Developments in Geotechnical Engineering, 83

Dynamic Soil-Structure Interaction

C. Zhang and J.P. Wolf
(Editors)

Elsevier

Developments in Geotechnical Engineering, 83

Dynamic Soil-Structure Interaction

Developments in Geotechnical Engineering, 83

Dynamic Soil-Structure Interaction
Current Research in China and Switzerland

Edited by

Zhang Chuhan

Tsinghua University, Beijing, People's Republic of China

and

John P. Wolf

Swiss Federal Institute of Technology, Lausanne, Switserland

1998

ELSEVIER

Amsterdam — Lausanne — New York — Oxford — Shannon — Singapore — Tokyo

ELSEVIER SCIENCE B.V.
Sara Burgerhartstraat 25
P.O. Box 211, 1000 AE Amsterdam, The Netherlands

Library of Congress Cataloging in Publication Data:

Dynamic soil-structure interaction : current research in China and
Switzerland / edited by Zhang Chuhan and John P. Wolf.
p. cm. -- (Developments in geotechnical engineering ; 83)
Proceedings of the Chinese-Swiss Workshop on Soil-Structure
Interaction, held July 14-18, 1997, at Tsinghua University, Beijing.
Includes bibliographical references and index.
ISBN 0-444-50035-9 (alk. paper)
1. Soil-structure interaction--Congresses. 2. Soil-structure
interaction--Research--China--Congresses. 3. Soil-structure
interaction--Research--Switzerland--Congresses. I. Zhang, Chuhan.
II. Wolf, John P. III. Chinese-Swiss Workshop on Soil-Structure
Interaction (1997 : Beijing, China) IV. Series.
TA711.5.D96 1998
624.1'5136--dc21 98-29711
CIP

ISBN: 0-444-50035-9

♾ The paper used in this publication meets the requirements of ANSI/NISO Z39.48-1992 (Permanence of Paper).

Printed in The Netherlands

Further titles in this series:
Volumes 2, 3, 5-7, 9, 10, 12, 13, 15, 16A, 22 and 26 are out of print

1. G. SANGLERAT – THE PENETROMETER AND SOIL EXPLORATION
4. R. SILVESTER – COASTAL ENGINEERING. 1 AND 2
8. L.N. PERSEN – ROCK DYNAMICS AND GEOPHYSICAL EXPLORATION
   Introduction to Stress Waves in Rocks
11. H.K. GUPTA AND B.K. RASTOGI – DAMS AND EARTHQUAKES
14. B. VOIGHT (Editor) – ROCKSLIDES AND AVALANCHES. 1 and 2
17. A.P.S. SELVADURAI – ELASTIC ANALYSIS OF SOIL-FOUNDATION INTERACTION
18. J. FEDA – STRESS IN SUBSOIL AND METHODS OF FINAL SETTLEMENT CALCULATION
19. Á. KÉZDI – STABILIZED EARTH ROADS
20. E.W. BRAND AND R.P. BRENNER (Editors) – SOFT-CLAY ENGINEERING
21. A. MYSLIVE AND Z. KYSELA – THE BEARING CAPACITY OF BUILDING FOUNDATIONS
23. P. BRUUN – STABILITY OF TIDAL INLETS – Theory and Engineering
24. Z. BAŽANT – METHODS OF FOUNDATION ENGINEERING
25. Á. KÉZDI – SOIL PHYSICS - Selected Topics
27. D. STEPHENSON – ROCKFILL IN HYDRAULIC ENGINEERING
28. P.E. FRIVIK, N. JANBU, R. SAETERSDAL AND L.I. FINBORUD (Editors) –
    GROUND FREEZING 1980
29. P. PETER – CANAL AND RIVER LEVÉES
30. J. FEDA – MECHANICS OF PARTICULATE MATERIALS - The Principles
31. Q. ZÁRUBA AND V. MENCL – LANDSLIDES AND THEIR CONTROL
    Second completely revised edition
32. I.W. FARMER (Editor) – STRATA MECHANICS
33. L. HOBST AND J. ZAJÍC – ANCHORING IN ROCK AND SOIL
    Second completely revised edition
34. G. SANGLERAT, G. OLIVARI AND B. CAMBOU – PRACTICAL PROBLEMS IN SOIL
    MECHANICS AND FOUNDATION ENGINEERING, 1 and 2
35. L. RÉTHÁTI – GROUNDWATER IN CIVIL ENGINEERING
36. S.S. VYALOV – RHEOLOGICAL FUNDAMENTALS OF SOIL MECHANICS
37. P. BRUUN (Editor) – DESIGN AND CONSTRUCTION OF MOUNDS FOR BREAKWATER
    AND COASTAL PROTECTION
38. W.F. CHEN AND G.Y. BALADI – SOIL PLASTICITY - Theory and Implementation
39. E.T. HANRAHAN – THE GEOTECTONICS OF REAL MATERIALS: THE $\varepsilon_g\varepsilon_k$ METHOD
40. J. ALDORF AND K. EXNER – MINE OPENINGS - Stability and Support
41. J.E. GILLOT – CLAY IN ENGINEERING GEOLOGY
42. A.S. CAKMAK (Editor) – SOIL DYNAMICS AND LIQUEFACTION
43. A.S. CAKMAK (Editor) – SOIL-STRUCTURE INTERACTION
44. A.S. CAKMAK (Editor) – GROUND MOTION AND ENGINEERING SEISMOLOGY
45. A.S. CAKMAK (Editor) – STRUCTURES, UNDERGROUND STRUCTURES, DAMS, AND
    STOCHASTIC METHODS
46. L. RÉTHÁTI – PROBABILISTIC SOLUTIONS IN GEOTECTONICS
47. B.M. DAS – THEORETICAL FOUNDATION ENGINEERING
48. W. DERSKI, R. IZBICKI, I. KISIEL AND Z. MROZ – ROCK AND SOIL MECHANICS
49. T. ARIMAN, M. HAMADA, A.C. SINGHAL, M.A. HAROUN AND A.S. CAKMAK (Editors) –
    RECENT ADVANCES IN LIFELINE EARTHQUAKE ENGINEERING
50. B.M. DAS – EARTH ANCHORS
51. K. THIEL – ROCK MECHANICS IN HYDROENGINEERING
52. W.F. CHEN AND X.L. LIU – LIMIT ANALYSIS IN SOIL MECHANICS
53. W.F. CHEN AND E. MIZUNO – NONLINEAR ANALYSIS IN SOIL MECHANICS

54. F.H. CHEN – FOUNDATIONS ON EXPANSIVE SOILS
55. J. VERFEL – ROCK GROUTING AND DIAPHRAGM WALL CONSTRUCTION
56. B.N. WHITTAKER AND D.J. REDDISH – SUBSIDENCE – Occurrence, Prediction and Control
57. E. NONVEILLER – GROUTING, THEORY AND PRACTICE
58. V. KOLÁŘ AND I. NĚMEC – MODELLING OF SOIL-STRUCTURE INTERACTION
59A. R.S. SINHA (Editor) – UNDERGROUND STRUCTURES – Design and Instrumentation
59B. R.S. SINHA (Editor) – UNDERGROUND STRUCTURES – Design and Construction
60. R.L. HARLAN, K.E. KOLM AND E.D. GUTENTAG – WATER-WELL DESIGN AND CONSTRUCTION
61. I. KASDA – FINITE ELEMENT TECHNIQUES IN GROUNDWATER FLOW STUDIES
62. L. FIALOVSZKY (Editor) – SURVEYING INSTRUMENTS AND THEIR OPERATION PRINCIPLES
63. H. GIL – THE THEORY OF STRATA MECHANICS
64. H.K. GUPTA – RESERVOIR-INDUCED EARTHQUAKES
65. V.J. LUNARDINI – HEAT TRANSFER WITH FREEZING AND THAWING
66. T.S. NAGARAI – PRINCIPLES OF TESTING SOILS, ROCKS AND CONCRETE
67. E. JUHÁSOVÁ – SEISMIC EFFECTS ON STRUCTURES
68. J. FEDA – CREEP OF SOILS – and Related Phenomena
69. E. DULÁCSKA – SOIL SETTLEMENT EFFECTS ON BUILDINGS
70. D. MILOVIĆ – STRESSES AND DISPLACEMENTS FOR SHALLOW FOUNDATIONS
71. B.N. WHITTAKER, R.N. SINGH AND G. SUN – ROCK FRACTURE MECHANICS – Principles, Design and Applications
72. M.A. MAHTAB AND P. GRASSO – GEOMECHANICS PRINCIPLES IN THE DESIGN OF TUNNELS AND CAVERNS IN ROCK
73. R.N. YONG, A.M.O. MOHAMED AND B.P. WARKENTIN – PRINCIPLES OF CONTAMINANT TRANSPORT IN SOILS
74. H. BURGER (Editor) – OPTIONS FOR TUNNELING 1993
75. S. HANSBO – FOUNDATION ENGINEERING
76. R. PUSCH – WASTE DISPOSAL IN ROCK
77. R. PUSCH – ROCK MECHANICS ON A GEOLOGICAL BASE
78. T. SAWARAGI – COASTAL ENGINEERING - WAVES, BEACHES, WAVE-STRUCTURE INTERACTIONS
79. O. STEPHANSSON, L. JING AND CHIN-FU TSANG (Editors) – COUPLED THERMO-HYDRO- MECHANICAL PROCESSES OF FRACTURED MEDIA
80. J. HARTLÉN AND W. WOLSKI (EDITORS) – EMBANKMENTS ON ORGANIC SOILS
81. Y. KANAORI (EDITOR) – EARTHQUAKE PROOF DESIGN AND ACTIVE FAULTS
82. A.M.O. MOHAMED AND H.E. ANTIA - GEOENVIRONMENTAL ENGINEERING

PREFACE

During the last several decades, seismic soil-structure interaction has been a major topic in earthquake engineering since it is closely related to the safety evaluation of many important engineering projects, such as nuclear power plants, to resist earthquakes. The significance of the interaction has long been recognized because of the massive and stiff nature of the structure and, often, soil softness. In recent years the importance of dynamic soil-structure interaction to earthquake behaviors of high arch dams has also been realized, since the effects of energy radiation through the infinite canyon and the non-uniform ground motions on the dam response may be significant. Nuclear power plants and high arch dams are only two examples for which dynamic soil-structure interaction is important and needs to be seriously considered in engineering practice.

In dealing with the analysis of dynamic soil-structure interactions, one of the most difficult tasks is the modelling of unbounded media. Many numerical methods or techniques have been developed to solve this problem, such as transmitting boundaries of different kinds, boundary elements, and infinite elements and their coupling procedures. It is noteworthy that the two recently published books, Finite Element Modelling of Unbounded Media by John P. Wolf and Chongmin Song and Foundation Vibration Analysis Using Simple Physical Models by John P. Wolf, are considered important developments in this aspect. Significant contributions have also been made on the Chinese side in recent years. These include a time domain transmitting boundary developed by Z. P. Liao and his co-workers and a 3-D infinite boundary element for modelling arch dam canyons developed by Zhang Chuhan and his colleagues. In addition, many engineering applications using advanced procedures are also being conducted both in China and Switzerland.

To exchange the current developments, the Chinese-Swiss Workshop on Soil-Structure Interaction was held during July 14-18, 1997 at Tsinghua University, Beijing, China. The idea of the workshop was initiated by John P. Wolf in Spring 1996. Many specific issues were settled in June 1996 by Zhang and Wolf in Acapulco, Mexico, during the 11WCEE. A Planning Committee co-chaired by Zhang and Wolf was then established. As part of the preparation, the above-mentioned two books were provided by the Swiss side to the Chinese participants before the workshop.

Twenty-three participants from China and Switzerland attended the workshop, and 18 presentations were given. Two presentation series were given by the Swiss scientists summarizing the advanced procedure of modelling unbounded media by the scaled boundary finite-element method and the simple physical methods for practical analysis of soil-structure interaction. Sixteen presentations were given by the Chinese scientists covering a rather wide range of the latest achievements of research in China.

The workshop consisted of nine half-day sessions, with one afternoon set aside for local sightseeing. Each session had 2-3 presentations, each followed by a 30-minute discussion. Due to the generous allotment of time and small number of participants, the discussions were rather thorough and lively. Before the closing ceremony, the final session was devoted to a panel meeting, in which urgent research needs and some benchmark examples were discussed.

As the final achievement of the workshop, we now publish these proceedings, It is hoped that the research and applications of dynamic soil-structure interaction will continue to progress, and the academic cooperation between the scientists from our two countries in this field will further advance.

Finally, we would like to express our thanks to the Swiss Federal Institute of Technology Lausanne; the Department of Sciences and Technology, the Ministry of Water Conservancy of China; the National Key Projects on Basic Research and Applied Research, State Commission of Sciences and Technology of China; and the National Science Foundation of China for their financial support for this workshop.

Zhang Chuhan
John P. Wolf

LIST OF PLANNING COMMITTEE

Co-chairmen: Prof. Zhang, Chuhan Dr. Wolf, John P.

Members:

Prof. Chen, Houqun
Prof. Liao, Zhenpeng
Prof. Xu, Zhixin
Dr. Yao, Zhenhan
Prof. Dong, Zheren
Prof. Chen, Shihui
Dr. Sarlos, Gerard
Prof. Lin, Gao
Dr. Wu, Shiming
Dr. Song, Chongmin
Dr. Liu, Xila
Prof. Wang, Guanglun

Secretary: Dr. Jin, Feng

LIST OF PARTICIPANTS

Bie Shean	Dept. of Hydraulic Engineering, Tsinghua University
Chen Houqun	China Institute of Water Resources and Hydropower Research
Chen Jianyun	Dept. of Civil Engineering, Dalian University of Technology
Ding Boyang	Lanzhou Earthquake Research Institute
Jin Feng	Dept. of Hydraulic Engineering, Tsinghua University
Liao Zhenpeng	Institute of Engineering Mechanics, State Seismological Bureau
Lin Gao	Dept. of Civil Engineering, Dalian University of Technology
Liu Jingbo	Dept. of Civil Engineering, Tsinghua University
Lou Menglin	Institute of Structural Theory, Tongji University
Qiu Zonglian	Dept. of Civil Engineering, Tsinghua University
Shao Xiumin	Institute of Mathematics, China Academy of Sciences
Song Chongmin	Dept. of Civil Engineering, Swiss Federal Institute of Technology
Song Erxiang	Dept. of Civil Engineering, Tsinghua University
Wang Guanglun	Dept. of Hydraulic Engineering, Tsinghua University
Wolf John P.	Dept. of Civil Engineering, Swiss Federal Institute of Technology
Wu Shiming	Dept. of Civil Engineering, Zhejiang University
Xiong Jianguo	Institute of Engineering Mechanics, State Seismological Bureau
Xu Zhixin	Institute of Structural Theory, Tongji University
Yao Zhenhan	Dept. of Engineering Mechanics, Tsinghua University
Yuan Xiaoming	Institute of Engineering Mechanics, State Seismological Bureau
Zhang Chuhan	Dept. of Hydraulic Engineering, Tsinghua University
Zhao Chongbin	CSIRO Division of Exploration and Mining, Australia
Zhou Xiyuan	China Academy of Building Research

CONTENTS

SIMPLE PHYSICAL MODELS FOR FOUNDATION DYNAMICS

JOHN P. WOLF
(Institute of Hydraulics and Energy, Department of Civil
Engineering, Swiss Federal Institute of Technology Lausanne,
CH-1015 Lausanne, Switzerland)

Abstract

As an alternative to rigorous boundary-element solutions, simple physical models can be used to determine e.g. the interaction force-displacement relationship (dynamic stiffness) of foundations and the seismic effective foundation input motion. Translational and rotational cones and their corresponding lumped-parameter models (spring-dashpot-mass models) together with simple one-dimensional wave patterns in the horizontal plane allow surface, embedded and pile foundations even for a layered site to be analyzed and thus form a major step towards developing a strength-of-materials approach to foundation-vibration analysis. The analysis can mostly be performed directly in the time domain. The physical models provide physical insight which is often obscured by the mathematical complexity of rigorous solutions, offer simplicity in application as well as in the physics and in the rigorous mathematical solution of the physical model, are sufficiently general to enable reasonably complicated practical cases to be solved, exhibit adequate accuracy, allow physical features to be demonstrated and offer the potential for generalizations.

Introduction

A key aspect of any foundation vibration or dynamic soil-structure interaction analysis is the calculation of the interaction force-displacement relationship (dynamic stiffness) on the basemat-soil interface. To discuss the concepts, a specific case is addressed (Fig. 1): the vertical degree of freedom with the force P_0 and displacement u_0 of a rigid, massless disk of radius r_0 on a soil layer of depth d resting on a flexible rock halfspace. G represents the shear modulus, ν Poisson's ratio and ρ the mass density, from which the dilatational wave velocity c_p follows. Indices L and R are introduced to identify constants associated with the layer and the rock respectively.

To determine the P_0-u_0 relationship, *rigorous methods* exist: either the region of the layer and part of the halfspace are modeled with axisymmetric finite elements and sophisticated *consistent transmitting boundaries* are introduced to represent wave propagation towards infinity or the *boundary-element method* is applied whereby the free surface and the interface between the layer and the halfspace must be discretized when the fundamental solution of the full space is used. In these rigorous methods a formidable theoretical background is required. A considerable amount of expertise in idealizing the actual dynamic system is necessary [8], and a significant amount of data preparation has to be performed. The computational expense for just one run is large, making it difficult from an economical point of view to perform the necessary parametric studies. A false sense of security could thus be provided to the user. The engineer tends to be intimidated by these procedures. The effort to interpret the results is also significant. These rigorous methods with their mathematical complexity obscure the physical insight and belong more to the discipline of applied computational mechanics than to civil engineering. They should only be used for large projects of critical facilities such as nuclear-power plants, bunkered military constructions, dams, etc. with the corresponding budget and available time to perform the analysis. For all other projects, the most majority, the *simple physical models to represent the unbounded soil* summarized in this paper should be used.

For instance, the soil below the disk is modeled as a truncated rod (bar) with its area varying as in a *cone* (Fig. 2). The vertical force $P_0(t)$ produces an incident dilatational wave propagating with the velocity c_p^L (for $\upsilon_L \leq 1/3$) along a cone (with Apex 1) with mass density ρ_L and a specific opening angle determined by z_0^L downwards from the disk. At the beginning of the excitation before the wave reaches the soil-rock interface, the wave pattern in the layer will be the same as that occurring in a halfspace. The corresponding displacement in the truncated semi-infinite cone is inversely proportional to the distance from apex 1

$$u(z,t) = \frac{z_0^L}{z_0^L + z} f\left(t - \frac{z}{c_p^L}\right) \tag{1}$$

with z measured from the free surface. Apex 1 is specified in such a way as to yield the same static-stiffness coefficients for the truncated semi-infinite cone $\rho\left(c_p^L\right)^2 \pi r_0^2 / z_0^L$ and the disk on a homogeneous halfspace with the material properties of the layer $4G_L r_0/(1-v_L)$, yielding

$$\frac{z_0^L}{r_0} = \frac{\pi}{2} \frac{(1-\upsilon_L)^2}{1-2\upsilon_L} \tag{2}$$

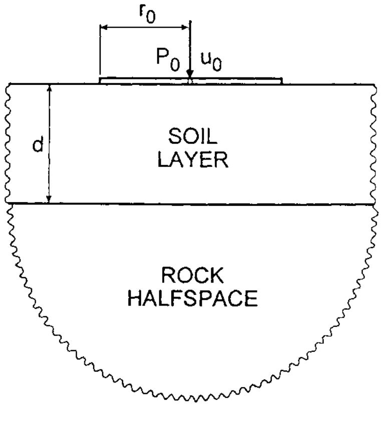

Fig. 1 Vertical motion of disk on surface layer resting on flexible rock halfspace.

At the interface of the layer and the rock (z=d) the incident wave f will lead to a refracted wave h propagating in the rock in the same direction as the incident wave along its own cone with the apex distance-to-radius ratio $z_0^R / \left(r_0\left(z_0^L + d\right) / z_0^L\right)$ (apex 2, dotted line). (Note that the aspect ratio of the rock's cone is generally different from that of the layer's cone. However, in the special case $\upsilon_R=\upsilon_L$, both cones have the same proportions and z_0^R equals $z_0^L + d$). The displacement in the rock $u_R(z,t)$ is formulated as

$$u_R(z,t) = \frac{\dfrac{z_0^L z_0^R}{z_0^L + d}}{z_0^R - d + z} h\left(t - \frac{d}{c_p^L} + \frac{d}{c_p^R} - \frac{z}{c_p^R}\right) \tag{3}$$

with the numerator chosen for convenience. In addition, a reflected wave g is created propagating back through the layer along the indicated cone (apex 3) in the opposite upward direction. The resulting displacement in the layer $u_L(z,t)$ then equals

$$u_L(z,t) = \frac{z_0^L}{z_0^L + z} f\left(t - \frac{z}{c_p^L}\right) + \frac{z_0^L}{z_0^L + 2d - z} g\left(t - \frac{2d}{c_p^L} + \frac{z}{c_p^L}\right) \tag{4}$$

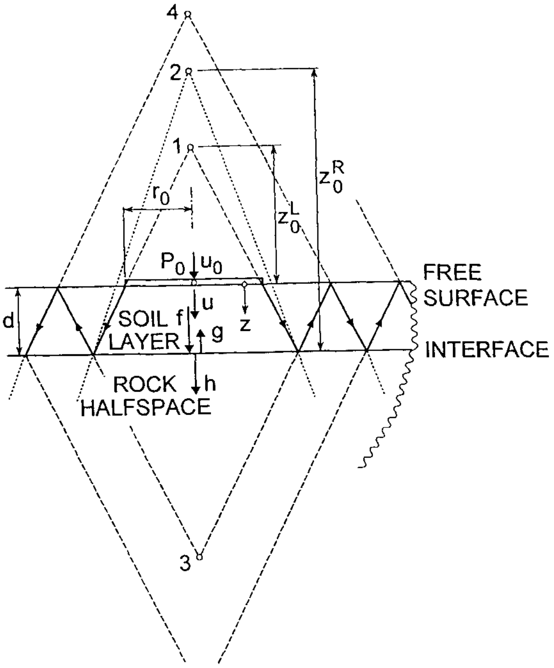

Fig. 2 Wave patterns of corresponding cones in soil layer and rock halfspace.

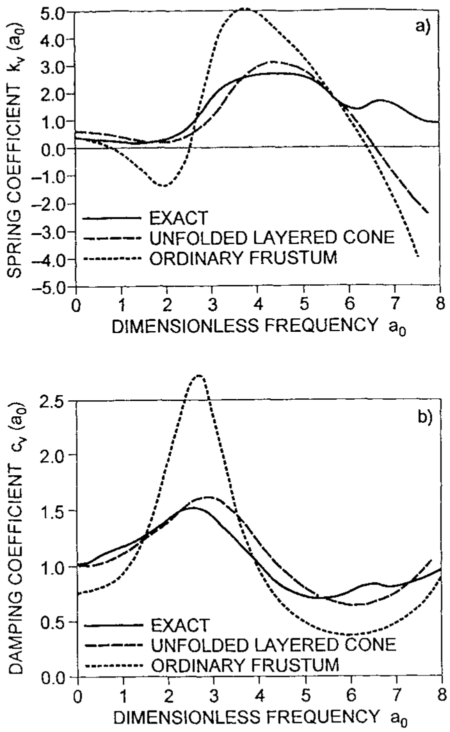

Fig. 3 Vertical dynamic-stiffness coefficient for disk on soil layer stiffer than rock halfspace.

Notice that the denominators in Eqs. 3 and 4 are the distances to the apexes of the respective cones. At the interface z=d the arguments of the three functions f, g and h are the same, $t - d / c_p^L$. The upwave g will reflect back at the free surface and then propagate downwards along the cone (apex 4) shown in Fig. 2. Upon reaching the interface of the layer and the rock, a refraction and a reflection again take place, etc. The reflection coefficient $-\alpha$, defined as the ratio of the reflected wave g to the incident wave f, is determined by formulating compatibility and equilibrium at the interface. From a practical point of view sufficient accuracy results from using the high-frequency limit which corresponds to replacing the cone by a prismatic bar.

$$-\alpha = \frac{\rho_L c_p^L - \rho_R c_p^R}{\rho_L c_p^L + \rho_R c_p^R} \tag{5}$$

The resulting displacement in the layer $u_L(t,z)$ is equal to the superposition of the contributions of all cones; i.e. the displacements of the incident wave and of all subsequent upwaves and downwaves are summed. Denoting the incident wave at z=0 as $\bar{u}_0(t)(=f(t))$ the displacement $u_L(z,t)$ of the layer at depth z and time t may be expressed as the wave pattern

$$\begin{aligned} &\qquad\qquad\text{incident wave} \\ &u_L(z,t) = \frac{z_0^L}{z_0^L + z}\bar{u}_0\left(t - \frac{z}{c_p^L}\right) \\ &\qquad\text{upwave from rock} \qquad\qquad \text{downwave from surface} \\ &+\sum_{j=1}^{k}(-\alpha)^j\left[\frac{z_0^L\bar{u}_0\left(t - \frac{2jd}{c_p^L} + \frac{z}{c_p^L}\right)}{z_0^L + 2jd - z} + \frac{z_0^L\bar{u}_0\left(t - \frac{2jd}{c_p^L} - \frac{z}{c_p^L}\right)}{z_0^L + 2jd + z}\right] \end{aligned} \tag{6}$$

The integer k is equal to the largest j for which at least one of the arguments of $\bar{u}_0$ for a specific z and t is positive.

The cones describing the wave propagation in the layer can be unfolded to form a single layered cone. This generalized *unfolded layered cone* represents a wave pattern whose amplitude decays with distance, that considers the reflections at the free surface and the reflections and refractions at the layer-rock interface and that spreads resulting in radiation of energy in the horizontal direction. Through the choice of the cone as a physical model, the complicated three-dimensional wave pattern with body and surface waves and three different velocities is replaced by the simple one-dimensional wave propagation governed by the one constant dilatational wave velocity of the conical rod, whereby *plane sections remain plane* (theory of strength of materials). Only the (one) unknown u_0 needs to be introduced.

As an example, the vertical dynamic-stiffness coefficient for harmonic loading of the disk on the soil layer-rock halfspace based on the refolded layered cone equals [45]

$$S(\omega) = K \frac{1 + i\dfrac{\omega T}{\kappa}}{1 + 2\sum\limits_{j=1}^{\infty}(-\alpha)^{j}\dfrac{e^{-ij\omega T}}{1 + j\kappa}} \tag{7}$$

where $K=4G_L r_0/(1-\nu_L)$ denotes the static-stiffness coefficient of the disk on a homogeneous halfspace with the properties of the layer, $T=2d/c_p^L$ and $\kappa=2d/z_0^L$. The numerator is equal to the dynamic-stiffness coefficient of the truncated semi-infinite cone modeling the halfspace which is multiplied by the transfer function $\bar{u}_0(\omega)/u_0(\omega)$ determined from Eq. 6 which introduces the reflections of the layered system. Equation 7 represents a compact expression with a clear physical interpretation.

To check the accuracy, the case of a stiffer and denser layer than the halfspace is examined. This situation can occur for a new sand fill over soft alluvial virgin soil. It is typical for some sea coast areas. The ratios $d/r_0=1$, $G_L/G_R=5$, $\rho_L/\rho_R=1.25$ and $\nu_L=\nu_R=1/3$ are selected, resulting in an impedance ratio $\rho_L c_L/(\rho_R c_R)=2.5$. The apex ratio for the vertical motion equals $z_0^L/r_0=2.094$ (Eq. 2) and the reflection coefficient $-\alpha=+3/7$ (Eq. 5). In this case $z_0^R = z_0^L+d$. The non-dimensionalized vertical dynamic-stiffness coefficient $S(\omega)/K$ (Eq. 7) is decomposed as $k_v(a_0)+ia_0\, c_v(a_0)$ with $a_0=\omega r_0/c_s^L$ (shear-wave velocity c_s). The spring and damping coefficients $k_v(a_0)$, $c_v(a_0)$ of the unfolded layered cone agree well with the rigorous result using the consistent-boundary formulation [38] denoted as exact in Fig. 3.

To capture the horizontal radiation of energy through a layer with cones, the sum in Eq. 7 must be evaluated up to a large j. The sum may be avoided if the layer is idealized by an ordinary non-radiating cone frustum (finite element of a tapered bar) with vertical dynamic-stiffness coefficients (index 1 for top ($r_1=r_0$), index 2 for bottom [25])

$$S_{11}(\omega) = \rho\left(c_p^L\right)^2 \pi r_1^2 \left[\frac{1}{z_0^L} + \frac{1}{d}\frac{\omega d/c_p^L}{\tan\left(\omega d/c_p^L\right)}\right] \tag{8a}$$

$$S_{12}(\omega) = S_{21}(\omega) = -\rho\left(c_p^L\right)^2 \pi r_1^2 \left[\frac{z_0^L + d}{z_0^L d}\frac{\omega d/c_p^L}{\sin\left(\omega d/c_p^L\right)}\right] \tag{8b}$$

$$S_{22}(\omega) = \rho\left(c_p^L\right)^2 \pi r_1^2 \left[\left(\frac{z_0^L + d}{z_0^L}\right)^2 \frac{1}{d}\frac{\omega d/c_p^L}{\tan\left(\omega d/c_p^L\right)} - \frac{z_0^L + d}{\left(z_0^L\right)^2}\right] \tag{8c}$$

In this ordinary frustum, waves reflected at the layer-rock interface cannot spread and radiate energy horizontally as they propagate back upwards. Instead, they are focused in the narrowing neck of the frustum. This disadvantage makes the ordinary frustum used to model the soil layer whose dynamic-stiffness matrix (Eq. 8) can be assembled with the dynamic-stiffness coefficient of the cone representing the rock halfspace to calculate the layered system clearly inferior (Fig. 3). The spring and damping coefficients of the ordinary frustum oscillate more than they should.

The simple physical models such as the unfolded layered cone easily fit the size and economics of a project, and no sophisticated computer code needs to be available. Use of these procedures leads to some loss of precision, which is more than compensated for by their many advantages. It cannot be the aim of the engineer to calculate the complex reality as closely as possible. For a well balanced design which is both safe and economical rigorous results are not called for in a standard project. Their accuracy is anyhow limited because of the many uncertainties (for instance in defining the soil profile), some of which can never be eliminated.

As the simple physical models cannot cover all cases, they do not supplant the more generally applicable rigorous boundary-element method, but rather supplement it. It should also be stressed that an improved understanding can be gained from the results of a rigorous analysis, which should thus be developed to enable progress. As experience increases, the key aspects of the behavior can be identified. This then leads to the development of simplified procedures which, however, still capture the salient features of the phenomenon. These physical models for soil dynamics are not the first attempt to capture the physics which has not been properly evaluated yet. On the contrary they make full use of the experience gained from the rigorous state-of-the-art formulations. The physical models are thus not only simple to use and lead to valuable physical insight, but they are also quite dependable incorporating implicitly much more know-how than meets the eye.

As described by Roesset in the foreword covering the early work on simple models of [50], the same researchers engaged in the derivation of rigorous procedures based on elasto-dynamics have at the same time tried to explain their results with simple models. These attempts dating back to the thirties were not always successful. Summaries, written by Roesset [29, 30], who contributed significantly to the advancement of the state of the art, influenced the development significantly. A brief historical review with a classification of the methods concentrating on certain key aspects influenced by the preferences of the author follows. For a more complete evaluation of the rich tradition the reader is referred to the literature mentioned in the references of this paragraph. The first group to calculate the interaction force-displacement relationship of a foundation on the surface of a halfspace consists of *truncated semi-infinite cones* introduced by Ehlers [5] for translational motion and much later by Meek and Veletsos [15] for rotational motion. An application to the torsional motion is described in Veletsos and Nair [35]. Wedges for plane-strain conditions are examined by Gazetas and Dobry [7]. It is important to stress that in a practical application the (one dimensional) wave propagation does not have to be addressed as the dynamic stiffness of the semi-infinite cone is exactly equal to that of a simple discrete-element model consisting of a spring and a dashpot (for rotation also of a mass moment of inertia with its own internal degree of freedom) with frequency-independent coefficients. Based on this arrangement the coefficients of the discrete elements are determined not from the cone model - but as an extension - from calibration with rigorous solutions of elasto-dynamics. This permits not only material damping to be considered (Veletsos and Nair [36]), but allows generalizations to embedded and inhomogeneous sites (Wolf and Somaini [40]) whereby also an additional discrete-element (a spring) can be introduced (de Barros and Luco [2]). In this second group, the *lumped-parameter models*, the early single-degree-of-freedom systems determined in an ad-hoc manner (Whitman [39], Richart, Hall and Woods [28]) are also included. Starting from the discrete-element model of the rotational cone, a family of lumped-parameter models also called *spring-dashpot-mass models* can be constructed systematically for any dynamic-stiffness coefficient (Wolf [41]). In the third group, *wave patterns in the horizontal plane* are prescribed. Dobry and Gazetas [4] assume simple cylindrical waves to calculate dynamic-interaction factors which permit a pile group to be analysed considering dynamic pile-soil-pile interaction. Finally, the fourth group consists of calibration procedures to determine *approximate expressions for the dynamic-stiffness coefficients in the frequency domain* and the static-stiffness coefficients for a wide range of foundations (Gazetas [9], [11], Pais and Kausel [27]), in many cases also being guided by the dynamic-stiffness coefficient of the rotational cone.

This paper concentrates on summarizing the research and development performed in an informal, enthusiastic, and collegial atmosphere from 1990 to 1994 with Dr. J.W. Meek. His role as leader and his significant contributions in generalizing the concept of cones (group 1 [18, 22]) and the wave pattern in the horizontal plane (group 3 [21]) are acknowledged. In addition, the extension of the systematic formulation to construct consistent lumped-parameter models (group 2 [42, 44]) is addressed. For details the reader can consult the references cited above or the book [50] which contains easy-to-follow derivations, many examples and engineering applications.

Concepts, Classification and Examples

Applications

The simple models to be summarized can be used in the majority of cases for the final dynamic analyses of foundation vibration and soil-structure interaction. In addition, the following considerations are appropriate. In certain cases, the effect of the interaction of the soil and the structure on the response of the latter will be negligible and need thus not be considered. This applies, for example, to a flexible high structure with small mass where the influence of the higher modes (which are actually affected significantly by soil-structure interaction) on the seismic response remains small. It is then possible to excite the base of the structure with the prescribed earthquake motion. For loads applied directly to the structure, the soil can in this case be represented by a static spring or the structure can even be regarded as built-in. In other cases, which include many everyday building structures, ignoring the interaction analysis can lead to an overly conservative design. It should be remembered that seismic-design provisions [26] allow for a significant *reduction* of the equivalent static lateral force (up to 30%) *for soil-structure interaction effects*. For these two categories, to determine if a dynamic interaction analysis is meaningful or not and to calculate the reduction in the response of everyday structures, i.e. to perform the actual dynamic analysis, physical models are well suited. They are also appropriate to help the analyst to identify the key parameters of the dynamic system, for preliminary design, to investigate alternative designs, to perform parametric studies varying the parameters with large uncertainties such as the soil properties or the contact conditions on the structure-soil interface. Finally, simple models are used to check the results of more rigorous procedures determined with sophisticated computer codes.

Overview

To construct a physical model, physical approximations are introduced for the cone models and the assumed wave patterns in the horizontal plane, which at the same time simplify the mathematical formulation. The latter can then be solved rigorously, in general in closed form. These assumptions of mechanics permit a much better evaluation of the consequences than when mathematical approximations are introduced, such as e.g. neglecting certain higher-order derivatives in the differential equations of the rigorous formulation. For the lumped-parameter models, which for more complicated cases does involve curve fitting, a visual check of the accuracy is possible by comparing the dynamic-stiffness coefficients of the rigorous procedure and the physical model.

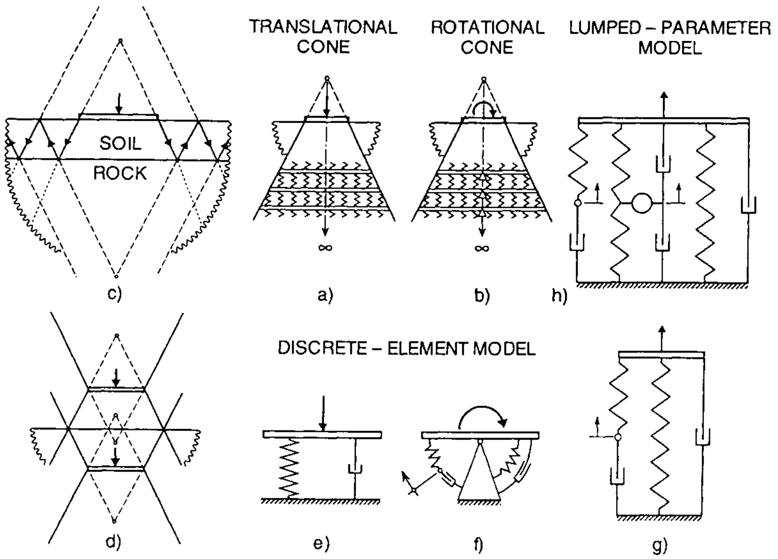

Fig. 4 Physical models to represent dynamic stiffness.

a) Disk on surface of halfspace with truncated semi-infinite translational cone
b) Disk on surface of halfspace with truncated semi-infinite rotational cone.
c) Disk on surface of soil layer resting on flexible rock halfspace with corresponding cones.
d) Anti-symmetry condition with respect to free surface for disk and mirror-image disk with corresponding double cones to calculate Green's function.
e) Discrete-element model for translational cone.
f) Discrete-element model for rotational cone.
g) Lumped-parameter model consisting of springs and dashpots with one internal degree of freedom corresponding to f.
h) Lumped-parameter model consisting of springs, dashpots and a mass with two internal degrees of freedom.

An overview of the physical models to calculate the interaction force-displacement relationship (dynamic stiffness) of the unbounded soil and the effective foundation input motion for seismic excitation is presented.

A summary of the key expressions used to model the various foundations is specified in the Appendix.

The simplest case consists of a rigid massless circular *basemat*, called disk in the following, resting *on the surface of a homogeneous soil halfspace*. A translational degree of freedom, e.g. the vertical motion, is examined (Fig. 4a). To determine the interaction force-displacement relationship of the disk and thus its dynamic stiffness, the disk's displacement (as a function of time) is prescribed and the corresponding interaction force, the load acting on the disk (as a function of time), is calculated. The halfspace below the disk is modeled as a *truncated semi-infinite rod (bar) with its area varying as in a cone* with the same material properties. A load applied to the disk on the free surface of a halfspace leads to stresses, due to geometric spreading, acting on an area that increases with depth, which is also the case for the translational cone. As already mentioned, by equating the static stiffness of the *translational cone* to that of the disk on a halfspace, the cone's opening angle is calculated. It turns out that the opening angle for a given degree of freedom depends only on Poisson's ratio of the soil. Through the choice of the physical model, the complicated three-dimensional wave pattern of the halfspace with body and surface waves and three different velocities is replaced by the simple one-dimensional wave propagation governed by the one constant dilatational-wave velocity of the conical rod, whereby plane cross-sections remain plane. The radiation condition (outwardly propagating waves only) is enforced straightforwardly by admitting waves traveling downwards only. For the horizontal motion a translational cone in shear with the shear-wave velocity is constructed analogously. For the rocking and torsional degrees of freedom, rotational cones can be identified using the same concepts (Fig. 4b).

The same cones can also be used to examine a *surface foundation* for a site consisting *of a soil layer resting on flexible rock halfspace*, as already discussed in the Introduction. The vertical degree of freedom is addressed in Fig. 4c using the corresponding translational cone. The same approach can be applied for the horizontal and rotational degrees of freedom. The vertical force applied to the disk produces dilatational waves propagating downwards from the disk. The opening angle of this cone follows again from equating the static stiffness of the truncated semi-infinite cone to that of the disk on a homogeneous halfspace with the material properties of the layer. At the interface of the soil layer and the rock halfspace the incident wave will lead to a refracted wave propagating in the rock in the same direction as the incident wave along its own cone (dotted lines). In addition, a reflected wave is created propagating back through the soil layer along the indicated cone (dashed lines) in the opposite upward direction. The latter will reflect back at the free surface and then propagate downwards along the cone shown in Fig. 4c. Upon reaching the interface of the layer and the rock, a refraction and a reflection again take place, etc. The waves in the layer thus decrease in amplitude and spread resulting in radiation of energy in the layer in the horizontal direction (in addition to the energy loss through the rock halfspace).

The concepts of cone models can be expanded to the analysis of *embedded cylindrical foundations*. Again, the vertical degree of freedom of a foundation embedded *in* a *halfspace* is addressed in Fig. 4d, but the following argumentation is just as valid for the horizontal, rocking or torsional ones. The embedded part is discretized with disks. To represent a disk within an elastic fullspace, a double-cone model is introduced. Its displacement field defines an approximate Green's function for use in an uncomplicated (one-dimensional) version of the boundary-element method. To enforce the stress-free condition at the free surface of the halfspace (Fig. 4d), a mirror-image disk (again modeled as a double cone) placed symmetrically (with respect to the free surface) and excited simultaneously by the same force is considered. Indeed, any halfspace problem amenable to a solution via cone models may also be solved in the fullspace. It is only necessary to augment the actual foundation in the lower halfspace by its mirror image in the upper halfspace. By exploiting principles of antisymmetry and superposition, the soil's flexibility matrix defined at the disks located within the embedded part of the foundation can be set up. The rest of the analysis follows via conventional matrix methods of structural analysis. The concept can be expanded to a fixed boundary and also to an interface with another halfspace. This permits *cylindrical foundations embedded in a soil layer resting on a rigid or flexible rock halfspace* to be calculated using cones. The methodology points towards a general *strength-of-materials approach to foundation dynamics* using the approximate *Green's functions of the double-cone models.*

A generalization is possible, enabling the dynamic-stiffness coefficients of a *foundation on the surface of or embedded in a layered halfspace* to be calculated. For each layer a dynamic-stiffness matrix based on cones is established. Assembling the dynamic-stiffness coefficients of the underlying halfspace and the dynamic-stiffness matrices of the layers yields that of the layered site.

Returning to the translational and rotational cones of Figs. 4a and b, it should be emphasized that in an actual soil-structure-interaction or foundation vibration analysis the cones are not represented physically by finite elements of a tapered rod. For practical applications it is not necessary to compute explicitly the displacements of the waves propagating along the cone. The attention can be restricted to the interaction force-displacement relationship at the disk. The translational cone's dynamic stiffness can rigorously be represented by the *discrete-element model* shown in Fig. 4e. It consists of a spring with the static stiffness (of the disk on a halfspace) in parallel with a dashpot with its coefficient determined as the product of the density, the dilatational-wave velocity (for the vertical degree of freedom) and the area of the disk. As the latter is equal to the disk on a halfspace's limit of the dynamic stiffness as the frequency approaches infinity, the cone's dynamic stiffness will be exact for the static case and for the limit of infinite frequencies (*doubly-asymptotic approximation*). For intermediate frequencies the cone is only an approximation of the disk on a halfspace. One rigorous representation of the rotational cone's dynamic stiffness is shown in Fig. 4f. The model again consists of a spring with the static stiffness in parallel with a dashpot with as coefficient the exact high-frequency limit of the dynamic stiffness (density times dilatational-wave velocity times disk's moment of inertia for the rocking degree of freedom). An additional internal degree of freedom is introduced, connected by a spring (with a coefficient equal to minus a third of the static-stiffness coefficient) to the footing and by a dashpot (with a coefficient equal to minus the high-frequency limit) to the rigid support. Again, the rotational cone's dynamic stiffness is doubly asymptotic. This is easily verified by noting that the internal degree of freedom of the discrete-element model is not activated in the two limits.

The model of Fig. 4f is shown for a translational degree of freedom in Fig. 4g, which forms the starting point to develop systematically a family of consistent *lumped-parameter models*, also called *spring-dashpot-mass models*. The direct spring is chosen to represent the static stiffness. The coefficients of the other spring and of the two dashpots are selected so as to achieve *an optimum fit* between the dynamic stiffness of the lumped-parameter model and the corresponding exact value (originally determined by a rigorous procedure such as the boundary-element method). If the direct dashpot is used to represent the high-frequency limit of the dynamic stiffness, the number of coefficients available for the optimum fit is reduced to two.

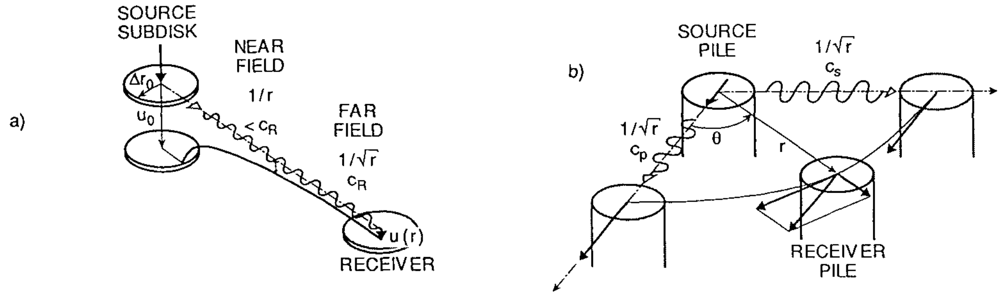

Fig. 5 Displacement patterns in horizontal plane.
a) Vertical displacement on free surface from loaded source subdisk.
b) Horizontal displacement from loaded source pile.

To increase the number of coefficients and thus the accuracy, several systems of Fig. 4g can be placed in parallel. Figure 4h shows the lumped-parameter model for three such systems, whereby two of them are combined to form a new system consisting of two springs, one independent dashpot (the two dashpots in series have the same coefficient) and a mass. A total of six coefficients keeping the doubly-asymptotic approximation thus results. It can be shown that these six frequency-independent coefficients, which can be determined using curve fitting applied to the dynamic stiffnesses (involving the solution of a linear system of equations only) will be real (but not necessarily positive). The *springs, dashpots and mass* will represent a *stable lumped-parameter model with only two additional internal degrees of freedom.* The fundamental lumped-parameter model of Fig. 4g is easy to interpret physically. This physical insight is, however, lost to a large extent in the model shown in Fig. 4h. But the latter does allow the analyst to model quite complicated cases, as will be demonstrated, such as a foundation embedded in a soil layer resting on rigid rock. Use is implicitly made of the results obtained with the state-of-the-art formulation which leads to the rigorous dynamic stiffnesses used in the optimum fit. By comparing visually the dynamic stiffness of the lumped-parameter model with the rigorous solution, the accuracy can be evaluated.

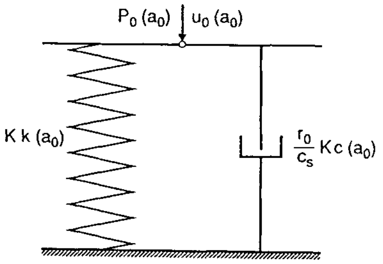

Fig. 6 Interpretation of dynamic-stiffness coefficient for harmonic excitation as spring and as dashpot in parallel with frequency-dependent coefficients.

As an example of an extension, spring-dashpot-mass models can also be constructed to determine the dynamic soil pressure acting on a vertical rigid wall retaining a semi-infinite uniform soil layer for horizontal seismic excitation.

Summarizing, two types of physical models are described in connection with Fig. 4: the translational and rotational cones [truncated semi-infinite single or double cones based on rod (bar) theory with the corresponding one-dimensional displacement and wave propagation] and the lumped-parameter models (spring-dashpot-mass models). The latter can conceptionally be constructed from the former by assembling the exact discrete-element models of the cones in parallel and using calibration with rigorous solutions.

The models shown in Fig. 4 prescribe a displacement pattern varying with depth along the axis of the cone. To extend the application, *displacement patterns in the horizontal plane* other than those corresponding to the strength-of-materials assumption of plane cross-sections remain plane are introduced as a third type of physical models in this text. One-dimensional wave propagation is again prescribed.

Two examples follow. For a vertical point load on the surface of an elastic halfspace the displacement in form of a Green's function may be deduced via non-mathematical physical reasoning, then calibrated with a few constants taken from a rigorous solution. By superposing point loads, an approximate *Green's function* is constructed for a subdisk of radius Δr_0 (Fig. 5a). In the near field the displacement amplitude is inversely proportional to the distance r from the center of the loaded source *subdisk* (body wave), and the wave propagates with a velocity which is slightly less than the Rayleigh-wave velocity c_R. In the far field the displacement amplitude decays inversely proportional to the square root of r (surface wave), and the wave propagates with c_R. Arbitrary shaped foundations can be treated as an assemblage of subdisks. The through-soil coupling of neighboring foundations can also be analyzed using subdisks.

To analyze a *pile group*, the *dynamic-interaction factor* describing the effect of the loaded source pile on the receiver pile is applied (Fig. 5b). To calculate the interaction factor e.g. for a horizontal motion of a source pile, it is assumed that dilatational waves propagating with the corresponding velocity c_p are generated in the direction of motion and shear waves propagating with the velocity c_s in the perpendicular direction. The amplitudes of both types of these cylindrical waves decay inversely proportional to the square root of the radius.

Examples

To illustrate the concepts of constructing physical models, some examples with selected results are presented, which also allow the accuracy to be evaluated.

Harmonic excitation with frequency ω is addressed. Complex-variable notation is used in the following. From the complex response $u(\omega)=\text{Re}u(\omega)+i\text{Im}u(\omega)$, the magnitude is calculated as $\sqrt{\text{Re}u^2(\omega)+\text{Im}u^2(\omega)}$ and the phase angle as arctan $[\text{Im}u(\omega)/\text{Re}u(\omega)]$. Applying a displacement with amplitude $u_0(\omega)$, the corresponding force amplitude $P_0(\omega)$ is formulated as

$$P_0(\omega)=S(\omega)u_0(\omega) \tag{9}$$

with the (complex) dynamic-stiffness coefficient $S(\omega)$. In foundation dynamics it is appropriate to introduce the dimensionless frequency a_0

$$a_0=\frac{\omega r_0}{c_s} \tag{10}$$

with r_0 representing a characteristic length of the foundation, for example, the radius of a disk, and c_s the shear-wave velocity. Using the static-stiffness coefficient K to nondimensionalize the dynamic-stiffness coefficient

$$S(a_0)=K[k(a_0)+ia_0c(a_0)] \tag{11}$$

is formulated. The spring coefficient $k(a_0)$ governs the force which is in phase with the displacement, and the damping coefficient $c(a_0)$ describes the force which is 90° out of phase. The dynamic-stiffness coefficient $S(a_0)$ can thus be interpreted as a spring with the frequency-dependent coefficient $Kk(a_0)$ and a dashpot in parallel with the frequency-dependent coefficient $(r_0/c_s)Kc(a_0)$ (Fig. 6).

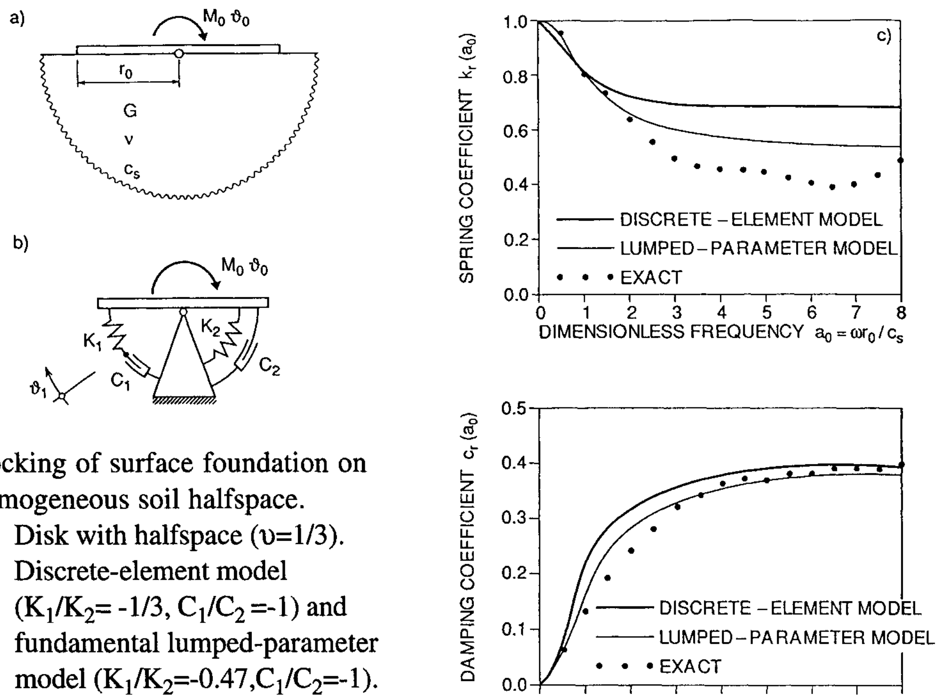

Fig. 7 Rocking of surface foundation on homogeneous soil halfspace.

a) Disk with halfspace (υ=1/3).

b) Discrete-element model (K_1/K_2= -1/3, C_1/C_2 =-1) and fundamental lumped-parameter model (K_1/K_2=-0.47,C_1/C_2=-1).

c) Dynamic-stiffness coefficient for harmonic excitation.

First, the rocking degree of freedom of a rigid disk with radius r_0 (Fig. 7a) resting on the surface of an undamped homogeneous soil halfspace with shear modulus G, Poisson's ratio υ and c_s is addressed. The rigorous result denoted as exact is specified in [32]. The discrete-element model representing exactly the rotational cone (which is a doubly-asymptotic approximation of the disk on a halfspace) is shown in Fig. 7b with $K_2 = 8Gr_0^3 / (3(1-\upsilon))$, $C_2 = \rho c_p \pi r_0^4 / 4$ (ρ=mass density, c_p=dilatational-wave velocity). The accuracy of the corresponding dynamic-stiffness coefficient (Fig. 7c) is acceptable. Better agreement is achieved when the coefficients of K_1 and C_1 are determined by an optimum fit based on the exact values, leading to the fundamental lumped-parameter model with the same arrangement of the springs and dashpots. The coefficients K_1, C_1 are presented in the caption.

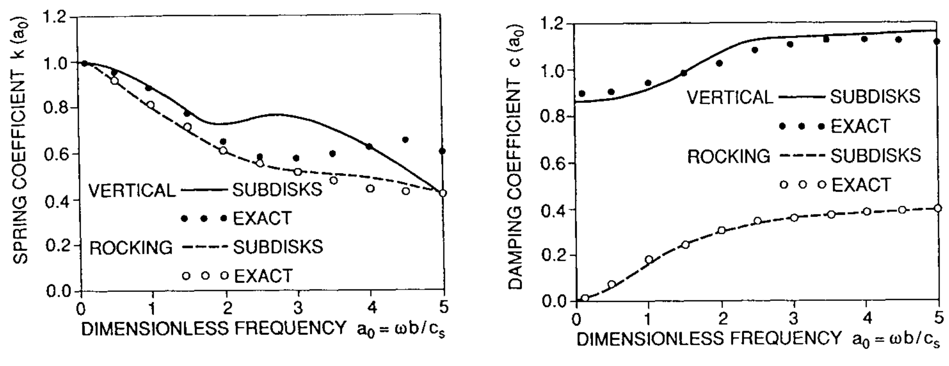

Fig. 8 Dynamic-stiffness coefficients of square foundation on surface of homogeneous soil halfspace modeled with subdisks (υ=1/3).

Second, the Green's function illustrated in Fig. 5a is applied. The vertical and rocking degrees of freedom of a rigid square foundation of length 2b resting on the surface of a soil halfspace is investigated with the exact result given in [52]. One quadrant is discretized with 7x7 subdisks. Figure 8 shows the dynamic-stiffness coefficients. The agreement is good.

As another application of the subdisks, the through-soil coupling in the vertical direction of two square rigid basemats of length 2b and distance d=2b on a halfspace is addressed (Fig. 9a). Each basemat is discretized into 10x10 subdisks. The dynamic-stiffness coefficient $S_{12}(a_0)$ representing the through-soil coupling of the two basemats in their centers of gravity points 1 and 2 in the vertical direction is normalized as

$$S_{12}(a_0)=Gb[k_{v12}(a_0)+ia_0c_{v12}(a_0)] \tag{12}$$

with $a_0=\omega b/c_s$. A good agreement (Fig. 9b) exists with the exact solution of [53].

Third, the vertical degree of freedom of a rigid disk on the surface of an undamped soil layer of depth d resting on rigid rock (Fig. 10a) is examined (with the exact solution specified in [12]). The cone model with the wave pattern representing the reflections at the rigid interface and the free surface is shown in Fig. 10b. The corresponding dynamic-stiffness coefficient (Fig. 10c) yields a smooth approximation in the sense of an average fit to the exact solution, which becomes increasingly irregular. The unit-impulse response function shown in Fig. 10d exhibits jump discontinuities from the reflected waves at the travel times from the disk at the surface to the rock and back and at multiples thereof. The unit-impulse response function of the halfspace is also shown. The lumped-parameter model (spring-dashpot-mass model) of Fig. 10e based on an optimum fit leads to the results shown in Fig. 10f.

Fourth, a rigid cylindrical foundation embedded with the depth e in a halfspace is addressed (Fig. 11a). In the embedded part of the foundation, 8 disks with their double cones are selected. For the rocking motion, the dynamic-stiffness coefficient is presented for three embedment ratios in Fig. 11b. The derivation from the exact result of [1] shown for $e/r_0=1$ is less than 10%. For vertically propagating S-waves with the amplitude $u^f(\omega)$ at the free surface (Fig. 11a) the effective foundation imput motion consisting of the horizontal component with amplitude $u_0^g(\omega)$ defined at the center of the basemat and of the rocking component with amplitude $\vartheta_0^g(\omega)$ are calculated (Fig. 11c and d). The agreement with the exact solution [14] is excellent.

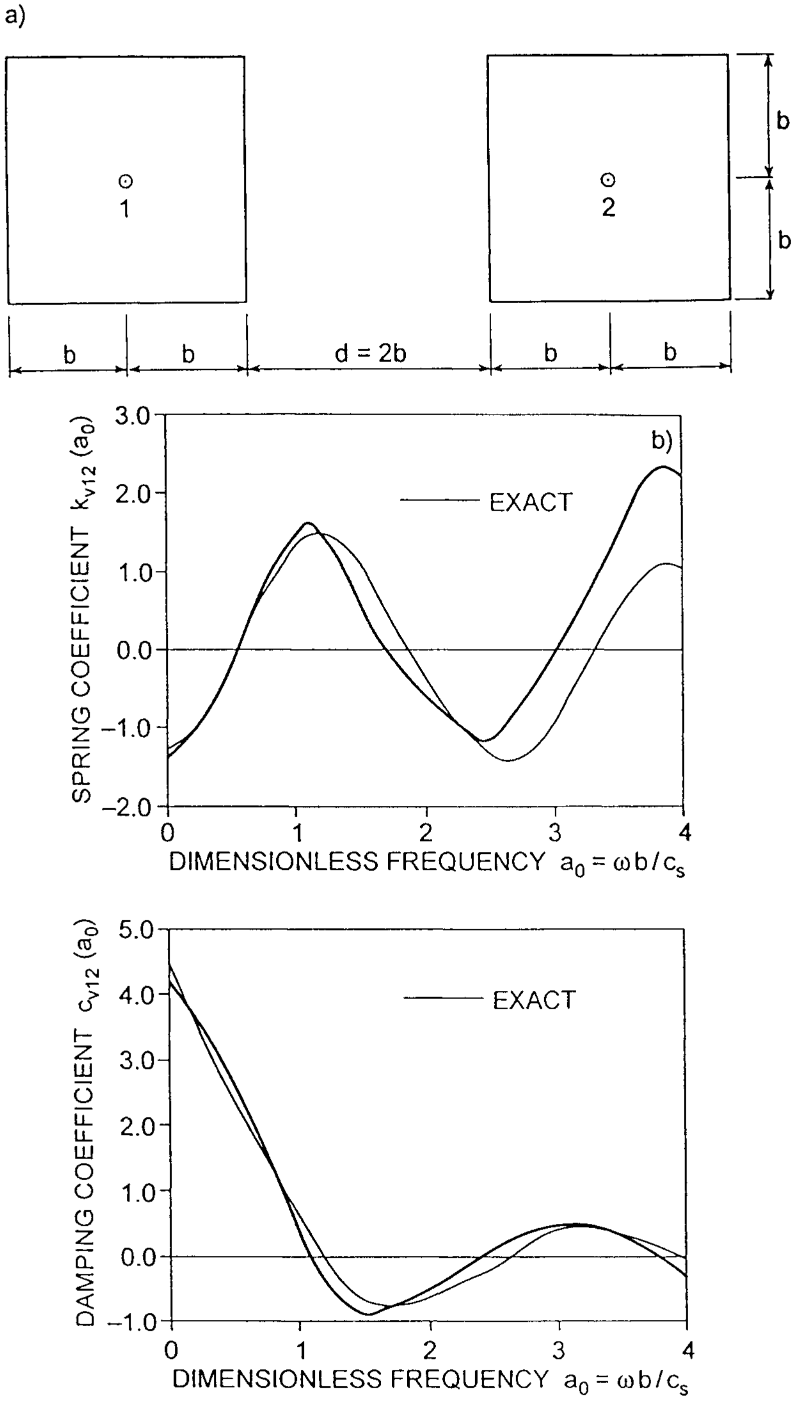

Fig. 9 Through-soil-coupling of two foundations modeled with subdisks.

a) Plan view of two square foundations (υ=1/3).

b) Vertical through-soil coupling dynamic-stiffness coefficient for harmonic excitation.

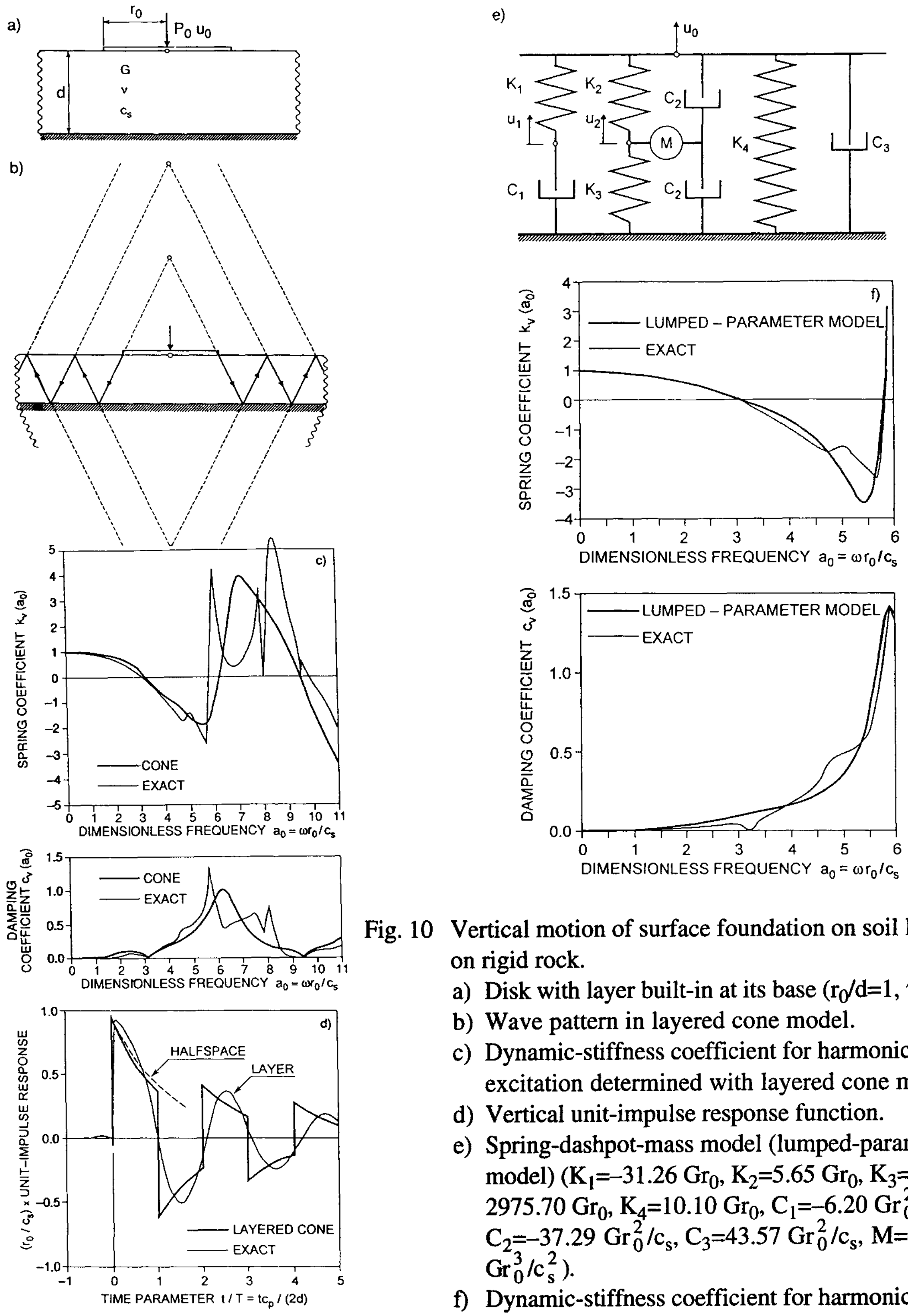

Fig. 10 Vertical motion of surface foundation on soil layer on rigid rock.

a) Disk with layer built-in at its base ($r_0/d=1$, $\nu=1/3$).

b) Wave pattern in layered cone model.

c) Dynamic-stiffness coefficient for harmonic excitation determined with layered cone model.

d) Vertical unit-impulse response function.

e) Spring-dashpot-mass model (lumped-parameter model) ($K_1=-31.26\ Gr_0$, $K_2=5.65\ Gr_0$, $K_3=-2975.70\ Gr_0$, $K_4=10.10\ Gr_0$, $C_1=-6.20\ Gr_0^2/c_s$, $C_2=-37.29\ Gr_0^2/c_s$, $C_3=43.57\ Gr_0^2/c_s$, $M=-89.68\ Gr_0^3/c_s^2$).

f) Dynamic-stiffness coefficient for harmonic excitation determined with lumped-parameter model.

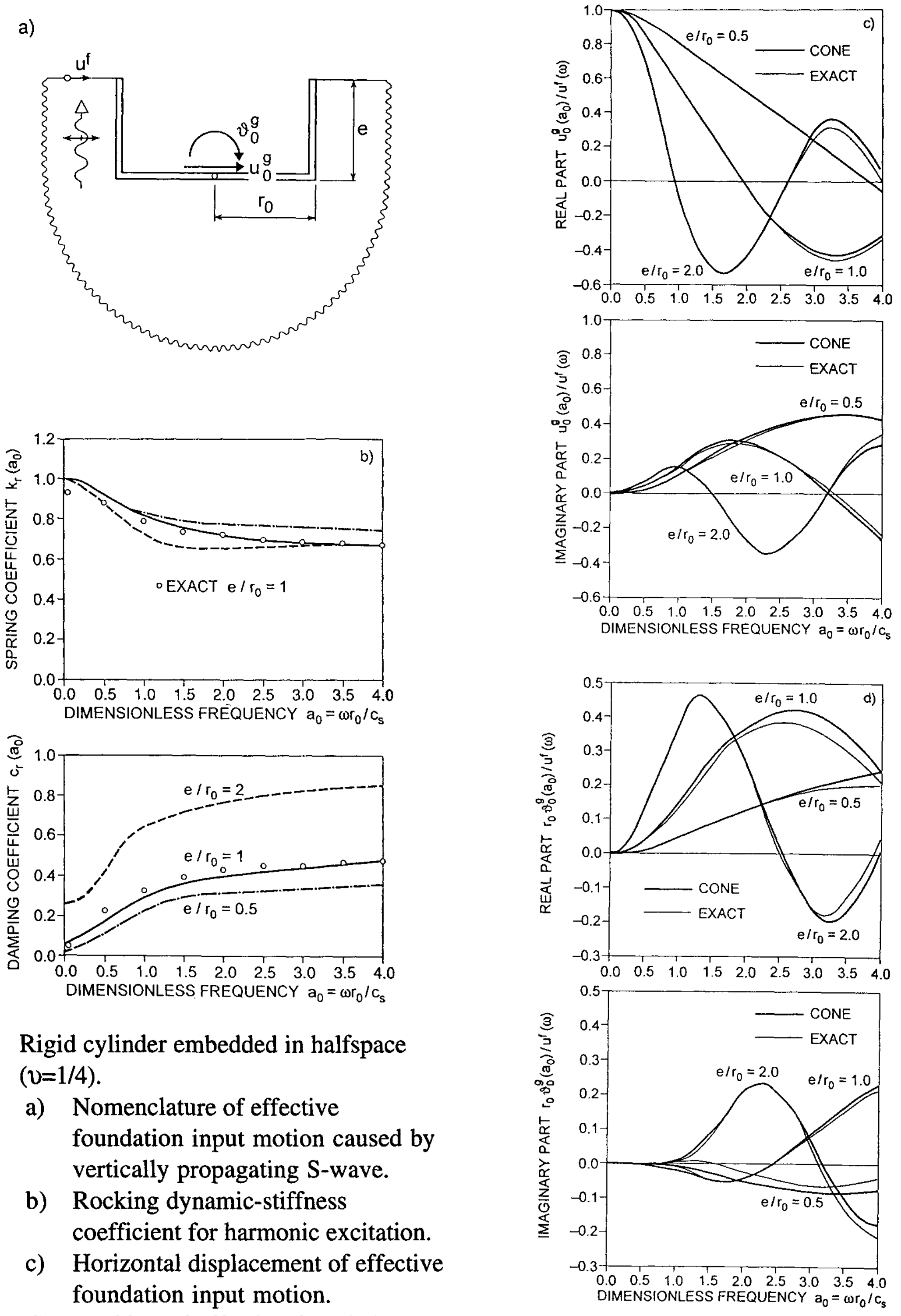

Fig. 11 Rigid cylinder embedded in halfspace (ν=1/4).

a) Nomenclature of effective foundation input motion caused by vertically propagating S-wave.
b) Rocking dynamic-stiffness coefficient for harmonic excitation.
c) Horizontal displacement of effective foundation input motion.
d) Rocking of effective foundation input motion.

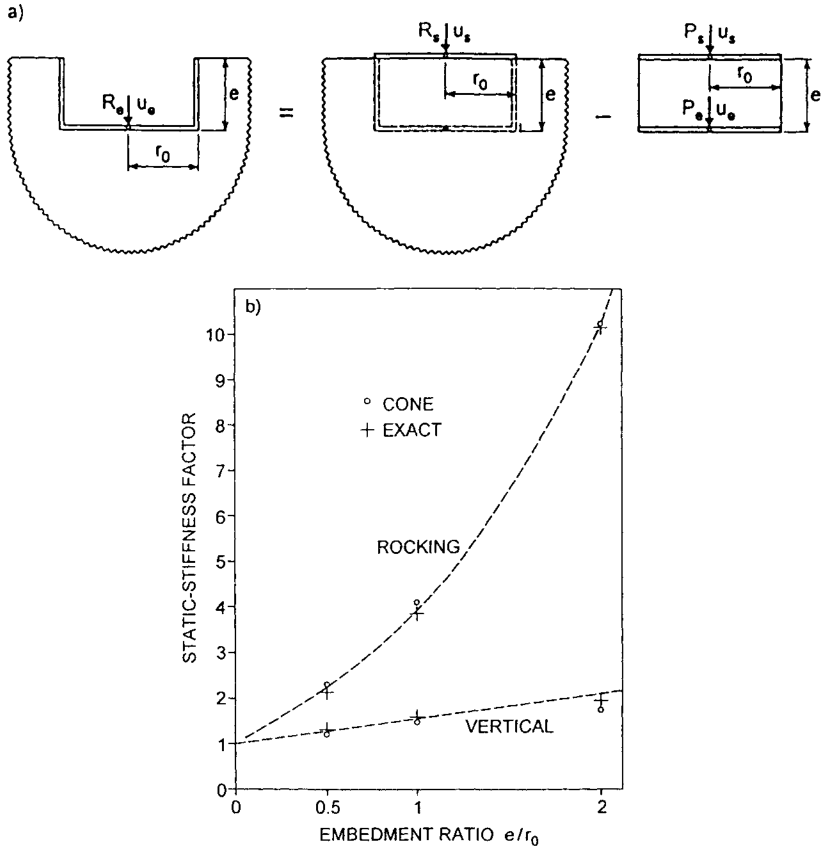

Fig. 12 Excavation-deletion method for rigid cylinder embedded in halfspace.
a) Nomenclature for vertical motion.
b) Static-stiffness factors.

Diverting somewhat, it is instructive to derive an approximate expression for the vertical static-stiffness coefficient of the embedded cylindrical foundation. The substructure-deletion method [3] is used which expresses the stiffness coefficient of the embedded foundation as a function of that of the surface foundation and of the stiffness matrix of the excavated part (Fig. 12a). Applying the strength-of-materials concept, the stiffness coefficient of the disk on the surface of the halfspace is calculated based on the cone (Eq. 13) and the stiffness matrix of the excavated part is determined for a cylindrical rod (Eq. 14)

$$R_s = K_s^{\infty} u_s \tag{13a}$$

where (Table A-1)

$$K_s^{\infty} = \frac{E_c}{z_0} \pi r_0^2 \tag{13b}$$

$$\begin{Bmatrix} P_s \\ P_e \end{Bmatrix} = \begin{bmatrix} K & -K \\ -K & K \end{bmatrix} \begin{Bmatrix} u_s \\ u_e \end{Bmatrix} \tag{14a}$$

where

$$K = \frac{E_c \pi r_0^2}{e} = K_s^\infty \frac{z_0}{e} \tag{14b}$$

with the interaction forces R and P, the displacement u, the constrained modulus E_c and the apex height of the cone z_0 (Fig. A-2). The subscripts s and e denote the surface and the embedded cases and the superscript ∞ the infinite halfspace. The stiffness coefficient of the embedded foundation is defined as

$$R_e = K_e^\infty u_e \tag{15}$$

Formulating equilibrium

$$R_s = P_s \tag{16a}$$

$$R_e = -P_e \tag{16b}$$

and eliminating all interaction forces and u_s yields

$$\left(-K\left(K - K_s^\infty\right)^{-1} K + K + K_e^\infty\right) u_e = 0 \tag{17}$$

Setting the coefficient equal to zero leads to

$$K_e^\infty = \frac{K^2}{K - K_s^\infty} - K \tag{18}$$

Substituting Eq. 14b results in

$$K_e^\infty = K_s^\infty \left[\frac{\frac{z_0}{e}}{1 - \frac{e}{z_0}} - \frac{z_0}{e} \right] \tag{19}$$

Applying a Taylor expansion for $e/z_0 << 1$ yields

$$K_e^\infty = K_s^\infty \left(1 + \frac{e}{z_0}\right) \tag{20}$$

For $\upsilon=0.25$, $e/z_0=(e/r_0)(r_0/z_0)=0.566e/r_0$, with z_0/r_0 specified in Table A-1 leading to

$$K_e^\infty = K_s^\infty \left(1 + 0.566\frac{e}{r_0}\right) \tag{21}$$

which hardly deviates from the expression determined from curve fitting [27] shown in Table A-6

$$K_e^\infty = K_s^\infty \left(1 + 0.54\frac{e}{r_0}\right) \tag{22}$$

In Fig. 12b, the vertical static-stiffness factor $1+0.566e/r_0$ is compared to that determined with cones and with the exact value. For the rocking motion, the solution using cones is very close to the exact result and the equation specified in Table A-6 (dashed line).

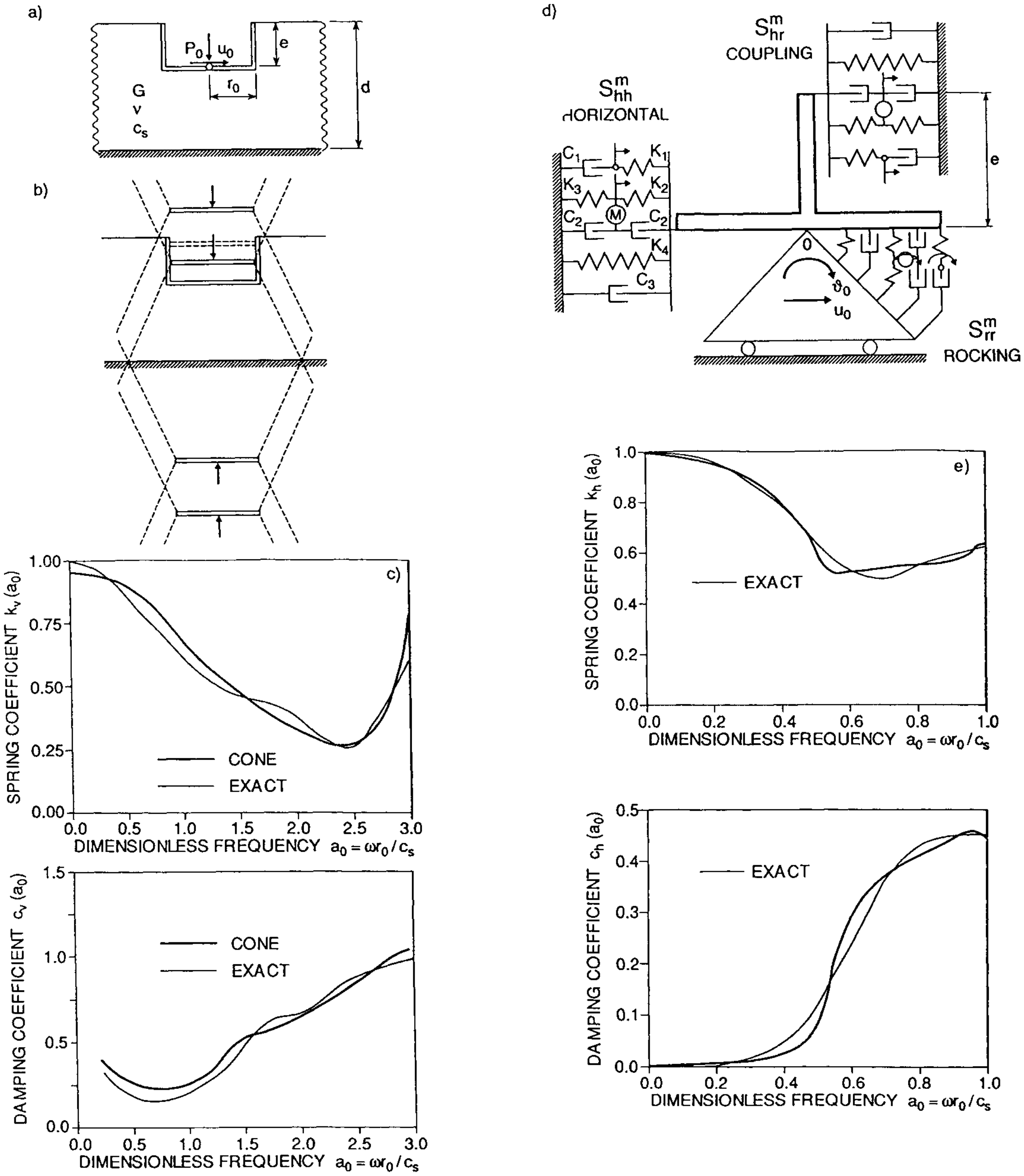

Fig. 13 Rigid cylinder embedded in soil layer on rigid rock.

a) Cylindrical foundation with layer fixed at its base ($r_0/e=1$, $r_0/d=1/3$, $\upsilon=1/3$).

b) Array of disks with double-cone models and mirror-image disks for vertical motion.

c) Vertical dynamic-stiffness coefficient for harmonic excitation with cone model (5% material damping).

d) Spring-dashpot-mass model with coupling of horizontal and rocking motions (coefficients see Table A-7).

e) Horizontal dynamic-stiffness coefficient for harmonic excitation with spring-dashpot-mass model (undamped).

Fifth, a rigid cylindrical foundation embedded with the depth e in a soil layer resting on rigid rock (Fig. 13a) is discussed. The cones are applied to calculate the dynamic-stiffness coefficient of the vertical degree of freedom and the lumped-parameter model that of the horizontal motion. In the embedded part of the foundation (Fig. 13b), 8 disks with doubles cones are selected (two are shown in the figure, one with a solid and one with a dashed line). To enforce approximately the stress-free condition at the free surface and the fixed boundary condition at the base of the layer, mirror images of the disk with the loads acting in the indicated directions with the corresponding double cones (dashed lines) are introduced. The dynamic-stiffness coefficient (Fig. 13c) is surprisingly accurate, as can be seen from a comparison with the exact solution determined with a very fine mesh of boundary elements [6]. The spring-dashpot-mass model for the coupled horizontal and rocking degrees of freedom is shown in Fig. 13d. The coupling term is represented by placing the spring-dashpot-mass model of Fig. 4h at the eccentricity e. The agreement for the horizontal dynamic-stiffness coefficient in Fig. 13e with the exact value [31] is good.

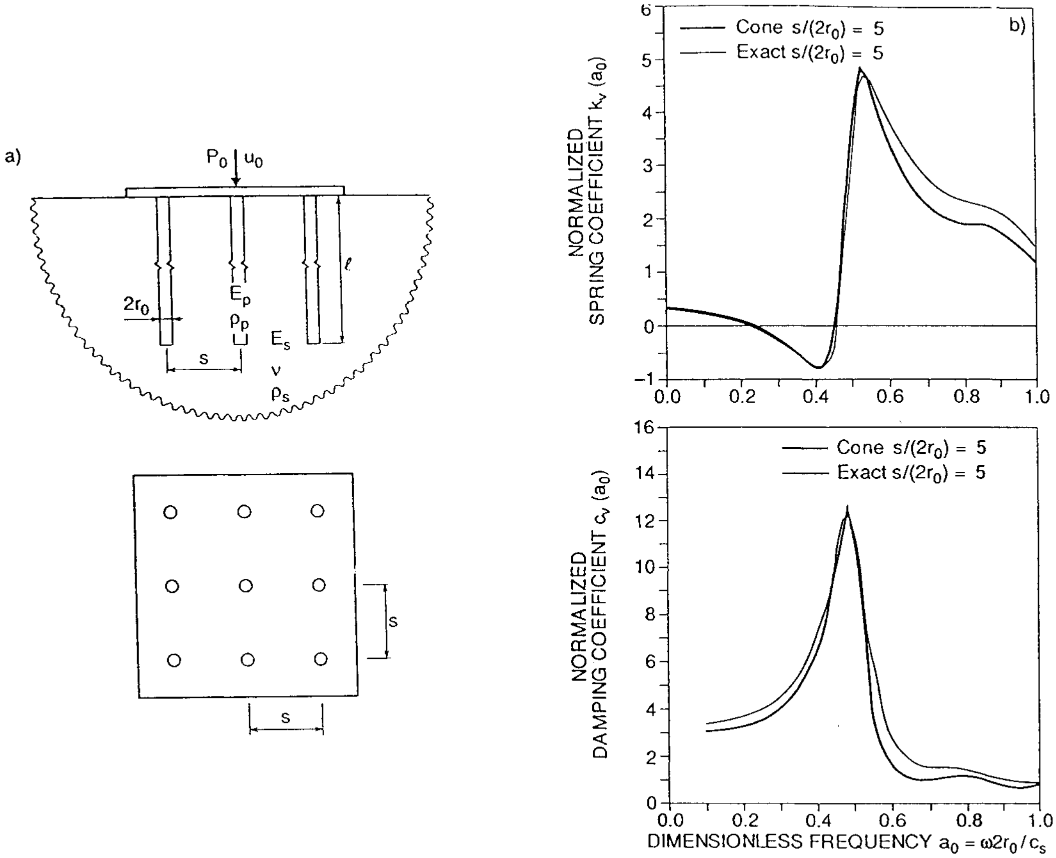

Fig. 14 Vertical motion of floating pile group in homogeneous soil halfspace.

a) Elevation and plan view of 3x3 pile group ($s/(2r_0)=5$, $\ell/(2r_0)=15$, $\nu=0.4$, $E_p/E_s=1000$, $\rho_p/\rho_s=1.43$, 5% material damping).

b) Dynamic-stiffness coefficient for harmonic excitation with cone model and dynamic-interaction coefficient.

Finally, a rigidly capped floating pile group taking pile-soil-pile interaction into consideration is addressed. The 3x3 pile group in a halfspace is shown in Fig. 14a (s=distance between axes of two neighboring piles, ℓ=length of pile, $2r_0$=diameter of pile, E=Young's modulus of elasticity, ρ=density). To model the single pile, 25 disks with the corresponding double cones are used. To calculate pile-soil-pile interaction, the dynamic-interaction factor based on the sound physical approximation illustrated in Fig. 5b - but for vertical motion - is determined. The dynamic-stiffness coefficient in the vertical direction of the pile group (normalized with the sum of the static-stiffness coefficients of the single piles) calculated with cones is astonishingly accurate (Fig. 14b) with the exact solution specified in [13]. Even details of the strong dependency on frequency are well represented.

Spring-dashpot-mass models with frequency-independent coefficients and with a few internal degrees of freedom can be constructed for practical use in many other cases. As an example, a spring-dashpot-mass model to calculate the dynamic pressure on a vertical rigid wall retaining a semi-infinite soil layer on rigid rock caused by a horizontal earthquake (Fig. 15) is addressed [51].

The model to perform a seismic analysis directly in the time domain is shown in Fig. 16. On the mass m with its degree of freedom u_0 acts the load $-m\ddot{u}^g(t)$ with the known seismic acceleration time history of the rock's interface $\ddot{u}^g(t)$. The spring-dashpot part has three internal degrees of freedom u_1, u_2, u_3. The coefficients of the mass, the 4 springs and 4 dashpots are equal to

$$m = 0.543\frac{2}{\sqrt{(1-\nu)(2-\nu)}}\rho h^2 \tag{23a}$$

$$K_1 = -0.682\omega_1^2 m \tag{23b}$$

$$K_2 = -0.318\omega_1^2 m \tag{23c}$$

$$K_3 = 0.273\omega_1^2 m \tag{23d}$$

$$K_4 = 2\omega_1^2 m \tag{23e}$$

$$C_1 = -0.658\omega_1 m \tag{23f}$$

$$C_2 = -0.344\omega_1 m \tag{23g}$$

$$C_3 = 0.232\omega_1 m \tag{23h}$$

$$C_4 = \omega_1 m \tag{23i}$$

with Poisson's ratio υ, mass density ρ and layer thickness d. ω_1 is the circular natural frequency of the layer ($=\pi c_s/2$) with shear-wave velocity $c_s = \sqrt{G/\rho} =$ and shear modulus G. The resultant dynamic soil pressure R acts at a height = 0.637h (Fig. 16). These coefficients apply for a soil layer without material damping. As for spring-dashpot-mass models of the dynamic-stiffness coefficients, material damping can be introduced directly into the algorithm [23, 50]. Excellent agreement of the results with those of the approximate but accurate solution of Reference [37] arises.

Requirements

1. Physical insight. The mathematical complexity of rigorous solutions in elastodynamics often obscures physical insight and intimidates practitioners. By simplifying the physics of the problem, *conceptual clarity* with *physical insight* results. As an example, the calculation of the dynamic stiffness of a disk on the surface of a soil layer resting on rigid rock (Fig. 10a) - a complicated three-dimensional mixed boundary-value problem with dispersive waves - is addressed. In the physical model made up of truncated cones (Fig. 10b), for which the familiar strength-of-materials theory applies, the wave pattern is clearly postulated. The one-dimensional waves propagate with the dilatational-wave velocity (a material constant), reflecting back and forth, spreading and decreasing in amplitude, and thus radiating energy towards infinity in the horizontal direction.

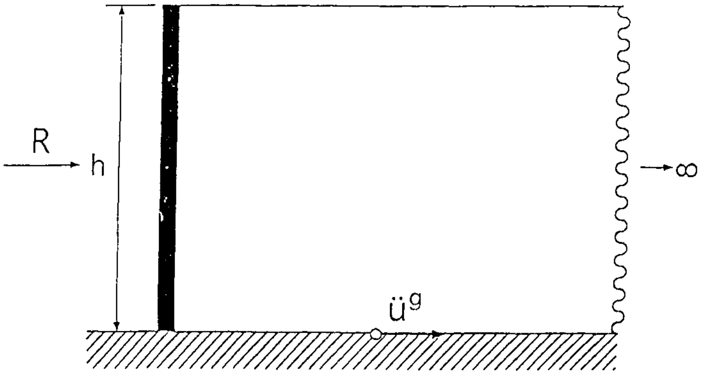

Fig. 15 Vertical rigid wall retaining a semi-infinite soil layer on rigid rock with prescribed horizontal seismic motion at its base.

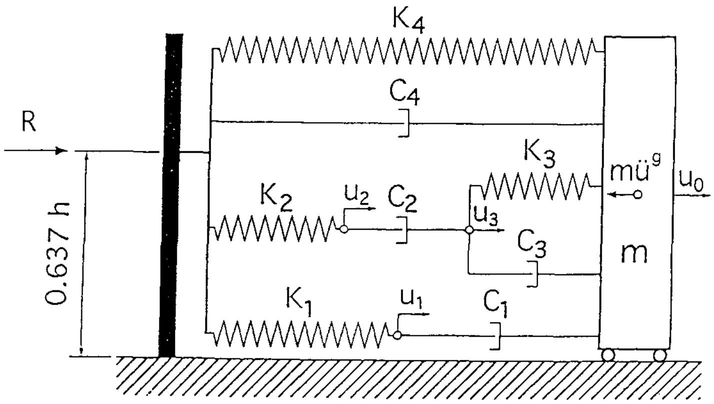

Fig. 16 Spring-dashpot-mass model to calculate resultant pressure on vertical rigid wall.

2. Simplicity. Due to the simplification of the physical problem, the physical model can be rigorously mathematically solved. The fundamental principles of wave propagation and dynamics are thus satisfied exactly for the simple physical model. Closed-form solutions (even in the time domain) exist for the (one-dimensional) cones. For instance, to calculate the dynamic stiffness of the disk on the soil layer resting on rigid rock with cones (Fig. 10b), the analysis can be performed with a hand calculator as no system of equations is solved; for the embedded cylindrical foundation with cones (Fig. 13b), a special-purpose computer code can easily be written; and when lumped-parameter models are applied (Figs. 10e, 13d), a standard general-purpose structural dynamics program which permits springs, dashpots, and masses as input can be used directly. The *practical application* of the physical models is thus also *simple*, together with the *physics* and the rigorous *mathematical solution.*

3. Generality. To be able to provide engineering solutions to reasonably complicated practical cases and not just to address academic examples, the physical models must reflect the following key aspects of the foundation-soil system for all translational and rotational degrees of freedom [8].

- *The shape of the foundation-soil (structure-soil) interface*: Besides the circle, the rectangle and the arbitrary shape, which can be modeled as an equivalent disk or directly (Fig. 8) without "smearing", can be represented as a three-dimensional case or, if applicable, as a two-dimensional slice of a strip foundation.
- *The nature of the soil profile*: The homogeneous halfspace, the layer resting on a flexible halfspace, and the layer resting of a rigid halfspace as well as the layered halfspace with many layers can be modeled.
- *The amount of embedment*: Surface, embedded (with soil contact along the total height of the wall or only on part of it), and pile foundations can be represented.

The physical models must also allow the calculation of the effective foundation input motion for seismic excitation. They must work well for the static case, for the low- and intermediate-frequency ranges important for machine vibrations and earthquakes, and for the limit of very high frequencies as occurring in impact loads.

4. Accuracy. Due to many uncertainties, the accuracy of any analysis will always be limited. A deviation of ±20% of the results of the physical models from those of the rigorous solution for one set of input parameters is, in general, acceptable. This *engineering accuracy* criterion is, in general, satisfied, as can be verified by examining the dynamic-stiffness coefficients shown in Figs. 7, 11, 13 and 14. It should also be remembered that for a transient loading such as an earthquake the deviations (with both signs) are "smeared" over the frequency range of the excitation and thus further reduced compared to the larger error for one frequency.

The use of the physical models does indeed lead to some loss of precision compared to applying the rigorous boundary-element procedure or the sophisticated finite-element-based method; however, this is more than compensated by the many advantages discussed in this section.

5. Demonstration of physical features. Besides leading (by construction of the physical model) to physical insight of the mechanisms involved in foundation vibration (item 1), the physical models are also well suited to demonstrate certain unexpected features and to derive further results. Four examples follow.

1. Placing a row of an infinite number of identical vertical point loads on the surface of a halfspace as a simple physical model, the vertical dynamic stiffness of a two-dimensional slice of a rigid surface strip foundation can be determined. An analytical solution can be derived. The static stiffness is zero, but the spring coefficient increases abruptly to a more or less constant value for larger frequencies. By contrast, the damping coefficient begins from infinity at zero frequency and then diminishes asymptotically for increasing frequency. The same features exist in the rigorous solution.
2. As can be shown, the radiation damping ratio in a two-dimensional model is significantly larger than in the corresponding three-dimensional case (just the contrary of what is expected intuitively). To model a two-dimensional slice of a strip foundation on a half-plane, wedges can be used which are again based on rod theory, just as cones represent a disk on a halfspace (three-dimensional situation). For both the translational and rotational motions, the damping ratios $\zeta=b_0c(b_0)/[2k(b_0)]$ of the wedges are significantly larger than those of the cones (Fig. 17). The dimensionless frequency parameter is defined as $b_0=\omega z_0/c$ with z_0 denoting the apex height of the cone or wedge and c the appropriate wave velocity. The multipliers are also specified in the figure.
3. For the frequency range below the cutoff frequency of the soil layer resting on rigid rock, the radiation damping and thus the damping coefficient of the dynamic stiffness vanish, which is well simulated using cones and lumped-parameter models. See Figs. 10c and 10f, where below the cutoff frequency for dilatational waves, $a_0=\pi$, $c(a_0)$ is very small.
4. The combined structure-soil system can be modeled approximately as an equivalent one-degree-of-freedom system. The corresponding effective natural frequency and damping ratio can be determined by modeling the soil as cones.

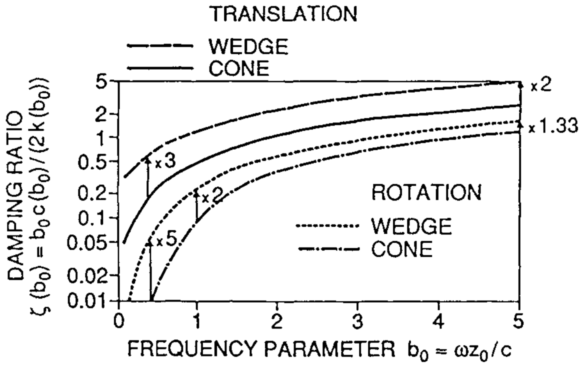

Fig. 17 Overestimation of radiation damping ratio of two-dimensional modeling with wedges when compared to that of three-dimensional modeling with cones for translational and rotational motions.

6. *Suitability for everyday practical foundation-vibration analysis.* Especially the ease in use, the sufficient generality and the good accuracy allow the physical models to be applied for foundation vibration and dynamic soil-structure-interaction analyses in a design office.

7. Potential for generalization. The *concepts and certain features of the physical models can be generalized* and the results applied in much more sophisticated calculations. Three examples of such extensions are listed.

1. The cone models lead to simple Green's functions, and the analysis of an embedded foundation can be interpreted as a straightforward application of the one-dimensional boundary-element method. The rigorous calculation can be performed also with a boundary-element method based on the same concept, the major difference being that the Green's function of the three-dimensional fullspace is used and not the one-dimensional solution derived from the rod theory of cones.
2. A consistent spring-dashpot-mass model (lumped-parameter model) for the dynamic-stiffness matrix of any general flexible foundation can be systematically constructed starting from the same fundamental lumped-parameter model (Fig. 4g). In general, a large number of these building blocks are assembled in parallel for each coefficient of the matrix to be represented.
3. The interaction force-displacement relationship of some physical models will involve convolution integrals which can be evaluated exactly very efficiently using a recursive formulation. The same procedure can also be applied to the corresponding relationship of any general flexible foundation.

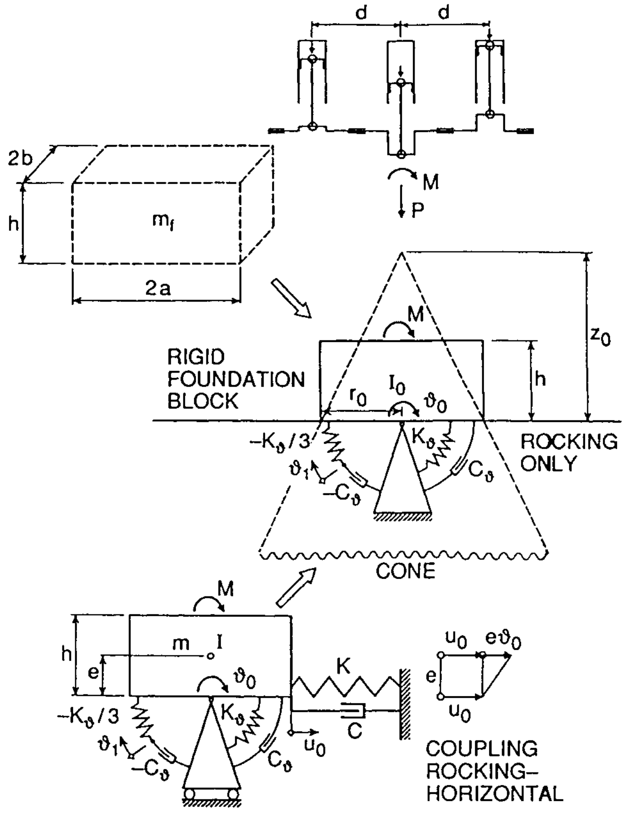

Fig. 18 Foundation of three-cylinder compressor with cranks at 120° with dynamic models.

Summarizing, the cone models with the prescribed deformation of rod (bar) theory, the spring-dashpot-mass models based on them, and the displacement patterns in the horizontal plane present a major step towards developing a *strength-of-materials approach to foundation dynamics*. The aim is the same as in stress analysis of structural engineering, where, for instance for very complicated skew-curved prestressed concrete bridges, beam theory is applied successively and the general three-dimensional theory of elasticity is not needed. As in stress analysis, each specific case has to be calculated based on the strength-of-materials approach. It is not sufficient just to use tables of dynamic-stiffness coefficients calculated for certain cases based on the rigorous formulation of elastodynamics. As the soil is a three-dimensional body without a dominant axial direction, the strength-of-materials approach, with prescribed displacement behavior taking all essential features into account, will be more difficult to formulate in foundation engineering than in structural engineering. Concluding, the dynamic analyst should always "make things as simple as possible but no simpler (H. Einstein). Or to state it differently: "*Simplicity that is based on rationality is the ultimate sophistication*" (A.S. Veletsos).

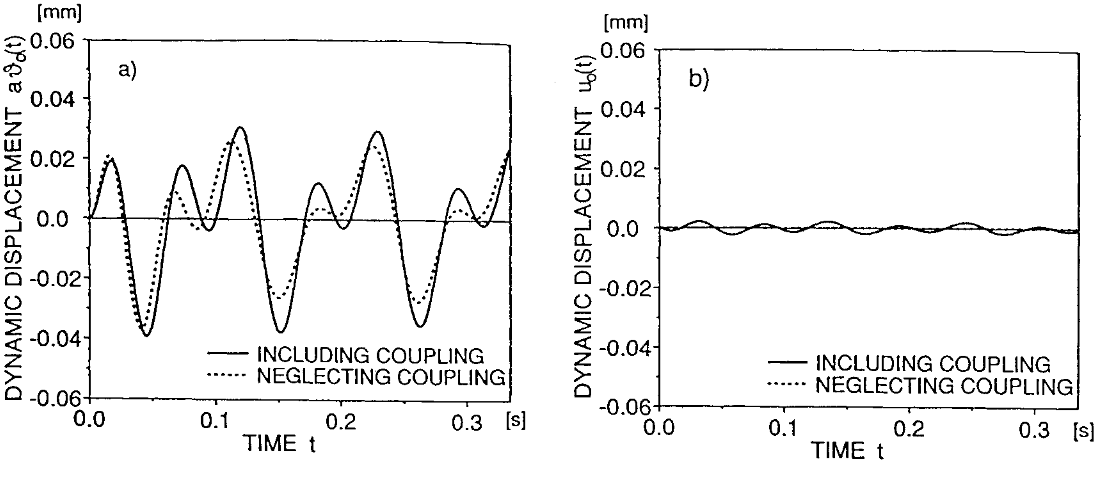

Fig. 19 Response including coupling of rocking motion with horizontal motion.

a) Vertical displacement at edge of foundation block.

b) Horizontal displacement

Engineering Applications

Selected simple engineering applications taken from [50] follow.

As a first example, a machine foundation on the surface of a soil halfspace excited by a three-cylinder compressor operating at 9 Hz with the cranks at 120° resulting in a moment (Fig. 18) is investigated. The discrete-element models of the cones shown in Figs. 4f and 4e are used to represent the soil in the rocking and horizontal motions. Including the coupling between the horizontal and rocking motions increases the rocking response (Fig. 19a).

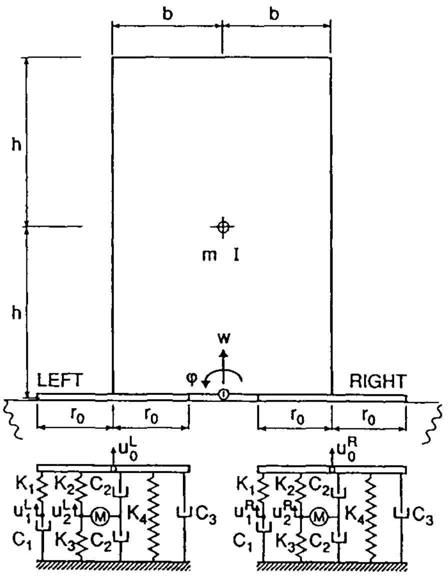

Fig. 20 Rigid block on disks with lumped-parameter models of disks on surface of soil layer resting on rigid rock.

The second example examines non-linear soil-structure-interaction analysis. A rigid block with individual footings, which can uplift, resting on the surface of a soil layer with c_s=750 m/s and $d/r_0=1$ is discussed (Fig. 20). An idealized horizontal earthquake acts during 2s. Only the vertical and rocking motions of the block's bottom center are considered in the calculation. The spring-dashpot-mass model of Fig. 4h is used to represent the soil neglecting through-soil coupling. As the fundamental frequency in rocking lies below the cutoff frequency of the layer, no radiation damping occurs during the free vibration phase after 2s. This leads to no decay occurring in the gaps (Fig. 21a). If the soil is a halfspace, the gaps are much smaller and decay rapidly after 2s (Fig. 21b).

The third example, also addressing nonlinear soil-structure-interaction analysis, discusses the vibration of a hammer foundation embedded in a soil layer on rigid rock ($d/r_0=2$) with an excentrically mounted anvil (Fig. 22). The head impacts with a velocity c_h=5 m/s against the anvil. As a tension-resistant connection for the pads of the anvil is not provided, the anvil will partially uplift from the block, when the dynamic stress in tension exceeds the static stress. The dynamic system with 14 degrees of freedom (Fig. 23) is constructed using the spring-dashpot-mass models of Figs. 13d and 4h. As expected, the partial uplift of the anvil increases the motion significantly when compared with the result of a linear analysis (Fig. 24). The response for a soil halfspace is also plotted.

As a final example, the vertical seismic motion of a structure founded on the surface of a soil layer on rigid rock (Fig. 25) for a record of the Loma Prieta earthquake is investigated. Two radius-to-depth ratios are addressed. For $d/r_0=1$, the vertical fundamental frequency of the structure-soil system is smaller than the corresponding fundamental frequency of the layer (=cutoff frequency) which eliminates radiation damping. For $d/r_0=4$, the opposite applies which results in radiation damping occurring. The analyses are performed with the layered cone model (Fig. 10b) and with the spring-dashpot-mass model (Fig. 10e). From the structural distortion $u^t - u_0^t$ plotted for the shallow and the deep layers in Fig. 26, the significant influence of radiation damping resulting in smaller peaks and a larger decay is clearly visible.

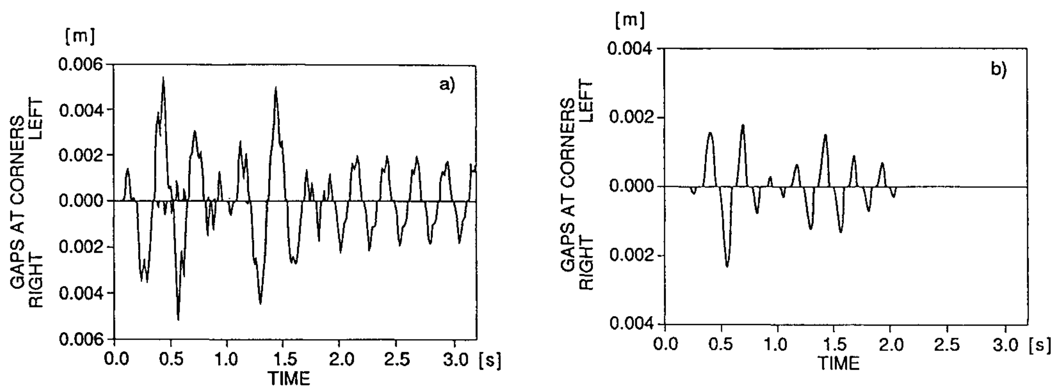

Fig. 21 Vertical gap between block and disk for soil modeled as
a) Layer. b) Halfspace.

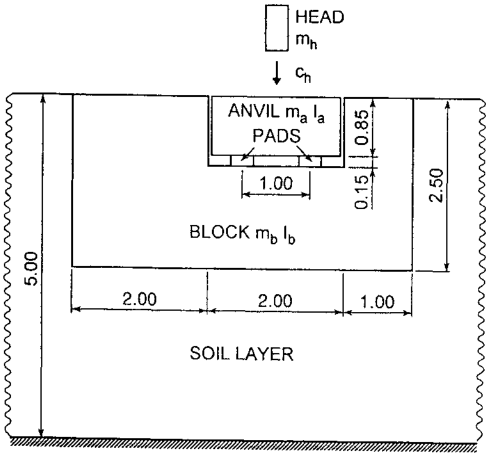

Fig. 22 Hammer foundation with inertial block embedded in soil layer resting on rigid rock.

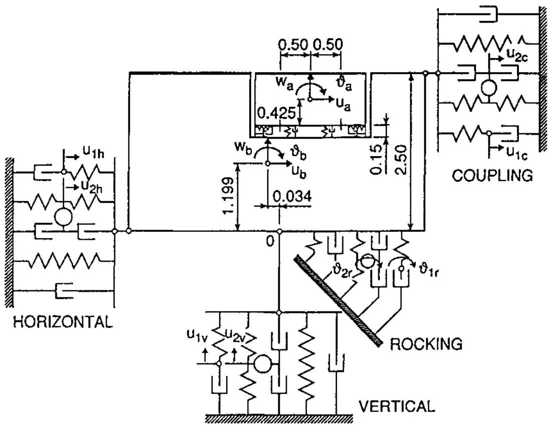

Fig. 23 Dynamic model of hammer foundation with spring-dashpot-mass models of soil layer.

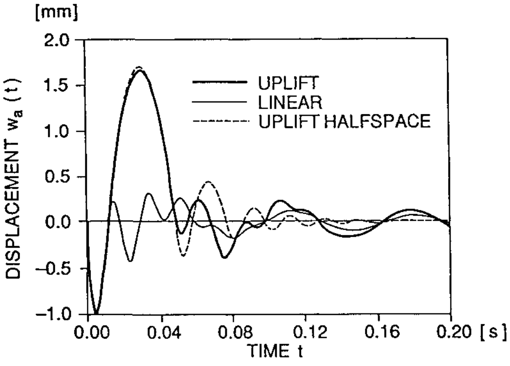

Fig. 24 Vertical displacement at center of anvil for load transmitted as initial velocity of anvil.

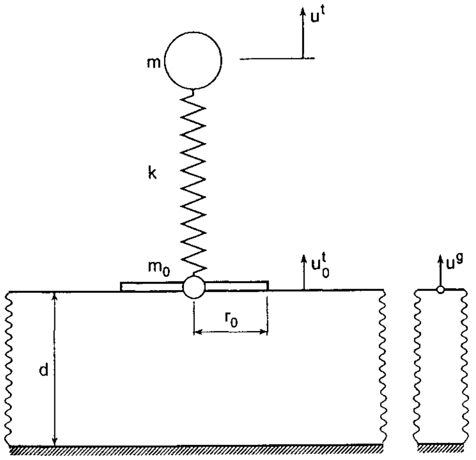

Fig. 25 Dynamic system with two degrees of freedom for vertical motion of structure on soil layer.

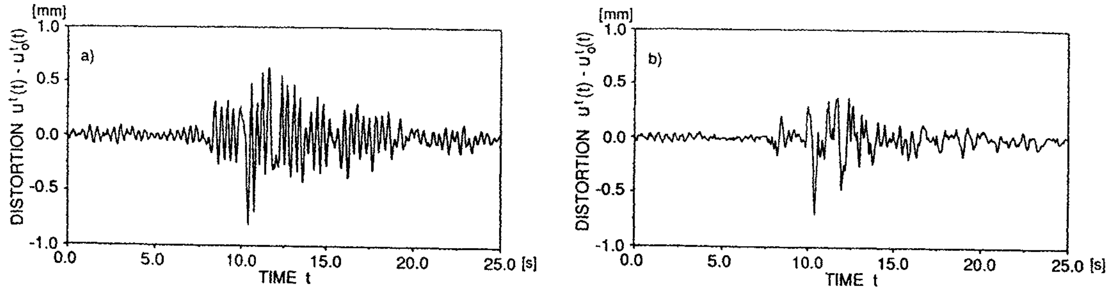

Fig. 26 Structural distortion.

a) Fundamental frequency of dynamic system below fundamental frequency of soil layer (cutoff frequency).

b) Fundamental frequency of dynamic system above fundamental frequency of soil layer (cutoff frequency).

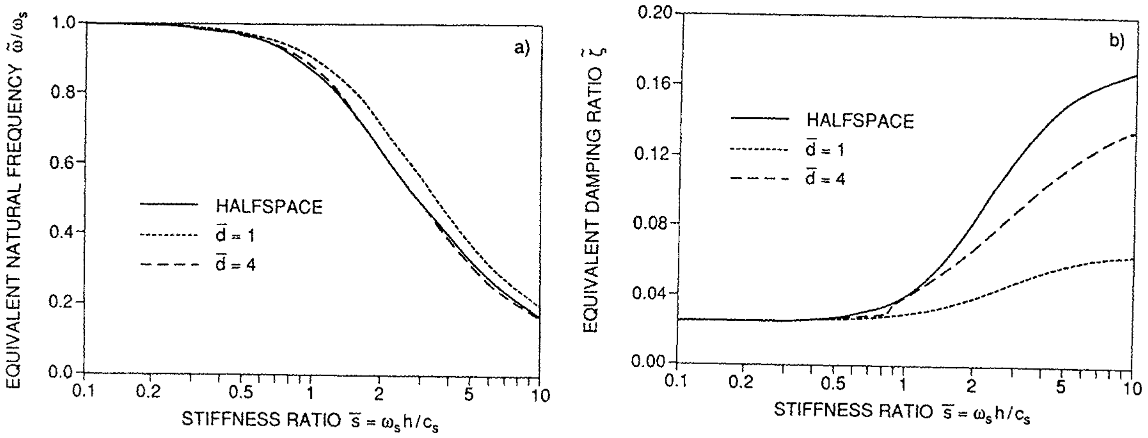

Fig. 27 Properties of equivalent one-degree-of-freedom system modeling coupled horizontal and rocking motions for horizontal earthquake varying depth of soil layer (see Fig. A-30, $h/r_0=2$, $m/(pr_0^3)=1$, $\upsilon=1/3$, $\zeta=0.025$, $\zeta_g=0.05$).

The same effect is also present for the coupled horizontal and rocking motions (see Fig. A-30) of a structure of height h, fixed-base frequency ω_s, mass m and material damping ratio ζ on a soil layer. While the natural frequency ratio $\tilde{\omega} / \omega_s$ of the equivalent one-degree-of-freedom system (Fig. A-31) is hardly effected by $\bar{d} = d / r_0 =$ (Fig. 27a), the equivalent damping ratio $\tilde{\zeta}$ depends for large $\bar{s}(= \omega_s h / c_s)$, i.e. for a significant soil-structure interaction effect, strongly on $\bar{d}$ (Fig. 27b). For the shallow layer $\bar{d}=1$, no radiation damping is activated, as $\tilde{\zeta}$ converges for large $\bar{s}$ essentially to the material damping of the soil $\zeta_g=0.05$. For the halfspace shown for comparison, $\tilde{\zeta}$ increases significantly for increasing $\bar{s}$, due to the large effect of radiation damping. For the intermediate site with $\bar{d}=4$, a transmission occurs.

Acknowledgment

This paper is a slightly updated version of the state-of-the-art lecture S0A9 with the same title presented at the Third International Conference on Recent Advances in Geotechnical Earthquake Engineering and Soil Dynamics, St. Louis, Missouri, April 2-7 1995, (Vol. II of the Proceedings, pages 943-984, edited by S. Prakash). The permission to include the material is gratefully acknowledged.

References

[1] R.J. Apsel and J.E. Luco, Impedance Functions for Foundations Embedded in a Layered Medium: An Integral Equation Approach, *Earthquake Engineering and Structural Dynamics*, 15 (1987): 213-231.

[2] F.C.P. de Barros and J.E. Luco, Discrete Models for Vertical Vibrations of Surface and Embedded Foundation, *Earthquake Engineering and Structural Dynamics*, 19 (1990), 289-303.

[3] G. Dasgupta, Foundation Impedance Matrices by Substructure Deletion, *Journal of the Engineering Mechanics Division*, ASCE, 106 (1980): 517-523.

[4] R. Dobry and G. Gazetas, Simple Method for Dynamic Stiffness and Damping of Floating Pile Groups, *Géotechnique*, 38 (1988): 557-574.

[5] G. Ehlers, The Effect of Soil Flexibility on Vibrating Systems, *Beton und Eisen*, 41 (1942): 197-203 [in German].

[6] J.M. Emperador and J. Dominguez, Dynamic Response of Axisymmetric Embedded Foundations, *Earthquake Engineering and Structural Dynamics*, 18 (1989): 1105-1117.

[7] G. Gazetas and R. Dobry, Simple Radiation Damping Model for Piles and Footings, *Journal of Engineering Mechanics*, ASCE, 110 (1984), 937-956.

[8] G. Gazetas, Simple Physical Methods for Foundation Impedances, in *Dynamic Behaviour of Foundations and Buried Structures* (Developments in Soil Mechanics and Foundation Engineering, Vol.3), edited by P.K. Banerjee and R. Butterfield, Chapter 2, pp. 45-93 (London: Elsevier Applied Science, 1987).

[9] G. Gazetas, Foundation Vibrations, in *Foundation Engineering Handbook*, 2nd Edition, edited by H.-J. Fang, Chapter 15, pp. 553-593 (New York: Van Nostrand Reinhold, 1991).

[10] G. Gazetas and N. Markis, Dynamic Pile-Soil-Pile Interaction, Part I: Analysis of Axial Vibration, *Earthquake Engineering and Structural Dynamics*, 20 (1991): 115-132.

[11] G. Gazetas, Formulas and Charts for Impedances of Surface and Embedded Foundations, *Journal of Geotechnical Engineering*, ASCE, 117 (1991): 1363-1381.

[12] E. Kausel, personal communication, 1990.

[13] A.M. Kaynia and E. Kausel, Dynamic Behavior of Pile Groups, *Proceedings of 2nd International Conference on Numerical Methods of Offshore Piling*, Austin, TX, 1982: 509-532.

[14] J.E. Luco and H.L. Wong, Seismic Response of Foundations Embedded in a Layered Half-space, *Earthquake Engineering and Structural Dynamics*, 15 (1987): 233-247.

[15] J.W. Meek and A.S. Veletsos, Simple Models for Foundations in Lateral and Rocking Motions, *Proceedings of the 5th World Conference on Earthquake Engineering*, Rome, 1974, Vol. 2: 2610-2613.

[16] J.W. Meek and J.P. Wolf, Insights on Cutoff Frequency for Foundation on Soil Layer, *Earthquake Engineering and Structural Dynamics*, 20 (1991): 651-665.

[17] J.W. Meek and J.P. Wolf, Cone Models for Homogeneous Soil, *Journal of Geotechnical Engineering*, ASCE, 118 (1992): 667-685.

[18] J.W. Meek and J.P. Wolf, Cone Models for Soil Layer on Rigid Rock, *Journal of Geotechnical Engineering*, ASCE, 118 (1992): 686-703.

[19] J.W. Meek and J.P. Wolf, Cone Models for Nearly Incompressible Soil, *Earthquake Engineering and Structural Dynamics*, 22 (1993): 649-663.

[20] J.W. Meek and J.P. Wolf, Why Cone Models Can Represent the Elastic Half-space, *Earthquake Engineering and Structural Dynamics*, 22 (1993): 759-771.

[21] J.W. Meek and J.P. Wolf, Approximate Green's Function for Surface Foundations, *Journal of Geotechnical Engineering*, ASCE, 119 (1993): 1499-1514.

[22] J.W. Meek and J.P. Wolf, Cone Models for an Embedded Foundation, *Journal of Geotechnical Engineering*, ASCE, 120 (1994): 60-80.

[23] J.W. Meek and J.P. Wolf, Material Damping for Lumped-Parameter Models of Foundations, *Earthquake Engineering and Structural Dynamics*, 23 (1994): 349-362.

[24] J.W. Meek and J.P. Wolf, Non-Linear Seismic Soil-Structure Interaction Using Simple Physical Models of the Soil, *Proceedings of the 8th International Conference on Computer Methods and Advances in Geomechanics*, Morgantown WV, 1994, edited by H.J. Siriwardane and M.M. Zaman, Vol. II: 943-948. (Rotterdam, Balkema, 1994).

[25] J.W. Meek and J.P. Wolf, Cones and Rigorous Solutions. A Good Marriage for Layered Systems? Radiating Versus Ordinary Cones, *Proceedings of Second International Conference on Earthquake Resistant Construction and Design*, Berlin, 1994, edited by S.A. Savidis, Vol. 1: 359-366 (Rotterdam, Balkema, 1994).

[26] National Earthquake Hazards Reduction Program (NEHRP), *Recommended Provisions for the Development of Seismic Regulations for New Buildings*, Building Seismic Safety Council, Washington DC, 1986.

[27] A. Pais and E. Kausel, Approximate Formulas for Dynamic Stiffnesses of Rigid Foundations, *Soil Dynamics and Earthquake Engineering*, 7 (1988): 213-227.

[28] F.E. Richart, J.R. Hall and R.D. Woods, *Vibrations of Soils and Foundations*. Englewood Cliffs, NJ: Prentice-Hall, 1970.

[29] J.M. Roesset, The Use of Simple Models in Soil-Structure Interaction, *Civil Engineering and Nuclear Power*, ASCE, N° 1/3, 1980, 1-25.

[30] J.M. Roesset, Stiffness and Damping Coefficients in Foundations, *Dynamic Response of Pile Foundations*, ed. M.O. Neil and R. Dobry, ASCE, 1980, 1-30.

[31] J.L. Tassoulas, *Elements for the Numerical Analysis of Wave Motion in Layered Media* (Research Report R81-2). Department of Civil Engineering, Massachusetts Institute of Technology, Cambridge, MA: 1981.

[32] A.S. Veletsos and Y.T. Wei, Lateral and Rocking Vibration of Footings, *Journal of the Soil Mechanics and Foundation Division*, ASCE, 97 (1971): 1227-1248.

[33] A.S. Veletsos and B. Verbic, Vibration of Viscoelastic Foundations, *Earthquake Engineering and Structural Dynamics*, 2 (1973):87-102.

[34] A.S. Veletsos and B. Verbic, Basic Response Functions for Elastic Foundations, *Journal of the Engineering Mechanics Division*, ASCE, 100 (1974): 189-202.

[35] A.S. Veletsos and V.D. Nair, Response of Torsionally Excited Foundations, *Journal of the Geotechnical Engineering Division*, ASCE, 100 (1974):476-482.

[36] A.S. Veletsos and V.D. Nair, Seismic Interaction of Structures on Hysteretic Foundations, *Journal of Structural Division*, ASCE, 101 (1975), 109-129.

[37] Veletsos and A.H. Younan, Dynamic Soil Pressure on Rigid Vertical Walls, *Earthquake Engineering and Structural Dynamics*, 23 (1994): 275-301.

[38] G. Waas, personal communication, 1992.

[39] R.V. Whitman, Soil-Platform Interaction, *Proceedings of Conference on Behaviour of Offshore Structures*, Vol. 1, Norwegian Geotechnical Institute, Oslo, 1976: 817-829.

[40] J.P. Wolf and D.R. Somaini, Approximate Dynamic Model of Embedded Foundation in Time Domain, *Earthquake Engineering and Structural Dynamics*, 14 (1986):683-703.

[41] J. P. Wolf, Consistent Lumped-Parameter Models for Unbounded Soil: Physical Representation, *Earthquake Engineering and Structural Dynamics*, 20 (1991): 11-32.

[42] J.P. Wolf and A. Paronesso, Lumped-Parameter Model for Foundation on Layer, *Proceedings of 2nd International Conference on Recent Advances in Geotechnical Earthquake Engineering and Soil Dynamics*, edited by S. Prakash, St. Louis MO, 1991; Vol. I: 895-905.

[43] J.P. Wolf, J.W. Meek and Ch. Song, Cone Models for a Pile Foundation, *Piles under Dynamic Loads*, Edited by S. Prakash. Geotechnical Special Publication No. 34, ASCE (1992): 94-113.

[44] J.P. Wolf and A. Paronesso, Lumped-Parameter Model for a Rigid Cylindrical Foundation Embedded in a Soil Layer on Rigid Rock, *Earthquake Engineering and Structural Dynamics*, 21 (1992): 1021-1038.

[45] J.P. Wolf and J.W. Meek, Cone Models for a Soil Layer on Flexible Rock Half-space, *Earthquake Engineering and Structural Dynamics*, 22 (1993): 185-193.

[46] J.P. Wolf and J.W. Meek, Insight on 2D- versus 3D-Modelling of Surface Foundations via Strength-of-Materials Solutions for Soil Dynamics, *Earthquake Engineering and Structural Dynamics*, 23 (1994): 91-112.

[47] J.P. Wolf and J.W. Meek, Rotational Cone Models for a Soil Layer on Flexible Rock Half-space, *Earthquake Engineering and Structural Dynamics*, 23 (1994): 909-925.

[48] J.P. Wolf and J.W. Meek, Dynamic Stiffness of Foundation on Layered Soil Halfspace Using Cone Frustums, *Earthquake Engineering and Structural Dynamics* , 23 (1994): 1079-1095.

[49] J.P. Wolf and J.W. Meek, Linear Seismic Soil-Structure Interaction Using Simple Physical Models of the Soil, *Proceedings of Fifth US National Conference on Earthquake Engineering*, Chicago 1994, Vol. IV: 5-14.

[50] J.P. Wolf, *Foundation Vibration Analysis Using Simple Physical Models*, Englewood Cliffs, NJ: Prentice-Hall, 1995.

[51] J.P. Wolf, Discussion on a paper by A.S. Veletsos and A.H. Younan, *Earthquake Engineering and Structural Dynamics*, 24 (1995): 1287-1291.

[52] H.L. Wong and J.E. Luco, Tables of Influence Functions for Square Foundations on Layered Media, *Soil Dynamics and Earthquake Engineering*, 4 (1985): 64-81.

[53] H.L. Wong and J.E. Luco, Dynamic Interaction between Rigid Foundations in a Layered Half-space, *Soil Dynamics and Earthquake Engineering*, 5 (1986): 149-158.

Appendix. Bare Essentials For Practical Application

The book *Foundation Vibration Analysis Using Simple Physical Models* [50] contains a summary at the end of each chapter with the key findings and relations. Of the latter those equations which are necessary to analyze practical cases are listed in the following. The subdivision corresponds to the chapters of the book [50] which should be consulted for a complete description including derivations and examples. Other tables for the analysis of foundations concentrating on harmonic loading are specified in the handbook [9].

A.1 Foundation on Surface of Homogeneous Soil Halfspace

A.1.1 Cone Model

For all components of motion a rigid basemat with area A_0 and (polar) moment of inertia I_0 on the surface of a homogeneous soil halfspace (three-dimensional foundation) with Poisson's ratio υ, shear-wave velocity c_s, dilatational-wave velocity c_p and density ρ (Fig. A-1) can be modeled as a truncated semi-infinite cone of equivalent radius r_0, apex height z_0 and wave velocity c (Fig. A-2a and Fig. A-3). For the horizontal and torsional cones deforming in shear the appropriate wave velocity c equals c_s. For the vertical and rocking cones deforming axially c equals c_p for $\upsilon \leq 1/3$ and is limited to $2c_s$ for $1/3 < \upsilon \leq 1/2$. The translational cone model for the displacement u_0 is dynamically equivalent to the spring K- and dashpot C-system (Fig. A-2b). The rotational cone for the rotation ϑ_0 corresponds exactly to the discrete-element models with one internal degree of freedom ϑ_1 and a small number of springs(s) K_ϑ, dashpot(s) C_ϑ and in the monkey-tail configuration a mass moment of inertia M_ϑ (Fig. A-2c). All coefficients are frequency independent. For the vertical and rocking motions in the case of nearly-incompressible soil ($1/3 < \upsilon \leq 1/2$), a trapped mass ΔM and a trapped mass moment of inertia ΔM_ϑ assigned to the basemat arise. The properties of the cones and the discrete-element models which are all that is necessary for the modeling of a basemat of arbitrary shape on the surface of the soil (e.g. in a general-purpose structural dynamics program working directly in the time domain) are summarized in a nutshell in Table A-1.

$$c_s = \sqrt{\frac{G}{\rho}} = \sqrt{\frac{E_c}{2\rho}\frac{1-2\upsilon}{1-\upsilon}} \qquad \text{shear modulus } G$$

$$c_p = \sqrt{\frac{E_c}{\rho}} = \sqrt{2\frac{G}{\rho}\frac{1-\upsilon}{1-2\upsilon}} \qquad \text{constrained modulus } E_c$$

Static-Stiffness Coefficient

$$K_h = \frac{8Gr_0}{2-\upsilon} \quad \text{horizontal} \qquad K_v = \frac{4Gr_0}{1-\upsilon} \quad \text{vertical}$$

$$K_r = \frac{8Gr_0^3}{3(1-\upsilon)} \quad \text{rocking} \qquad K_t = \frac{16}{3}Gr_0^3 \quad \text{torsional}$$

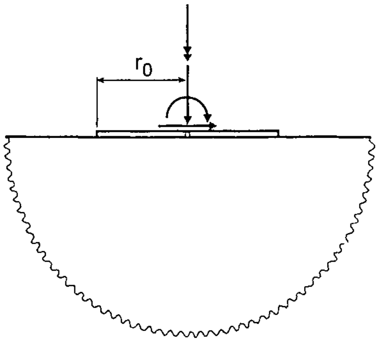

Fig. A-1 Disk on surface of homogeneous soil halfspace.

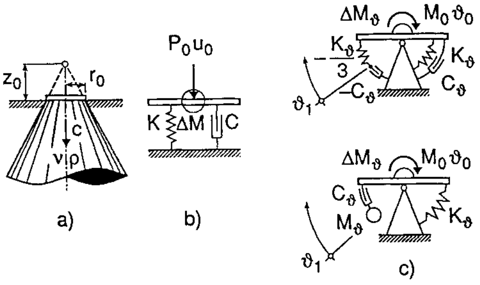

Fig. A-2 Cone model and equivalent discrete-element model.
a) Cone
b) Discrete-element model for translation
c) Discrete-element models for rotation.

Radiation-Dashpot Coefficient (high-frequency behavior)

$C = \rho c A_0$ translational $\quad C_\vartheta = \rho c I_0$ rotational

Translational Cone

Stiffness Formulation

Interaction force-displacement relationship (Fig. A-2b)

$$P_0(t) = Ku_0(t) + C\dot{u}_0(t) + \Delta M\ddot{u}_0(t)$$

($\Delta M=0$ for horizontal motion and for vertical motion when $\upsilon \leq 1/3$)

Dynamic-stiffness coefficient for harmonic loading

$$S(a_0) = K\left[k(a_0) + ia_0c(a_0)\right]$$

with dimensionless spring coefficient $k(a_0)$ for horizontal motion and for vertical motion when $\upsilon \leq 1/3$

$$k(a_0)=1$$

for vertical motion when $1/3<\upsilon\leq 1/2$

$$k(a_0) = 1 - 0.6\pi(1-\upsilon)\left(\upsilon - \frac{1}{3}\right)a_0^2$$

dimensionless damping coefficient

$$c(a_0) = \frac{z_0}{r_0}\frac{c_s}{c}$$

and dimensionless frequency

$$a_0 = \frac{\omega r_0}{c_s}$$

Table A-1 Key Expressions to Model a Three-Dimensional Foundation on the Surface of a Homogeneous Soil Halfspace with a Cone

Motion	Horizontal	Vertical		Rocking		Torsional
Equivalent Radius r_0	$\sqrt{\frac{A_0}{\pi}}$	$\sqrt{\frac{A_0}{\pi}}$		$\sqrt[4]{\frac{4I_0}{\pi}}$		$\sqrt[4]{\frac{2I_0}{\pi}}$
Aspect Ratio $\frac{z_0}{r_0}$	$\frac{\pi}{8}(2-\upsilon)$	$\frac{\pi}{4}(1-\upsilon)\left(\frac{c}{c_s}\right)^2$		$\frac{9\pi}{32}(1-\upsilon)\left(\frac{c}{c_s}\right)^2$		$\frac{9\pi}{32}$
Poisson's Ratio υ	all υ	$\leq\frac{1}{3}$	$\frac{1}{3}<\upsilon\leq\frac{1}{2}$	$\leq\frac{1}{3}$	$\frac{1}{3}<\upsilon\leq\frac{1}{2}$	all υ
Wave Velocity c	c_s	c_p	$2c_s$	c_p	$2c_s$	c_s
Trapped Mass ΔM ΔM_ϑ	0	0	$2.4\left(\upsilon-\frac{1}{3}\right)\rho A_0 r_0$	0	$1.2\left(\upsilon-\frac{1}{3}\right)\rho I_0 r_0$	0
Discrete-Element Model	$K=\rho c^2\frac{A_0}{z_0}$ $C=\rho cA_0$			$K_\vartheta=3\rho c^2\frac{I_0}{z_0}$ $C_\vartheta=\rho cI_0$ $M_\vartheta=\rho I_0 z_0$		

Flexibility Formulation

Displacement-interaction force relationship (Fig. A-2b)
For horizontal motion and for vertical motion when $\upsilon \leq 1/3$

$$u_0(t) = \int_0^t h_1(t-\tau)\frac{P_0(\tau)}{K}d\tau$$

with unit-impulse response function

$$h_1(t) = \frac{c}{z_0}e^{-\frac{c}{z_0}t} \qquad t \geq 0$$
$$= 0 \qquad t < 0$$

The convolution integral with the first-order term $h_1(t)$ (Duhamel integral) at time station n can be evaluated efficiently by the recursive procedure expressing the displacement at time station n as a linear function of the displacement at the previous time station n-1 and of the normalized interaction forces at the same two time stations

$$u_{0n} = au_{0n-1} + b_0\frac{P_{0n}}{K} + b_1\frac{P_{0n-1}}{K}$$

where the recursive coefficients are specified as (Δt=time step)

$$a = e^{-\frac{c\Delta t}{z_0}}$$

$$b_0 = 1 + \frac{e^{-\frac{c\Delta t}{z_0}} - 1}{\frac{c\Delta t}{z_0}} \qquad b_1 = \frac{-e^{-\frac{c\Delta t}{z_0}} + 1}{\frac{c\Delta t}{z_0}} - e^{-\frac{c\Delta t}{z_0}}$$

The unconditionally stable recursive evaluation which is suitable even for a hand calculation is exact when $P_0(t)$ is piecewise linear.
For vertical motion when $1/3 < \upsilon \leq 1/2$

$$u_0(t) = \int_0^t h_4(t-\tau)\frac{P(\tau)}{K}d\tau$$

$$\text{with} \left(\gamma = \frac{\pi}{2.4}\frac{1-\upsilon}{\upsilon - \frac{1}{3}}\right)$$

$$h_4(t) = \frac{4}{\pi(1-\upsilon)}\frac{c_s}{r_0}\frac{1}{\sqrt{1-\frac{4}{\gamma}}}e^{-\frac{1}{2.4\left(\upsilon-\frac{1}{3}\right)}\frac{c_s}{r_0}t}$$

$$*\sinh\frac{1}{2.4\left(\upsilon-\frac{1}{3}\right)}\frac{c_s}{r_0}\sqrt{1-\frac{4}{\gamma}}t \qquad t\geq 0$$

$$=0 \qquad t<0$$

The recursive evaluation with the second-order term $h_4(t)$ proceeds as

$$u_{0n}=a_1u_{0n-1}+a_2u_{0n-2}+b_0\frac{P_{0n}}{K}+b_1\frac{P_{0n-1}}{K}+b_2\frac{P_{0n-2}}{K}$$

where

$$a_1=2e^{-\frac{1}{2.4\left(\upsilon-\frac{1}{3}\right)}\frac{c_s}{r_0}\Delta t}\cosh\frac{1}{2.4\left(\upsilon-\frac{1}{3}\right)}\frac{c_s}{r_0}\sqrt{1-\frac{4}{\gamma}}\Delta t$$

$$a_2=-e^{-\frac{1}{1.2\left(\upsilon-\frac{1}{3}\right)}\frac{c_s}{r_0}\Delta t}$$

and

$$b_0=\frac{r(\Delta t)}{\Delta t} \qquad b_1=\frac{r(2\Delta t)-(2+a_1)r(\Delta t)}{\Delta t}$$

$$b_2=\frac{r(3\Delta t)-(2+a_1)r(2\Delta t)+(1+2a_1-a_2)r(\Delta t)}{\Delta t}$$

with $r(t)=r_4(t)$

$$r_4(t)=-\frac{\pi(1-\upsilon)}{2}\frac{r_0}{c_s}+t+\frac{1-\frac{2}{\gamma}}{\sqrt{1-\frac{4}{\gamma}}}\frac{\pi(1-\upsilon)}{2}\frac{r_0}{c_s}e^{-\frac{1}{2.4\left(\upsilon-\frac{1}{3}\right)}\frac{c_s}{r_0}t}$$

$$*\sinh\frac{1}{2.4\left(\upsilon-\frac{1}{3}\right)}\frac{c_s}{r_0}\sqrt{1-\frac{4}{\gamma}}\ t$$

$$+\frac{\pi(1-\upsilon)}{2}\frac{r_0}{c_s}e^{-\frac{1}{2.4\left(\upsilon-\frac{1}{3}\right)}\frac{c_s}{r_0}t} \qquad t\geq 0$$

$$*\cosh\frac{1}{2.4\left(\upsilon-\frac{1}{3}\right)}\frac{c_s}{r_0}\sqrt{1-\frac{4}{\gamma}}\ t$$

$$=0 \qquad t<0$$

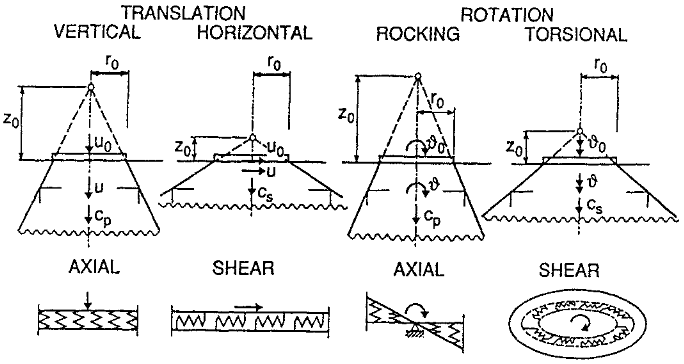

Fig. A-3 Cones for various degrees of freedom with corresponding apex ratio (opening angle), wave-propagation velocity and distortion.

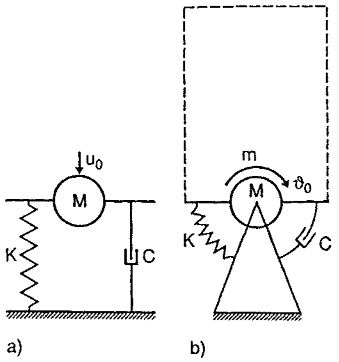

Fig. A-4 Standard spring-dashpot-mass model with no internal degree of freedom for

a) Translational motion.
b) Rotational motion.

Rotational Cone

Stiffness Formulation

Interaction moment-rotation relationship (Fig. A-2c)

$$M_0(t) = K_\vartheta \vartheta_0(t) + C_\vartheta \dot{\vartheta}_0(t) + \Delta M_\vartheta \ddot{\vartheta}_0(t) - \int_0^t h_1(t-\tau)\ C_\vartheta \dot{\vartheta}_0(\tau) d\tau$$

($\Delta M_\vartheta = 0$ for torsional motion and for rocking motion when $\upsilon \leq 1/3$)

The recursive evaluation of the convolution integral with $h_1(t)$ is described above.

Dynamic-stiffness coefficient for harmonic loading

$$S_\vartheta(a_0) = K_\vartheta\left[k_\vartheta(a_0) + ia_0c_\vartheta(a_0)\right]$$

with dimensionless spring coefficient $k_\vartheta(a_0)$ for torsional motion and for rocking motion when $\upsilon\leq 1/3$

$$k_\vartheta(a_0) = 1 - \frac{1}{3}\frac{a_0^2}{\left(\frac{r_0c}{z_0c_s}\right)^2 + a_0^2}$$

for rocking motion when $1/3<\upsilon\leq 1/2$

$$k_\vartheta(a_0)=1-\frac{1}{3}\frac{a_0^2}{\left(\frac{16}{9\pi(1-\upsilon)}\right)^2+a_0^2} - \frac{0.9\pi(1-\upsilon)\left(\upsilon-\frac{1}{3}\right)}{8}a_0^2$$

and dimensionless damping coefficient

$$c_\vartheta(a_0) = \frac{z_0c_s}{3r_0c}\frac{a_0^2}{\left(\frac{r_0c}{z_0c_s}\right)^2 + a_0^2}$$

<u>Flexibility Formulation</u>

Rotation-interaction moment relationship (Fig. A-2c)

For torsional motion and for rocking motion when $\upsilon\leq 1/3$

$$\vartheta_0(t)=\int_0^t h_2(t-\tau)\frac{M_0(\tau)}{K_\vartheta}d\tau$$

with unit-impulse response function

$$\begin{aligned} h_2(t) &= \frac{c}{z_0}e^{-\frac{3}{2}\frac{c}{z_0}t} \\ &\quad *\left(3\cos\frac{\sqrt{3}}{2}\frac{c}{z_0}t-\sqrt{3}\sin\frac{\sqrt{3}}{2}\frac{c}{z_0}t\right) \quad t \geq 0 \\ &= 0 \quad\quad t < 0 \end{aligned}$$

The recursive evaluation with the second order term $h_2(t)$ proceeds as:

$$\vartheta_{0n} = a_1\vartheta_{0n-1} + a_2\vartheta_{0n-2} + b_0\frac{M_{0n}}{K_\vartheta} + b_1\frac{M_{0n-1}}{K_\vartheta} + b_2\frac{M_{0n-2}}{K_\vartheta}$$

where

$$a_1 = 2e^{-\frac{3}{2}\frac{c\Delta t}{z_0}}\cos\frac{\sqrt{3}}{2}\frac{c\Delta t}{z_0}$$

$$a_2 = -e^{-3\frac{c\Delta t}{z_0}}$$

and substituting $r(t) = r_2(t)$

$$\begin{aligned} r_2(t) &= t - \frac{2\sqrt{3}}{3}\frac{z_0}{c}\, e^{-\frac{3}{2}\frac{ct}{z_0}} \sin\frac{\sqrt{3}}{2}\frac{ct}{z_0} && t \geq 0 \\ &= 0 && t < 0 \end{aligned}$$

b_0, b_1 and b_2 follow from the equations specified in connection with the convolution with $h_4(t)$(end of Section Translational Cone).

A.1.2 Spring-Dashpot-Mass Model

Standard Spring-Dashpot-Mass Model

Besides a spring with the static-stiffness coefficient K ($=K_\vartheta$ for rotational motion) a dashpot and a mass (mass moment of inertia for rotational motion) are present (Fig. A-4) with the coefficients

$$C = \frac{r_0}{c_s}\,\gamma\, K \qquad M = \frac{r_0^2}{c_s^2}\,\mu\, K$$

γ and μ are specified in Table A-2 with the mass moment of inertia of the disk (rigid structure) m.

Table A-2 Static Stiffness and Dimensionless Coefficients of the Standard Spring-Dashpot-Mass Model for a Disk with Mass on a Homogeneous Halfspace

		Dimensionless Coefficients of	
	Static Stiffness K	Dashpot γ	Mass μ
Horizontal	$\frac{8Gr_0}{2-\nu}$	0.58	0.095
Vertical	$\frac{4Gr_0}{1-\nu}$	0.85	0.27
Rocking	$\frac{8Gr_0^3}{3(1-\nu)}$	$\frac{0.3}{1+\frac{3(1-\nu)m}{8r_0^5\rho}}$	0.24
Torsional	$\frac{16Gr_0^3}{3}$	$\frac{0.433}{1+\frac{2m}{r_0^5\rho}}\sqrt{\frac{m}{r_0^5\rho}}$	0.045

Fundamental Spring-Dashpot-Mass Model

Besides a spring with the static-stiffness coefficient K (= K_ϑ for rotational motion) and a direct dashpot C_0 connecting the basemat node with mass M_0 (mass moment of inertia for rotational motion) to the rigid support (Fig. A-5), an internal degree of freedom with its own mass M_1 (mass moment of inertia for rotational motion) is introduced which is attached to the disk node by a dashpot C_1

$$C_0 = \frac{r_0}{c_s}\gamma_0 K \qquad C_1 = \frac{r_0}{c_s}\gamma_1 K$$

$$M_0 = \frac{r_0^2}{c_s^2}\mu_0 K \qquad M_1 = \frac{r_0^2}{c_s^2}\mu_1 K$$

γ_0, γ_1, μ_0 and μ_1 are specified in Table A-3.

A.1.3 Wedge Model

For the horizontal and rocking motions a rigid basemat with width 2b on the surface of a homogeneous soil halfplane (two-dimensional strip foundation) can be modeled with a truncated semi-infinite wedge with apex height z_0 and wave velocity c (Fig. A-6). For the horizontal wedge deforming in shear c equals c_s and for the rocking wedge deforming axially c equals c_p for $\upsilon<1/3$ and is limited to $2c_s$ for $1/3<\upsilon\leq 1/2$. For the rocking motion in the case of the nearly-incompressible soil ($1/3<\upsilon\leq 1/2$) a trapped mass moment of inertia ΔM_ϑ assigned to the basemat arises. The properties are summarized in Table A-4.

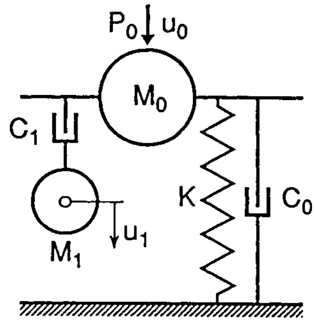

Fig. A-5 Fundamental spring-dashpot-mass model (monkey-tail arrangement) with one internal degree of freedom.

Static-Stiffness Coefficient

$K_h = 0$ horizontal $\qquad K_r = \dfrac{\pi G b^2}{2(1-\upsilon)}$ rocking

Radiation-Dashpot Coefficient (high-frequency behavior)

$C_h = \rho c_s 2b$ horizontal $\qquad C_r = \rho c \dfrac{8b^3}{12}$ rocking

Table A-3 Static Stiffness and Dimensionless Coefficients of the Fundamental Spring-Dashpot-Mass Model (Monkey-Tail Arrangement) for a Disk on a Homogeneous Halfspace

		Dimensionless Coefficients of			
		Dashpots		Masses	
	Static Stiffness K	γ_0	γ_1	μ_0	μ_1
Horizontal	$\frac{8Gr_0}{2-\upsilon}$	$0.78-0.4\upsilon$	- —	—	—
Vertical	$\frac{4Gr_0}{1-\upsilon}$	0.8	$0.34-4.3\ \upsilon^4$	$\upsilon<\frac{1}{3}\quad 0$ $\upsilon>\frac{1}{3}\quad 0.9\left(\upsilon-\frac{1}{3}\right)$	$0.4-4\ \upsilon^4$
Rocking	$\frac{8Gr_0^3}{3(1-\upsilon)}$	—	$0.42-0.3\ \upsilon^2$	$\upsilon<\frac{1}{3}\quad 0$ $\upsilon>\frac{1}{3}\quad 0.16\left(\upsilon-\frac{1}{3}\right)$	$0.34-0.2\ \upsilon^2$
Torsional	$\frac{16Gr_0^3}{3}$	—	0.29	—	0.2
		(0.017)	(0.291)	(—)	(0.171)

Dynamic-Stiffness Coefficient for Harmonic Loading

$$\text{horizontal} \quad S(b_0)=\frac{b_0 H_1^{(2)}(b_0)}{H_0^{(2)}(b_0)}\,\frac{\rho c_s^2\, 2b}{z_0}$$

$$\text{rocking} \quad S(b_0)=\frac{b_0 H_2^{(2)}(b_0)}{H_1^{(2)}(b_0)}\,\frac{\rho c^2}{z_0}\,\frac{8b^3}{12}$$

with dimensionless frequency parameter defined with respect to properties of wedge

$$b_0=\frac{\omega z_0}{c}$$

and Hankel functions of second kind $H^{(2)}$.

Table A-4 Key Expressions to Model a Two-Dimensional Foundation on the Surface of a Homogeneous Soil Halfplane with a Wedge

Motion	Horizontal	Rocking	
Aspect Ratio $\frac{z_0}{b}$	$\frac{2-\upsilon}{\pi}$	$\frac{8(1-\upsilon)}{3\pi}\,\frac{c^2}{c_s^2}$	
Poisson's Ratio υ	all υ	$\leq\frac{1}{3}$	$\frac{1}{3}<\upsilon\leq\frac{1}{2}$
Wave Velocity c	c_s	c_p	$2c_s$
Trapped Mass Moment of Inertia ΔM_ϑ	0	0	$\frac{3}{4}\left(\upsilon-\frac{1}{3}\right)\rho\frac{8b^3}{12}b$

A1.4 Material Damping

Material damping is introduced in the frequency domain based on the correspondence principle applied to the elastic solution. For non-causal linear-hysteretic damping the shear modulus G and constrained modulus E_c are multiplied by $1 + 2i\zeta_g$ (ζ_g = hysteretic-damping ratio), resulting in the solution for the damped case. The corresponding spring and damping coefficients $k_\zeta(a_0)$, $c_\zeta(a_0)$ are expressed approximately as a function of the elastic values $k(a_0)$, $c(a_0)$

$$k_\zeta(a_0)=k(a_0)-\zeta_g a_0 c(a_0)$$

$$c_\zeta(a_0)=c(a_0)+\frac{2\zeta_g}{a_0}k(a_0)$$

Table A-5 Dimensionless Coefficients of the Basic Spring-Dashpot-Mass Model for a Disk on the Surface of a Soil Layer on Rigid Rock

Horizontal			Vertical			Rocking			Torsional
Poisson's Ratio υ									
0	1/3	0.45	0	1/3	0.45	0	1/3	0.45	
-.109636 E+02	-.125658 E+02	-.107091 E+02	-.185216 E+02	-.312572 E+02	-.585650 E+02	-.538137 E+01	-.127100 E+02	-.125057 E+02	-.920277 E+01
-.199616 E+02	-.100143 E+02	-.277613 E+02	-.689058 E+02	+.564651 E+01	+.533868 E+02	-.118019 E+02	-.127000 E+01	-.102097 E+02	-.488643 E+01
-.596293 E+03	-.236814 E+03	-.837270 E+03	-.803915 E+04	-.297570 E+04	-.972054 E+05	-.370561 E+03	-.106411 E+03	-.114401 E+05	-.762034 E+02
+.262006 E+02	+.172890 E+02	+.350886 E+02	+.781698 E+02	+.101028 E+02	-.297301 E+02	+.152717 E+02	+.665102 E+01	+.171002 E+02	+.104850 E+02
-.423955 E+01	-.391585 E+01	-.443420 E+01	-.564579 E+01	-.620122 E+01	-.533597 E+01	-.152562 E+01	-.168764 E+01	-.159579 E+01	-.209847 E+01
-.144980 E+02	-.969345 E+01	-.164981 E+02	-.573623 E+02	-.372925 E+02	-.162817 E+03	-.511671 E+01	-.464871 E+01	-.205038 E+02	-.424955 E+01
+.176380 E+02	+.128349 E+02	+.196381 E+02	+.618023 E+02	+.435725 E+02	+.173237 E+03	+.622671 E+01	+.621871 E+01	+.231038 E+02	+.581955 E+01
-.444888 E+02	-.177585 E+02	-.804875 E+02	-.355432 E+03	-.896786 E+02	-.759400 E+03	-.136958 E+02	-.294864 E+01	-.748688 E+02	-.501042 E+01
-.101741 E+02	-.756096 E+01	-.103098 E+02	-.869429 E+01	-.178038 E+02	-.211241 E+02	-.558202 E+01	-.315920 E+01	-.544861 E+01	-.584813 E+01
-.711128 E+01	+.221036 E+01	+.353643 E+00	-.211429 E+02	+.869558 E+01	+.237930 E+02	-.260867 E+01	+.429538 E+00	+.544528 E+01	+.779373 E+00
-.376551 E+02	-.183990 E+02	-.386290 E+02	-.301954 E+03	-.648930 E+02	-.574768 E+04	-.120186 E+02	-.563639 E+00	-.495529 E+02	-.267204 E+01
+.114651 E+02	+.370791 E+01	+.631911 E+01	+.266455 E+02	+.167960 E+00	-.104560 E+02	+.553603 E+01	+.268680 E+01	-.714571 E+00	+.448746 E+01
-.563146 E+01	-.169515 E+01	-.312323 E+01	-.635435 E+01	-.300736 E+01	-.885920 E+01	-.180105 E+01	-.217449 E+00	-.226588 E+01	-.873265 E+00
-.853329 E+01	-.484337 E+01	-.900332 E+01	-.118278 E+02	-.967485 E+01	-.348879 E+02	-.209944 E+01	-.485884 E-01	-.872006 E+00	-.664093 E+00
+.116733 E+02	+.798337 E+01	+.121433 E+02	+.162678 E+02	+.159548 E+02	+.453079 E+02	+.320944 E+01	+.161859 E+01	+.347201 E+01	+.223409 E+01
-.125108 E+02	-.142805 E+02	-.222875 E+02	-.438319 E+02	-.104698 E+02	-.156304 E+03	-.166034 E+01	-.550887 E-01	-.105920 E+01	-.758683 E+00
-.500393 E+01	-.569922 E+01	-.635602 E+01	-.650348 E+01	-.866267 E+01	-.939217 E+01	-.197103 E+01	-.131566 E+01	-.185845 E+01	-.317223 E+01
+.117908 E+01	+.113372 E+01	+.126563 E+01	+.212837 E+01	+.360033 E+01	+.591506 E+01	-.908392 E+00	-.159178 E+01	+.140842 E+01	-.110204 E+02
-.531658 E+01	-.627809 E+01	-.861155 E+01	-.111486 E+02	-.206851 E+02	-.294639 E+02	+.320667 E+00	+.889908 E+00	-.198123 E+01	-.272014 E+02
+.330564 E+01	+.414181 E+01	+.444955 E+01	+.290606 E+01	+.353509 E+01	+.239510 E+01	+.280516 E+01	+.228996 E+01	+.228257 E+00	+.133791 E+02
-.753687 E+00	-.123420 E+01	-.118324 E+01	-.147587 E+01	-.301652 E+01	-.652332 E+01	-.111891 E+01	-.117566 E+01	-.166191 E+01	-.175255 E+01
-.320391 E+01	-.343160 E+01	-.476257 E+01	-.545496 E+01	-.633133 E+01	-.153512 E+01	-.192001 E-01	-.120420 E+00	-.608065 E-01	-.576183 E+00
+.634391 E+01	+.657160 E+01	+.790257 E+01	+.989496 E+01	+.126113 E+02	+.119551 E+02	+.131920 E+01	+.199042 E+01	+.266081 E+01	+.214618 E+01
-.197705 E+02	-.277938 E+02	-.353939 E+02	-.202557 E+02	-.262470 E+02	-.217797 E+01	-.496405 E-02	-.234838 E-01	-.166728 E-01	-.408057 E+00
-.135004 E+02	-.388471 E+01	-.517262 E+01	-.196175 E+01	-.741830 E+01	-.174454 E+02	-.177328 E+01	-.371794 E+01	-.398695 E+01	-.347454 E+01
-.953646 E+01	-.159784 E+02	+.239313 E+00	-.586095 E+00	+.149859 E+01	+.318590 E+01	-.825315 E+01	-.530262 E+01	+.488296 E+01	+.161189 E+00
-.152937 E+02	-.214052 E+02	-.491200 E+01	+.418313 E+00	-.108130 E+02	-.145871 E+03	-.960129 E+00	-.456729 E+01	-.157465 E+02	-.175021 E+00
+.100318 E+02	+.139890 E+02	+.491843 E+01	+.253876 E+01	+.426031 E+01	+.401297 E+01	+.363207 E+01	+.648378 E+01	-.222776 E+01	+.329151 E+01
-.108173 E+01	-.406936 E+00	-.431719 E-01	-.540639 E+00	-.308148 E+00	-.287195 E+01	-.105544 E+01	-.150532 E+01	-.158356 E+01	-.257114 E-01
-.164199 E+01	-.441082 E+00	-.433318 E-01	-.316451 E-02	-.760091 E+00	-.496738 E+01	-.396130 E+00	-.400894 E+00	-.408329 E+00	-.525606 E-02
+.478349 E+01	+.358258 E+01	+.318483 E+01	+.470316 E+01	+.704009 E+01	+.153874 E+02	+.150613 E+01	+.197089 E+01	+.300833 E+01	+.157526 E+01
-.207315 E+00	-.331202 E-01	-.126178 E+00	-.110135 E-02	-.348161 E+00	-.240813 E+01	-.245402 E-01	-.633544 E-01	-.125199 E+00	-.126499 E-02

For Voigt visco-elasticity with damping proportional to frequency (defined as the ratio ζ_0 at ω_0) the factor equals $1+i\omega 2\zeta_0/\omega_0$, and the correspondence principle is applied directly to the discrete-element model (or lumped-parameter model). Each original spring with coefficient K is augmented by a dashpot with coefficient $C = 2(\zeta_0/\omega_0)K$ in parallel, and each original dashpot with coefficient C by a pulley-mass with coefficient $(\zeta_0/\omega_0)C$ (Fig. A-7). Masses in the original model remain unchanged.

For frictional (hysteretic) material damping which preserves causality, non-linear frictional elements replace the augmenting dashpot and pulley-mass. The corresponding forces acting between the nodes with displacements u_0 and u_1 are equal to (sgn () returns the algebraic sign of the argument)

$$P = K\left|\overline{u_0 - u_1}\right| \tan\delta \ \operatorname{sgn}\left(\dot{u}_0 - \dot{u}_1\right)$$

$$P = C\left|\overline{\dot{u}_0 - \dot{u}_1}\right| 0.5 \tan\delta \ \operatorname{sgn}\left(\ddot{u}_0 - \ddot{u}_1\right)$$

with the overbar denoting the short-term memory (current or last peak value) and $\tan\delta = 2\zeta_g$ (δ=friction angle). Incorporation of these frictional elements in the discrete-element model (or spring-dashpot-mass model) permits causal analysis in the time domain taking hysteretic damping independent of frequency into consideration.

These concepts also apply to the spring-dashpot-mass models for a foundation on the surface of a layer on rigid rock (Appendix A2) and for a foundation embedded in a halfspace or in a layer (Appendix A3).

A.2 Foundation on Surface of Soil Layer on Rigid Rock

A.2.1 Unfolded Layered Cone Model

For all components of motion a rigid basemat with equivalent radius r_0 on the surface of a soil layer of depth d resting on rigid rock (Fig. A-8) can be visualized as a folded cone. When unfolded, this layered cone enables a wave pattern to be postulated which incorporates the decay of amplitude as the waves propagate away from the basemat as well as the reflections at rock interface and at the free surface. The aspect ratio z_0/r_0 (opening angle) of the unfolded layered cone is the same as that of the truncated semi-infinite cone used to model a disk on a homogeneous halfspace with the same material properties as the layer (Table A-1).

From the wave pattern it follows that the translation $u_0(t)$ (or rotation $\vartheta_0(t)$) of the basemat on a layer is equal to that of the basemat, with the same load acting, on a homogeneous halfspace ($\bar{u}_0(t)$ or $\bar{\vartheta}_0(t)$) (generating function), augmented by echoes of the previous response (Fig. A-9). The appropriate echo constants are derived for the flexibility formulation, then inverted to obtain the echo constants of the stiffness formulation.

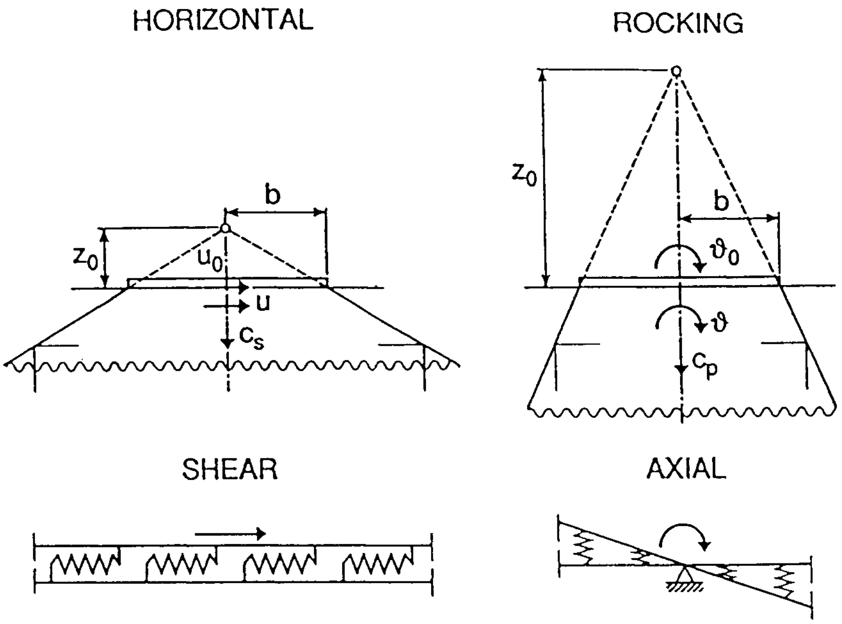

Fig. A-6 Horizontal and rocking wedges with corresponding apex ratio (opening angle), wave-propagation velocity and distortion.

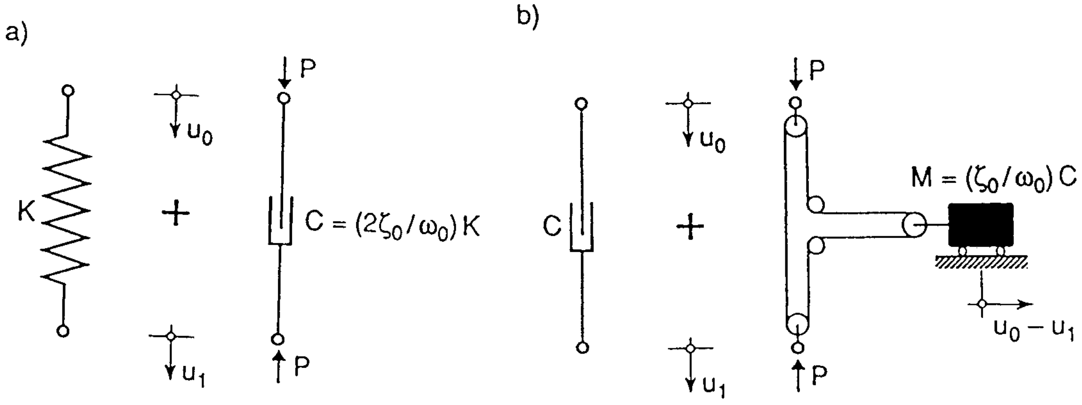

Fig. A-7 Augmenting elements to represent Voigt visco-elasticity.

a) Original spring with augmenting dashpot.

b) Original dashpot with augmenting pulley mass.

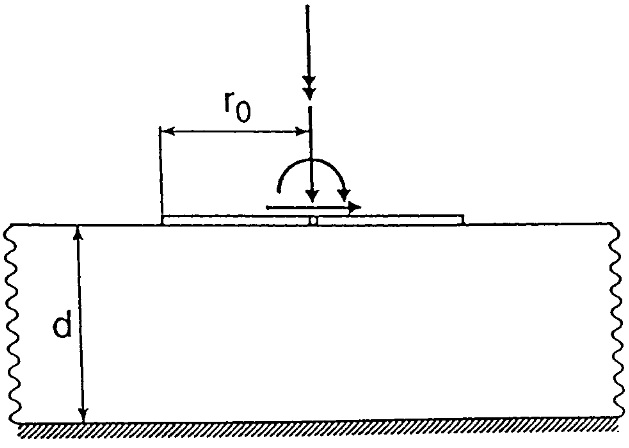

Fig. A-8 Disk on surface of soil layer resting on rigid rock.

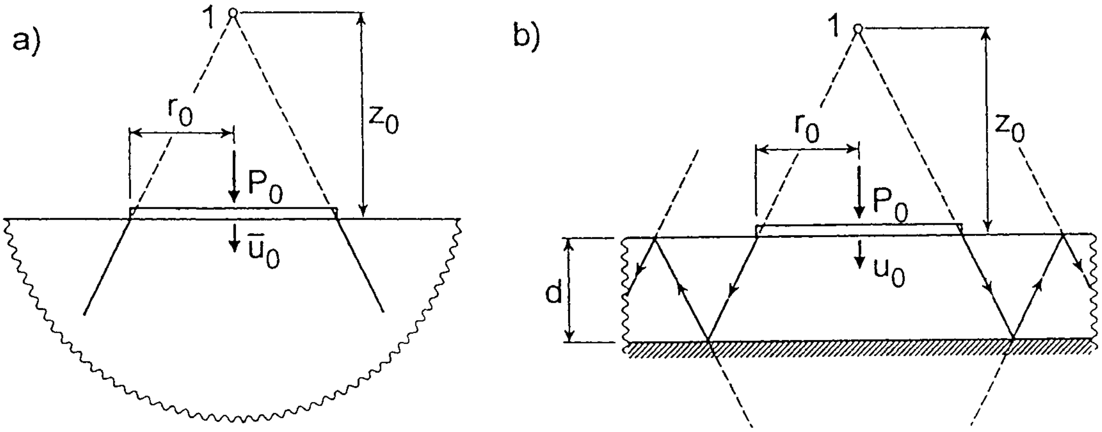

Fig. A-9 Nomenclature for loaded disk in vertical motion on surface of soil.

a) Halfspace with generating displacement.

b) Layer with resulting displacement.

Echo Constant

Echo formula for translation in a flexibility formulation

$$u_0(t)=\sum_{j=0}^{k} e_j^F \bar{u}_0(t-jT)$$

with flexibility echo constants

$$e_0^F = 1 \qquad e_j^F=\frac{2(-1)^j}{1+j\kappa} \qquad j \geq 1$$

and

$$T=\frac{2d}{c} \qquad \kappa=\frac{2d}{z_0}$$

and appropriate wave velocity c and aspect height z_0 (Table A-1). The integer k is equal to the largest index j for which the argument t-jT of $\bar{u}_0$ is positive.

Echo formula for rotation in a flexibility formulation

$$\vartheta_0(t) = \sum_{j=0}^{k} e_{0j}^F \bar{\vartheta}_0(t-jT) + \sum_{j=0}^{k} e_{1j}^F \bar{\vartheta}_1(t-jT)$$

with flexibility echo constants

$$e_{00}^F=1 \quad e_{0j}^F=\frac{2(-1)^j}{(1+j\kappa)^2} \qquad j\geq 1$$

$$e_{10}^F=0 \quad e_{1j}^F=2(-1)^j\left[\frac{1}{(1+j\kappa)^3}-\frac{1}{(1+j\kappa)^2}\right] \qquad j\geq 1$$

and

$$\bar{\vartheta}_1(t)=\int_0^t h_1(t-\tau)\bar{\vartheta}_0(\tau)\, d\tau$$

with unit-impulse response function

$$\begin{aligned} h_1(t) &= \frac{c}{z_0}e^{-\frac{c}{z_0}t} \qquad && t \geq 0 \\ &= 0 && t < 0 \end{aligned}$$

Alternatively, using pseudo-echo constants e_{rm}^F (influence functions) which follow from e_{0j}^F and e_{1j}^F (see [50], p. 175-177) the echo formula for rotation equals

$$\vartheta_0(t) = \sum_{m=0}^{k} e_{rm}^F \bar{\vartheta}_0(t-m\Delta t)$$

with time step Δt.

Echo formula for translation in a stiffness formulation

$$\bar{u}_0(t) = \sum_{j=0}^{k} e_j^K u_0(t-jT)$$

with stiffness echo constants

$$e_0^K = 1 \qquad e_j^K = -\sum_{\ell=0}^{j-1} e_\ell^K e_{j-\ell}^F \quad j \geq 1$$

and for rotation

$$\bar{\vartheta}_0(t) = \sum_{m=0}^{k} e_{rm}^K \vartheta_0(t - m\Delta t)$$

with stiffness echo constants

$$e_{r0}^K = 1 \qquad e_{rm}^K = -\sum_{\ell=0}^{m-1} e_{r\ell}^K e_{rm-\ell}^F \qquad j \geq 1$$

Flexibility Formulation

In a flexibility formulation, in the first step, the prescribed interaction force $P_0(t)$ (or moment $M_0(t)$) is applied to the cone modeling a disk on the associated homogeneous halfspace with the same material properties as the layer, resulting in the surface displacement $\bar{u}_0(t)$ (or rotation $\bar{\vartheta}_0(t)$) using the procedure described in Section A1.1 (Fig. A-9a). In the second step, the displacement $u_0(t)$ (or rotation $\vartheta_0(t)$) of the basemat on the layer follows from $\bar{u}_0(t)$ (or $\bar{\vartheta}_0(t)$) using the corresponding echo formula.

Stiffness Formulation

In a stiffness formulation, in the first step, the prescribed surface displacement $u_0(t)$ (or rotation $\vartheta_0(t)$) is converted to the displacement $\bar{u}_0(t)$ (or rotation $\bar{\vartheta}_0(t)$) of a disk on the associated homogeneous halfspace using the corresponding echo formula. In the second step, insertion into the interaction force-displacement relationship of the cone modelling a disk on the associated homogeneous halfspace leads to the interaction force $P_0(t)$ (or moment $M_0(t)$) acting on the basemat using the procedure described in Section A1.1 (Fig. A-9a).

Static-Stiffness Coefficient

$$K^L = K \frac{1}{\sum\limits_{j=0}^{\infty} e_j^F} \qquad K_\vartheta^L = K_\vartheta \frac{1}{\sum\limits_{j=0}^{\infty} e_{0j}^F + \sum\limits_{j=0}^{\infty} e_{1j}^F}$$

index L for disk on layer, no index for disk on homogeneous halfspace with material properties of layer

$$\begin{array}{lll}
K_h^L = \dfrac{8Gr_0}{2-\upsilon}\left(1+\dfrac{1}{2}\dfrac{r_0}{d}\right) & & \text{horizontal} \\
K_v^L = \dfrac{4Gr_0}{1-\upsilon}\left(1+1.3\dfrac{r_0}{d}\right) & & \text{vertical} \\
K_r^L = \dfrac{8Gr_0^3}{3(1-\upsilon)}\left(1+\dfrac{1}{6}\dfrac{r_0}{d}\right) & & \text{rocking} \\
K_t^L = \dfrac{16}{3}Gr_0^3\left(1+\dfrac{1}{10}\dfrac{r_0}{d}\right) & & \text{torsional}
\end{array}$$

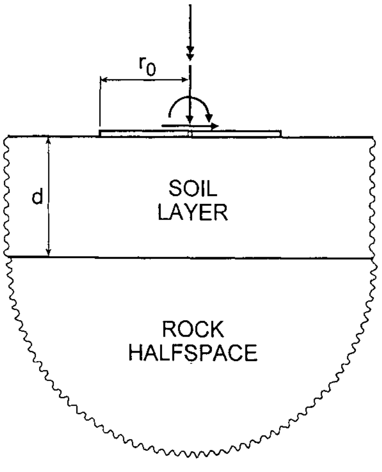

Fig. A-10 Disk on surface of soil layer resting on flexible rock halfspace.

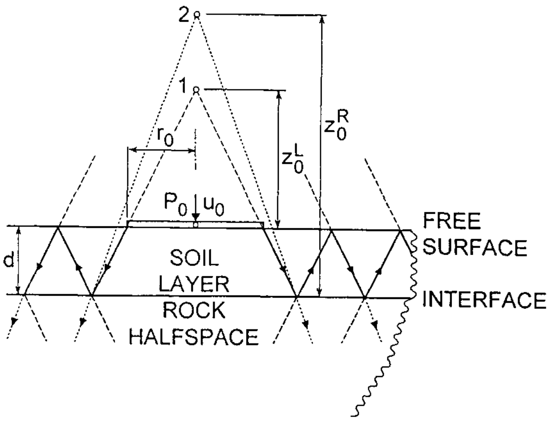

Fig. A-11 Disk in vertical motion on soil layer resting on flexible rock halfspace with wave pattern in corresponding cones.

Dynamic-Stiffness Coefficient for Harmonic Loading

translation

$$S(\omega) = K\frac{1+i\dfrac{\omega T}{\kappa}}{1+2\sum\limits_{j=1}^{\infty}(-1)^j\dfrac{e^{-ij\omega T}}{1+j\kappa}}$$

rotation

$$S_\vartheta(\omega) = K_\vartheta$$

$$*\frac{1-\dfrac{1}{3}\dfrac{(\omega T)^2}{\kappa^2+(\omega T)^2}+i\dfrac{\omega T}{3\kappa}\dfrac{(\omega T)^2}{\kappa^2+(\omega T)^2}}{1+\dfrac{2}{1+i\dfrac{\omega T}{\kappa}}\left(\sum\limits_{j=1}^{\infty}(-1)^j\dfrac{e^{-ij\omega T}}{(1+j\kappa)^3}+i\dfrac{\omega T}{\kappa}\sum\limits_{j=1}^{\infty}(-1)^j\dfrac{e^{-ij\omega T}}{(1+j\kappa)^2}\right)}$$

with static-stiffness coefficients of homogeneous halfspace with material properties of layer K, K_ϑ (Table A-2).

Foundation on Surface of Soil Layer on Flexible Rock Halfspace

The unfolded cone can be generalized to the case of a layer on flexible rock (Fig. A-10) considering the refraction at the layer-rock interface. The only modification consists of replacing in the expressions for the echo constants the reflection coefficient associated with the rigid rock,

-1, by the corresponding value -α for the flexible rock. All flexibility and stiffness formulations for the dynamic analysis remain valid.

$$-\alpha = \frac{\dfrac{\rho_L c_L^2}{z_0^L + d} - \dfrac{\rho_R c_R^2}{z_0^R}}{\dfrac{\rho_L c_L^2}{z_0^L + d} + \dfrac{\rho_R c_R^2}{z_0^R}} \quad \left(= \frac{\rho_L c_L^2 - \rho_R c_R^2}{\rho_L c_L^2 + \rho_R c_R^2} \text{ for } \upsilon_L = \upsilon_R \right)$$

Indices L and R refer to the layer and the rock. z_0^R measured from the interface determined with the properties of the rock halfspace (Table A-1) leads to the apex 2 of the rock's truncated semi-infinite cone (Fig. A-11).

For the dynamic-stiffness coefficients frequency-dependent reflection coefficients for translation and rotation -α(ω) can also be used ([50], pages 193 and 196). A generalization to the halfspace with many layers exists ([50], Appendix D).

A.2.2 Basic Spring-Dashpot-Mass Model

The basic spring-dashpot-mass model can be used to represent the dynamic behavior for all components of motion of a disk on the surface of a soil layer on rigid rock in a standard finite-element program for structural dynamics in the time domain. The model (Fig. A-12) with two additional internal degrees of freedom (u_1, u_2) consists of four springs K_i, three dashpots C_i and one mass M whose real frequency-independent coefficients are specified for various ratios of the radius r_0 of the disk to the depth d of the layer and Poisson's ratio υ for the horizontal, vertical, rocking and torsional motions in Table A-5.

$$K_i = k_i G r_0 \quad i = 1, \ldots, 4$$

$$C_i = c_i G \frac{r_0^2}{c_s} \quad i = 1, \ldots 3, \quad M = mG\frac{r_0^3}{c_s^2}$$

To construct a lumped-parameter model for the rotational motions representing the relationship between the rotation and the moment, the right-hand side has to be multiplied by r_0^2.

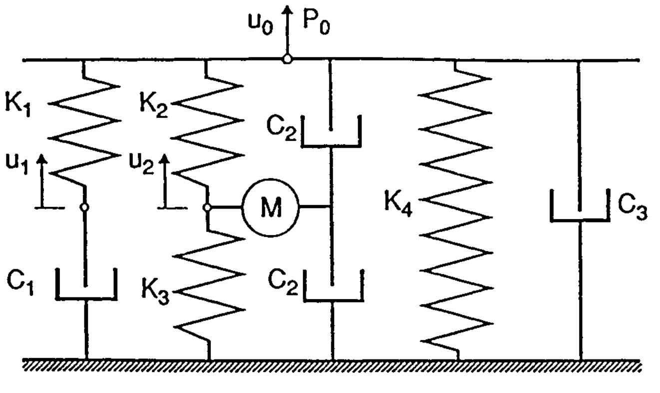

Fig. A-12 Basic spring-dashpot mass model with two internal degrees of freedom.

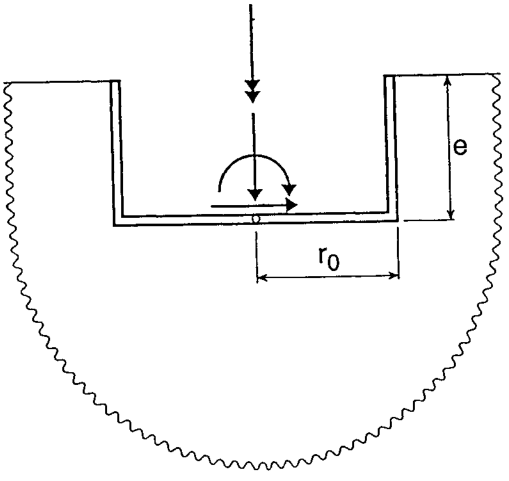

Fig. A-13 Cylindrical foundation embedded in soil halfspace.

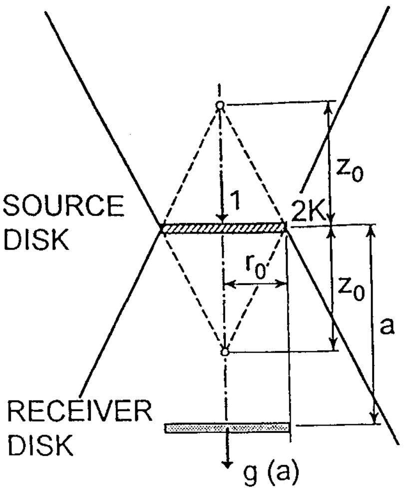

Fig. A-14 Green's function based on disk embedded in fullspace with double-cone model.

A.3 Embedded Foundation and Pile Foundation

A.3.1 Double-Cone Model

To analyze a foundation with embedment e for all components of motion (Fig. A-13), a rigid disk of radius r_0 embedded in a full-space, which is modeled with a double-cone model, is the building block (Fig. A-14). The aspect ratio z_0/r_0 and the wave velocity c are the same as for the one-sided cone used to model a surface disk (Table A-1). The only change consists of doubling the static-stiffness coefficients K and K_ϑ (Table A-2). The double cone's displacement field defines approximate Green's functions for use in a matrix formulation of structural mechanics.

Green's Function

Translational Double Cone (Fig. A-14)

distance a

$$g(a,\ t) \ = \ \frac{1}{2K}\ \frac{1}{1+\dfrac{a}{z_0}}\ h_1\!\left(t-\frac{a}{c}\right)$$

with unit-impulse response function

$$\begin{aligned} h_1(t) &= \frac{c}{z_0}\ e^{-\frac{c}{z_0}t} && t \geq 0 \\ &= 0 && t < 0 \end{aligned}$$

$$g(a,\omega) \ = \ \frac{1}{2K}\ \frac{1}{1+\dfrac{a}{z_0}}\ \frac{e^{-i\frac{\omega a}{c}}}{1+i\dfrac{\omega z_0}{c}}$$

Rotational Double Cone

$$g_\vartheta(a,t) = \frac{1}{2K_\vartheta}\frac{1}{\left(1+\dfrac{a}{z_0}\right)^2}\left[h_2\!\left(t-\frac{a}{c}\right)+\left(-1+\frac{1}{1+\dfrac{a}{z_0}}\right)h_3\!\left(t-\frac{a}{c}\right)\right]$$

with

$$\begin{aligned} h_2(t) &= \frac{c}{z_0}e^{-\frac{3}{2}\frac{c}{z_0}t}\left(3\cos\frac{\sqrt{3}}{2}\ \frac{c}{z_0}t-\sqrt{3}\sin\frac{\sqrt{3}}{2}\ \frac{c}{z_0}t\right) && t \geq 0 \\ &= 0 && t<0 \\ h_3(t) &= 2\sqrt{3}\ \frac{c}{z_0}e^{-\frac{3}{2}\frac{c}{z_0}t}\sin\frac{\sqrt{3}}{2}\frac{c}{z_0}t && t \geq 0 \\ &= 0 && t<0 \end{aligned}$$

$$g_\vartheta(a,\omega) = \frac{3}{2K_\vartheta}\left(\frac{1}{\left(1+\dfrac{a}{z_0}\right)^3} + i\frac{\omega z_0}{c}\,\frac{1}{\left(1+\dfrac{a}{z_0}\right)^2}\right) * \frac{1}{3 + 3i\dfrac{\omega z_0}{c} + \left(i\dfrac{\omega z_0}{c}\right)^2}\, e^{-i\frac{\omega a}{c}}$$

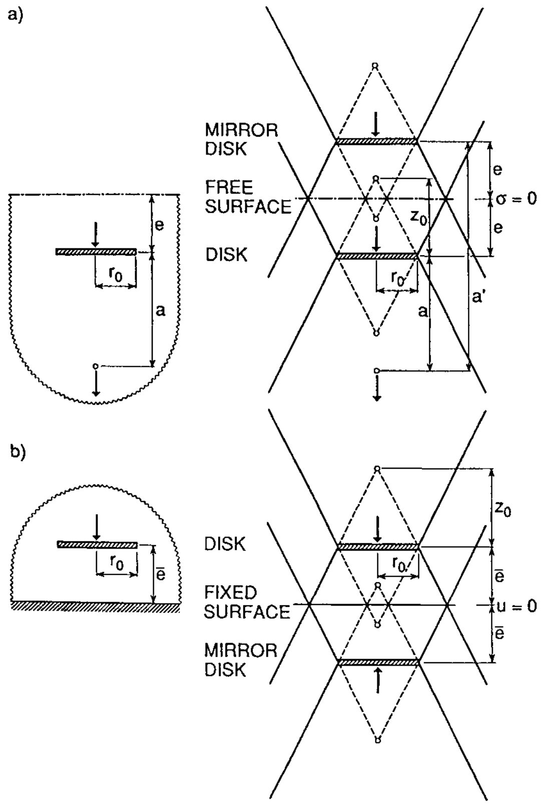

Fig. A-15 Modeling of free and fixed boundaries.
a) Disk embedded in halfspace with free boundary with anti-symmetrically loaded mirror-image disk to represent free surface.
b) Disk embedded in halfspace with fixed boundary with symmetrically loaded mirror-image disk to represent fixed boundary

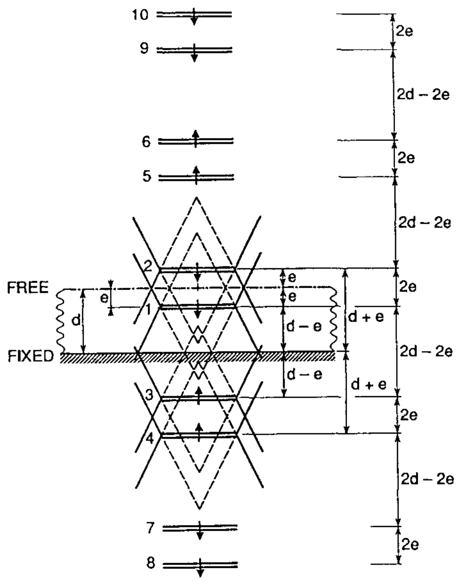

Fig. A-16 Arrangements of mirror-image disks embedded in fullspace with loads and double cones to model disk embedded in soil layer resting on rigid rock.

For vertical motion of a *pile* the weighted Green's function of the double cone g_{cone} (a,ω) as above and of the fullspace for a point load $g_{fullspace}$ (a,ω) is used

$$g(a,\omega) = w(a)\ g_{cone}(a,\omega) + (1 - w(a))g_{fullspace}(a,\omega)$$

with the weighting function

$$\begin{aligned} w(a) &= 1 & a &\le r_0 \\ &= e^{-0.8\frac{a-r_0}{r_0}} & a &> r_0 \end{aligned}$$

and where

$$g_{fullspace}(a,\omega) = \frac{1}{4\pi G}\left[\psi - \left(\frac{a}{r}\right)^2 \chi\right]$$

and with

$$\psi = \left(1 - i\frac{1}{a_0} - \frac{1}{a_0^2}\right)\frac{e^{-ia_0}}{r} + \left(i\frac{c_s}{c_p a_0} + \frac{1}{a_0^2}\right)\frac{e^{-i\frac{c_s}{c_p}a_0}}{r}$$

$$\chi = \left(1 - i\frac{3}{a_0} - \frac{3}{a_0^2}\right)\frac{e^{-ia_0}}{r} - \left(\frac{c_s^2}{c_p^2} - i\frac{3c_s}{c_p a_0} - \frac{3}{a_0^2}\right)\frac{e^{-i\frac{c_s}{c_p}a_0}}{r}$$

$$r = \sqrt{a^2 + r_0^2} \qquad a_0 = \frac{\omega r}{c_s}$$

To model the free surface of a soil, a mirror-image disk (embedded in the fullspace and also represented by a double cone) loaded by the same time history of force as the original disk and with the same sign is introduced (Fig. A-15a). The same procedure can be used to model a fixed boundary, but the force on the mirror-image disk acts in the opposite direction (Fig. A-15b). To model a disk embedded in a soil layer resting on rigid rock, the concept of anti-symmetrically loaded mirror-image disks to represent the free surface and of symmetrically loaded mirror-image disks for the fixed boundary is applied repeatedly (Fig. A-16).

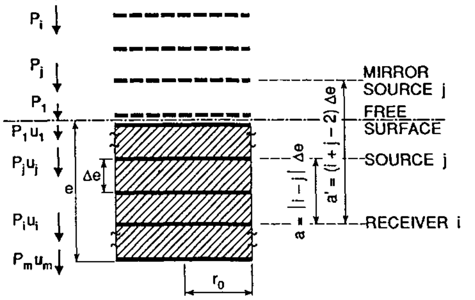

Fig. A-17 Stack of disks to model embedded cylindrical foundation with anti-symmetrically loaded mirror-image disks.

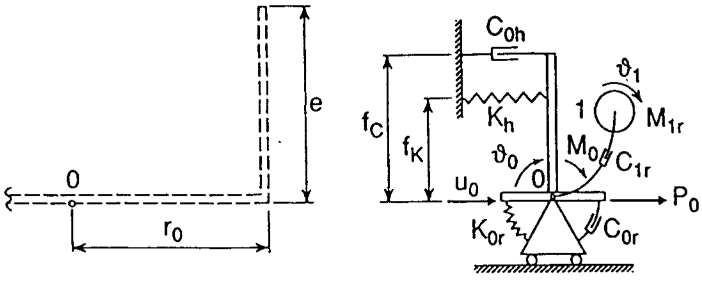

Fig. A-18 Fundamental spring-dashpot-mass model for foundation embedded in halfspace with coupling of horizontal and rocking motions.

Matrix Formulation

Modeling the soil region which will later be excavated by a stack of rigid disks separated by soil (Fig. A-17), the dynamic-stiffness matrix for harmonic loading $\left[S^g_{00}(\omega)\right]$ of an embedded cylindrical foundation with respect to the rigid-body displacement amplitudes $\{u_0(\omega)\}$ and corresponding force amplitudes $\{P_0(\omega)\}$ is formulated with standard matrix methods of structural analysis as

$$\{P_0(\omega)\} = \left[S^g_{00}(\omega)\right] \{u_0(\omega)\}$$

where

$$\left[S^g_{00}(\omega)\right] = [A]^T \left[S^f(\omega)\right] [A] + \omega^2[M]$$

[A] is the kinematic-constraint matrix of the rigid foundation with $\{u(\omega)\}$ denoting the displacement amplitudes of the disks

$$\{u(\omega)\} = [A] \{u_0(\omega)\}$$

[M] is the rigid-body mass matrix of the excavated soil and $\left[S^f(\omega)\right]$ the dynamic-stiffness matrix of the free field

$$\left[S^f(\omega)\right] = [G(\omega)]^{-1}$$

where the dynamic-flexibility matrix of the disks embedded in the soil equals

$$\{u(\omega)\} = [G(\omega)] \{P(\omega)\}$$

with the corresponding force amplitudes $\{P(\omega)\}$. In $[G(\omega)]$ the sum of the Green's functions $g(a,\omega)$ of the source disk and $g(a',\omega)$ of the mirror-image disk appears (Fig. A-17).

In the time domain, the corresponding interaction force-displacement relationship of an embedded foundation at time $n\Delta t$ equals

$$\{P_0\}_n = [A]^T\left[S^f\right]_0[A]\{u_0\}_n - [A]^T\left[S^f\right]_0\{\bar{u}\}_n - [M]\{\ddot{u}_0\}_n$$

$\left[S^f\right]_0$ is the instantaneous dynamic-stiffness matrix of the free field

$$\left[S^f\right]_0 = [G]_0^{-1}$$

where the displacement-force relationship of the disks equals

$$\{u\}_n = \{\bar{u}\}_n + [G]_0\{P\}_n$$

with

$$\{\bar{u}\}_n = \sum_{k=1}^{n-1}[G]_{n-k}\{P\}_k$$

$[G]_{n-k}$ is the dynamic-flexibility matrix in the time domain (displacements at time n caused by unit forces acting at time k).

Table A-6 Static Stiffness and Dimensionless Coefficients of the Fundamental Spring-Dashpot-Mass Model (Monkey-Tail Arrangement) for a Cylinder Embedded in a Halfspace

	Static Stiffness K	Dimensionless Coefficients of		
		Dashpots		Mass
		γ_0	γ_1	μ_1
Horizontal	$\frac{8Gr_0}{2-\upsilon}\left(1+\frac{e}{r_0}\right)$	$0.68+0.57\sqrt{\frac{e}{r_0}}$	———	———
Vertical	$\frac{4Gr_0}{1-\upsilon}\left(1+0.54\frac{e}{r_0}\right)$	$0.80+0.35\frac{e}{r_0}$	$0.32-0.01\left(\frac{e}{r_0}\right)^4$	0.38
Rocking	$K_r=\frac{8Gr_0^3}{3(1-\upsilon)}\left[1+2.3\frac{e}{r_0}+0.58\left(\frac{e}{r_0}\right)^3\right]$ $K_{0r}=K_r-\frac{Gr_0^3}{2(2-\upsilon)}\left(1+\frac{e}{r_0}\right)\left(\frac{e}{r_0}\right)^2$	$0.15631\frac{e}{r_0}$ $-0.08906\left(\frac{e}{r_0}\right)^2$ $-0.00874\left(\frac{e}{r_0}\right)^3$	$0.40+0.03\left(\frac{e}{r_0}\right)^2$	$0.33+0.10\left(\frac{e}{r_0}\right)^2$
Torsional	$\frac{16Gr_0^3}{3}\left(1+2.67\frac{e}{r_0}\right)$	———	$0.29+0.09\sqrt{\frac{e}{r_0}}$	$0.20+0.25\sqrt{\frac{e}{r_0}}$

Static-Stiffness Coefficient

cylindrical foundation of radius r_0 embedded with height e in a soil layer of depth d on rigid rock (d=∞: embedded in halfspace)

$$K_h = \frac{8Gr_0}{2-\upsilon}\left(1+\frac{1}{2}\frac{r_0}{d}\right)\left(1+\frac{e}{r_0}\right)\left(1+\frac{e}{d}\right) \qquad \text{horizontal}$$

$$K_v = \frac{4Gr_0}{1-\upsilon}\left(1+1.3\frac{r_0}{d}\right)\left(1+0.54\frac{e}{r_0}\right)$$

$$* \left[1+\left(0.85-0.28\frac{e}{r_0}\right)\frac{\frac{e}{d}}{1-\frac{e}{d}}\right] \qquad \text{vertical}$$

$$K_r = \frac{8Gr_0^3}{3(1-\upsilon)}\left(1+\frac{1}{6}\frac{r_0}{d}\right)$$

$$* \left[1+2.3\frac{e}{r_0}+0.58\left(\frac{e}{r_0}\right)^3\right]\left(1+0.7\frac{e}{d}\right) \qquad \text{rocking}$$

$$K_t = \frac{16}{3}Gr_0^3\left(1+\frac{1}{10}\frac{r_0}{d}\right)\left(1+2.67\frac{e}{r_0}\right) \qquad \text{torsional}$$

$$K_{hr} = \frac{e}{3}K_h \qquad \text{coupling}$$

A.3.2 Spring-Dashpot-Mass Model

Fundamental Spring-Dashpot-Mass Model

A cylindrical rigid foundation with embedment e in a *halfspace* can be modeled with the fundamental spring-dashpot-mass model described in Section A1.2 (Fig. A-5). The coupling between the horizontal and rocking motions is achieved by connecting the horizontal spring-dashpot-mass model with eccentricities f_K, f_C to the base (Fig. A-18).

$$f_K = 0.25e \qquad f_C = 0.32e + 0.03e\left(\frac{e}{r_0}\right)^2$$

The coefficients are specified as a function of the embedment ratio e/r_0 in Table A-6 (υ=1/4). Note that the coefficients of the rocking spring-dashpot-mass model are defined with respect to K_r (and not K_{0r}), although K_{0r} is the coefficient of the direct spring (Fig. A-18).

$$C_{0r} = \frac{r_0}{c_s}\gamma_0 K_r \quad C_{1r} = \frac{r_0}{c_s}\gamma_1 K_r \quad M_{1r} = \frac{r_0^2}{c_s^2}\mu_1 K_r$$

Basic Spring-Dashpot-Mass Model

To represent a cylindrical rigid foundation with embedment e in a *soil layer* resting on rigid rock (Fig. A-19), a spring-dashpot-mass model for all degrees of freedom is described. For the vertical and torsional motions the basic spring-dashpot-mass model with four springs, three dashpots and a mass introducing two internal degrees of freedom (Fig. A-12) is directly applicable (described in Section A2.2). For the coupled horizontal and rocking motions, a physical representation (Fig. A-20) exists, consisting of three basic spring-dashpot-mass models, one of which is attached with the eccentricity e to take the coupling into consideration. For various ratios of the radius r_0 of the foundation to the depth d of the layer and lateral contact ratios e_c/e, the frequency-independent real coefficients for all springs, dashpots and masses are specified in Table A-7 (υ=1/3).

Table A-7 Dimensionless Coefficients of the Basic Spring-Dashpot-Mass Model for a Cylinder Embedded in a Soil Layer on Rigid Rock (Embedment Ratio e/r_0=1)

Ratio of Radius to Depth r_0/d	Contact Ratio e_c/e		Vertical	Horizontal	Rocking	Coupling	Torsional
$\frac{1}{2}$	1.00	k_1	-.203759 E+02	-.124401 E+02	-.125229 E+02	-.618776 E+01	-.139252 E+02
		k_2	+.339543 E+01	+.286199 E+01	-.583152 E+00	+.202777 E+01	-.275441 E+01
		k_3	-.617014 E+01	-.208541 E+02	-.814822 E-01	-.141784 E+02	+.178780 E+01
		k_4	+.166202 E+02	+.794575 E+01	+.130945 E+02	+.337083 E+01	+.161164 E+02
		c_1	-.918456 E+01	-.590158 E+01	-.315268 E+01	-.333135 E+01	-.774712 E-02
		c_2	-.596381 E+00	-.516028 E+01	-.885823 E-01	-.340080 E+01	-.736101 E+00
		c_3	+.131164 E+02	+.130103 E+02	+.322858 E+01	+.811310 E+01	+.858610 E+01
		m	-.987169 E+00	-.163126 E+02	-.680666 E+00	-.146553 E+02	-.962102 E+00
	0.50	k_1	-.190169 E+02	-.123585 E+02	-.918010 E+01	-.311508 E+01	-.150459 E+02
		k_2	+.102770 E+02	+.382788 E+01	+.934512 E+00	+.786487 E+00	+.149201 E+01
		k_3	-.256293 E+02	-.116229 E+02	-.466308 E+01	-.869559 E+01	-.230599 E+01
		k_4	+.480379 E+01	+.697738 E+01	+.821627 E+01	+.184030 E+01	+.132374 E+02
		c_1	-.803919 E+00	-.129978 E+01	-.212247 E+01	-.715314 E+00	-.513171 E+00
		c_2	-.378972 E+01	-.357027 E+01	-.316747 E+00	-.208337 E+01	-.403901 E+00
		c_3	+.131677 E+02	+.102413 E+02	+.266675 E+01	+.326137 E+01	+.511390 E+01
		m	-.364874 E+01	-.820645 E+01	-.342125 E+01	-.888905 E+01	-.515523 E+00
	0.00	k_1	-.199866 E+02	-.113528 E+02	-.801960 E+01		-.820959 E+01
		k_2	+.324059 E+01	+.187819 E+01	+.103933 E+01		+.236828 E+00
		k_3	-.138239 E+03	-.141228 E+02	-.800817 E+01		-.295213 E+00
		k_4	+.151110 E+02	+.837372 E+01	+.584466 E+01		+.794727 E+01
		c_1	-.577181 E+01	-.169786 E+01	-.101867 E+01		-.288545 E+00
		c_2	-.891247 E+01	-.396633 E+01	-.157192 E+01		-.308176 E-01
		c_3	+.151425 E+02	+.710633 E+01	+.313092 E+01		+.160082 E+01
		m	-.485815 E+02	-.142894 E+02	-.217586 E+01		-.372596 E-01
$\frac{1}{3}$	1.00	k_1	-.215677 E+02	-.800686 E+01	-.112339 E+02	-.531331 E+01	-.158881 E+02
		k_2	+.995664 E+01	+.248098 E+01	+.271244 E+01	+.128879 E+01	-.216892 E+01
		k_3	-.299529 E+02	-.530555 E+01	-.112792 E+02	-.117090 E+02	+.122884 E+01
		k_4	+.122789 E+01	+.460883 E+01	+.830774 E+01	+.314281 E+01	+.175253 E+02
		c_1	-.214856 E+01	-.638370 E-01	-.185381 E+01	-.345899 E+01	-.770582 E+00
		c_2	-.703468 E+01	-.234186 E+01	-.147482 E+01	-.442673 E+01	-.114118 E+01
		c_3	+.195563 E+02	+.101919 E+02	+.461482 E+01	+.913903 E+01	+.899118 E+01
		m	-.476605 E+01	-.598035 E+01	-.101760 E+02	-.222249 E+02	-.244900 E+01
	0.50	k_1	-.263609 E+02	-.105510 E+02	-.812675 E+01	-.258694 E+01	-.164865 E+02
		k_2	+.106994 E+02	+.323771 E+01	+.327590 E+01	+.487010 E+00	+.162631 E+01
		k_3	-.415582 E+02	-.101866 E+02	-.183711 E+02	-.708382 E+01	-.359665 E+01
		k_4	+.391023 E+00	+.579774 E+01	+.434718 E+01	+.155304 E+01	+.138158 E+02
		c_1	-.734715 E-02	-.691681 E-01	-.831614 E+00	-.752538 E+00	-.786309 E+00
		c_2	-.101472 E+02	-.475156 E+01	-.272228 E+01	-.265221 E+01	-.129218 E+01
		c_3	+.195330 E+02	+.114226 E+02	+.507228 E+01	+.383021 E+01	+.600218 E+01
		m	-.674277 E+01	-.148975 E+02	-.147137 E+02	-.128622 E+02	-.159889 E+01
	0.00	k_1	-.147108 E+02	-.922525 E+01	-.736535 E+01		-.790274 E+01
		k_2	+.600489 E+01	+.187933 E+01	-.907967 E+00		+.176502 E-01
		k_3	-.355109 E+02	-.788239 E+01	-.157724 E+03		-.179897 E-01
		k_4	+.527313 E+01	+.637232 E+01	+.684877 E+01		+.788488 E+01
		c_1	-.203850 E+01	-.425306 E-01	-.168579 E+01		-.128670 E+00
		c_2	-.830045 E+01	-.368700 E+01	-.114538 E+02		-.263292 E-03
		c_3	+.145304 E+02	+.682700 E+01	+.130128 E+02		+.157125 E+01
		m	-.200705 E+02	-.139626 E+02	-.920928 E+02		-.331649 E-03

A.3.3 Pile Foundation

Single Pile

The formulation based on disks embedded in a fullspace with their corresponding double cones and anti-symmetrically and symmetrically loaded mirror-image disks to model a free surface and a fixed boundary can straightforwardly be applied to the dynamic analysis of a single pile (Fig. A-21). The cylindrical soil region between the disks is not just analytically excavated as for an embedded foundation, but replaced by the difference of the material properties of the pile and the soil.

Pile Group

For a pile group, pile-soil-pile interaction can be considered with one dynamic-interaction factor in vertical direction and one in the lateral direction $\alpha(\omega)$, defined as the amplitude ratio of the displacement at the head of a receiver pile $u_r\omega)$ to the corresponding displacement of the loaded source pile $u_S(\omega)$ under its own dynamic load (Fig. A-22).

$$\alpha(\omega) = \frac{u_r(\omega)}{u_s(\omega)}$$

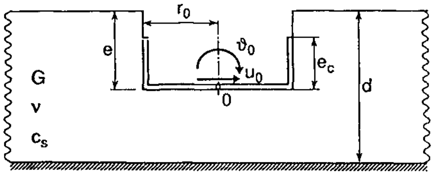

Fig. A-19 Cylindrical foundation with partial contact over embedment height embedded in soil layer resting on rigid rock.

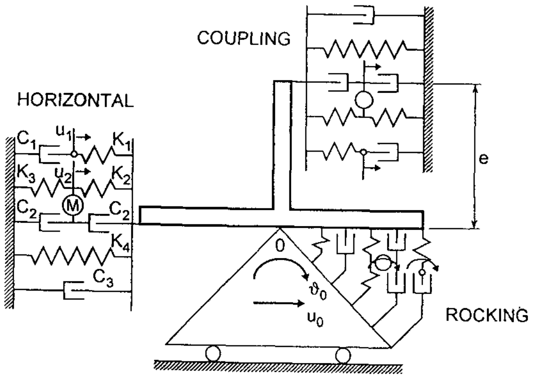

Fig. A-20 Basic spring-dashpot mass model for embedded foundation with coupling of horizontal and rocking motions.

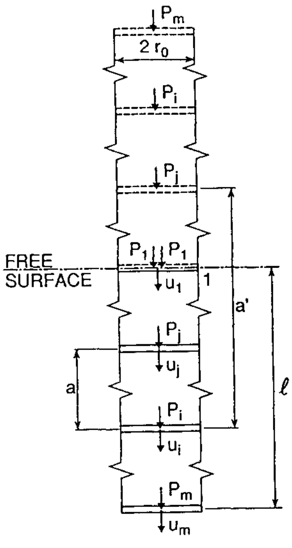

Fig. A-21 Stack of disks to model pile embedded in halfspace with anti-symmetrically loaded mirror-image disks.

Dynamic-Interaction Factor

vertical (Fig. A-22 a)

$$\alpha_v(\omega) = \sqrt{\frac{r_0}{d}}\, e^{-\zeta_g \omega \frac{d}{c_s}}\, e^{-i\omega \frac{d}{c_s}}$$

with the radius r_0, pile distance d and material damping ratio ζ_g.
lateral (horizontal) (Fig. A-22 b)

$$\alpha_h^f(\omega) = \cos^2\theta\alpha_h^f(0°,\omega) + \sin^2\theta\alpha_h^f(90°,\omega)$$

with the angle θ between the horizontal load and the line connecting the source and the receiver piles.

$$\alpha_h^f(0°,\omega) = \sqrt{\frac{r_0}{d}} e^{-\zeta_g \omega \frac{d}{c_p}} e^{-i\omega \frac{d}{c_p}}$$

$$\alpha_h^f(90°,\omega) = \alpha_v(\omega)$$

The dynamic-interaction factor referred to the free-field of the soil (at the location of the receiver pile) $\alpha_h^f(\omega)$ can be transformed to the corresponding factor referred to the head of the receiver pile itself $\alpha_h(\omega)$ based on the concept of substructuring with replacement (see [50], p. 283).

Matrix Formulation

Dynamic-stiffness matrix for harmonic loading with rigid pile cap

$$[S(\omega)] = [A]^T[G(\omega)]^{-1}[A]$$

with kinematic-constraint matrix [A] and dynamic-flexibility matrix [G(ω)] discretized at pile heads. For instance, for vertical motion (Fig. A-23) and with the dynamic-stiffness coefficient S(ω) of a single pile

$$u_i(\omega) = \frac{1}{S(\omega)}$$
$$* \left(\sum_{j=1}^{i-1} \alpha_v(d_{ij},\omega)P_j(\omega) + P_i(\omega) + \sum_{j=i+1}^{n} \alpha_v(d_{ij},\omega)P_j(\omega) \right)$$
$$i = 1, \ldots, n$$

which is generalized to

$$\{u(\omega)\} = [G(\omega)]\,\{P(\omega)\}$$

A.4 Simple Vertical Dynamic Green's Function

To calculate the vertical and rocking dynamic-stiffness coefficients for harmonic loading of an irregular basemat which cannot by represented by an equivalent disk on the surface of a homogeneous halfspace, the basemat is modeled as an assemblage of subdisks.

A.4.1 Dynamic-Flexibility Matrix of Subdisk

For small values of the dimensionless frequency $a_0 = \omega r_0 / c_s$, the amplitude of the vertical displacement $u_0(a_0)$ produced by a vertical load with amplitude $P(a_0)$ acting on the source disk of radius r_0 equals (Fig. A-24)

$$u_0(a_0) = \frac{P(a_0)}{K(1+0.74ia_0)}$$

with static-stiffness coefficient

$$K = 6Gr_0 \text{ for } \nu = 1/3$$

The Green's function outside the disk is approximated as

$$u(r,a_0) = u_0(a_0)Ae^{-i\varphi(a_0)}$$

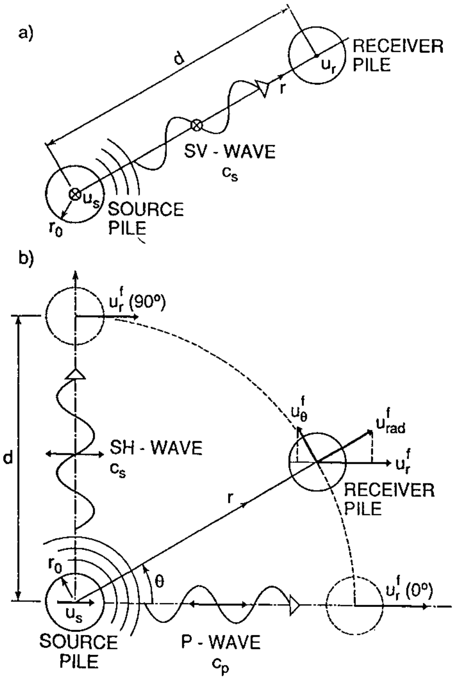

Fig. A-22 Cylindrical waves emitted from shaft of loaded source pile and propagating towards receiver pile determining dynamic-interaction factors.

a) Vertical.

b) Lateral (horizontal).

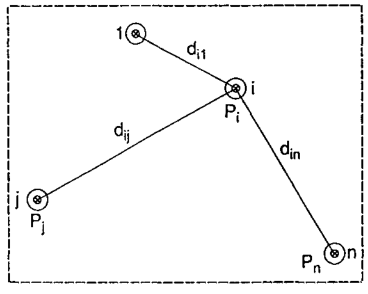

Fig. A-23 Plan view of arrangement of piles in group.

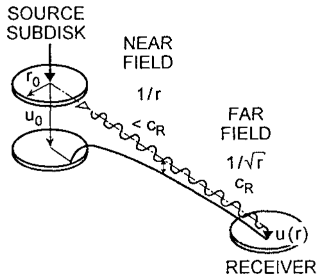

Fig. A-24 Vertical displacement on free surface from source subdisk loaded vertically.

The amplitude-reduction factor A equals

$$A = \frac{2}{\pi}\frac{r_0}{r} \qquad \text{for} \quad r \le r_f \quad \text{(near field)}$$

$$A = \frac{2}{\pi}\frac{r_0}{\sqrt{r_f r}} \qquad \text{for} \quad r > r_f \quad \text{(far field)}$$

with (index R for Rayleigh wave)

$$r_f = 0.3\lambda_R = \frac{1.76}{a_0} r_0$$

The phase angle $\varphi(a_0)$ equals

$$\varphi(a_0) = 1.16\ a_0\left(\frac{r}{r_0} - \frac{2}{\pi}\right) \qquad \text{for } r - \frac{2r_0}{\pi} \le 5r_f$$

$$\varphi(a_0) = \frac{\pi}{4} + 1.07\ a_0\left(\frac{r}{r_0} - \frac{2}{\pi}\right) \qquad \text{for } r - \frac{2r_0}{\pi} > 5r_f$$

With the amplitudes of the vertical forces $\{P(a_0)\}$ acting on the subdisks and of the vertical displacements $\{u(a_0)\}$

$$\{u(a_0)\} = [G(a_0)]\{P(a_0)\}$$

where the dynamic-flexibility matrix $[G(a_0)]$ is constructed based on the approximate Green's function of the subdisk.

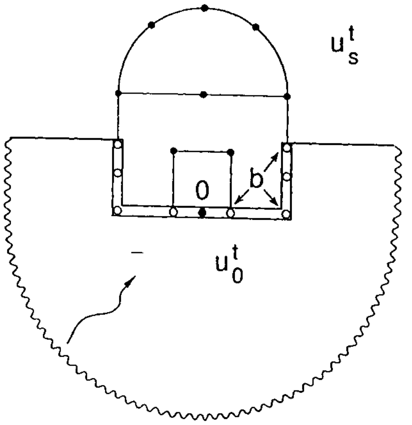

Fig. A-25 Structure-soil system with rigid base.

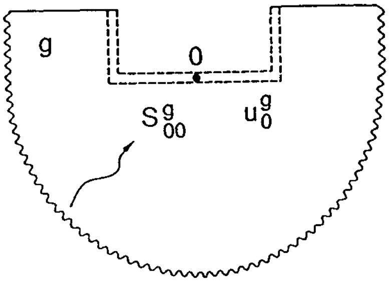

Fig. A-26 Soil system ground with excavation and rigid structure-soil interface.

A.4.2 Matrix Formulation

The dynamic-stiffness matrix with respect to the displacement amplitudes of the rigid basemat $\{u_0(a_0)\}$ equals

$$[S(a_0)] = [A]^T[G(a_0)]^{-1}[A]$$

with the kinematic-constraint matrix [A] defined as

$$\{u(a_0)\} = [A]\,\{u_0(a_0)\}$$

A.5 Seismic Excitation

A.5. 1 Basic Equation of Motion

Frequency Domain

Basic equation of motion of substructure method for harmonic loading for analysis of dynamic soil-structure interaction for seismic excitation (Fig. A-25)

$$\begin{bmatrix} [S_{ss}(\omega)][S_{s0}(\omega)] \\ [S_{0s}(\omega)][S^{s}_{00}(\omega)] \end{bmatrix} \begin{Bmatrix} \{u^{t}_{s}(\omega)\} \\ \{u^{t}_{0}(\omega)\} \end{Bmatrix} = \begin{Bmatrix} \{0\} \\ -\{P_0(\omega)\} \end{Bmatrix}$$

with amplitudes of total displacements in nodes within structure $\{u^{t}_{s}(\omega)\}$ and on rigid structure-soil interface $\{u^{t}_{0}(\omega)\}$ and dynamic-stiffness matrix of structure (static-stiffness matrix [K], mass matrix [M], hysteretic damping ratio ζ).

$$[S^{s}(\omega)] = [K](1+2i\zeta) - \omega^2[M]$$

$[S^{g}_{00}(\omega)]$ denotes the dynamic-stiffness matrix of unbounded soil with excavation (ground, Fig. A-26). Amplitudes of soil's interaction forces are formulated as

$$\{P_0(\omega)\} = [S^{g}_{00}(\omega)]\left(\{u^{t}_{0}(\omega)\} - \{u^{g}_{0}(\omega)\}\right)$$

with the effective foundation input motion $\{u^{g}_{0}(\omega)\}$ (Fig. A-26). Defining driving loads as

$$\{P^{g}_{0}(\omega)\} = [S^{g}_{00}(\omega)]\,\{u^{g}_{0}(\omega)\}$$

the equation of motion equals

$$\begin{bmatrix} [S_{ss}(\omega)]\vdots[S_{s0}(\omega)] \\ [S_{0s}(\omega)]\vdots[S^{s}_{00}(\omega)]+[S^{g}_{00}(\omega)] \end{bmatrix} \begin{Bmatrix} \{u^{t}_{s}(\omega)\} \\ \{u^{t}_{0}(\omega)\} \end{Bmatrix} = \begin{Bmatrix} \{0\} \\ \{P^{g}_{0}(\omega)\} \end{Bmatrix}$$

Time Domain

Basic equation in time domain (viscous damping matrix of structure)

$$\begin{bmatrix} [M_{ss}][M_{s0}] \\ [M_{0s}][M_{00}] \end{bmatrix} \begin{Bmatrix} \{\ddot{u}^{t}_{s}(t)\} \\ \{\ddot{u}^{t}_{0}(t)\} \end{Bmatrix} + \begin{bmatrix} [C_{ss}][C_{s0}] \\ [C_{0s}][C_{00}] \end{bmatrix} \begin{Bmatrix} \{\dot{u}^{t}_{s}(t)\} \\ \{\dot{u}^{t}_{0}(t)\} \end{Bmatrix} +$$

$$\begin{bmatrix} [K_{ss}][K_{s0}] \\ [K_{0s}][K_{00}] \end{bmatrix} \begin{Bmatrix} \{u^{t}_{s}(t)\} \\ \{u^{t}_{0}(t)\} \end{Bmatrix} = \begin{Bmatrix} \{0\} \\ -\{P_0(t)\} \end{Bmatrix}$$

A.5.2 Interaction Force of Soil and Driving Load

Disk on Homogeneous Halfspace Modeled with Cones

(Section A1.1)
translation

$$\begin{aligned} P_0(t) &= K\left(u_0^t(t) - u_0^g(t)\right) + C\left(\dot{u}_0^t(t) - \dot{u}_0^g(t)\right) \\ &= K u_0^t(t) + C\dot{u}_0^t(t) - P_0^g(t) \\ \text{with}\quad P_0^g(t) &= K u_0^g(t) + C\dot{u}_0^g(t) \end{aligned}$$

rotation

$$\begin{aligned} M_0(t) &= K_\vartheta\left(\vartheta_0^t(t) - \vartheta_0^g(t)\right) + C_\vartheta\left(\dot{\vartheta}_0^t(t) - \dot{\vartheta}_0^g(t)\right) \\ &\quad - \int_0^t h_1(t-\tau) C_\vartheta\left(\dot{\vartheta}_0^t(\tau) - \dot{\vartheta}_0^g(\tau)\right) d\tau \end{aligned}$$

$$= K_\vartheta \vartheta_0^t(t) + C_\vartheta \dot{\vartheta}_0^t(t) - \int_0^t h_1(t-\tau)\, C_\vartheta \dot{\vartheta}_0^t(\tau) d\tau - M_0^g(t)$$

with

$$M_0^g(t) = K_\vartheta \vartheta_0^g(t) + C_\vartheta \dot{\vartheta}_0^g(t) - \int_0^t h_1(t-\tau) C_\vartheta \dot{\vartheta}_0^g(\tau) d\tau$$

Disk on Layer on Rock Modeled with Unfolded Layered Cone

(Section A2.1)
translation

$$\begin{aligned} P_0(t) &= K\left(\sum_{j=0}^{k} e_j^K\left(u_0^t(t-jT) - u_0^g(t-jT)\right)\right) \\ &\quad + C\left(\sum_{j=0}^{k} e_j^K\left(\dot{u}_0^t(t-jT) - \dot{u}_0^g(t-jT)\right)\right) \\ &= K\sum_{j=0}^{k} e_j^K u_0^t(t-jT) + C\sum_{j=0}^{k} e_j^K \dot{u}_0^t(t-jT) - P_0^g(t) \end{aligned}$$

with

$$P_0^g(t) = K\sum_{j=0}^{k} e_j^K u_0^g(t-jT) + C\sum_{j=0}^{k} e_j^K \dot{u}_0^g(t-jT)$$

analogously for rocking unfolded layered cone

Embedded Foundation Modeled with Stack of Disks

for vertically propagating free-field motion $\{u^f(t)\}$

$$
\begin{aligned}
\{P_0\}_n &= [A]^T[S^f]_0[A]\{u_0^t\}_n - [A]^T[S^f]_0\{\bar{u}\}_n \\
&\quad - [M]\{\ddot{u}_0^t\}_n - [A]^T[S^f]_0\{u^f\}_n \\
&= [A]^T[S^f]_0[A]\{u_0^t\}_n - [A]^T[S^f]_0\{\bar{u}\}_n \\
&\quad - [M]\{\ddot{u}_0^t\}_n - \{P_0^g\}_n
\end{aligned}
$$

with

$$\{P_0^g\}_n = [A]^T[S^f]_0\{u^f\}_n$$

A.5.3 Effective Foundation Input Motion

Effective Foundation Input Motion for Harmonic Loading

$$\{u_0^g(\omega)\} = [S_{00}^g(\omega)]^{-1}[A]^T[S_{bb}^f(\omega)]\{u_b^f(\omega)\}$$

with dynamic-stiffness matrix $[S_{bb}^f(\omega)]$ and motion of free field $\{u_b^f(\omega)\}$ in those nodes (disks) b which will later lie on the structure-soil interface and with kinematic-constraint matrix [A] (see Fig. A-27).

Surface Foundation on Homogeneous Halfspace Modeled with Subdisks

(Section A4)
vertical and rocking motions $\{u_0^g(\omega)\}$ caused by vertical free-field displacement with amplitude

$$u_z^f(x,\omega) = u_z^f(\omega)e^{-i\frac{\omega}{c_a}x}$$

propagating horizontally in x-direction with apparent velocity c_a

$$\{u_0^g(\omega)\} = \left([A]^T[G(a_0)]^{-1}[A]\right)^{-1}[A]^T[G(a_0)]^{-1}\{u_b^f(\omega)\}$$

with $\{u_b^f(\omega)\}$ equal to $\{u_z^f(x,\omega)\}$ evaluated in nodes b.

Surface Foundation Modeled with Distributed Springs

Vertical and rocking motions w_0^g, β_0^g caused by vertical free-field displacement propagating horizontally with apparent velocity c_a

$$u_z^f(x,t) = u^f\left(t - \frac{x}{c_a}\right)$$

for square foundation of length 2a and spring constant k (Fig. A-28)

$$w_0^g(t) = \frac{1}{k4a^2}\int_{-a}^{+a} k2a\ u^f\left(t-\frac{x}{c_a}\right)dx = \frac{c_a}{2a}\int_{t-a/c_a}^{t+a/c_a} u^f(\bar{x})d\bar{x}$$

$$\beta_0^g(t) = -\frac{1}{k\frac{4}{3}a^4}\int_{-a}^{+a} xk2a\; u^f\left(t-\frac{x}{c_a}\right)dx$$

$$= \frac{3}{2}\frac{c_a^2}{a^3}\left(\int_{t-a/c_a}^{t+a/c_a} \bar{x}u^f(\bar{x})d\bar{x} - t\int_{t-a/c_a}^{t+a/c_a} u^f(\bar{x})d\bar{x}\right)$$

Embedded Foundation Modeled with Stacks of Disks

(Section A3.1)

for vertically propagating free-field motion with amplitude $\{u^f(\omega)\}$

$$\{u_0^g(\omega)\} = \left[S_{00}^g(\omega)\right]^{-1}[A]^T\left[S^f(\omega)\right]\{u^f(\omega)\}$$

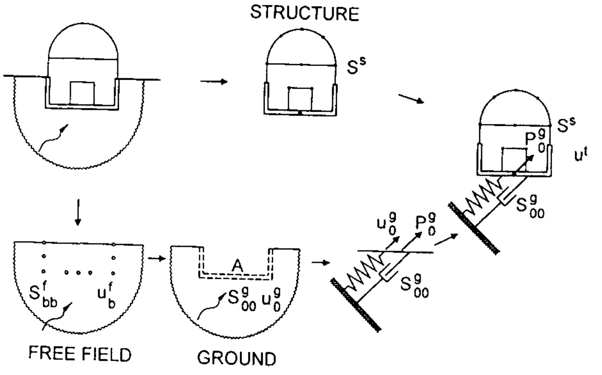

Fig. A-27 Physical interpretation of basic equation of motion in total displacements with effective foundation input motion and driving loads.

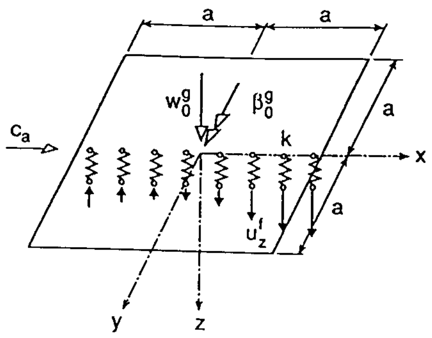

Fig. A-28 Effective foundation input motion for vertical component of horizontally propagating wave acting on rigid square basemat with distributed springs beneath.

A.5.4 Foundation Represented by Spring-Dashpot-Mass Model

When a spring-dashpot-mass model for the soil is used, the effective seismic input motion $\{u_0^g(t)\}$ is in a first step applied at the base (where the structure will later be connected) of the soil model, leading to the reaction forces (driving loads) $\{P_0^g(t)\}$. The latter are then applied to the total dynamic model in the second step, yielding the total dynamic response. The procedure is summarized in Fig. A-27. As an example the rocking motion of a rigid block on a homogeneous halfspace modeled with the lumped-parameter model (discrete-element model) of Fig. A-2c is addressed in Fig. A-29.

A.6 Dynamic Soil-Structure Interaction

A simple coupled dynamic model (Fig. A-30) consisting of a vertical rigid bar with the horizontal and rocking springs and dashpots with frequency-dependent coefficients $Kk(a_0)$, $(r_0/c_s)\ Kc(a_0)$ and $K_\vartheta k_\vartheta(a_0)$, $r_0/c_s)\ K_\vartheta c_\vartheta(a_0)$ representing the soil attached at one end and at the other one, at a distance equal to the height h, a spring with coefficient k connected to a mass m, which models the structure, correctly captures the essential effects of soil-structure interaction for a horizontal seismic excitation u^g. The dynamic-stiffness coefficients of the soil are calculated with cones for a halfspace (Section A1.1) and with unfolded layered cones for a layer resting on rigid or flexible rock (Section A2.1).

The coupled system can be replaced by an equivalent one-degree-of-freedom system (Fig. A-31) enforcing the same structural distortion u as in the coupled dynamic system with the same mass m, the effective natural frequency $\tilde{\omega}$, the effective damping ratio $\tilde{\zeta}$ and the effective input motion $\tilde{u}^g$.

$$\frac{1}{\tilde{\omega}^2} = \frac{1}{\omega_s^2} + \frac{1}{\omega_h^2(\tilde{a}_0)} + \frac{1}{\omega_r^2(\tilde{a}_0)}$$

$$\tilde{\zeta} = \frac{\tilde{\omega}^2}{\omega_s^2}\zeta + \left(1 - \frac{\tilde{\omega}^2}{\omega_s^2}\right)\zeta_g + \frac{\tilde{\omega}^2}{\omega_h^2(\tilde{a}_0)}\zeta_h(\tilde{a}_0) + \frac{\tilde{\omega}^2}{\omega_r^2(\tilde{a}_0)}\zeta_r(\tilde{a}_0)$$

$$\tilde{u}^g = \frac{\tilde{\omega}^2}{\omega_s^2}u^g$$

with the natural frequencies

$$\omega_s = \sqrt{\frac{k}{m}} \qquad \text{fixed-base structure}$$

$$\omega_h(\tilde{a}_0) = \sqrt{\frac{Kk(\tilde{a}_0)}{m}} \qquad \text{rigid structure and rocking motion prevented}$$

$$\omega_r(\tilde{a}_0) = \sqrt{\frac{K_\vartheta k_\vartheta(\tilde{a}_0)}{mh^2}} \qquad \text{rigid structure and horizontal motion prevented}$$

the damping ratios

$$\zeta_h(\tilde{a}_0) = \frac{\tilde{a}_0 c(\tilde{a}_0)}{2k(\tilde{a}_0)} \qquad \text{horizontal radiation}$$

$$\zeta_r(\tilde{a}_0) = \frac{\tilde{a}_0 c_\vartheta(\tilde{a}_0)}{2k_\vartheta(\tilde{a}_0)} \qquad \text{rocking radiation}$$

and the hysteretic material damping of the structure ζ and of the soil ζ_g.

For a redundant coupled structure-soil system where the mass of the structure can only displace horizontally but not rotate (Fig. A-32), the equivalent one-degree-of-freedom system for horizontal seismic excitation is defined by the parameters

$$\frac{1}{\tilde{\omega}^2} = \frac{1}{\omega_s^2} + \frac{1}{\omega_h^2(\tilde{a}_0)} + \frac{3}{\omega_s^2 + 12\omega_r^2(\tilde{a}_0)}$$

$$\begin{aligned}\tilde{\zeta} &= \zeta - \frac{\tilde{\omega}^2}{\omega_h^2(\tilde{a}_0)}\left[\zeta - \zeta_g - \zeta_h(\tilde{a}_0)\right] \\ &\quad - \frac{36\tilde{\omega}^2\omega_r^2(\tilde{a}_0)}{\left(\omega_s^2 + 12\omega_r^2(\tilde{a}_0)\right)^2}\left[\zeta - \zeta_g - \zeta_r(\tilde{a}_0)\right] \\ \tilde{u}^g &= \frac{\tilde{\omega}^2}{\omega_s^2}u^g\end{aligned}$$

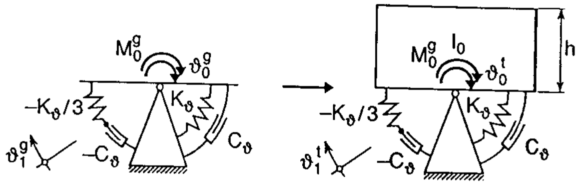

Fig. A-29 Rigid structure on soil halfspace. Discrete-element model of soil with applied effective foundation input rotational motion yielding reaction moment, which as driving moment acts on total dynamic system leading to total rotation.

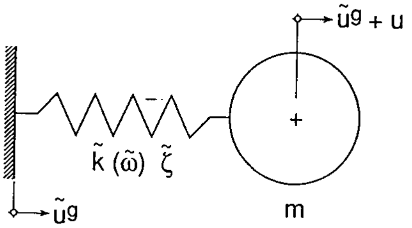

Fig. A-31 Equivalent one-degree-of-freedom system leading to same structural distortion with same mass, effective input motion, effective damping ratio and effective natural frequency determining effective spring.

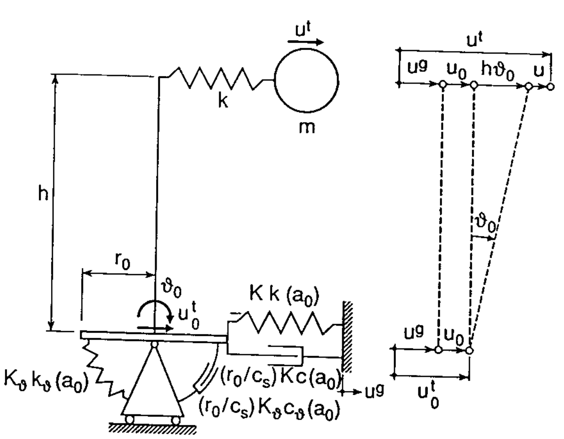

Fig. A-30 Coupled dynamic model of structure and soil for horizontal and rocking motions.

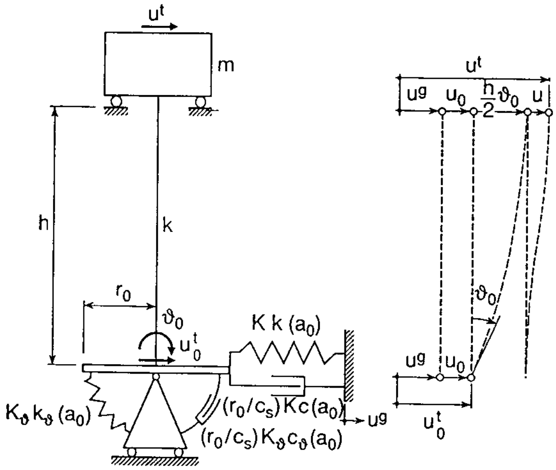

Fig. A-32 Redundant coupled dynamic model of structure with zero rotation of mass and of soil for horizontal and rocking motions.

THE SCALED BOUNDARY FINITE-ELEMENT METHOD - ALIAS CONSISTENT INFINITESIMAL FINITE-ELEMENT CELL METHOD - FOR UNBOUNDED MEDIA

Song Chongmin and John P. Wolf
(Institute of Hydraulics and Energy, Department of Civil Engineering, Swiss Federal Institute of Technology Lausanne, CH-1015 Lausanne, Switzerland)

Abstract

The scaled boundary finite-element method, alias the consistent infinitesimal finite-element cell method, is developed. The governing partial differential equations of linear elastodynamics are transformed to a system of linear second-order ordinary differential equations of displacements as functions of the radial coordinate. Introducing the definition of the dynamic stiffness a system of nonlinear first-order ordinary differential equations of the dynamic-stiffness matrix as functions of frequency results. The asymptotic expansion for high frequency yields the boundary condition satisfying the radiation condition. In an application only the boundary of the medium is discretized with surface finite elements yielding a reduction of the spatial dimension by one. No fundamental solution is necessary, and thus no singular integrals must be evaluated. General anisotropic material is analysed without any increase in computational effort. Boundary conditions on free surfaces and on interfaces between different materials are enforced exactly without any discretization. This method is exact in the radial direction and converges to the exact solution in the finite-element sense in the circumferential directions.

1 Introduction

To analyse dynamic medium-structure interaction based on the substructure method in the frequency domain, the dynamic-stiffness matrix in the degrees of freedom on the structure-medium interface of the unbounded medium is determined. For a transient load the dynamic-stiffness matrix throughout the frequency range of interest is needed. The *boundary-element method* can be used. Only the boundary is discretized, leading to a reduction of the spatial dimension by one. A fundamental solution satisfying the governing equations in the domain must be determined. This analytical solution is often very complicated exhibiting singularities and for general anisotropy does not even exist. In each boundary element shape functions in the form of polynomials interpolate the displacements and surface tractions. Numerical integration of the polynomials with the fundamental solution involving singularities yields the non-symmetric coefficient matrices. As the fundamental solution satisfies exactly the radiation condition at infinity, the boundary-element method is well suited to analyse unbounded (infinite and semi-infinite) media.

It is the goal of the present paper to describe a novel procedure, called the *scaled boundary finite-element method*, which is based entirely on finite elements but with a discretization on the boundary only. Thus, the *advantages of the finite-element method and the boundary-element method are combined.*

To develop the scaled boundary finite-element method, a three-dimensional linear elastic unbounded medium with a section shown in Fig. 1 is addressed. The total boundary must be visible from a zone outside the medium where the so-called scaling centre O is chosen. In the medium with volume V the governing equations of elastodynamics apply. On the doubly-curved boundary S of the medium, the displacements and surface tractions are prescribed on S_u and S_t, respectively. The radial direction points from the scaling centre

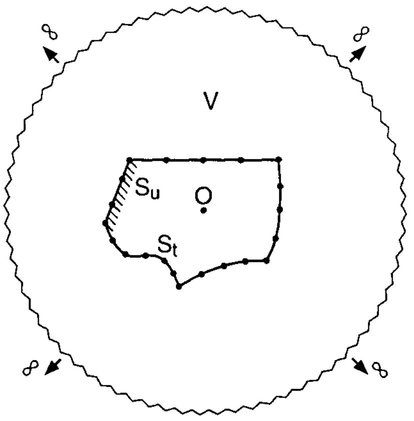

Fig. 1 Modelling of unbounded medium with surface finite elements with scaling centre outside medium (section).

to a point on the boundary, where two circumferential directions tangential to the boundary are identified. The boundary is discretized with doubly-curved surface finite elements with any arrangement of nodes.

For an unbounded medium the dynamic behaviour is described by the dynamic-stiffness matrix in the frequency domain $[S^{\infty}(\omega)]$, relating the displacement amplitudes in the degrees of freedom on the boundary S to the corresponding force amplitudes. Alternatively, the same force-displacement relationship can be represented in the time domain by the unit-impulse response matrix.

In general terms, the concept of the scaled boundary finite-element method can be described as follows. By scaling the boundary in the radial direction with respect to the scaling centre O with a scaling factor larger than 1, the whole domain is covered (Fig. 2). The scaling applies to each surface finite element. Its discretized surface on the boundary is denoted as S^e (superscript e for element). Continuous scaling of the element yields a truncated semi-infinite pyramid with volume V^e. The scaling centre O is at its apex. The "top" of the truncated pyramid is the surface finite element. The sides of the truncated pyramid forming the boundary A^e follow from extending straight lines passing through the scaling center from the curved edge of the surface finite-element to infinity. Note that no discretization on A^e occurs. Obviously, assembling all the truncated pyramids by connecting their sides which corresponds to enforcing compatibility and equilibrium results in the total medium with volume V and the closed boundary S. No boundaries A^e whose extensions passing through the scaling centre remain. Mathematically, the scaling corresponds to a transformation of the coordinates for each finite element, resulting in the two curvilinear local coordinates in the circumferential directions on the surface and the dimensionless radial coordinate representing the scaling factor. This transformation is unique due to the choice of the scaling centre. Summarizing, scaling of the boundary discretized with finite elements is applied, which explains the name of the scaled boundary finite-element method.

A powerful extension of the basic case with the scaling centre not located on the boundary shown in Fig. 1 is addressed. When during the assemblage process some sides of the truncated pyramids are not connected or some truncated pyramids are missing, an additional boundary A with its extension passing through the scaling centre is created. The case of a missing truncated pyramid is illustrated in Fig. 3 with the displacements and surface tractions prescribed on A_u and A_t, respectively. Thus, the boundary conditions on A_u and A_t can be modelled without spatial discretization by formulating them only on the finite-element edges P_1 and P_2 located on the boundary. The tops of all truncated pyramids form the boundary S which is not a closed surface. The total boundary of the medium consists of S and A. The scaling centre O is thus chosen on the (total) boundary. This applies when modelling a foundation embedded in a half-space where the free surface is not discretized.

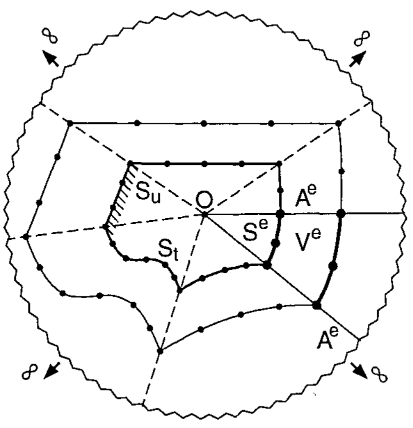

Fig. 2 Scaled boundary (section).

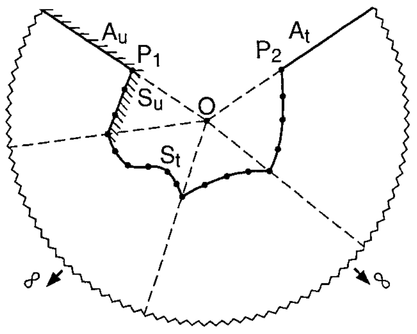

Fig. 3 Modelling of unbounded medium with surface finite elements with scaling centre on extension of boundary (section).

This transformation of the geometry involving the discretization of the boundary with finite elements and scaling in the radial direction leads to a system of linear second-order differential equations for the displacements with the dimensionless radial coordinate as the independent variable. The coefficient matrices are constant. No approximation other than that of the finite elements in the circumferential directions is introduced. After substituting the definition of the dynamic-stiffness matrix in the differential equations, it is shown that the dynamic-stiffness matrix is a function of the dimensionless frequency which is proportional to the product of the frequency and the dimensionless radial coordinate. This permits the equation for the dynamic-stiffness matrix on the boundary to be expressed as a system of nonlinear first-order ordinary differential equations in the frequency as the independent variable with constant coefficient matrices.

In comparison with the conventional finite-element method and the boundary-element method, the scaling boundary finite-element method has the following features which will be discussed. As is shown in Table 1, the scaled boundary finite-element method not only combines the advantages of the finite-element method and the boundary-element method but also exhibits additional advantages:

1. reduction of the spatial dimension by one, reducing the discretization effort and the number of degrees of freedom
2. no fundamental solution required which permits general anisotropic material to be addressed and eliminates singular integrals
3. radiation condition at infinity satisfied exactly for unbounded media
4. no discretization on that part of the boundary and interfaces between different materials passing through the scaling centre
5. exact in the radial direction
6. converges to the exact solution in the finite-element sense in the circumferential directions

The novel approach is described for the three-dimensional vector wave equation addressing an unbounded medium in Reference [1]. The corresponding derivation is based on the assemblage of an infinitesimal finite-element cell and on similarity. This physically motivated derivation leads to the same final equation for the dynamic-stiffness matrix after performing the limit of the cell width analytically as that derived

Table 1 Advantages of scaled boundary finite-element method compared with those of finite-element and boundary-element methods.

	FINITE-ELEMENT METHOD	BOUNDARY-ELEMENT METHOD	SCALED BOUNDARY FINITE-ELEMENT METHOD
reduction of spatial dimension by one		X	X
no fundamental solution required	X		X
no singular integrals to be evaluated	X		X
suitable for anisotropic material	X		X
radiation condition satisfied exactly		X	X
boundary conditions on free and fixed surfaces and interfaces between different meaterials satisfied without discretization			X

in the scaled boundary finite-element method. The procedure is called the *consistent infinitesimal finite-element cell method* reflecting its derivation, which could also be applied to a bounded medium. The consistent infinitesimal finite-element cell method is described in great detail in the book (Reference [2]) where the parabolic and elliptic partial differential equations are also addressed. The historical development is described in Reference [1] citing references, and will not be repeated.

The governing equations of three-dimensional elastodynamics are summarized in Section 2. The scaled boundary transformation of the geometry is derived in Section 3 and then applied to the governing equations of elastodynamics in Section 4. The boundary is discretized with surface finite elements in Section 5, which leads to the scaled boundary finite-element equation in displacement with the dimensionless radial coordinate as the independent variable. The scaled boundary finite-element equation in the dynamic-stiffness matrix is derived in Section 6. The boundary condition which is necessary to be able to start the solution procedure of the differential equation follows from an asymptotic expansion for high frequency in Section 7. Examples demonstrating the high accuracy and versatility of the scaled boundary finite-element method are described in Section 8. Conclusions are stated in Section 9. The key equations for the two-dimensional case are specified in Appendix A.

2 Governing Equations of Elastodynamics

The governing equations of three-dimensional elastodynamics are formulated in Cartesian coordinates $\hat{x}$, $\hat{y}$, $\hat{z}$. A circumflex ($\hat{\ }$) is introduced to denote a point in space, as the coordinates x, y, z are reserved for the boundary, which is discretized in an application. To simplify the nomenclature, the circumflex is omitted when used in a subscript to indicate a direction.

The unbounded medium shown in Fig. 3 is addressed. The boundary consisting of S_u and S_t is discretized, and the boundary A_u and A_t, whose extension passing through the scaling centre, is not discretized.

The differential equations of motion in the frequency domain expressed in displacement amplitudes $\{u\} = \{u(\hat{x},\hat{y},\hat{z})\} = [\ u_x \quad u_y \quad u_z\ ]^T$ are formulated as

$$[L]^T\{\sigma\} + \{p\} + \omega^2\rho\{u\} = 0 \tag{1}$$

with the mass density ρ and the amplitudes of the body forces $\{p\}$. The stress amplitudes $\{\sigma\}$ follows from

Hooke's law with the elasticity matrix $[D]$ as

$$\{\sigma\} = [\ \sigma_x \quad \sigma_y \quad \sigma_z \quad \tau_{yz} \quad \tau_{xz} \quad \tau_{xy}\ ]^T = [D]\{\varepsilon\} \tag{2}$$

The strain amplitudes $\{\varepsilon\}$ are defined from the strain-displacement relationship

$$\{\varepsilon\} = [\ \varepsilon_x \quad \varepsilon_y \quad \varepsilon_z \quad \gamma_{yz} \quad \gamma_{xz} \quad \gamma_{xy}\ ]^T = [L]\{u\} \tag{3}$$

with the differential operator $[L]$

$$[L] = \begin{bmatrix} \frac{\partial}{\partial \hat{x}} & & \\ & \frac{\partial}{\partial \hat{y}} & \\ & & \frac{\partial}{\partial \hat{z}} \\ & \frac{\partial}{\partial \hat{z}} & \frac{\partial}{\partial \hat{y}} \\ \frac{\partial}{\partial \hat{z}} & & \frac{\partial}{\partial \hat{x}} \\ \frac{\partial}{\partial \hat{y}} & \frac{\partial}{\partial \hat{x}} & \end{bmatrix} \tag{4}$$

The boundary conditions are equal to

$$\{u\} = \{\bar{u}\} \qquad \text{on } S_u \tag{5a}$$

$$\{t\} = \{\bar{t}\} \qquad \text{on } S_t \tag{5b}$$

and

$$\{u\} = 0 \qquad \text{on } A_u \tag{6a}$$

$$\{t\} = 0 \qquad \text{on } A_t \tag{6b}$$

with the prescribed displacement amplitudes $\{\bar{u}\}$ and prescribed surface traction amplitudes $\{\bar{t}\}$. For simplicity, the right-hand sides of (6) are assumed to be zero.

3 Scaled Boundary Transformation of Geometry

The transformation of the geometry corresponding to the scaled boundary discussed in Section 1 is addressed. The coordinates on the (doubly-curved) boundary are denoted as x, y, z. A point on the boundary is described by its position vector (unit vectors $\vec{i}$, $\vec{j}$, $\vec{k}$)

$$\vec{r} = x\vec{i} + y\vec{j} + z\vec{k} \tag{7}$$

The Cartesian coordinates $\hat{x}$, $\hat{y}$, $\hat{z}$ are transformed to the curvilinear coordinates ξ, η, ζ (Fig. 4). The scaling centre is selected outside of the domain (Fig. 1) or on the boundary (Fig. 3). It coincides with the origin of the coordinate system $\hat{x}$, $\hat{y}$, $\hat{z}$. The dimensionless radial coordinate ξ is measured from the scaling centre along the position vector

$$\vec{\hat{r}} = \hat{x}\vec{i} + \hat{y}\vec{j} + \hat{z}\vec{k} \tag{8}$$

ξ is constant (equal to 1) on the boundary. In a practical application, the geometry of the boundary is so general that only a piecewise description is feasible. (Doubly-curved) surface finite elements are used.

A specific finite element is addressed. The geometry of this finite element on the boundary is represented by interpolating its nodal coordinates $\{x\}$, $\{y\}$ and $\{z\}$ using the local coordinates η, ζ

$$x(\eta,\zeta) = [N(\eta,\zeta)]\{x\} \tag{9a}$$

$$y(\eta,\zeta) = [N(\eta,\zeta)]\{y\} \tag{9b}$$

$$z(\eta,\zeta) = [N(\eta,\zeta)]\{z\} \tag{9c}$$

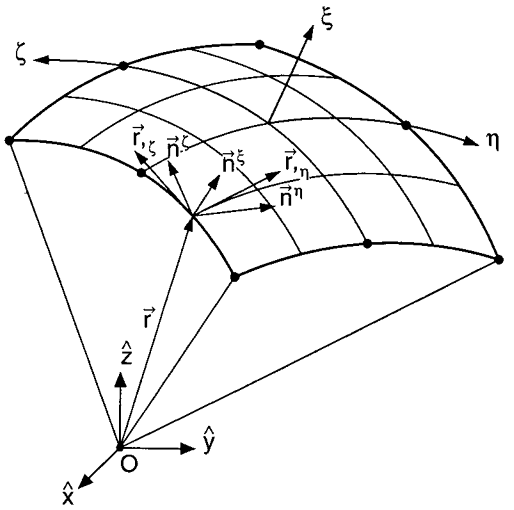

Fig. 4 Scaled boundary transformation of geometry of surface finite element.

with the mapping functions

$$[N(\eta,\zeta)] = [\; N_1(\eta,\zeta) \quad N_2(\eta,\zeta) \quad \ldots \;] \tag{10}$$

A point in the domain is obtained by scaling that on the boundary

$$\hat{\vec{r}} = \xi \vec{r} \tag{11}$$

Expressed in coordinates

$$\hat{x}(\xi,\eta,\zeta) = \xi x(\eta,\zeta) \tag{12a}$$
$$\hat{y}(\xi,\eta,\zeta) = \xi y(\eta,\zeta) \tag{12b}$$
$$\hat{z}(\xi,\eta,\zeta) = \xi z(\eta,\zeta) \tag{12c}$$

applies with $\xi = 1$ on the boundary and $= 0$ in the scaling centre. The uniqueness of the transformation is guaranteed by the choice of the scaling centre, from which the total boundary must be visible.

To transform the differential operator $[L]$ in the $\hat{x}$, $\hat{y}$, $\hat{z}$ coordinate system (Eq. (4)) to that in the ξ, η, ζ coordinate system, the Jacobian matrix is required

$$[\hat{J}(\xi,\eta,\zeta)] = \begin{bmatrix} \hat{x}_{,\xi} & \hat{y}_{,\xi} & \hat{z}_{,\xi} \\ \hat{x}_{,\eta} & \hat{y}_{,\eta} & \hat{z}_{,\eta} \\ \hat{x}_{,\zeta} & \hat{y}_{,\zeta} & \hat{z}_{,\zeta} \end{bmatrix} \tag{13}$$

The partial derivatives are calculated using (12) and (9), leading, for instance, to

$$\hat{x}_{,\xi} = x = [N]\{x\} \tag{14a}$$
$$\hat{x}_{,\eta} = \xi x_{,\eta} = \xi[N_{,\eta}]\{x\} \tag{14b}$$
$$\hat{x}_{,\zeta} = \xi x_{,\zeta} = \xi[N_{,\zeta}]\{x\} \tag{14c}$$

Substituting in (13) yields

$$[\hat{J}(\xi,\eta,\zeta)] = \begin{bmatrix} 1 & \xi & \xi \end{bmatrix} [J(\eta,\zeta)] \tag{15}$$

with the abbreviation

$$[J(\eta,\zeta)] = \begin{bmatrix} x & y & z \\ x_{,\eta} & y_{,\eta} & z_{,\eta} \\ x_{,\zeta} & y_{,\zeta} & z_{,\zeta} \end{bmatrix} \tag{16}$$

The argument η and ζ is omitted for conciseness. $[J]$ depends on the geometry of the boundary only. Its determinant is equal to

$$|J| = x(y_{,\eta} z_{,\zeta} - z_{,\eta} y_{,\zeta}) + y(z_{,\eta} x_{,\zeta} - x_{,\eta} z_{,\zeta}) + z(x_{,\eta} y_{,\zeta} - y_{,\eta} x_{,\zeta}) \tag{17}$$

$[J]$ and $|J|$ can be non-dimensionalized with a characteristic length r_0 with respect to the boundary as

$$[J] = r_0[\bar{J}] \tag{18a}$$

$$|J| = r_0^3|\bar{J}| \tag{18b}$$

where $[\bar{J}]$ and $|\bar{J}|$ are dimensionless. The inverse of the matrix $[J]$ is written as

$$[J]^{-1} = \frac{1}{|J|} \begin{bmatrix} y_{,\eta} z_{,\zeta} - z_{,\eta} y_{,\zeta} & zy_{,\zeta} - yz_{,\zeta} & yz_{,\eta} - zy_{,\eta} \\ z_{,\eta} x_{,\zeta} - x_{,\eta} z_{,\zeta} & xz_{,\zeta} - zx_{,\zeta} & zx_{,\eta} - xz_{,\eta} \\ x_{,\eta} y_{,\zeta} - y_{,\eta} x_{,\zeta} & yx_{,\zeta} - xy_{,\zeta} & xy_{,\eta} - yx_{,\eta} \end{bmatrix} \tag{19}$$

The coefficients in (19) satisfy the identities

$$(zy_{,\zeta} - yz_{,\zeta})_{,\eta} + (yz_{,\eta} - zy_{,\eta})_{,\zeta} = -2(y_{,\eta} z_{,\zeta} - z_{,\eta} y_{,\zeta}) \tag{20a}$$

$$(xz_{,\zeta} - zx_{,\zeta})_{,\eta} + (zx_{,\eta} - xz_{,\eta})_{,\zeta} = -2(z_{,\eta} x_{,\zeta} - x_{,\eta} z_{,\zeta}) \tag{20b}$$

$$(yx_{,\zeta} - xy_{,\zeta})_{,\eta} + (xy_{,\eta} - yx_{,\eta})_{,\zeta} = -2(x_{,\eta} y_{,\zeta} - y_{,\eta} x_{,\zeta}) \tag{20c}$$

The derivatives with respects to $\hat{x}$, $\hat{y}$, $\hat{z}$ are transformed to those with respect to ξ, η, ζ using (15)

$$\begin{Bmatrix} \frac{\partial}{\partial \hat{x}} \\ \frac{\partial}{\partial \hat{y}} \\ \frac{\partial}{\partial \hat{z}} \end{Bmatrix} = [\hat{J}]^{-1} \begin{Bmatrix} \frac{\partial}{\partial \xi} \\ \frac{\partial}{\partial \eta} \\ \frac{\partial}{\partial \zeta} \end{Bmatrix} = [J]^{-1} \begin{Bmatrix} \frac{\partial}{\partial \xi} \\ \frac{1}{\xi}\frac{\partial}{\partial \eta} \\ \frac{1}{\xi}\frac{\partial}{\partial \zeta} \end{Bmatrix} \tag{21}$$

The geometrical interpretation of the coordinate transformation is discussed (Fig. 4). The derivatives of the position vector of a point on the boundary (Eq. (7)) with respect to η and ζ represent two tangential vectors

$$\vec{r}_{,\eta} = x_{,\eta}\vec{i} + y_{,\eta}\vec{j} + z_{,\eta}\vec{k} \tag{22a}$$

$$\vec{r}_{,\zeta} = x_{,\zeta}\vec{i} + y_{,\zeta}\vec{j} + z_{,\zeta}\vec{k} \tag{22b}$$

with ζ, η, respectively, being constant. The three vectors $\vec{r}$, $\vec{r}_{,\eta}$, $\vec{r}_{,\zeta}$ form the base of the transformed coordinate system of the finite element. Eq. (17) is equivalent to

$$|J| = \vec{r} \cdot (\vec{r}_{,\eta} \times \vec{r}_{,\zeta}) \tag{23}$$

The infinitesimal volume $\mathrm{d}V$ for any ξ is calculated as

$$\mathrm{d}V = \vec{r}_{,\xi} \cdot (\vec{r}_{,\eta} \times \vec{r}_{,\zeta})\mathrm{d}\xi\mathrm{d}\eta\mathrm{d}\zeta \tag{24}$$

Using (11) and (23) leads to

$$\mathrm{d}V = \xi^2|J|\mathrm{d}\xi\mathrm{d}\eta\mathrm{d}\zeta \tag{25}$$

The outward normal vectors to the surfaces (η, ζ), (ζ, ξ) and (ξ, η), where the coordinates ξ, η and ζ, respectively, are constant, are equal on the boundary ($\xi = 1$) to

$$\vec{g}^{\xi} = \vec{r}_{,\eta} \times \vec{r}_{,\zeta} = (y_{,\eta} z_{,\zeta} - z_{,\eta} y_{,\zeta})\vec{i} + (z_{,\eta} x_{,\zeta} - x_{,\eta} z_{,\zeta})\vec{j} + (x_{,\eta} y_{,\zeta} - y_{,\eta} x_{,\zeta})\vec{k} \tag{26a}$$

$$\vec{g}^{\eta} = \vec{r}_{,\zeta} \times \vec{r} = (zy_{,\zeta} - yz_{,\zeta})\vec{i} + (xz_{,\zeta} - zx_{,\zeta})\vec{j} + (yx_{,\zeta} - xy_{,\zeta})\vec{k} \tag{26b}$$

$$\vec{g}^{\zeta} = \vec{r} \times \vec{r}_{,\eta} = (yz_{,\eta} - zy_{,\eta})\vec{i} + (zx_{,\eta} - xz_{,\eta})\vec{j} + (xy_{,\eta} - yx_{,\eta})\vec{k} \tag{26c}$$

The magnitude of a vector is denoted with the same symbol omitting the arrow sign (e.g. $g^{\xi} = |\vec{g}^{\xi}|$).

The transformation of infinitesimal surfaces for any ξ between the two coordinate systems is specified using (11) and (26) as

$$\mathrm{d}S^{\xi} = |\vec{\hat{r}}_{,\eta} \times \vec{\hat{r}}_{,\zeta}|\mathrm{d}\eta\mathrm{d}\zeta = |\xi\vec{r}_{,\eta} \times \xi\vec{r}_{,\zeta}|\mathrm{d}\eta\mathrm{d}\zeta = \xi^2 g^{\xi}\mathrm{d}\eta\mathrm{d}\zeta \tag{27a}$$

$$\mathrm{d}S^{\eta} = |\vec{\hat{r}}_{,\zeta} \times \vec{\hat{r}}_{,\xi}|\mathrm{d}\zeta\mathrm{d}\xi = |\xi\vec{r}_{,\zeta} \times \vec{r}|\mathrm{d}\zeta\mathrm{d}\xi = \xi g^{\eta}\mathrm{d}\zeta\mathrm{d}\xi \tag{27b}$$

$$\mathrm{d}S^{\zeta} = |\vec{\hat{r}}_{,\xi} \times \vec{\hat{r}}_{,\eta}|\mathrm{d}\xi\mathrm{d}\eta = |\vec{r} \times \xi\vec{r}_{,\eta}|\mathrm{d}\xi\mathrm{d}\eta = \xi g^{\zeta}\mathrm{d}\xi\mathrm{d}\eta \tag{27c}$$

The unit normal vectors of the three surfaces (Fig. 4) follow from (26) as

$$\vec{n}^{\xi} = n_x^{\xi}\vec{i} + n_y^{\xi}\vec{j} + n_z^{\xi}\vec{k} = \frac{\vec{g}^{\xi}}{g^{\xi}} \tag{28a}$$

$$\vec{n}^{\eta} = n_x^{\eta}\vec{i} + n_y^{\eta}\vec{j} + n_z^{\eta}\vec{k} = \frac{\vec{g}^{\eta}}{g^{\eta}} \tag{28b}$$

$$\vec{n}^{\zeta} = n_x^{\zeta}\vec{i} + n_y^{\zeta}\vec{j} + n_z^{\zeta}\vec{k} = \frac{\vec{g}^{\zeta}}{g^{\zeta}} \tag{28c}$$

Eqs. (19), (26) and (28) yield

$$[J]^{-1} = \frac{1}{|J|}\begin{bmatrix} g^{\xi}n_x^{\xi} & g^{\eta}n_x^{\eta} & g^{\zeta}n_x^{\zeta} \\ g^{\xi}n_y^{\xi} & g^{\eta}n_y^{\eta} & g^{\zeta}n_y^{\zeta} \\ g^{\xi}n_z^{\xi} & g^{\eta}n_z^{\eta} & g^{\zeta}n_z^{\zeta} \end{bmatrix} \tag{29}$$

Substituting (29) in (21) results in

$$\begin{Bmatrix} \frac{\partial}{\partial \hat{x}} \\ \frac{\partial}{\partial \hat{y}} \\ \frac{\partial}{\partial \hat{z}} \end{Bmatrix} = \frac{g^{\xi}}{|J|}\{n^{\xi}\}\frac{\partial}{\partial \xi} + \frac{1}{\xi}\left(\frac{g^{\eta}}{|J|}\{n^{\eta}\}\frac{\partial}{\partial \eta} + \frac{g^{\zeta}}{|J|}\{n^{\zeta}\}\frac{\partial}{\partial \zeta}\right) \tag{30}$$

The partial derivatives with respect to $\hat{x}$, $\hat{y}$, $\hat{z}$ are expressed as a function of those with respect to ξ, η, ζ.

4 Governing Equations of Elastodynamics with Geometry in Transformed Coordinate System

For the governing equations of elastodynamics in Section 2, the scaled boundary transformation of Section 3 is applied to the geometry of the domain. Only the spatial coordinates are affected. The components of the displacements, strains and stresses are still defined in the original coordinate system $\hat{x}$, $\hat{y}$, $\hat{z}$. This is analogous to the procedure of mapping parent elements to curvilinear elements in the finite-element method.

Thus, only the differential operator $[L]$ in (4) is addressed. Substituting (30) in (4) yields

$$[L] = [b^1]\frac{\partial}{\partial \xi} + \frac{1}{\xi}\left([b^2]\frac{\partial}{\partial \eta} + [b^3]\frac{\partial}{\partial \zeta}\right) \tag{31}$$

with

$$[b^1] = \frac{g^\xi}{|J|}\begin{bmatrix} n_x^\xi & 0 & 0 \\ 0 & n_y^\xi & 0 \\ 0 & 0 & n_z^\xi \\ 0 & n_z^\xi & n_y^\xi \\ n_z^\xi & 0 & n_x^\xi \\ n_y^\xi & n_x^\xi & 0 \end{bmatrix} \tag{32a}$$

$$[b^2] = \frac{g^\eta}{|J|}\begin{bmatrix} n_x^\eta & 0 & 0 \\ 0 & n_y^\eta & 0 \\ 0 & 0 & n_z^\eta \\ 0 & n_z^\eta & n_y^\eta \\ n_z^\eta & 0 & n_x^\eta \\ n_y^\eta & n_x^\eta & 0 \end{bmatrix} \tag{32b}$$

$$[b^3] = \frac{g^\zeta}{|J|}\begin{bmatrix} n_x^\zeta & 0 & 0 \\ 0 & n_y^\zeta & 0 \\ 0 & 0 & n_z^\zeta \\ 0 & n_z^\zeta & n_y^\zeta \\ n_z^\zeta & 0 & n_x^\zeta \\ n_y^\zeta & n_x^\zeta & 0 \end{bmatrix} \tag{32c}$$

Note that $[b^1]$, $[b^2]$ and $[b^3]$ are independent of ξ. The following identity can be verified by substituting (32), (28), (26) and (20)

$$(|J|[b^2])_{,\eta} + (|J|[b^3])_{,\zeta} = -2|J|[b^1] \tag{33}$$

The amplitudes of the surface tractions $\{t\} = [\ t_x \quad t_y \quad t_z\ ]^T$ on any boundary with the outward unit normal vector $\vec{n} = n_x\vec{i} + n_y\vec{j} + n_z\vec{k}$ equal

$$\{t\} = \begin{bmatrix} n_x & 0 & 0 & 0 & n_z & n_y \\ 0 & n_y & 0 & n_z & 0 & n_x \\ 0 & 0 & n_z & n_y & n_x & 0 \end{bmatrix}\{\sigma\} \tag{34}$$

By comparing (34) and (32), the traction amplitudes on the surfaces (η, ζ), (ζ, ξ) and (ξ, η), where the coordinates ξ, η and ζ, respectively, are constant, are written as

$$\{t^\xi\} = \frac{|J|}{g^\xi}[b^1]^T\{\sigma\} \tag{35a}$$

$$\{t^\eta\} = \frac{|J|}{g^\eta}[b^2]^T\{\sigma\} \tag{35b}$$

$$\{t^\zeta\} = \frac{|J|}{g^\zeta}[b^3]^T\{\sigma\} \tag{35c}$$

5 Boundary Discretization with Finite Elements

The exact differential equations in the frequency domain with the geometry in the transformed coordinate system are specified in (1) with $[L]$ in (31). The truncated semi-infinite pyramid whose top is one finite element on the boundary (Fig. 2) is addressed. The superscript e is dropped for conciseness. To derive a finite-element approximation, (1) is multiplied by a weighting function $\{w\} = \{w(\xi,\eta,\zeta)\}$ and integrated over the domain of the truncated pyramid

$$\int_V \{w\}^T[b^1]^T\{\sigma_{,\xi}\}\mathrm{d}V + \int_V \{w\}^T\frac{1}{\xi}\left([b^2]^T\{\sigma_{,\eta}\} + [b^3]^T\{\sigma_{,\zeta}\}\right)\mathrm{d}V$$
$$+\int_V \{w\}^T\{p\}\mathrm{d}V + \omega^2\int_V \{w\}^T\rho\{u\}\mathrm{d}V = 0 \quad (36)$$

The second term of (36) denoted as I is examined. Substituting (25) yields

$$I = \int_1^\infty \xi\left(\int_{S^\xi}\{w\}^T|J|\left([b^2]^T\{\sigma_{,\eta}\} + [b^3]^T\{\sigma_{,\zeta}\}\right)\mathrm{d}\eta\mathrm{d}\zeta\right)\mathrm{d}\xi \quad (37)$$

where S^ξ denotes the surface with a constant ξ. Applying Green's theorem to the surface integral results in

$$I = \int_1^\infty \xi\left(\oint_{\Gamma^\xi}\{w\}^T\left(|J|[b^3]^T\{\sigma\}\mathrm{d}\eta + |J|[b^2]^T\{\sigma\}\mathrm{d}\zeta\right)\right.$$
$$\left.-\int_{S^\xi}\left(\left(\{w\}^T|J|[b^2]^T\right)_{,\eta} + \left(\{w\}^T|J|[b^3]^T\right)_{,\zeta}\right)\{\sigma\}\mathrm{d}\eta\mathrm{d}\zeta\right)\mathrm{d}\xi \quad (38)$$

with the contour Γ^ξ (resulting from scaling the edge of the surface finite element) of S^ξ. Substituting (35b) and (35c) in (38) and using (33) leads to

$$I = \int_1^\infty \xi\left(\oint_{\Gamma^\xi}\{w\}^T\left(\{t^\zeta\}g^\zeta\mathrm{d}\eta + \{t^\eta\}g^\eta\mathrm{d}\zeta\right)\right.$$
$$\left.-\int_{S^\xi}\left(-2\{w\}^T[b^1]^T + \{w_{,\eta}\}^T[b^2]^T + \{w_{,\zeta}\}^T[b^3]^T\right)\{\sigma\}|J|\mathrm{d}\eta\mathrm{d}\zeta\right)\mathrm{d}\xi \quad (39)$$

Substituting (25) in the first, third and fourth terms in (36) and using (39) yields

$$\int_1^\infty\left(\xi^2\int_{S^\xi}\{w\}^T[b^1]^T\{\sigma_{,\xi}\}|J|\mathrm{d}\eta\mathrm{d}\zeta + \xi\oint_{\Gamma^\xi}\{w\}^T\left(\{t^\zeta\}g^\zeta\mathrm{d}\eta + \{t^\eta\}g^\eta\mathrm{d}\zeta\right)\right.$$
$$-\xi\int_{S^\xi}\left(-2\{w\}^T[b^1]^T + \{w_{,\eta}\}^T[b^2]^T + \{w_{,\zeta}\}^T[b^3]^T\right)\{\sigma\}|J|\mathrm{d}\eta\mathrm{d}\zeta$$
$$\left.+\xi^2\int_{S^\xi}\{w\}^T\{p\}|J|\mathrm{d}\eta\mathrm{d}\zeta + \omega^2\xi^2\int_{S^\xi}\{w\}^T\rho\{u\}|J|\mathrm{d}\eta\mathrm{d}\zeta\right)\mathrm{d}\xi = 0 \quad (40)$$

Eq. (40) is satisfied by setting the integrand of the integral over ξ equal to zero. This corresponds to *enforcing the equation of motion (1) exactly in the* ξ *direction*

$$\xi^2\int_{S^\xi}\{w\}^T[b^1]^T\{\sigma_{,\xi}\}|J|\mathrm{d}\eta\mathrm{d}\zeta + \xi\oint_{\Gamma^\xi}\{w\}^T\left(\{t^\zeta\}g^\zeta\mathrm{d}\eta + \{t^\eta\}g^\eta\mathrm{d}\zeta\right)$$
$$-\xi\int_{S^\xi}\left(-2\{w\}^T[b^1]^T + \{w_{,\eta}\}^T[b^2]^T + \{w_{,\zeta}\}^T[b^3]^T\right)\{\sigma\}|J|\mathrm{d}\eta\mathrm{d}\zeta$$
$$+\xi^2\int_{S^\xi}\{w\}^T\{p\}|J|\mathrm{d}\eta\mathrm{d}\zeta + \omega^2\xi^2\int_{S^\xi}\{w\}^T\rho\{u\}|J|\mathrm{d}\eta\mathrm{d}\zeta = 0 \quad (41)$$

Note that no volume integrals are present in (41).

The displacement amplitudes of the finite element on the boundary ($\xi = 1$) are interpolated using shape functions $[N^u(\eta,\zeta)]$. It is postulated that the same shape functions apply with the displacement amplitudes $\{u(\xi)\}$ for all surfaces S^ξ with a constant ξ

$$\{u(\xi,\eta,\zeta)\} = [N^u(\eta,\zeta)]\{u(\xi)\} \quad (42)$$

The stress amplitudes are calculated substituting (42) and (31) in (3) using (2)

$$\{\sigma\} = [D]\left([B^1]\{u(\xi)\},_{\xi} + \frac{1}{\xi}[B^2]\{u(\xi)\}\right) \tag{43}$$

with

$$[B^1] = [b^1][N^u(\eta,\zeta)] \tag{44a}$$

$$[B^2] = [b^2][N^u(\eta,\zeta)],_{\eta} + [b^3][N^u(\eta,\zeta)],_{\zeta} \tag{44b}$$

$[B^1]$ and $[B^2]$ are independent of ξ. The displacement discretization also applies to the weighting function $\{w\} = \{w(\xi,\eta,\zeta)\}$

$$\{w(\xi,\eta,\zeta)\} = [N^u(\eta,\zeta)]\{w(\xi)\} \tag{45}$$

Substituting (45) in (41) for arbitrary $\{w(\xi)\}$ yields

$$\xi^2 \int_{S^\xi} [B^1]^T\{\sigma,_{\xi}\}|J|\mathrm{d}\eta\mathrm{d}\zeta - \xi \int_{S^\xi} \left(-2[B^1]^T + [B^2]^T\right)\{\sigma\}|J|\mathrm{d}\eta\mathrm{d}\zeta \\ + \omega^2\xi^2 \int_{S^\xi} [N^u(\eta,\zeta)]^T \rho\{u\}|J|\mathrm{d}\eta\mathrm{d}\zeta + \xi\{T\} + \xi^2\{P\} = 0 \tag{46}$$

with

$$\{T\} = \oint_{\Gamma^\xi} [N^u(\eta,\zeta)]^T \left(\{t^\zeta\}g^\zeta \mathrm{d}\eta + \{t^\eta\}g^\eta \mathrm{d}\zeta\right) \tag{47}$$

$$\{P\} = \int_{S^\xi} [N^u(\eta,\zeta)]^T\{p\}|J|\mathrm{d}\eta\mathrm{d}\zeta \tag{48}$$

$\{T\}$ corresponds to the amplitudes of the nodal forces resulting from the surface tractions acting on those surfaces A whose extensions pass through the scaling centre (Fig. 2) and $\{P\}$ to the body forces. Substituting the stress amplitudes of (43) in (46) results in the differential equations expressed in displacement amplitudes

$$\xi^2 \int_{S^\xi} [B^1]^T[D]\left([B^1]\{u(\xi)\},_{\xi\xi} + \frac{1}{\xi}[B^2]\{u(\xi)\},_{\xi} - \frac{1}{\xi^2}[B^2]\{u(\xi)\}\right)|J|\mathrm{d}\eta\mathrm{d}\zeta \\ - \xi \int_{S^\xi} \left(-2[B^1]^T + [B^2]^T\right)[D]\left([B^1]\{u(\xi)\},_{\xi} + \frac{1}{\xi}[B^2]\{u(\xi)\}\right)|J|\mathrm{d}\eta\mathrm{d}\zeta \\ + \omega^2\xi^2 \int_{S^\xi} [N^u(\eta,\zeta)]^T\rho[N^u(\eta,\zeta)]\{u(\xi)\}|J|\mathrm{d}\eta\mathrm{d}\zeta + \xi\{T\} + \xi^2\{P\} = 0 \tag{49}$$

Introducing the coefficient matrices

$$[E^0] = \int_{S^\xi} [B^1]^T[D][B^1]|J|\mathrm{d}\eta\mathrm{d}\zeta \tag{50a}$$

$$[E^1] = \int_{S^\xi} [B^2]^T[D][B^1]|J|\mathrm{d}\eta\mathrm{d}\zeta \tag{50b}$$

$$[E^2] = \int_{S^\xi} [B^2]^T[D][B^2]|J|\mathrm{d}\eta\mathrm{d}\zeta \tag{50c}$$

and

$$[M^0] = \int_{S^\xi} [N^u(\eta,\zeta)]^T\rho[N^u(\eta,\zeta)]|J|\mathrm{d}\eta\mathrm{d}\zeta \tag{51}$$

yields

$$[E^0]\xi^2\{u(\xi)\}_{,\xi\xi}+(2[E^0]-[E^1]+[E^1]^T)\xi\{u(\xi)\}_{,\xi} \\ +([E^1]^T-[E^2])\{u(\xi)\}+\omega^2[M^0]\xi^2\{u(\xi)\}+\xi\{T\}+\xi^2\{P\}=0 \quad (52)$$

Note that the coefficient matrices $[E^0]$, $[E^1]$, $[E^2]$, $[M^0]$ are independent of ξ. Integrations over the surface finite element (at $\xi = 1$) only are involved. For later use, the coefficient matrices are non-dimensionalized

$$[E^0] = Gr_0[\bar{E}^0] \quad (53a)$$

$$[E^1] = Gr_0[\bar{E}^1] \quad (53b)$$

$$[E^2] = Gr_0[\bar{E}^2] \quad (53c)$$

and

$$[M^0] = \rho r_0^3[\bar{M}^0] \quad (54)$$

with the shear modulus G.

Eq. (52) applies to the domain of the truncated pyramid corresponding to one finite element on the boundary. To model the total domain, an assemblage as in the conventional finite-element method is performed. To simplify the nomenclature, the same symbols are used for the assembled coefficient matrices and the assembled displacement amplitudes in the following. In the assemblage process the nodal forces $\{T\}$ in (47) will cancel with the exception of those on the part A_t of the total boundary passing through the scaling centre with prescribed surface tractions. The case of the free surface (6b) and vanishing body forces leading to $\{\bar{T}\} = 0$ and $\{P\} = 0$ is addressed. The assemblage process yields

$$[E^0]\xi^2\{u(\xi)\}_{,\xi\xi}+(2[E^0]-[E^1]+[E^1]^T)\xi\{u(\xi)\}_{,\xi}+([E^1]^T-[E^2])\{u(\xi)\}+\omega^2[M^0]\xi^2\{u(\xi)\}=0 \quad (55)$$

Eq. (55) represents the *scaled boundary finite-element equation in displacement* formulated in the frequency domain in three dimensions. It is a system of linear second-order ordinary differential equations for the displacement amplitude $\{u(\xi)\}$ in the dimensionless radial coordinate ξ as the independent variable. As already pointed out, the coefficient matrices $[E^0]$, $[E^1]$, $[E^2]$, $[M^0]$ are independent of ξ. In the scalar case, a transformation to the Bessel differential equation is possible.

6 Dynamic-Stiffness Matrix on Boundary

The dynamic-stiffness matrix of the unbounded medium corresponding to all the degrees of freedom on the boundary $[S^\infty(\omega)]$ is addressed. For any surface S^ξ with a constant ξ, the virtual work is formulated as

$$\{w(\xi)\}^T\{R(\xi)\} = \int_{S^\xi}\{w\}^T\{t^\xi\}\mathrm{d}S^\xi \quad (56)$$

with the amplitudes of the resultant forces $\{R(\xi)\}$ and of the surface tractions $\{t^\xi\}$. Substituting the weighting function $\{w\}$ (Eq. (45)) and the infinitesimal surface $\mathrm{d}S^\xi$ (Eq. (27a)) yields for an arbitrary $\{w(\xi)\}$

$$\{R(\xi)\} = \int_{S^\xi}[N^u(\eta,\zeta)]^T\{t^\xi\}\xi^2 g^\xi \mathrm{d}\eta\mathrm{d}\zeta \quad (57)$$

Substituting (43) in (35a) and then in (57) and using (44) leads to

$$\{R(\xi)\} = \int_{S^\xi}[B^1]^T[D]\left([B^1]\{u(\xi)\}_{,\xi}+\frac{1}{\xi}[B^2]\{u(\xi)\}\right)\xi^2|J|\mathrm{d}\eta\mathrm{d}\zeta \quad (58)$$

Introducing $[E^0]$, $[E^1]$ (Eqs. (50a) and (50b)) results in

$$\{R(\xi)\} = [E^0]\xi^2\{u(\xi)\}_{,\xi}+[E^1]^T\xi\{u(\xi)\} \quad (59)$$

The dynamic-stiffness matrix on a surface with constant ξ is defined as (superscript ∞ for unbounded)

$$-\{R(\xi)\} = [S^{\infty}(\omega,\xi)]\{u(\xi)\} \tag{60}$$

Equating the right-hand sides of (59) and (60) yields

$$-[S^{\infty}(\omega,\xi)]\{u(\xi)\} = [E^0]\xi^2\{u(\xi)\},_{\xi} + [E^1]^T\xi\{u(\xi)\} \tag{61}$$

From (55) and (61) the equation for $[S^{\infty}(\omega,\xi)]$ can be derived. Differentiating (61) with respect to ξ leads to

$$\begin{aligned} &-[S^{\infty}(\omega,\xi)],_{\xi}\{u(\xi)\} - [S^{\infty}(\omega,\xi)]\{u(\xi)\},_{\xi} - [E^0]\xi^2\{u(\xi)\},_{\xi\xi} \\ &\qquad - (2[E^0] + [E^1]^T)\xi\{u(\xi)\},_{\xi} - [E^1]^T\{u(\xi)\} = 0 \end{aligned} \tag{62}$$

Adding (55) and (62) results in

$$-[S^{\infty}(\omega,\xi)],_{\xi}\{u(\xi)\} - ([S(\omega,\xi)] + \xi[E^1])\{u(\xi)\},_{\xi} - [E^2]\{u(\xi)\} + \omega^2[M^0]\xi^2\{u(\xi)\} = 0 \tag{63}$$

Solving (61) for $\{u(\xi)\},_{\xi}$ and substituting in (63) yields for arbitrary $\{u(\xi)\}$

$$([S^{\infty}(\omega,\xi)] + \xi[E^1])(\xi[E^0])^{-1}([S^{\infty}(\omega,\xi)] + \xi[E^1]^T) - \xi[S(\omega,\xi)],_{\xi} - \xi[E^2] + \omega^2\xi^3[M^0] = 0 \tag{64}$$

Introducing the dimensionless dynamic-stiffness matrix denoted with a bar

$$[S^{\infty}(\omega,\xi)] = Gr_0\xi[\bar{S}^{\infty}(\omega,\xi)] \tag{65}$$

and substituting (53) and (54) in (64) leads to

$$\begin{aligned} &([\bar{S}^{\infty}(\omega,\xi)] + [\bar{E}^1])[\bar{E}^0]^{-1}([\bar{S}^{\infty}(\omega,\xi)] + [\bar{E}^1]^T) - [\bar{S}^{\infty}(\omega,\xi)] \\ &\qquad - \xi[\bar{S}^{\infty}(\omega,\xi)],_{\xi} - [\bar{E}^2] + \left(\frac{\omega r_0}{c_s}\xi\right)^2[\bar{M}^0] = 0 \end{aligned} \tag{66}$$

with the shear-wave velocity $c_s = \sqrt{G/\rho}$. The coefficient of the last term defines the dimensionless frequency for any ξ

$$a_0(\omega,\xi) = \frac{\omega r_0}{c_s}\xi \tag{67}$$

The second-last term is written as

$$\xi[\bar{S}^{\infty}(\omega,\xi)],_{\xi} = a_0[\bar{S}^{\infty}(\omega,\xi)],_{a_0} \tag{68}$$

After substituting (67) and (68) in (66), the only independent variable in the equation is a_0. Thus, the dimensionless dynamic-stiffness matrix is a function of a_0 only

$$[\bar{S}^{\infty}(\omega,\xi)] = [\bar{S}^{\infty}(a_0)] \tag{69}$$

The term with the derivative $a_0[\bar{S}^{\infty}(a_0)],_{a_0}$ can be interpreted either for varying ξ with fixed ω or for varying ω with fixed ξ

$$a_0[\bar{S}^{\infty}(a_0)],_{a_0} = \xi[\bar{S}^{\infty}(a_0)],_{\xi} = \omega[\bar{S}^{\infty}(a_0)],_{\omega} \tag{70}$$

Differentiating (65) with respect to ξ and using (69) and (70) yields

$$\xi[S^{\infty}(\omega,\xi)],_{\xi} = [S^{\infty}(\omega,\xi)] + \omega[S^{\infty}(\omega,\xi)],_{\omega} \tag{71}$$

Substituting (71) in (64) results in

$$([S^{\infty}(\omega,\xi)]+\xi[E^1])(\xi[E^0])^{-1}([S^{\infty}(\omega,\xi)]+\xi[E^1]^T)-[S^{\infty}(\omega,\xi)]-\omega[S^{\infty}(\omega,\xi)]_{,\omega}-\xi[E^2]+\omega^2\xi^3[M^0]=0 \qquad (72)$$

For the boundary ($\xi = 1$) the dynamic-stiffness matrix is expressed as

$$([S^{\infty}(\omega)]+[E^1])[E^0]^{-1}([S^{\infty}(\omega)]+[E^1]^T)-[S^{\infty}(\omega)]-\omega[S^{\infty}(\omega)]_{,\omega}-[E^2]+\omega^2[M^0]=0 \qquad (73)$$

This represents the *scaled boundary finite-element equation in dynamic stiffness* formulated in the frequency domain for a three-dimensional unbounded medium. It is a system of nonlinear first-order ordinary differential equations in the independent variable, which is the frequency.

Comparing (73) for the three-dimensional case and (A.13) for the two-dimensional case the scaled boundary finite-element equation can be unified using the spatial dimension s ($= 2$ or $= 3$)

$$([S^{\infty}(\omega)]+[E^1])[E^0]^{-1}([S^{\infty}(\omega)]+[E^1]^T)-(s-2)[S^{\infty}(\omega)]-\omega[S^{\infty}(\omega)]_{,\omega}-[E^2]+\omega^2[M^0]=0 \qquad (74)$$

This equation is identical to equation (56) for the unbounded medium in Reference [1].

7 Asymptotic Expansion for High Frequency

The dynamic-stiffness matrix $[S^{\infty}(\omega)]$ at high frequency is expanded in a power series of $i\omega$ in descending order starting at one

$$[S^{\infty}(\omega)] \approx i\omega[C_{\infty}]+[K_{\infty}]+\sum_{j=1}^{m}\frac{1}{(i\omega)^j}[A_j] \qquad (75)$$

The first two terms on the right-hand side represent the singular part $[S_s^{\infty}(\omega)]$ with the constant dashpot matrix $[C_{\infty}]$ and the constant spring matrix $[K_{\infty}]$ (Reference [4], p. 256). The third term denotes the asymptotic expansion with m terms of the regular part $[S_r^{\infty}(\omega)]$ with the unknown coefficient matrices $[A_j]$ ($j = 1,\dots,m$). A concise formulation results when the transformation based on the following eigenvalue problem is introduced

$$[M^0][\Phi] = [E^0][\Phi]\lceil\Lambda^2\rfloor \qquad (76)$$

$[M^0]$ and $[E^0]$ are positive definite matrices resulting in positive eigenvalues $\lceil\Lambda^2\rfloor$. The eigenvectors $[\Phi]$ are normalized as

$$[\Phi]^T[E^0][\Phi] = [I] \qquad (77)$$

yielding

$$[\Phi]^T[M^0][\Phi] = \lceil\Lambda^2\rfloor \qquad (78)$$

and

$$[E^0]^{-1} = [\Phi][\Phi]^T \qquad (79)$$

Premultiplying (74) by $[\Phi]^T$ and postmultiplying by $[\Phi]$ results in

$$([s^{\infty}(\omega)]+[e^1])([s^{\infty}(\omega)]+[e^1]^T)-(s-2)[s^{\infty}(\omega)]-\omega[s^{\infty}(\omega)]_{,\omega}-[e^2]+\omega^2\lceil\Lambda^2\rfloor=0 \qquad (80)$$

where

$$[s^{\infty}(\omega)] = [\Phi]^T[S^{\infty}(\omega)][\Phi] \qquad (81)$$

and

$$[e^1] = [\Phi]^T [E^1][\Phi] \tag{82a}$$

$$[e^2] = [\Phi]^T [E^2][\Phi] \tag{82b}$$

Substituting (75) in (81) yields

$$[s^\infty(\omega)] \approx \mathrm{i}\omega[c_\infty] + [k_\infty] + \sum_{j=1}^{m} \frac{1}{(\mathrm{i}\omega)^j}[a_j] \tag{83}$$

with

$$[c_\infty] = [\Phi]^T [C_\infty][\Phi] \tag{84a}$$

$$[k_\infty] = [\Phi]^T [K_\infty][\Phi] \tag{84b}$$

$$[a_j] = [\Phi]^T [A_j][\Phi] \tag{84c}$$

Substituting (83) in (80) and rearranging in descending order of the power series of iω leads to

$$\begin{aligned}(\mathrm{i}\omega)^2 \left([c_\infty]^2 - \lceil \Lambda^2 \rfloor\right) &+ \mathrm{i}\omega \left([c_\infty][k_\infty] + [k_\infty][c_\infty] + [c_\infty][e^1]^T + [e^1][c_\infty] - (s-1)[c_\infty]\right) \\ &+ [c_\infty][a_1] + [a_1][c_\infty] + \left([k_\infty] + [e^1]\right)\left([k_\infty] + [e^1]^T\right) - (s-2)[k_\infty] - [e^2] \\ &+ \frac{1}{\mathrm{i}\omega}\left([c_\infty][a_2] + [a_2][c_\infty] + \left([k_\infty] + [e^1]\right)[a_1] + [a_1]\left([k_\infty] + [e^1]^T\right) - (s-3)[a_1]\right) \approx 0\end{aligned} \tag{85}$$

In (85), $m = 2$ is selected. The generalization to any m leading to additional terms is straightforward.

The coefficient matrix of each term of the power series in iω is set equal to zero in descending order. The first yields

$$[c_\infty]^2 = \lceil \Lambda^2 \rfloor \tag{86}$$

Selecting the positive roots of each element on the diagonal of $\lceil \Lambda^2 \rfloor$ leads to

$$[c_\infty] = \lceil \Lambda \rfloor \tag{87}$$

The dashpot matrix $[C_\infty]$ follows from (84a) as

$$[C_\infty] = \left([\Phi]^{-1}\right)^T \lceil \Lambda \rfloor [\Phi]^{-1} \tag{88}$$

As each coefficient of $\lceil \Lambda \rfloor$ is positive, $[C_\infty]$ will be positive definite.

The second term in (85) results after substituting (87) in

$$\lceil \Lambda \rfloor [k_\infty] + [k_\infty] \lceil \Lambda \rfloor = -\lceil \Lambda \rfloor [e^1]^T - [e^1] \lceil \Lambda \rfloor + (s-1) \lceil \Lambda \rfloor \tag{89}$$

This linear equation for $[k_\infty]$ is a Lyapunov equation with a diagonal coefficient matrix $\lceil \Lambda \rfloor$. Its solution for each element $k_{\infty kl}$ equals

$$k_{\infty kl} = \frac{1}{\Lambda_k + \Lambda_l}\left(-\Lambda_k e^1_{lk} - \Lambda_l e^1_{kl} + (s-1)\Lambda_k \delta_{kl}\right) \tag{90}$$

with the Kronecker delta δ_{kl} (=1 for $k = l$; =0 for $k \neq l$). The spring matrix $[K_\infty]$ is calculated from (84b) as

$$[K_\infty] = \left([\Phi]^{-1}\right)^T [k_\infty][\Phi]^{-1} \tag{91}$$

The third term in (85) leads after substituting (87) with the known $[k_\infty]$ to

$$\lceil \Lambda \rfloor [a_1] + [a_1] \lceil \Lambda \rfloor = -\left([k_\infty] + [e^1]\right)\left([k_\infty] + [e^1]^T\right) + (s-2)[k_\infty] + [e^2] \tag{92}$$

This equation for $[a_1]$ is in the same form as (89). Analogously, $[a_2]$ is determined from the fourth term in (85) with the known $[c_\infty] = \lceil \Lambda \rfloor$, $[k_\infty]$ and $[a_1]$

$$\lceil \Lambda \rfloor [a_2] + [a_2] \lceil \Lambda \rfloor = -\left([k_\infty] + [e^1]\right)[a_1] - [a_1]\left([k_\infty] + [e^1]^T\right) + (s-3)[a_1] \tag{93}$$

The coefficient matrices $[A_j]$ result from (84c) as

$$[A_j] = \left([\Phi]^{-1}\right)^T \lceil a_j \rfloor [\Phi]^{-1} \tag{94}$$

After calculating $[C_\infty]$, $[K_\infty]$, $[A_1]$ and $[A_2]$, the asymptotic behaviour for $m = 2$ follows from (75).

In an actual application of the scaled boundary finite-element method in the frequency domain the boundary condition at the specified high frequency ω_h $[S^\infty(\omega_h)]$ follows from (75) for a selected m. The dashpot matrix $[C_\infty]$ is calculated after solving an eigenvalue problem (Eq. (88)), and the spring matrix $[K_\infty]$ (Eq. (91)) as well as the coefficient matrices of the asymptotic expansion $[A_j]$ (Eq. (94)) follow from Lyapunov equations. $[S^\infty(\omega_h)]$ is then used as the starting value to integrate the scaled boundary finite-element equation in frequency (Eq. (74)) for decreasing ω.

The scaled boundary finite-element equation is processed for decreasing frequencies starting at a very large value ω_h which replaces $\omega \to \infty$. The starting value of $[S^\infty(\omega_h)]$ is determined based on an asymptotic expansion at high frequency (Eq. (75)).

8 Examples

(1) Spherical Cavity Embedded in Full-Space

The spherical cavity of radius r embedded in a full-space with shear modulus G, Poisson's ratio ν and mass density ρ is addressed. A uniform normal displacement amplitude $u_0(\omega)$ is prescribed on its wall, the structure-medium interface, yielding the pressure amplitude $p(\omega)$. This one-dimensional problem is solved in Section 2.3 of Reference [4]. The analytical solution of the dynamic-stiffness coefficient relating $u_0(\omega)$ to the total interaction force $R(\omega) = 4\pi r^2 p(\omega)$ is specified as

$$S^\infty(\omega) = 16\pi G r \left(1 + \frac{1-\nu}{2(1-2\nu)} \frac{1}{c_p} \frac{(\mathrm{i}\omega r)^2}{c_p + \mathrm{i}\omega r}\right) \tag{95}$$

with the dilatational-wave velocity c_p.

The coefficients E^0, E^1, E^2 and M^0 follow as

$$E^0 = 8\pi \frac{1-\nu}{1-2\nu} G r \tag{96a}$$

$$E^1 = 16\pi \frac{\nu}{1-2\nu} G r \tag{96b}$$

$$E^2 = 16\pi \frac{1}{1-2\nu} G r \tag{96c}$$

$$M^0 = 4\pi \rho r^3 \tag{97}$$

Substituting (96) and (97) in (74) yields

$$\frac{1}{8\pi} \frac{1-2\nu}{1-\nu} \frac{1}{Gr} (S^\infty(\omega))^2 - \frac{1-5\nu}{1-\nu} S^\infty(\omega) - \omega S^\infty(\omega)_{,\omega} + 4\pi r^3 \rho \omega^2 - 16\pi \frac{1+\nu}{1-\nu} G r = 0 \tag{98}$$

The accuracy of the scaled boundary finite-element method is investigated. First, the asymptotic expansion for high frequency, which provides the boundary condition, is examined. An asymptotic expansion can be derived from the analytical solution and used in a comparison with that of the scaled boundary finite-element method. The coefficients of the asymptotic expansion of the analytical solution of $S^{\infty}(\omega)$ specified in (95) for high frequency are

$$C_{\infty} = 4\pi r^2 \rho c_p \tag{99a}$$

$$K_{\infty} = 8\pi \frac{1-3\nu}{1-2\nu} Gr \tag{99b}$$

$$A_1 = 4\pi \rho c_p^3 \tag{99c}$$

$$A_2 = -4\pi \rho c_p^4 \frac{1}{r} \tag{99d}$$

The coefficients of the asymptotic expansion are calculated from the scaled boundary finite-element method. From (76) and (77)

$$\Lambda^2 = \frac{M^0}{E^0} \tag{100}$$

$$\Phi = (E^0)^{-0.5} \tag{101}$$

result. The dashpot coefficient C_{∞} follows from (88) as

$$C_{\infty} = \frac{\Lambda}{\Phi^2} = 4\pi r^2 \rho c_p \tag{102}$$

and the spring coefficient K_{∞} from (89) and (91) as

$$K_{\infty} = E^0 - E^1 = 8\pi \frac{1-3\nu}{1-2\nu} Gr \tag{103}$$

The coefficients A_1 and A_2 result from (92), (93) and (94) as

$$A_1 = 4\pi \rho c_p^3 \tag{104a}$$

$$A_2 = -4\pi \rho c_p^4 \frac{1}{r} \tag{104b}$$

As expected, the coefficients of the asymptotic expansion C_{∞}, K_{∞}, A_1, A_2 determined from the scaled boundary finite-element equation are identical to those of the analytical solution (Eq. (99)).

The scaled boundary finite-element equation (Eq. (98)) is solved starting from the boundary condition evaluated at different frequencies ω_h

$$S^{\infty}(\omega_h) \approx \mathrm{i}\omega_h C_{\infty} + K_{\infty} + \sum_{j=1}^{m} \frac{1}{(\mathrm{i}\omega_h)^j} A_j \tag{105}$$

The analysis is performed for Poisson's ratio $\nu = 0.25$ using the Bulirsch-Stoer method described in Reference [3], starting at $\omega_h = a_{0h} c_p / r$ for $a_{0h} = 3$ and $= 6$. The dynamic-stiffness coefficient is decomposed in the dimensionless spring coefficient $k(a_0)$ and damping coefficient $c(a_0)$ as

$$S^{\infty}(a_0) = K^{\infty}(k(a_0) + \mathrm{i}a_0 c(a_0)) \tag{106}$$

with the static-stiffness coefficient K^{∞} and the dimensionless frequency $a_0 = \omega r / c_p$. As shown in Fig. 5, the (small) error of the boundary condition decreases for decreasing a_0. Even for $a_{0h} = 3$ with the boundary condition $K^{\infty}(0.333 + \mathrm{i}2)$ (the analytical solution equals $K^{\infty}(0.325 + \mathrm{i}2.025)$), the results are highly accurate.

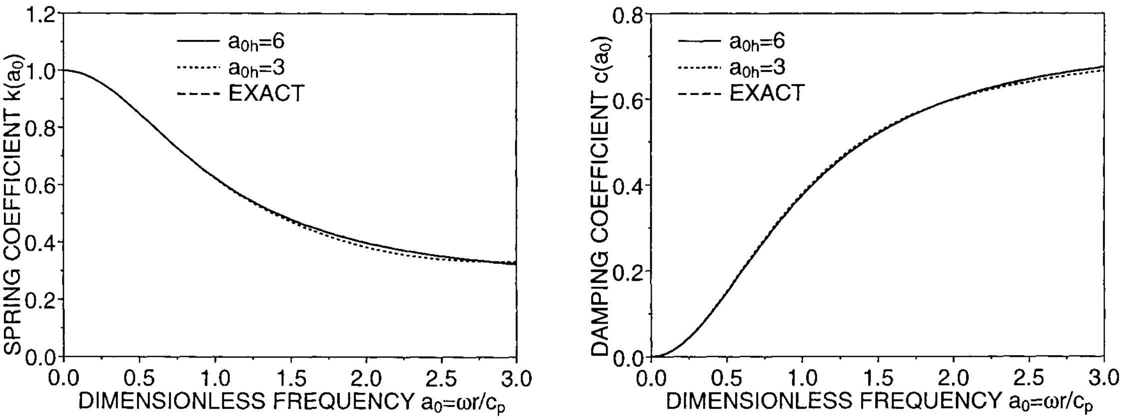

Fig. 5 Dynamic-stiffness coefficient of spherical cavity for different starting values.

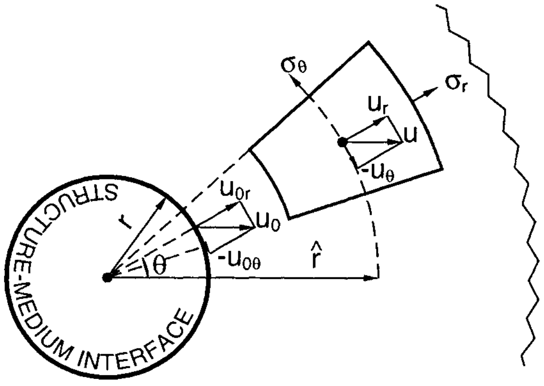

Fig. 6 Circular cavity embedded in full-plane with prescribed translational motion.

(2) Circular Cavity Embedded in Full-Plane

As a two-dimensional in-plane wave propagation problem with an analytical solution available, the circular cavity embedded in a full-plane is discussed (Fig. 6). On its rigid wall, the structure-medium interface, a constant horizontal displacement u_0 is enforced. The radius of the cavity is r, and the material properties of the full-plane are chosen as the Lamé parameters λ and G, the shear modulus ($\lambda = 2G\nu/(1-2\nu)$ with Poisson's ratio ν). The shear- and dilatational-wave velocities equal

$$c_s = \sqrt{\frac{G}{\rho}} \tag{107a}$$

$$c_p = \sqrt{\frac{\lambda+2G}{\rho}} = \sqrt{\frac{2(1-\nu)}{1-2\nu}}c_s \tag{107b}$$

The analytical solution for the dynamic-stiffness coefficient equals[5]

$$S^{\infty}(a_0) = \pi G a_0^2 \frac{\alpha+\beta-4}{\alpha\beta-\alpha-\beta} \tag{108}$$

with

$$\alpha = a_0 \frac{H_0^{(2)}(a_0)}{H_1^{(2)}(a_0)} \tag{109a}$$

$$\beta = \frac{c_s}{c_p} a_0 \frac{H_0^{(2)}\left(\frac{c_s}{c_p} a_0\right)}{H_1^{(2)}\left(\frac{c_s}{c_p} a_0\right)} \tag{109b}$$

$$a_0 = \frac{\omega r}{c_s} \tag{110}$$

Due to symmetry only one quarter of the structure-medium interface is discretized with 4 3-node line elements of equal length. The boundary condition of the dynamic-stiffness matrix $[S^\infty(\omega_h)]$ is determined from the asymptotic expansion with $m = 2$ (Eq. (75)) at $\omega_h = a_{0h} c_s / r_0$ for $a_{0h} = 6$. $[S^\infty(\omega)]$ of order 16×16 is calculated for decreasing ω with the scaled boundary finite-element method based on the Bulirsch-Stoer method of Reference [3]. The dynamic-stiffness coefficient $S^\infty(\omega)$ follows from

$$S^\infty(\omega) = \{\phi\}^T [S^\infty(\omega)] \{\phi\} \tag{111}$$

with the vector $\{\phi\}$ determined from the translational motion of the rigid structure-medium interface. $S^\infty(\omega)$ non-dimensionalized with the shear modulus G is decomposed in $k(a_0)$ and $c(a_0)$. Excellent agreement with the analytical solution for $\nu = 1/3$ of (108) results (Fig. 7).

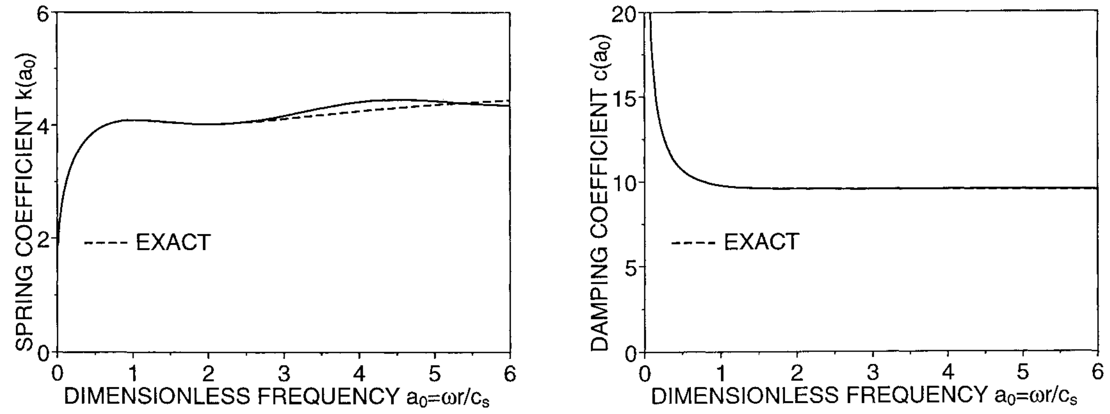

Fig. 7 Dynamic-stiffness coefficient of circular cavity.

(3) Prism Embedded in Half-Space

The three-dimensional motion of a prism of length $2b$ embedded with depth e in a half-space of shear modulus G, Poisson's ratio ν and mass density ρ (Fig. 8) is calculated. The embedment ratio $e/b = 2/3$ and $\nu = 1/3$ are selected. The finite-element discretization of one quarter of the structure-medium interface is shown in Fig. 9. The dynamic-stiffness matrix $[S^\infty(\omega)]$ is calculated for decreasing ω using the scaled boundary finite-element method based on the Bulirsch-Stoer method of Reference [3], starting from the boundary condition $[S^\infty(\omega_h)]$ determined from the asymptotic expansion with $m = 2$ (Eq. (75)) at $\omega_h = a_{0h} c_s / r_0$ for $a_{0h} = 40$. A rigid interface is introduced. $\{\phi_h\}$, $\{\phi_v\}$, $\{\phi_r\}$ and $\{\phi_t\}$ correspond to the motion patterns of the nodes on the structure-medium interface associated with the horizontal, vertical,

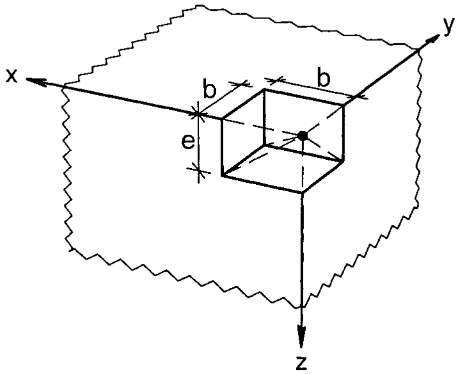

Fig. 8 One quarter of square prism embedded in half-space.

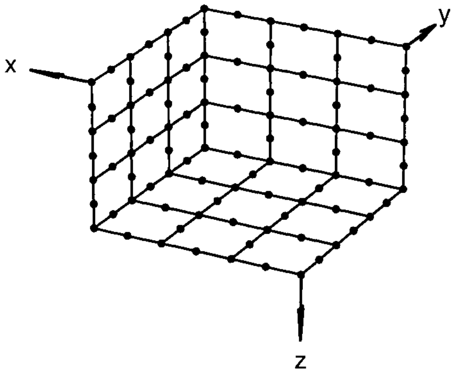

Fig. 9 Finite-element mesh of one quarter of structure-medium interface of square prism.

rocking and torsional motions, respectively. The dynamic-stiffness coefficients $S_h^{\infty}(\omega)$, $S_v^{\infty}(\omega)$, $S_r^{\infty}(\omega)$ and $S_t^{\infty}(\omega)$ are calculated from (111). After normalization with the static-stiffness coefficients a decomposition in the dimensionless spring coefficients and damping coefficients is performed as specified in (106). The dynamic-stiffness coefficients plotted in Fig. 10 are compared with the results of the boundary-element method for the horizontal, vertical and rocking degrees of freedom in the frequency domain[7] and with those of the hybrid method for the torsional degree of freedom[8].

9 Conclusions

The consistent infinitesimal finite-element cell method, which was originally developed using finite-element assemblage and similarity, is reexamined for an unbounded medium starting from the governing equations of elastodynamics. The procedure is called the scaled boundary finite-element method.

1. Applying the scaled boundary transformation to the geometry, the governing equations of elastodynamics yields the scaled boundary finite-element equation in displacements with the dimensionless radial coordinate as the independent variable. No approximation other than that of the surface finite elements is introduced. The scaled boundary finite-element equation in dynamic stiffness with the frequency as the independent variable is independent of the radial coordinate which can be solved without addressing the radial direction.
2. A reduction of the spatial dimension by one is achieved with this finite-element procedure, as only the boundary is discretized with surface finite elements. Furthermore, no discretization of that part of the boundary and material interfaces whose extensions pass through the scaling centre is required.
3. In contrast to the boundary-element method no fundamental solution is required. This expands the scope of application and avoids the singular integrals. When applied to an unbounded medium, the scaled boundary finite-element method satisfies the radiation condition at infinity exactly.
4. The scaled boundary finite-element method is exact in the radial direction and converges to the exact solution in the finite-element sense in the circumferential directions.
5. Examples demonstrate the high accuracy achieved with a small number of surface finite elements.

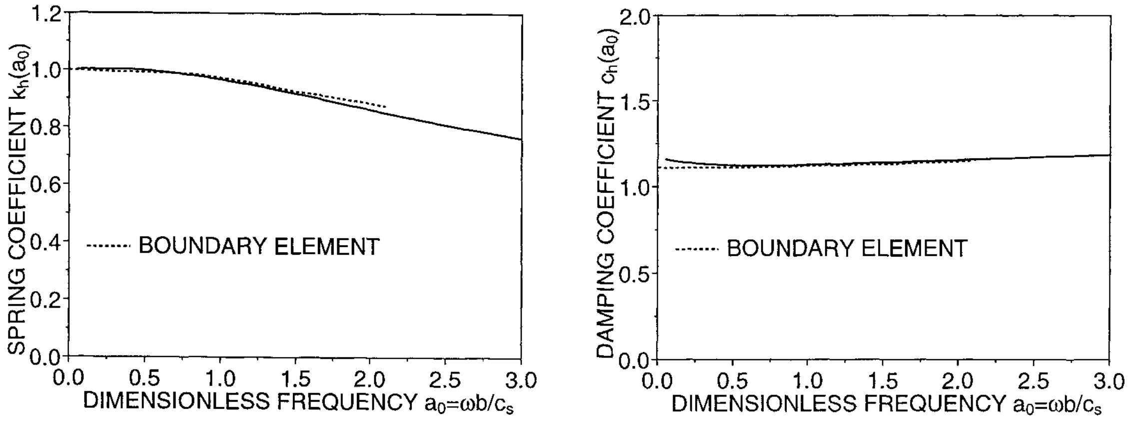

(a) horizontal

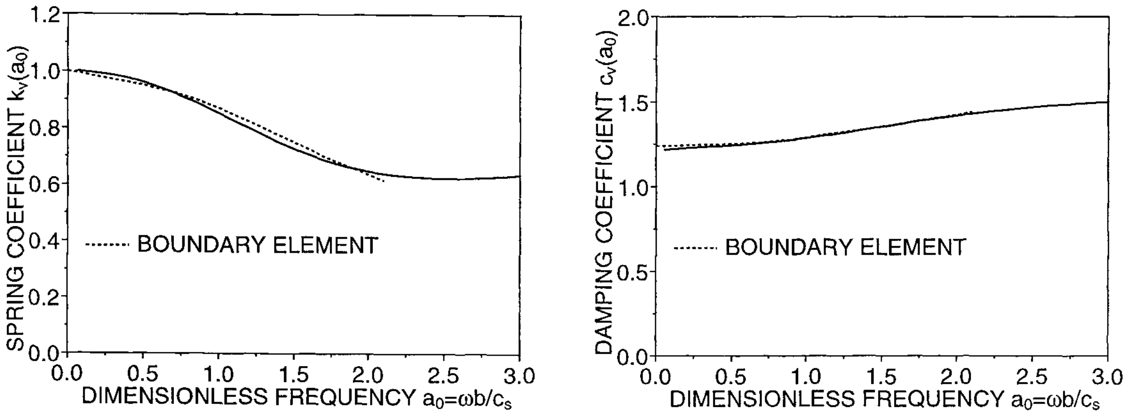

(b) vertical

Fig. 10 Dynamic-stiffness coefficients of rigid prism embedded in half-space.

A Summary of Equations for Implementation of Two-Dimensional Elastodynamics

The derivation of the scaled boundary finite-element equations for two-dimensional elastodynamics follows closely that of the three-dimensional case. For easy reference the key equations used for the implementation of the method are listed.

The differential equations of motion (Eq. (1)) still hold for the two-dimensional case with displacement amplitudes $\{u\} = [\ u_x \quad u_y\ ]^T$ and stress amplitudes $\{\sigma\} = [\ \sigma_x \quad \sigma_y \quad \tau_{xy}\ ]^T$ where the differential operator equals

$$[L] = \begin{bmatrix} \frac{\partial}{\partial \hat{x}} & \\ & \frac{\partial}{\partial \hat{y}} \\ \frac{\partial}{\partial \hat{y}} & \frac{\partial}{\partial \hat{x}} \end{bmatrix} \tag{A.1}$$

The scaled boundary transformation of the geometry is defined with the dimensionless radial coordinate

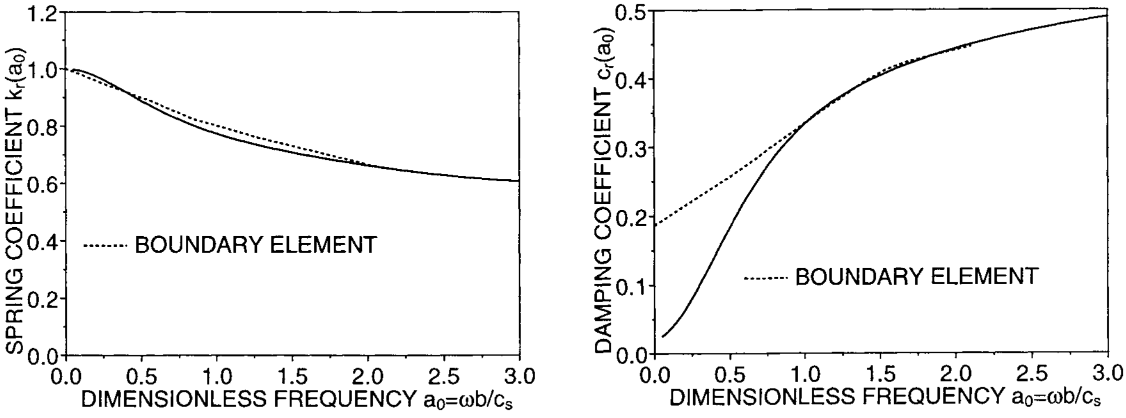

(c) rocking

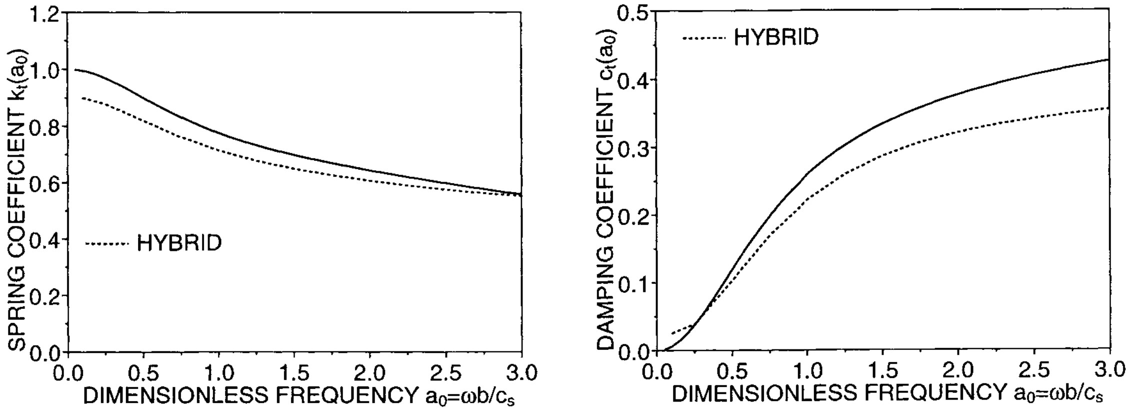

(d) torsional

Fig. 10 Dynamic-stiffness coefficients of rigid prism embedded in half-space.

ξ by

$$\hat{x}(\xi,\eta) = \xi x(\eta) \tag{A.2a}$$

$$\hat{y}(\xi,\eta) = \xi y(\eta) \tag{A.2b}$$

where the coordinates on the boundary

$$x(\eta) = [N(\eta)]\{x\} \tag{A.3a}$$

$$y(\eta) = [N(\eta)]\{y\} \tag{A.3b}$$

are represented by interpolating the nodal coordinates $\{x\}$, $\{y\}$ using the mapping function $[N(\eta)]$.

The coefficients for a (curved) line finite element in the scaled boundary finite-element method are specified in the same form as those for the three-dimensional case (Eqs. (50) and (51))

$$[E^0] = \int_{-1}^{+1} [B^1]^T [D][B^1]|J|\mathrm{d}\eta \tag{A.4a}$$

$$[E^1] = \int_{-1}^{+1} [B^2]^T [D][B^1]|J|\mathrm{d}\eta \tag{A.4b}$$

$$[E^2] = \int_{-1}^{+1} [B^2]^T [D][B^2]|J| d\eta \tag{A.4c}$$

and

$$[M^0] = \int_{-1}^{+1} [N^u(\eta)]^T \rho [N^u(\eta)]|J| d\eta \tag{A.5}$$

The curvilinear coordinate η in $[N(\eta)]$ equals $+1$ and -1 at the two ends of the line element. $[D]$ denotes the two-dimensional elasticity matrix. The determinant equals

$$|J| = xy,_\eta - yx,_\eta \tag{A.6}$$

where x, y are functions of η described in (A.3). The matrices

$$[B^1] = [b^1][N^u(\eta)] \tag{A.7a}$$

$$[B^2] = [b^2][N^u(\eta)],_\eta \tag{A.7b}$$

are calculated with

$$[b^1] = \frac{1}{|J|} \begin{bmatrix} y,_\eta & 0 \\ 0 & -x,_\eta \\ -x,_\eta & y,_\eta \end{bmatrix} \tag{A.8a}$$

$$[b^2] = \frac{1}{|J|} \begin{bmatrix} -y & 0 \\ 0 & x \\ x & -y \end{bmatrix} \tag{A.8b}$$

and the shape functions $[N^u(\eta)]$

$$\{u(\xi,\eta)\} = [N^u(\eta)]\{u(\xi)\} \tag{A.9}$$

The scaled boundary finite-element equation in displacement equals

$$[E^0]\xi^2\{u(\xi)\},_{\xi\xi} + ([E^0] - [E^1] + [E^1]^T)\xi\{u(\xi)\},_\xi - [E^2]\{u(\xi)\} + \omega^2[M^0]\xi^2\{u(\xi)\} = 0 \tag{A.10}$$

which should be compared with that for the three-dimensional case in (55).

Using the dynamic-stiffness matrix

$$-[S^\infty(\omega,\xi)]\{u(\xi)\} = [E^0]\xi\{u(\xi)\},_\xi + [E^1]^T\{u(\xi)\} \tag{A.11}$$

with

$$[S^\infty(\omega,\xi)] = G[\bar{S}^\infty(a_0)] \tag{A.12}$$

the scaled boundary finite-element equation in dynamic stiffness is derived as

$$([S^\infty(\omega)] + [E^1])[E^0]^{-1}([S^\infty(\omega)] + [E^1]^T) - \omega[S^\infty(\omega)],_\omega - [E^2] + \omega^2[M^0] = 0 \tag{A.13}$$

Eq. (A.12) should be compared with (65) and (69) for the three-dimensional case, and (A.13) with (73).

References

[1] Song Chongmin and Wolf J. P., Consistent infinitesimal finite-element cell method: three-dimensional vector wave equation, *International Journal for Numerical Methods in Engineering,* **39** (1996) 2189-2208.

[2] Wolf J. P. and Song Chongmin, *Finite-Element Modelling of Unbounded Media,* John Wiley & Sons (1996).

[3] Press W. H., Flannery B. P., Teukolsky S. A. and Vetterling W. T., *Numerical Recipes,* Chapter 15, Cambridge University Press (1988).

[4] Wolf J. P., *Soil-Structure-Interaction Analysis in Time Domain,* Prentice-Hall (1988).

[5] Novak M., 'Dynamic stiffness and damping of piles', *Canadian Geotechnical Journal,* **11** (1974) 574–598.

[6] Wang Y. and Rajapakse R. K. N. D., 'Dynamics of rigid strip foundations embedded in orthotropic elastic soils', *Earthquake Engineering and Structural Dynamics,* **20** (1991) 927–947.

[7] Dominguez J., *Boundary Elements in Dynamics,* Computational Mechanics Publications (1993).

[8] Mita A. and Luco J. E., 'Impedance functions and input motions for embedded square foundations', *Journal of Geotechnical Engineering,* ASCE, **115** (1989) 491–503.

EFFECTS OF SOIL-STRUCTURE INTERACTION ON NONLINEAR RESPONSE OF ARCH DAMS

Zhang Chuhan, Xu Yanjie and Jin Feng
(Tsinghua University, Beijing, China, 100084)

Summary

Effects of two important factors on earthquake response of high arch dams are considered and combined into one program. These factors are: effects of dam-canyon interaction and that of local nonlinearity of the contraction joint opening between the dam monoliths. The substructuring technique is employed, thus the equilibrium iteration involves only the degrees of freedom in nonlinear substructure. For modeling of rock canyon, the discrete parameters are obtained based on a curve fitting, thus allowing the nonlinear dam system to be solved in the time domain. A simplified earthquake input procedure is also used, which takes into account the radiation damping of the infinite canyon while preventing the artificial amplification of the ground motion through the rock mass. Two engineering examples are given to demonstrate the significant effects of the above-mentioned two factors on the response of the structure.

Introduction

Starting from the end of this century, construction of a series of high arch dams up to 250m-300m in height are being planned or conducted. These projects include: the Ertan arch dam (240m high, under construction) on the Yalun River, the Laxiwa arch dam (250m high, in preliminary design) on the Yellow River, the Xiaowan arch dam (292m high, in preliminary design) on the Lanchang River, and the Xiluodu arch dam (275m high, in feasibility study) on the Jinsha River. All these projects are located in seismically active regions with design basis earthquakes between a PVA of 0.22g and 0.32g. For seismic analysis of such high arch dams to resist strong earthquakes, it is necessary to consider some important factors which are not accounted for in the current procedures. These factors include (1)complete interaction effects between the dam and the rock foundation; (2)nonlinearities of the dam with contraction joint opening during the extreme ground motions.

State-of-the-art procedures dealing with seismic analysis of arch dams assume a truncated massless rock foundation and apply the design earthquake input at the rigid base beneath the truncated rock foundation. These assumptions neglect the interaction effects due to radiation damping of the infinite mass rock and the non-uniform input motions along the canyon. Recent studies[1]-[4] have revealed that these interaction effects are important and should be included in the analysis. With this objective, a time domain procedure of coupling finite elements (FEs), boundary elements (BEs) and infinite boundary elements (IBEs) has been developed by the authors[5][6]. Studies on the effects of interaction on the response of the dam have been conducted in detail for some of the above-mentioned arch dams[7].

With regard to the nonlinear behaviors of arch dams, the most important nonlinearity is initiated by the contraction joint opening during strong ground motions. This phenomenon often occurs in the upper portion of a dam where the largest tensile stresses up to 5-6MPa are expected to occur in the arch direction for moderately strong earthquake motion. It is evident that the contraction joints can only sustain very limited values of tensile stress even if they are properly grouted. Thus, the opening of contraction joints is inevitable leading to a substantial reduction of tensile stresses in arch direction, while, on the other hand, a significant increase in the possibility of cracking of vertical cantilevers. Problems of such nonlinearities of arch dams were first raised by Clough[8]. Dowling and Hall [9] presented a 2-D discrete joint element for simulation of gradual opening and closing of joints of 3-D arch dams in an approximate manner. The nonlinear analysis of the Pacoima dam subjected to the 1971 San Fernando earthquake is performed as a case study. Following up, Fenves[10] used a 3-D nonlinear joint element and an efficient numerical procedure for solving this problem. The F.E. substructuring technique is employed by considering the set of joint elements as a single nonlinear substructure while the cantilevers between joints as linear ones and their degrees of freedom can be condensed out. A typical arch dam-Big Tujunga was analyzed using the presented method.

The objective of this study is to combine the above-mentioned two factors into one program, i.e. the complete interaction effects between arch dam and foundation, and the nonlinearities of the contraction joint opening. The development of the time domain BE-IBE coupling model for simulation of rock canyon provides a means for solving problems with structural nonlinearities. The joint element and the solution technique for dam substructure developed by Fenves are retained in this new program and the discrete parameters for simulation of infinite rock canyon are incorporated into the program. For examination of the effects of these two factors on the dam response, the earthquake analysis of the Laxiwa arch dam and Big Tujunga arch dam are performed.

System Analyzed

Shown in Figure 1 is a complete dam-canyon-reservoir system.

Finite elements are used for discretization of the dam and the reservoir, assuming the latter being incompressible. The dam may be viewed to consist of a series of cantilever elements separated by nearly vertical contraction joints. Since the joints can be expected to open and close during an earthquake, it is evident that the dam behaves as a locally nonlinear subsystem, provided the dam body, excluding the joints remains linear elastic. Preliminary analysis showed that a significant redistribution of stresses will occur due to this nonlinearity, thus raising a concern of the integrity and safety of the dam. The substructure of the canyon is discretized into boundary elements and infinite boundary elements. Frequency-dependent impedance functions are first obtained for all degrees of freedom on the dam canyon interface. By using a curve fitting, these impedance functions are transformed into a mass-spring-dashpot system which is frequency independent. Finally, these discrete parameters together with the linear substructure of cantilevers of the dam body are condensed into the boundaries of the nonlinear substructure-a set of contraction joint elements. The equilibrium iteration during a time step is conducted only for the degrees-of-freedom for the nonlinear substructure.

1. Modeling of Rock Canyon and Free Field Input

3-D boundary elements (BEs) and infinite boundary elements (IBEs) are used for discretization of the canyon, taking into account the irregular geometrical conditions in the near field of the canyon. The detailed formulations of the infinite boundary elements can be found elsewhere[11].

Numerical integration of the boundary integral equation by BE-IBE coupling leads to a series of linear equations

$$[H]\{u\} = [G]\{p\} \tag{1-1}$$

where $[H]$ and $[G]$ are coefficient matrices assembled from individual elements including the contribution due to IBEs to $[H]$, with no contribution to $[G]$ from these elements due to the traction-free condition. Equation (1-1) can then be used to obtain impedance functions at all defined nodes on canyon surface in frequency domain. It is, therefore, necessary to condense the impedance functions into the dam canyon interface.

Partitioning equation (1-1) according to the degrees-of-freedom associated with the dam-canyon interface c and the remaining portion of the canyon surface r leads to equation(1-1) rewritten as

$$\begin{bmatrix} H_{cc} & H_{cr} \\ H_{rc} & H_{rr} \end{bmatrix} \begin{Bmatrix} u_c \\ u_r \end{Bmatrix} = \begin{bmatrix} G_{cc} & G_{cr} \\ G_{rc} & G_{rr} \end{bmatrix} \begin{Bmatrix} p_c \\ p_r \end{Bmatrix} \tag{1-2}$$

After condensation and recognizing the traction-free condition $p_r = 0$, equation (1-2) becomes

$$H'_{cc}\, u_c = G'_{cc}\, p_c \tag{1-3}$$

where

$$\begin{aligned} H'_{cc} &= H_{cc} - H_{cr} H_{rr}^{-1} H_{rc} \\ G'_{cc} &= G_{cc} - H_{cr} H_{rr}^{-1} G_{rc} \end{aligned} \tag{1-4}$$

Introducing now the following relationship between the nodal forces F_c and traction p_c

$$F_c = \psi p_c \tag{1-5}$$

into equation (1-3) leads to

$$S_{cc} u_c = F_c \tag{1-6}$$

and

$$S_{cc} = \psi G'^{-1}_{cc} H'_{cc} \tag{1-7}$$

where ψ is the transformation matrix constructed from the interpolation shape functions; S_{cc} is by definition the impedance matrix defined on the dam-canyon interface.

Since $S_{cc}(\omega)$ in equation (1-6) are frequency dependent, it is necessary to transform them into discrete parameters so that the entire dam-canyon system can be solved in the time domain for nonlinearities of the structure. Applying the following relationship

$$S_{cc} = -\omega^2 \overline{m}_{cc} + i\omega \overline{c}_{cc} + \overline{k}_{cc} \tag{1-8}$$

to each coefficient of the impedance matrix yields the discrete parameters $\overline{m}_{cc}, \overline{c}_{cc}, \overline{k}_{cc}$, which are the elements of equivalent mass $\overline{M}_{cc}$, damping $\overline{C}_{cc}$ and stiffness $\overline{K}_{cc}$ matrices respectively.

Assuming that ω_1 and ω_2 represent the prescribed excitation frequency at the two boundary points within the frequency range of interest and that the corresponding impedance functions $S_{cc}(\omega_1)$ and $S_{cc}(\omega_2)$ are known, the substitution of S_{cc} at the above points into equation (1-8) leads to

$$\begin{aligned} \overline{m}_{cc} &= \frac{1}{\omega_2^2 - \omega_1^2} \{\mathrm{Re}[S_{cc}(\omega_1)] - \mathrm{Re}[S_{cc}(\omega_2)]\} \\ \overline{c}_{cc} &= \frac{1}{2}\{\frac{1}{\omega_1}\mathrm{Im}[S_{cc}(\omega_1)] + \frac{1}{\omega_2}\mathrm{Im}[S_{cc}(\omega_2)]\} \\ \overline{k}_{cc} &= \mathrm{Re}[S_{cc}(\omega_1)] + \omega_1^2 \overline{m}_{cc} \end{aligned} \tag{1-9}$$

in which $\overline{m}_{cc}, \overline{k}_{cc}$ are obtained by equating the real parts of S_{cc}, and $\overline{c}_{cc}$ is based on averaging the imaginary parts at the boundary points.

The three parameters for all degrees-of-freedom and their coupling terms on the dam-canyon interface can be obtained from equation (1-9) and then assembled to give matrices $\overline{M}_{cc}, \overline{C}_{cc}$ and $\overline{K}_{cc}$ and to form the corresponding equation of motion for the canyon

$$\overline{M}_{cc}\ddot{u}_c + \overline{C}_{cc}\dot{u}_c + \overline{K}_{cc}u_c = \overline{F}_c \tag{1-10}$$

in which $u_c, \dot{u}_c$ and $\ddot{u}_c$ denote the interaction displacement, velocity and acceleration vectors of the canyon respectively, and $\overline{F}_c$ represents the interaction forces acting on the canyon interface.

For coupling the equations of the canyon motion with the dam, the total response of the arch dam and its boundary connection with canyon can be written in partitioned form as

$$\begin{bmatrix} M_{dd} & M_{dc} \\ M_{cd} & M_{cc} \end{bmatrix} \begin{Bmatrix} \ddot{U}_d \\ \ddot{U}_c \end{Bmatrix} + \begin{bmatrix} C_{dd} & C_{dc} \\ C_{cd} & C_{cc} \end{bmatrix} \begin{Bmatrix} \dot{U}_d \\ \dot{U}_c \end{Bmatrix} + \begin{bmatrix} K_{dd} & K_{dc} \\ K_{cd} & K_{cc} \end{bmatrix} \begin{Bmatrix} U_d \\ U_c \end{Bmatrix} = \begin{Bmatrix} F_d \\ F_c \end{Bmatrix} \tag{1-11}$$

where M, C, K are the mass, damping and stiffness matrices of the system respectively; F denotes the load vector; subscripts d and c refer to the degrees of freedom associated with the internal nodes of the dam and the boundary nodes connecting with the canyon respectively.

Combining equation (1-10) and (1-11) and noting that

$$\begin{aligned} F_c &= -\overline{F}_c \\ U_c &= \overline{u}_c + u_c \end{aligned} \tag{1-12}$$

the equation of motion for dam-canyon interaction are finally obtained as

$$\begin{bmatrix} M_{dd} & M_{dc} \\ M_{cd} & M_{cc} + \overline{M}_{cc} \end{bmatrix} \begin{Bmatrix} \ddot{U}_d \\ \ddot{u}_c \end{Bmatrix} + \begin{bmatrix} C_{dd} & C_{dc} \\ C_{cd} & C_{cc} + \overline{C}_{cc} \end{bmatrix} \begin{Bmatrix} \dot{U}_d \\ \dot{u}_c \end{Bmatrix} + \begin{bmatrix} K_{dd} & K_{dc} \\ K_{cd} & K_{cc} + \overline{K}_{cc} \end{bmatrix} \begin{Bmatrix} U_d \\ u_c \end{Bmatrix}$$

$$= \begin{Bmatrix} -[M_{dc}\ddot{\overline{u}}_c + C_{dc}\dot{\overline{u}}_c + K_{dc}\overline{u}_c] \\ -[M_{cc}\ddot{\overline{u}}_c + C_{cc}\dot{\overline{u}}_c + K_{cc}\overline{u}_c] \end{Bmatrix} \tag{1-13}$$

Solving equation (1-13) and using equation (1-12), the total displacement field $(U_d \ \ U_c)^T$ for the dam can be obtained.

It should be noted that the terms of the right hand side of equation (1-13) are now free-field motions acting on the dam-canyon interface. The equation (1-13) can either be linear or nonlinear and be solved by a typical numerical scheme such as the Newmark average acceleration method.

As a linear application example, the Laxiwa arch dam (250m high) is selected to perform the interaction analysis. Figure 2 shows the profiles of the canyon and the dam. The corresponding parameters are: for concrete, E=3.5 × 10^4MPa; ρ=2400kg/m^3; ν=0.167, for rock, G=1.4 × 10^4MPa; ρ=2680kg/m^3; ν=0.23. Figure 3 shows the impedance functions of the canyon. They behave in gradual monotonic fashion within the frequency range considered due primarily to the high shear modulus of the canyon rock.

The comparison of the response functions at the dam crest between the interaction model (i.e. infinite mass foundation) and the standard massless foundation is shown in Figure 4. Significant reduction in the dam response in the entire frequency range for interaction model is observed.

2. Modeling of Nonlinear Contraction Joints of Dam

A 3-D nonlinear joint element[12] is shown in Figure 5. The element is of isoparametric and consists of two coincident surfaces each of which is defined by four nodes. The coordinate transformation between the global and natural coordinate system can be written as the form:

$$X = \sum_{j=1}^{4} N_j X_j \tag{2-1}$$

where

$$N_j = N_{j+4} = \frac{1}{4}(1 + r_j r)(1 + s_j s) \quad j = 1,2,3,4 \tag{2-2}$$

in which X are global coordinates of a point on the joint surface and X_j are coordinates of nodes j and $j+4$; N_j are shape functions in the natural coordinate system; r_j, s_j are the coordinates of node j.

The global displacements of the bottom and the top surfaces of the joint are expressed in terms of nodal displacements u_j as follows:

$$u_{bot} = \sum_{j=1}^{4} N_j u_j \tag{2-3a}$$

$$u_{top} = \sum_{j=5}^{8} N_j u_j \tag{2-3b}$$

The displacements of the bottom and the top surfaces can be further transformed into the orthonormal coordinate system by

$$\bar{u}_{bot} = \mathrm{a} u_{bot} \tag{2-4a}$$

$$\bar{u}_{top} = \mathrm{a} u_{top} \tag{2-4b}$$

where a is a function of the natural coordinates r and s and can be constructed through coordinate transformation between global and local orthonormal coordinate systems.

The relative displacements between the two surfaces of the joint element are given by

$$v = \bar{u}_{top} - \bar{u}_{bot} \tag{2-5}$$

Substituting equation (2-4) and (2-3) into (2-5) provides the relative displacements v in terms of nodal displacements

$$v = Bu \tag{2-6}$$

$$u = [u_1^T \ u_2^T \ u_3^T \ u_4^T \ u_5^T \ u_6^T \ u_7^T \ u_8^T \ ]^T$$

$$B = [-\mathrm{N}_1 - \mathrm{N}_2 - \mathrm{N}_3 - \mathrm{N}_4 \ \mathrm{N}_1 \ \mathrm{N}_2 \ \mathrm{N}_3 \ \mathrm{N}_4] \tag{2-7}$$

and

$$\mathrm{N}_\mathrm{j} = N_j a \tag{2-8}$$

The constitutive relationship between resisting stresses and the relative displacements of the joint can be assumed as follows

$$q_i = \begin{cases} k_i v_i & v_i \le q_{oi} / k_i \\ 0 & v_i > q_{oi} / k_i \end{cases} \quad i = 1,2,3 \tag{2-9}$$

where q_i denotes the resisting stresses in i direction. k_i is the stiffness of the joint in compression. v_i is the relative displacement in i direction. q_{oi} is a specified tensile strength of the joint. Figure 6 shows the nonlinear constitutive relationship. It is reasonable to assume that the subsequent tensile strength of the joint will drop down to zero after the first opening of the joint when $v_i > q_{oi} / k_i$. The tangent stiffness matrix for the nonlinear joint element can be constructed. We start with the equilibrium condition between resisting stresses q and the nodal forces p by using the virtual work principle:

$$p = \int_A B^T q dA \tag{2-10}$$

where p is the nodal force vector in the global coordinate system.

From equation (2-10), the tangent stiffness matrix k_T is given by

$$k_T = \frac{\partial p}{\partial u} = \int_A B^T \frac{\partial q}{\partial v} \frac{\partial v}{\partial u} dA \tag{2-11}$$

Using equations (2-9) and (2-6) for $\frac{\partial q}{\partial v}$ and $\frac{\partial v}{\partial u}$ in equation (2-11) yields

$$k_T = \int_A B^T \bar{k}_T(v) B dA \tag{2-12}$$

where $\bar{k}_T$ is a diagonal matrix, in which the diagonal terms are

$$\bar{k}_{T_i} = \begin{cases} k_i & v_i \le q_{oi} / k_i \\ 0 & v_i > q_{oi} / k_i \end{cases} \tag{2-13}$$

The integration of equations (2-10) and (2-11) are carried out for the nodal forces p and the tangent stiffness matrix k_T using the standard Gauss integration in the natural coordinate system as in the normal finite element procedure.

3. Solution scheme for nonlinearities of dams

As noted previously, the arch dam-canyon system can be first divided into substructures of dam body and canyon respectively. The effects of reservoir water can be viewed as added mass by finite elements and attached to the dam-fluid interface. The impedance of the canyon rock are transformed into discrete parameters and attached to the dam-canyon interface. The remaining task is to solve the equations of motion of the dam body which includes linear elastic cantilevers and a set of nonlinear contraction joints.

Fenves[10] presented a procedure to achieve this objective based on a substructuring technique for local nonlinearities given by Clough and Wilson[13]. The procedure is summarized as follows:

The equations of motion at time t_{j+1} for a linear substructure is given by

$$m\ddot{u}_{j+1} + c\dot{u}_{j+1} + ku_{j+1} = f_{j+1} + q_{j+1} \tag{3-1}$$

where m, c, k are the mass, damping and stiffness matrices, respectively; f is the time depending loads; q denotes the forces at the boundary of the substructure.

If the Newmark integration scheme is employed for the solution, equation (3-1) can be written as

$$k^* u_{j+1} = p^*_{j+1} + q_{j+1} \tag{3-2}$$

in which the effective stiffness and effective load are:

$$k^* = a_0 m + a_1 c + k \tag{3-3a}$$

$$p^*_{j+1} = f_{j+1} + m[a_0 u_j + a_2 \dot{u}_j + a_3 \ddot{u}_j] + c[a_1 u_j + a_4 \dot{u}_j + a_5 \ddot{u}_j] \tag{3-3b}$$

The integration constants $a_0\ a_1 \cdots a_5$ have the form

$$\begin{aligned} a_0 &= \frac{1}{\alpha \Delta t^2};\ a_1 = \frac{\delta}{\alpha \Delta t};\ a_2 = \frac{1}{\alpha \Delta t}; \\ a_4 &= \frac{\delta}{\alpha} - 1;\ a_5 = \frac{1}{2}(\frac{\delta}{\alpha} - 2) \end{aligned} \tag{3-4a}$$

in which

$$\delta \ge 0.50;\ \alpha \ge 0.25(0.5 + \delta)^2 \tag{3-4b}$$

Assuming the damping matrix has the form of Rayleigh damping, i.e.

$$c = b_0 m + b_1 k \tag{3-4c}$$

the effective stiffness matrix k^* and the effective load vector p^*_{j+1} can be expressed in terms of $m, k, u_j, \dot{u}_j, \ddot{u}_j$ at time j and f_{j+1}.

Since the linear substructure is coupled with the nonlinear substructure at the boundaries between the two, the iteration of equations of motion for the nonlinear substructure involves computation of boundary displacements and forces in the linear substructure. Equation (3-2) is valid for the solution of iteration n for the response at time t_{j+1}

$$k^* u^n_{j+1} = p^*_{j+1} + q^n_{j+1} \tag{3-5}$$

in which k^* and p^*_{j+1} do not depend on the response at time t_{j+1}. Partitioning the domain into the internal and boundary degrees of freedom denoted by subscripts i and b with the latter being connected with the nonlinear substructure, we obtain

$$\bar{k}^* u^n_{b(j+1)} = \bar{p}^*_{j+1} + q^n_{j+1} \tag{3-6}$$

where

$$\bar{k}^* = k^*_{bb} - k^*_{bi}(k^*_{ii})^{-1} k^*_{ib} \tag{3.7a}$$

$$\bar{p}^*_{j+1} = p^*_{b(j+1)} - k^*_{bi}(k^*_{ii})^{-1} p^*_{i(j+1)} \tag{3.7b}$$

Similar equations of motion to equation (3-1) for nonlinear substructure at time t_{j+1} can be written as

$$M\ddot{U}_{j+1} + P(\dot{U}_{j+1}, U_{j+1}) = F_{j+1} + Q_{j+1} \tag{3-8}$$

where M is the mass matrix; $P(\dot{U}_{j+1}, U_{j+1})$ is the vector of restoring forces which is a nonlinear function of $\dot{U}_{j+1}$ and U_{j+1}; F_{j+1} is the time dependent loads; and Q_{j+1} is the boundary forces of the nonlinear substructure.

Applying the Newmark integration scheme to equation (3-8) gives an incremental form for $n+1$ iteration

$$K^* \Delta U = \Delta P^* \tag{3-9}$$

where

$$K^* = a_0 M + a_1 C_T + K_T - \frac{\partial Q}{\partial U} \tag{3-10a}$$

$$\Delta P^* = F_{j+1} - M\ddot{U}^n_{j+1} - P(\dot{U}^n_{j+1}, U^n_{j+1}) + Q^n_{j+1} \tag{3-10b}$$

in which, K_T and C_T are the tangent stiffness and tangent damping matrix respectively, and have the form $K_T = \frac{\partial P}{\partial U}$, $C_T = \frac{\partial P}{\partial \dot{U}}$. For equilibrium and compatibility conditions between the nonlinear substructure and the linear ones, the following relation is applied.

$$Q^n_{j+1} = -\sum q^n_{j+1} \tag{3-11a}$$

$$u_b = a_b U \tag{3-11b}$$

where a_b is a Boolean matrix.
Substituting equation (3-6) into (3-11) yields

$$Q^n_{j+1} = \sum \bar{p}^*_{j+1} - \sum \bar{k}^* u^n_{b(j+1)} \tag{3-12a}$$

and

$$\frac{\partial Q}{\partial U} = -\sum \bar{k}^* \tag{3-12b}$$

Substituting (3-12a,b) into (3-10a,b) yields

$$K^* = a_0 M + a_1 C_T + K_T + \sum \bar{k}^* \tag{3-13a}$$

$$\Delta P^* = F_{j+1} + \sum \bar{p}^*_{j+1} - M\ddot{U}^n_{j+1} - P(\dot{U}^n_{j+1}, U^n_{j+1}) - \sum \bar{k}^* u^n_{b(j+1)} \tag{3-14}$$

Solving the equation (3-9) iteratively under the effective load of earthquake ground motion, the response of the nonlinear substructure can be obtained, and then the responses of the whole system are solved.

Two important points should be noted in the analysis. (1)The equilibrium iteration during a time step involves only the degrees of freedom in nonlinear substructure leading to a substantial reduction of computation for structures with local nonlinearities; (2)The effective stiffness matrices of the linear substructures $\bar{k}^*$ are computed once. Only the tangent stiffness matrix K_T and the tangent damping matrix C_T need to be evaluated and assembled into K^* during the equilibrium iteration.

4. A Simplified Input Procedure for Earthquake Ground Motions

Although the free-field input expressed in equation (1-13) is feasible, a simplified procedure is used in current stage, which takes into account the discrete parameters of the canyon, i.e. the effects of radiation damping while eliminating the amplification of the input motions due to the canyon rock mass. Assuming a uniform earthquake ground motion is applied at the rigid base beneath the truncated rock foundation, the dynamic load on a linear substructure is given by

$$f = -(mr + m_g)\ddot{u}_g \tag{4-1}$$

where $\ddot{u}_g$ is the free-field ground acceleration at the supports; r is an influence coefficient vector, and m_g is the mass matrix that couples the DOF in the substructure and the support points. (For lumped mass formulation $m_g = 0$). The dynamic load on the nonlinear substructure is

$$F = -(Mr + M_g)\ddot{u}_g \tag{4-2}$$

where similar definition of the terms apply. In the current version of ADAP-88, the model of massless foundation is still being used, and hence the propagation of seismic waves through the foundation rock and radiation damping of the rock canyon are neglected. For inclusion of this dam-canyon interaction effect, this paper uses the matrices of discrete parameters $\overline{M}_{cc}, \overline{C}_{cc}$ and $\overline{K}_{cc}$ from equation (1-9) to form the effective stiffness k^* in equation (3-3a) and to replace the massless rock for foundation substructure. For computation of effective load vector p^*_{j+1} in equation (3-3b), the free-field input at the dam-canyon interface should have been used. However, in the current stage, a simplified and approximate procedure is employed, i.e. to input the earthquake ground motion at the base beneath the discrete parameter system without considering the equivalent mass $\overline{M}_{cc}$ in the system. This simplified procedure is approximate to the massless foundation input for effective forces while retaining the foundation mass in the response system. Thus, it takes into account the radiation damping but prevents an arbitrary amplification of the input motion through the foundation mass.

Engineering Applications

The Big Tujunga arch dam, located in Big Tujunga canyon, Los Angeles County, California was chosen as an engineering example for nonlinear analysis to examine the effects of dam-canyon interaction on the structural response. In order to compare the present results with those provided by Fenves, all the parameters related to the dam, rock canyon and earthquake ground motion are the same as the reference[10]. The dam has a crest length of 132m and the maximum dam height is 84m. The thickness varies from 24m at the base to 2.8m at the crest. The contraction joints are spaced approximately 16.5m along the crest. The finite element mesh of the dam with three contraction joints is shown in Figure 7. where six mesh elevations consisting of 12 thick shell elements and 18 3-D shell elements are used. The foundation for massless model is discretized into 80 3-D solid elements to a depth of 80m, the rock canyon for infinite mass foundation model is discretized into 60 boundary elements plus 38 infinite boundary elements. The impedance functions are then transferred to be the discrete parameters and attached to the dam-canyon interface. The material properties for the concrete are: unit weight=2400 kg/m^3; modulus of elasticity=2.75 × 10^{4}MPa; Poisson's ratio=0.2; for the foundation rock: unit weight=2580kg/m^3; modulus of elasticity=1.80 × 10^{4}MPa; Poisson's ratio=0.32. Rayleigh damping in the dam is represented by a viscous damping ratio of 0.05 in the first and fifth modes. No material damping in the foundation is assumed for both mass and massless models. Full reservoir water with Westergaard's added mass approximation is employed.

The earthquake ground motion used in the analysis is the Lake Hughes No.12 record obtained during the 1971 San Fernando earthquake. The three components are scaled and shown in Figure 8 with the maximum peak acceleration of 0.6*g* acting in the cross-canyon direction. Time step Δt of $0.01s$ is used, although $\Delta t = 0.005s$ was also examined to verify the convergence of the response.

Static analysis of the dam-reservoir-foundation system is first performed before a nonlinear dynamic analysis can be carried out. This includes stress analysis under self-weight of concrete and hydrostatic pressure of the reservoir water.

Dynamic analysis is first conducted for linear analysis assuming the contraction joints are closed. Nonlinear analysis is then performed allowing for the opening of the contraction joints. Both linear and nonlinear analysis are performed using massless and infinite mass foundation for comparison. Figure 9-10 show comparisons of displacements at dam crest between massless and infinite mass foundation for cases of joints closed and joints open respectively. The comparison of joint opening between the two foundation models is shown in Figure 11. Vivid reduction can be observed in joint opening and crest displacements when infinite mass of the foundation is considered. Comparing the displacements for joints closed with that of joints open, the latter shows significant increase in displacements in all three directions. In addition, the displacements behave asymmetrically during the periods of joint opening.

Comparisons of stresses between the two foundation models and between the two cases of contraction joint conditions (i.e. joints closed and joints open) are shown in Figures 12-15. The comparisons of maximum tensile and compressive stresses in arch and cantilever between different cases are also listed in Tables 1 and 2. The observations from these results are summarized as follows

Table 1. Comparison of maximum tensile stresses between
infinite mass and massless foundation (MPa)

Foundation		Upstream		Downstream	
Model	Case	Arch	Cantilever	Arch	Cantilever
Massless	Joints closed	16.28	6.64	11.50	6.49
	Joints open	11.10	8.44	7.72	11.93
Inf. Mass	Joints closed	14.07	5.77	9.87	5.32
	Joints open	9.33	7.92	7.86	10.28

Table 2. Comparison of maximum compressive stresses between
infinite mass and massless foundation (MPa)

Foundation		Upstream		Downstream	
Model	Case	Arch	Cantilever	Arch	Cantilever
massless	Joints closed	21.77	7.87	16.27	5.89
	Joints open	19.08	10.72	14.90	7.32
inf. mass	Joints closed	16.80	6.56	12.87	5.21
	Joints open	15.41	10.48	13.06	6.52

(1)From tables 1 and 2 significant reduction in arch stresses for the case of joints open is observed especially for the tensile stresses. However, the increase in cantilever stresses is also obvious due to a load transfer from the horizontal arch system to the vertical elements. The reduction and the increase of stresses in both directions can reach 25-30% for tensile stresses.

(2)Consideration of the infinite mass foundation with radiation damping receives benefits of further reduction in arch stresses. In the meantime, the increase of cantilever stresses due to the joints open is still significant, but the final stress level has a slight drawdown when compared with that of the massless foundation.

(3) From Figures 14 and 15, changes in stress pattern both in arch and in cantilever directions are important due to joint opening. An abrupt dropdown of arch stresses near the contraction joints is evident as shown in Fig. 14. The cantilever stresses are redistributed, and the maximum stresses increase and move upward in comparing the cases of joints closed.

Conclusions

The objective of this paper is to attempt to consider two important factors in earthquake analysis of high arch dams, i.e. dam-canyon interaction and nonlinearity of dam response due to the contraction joint opening. Findings from the results of investigation are:

(1)Effects of contraction joint opening of arch dams on the response are significant, resulting in a substantial stress reduction in the arch direction due to the release of constraint between the dam monoliths. However, a significant increase in cantilever stresses is also observed, implying that the dynamic loads are partially transferred to the vertical components of the structure.

(2)Effects of canyon radiation due to the infinite mass foundation are also significant on both linear and nonlinear responses of dams (i.e. joints closed and joints open respectively). Although the patterns of influence due to contraction joint opening are similar for both massless foundation and the infinite mass canyon, consideration of the latter results in a further reduction of arch stresses, and, in the mean time, reduces the net increase in cantilever stresses when compared with the massless foundation.

(3)The computer program which combines the above two factors is in a preliminary stage-a simplified earthquake input procedure is being used, which takes into account the radiation damping of the canyon but prevents the amplification of ground motion through the rock mass. Further efforts should be devoted to incorporating the free-field input procedure into the program.

Acknowledgment

The authors gratefully acknowledge the financial support for this work, which was provided by the National Key Projects on Basic Research and Applied Research: Applied Research on Safety and Durability of Major Construction Projects and the Ministry of Electric Power under contract: 96-221-03-02-02(1) 'Study on Earthquake Responses of High Arch Dams due to Contraction Joint Opening'.

References

1. P. S. Nowak and J. F. Hall, 'Arch dam response to non-uniform seismic input', *J. eng. mech. ASCE* **116**, 1125-1139(1990).
2. S. B. Kojic and M. D. Trifunac, 'Earthquake stresses in arch dams, 1: theory and antiplane excitation', *J. eng. mech. ASCE* **117**, 532-552(1991).
3. J. Dominguez and O. Maeso, 'Model for the seismic analysis of arch dams including interaction effects', *Proc. 10th world conf. earthquake eng.* Madrid **8**, 4601-4606 (1992).
4. A. K. Chopra and H. Tan, 'Modeling of dam-foundation interaction in analysis of arch dams', *Proc. 10th world conf. earthquake eng.* Madrid **8**, 4623-4626(1992).
5. Zhang Chuhan, Jin Feng and Wang Guanglun, 'A method of FE-BE-IBE coupling for seismic interaction of arch dam-canyons', Boundary Element Methods, *Proc. 5th Japan-China symposium on boundary element methods*, Elsevier, Amsterdam, 293-302(1993).
6. Zhang Chuhan, Jin Feng and O. A. Pekau, 'Time domain procedure of FE-BE-IBE coupling for seismic interaction of arch dams and canyons', *Earthquake eng. struct. dyn.* **24,** 1651-1666(1995).
7. Zhang Chuhan, Jin Feng and Wang Guanglun, 'Seismic interaction between arch dam and rock

canyon', *Proc. 11th world conf. earthquake eng.* Acapulco, Paper No. **595,** 41-48.

8. R. W. Clough, 'Nonlinear mechanisms in the seismic response of arch dams', *International research conf. on earthquake eng.*, Skopje, Yugoslavia (1980).
9. M. J. Dowling and J. F. Hall, 'Nonlinear seismic analysis of arch dams', *J. eng. mech. ASCE* **115,** 768-789 (1989).
10. G. L. Fenves, S. Mojtahedi and R. B. Reimer, 'ADAP-88: A computer program for nonlinear earthquake analysis of concrete arch dams', *Report No. EERC 89-12,* Earthquake Engineering Research Center, University of California, Berkeley, CA, 1989.
11. Zhang Chuhan, Song Chongmin and O. A. Pekau, 'Infinite boundary elements for dynamic problems of 3-D half space', *Int. J. numer. methods eng.* **31,** 447-462 (1991).
12. J. Ghaboussi, E. L. Wilson and J. Isenberg, 'Finite element for rock joints and interfaces', *J. soil mech. found. div. ASCE* **99**, 833-848 (1973).
13. R. W. Clough and E. L. Wilson, 'Dynamic analysis of large structural systems with local nonlinearities', *computer methods in applied mech. and eng.,* vol. **17/18**, 107-129(1979).

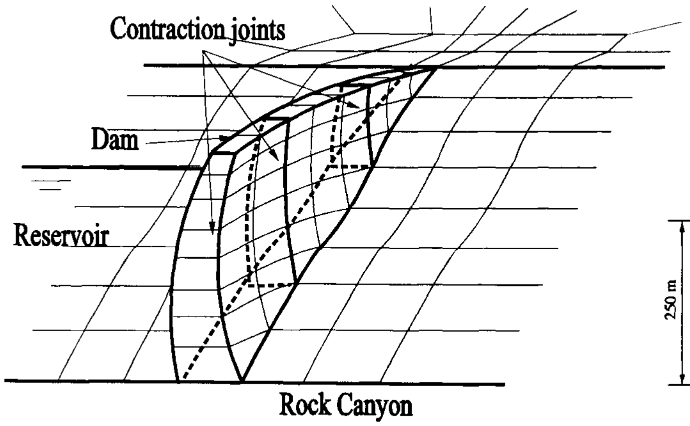

Fig. 1 Schematic layout of dam-canyon system

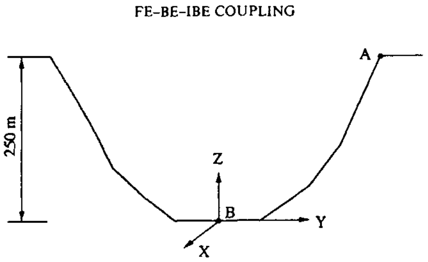

Fig. 2 Canyon profile for computed impedance functions

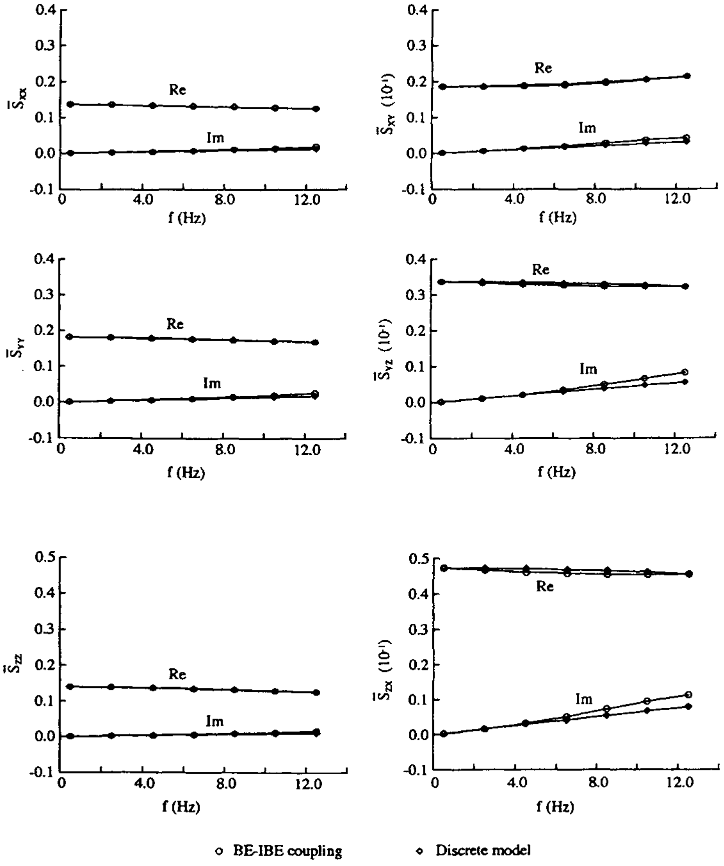

Fig. 3 Impedance functions of dam-canyon interface at point A

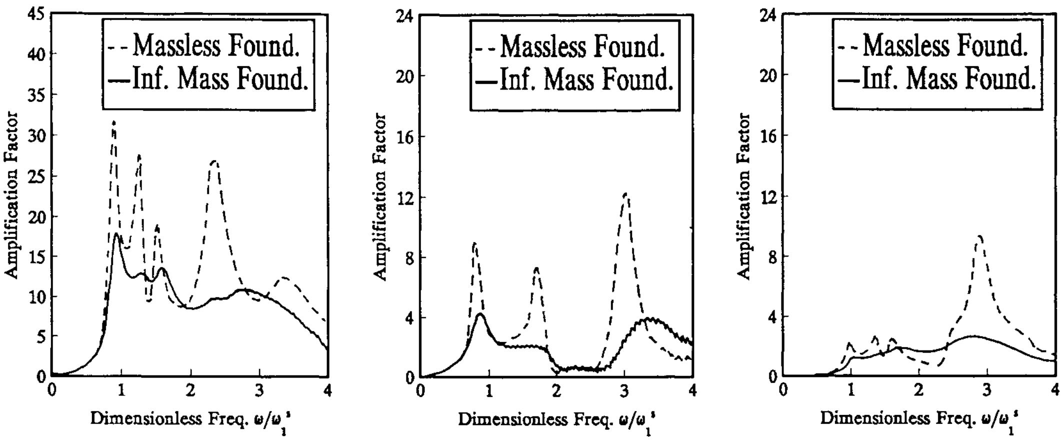

(a) Stream (b) Cross-stream (c) Vertical

Fig. 4 Comparison of response functions between the massless and infinite mass foundation

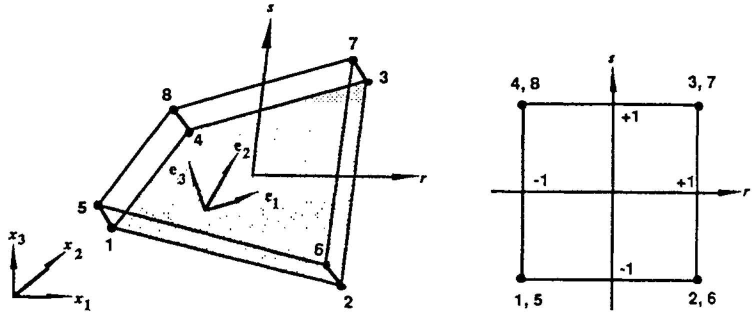

a) LOCAL AND GLOBAL COORDINATE SYSTEMS

b) NATURAL COORDINATE SYSTEM

Fig. 5 Nonlinear joint element

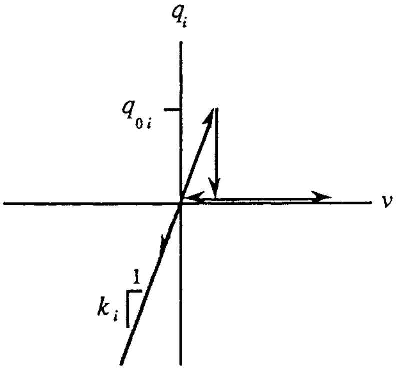

Fig. 6 Stress-relative displacement relationship for joint element

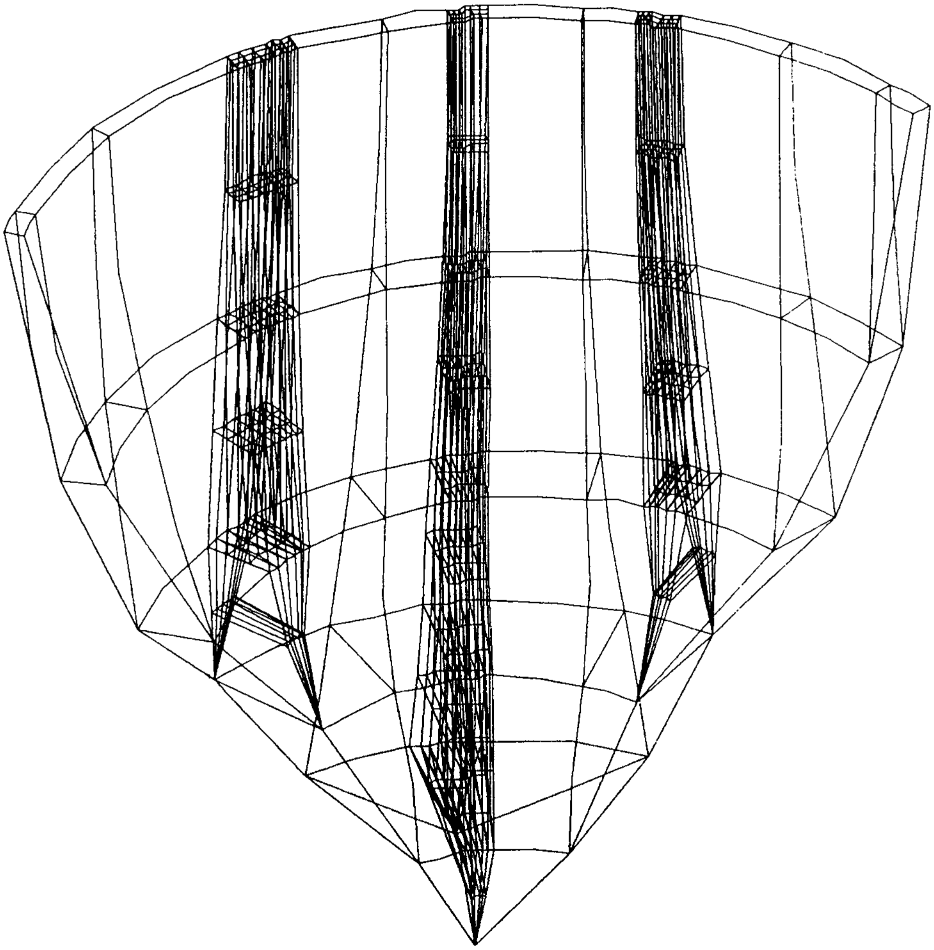

Fig. 7 F.E. discretization of Big Tujunga dam with three contraction joints (After Fenves et al. [10])

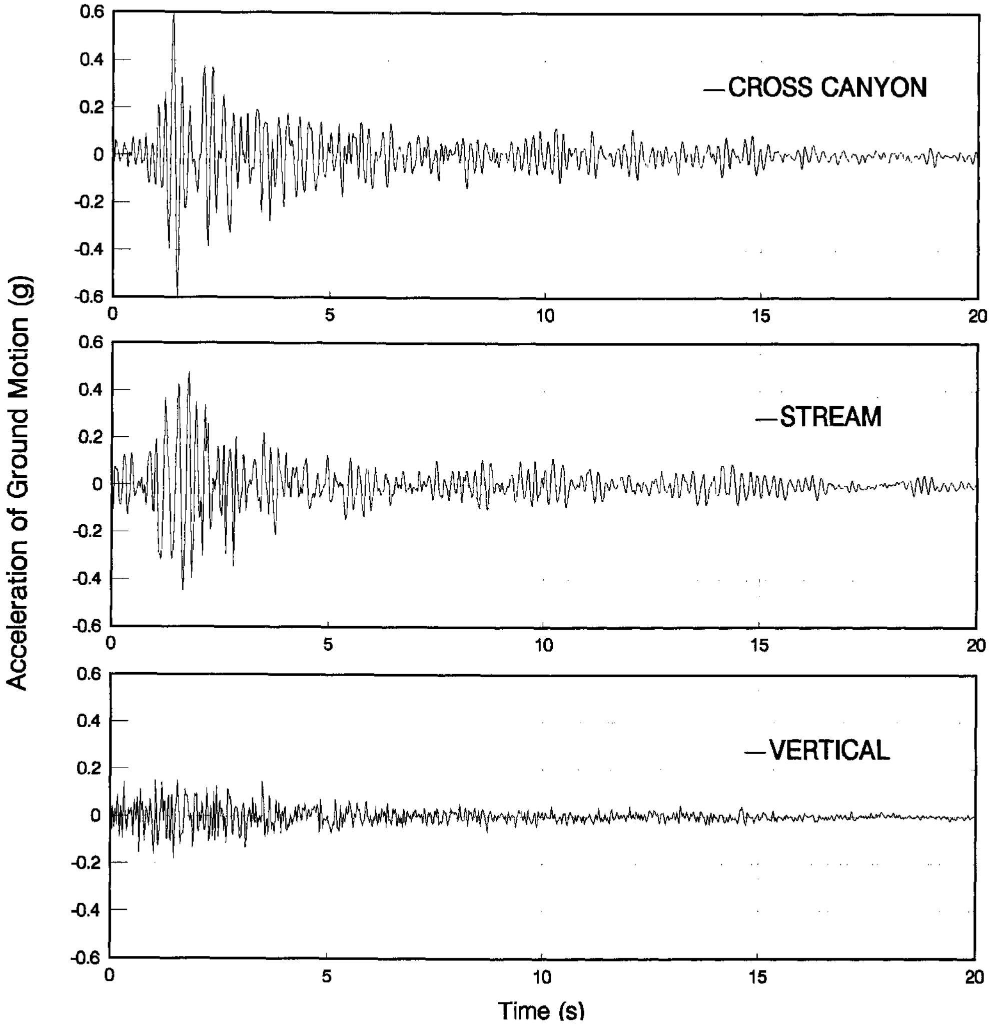

Fig. 8 Ground motion for the analysis of Big Tujunga dam, as scaled from Hughes No. 12 records

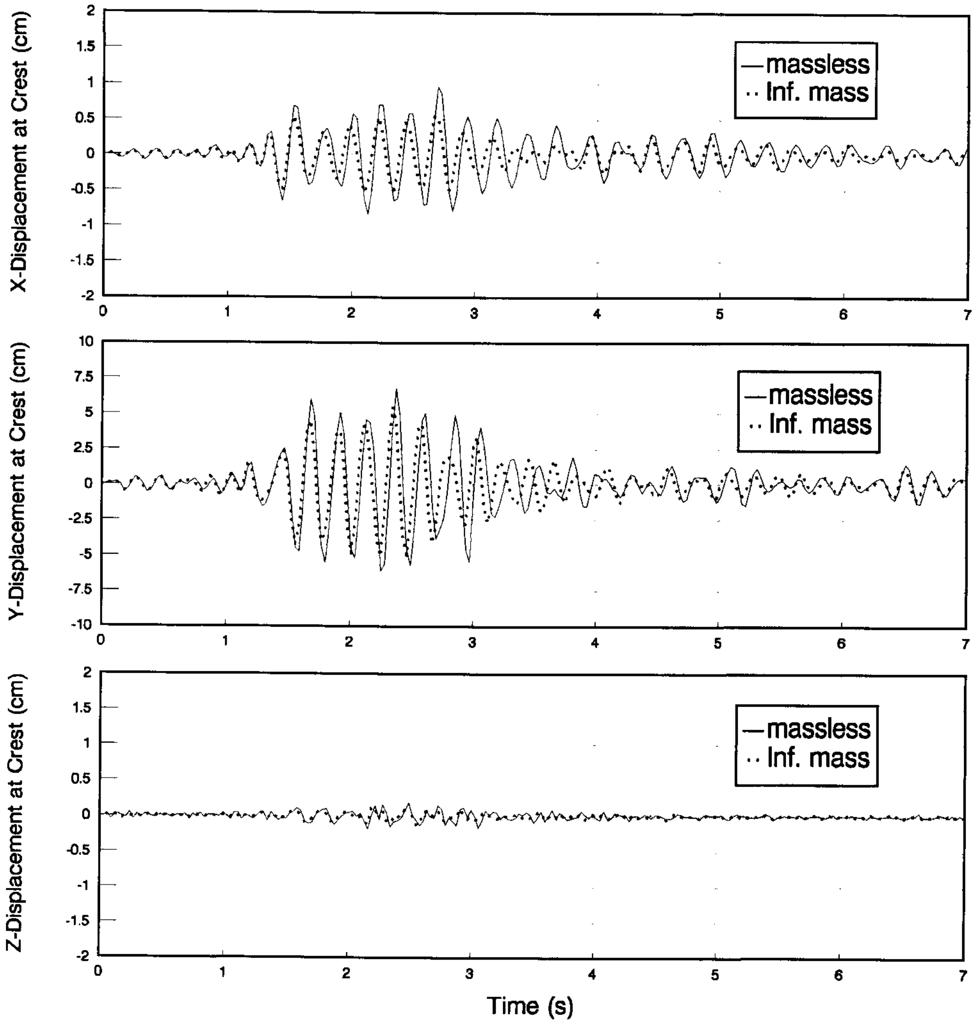

Joints Closed (Linear Response)

Fig. 9 Comparison of displacements at dam crest between the infinite mass and massless foundation

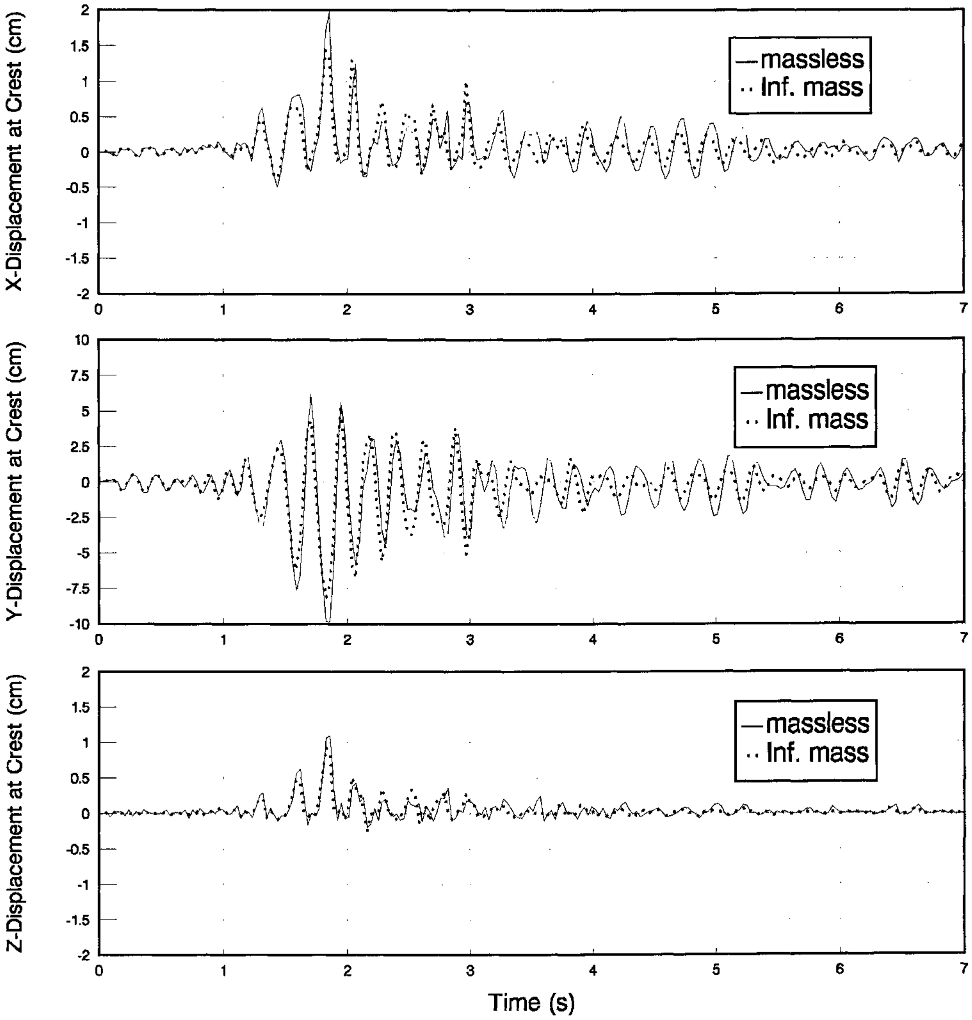

Joints Open (Nonlinear Response)

Fig. 10 Comparison of displacements at dam crest between the infinite mass and massless foundation

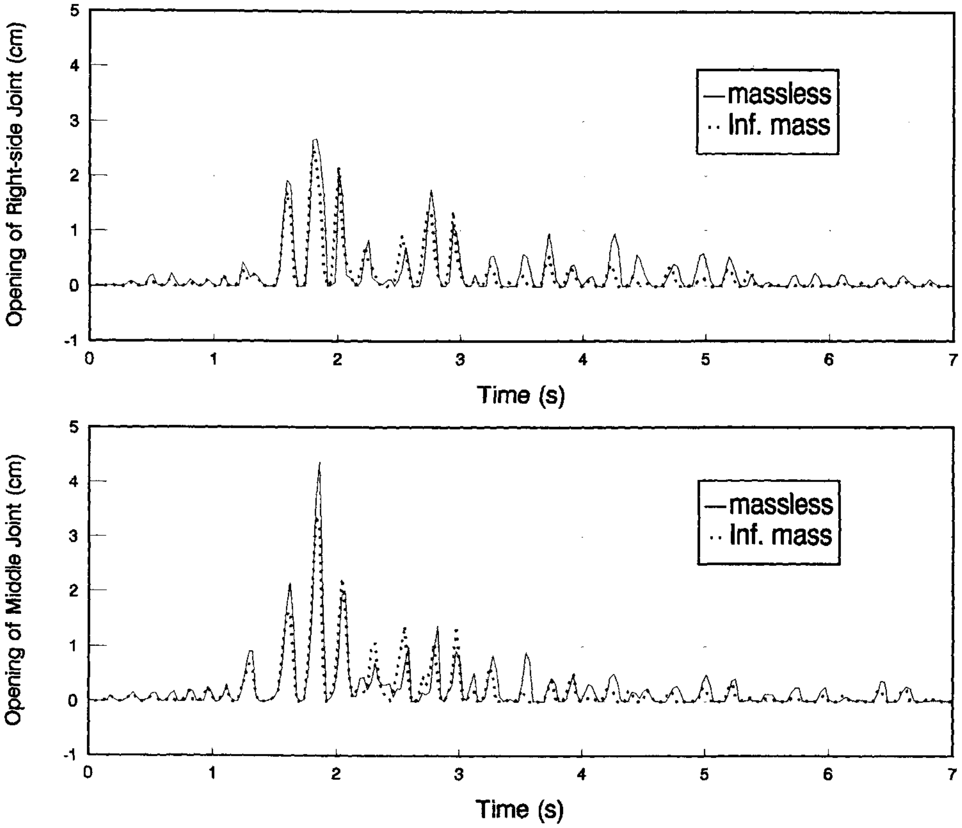

Fig. 11 Comparison of joint openings between the infinite mass and massless foundation

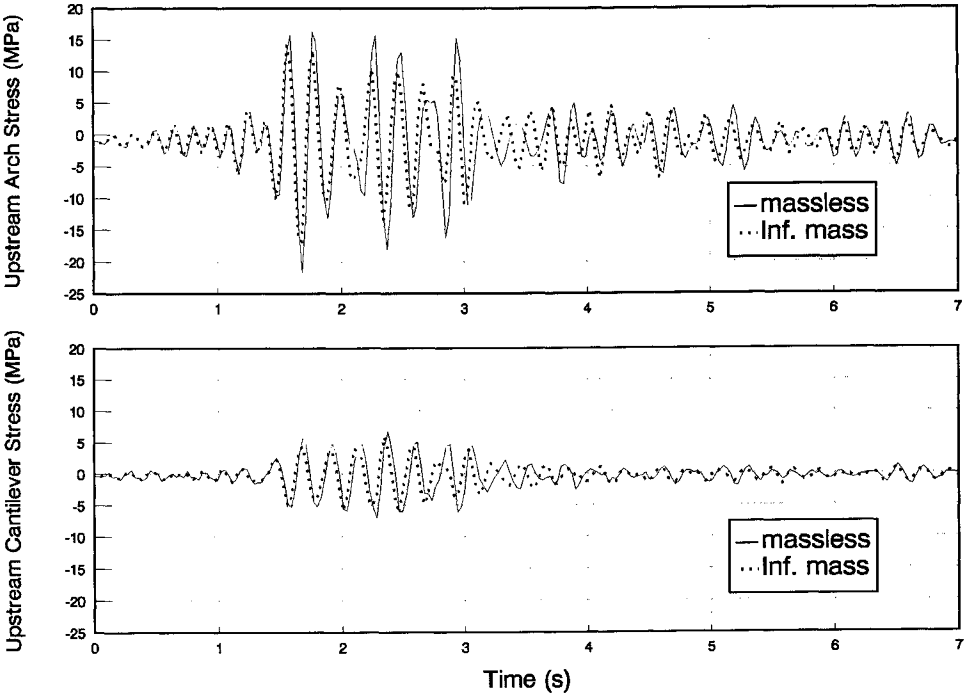

Fig. 12 Comparison of linear responses of the dam between the infinite mass and massless foundation

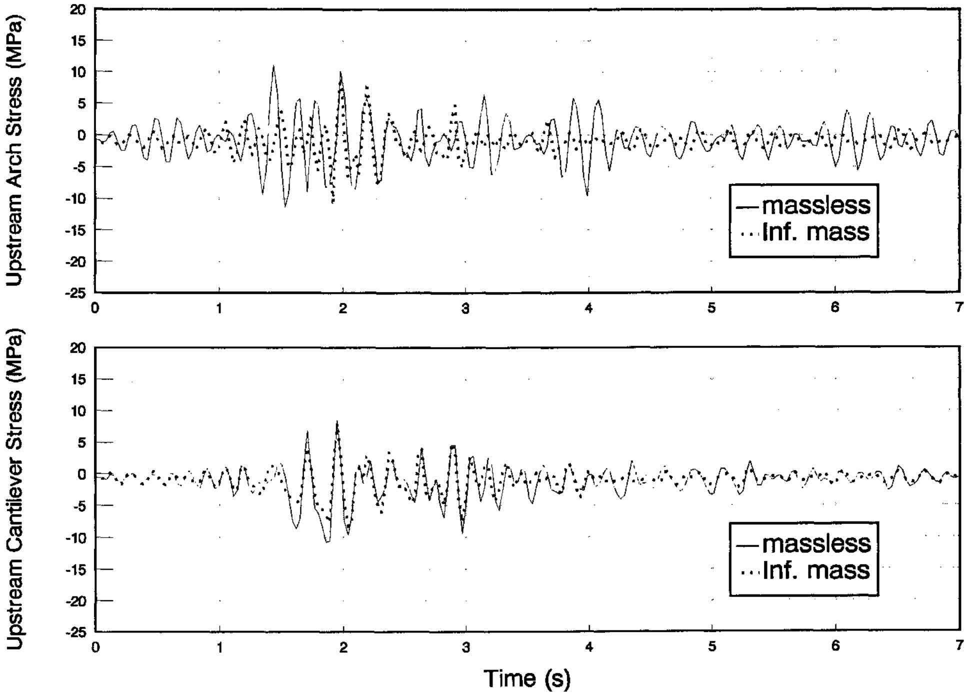

Fig. 13 Comparison of nonlinear responses of the dam between the infinite mass and massless foundation

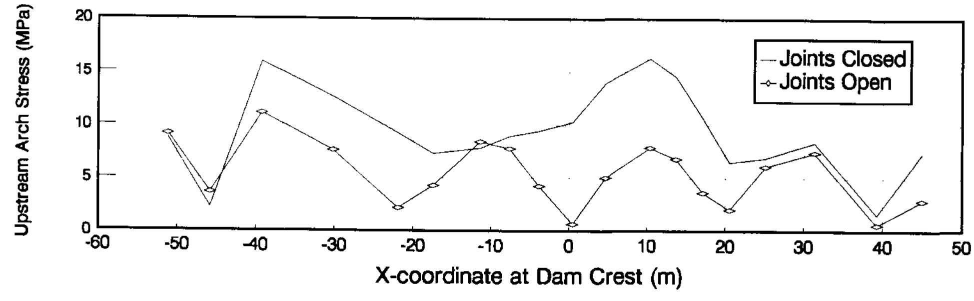

(a) Massless Foundation

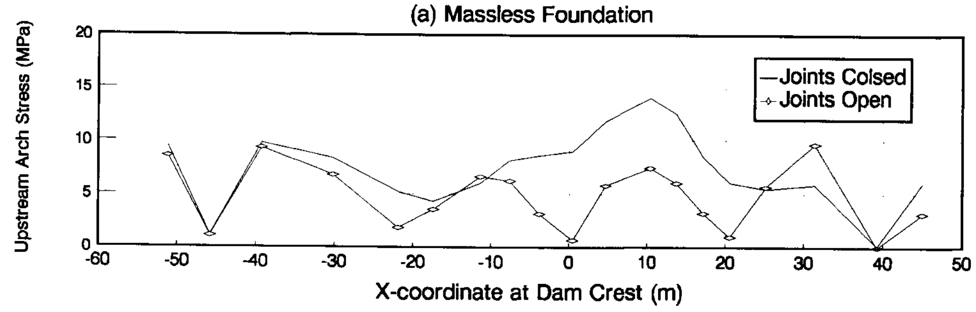

(b) Infinite Mass Foundation

Fig. 14 Comparison of upstream arch stress distributions along the dam crest between the infinite mass and massless foundation

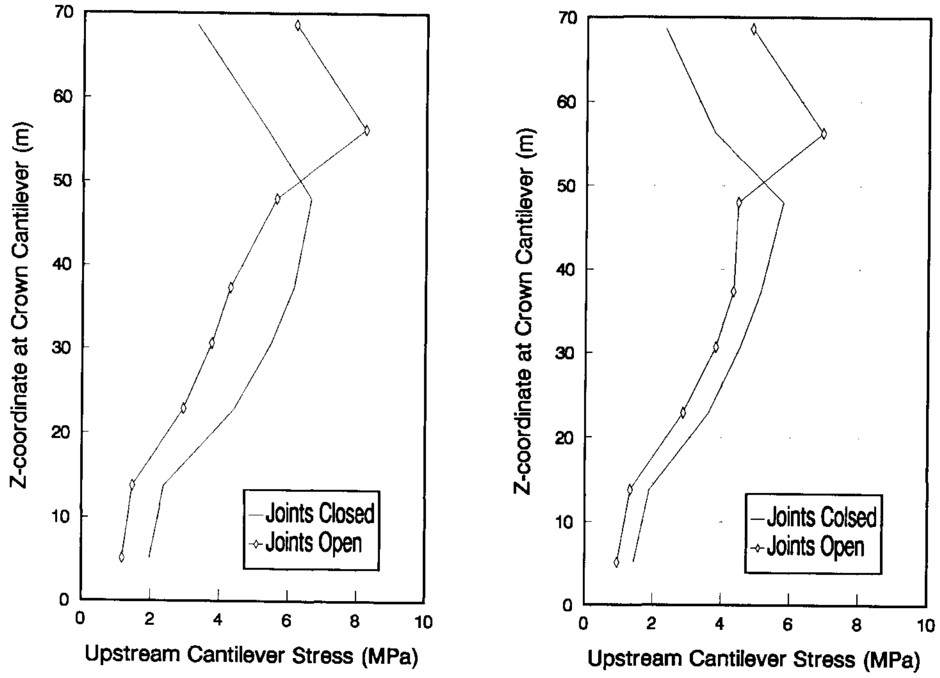

(a) Massless Foundation

(b) Infinite Mass Foundation

Fig. 15 Comparison of upstream cantilever stress distributions along the crown cantilever between the infinite mass and massless foundation

Application of Transmitting Boundaries to Non-Linear Dynamic Analysis of an Arch Dam-Foundation-Reservoir System

Chen Houqun Du Xiuli Hou Shunzai
(China Institute of Water Resources and Hydropower Research)

Key words :

arch dam, dynamic interaction, transmitting boundary, non-linear seismic response

Introduction

In China a series of important arch dam with a height of about 300m has been designed and planned to be constructed in the areas with high seismicity. Seismic safety becomes one of the most critical problems for hydropower construction at present in China.

The importance of foundation interaction on the displacements and stresses resulting from loading an arch dam has long been recognized for static as well as dynamic loads. With the introduction of the finite element method, the validity of the foundation interaction model was greatly improved for static loads as the foundation flexibility can be considered by including some adjacent rock mass to a certain extent to form a dam-foundation model with fixed boundaries. However the matters are much more complicated in seismic analysis. At least following three factors should be considered in this case, such as:

1.the spatial variation both in amplitude and the phase angle of a seismic input along the canyon of dam base, particularly, for a high dam in deep valley which is more sensitive to the differential ground motion of dam abutments;

2.the energy dispersion of seismic wave in the semi-infinite rock foundation media;

3.the effects of the spatial topographical features of a canyon and the non-linear behaviors of geological structures almost unavoidably existed in the near-field foundation for every dam site.

To solve the problem mentioned above some artificial boundary conditions have to be involved to prevent wave reflections at the boundaries of finite discrete models for infinite medium under the action of seismic incident waves. For earthquake engineering of dams some approaches with artificial boundary conditions represented through dynamic impedance of infinite foundation medium are commonly used in practice. However, those approaches not only couple all boundary points but also are basicly formulated in frequency domain. They are non-local both in space and in time, therefore, usually require too large computer storage and high computer speed for a three-dimensional arch dam system. Particularly, they are difficult to be efficiently and precisely used, while the non-linearities both of the geological structures in foundation and of the dam with joints must be considered.

In this paper a study of seismic behavior of a high arch dam with dynamic interation with reservoir and foundation based on the wave propagation in a non-uniform and local non-linear medium by using an explicite finite element method with transmitting boundaries is presented. Together with its easy implementation and high accuracy enough for engineering practice, the applied approaches is distinguished from others for its features of decoupling motion of any node on the artificial boundary of a discretized model from the others except its neighboring ones. Some results of the application of this approach to seismic analysis of a designed Xiaowan arch dam with a maximum height of 292m in China is illustrated and a comparison is made with the conventional method.

Brief description of the approach

The arch dam foundation system can be divided into an interior region with a discrete dam and its adjacent near-field foundation. and a far-field foundation region by a set of artificial boundaries. All important near-field topographical and geological features can be contained within the interior discrete model of a reasonable size. At the artificial transmitting boundaries the outgoing waves from the interior region can be transmitted without reflection and also the effects of the spatial variation of the motions at dam base along the canyon can be included under the action of incident seismic wave.

The equation of motion at any interior node of the finite element model at time t has the form

$$m_i\ddot{U}_{ij}(t) + D_{ij}(t) + F_{ij}(t) = R_{ij}(t) \tag{1}$$

in which m_i is the lumped mass of node i ; $\ddot{U}_{ij}$ is the acceleration of j direction at node i ; $D_{ij}(t)$、$F_{ij}(t)$、$R_{ij}(t)$ are the damping 、 restoring and external forces of j direction at node i , respectively. The m_i includes the added mass due to hydrodynamic pressure with an assumption of incompressible reservoir water. A Raleigh damping is adopted for derivation of $D_{ij}(t)$ as

$$D_{ij}(t) = 2\xi\omega_0 m_i\dot{U}_{ij}(t) \tag{2}$$

in which ξ is the damping ratio of material; ω_0 can be taken as the fundamental frequency of the system.

Using central differences for the derivatives for lumpd-mass finite element model, a simple step-by-step solution can be provided by an explicit integration scheme as follows:

$$(\tfrac{1}{\Delta t^2} + \tfrac{1}{\Delta t}\xi\omega_0)m_iU_{ij}^{t+\Delta t} = R_{ij}^t - F_{ij}^t + \tfrac{2}{\Delta t^2}m_iU_{ij}^t - (\tfrac{1}{\Delta t^2} - \tfrac{1}{\Delta t}\xi\omega_0)m_iU_{ij}^{t-\Delta t} \tag{3}$$

in which the restoring force F_{ij}^t at right-hand side is only related to the nodal displacements of elements correlated with node i .

The formula (3) is conditional stable, therefore, the time step for integration is limited as

$$\Delta t \le \min(\frac{\Delta R_{\min}^1}{C_{\max}^1}, \cdots\cdots, \frac{\Delta R_{\min}^n}{C_{\max}^n}) \tag{4}$$

in which n is the number of media; $\Delta R_{\min}^j$ 、$C_{\max}^j$ are the minimum element size and maximum wave velocity of medium i , respectively.

In general, it is required, that

$$\Delta R_{\max} \le (\frac{1}{8} \sim \frac{1}{12})\lambda_{\min} \tag{5}$$

here, $\Delta R_{\max} = \max(\Delta R_{\max}^1, \Delta R_{\max}^2, \cdots\cdots \Delta R_{\max}^n)$, $\lambda_{\min}$ is the minimum incident wave length.

A general expression of one way wave motion at transmitting boundary can be derivated based solely on wave propagation. It is not geared to any particular system of equations[1]

All outgoing waves impinging upon the transmitting boundary with different wave speeds (C_i) and incident angles (Q_i) may be expressed by their apparent propagation along the x-axis, normal to the boundary (Fig-1).

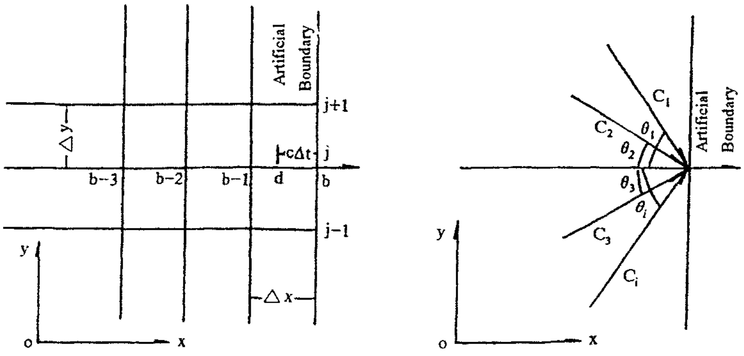

(a) (b)

Fig-1 Artificial Boundaey and Outgoing Waves

For one-wave propagation any outgoing wave U_i of boundary point b at time $(t+\Delta t)$ should be equal to its value of a point which is at a distance of $(C_i\Delta t)$ from the point b along the x-axis at forward time t as

$$U_i(x_b,y_b,z_b,t+\Delta t)=U_I(x_b-C\Delta t,x_b,y_b,t) \tag{6}$$

For linear wave field in the region of artificial boundary, If all outgoing waves are combined in a resultant outgoing wave with a constant artificial wave speed (C_a), as a consequence a error will be introduced as

$$\Delta U(x_{b.}y_b,z_b,t+\Delta t)=U(x,y,z,t+\Delta t)-U(x_b-c_a\Delta t,y_b,z_b,t) \tag{7}$$

It is easy to be proved that the error is also a wave propagating along the x-axis with the same speed and can be transmitted according to formula (6) too. Therefore a multi-transmitting formula of N-order can be written as

$$U(x_b,y_b,z_b,t+\Delta t)\approx\sum_{n=i}^{N}(-1)^{n+1}C_n^N U(x_b-nc_a\Delta t,y_b,z_b,t(n-1)\Delta t) \tag{8}$$

where $C_n^N=N!/[(N-n)!n!]$

By using a quadratic interpolation, the displacement at the computational points in finite element model can be written as

$$U(x_b,y_b,z_b,t+\Delta t)=\sum_{n=i}^{N}(-1)^{n+1}C_n^N\,\bar{T}_n\bar{U}_n \tag{9}$$

where

$$\bar{U}_n=[x_b,y_b,z_b,t-(n-1)\Delta t),U(x_b-\Delta x,y_b,z_b,t-(n-1)\Delta t),\cdots\cdots$$

$$U(x_b - 2n\Delta x, y_b, z_b, t-(n-1)\Delta t)]^T \tag{10}$$

$\bar{T}$ is a function of c_a, Δt and Δx and it can be calculated using the formula in Ref. [2].

In order to separate the outgoing waves from the total displacement in the region of artificial boundary, the incident seismic wave, which can be calculated from wave theory in continues medium, should be subtracted from the displacement obtained from formula (3).

In principle, the adopted approach can also be used for any oblique incident waves. Even for vertical incident seismic wave, the ground motions will variate along the canyon of an arch dam base.

Application to non-linear dynamic analysis

A study on a three-dimensional response of a high arch dam-foundation-reservoir system based on the seismic wave propagating in a foundation with nonlinear fault and transmitting boundaries in time domain was firstly carried out. The calculated Xiawan arch dam is located in the upper reach of the Lanchuang River in Yunnan province. It is a parablical double curvature arch dam of 292m high. Its design earthquake intensity is IX degree with a horizontal peak acceleration of 0.308g, while the vertical peak acceleration is 2/3 of the horizontal one. The sketch of the mathematical model is shown in Fig-2 In the V-type canyon only the most important fault F_7 located 76m apart from the dam heel was considered in the analysis. A non-linear constitutive relation with Druker-Prager cap model was adopted for fault F_7. A finite element mesh automatically generated in the program and the dam-foundation system was modeled by 1364 8-node three-dimensional solid elements. For simplicity the dam-reservoir interaction was considered through added mass with neglect of the compressibility of reservoir water.

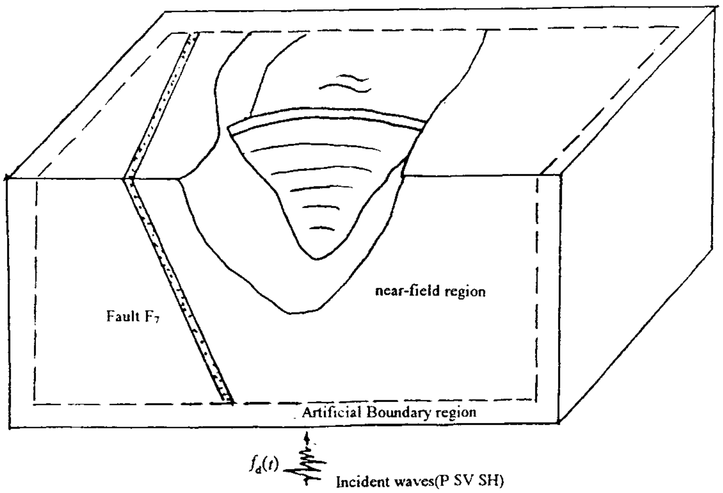

Fig-2 Sketch of the Mathematical Model

The acceleration recorded at rock foundation during an after shock of Tangshan earthquake in 1976 with its peak acceleration scaled to one half of the design values were used as the incident s and p waves in the analyses. For comparison, three alternatives of input, with one streamwise component, one cross-stream component, and all three components simultaneously were applied respectively. In order to reveal the effect of fault F_7, three foundation models ware analyzed separately. They are: Model 1-without fault, Model 2 with fault of linear property and Model 3-with fault of non-linear property. There are altogether 5 different analytical cases as shown in Table-1

Table-1 Analytical Cases

Analytical Cases	1	2	3	4	5
Seismic Input	X	Y	X+Y+Z	X+Y+Z	X+Y+Z
Foundation Model	1	1	1	2	3

For analytical cases 1 、2 、 and 3, the responses of arch dam system were also analyzed by using conventional program ADAP-CH84 with massless foundation and fixed boundaries.

Some analytical results are illustrated as follows.

The time-history plots of acceleration and displacement responses at crest and heel of the dam are shown in Figs. 3 and 4, respectively. The stress responses of dam at centroid of upstream element are shown in Fig 5 for example.

Peak dynamic stresses at centroid of elements at different part of dam are indicated in Table-2. A comparison of arch and cantilever stresses at crown of dam by using presented method and conventional method are shown in Table-3. In Table-4 the stresses of dam at some typical positions are compared for 3 different foundation Model

Table-2 Peak dynamic Stress at Centroid of Element (MPa)

		Upstream			Down stream		
		A	B	(A-B)/A(%)	A	B	(A-B)/A(%)
Right Abutment Ñ1222.5	s_x	2.42	1.73	-29	0.94	0.44	-53
	s_y	1.09	0.68	-38	1.94	1.01	-48
	s_z	1.09	0.29	-73	0.64	0.12	-81
Crown Ñ1222.5	s_x	2.17	2.85	31	2.18	2.51	15
	s_y	0.26	0.29	12	0.28	0.34	21
	s_z	0.62	0.56	-10	0.73	1.07	47
Left Abutment Ñ1222.5	s_x	1.09	0.68	-38	1.60	0.36	-78
	s_y	1.76	0.32	-82	1.23	0.67	-46
	s_z	1.06	0.42	-60	0.99	0.09	-91
Crown Ñ1120.0	s_x	1.31	1.40	7	1.03	0.83	-19
	s_y	0.31	0.16	-48	0.99	0.29	-12
	s_z	1.75	0.95	-46	1.03	1.36	32
Heel Ñ966.5	s_x	0.73	0.97	33	0.54	0.27	-50
	s_y	0.50	0.86	72	0.58	0.27	-53
	s_z	2.23	4.29	92	1.24	0.26	-79

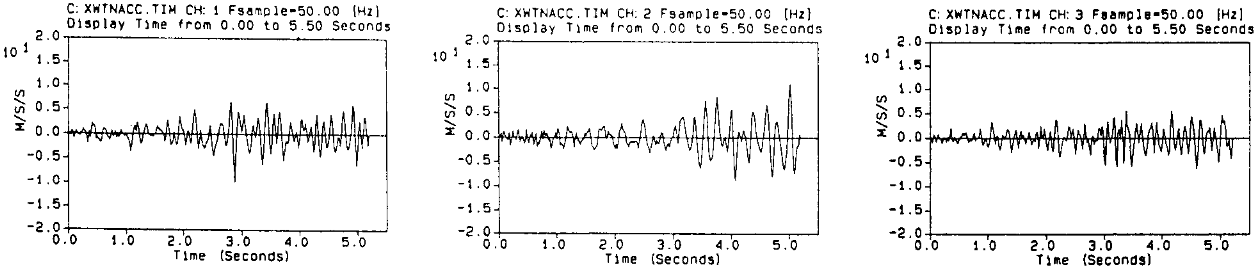

Right 1/4 Point at Crest

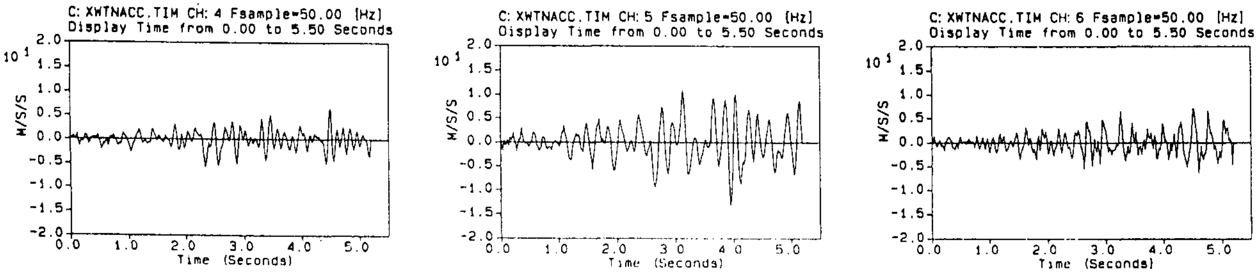

Crown at Crest

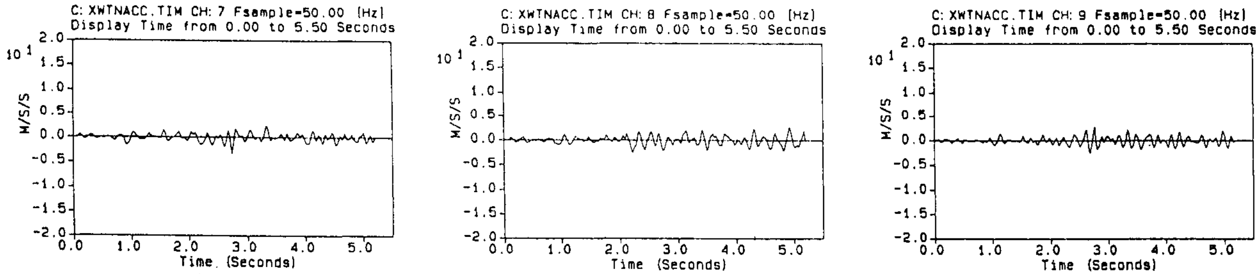

Cross-Stream Dam Heel Streamwise Vertical

Fig-3 Acceleration Responses of Dam (Case 5)

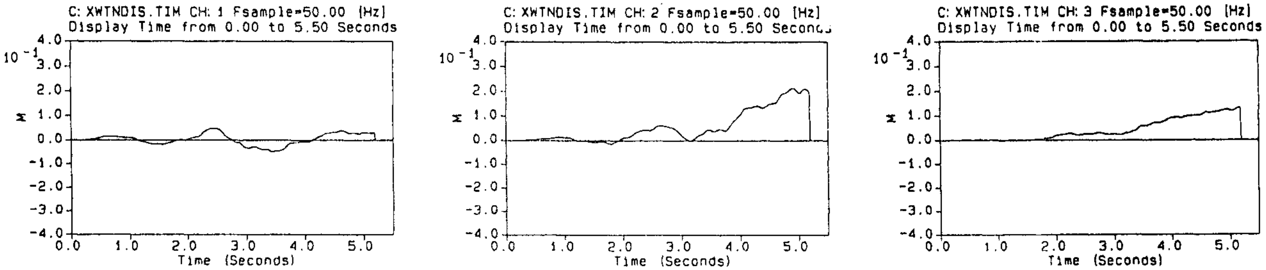

Right 1/4 Point at Crest

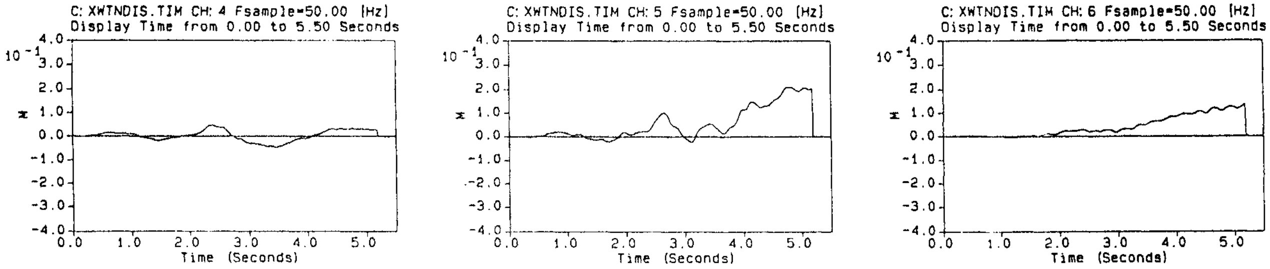

Crown at Crest

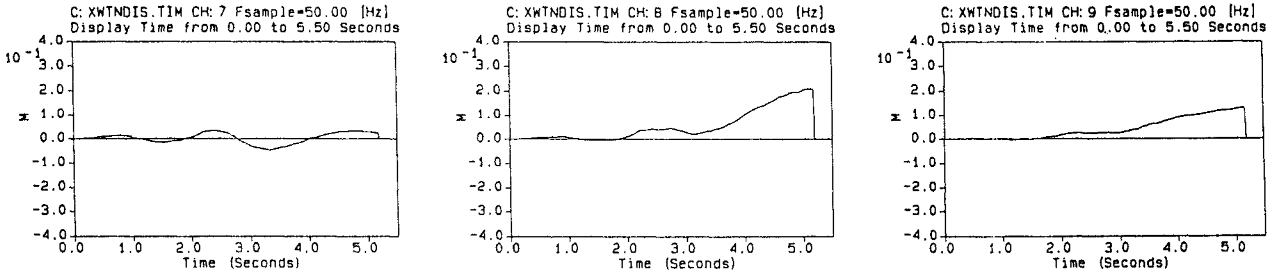

Cross-Stream Dam Heel Streamwise Vertical

Fig-4 Displacement Responses of Dam (Case 5)

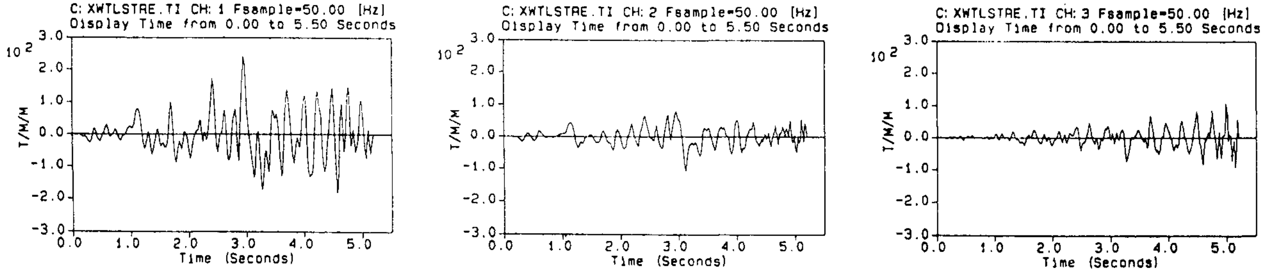

Right Abutment (∇1222.5)

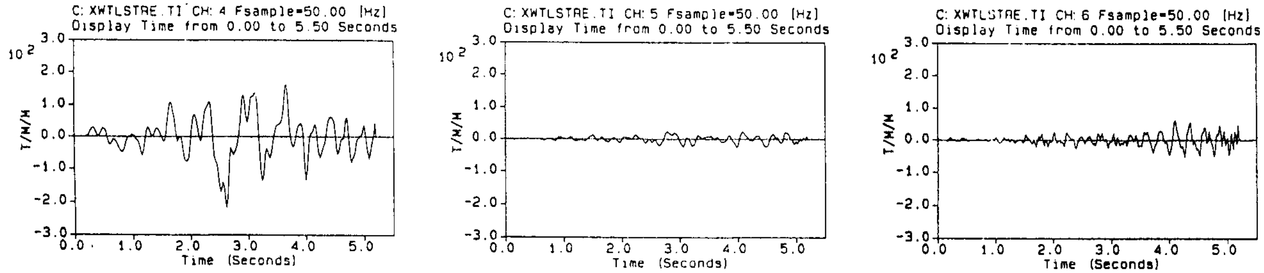

Crown (∇1222.5)

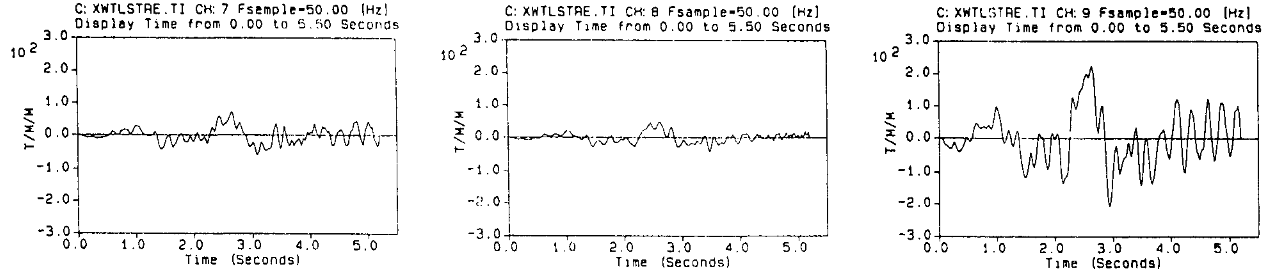

Cross-Stream

Heel (∇966.5)

Streamwise

Vertical

Fig-5 Stress Responses of Dam at Centroid of Upsteam Element

Conclusion and remark

The transmitting boundary approach is first successfully applied in a three-dimensional non-linear arch dam system with consideration of the dynamic interactions of dam-foundation-reservoir. From the study on dynamic behavior of Xiaowan arch dam, some conclusions aid in understanding the important seismic behavior of arch dam for engineers can be drawn as follows.

Table-3 Arch and Cantilever stresses at crown (Mpa)

			Ñ1222.5		Ñ1120.0		Ñ966.5	
			Arch	Cantilever	Arch	Cantilever	Arch	Cantilever
	1	A	0.76	0.32	0.61	0.76	0.43	0.55
		B	0.88	0.36	0.51	0.57	0.60	0.43
		(A-B)/A(%)	16	-16	-16	-25	40	-22
	2	A	2.34	1.07	1.07	1.30	0.76	3.88
		B	2.79	1.92	1.92	1.70	0.71	3.61
		(A-B)/A(%)	19	79	79	31	-7	-7
	3	A	2.17	1.55	1.55	1.99	1.08	3.89
		B	3.23	1.75	1.75	1.40	1.13	5.60
		(A-B)/A(%)	49	13	13	-30	5	44
	1	A	0.56	0.43	0.43	0.49	0.41	0.54
		B	0.59	0.82	0.82	0.34	0.35	0.16
		(A-B)/A(%)	5	91	91	-31	-15	-70
	2	A	1.83	0.68	0.68	0.86	0.40	1.25
		B	1.54	0.48	0.48	1.05	0.36	1.52
		(A-B)/A(%)	-16	-29	-29	22	-10	22
	3	A	2.19	1.14	1.14	1.44	0.55	1.99
		B	2.57	1.06	1.06	1.95	0.37	0.92
		(A-B)/A(%)	17	-7	-7	35	-33	-54

* Arch and cantilever stress mean s_x, s_z, recpectively for method with transmitting boundaries.

1.As the energy dispersion through transmitting boundaries for xiaowan dam in the central part with more significant dynamic effects the stresses calculated by presented method are reduced by (40-49)% for arch and cantilever, recpectively comparing with the conventional method with the assumptions of a massless foundation and its fixed boundaries. However, for the abutments, the stresses by presented method are significantly increased by (30-80)%. It obviously reveal the effect of non-uniform input at dam base along the canyon.

2. With consideration of the fault F_7 in foundation the dam stresses have some reduction, but at abutments the stresses are increased by(20-30)%. However, the effect of non-linearity in this case is less than 10%.

As for the applies approach, following problems warranted further study can be remarked:

1. A criteria for unstability with high frequency oscillation near the transmitting boundaries and its countermeasures need to be investigated with consideration both the coupling effect of interior motion equation with artificial boundary conditions and the effect of numerical discretization.

2. The material damping effect of foundation media for wave propagation in time domain need to be improved.

Table-4 Stresses of Dam with Different Foundation Model (Mpa)

		Upstream			Down stream		
		Case 1	Case 2	Case 3	Case 1	Case 2	Case 3
Right Abutment Ñ1222.5	s_x	3.18	3.44	3.42	1.14	1.65	1.54
	s_y	1.29	1.32	1.29	2.12	2.53	2.64
	s_z	1.26	1.33	1.29	0.74	0.99	1.00
Crown Ñ1222.5	s_x	2.17	1.87	1.88	2.19	1.95	1.77
	s_y	0.25	0.28	0.27	0.33	0.43	0.43
	s_z	0.83	0.49	1.48	0.90	0.87	0.84
Left Abutment Ñ1222.5	s_x	1.20	1.21	1.17	1.81	1.84	1.83
	s_y	1.78	1.71	1.70	1.36	1.16	1.25
	s_z	1.56	1.98	2.03	1.28	1.23	1.27
Crown Ñ1120.0	s_x	1.55	1.30	1.20	1.14	0.66	0.64
	s_y	0.34	0.20	0.20	0.32	0.32	0.31
	s_z	1.99	1.53	1.45	1.44	1.28	1.23
Heel Ñ966.5	s_x	1.08	0.90	1.00	0.55	.067	0.73
	s_y	0.79	0.49	0.55	0.76	0.92	0.85
	s_z	3.89	2.81	3.06	1.99	1.40	1.48

Acknowledgements

The authors are grateful to Mr. Liao Z. P., Li X. J and Liu J. B for their concern and help.

References

[1] Liao Z. P. and Liu J.P., " Fundamental problems of finit element simulation of wave motion " , scientia sinica (series B), 1992, 8, 874-82

[2] Liao Z. P., " Extrapolation non-reflecting boundary conditions " , Wave Motion 24 (1996) 117-138

A DECOUPLING NUMERICAL SIMULATION OF WAVE MOTION

Liao Zhen-Peng
(Institute of Engineering Mechanics, 9 Xue-fu Rd. Harbin China 150080)

Abstract

A direct numerical simulation of wave motion has been studying since the late 70s for analysis of the soil-structure dynamic interaction and other near-field wave motion problems in various fields. This paper provides a brief summarization of the studies carried out so far.

I Introduction

The soil-structure system consists of two distinct parts: the bounded structure and the unbounded soil. The structure whose dynamic response is to be determined consists of the actual structure and possibly an irregular adjacent soil region. The unbounded soil whose effects on the structure response is to be determined contains no wave ource or scattering wave source. To analyze the structure response using the direct numerical method, a finite soil box which encloses the structure is introduced. Having discretized the box, the fundamental problem of the analysis is to set up two types of equations, that is, the equations governing the motion of nodes within the box and the Artificial Boundary Conditions (ABCs) which govern the motion of nodes on the edge of the box. Great efforts for establishing and solving the two types of equations have led to considerable development of computational approaches for the analysis [1-8]. The author and his co-workers have been working on the topic since the late 70s. Our studies is based on a physical understanding of the local characteristic of wave motion, that is, a disturbance at a space point at a time station is only transmitted to its adjacent space points at the next time station; and our methodology may be described as a natural simulation of the essential feature of wave motion. The simple idea has been run through our studies either to set up the two types of equations of motion or to clarify accuracy and stability of numerical integration of the equations. This paper provides a brief summarization of our studies carried out so far. An outline of the remainder of the paper is as follows. In Section II, a general set of local ABCs are formulated based on a straightforward simulation of the one-way wave propagation. Accuracy of the boundary conditions and their relationships with other famous schemes are also discussed. In Section III, explicit lumped-mass finite element equations of motion of the interior nodes are presented based on the above mentioned essential feature of wave motion. Accuracy of the equations are then studied via clarifying differences of wave motions in the discrete model from those in the corresponding continuous model. Justification of using the lumped-mass equations instead of the consistent-mass ones is also discussed. In the final Section IV, the stable numerical integration of the ABCs in coupling with the equations of interior nodes are studies for practical implementation of the direct method.

II Local Artificial Boundary Conditions

1. Multi-Transmitting Formula

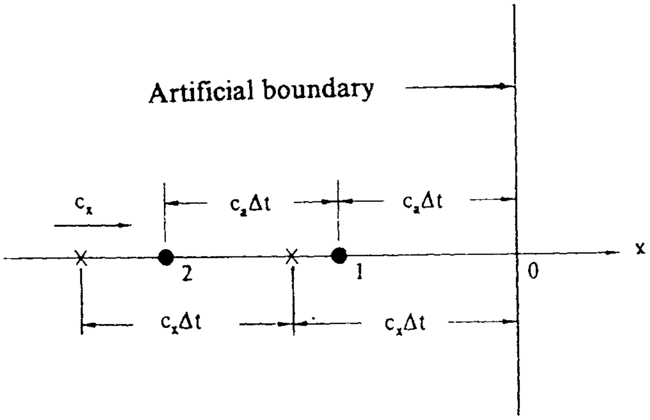

Fig. 1. Schematic of apparent propagation of a one-way wave along the x -axis approaching the artificial boundary.

Since ABCs are used to prevent the wave reflection at the edge of the soil box, a natural approach to set up the boundary conditions is a direct simulation of the one-way wave motion, which are passing through the edge from the interior to the exterior of the box. The starting point to perform the simulation is a general expression of the out-going waves. Having considered the local characteristic of wave motion, the expression may be presented in the local sense, that is, it describes the wave motion merely for a boundary point and its neighborhood within a short time interval containing the time station under consideration. Suppose that a point o on the boundary is considered (Fig.1). Let the x-axis pointing to the exterior of the box pass this point and be perpendicular to the boundary. The outgoing waves impinging upon the boundary point may be expressed by their apparent propagation along the x-axis,

$$u(t,x) = \sum_{j=1} f_j(c_{xj}t - x) \tag{1}$$

where $u(t,x)$ is a function of t and x and consists of arbitrary number of one-way waves $f_j(c_{xj}t - x)$, each of which propagates along the x -axis with an apparent speed c_{xj}, f_j are arbitrary functions. It can be shown that a system of local ABCs can be derived via a direct simulation of Eq.(1) using the space-time extrapolation without knowing any detail of Eq.(1). The apparent propagation of one of the one-way waves in Eq.(1) is written (neglecting the subscript j) as

$$u(t,x) = f(c_x t - x), \tag{2}$$

where f is an arbitrary and unknown function and the apparent speed c_x is an unknown real positive number. Using the forward characteristic, $c_x t - x$, it is easy to see that

$$u(t+\Delta t,x)=u(t,x-c_x\Delta t), \tag{3}$$

where Δt is the time step. Although this type of space-time extrapolation equation in association with Kirchhoff 's formula may be used to set up an exact ABC in some simple cases [9] , it is impossible to derive ABCs directly from Eq.(3) in general cases, because c_x is unknown. However, if an artificial wave speed c_a is introduced to replace the unknown physical speed c_x in Eq.(3), approximate ABCs can be derived from Eq.(3) as follows. First, Eq.(3) is replaced by

$$u(t+\Delta t,x)=u(t,x-c_a\Delta t)+\Delta u(t+\Delta t,x), \tag{4}$$

where $\Delta u(t+\Delta t,x)$ expresses the error caused by c_a replacing c_x. Eq. (4) yields

$$\Delta u(t+\Delta t,x)=u(t+\Delta t,x)-u(t,x-c_a\Delta t) \tag{5}$$

Substituting Eq.(2) into Eq.(5) leads to that $\Delta u(t+\Delta t,x)$ would be a function of c_x, c_a, Δt and $c_x t-x$. If c_x, c_a and Δt are fixed, we may write

$$\Delta u(t+\Delta t,x)=f_1(c_x t-x) \tag{6}$$

where f_1 is a function of the forward characteristic. Eq.(6) means that the error $\Delta u(t+\Delta t,x)$ is also a wave propagating along the x-axis with the same speed c_x. Recognition of $\Delta u(t+\Delta t,x)$ being a wave is the point in this derivation. Following Eq.(4) the error wave may be written as

$$\Delta u(t+\Delta t,x)=\Delta u(t,x-c_a\Delta t)+\Delta^2 u(t+\Delta t,x) \tag{7}$$

Having replaced t and x in Eq.(5) by $t-\Delta t$ and $x-c_a\Delta t$, respectively, the first term in the right-hand side of Eq.(7) is written as

$$\Delta u(t,x-c_a\Delta t)=u(t,x-c_a\Delta t)-u(t-\Delta t,x-2c_a\Delta t) \tag{8}$$

and the error term in Eq.(7) is written:

$$\Delta^2 u(t-\Delta t,x)=\Delta u(t+\Delta t,x)-\Delta u(t,x-c_a\Delta t) \tag{9}$$

Substitution of Eq.(7)into Eq.(4) yields

$$u(t+\Delta t,x)=u(t,x-c_a\Delta t)-\Delta u(t,x-c_a\Delta t)+\Delta^2 u(t+\Delta t,x) \tag{10}$$

It is easy to see that $\Delta^2(t+\Delta t,x)$ and the higher-order error terms similarly introduced are all functions of the forward characteristic $(c_x t-x)$. Following the above formulation we obtain

$$u(t+\Delta t,x)=u(t,x-c_a\Delta t)+\sum_{n=1}^{N-1}\Delta^n u(t,x-c_a\Delta t)+\Delta^N u(t+\Delta t,x), \tag{11}$$

where

$$\Delta^n u(t, x - c_a\Delta t) = \Delta^{n-1}u(t, x - c_a\Delta t) - \Delta^{n-1}u(t - \Delta t, x - 2c_a\Delta t)\,, \qquad n = 1, \cdots, N - 1 \tag{12}$$

$$\Delta^N u(t + \Delta t, x) = \Delta^{N-1}u(t + \Delta t, x) - \Delta^{N-1}u(t, x - c_a\Delta t) \tag{13}$$

Next, suppose that the origin of the x-axis is the boundary point o underconsideration. Substituting x=0 and $t = p\Delta t$ into Eq.(11) and neglecting the higher-order term $\Delta^N u(t + \Delta t, 0)$ yield

$$u((p + 1)\Delta t, 0) = \sum_{n=1}^{N} \Delta^{n-1}u(p\Delta t, -c_a\Delta t), \tag{14}$$

where $\Delta^0 u = u$, the integer p stands for the time station. If c_a used for simulating the nth error wave $\Delta^{n-1}u(t + \Delta t, x)$ is replaced by c_{an} Eq.(14) may be written

$$u((p + 1)\Delta t, 0) = \sum_{n=1}^{N} \Delta^{n-1}u(p\Delta t, -c_{an}\Delta t) \tag{15}$$

Since Eq.(14) or (15) is valid for each one-way wave in Eq.(1), it remains valid for the wave system expressed by Eq.(1) if a common artificial speed is used for transmitting the same order error wave of each wave in Eq.(1). The discrete quantities of $u(t, x)$ in Eq.(14) or (15) stand now for the total displacements contributed by all the incident one-way waves. Although Eq.(15) seems more general than Eq.(14), Eq.(14) is more practical and simpler than Eq.(15), because the physical speeds c_{an} are unknown. If a single artificial speed is used, it can be shown using Eq.(12) that [10-12]

$$\Delta^n u(p\Delta t, -c_a\Delta t) = \sum_{j=1}^{n+1} -1^{j+1} C_{j-1}^{n} u((p + 1 - j)\Delta t, -jc_a\Delta t), \tag{16}$$

where C_j^n are the binomial coefficients. Substituting Eq.(16) into Eq.(14) yields

$$u((p + 1)\Delta t, 0) = \sum_{n=1}^{N-1} A_{N,j} u((p + 1 - j)\Delta t, -jc_a\Delta t), \tag{17}$$

$$A_{N,j} = (-1)^{j+1} C_j^N \tag{18}$$

The local ABC Eq.(17) is the Multi-Transmitting Formula (MTF), which provides a family of ABCs with variable approximation orders. The formula was derived in the early 80s for the incidence of plane waves in homogeneous media[10-12], therefore, the range of applicability of MTF was not fully revealed. The present derivation of MTF[13-14] is based on Eq.(1), the general expression of linear one-way wave motion, therefore, MTF can be applied to all cases where Eq.(1) valids in principle.

The common methodology in derivation of ABCs is started with some assumptions on material properties of the unbounded exterior medium (for example, homogeneous or layered, acoustic or elastic, ...) and the mode of wave motion (for example, anti-plane or in-plane, 2-or 3-dimensional, ...). A specific type of ABCs may then be derived from a particular set of partial differential equations which govern the wave motion in the exterior medium. This common methodology has led to a number of valuable results, however, ABCs thus derived must be set up for each particular case[15-19]. The distinguishing feature of MTF is that it is not geared to any particular set of differential equations of motion, but instead of the particular assumptions on the exterior medium and the wave mode, it is based on a general assumption of the common process of various one-way wave motions, therefore, it applies without modification to all the cases where Eq.(1) valids in principle, for example, the unbounded exterior may be homogeneous or layered, acoustic or elastic, isotropic or anisotropic, and the one-way wave may be either 2- or 3- dimensional, transient or time harmonic, and so on.

2. A generalization of MTF

Suppose that Eq.(1) is generalized into

$$u(t,x)=\sum_j f_j(c_{x_j}t-x)+\sum_j g_j(t)h_j(x) \tag{19}$$

where g_j and h_j in the second summation are arbitrary and unknown functions, which represent some extreme cases of the one-way wave motion. For example, the summation represents the waves propagating parallel to the boundary as $h_j(x)$ are constant, and the static field as $g_j(t)$ are constant, and so on. In order to facilitate generalizing MTF for the expression Eq.(19), Eq.(17) is first rewritten as

$$Su_0^{p+1}=0 \tag{20}$$

where $u_n^p=u(p\Delta t,-nc_a\Delta t)$ and the discrete linear operator S is given by

$$S=B_0^0-\sum_{j=1}^{N}A_{N,j}B_j^j \tag{21}$$

where the backward shift operator B_m^j is defined by

$$B_m^j u_n^p=u_{n+m}^{p-j} \tag{22}$$

Eq.(20) is used to simulate the first summation in Eq.(19). We now consider the simulation of the second summation in Eq.(19). Following the time-space extrapolation Eq.(17), the corresponding space extrapolation at the time station $t=(p+1)\Delta t$ may by written

$$u_0^{p+1}=\sum_{q=1}^{M}A_{M,q}u_q^{p+1} \tag{23}$$

or

$$Tu_0^{p+1}=0 \tag{24}$$

where

$$T=B_0^0-\sum_{q=1}^{M}A_{M,q}B_q^0 \tag{25}$$

The linear combination of the generalized one-way waves expressed by Eq.(19) is approximately simulated by

$$(ST)u_0^{p+1}=0 \tag{26}$$

Substituting Eqs.(21) and (25) into Eq.(26) and using the operational rule

$$B_n^j B_q^p=B_{n+q}^{j+p}$$

lead to

$$u_0^{p+1} = \sum_{j=1}^{N} A_{N,j} u_j^{p+1-j} + \sum_{q=1}^{M} A_{M,q} u_q^{p+1} - \sum_{j=1}^{N} \sum_{q=1}^{M} A_{N,j} A_{M,q} u_{q+j}^{p+1-j} \tag{27}$$

The approximation order of Eq.(27) is given by the integers N and M, $A_{N,j}$ and $A_{M,q}$ are determined by Eq.(18). Eq.(27) is reduced to MTF as M=0. Displacements in Eq.(27) are sampled at the computational points $x = -jc_a \Delta t$. These points do not generally coincide with the nodal points $x = -n\Delta x$ in finite elements or finite differences, Δx is the space step. In order to implement Eq.(27) in the domain discretization computation, an interpolation scheme is required to express displacements at the computational points in terms of those at the nodal points. The interpolation may be realized in a number of ways, as summarized in [2].

3. Spurious reflection analysis

The spurious reflection from an artificial boundary may be described by a reflection coefficient R defined by

$$R = \left| U_0^R / U_0^I \right| \tag{28}$$

where U_0^I and U_0^R are the amplitudes at the boundary point $x = 0$ caused by a harmonic plane wave of incidence and the wave reflected from the boundary, respectively. Analyses of R are usually carried out in the steady-state case. These analyses are appropriate for the transient-state computation if it is performed by the . Fourier transform. However, if the transient computation is performed by the step-by-step integration, R in the steady-state case is no longer completely appropriate. For this reason, the transient-state case in the definition of R has been suggested to account for the reflection in the step-by-step integration [10-12]. In this case, it is assumed that the wave field merely consists of the incident wave in implementation of the ABCs. Suppose that a plane acoustic wave with an speed c impinges upon the boundary at an angle of incidence θ with respect to the x-axis, the explicit formulas of R have been obtained[2, 13].

$$R = \left| 2\sin\left(\pi \frac{\Delta t}{T} \left(\frac{c_a}{c} \cos\theta - 1 \right) \right) \right|^N \left| 2\sin\left(\pi \frac{\Delta t}{T} \frac{c_a}{c} \cos\theta \right) \right|^M, \quad \text{in the transient -state} \tag{29}$$

$$R = \left| \frac{\sin(\pi(\Delta_t / T)(1 \quad (c_a / c)\cos\theta))}{\sin(\pi(\Delta t / T)(1 + (c_a / c)\cos\theta))} \right|^N, \quad \text{in the steady -state} \tag{30}$$

where T stands for the vibration period. Numerical results of R versus θ in the entire range of $0 \leqslant \theta \leqslant 90°$ in the two extreme cases are shown in Fig.2 for Eq.(27), $c_a = c$ and $\Delta t / T = 0.1$. Conclusions drawn from the figure are as follows. The first, a coupling of the space extrapolation to MTF does reduce substantially R in the transient case, particularly for the large incident angles. However, the coupling has no effect on R in the steady case. The second considerable differences between R values in the two cases appear for the large incident angles. The differences become more obvious as $\Delta t / T$ approaches zero. In fact, R in the ideal transient-state case approaches zero with an order of magnitude of $(\Delta t / T)^{N+M}$ within the entire range $|\theta| \leq \pi / 2$, as shown by Eq.(29) with $\Delta t / T \to 0$; while R in the steady-state case is reduced to

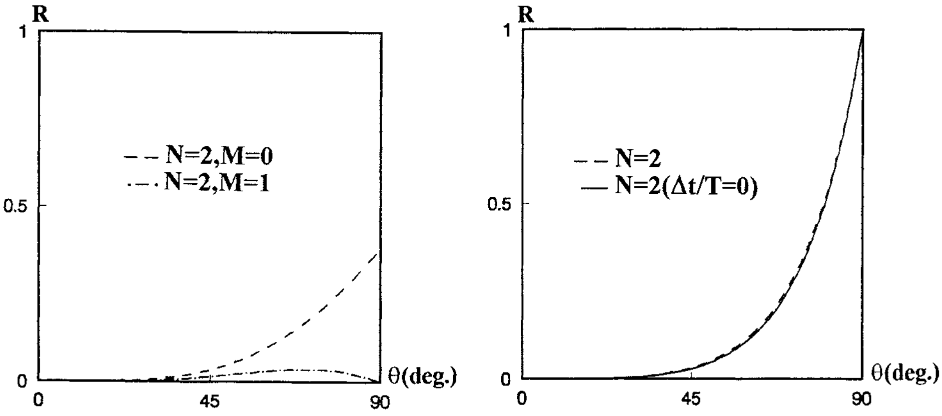

(a) Transient-state

(b) Steady-state

Fig.2 R in the transient- and steady-state cases for Eq.(27), c_a=c and Δt/T=0.1

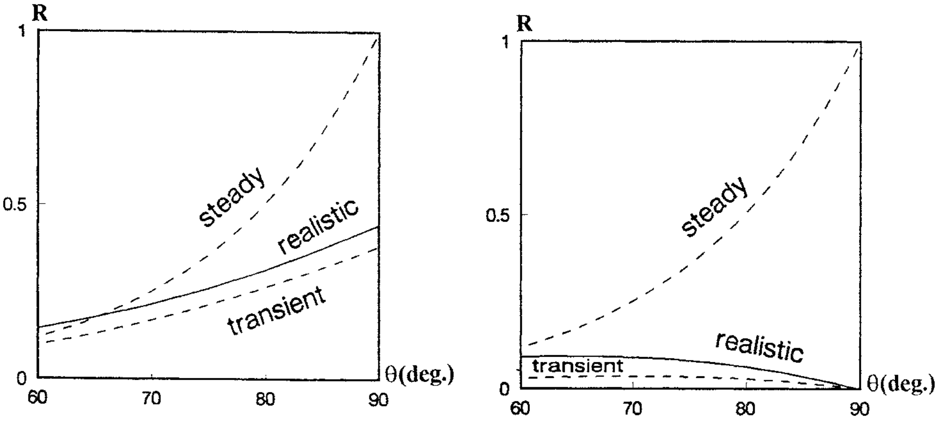

(a) Eq.(27),N=2,M=0

(b) Eq.(27),N=2,M=1

Fig.3 Comparison of R in the realistic case with R in the two extreme cases for Eq.(27), c_a=c and Δt/T=1/40

$$R = \left| \frac{c - c_a \cos\theta}{c + c_a \cos\theta} \right| \tag{31}$$

which means that R in this case would not be further reduced as $\Delta t / T \to 0$, as shown by the solid line in Fig.2(b). Since the differences of R values in the two extreme cases are significant, particularly, for the large angles of incidence, a question arises: which R would be more appropriate for describing the spurious reflection from the boundary in the step-by-step integration? To answer this question, a realistic reflection analysis has been performed by a numerical simulation of the reflection for incidence of a plane acoustic wave ([13] and [20]). The numerical simulation is summarized as follows. Consider a rectangular computational domain, a ABC is imposed on its one edge, whose center is the artificial boundary point under consideration, and the displacements of the other edges are assigned by the given incident wave. Having discretized the computational domain, the numerical simulation is started with t=0, at which the wavefront of the incident wave just arrives at the boundary point under consideration. Having assigned the initial values of the discrete grid in terms of the incident wave, the numerical simulation is performed by the step-by-step integration. If the computed displacement of the boundary point is denoted by $u(t,\theta)$, which is a function of time t and the angle θ of incidence, the total error of the computed displacement is

$$e(t,\theta) = f(t) - u(t,\theta) \tag{32}$$

where $f(t)$ is the displacement of the incident wave at the boundary point. Since all sorts of numerical errors except the one caused by the ABC have been carefully reduced to a negligible extent in the numerical simulation by using a sufficient large size of the computational domain, refining the grid, selecting the total computing time length and the time increment, $e(t, \theta)$ would represent the realistic spurious reflection from the artificial boundary. Substituting the Fourier amplitude spectra of $e(t, \theta)$ and the incidence wave into Eq.(28) leads to the realistic reflection coefficients needed. Fig.3 presents a comparison of R values in the realistic case with R values in the two extreme cases for Eq.(27), $c_a = c$ and $\Delta t/T$=0.025. The close relation between R values in the transient and realistic cases shown in Fig.3 speaks that R in the transient case does play a more important role than R in the steady case in governing accuracy of local ABCs in the numerical simulation performed by the step-by-step integration. The conclusion has been demonstrated by a number of numerical experiments, for example, Fig. 7 in [13]. This conclusion also greatly simplifies analysis of the spurious reflection, because the formulation of R in the transient case does not involve the reflection waves. Therefore, Eq.(29) is correct for all sorts of one-way waves of incidence though it was originally derived for the acoustic case.

4. Relationships between MTF and other local ABCs

Most local ABCs are derived from a particular set of partial differential equations, which govern the motion in the unbounded exterior. Therefore, their derivations are based on an particular assumption on the exterior model including the mechanical properties of the media and the motion mode under consideration. This methodology has led to a number of valuable results, as summarized in [1]. Since all the local ABCs are approximate one-way wave equations, some relationship between MTF and these local ABCs must exist. To clarify the relationship, the differential form of MTF is derived from Eq.(17) in the limit of Δt approaching to zero as following [2, 21],

$$\left(\frac{\partial}{\partial t}+c_a\frac{\partial}{\partial x}\right)^N u=0 \tag{33}$$

It can be shown that Eq.(15) with several artificial speeds reduces to the following equation as Δt approaches zero,

$$\left[\prod_{j=1}^{N}\left(\frac{\partial}{\partial t}+c_{aj}\frac{\partial}{\partial x}\right)\right]u=0 \tag{34}$$

Similarities and differences between MTF in the above differential forms and the other two major types of local ABCs, that is, the Clayton-Engquist's and Higdon's ABCs, are discussed as follows.

(1) MTF and Clayton-Engquist ABC

It has been shown that Eq.(33) is equivalent to the Clayton-Engquist ABC in the acoustic case if c_a is equal to the acoustic wave speed [22]. However, the artificial speed c_a in MTF can be adjusted so that perfect transmission may be achieved by MTF for a particular angle of incidence, as pointed out in [2, 21]. A more important difference between the two types of ABCs is in their ranges of applicability. The Clayton-Engquist ABCs in the acoustic case are derived from the paraxial rational expansion of the dispersion relation of the acoustic equation. The derivation of the ABCs cannot be directly extended to even the case of vector waves in homogeneous, isotropic and elastic media because the vector wave equations are not uniquely specified from their dispersion relations. In order to generalize the ABCs to the elastic case, a general form of the paraxial approximation must be additionally assumed using the hint provided in the acoustic case and the general form is then specified by matching it to the full elastic wave equations [15]. The ABCs thus derived for the elastic case are more complicated than that for the acoustic case. On the contrary, MTF applies without modification to all situations in which the one-way waves concerned can be expressed by Eq.(1) in principle, as mentioned earlier.

(2) MTF and Higdon ABC

Started with the finite difference approximation of the acoustic equation, Higdon presented a set of local ABCs [23]:

$$\left[\prod_{j=1}^{N}\left(\cos\theta_j\frac{\partial}{\partial t}+c\frac{\partial}{\partial x}\right)\right]u=0 \tag{35}$$

where $|\theta_j|<\pi/2, c$ is the acoustic speed. Since Eq.(35) is derived from the acoustic equation and using the notion of plane wave incidence, the acoustic speed **c** and the incident angle θ_j are inherent in Eq. (35). The relation between Eq.(34) and Eq.(35) is easily seen by substituting $c_{aj}=c/\cos\theta_j$ into Eq.(34). Eq.(35) has been then generalized to the elastic case with modification of the physical wave speed c in the equation [24-26]. It is interesting to note that the Higdon's generalization is much simpler than the Clayton-Engquist's. This may be explained by the close relation of the Higdon's theory with Eq.(34), which applies without modification to all cases where Eq.(1) valids in principle. In fact, using the artificial speed c_a instead of the physical speed c, Higdon's theory may be regarded as that the one-dimensional apparent wave propagation of the form $u=f(ct-x)$ satisfies the first-order differential relation

$$\left(\frac{\partial}{\partial t}+c_a\frac{\partial}{\partial x}\right)u=0 \tag{36}$$

if $c_a = c$, and Higdon's ABCs are then a combination of the first-order differential relations, which is identical to Eq.(34).

III Wave Motions in Discrete Grids

Having performed the spatial discretization, the inertial force term in the resulted ordinary differential dynamic equation of the interior nodes is proportional to the mass matrix. The conventional consistent mass matrix is not diagonal, which leads to not only increasing the cost of computation but also violating the causality of wave propagation with a finite speed. With the local characteristic of wave motion in mind, the author in the early 80s suggested using the lumped mass matrix instead of the consistent one for numerical simulation of wave motion in the computational region [27]. In order to justify the suggestion, wave motions in discrete grids with lumped-mass and consistent-mass matrices are studied and compared with those in the corresponding continuum. The studies are briefly summarized as follows.

1. One-dimensional wave motions in discrete grids

Elementary notions of wave motion in discrete grids may be clarified in a simple 1-D case. Consider the 1-D wave equation

$$\frac{\partial^2 u}{\partial t^2}=c_0^2\frac{\partial^2 u}{\partial x^2} \tag{37}$$

where the constant c_0 is the wave speed in the continuous model. It is well-known that harmonic waves with wave number ω / c_0 satisfy Eq.(37) for any frequency ω. If Eq.(37) is discretized in space by finite elements of space step Δx and in time by central finite differences of time step Δt, the equation of motion of the discrete model in the frequency domain is written

$$U_{j+1}+2bU_j+U_{j-1}=0 \tag{38}$$

where b is a function of ω, which is governed by $\Delta\tau = c_0\Delta t / \Delta x, \omega_N = \pi / \Delta t$ and the mass matrix being lumped or consistent [2]. Analysis of Eq.(38) yields that wave motions satisfying Eq.(38) are strongly frequency-dependent [28-29]:

(1) **Nyquist frequency and frequency aliasing** The time discretization leads to so-called Nyquist frequency ω_N, and wave motions in the discrete model at any frequency $\omega > \omega_N$ would appear at a frequency within the band $[0, \omega_N]$. This frequency aliasing implies that the discrete model cannot be used to simulate wave motions at $\omega (> \omega_N)$; and that if wave motions at $\omega > \omega_N$ are introduced (say, by dynamic loading or the round-off errors in the numerical simulation), they would not only reduce accuracy but also might cause numerical instabilities of the simulation, which will be discussed later.

(2) **Cut-off frequency and accuracy** The time and space discretizations lead to another characteristic frequency $\omega_u(<\omega_N)$, which is so-called the cut-off frequency. Wave motions are dispersive in $0 \le \omega \le \omega_u$ and reduced to the parasitic oscillation in $\omega_u \le \omega \le \omega_N$, which is non-traveling and concentrated in the neighborhood of the exciting source. Let the desired frequency upper limit be denoted by ω_c, wave motions in the desired band of $0 \le \omega < \omega_c$ may be simulated for an allowable error caused by the dispersion, if the grid is refined such that ω_u is properly larger than ω_c.

It is interesting to point out that the dispersive errors of the consistent mass model are not less than those of the corresponding lumped-mass one within the desired frequency band $\omega \le \omega_c$, and that the parasitic oscillations attenuate much faster for the lumped-mass model than the consistent-model.

(3) **Stability criteria** The stability criterion of the step-by-step numerical integration of the equations of motion may be set up in the frequency domain according to the dispersion equation. The criterion is that if the wave number is independent and real, the stability is guaranteed by the frequency in the dispersion equation being real. The stability criteria thus derived for the lumped- and consistent-mass models are as follows:

$$\left.\begin{array}{ll} c_0 \Delta t \le \Delta x & \textit{for lumped}-\textit{mass} \\ c_0 \Delta t \le \Delta x / \sqrt{3} & \textit{for consistent}-\textit{mass} \end{array}\right\} \tag{39}$$

The criterion for the consistent-mass is harsher than that for the lumped-mass in selecting the time step Δt.

2. Multi-dimensional wave motions in discrete grids

Wave motions in discrete grids have been analyzed for the anti-plane, in-plane and 3-dimensional cases using the approach similar to the 1-D case. For simplicity, the uniform square or cubic finite elements are used to discretize the interior medium which is homogeneous, isotropic, and linear elastic,. The results are as follows [30-32].

(1) **Stability criteria** It is like the 1-D case that the numerical stability criterion for the consistent-mass is harsher than that for the lumped-mass in the multi-D cases. For example, in the anti-plane case,

$$\left.\begin{array}{ll} c_s \Delta t \le \Delta x & \textit{for lumped}-\textit{mass}, \\ c_s \Delta t \le \Delta x / \sqrt{6} & \textit{for consistent}-\textit{mass}, \end{array}\right\} \tag{40}$$

where c_s is the S-wave speed, Δx is the size of the square finite elements; and in the in-plane case,

$$\left.\begin{array}{ll} c_p \Delta t \le \Delta x & \textit{for lumped}-\textit{mass}, \\ c_p \Delta t \le \left[3\left(1 + c_s^2 / c_p^2\right)\right]^{-1/2} \Delta x & \textit{for consistent}-\textit{mass}, \end{array}\right\} \tag{41}$$

where c_p is the P-wave speed.

(2) **Anisotropy and polarization drift** Besides the dispersion, the anisotropy and the polarization drift appear in wave motions in the multi-D discrete models. The anisotropy is shown by the direction-dependent dispersion curves in Fig.5.7 in [2] for the anti-plane case. Besides that the dispersion carves are

direction-dependent for the P-and SV-waves in the in-plane case, the polarization drift of the waves may appear. The drift is described by the deviation of the angle between the wave propagating direction and the particle vibrating direction in the discrete grid from that in the corresponding continuum. The drift shown in Fig.5.10 in [2] for the in-plane case reveals that the direction of the particle vibration in the discrete model is no longer parallel or perpendicular to the direction of wave propagation for the P- or SV- wave, respectively, at the higher frequencies. The polarization drift might also appear in the SH type of waves in the 3-D discrete model. All the above discretization effects are not desired in the numerical simulation and appear at high frequencies. They can be reduced to an allowable extent in the desired frequency band by appropriately refining the discrete grids. However, understanding them is important in choosing the proper discrete model parameters to guarantee accuracy and stability of the numerical simulation, because these effects are inherent in wave motions in the discrete models, which are the counterparts in the corresponding continuum.

(3) **Complexity of wave motions in multi-D discrete grids** The number of wave motion types in the discrete models is much larger than that in the corresponding continuum. To have a general picture of the complexity, let the frequency be independent and real. All types of wave motion in discrete models may be revealed by considering the wave numbers being complex, which satisfy the dispersion equation. There might be four types of wave motion in each characteristic direction for each dispersion equation, that is, the traveling wave, attenuated traveling wave, evanescent motion and parasitic oscillation. Having combined the motions in two characteristic directions, 16 types of motions might appear in the anti-plane case. Since there are two independent dispersion equations in the in-plane case, 32 types of motions might appear there, half of them are P-type and the other half are SV-type. In the 3-dimensional case, there are 3 independent dispersion equations for P-, SV- and SH-type of motions; 64 type of motion might appear for each dispersion equation and total number of the wave types reaches 3 × 64=192. Since most of the wave types never appear in the continua, they are not desired in the numerical simulation. Although they occur merely at the undesired high frequencies and may be eliminated by refining the discrete grids and considering the realistic damping effects, understanding them is again helpful for the accurate and stable implementation of the numerical simulation.

IV Stable Implementation of the Numerical Simulation

Since the discrete equations of motion for both the boundary nodes and the interior nodes are local and explicit, the step-by step numerical integration of the equations is simple and easy in programming. (Note that Eq.(27) samples the wave field at points which are not gemerally on the discrete grid, so an interpolation scheme might be needed in the implementation.) The numerical simulation has been used in analyses of soil-structure interaction and other near-field wave motion problems in complicated situations including the infinite exterior medinum being layered, anisotropic and elastic[33-36]. The common problem encountered in the implementation is the instability of the numerical integration. Studies on the problem have yielded some semi-empirical schemes, which lead to stable implementation without effects on the accuracy desired. Such schemes include the smoothing technique [37, 2], the boundary damping layer [2], the special interpolation schemes [38, 2]. Although the stability problem seems not serious from a practical point of view, it is worthy to be further studied for the numerical simulation to be based on a solid theoretical basis. Among the studies carried out so far [1], the following is our preliminary ones.

1. Mechanism of the instability

Consider the longitudinal wave propagation in a semi-infinite uniform elastic rod, excited by a given vibration at the end of the rod. The wave is simulated by the decoupling numerical approach suggested in the present paper. The instability phenomenon encountered in the simulation is shown in Fig.4. It can be seen that the instability is of the form of oscillation at frequencies higher than the desired but less than the cut-off frequency ω_u, and that it does not always occur (Fig.4(b)). In order to understand the phenomena, the exact solution of the discrete model has been derived in the frequency domain. It is found that the necessary and sufficient condition for the exact solution being finite is

$$|R| < 1, \quad \omega < \omega_u \tag{42}$$

where R is the reflection coefficient in the steady state. Fig.5 shows the relation of $|R|^{1/N}$ versus ω for $\omega \le \omega_u$. This figure plus the stability condition (42) provide a full explanation of major features of the stability phenomena. First, the stability criterion derived from the condition (42) for the simple 1-D model is

$$\Delta\tau\, c_a / c_0 < 1.5 \tag{43}$$

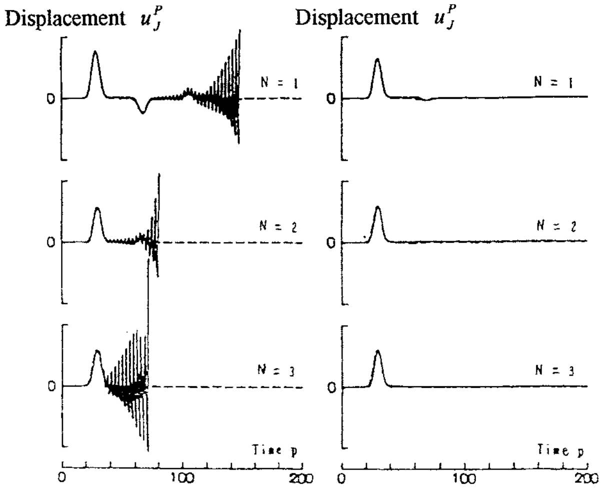

a. $c_a / c_0 = 2.0$ *b.* $c_a / c_0 = 1.2$

Figure 4. Numerical solutions of the motion at the artificial boundary node ($J = 20$, $\Delta\tau = 1$)

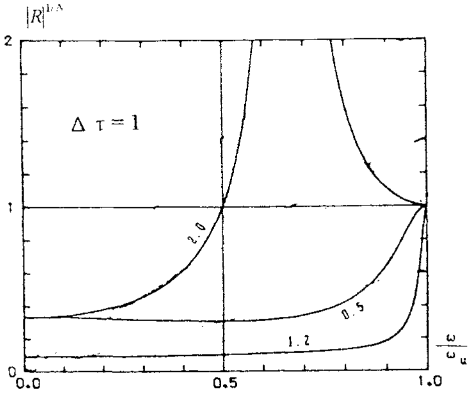

$\alpha = 0.5, 1.2, 2.0$

Figure 5. The reflection factor for the one-dimensional model: in the steady case

The criterion (43) explains why does the instability occur in Fig.4(a) but not in Fig.4(b). This is because $\Delta\tau = 1, c_a / c_0 = 2.0$ and $\Delta\tau = 1, c_a / c_0 = 1.2$ for 4(a) and Fig.4(b), respectively; the former does not satisfy (43), but the later does. Second, the frequences at which the unstable oscillation takes place in Fig.4(a) are within the range of $0.5\omega_n < \omega < \omega_u$, as counted from the time domain numerical results, which coincide with those frequencies at which $|R| > 1$, as shown by the curve of $\alpha = c_a / c_0 = 2.0$ in Fig.5. In conclusion, the instability comes from the multi-reflection of the traveling waves at the undesired high frequencies and their multi-amplification ($|R| > 1$) at the artificial boundary point. Therefore, the stable implementation may be guaranteed by eliminating the motion at the undesired high frequencies. This thought has led to some stable implementation schemes, as mentioned earlier.

2. Approximate stability criteria

The above study in the frequency domain for the 1-D model is helpful for understanding the mechanism of instability. However, it is questionable whether the condition of stability (42) for the 1-D case is still valid for the multi-D cases becuase of the coupling effcts of several intersected artificial boundaries. Further more, the stability criterion derived from Fourier analysis in the frequency domain cannot fully explain all the instability phenomena in the time domain, for example, the drift instability, which is caused by accumulation and propagation of the round-off error in the step-by-step integration. These considerations have led to searching for an approach in the time domain. As for the explicit step-by-step integration of a system of linear equations concerned here, the equations of all boundary and interior nodes may be written

$$\mathbf{Y}^{p+1} = \mathbf{A}\mathbf{Y}^{p} \tag{44}$$

where the vector $\mathbf{Y}^p$ stands for displacements and velocities of all nodes at the time station $t = p\Delta t$ and the previous time stations, **A** is a square matrix, whose elements are determined by the coefficients of the equations. Following the approach developed in structure dynamics [39], the stability condition may be written

$$\rho(\mathbf{A}) < 1 \tag{45}$$

where $\rho(\mathbf{A})$ is the spectral radius of **A**, that is , the maximum modulus of eigenvalues of **A**. The inequality (45) may be used to judge the stability for any particular discrete model numerically. However, it is difficult to derive the stability criterion from the condition directly for a class of discrete models. In order to cope with this difficulty, the following approximate approach has been proposed [2,40]. A local discrete system is first taken from a class of discrete models under consideration. The local system, which is composed of a few nodes on an artificial boundary and their adjacent interior nodes of the original discrete models, is then decoupled by imposing the fixed or free boundary condition on its all boundaries accept the artificial one to prevent waves going out of the boundaries. The approximate criterion of stability for the original discrete models may be then determined numerically using the matrix **A** of the local system according to the inequalily (45). To illustrate this approach, the above mentioned 1-D model is considered again. Since the elements of **A** are determined by $\Delta\tau = \Delta t c_0 / \Delta x, \alpha = c_a / c_0$ and the total number J of nodes of the local system, the values of $\rho(\mathbf{A})$ are also governed by the parameters. Define a critical value α_0 for given values of $\Delta\tau$ and J such that $\rho(\mathbf{A})<1$ for $\alpha < \alpha_0$ and $\rho(\mathbf{A})>1$ for $\alpha > \alpha_0$. A few values of α_0 thus computed are listed in Table 1, the last row in the Table is for comparison, the numbers in the row are computed from Eq.(43), which is derived from the exact solution in the frequency domain.

Table 1 the critical value α_0 for the 1-D discrete model

J \ $\Delta\tau$	0.5	0.6	0.7	0.8	0.9	1.0
10	3.025	2.521	2.161	1.891	1.681	1.513
20	3.006	2.505	2.147	1.879	1.670	1.503
Eq. (43)	3.000	2.500	2.143	1.875	1.667	1.500

In conclusion, the author feels justified in saying that the decoupling numerical simulation of wave motion is one of the most practical and promising approaches proposed so far for solving problems in the fields of the soil-structure dynamic interaction and the near-field wave motion, and worthy to be further studied.

References

[1] *Liao ZP, Numerical simulation of near-field wave motion, Advances in Mechanics,* **27**(2), 193-216, 1997(in Chinese).

[2] *Liao ZP, An Introduction to Wave Motion Theories in Engineering, Beiging, China,Academic press,*165-322, 1996 (in Chinese).

[3] *Wolf J. P., Dynamic Soil-Structure Interaction, Prentice-Hall, Englewood Cliffs, N J*, 1985.

[4] *Wolf J. P., Soil-Structure-Interaction Analysis in Time Domain, Prentice-Hall, Englewood Cliffs, N J,* 1988.

[5] *Wolf J. P., and Song Ch, Finite-Element Modeling of Unbounded Media, John Wiley & Sons Ltd,* 1996.

[6] *Wolf J. P., Foundation Vibration Analysis Using Simple Physical Models, Prentice-Hall,*1994.

[7] *D. Givoli, Review article: Non-reflecting boundary conditions, J. Comput.* **94,** 1-29 (1991).

[8] *Frankel A. A review of numerical experiments on seismic wave scattering. PAGEOPH,* **131**:639-685, 1989.

[9] *Lu Ting and M. J. Miksis, Exact boundary conditions for scattering problems, J. Acoust. Soc. Amer.* **80**, 1825-1827, 1986.

[10] *Liao ZP, A finite model for problems of transient scalar waves in an infinite domain (in Chinese), Earthq. Eng. Eng. Vib.* **2**(1), 38-53, 1982.

[11] *Liao ZP, H. L. Wong, B. P. Yang and Y. F. Yuan, A transmitting boundary for transient wave analyses, Scienta Sinica (Series A),***27,** 1063-1076, 1984.

[12] *Liao ZP and H. L. Wong, A transmitting boundary for the numerical simulation of elastic wave propagation, Soil Dyn, Earthq. Eng.* **3,** 174-183, 1984.

[13] *Liao Z P, Extrapolation Non-reflecting Boundary Conditions. Wave Motion, 1996,* **24,** 117-138,.

[14] *Liao Z P, Normal transmitting boundary conditions, Scientia Sinica (Series E)* **39**(3), 244-254,1996.

[15] *R. Clayton and B. Engquist, Absorbing boundary conditions for acoustic and elastic wave equations, Bull. Seism. Soc. Am.* **76**, 1529-1540, 1977.

[16] *R. Clayton and B. Engquist, Absorbing boundary conditions for wave-equation migration, Geophysics* **45,** 895-904, 1980.

[17] *B. Engquist and A. Majda, Absorbing boundary conditions for the numerical simulation of waves, Math. Comput.* **31**, 629-652, 1979.

[18] *B. Engquist and A. Majda, Radiation boundary conditions for acoustic and elastic calculations, Comm. Pure Appl. Math,.* **32**, 313-336, 1979.

[19] *L. Halpern and L. N. Trefethen, Wide-angle one-way wave equations, J. Acoust. Soc. Amer.* **84,** 1397-1404, 1988.

[20] *Jing LP and Liao ZP, A Study on realistic reflection coefficients of transmitting boundaries, Earthq. Eng. Eng. Vib.,* **17**(2): 21-26, 1977.(in Chinese)

[21] *N. Cheng and C. H. Cheng, Relationship between Liao and Clayton-Engquist absorbing boundary conditions: Acoustic case, Bull. Seisml. Soc. Amer.* **85**,954-956,1995.

[22] *E. Kausel, Local transmitting boundaries, J. Eng. Mech. Div. ASCE* **114,** 1011-1027, 1988.

[23] *R. L. Higdon, Absorbing boundary conditions for difference approximations to the multi-dimensional wave equation, Math. Comput.* **47** 437-459, 1986.

[24] *R. L. Higdon, Numerical absorbing boundary conditions for the wave equation, Math. Comput.* **49,** 65-90, 1987.

[25] *R. L. Higdon, Absorbing boundary conditions for elastic waves, Geophysics* **56**(2), 231-241, 1991.

[26] *R. L. Higdon, Absorbing boundary conditions for acoustic and elastic waves in stratified media, J. Comput. Phys.* **101,** 386-418, 1992.

[27] *Liao ZP, A finite element method for near-field problems of wave motions in heterogeneous materials Eqrth. Eng. Eng. Vib.* **4**(2), 1-14, 1984. *(in Chinese)*

[28] *Liao ZP and Liu JP , Elastic wave motions in discrete grids (1), Earthq. Eng. Eng. Vib.,* **6**(2), 1-14, 1986(in Chinese).

[29] *Liu JP and Liao ZP, Elastic wave motions in discrete grids (II, III), Earthq. Eng. Eng. Vib., II:* **9** (2), 1-11, 1989; III: **10**(2), 1-11, 1990. (in Chinese)

[30] *Liu JP and Liao ZP, Anti-plane wave motion in finite element discrete model, Acta Mechanica, Sinica,* **24**(2), 207-216, 1992 (in Chinese)

[31] *Liu JP and Liao ZP, In-plane wave motion in finite element discrete model, Acta Mechanica Sinica,* **8**(1), 80-91, 1992.

[32] *Guan HM and Liao ZP, Elastic waves in 3-d discrete grids, Acta Mechanica Solida, Sinica,* **8**(4), 283-293, 1995.

[33] *Liao ZP, Seismic Microzonation, Seismological Press, Beijing, China, 1990 (in Chinese)* .

[34] *Shao XM, Lan ZL, Absorbing boundary conditions for anisotropic elastic wave equations, Acta Geophysica Sinica,* **38**(Supplement I), 56-73, 1996.

[35] *Chen HJ, et al., 3-d dynamic analysis and aseismic measures of an arch dam system, Report No. 85-208 -01-01-36, China Institute of Water Resource and Hydropower Research,* Beijing, 1995.

[36] *Yuan YF, Yang BP and S. Huang, "Damage distribution and estimation of ground motion in Shidian basin", Proc. Int. Symp. on the Effects of Surface Geology on Seismic Motion* (Odawara, Japan) 281-286, 1992.

[37] *Liao ZP and J. B. Liu, "Numerical instabilities of a local transmitting boundary", Earthq. Eng. Struct. Dyn.* **21**, 65-77 (1992).

[38] *Shao XM, Lan ZL, Numerical simulation of the seismic wave propagation in inhomogeneous isotropic media, Acta Geophysica Sinica,* **38**(Supplement 1), 55-72, 1996 (in Chinese)

[39] *T. J. R. Hughes, Analysis of transient algorithms with particular reference to stability behavior, Computational Methods for Transient Analysis, Edited by T. Belytschko and T. J. R. Hughes, Elsevier Science Publishers B. V., 67-155, 1983.*

[40] *Guan HM, Liao ZP, A method for the stability analysis of local artificial boundaries, Acta Mechanica Sinica,* **28**(3), 376-380, 1996.

SCATTERING OF PLANE SH WAVES BY CYLINDRICAL SURFACE TOPOGRAPHY OF CIRCULAR–ARC CROSS–SECTION

Yuan Xiaoming and Liao Zhenpeng
(Institute of Engineering Mechanics,SSB,9 Xuefu Road,Harbin 150080,China)
Xu Shumei
(Harbin Normal University,Harbin 150080,China)

Abstract

The main points in formulating the closed–form solutions of two–dimensional scattering of plane SH waves by cylindrical suface topography of hill and canyon with circular–arc cross–section in a half–space are presented. The solutions are reduced to solving a set of infinite linear algebraic equations using the auxiliary functions and the exterior region form of Graf's addition theorem. The effects of the height(depth)–to–width ratio of the surface topography on surface ground motion are finally illustrated.

Introduction

Field investigation and strong motion records have shown that the local suface topography might play an important role in interpretation of wave propagation phenomena and earthquake damages. Although numerical methods[1–4]are a powerful tool for studying scattering of elastic waves by suface topography of arbitrary shape, the analytical solutions for comparatively simple cases are still valuable for checking accuracies of approximate solutions and providing insight into the physical nature of the problem. However, the exact solutions available so far for the problem under consideration are very limited[5–9]. The two–dimensional scattering of plane SH waves by cylindrical suface topography of circular–arc cross–section in a half–space is studied using the wave functions expansion method in this paper. Two difficulties in formulating the closed–form solution of the problem are solved by using the exterior region form of Graf's addition theorem[8]and the auxiliary functions method[9]. The solution presented here will be separately reduced to the known one[9,5]when the hill and canyon have a semi–circular cross–section.

Formulation

The cross–section of two–dimensional model to be analyzed is shown in Fig.1. It represents an elastic, isotropic and homogeneous half–space with circular–arc topography of a cylinder of radius a. In the Figure, (a) and (b) stand for hill and canyon topography respectively. The shape of the topography is characterized by the ratio of height(depth)–to–half–width, d/L, as shown in Fig.1. Two rectangular coordinate systems and the two corresponding polar systems employed in the paper are shown in Figs.2 and 3 for the hill and canyon, separately.u_0, λ, β and α are amplitude, wavelength, wavenumber and incident angle of the incident plane SH wave, respectively.

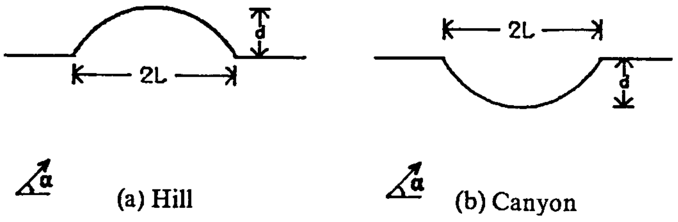

(a) Hill (b) Canyon

Fig.1 The half–space with circular–arc hill and canyon topography

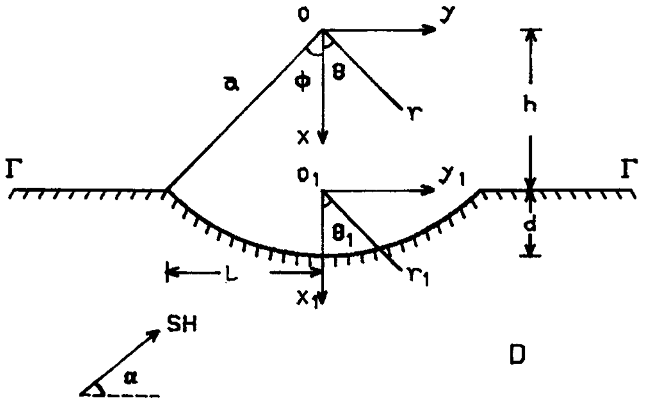

Fig.2 Coordinate systems for canyon model

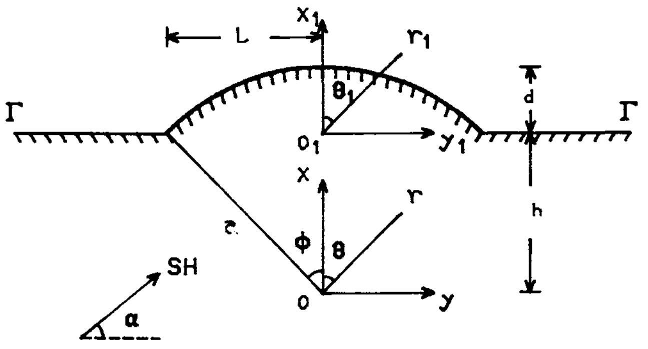

Fig.3 Coordinate systems for hill model

The general solution of the scattering displacements satisfying the wave equation and the boundary condition on the flat surface for the above two models can be written in the coordinate (x_1, y_1)

$$u^{(d)}(r_1,\ \theta_1)=u_0\sum_{n=0}^{\infty}H_n^{(1)}(\beta r_1)(\delta_n^{(1)}A_n cosn\theta_1+\delta_n^{(2)}B_n sinn\theta_1) \tag{1}$$

where A_n, B_n are constants to be determined and $H_n^{(1)}(\cdot)$ are the Hankel functions of the first kind with order n and

$$\delta_n^{(1)} = 1 + (-1)^n \quad , \quad \delta_n^{(2)} = 1 - (-1)^n \tag{2}$$

For the circular–arc canyon model, Cao and Lee[10]recently studied the same scattering problem as one in this paper.They appoximated the flat surface of the half–space close to the canyon by the surface of a circle of large radius.However, the value of the radius can not too be large because accuracies of numerical results available for Bessel functions are limited. This would result in an ad hoc choice of the radius and prevent a strict test on its accuracies for cases where the canyon does not have a semi–circular section. Therefore, their solution is appoximate. The key in the formulation of the exact solution in our paper is to present a transform formula of Hankel functions from coordinates (r_1, θ_1) into (r, θ) in the region D (Fig.2).As shown in Fig.4 and Fig.5, the circle with radius h divided x–y plane into the 'interior region' Ω and the 'exterior region' R.The transform formula quoted in Cao and Lee′paper is suitable for the interior region Ω but not for region D.The transform for the Hankel functions of integer n is written according to the Graf′s addition theorem

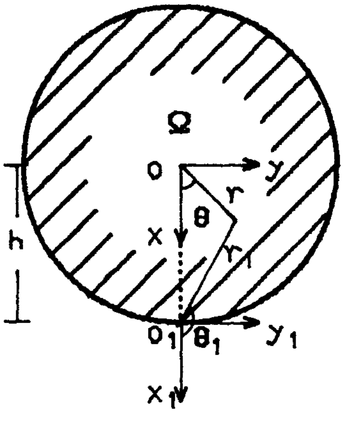

Fig.4 interior region Ω for the transform formula

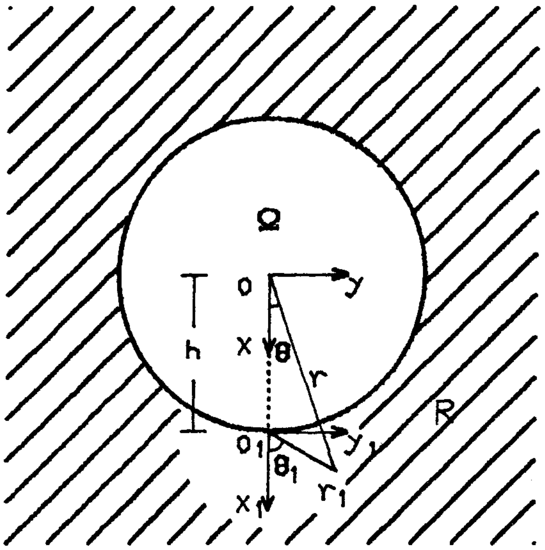

Fig.5 exterior region R for the transform formula

$$H_n^{(1)}(U)\left\{\begin{matrix}\cos n\psi\\ \sin n\psi\end{matrix}\right\} = \sum_{m=-\infty}^{\infty} H_{n+m}^{(1)}(V)J_m(W)\left\{\begin{matrix}\cos m\chi\\ \sin m\chi\end{matrix}\right\} \quad for|W|<|V| \tag{4}$$

where U, V, W, ψ and χ are real values of variables, and angle ψ is defined by the equations

$$V - W\cos\psi = U\cos\chi \tag{5}$$

$$W\sin\psi = U\sin\chi \tag{6}$$

To preform the transform in the region R, the variables in (4) can be replaced by

$$U = \beta r_1, \quad \psi = \theta_1 - \theta, \quad V = \beta r, \quad W = \beta h, \quad \chi = \theta \tag{7}$$

Using the relationships of the coordinate systems in Fig.2, equations (5) and (6) are satisfied.Inserting (7) into (4) results in

$$H_n^{(1)}(\beta r_1)\left\{\begin{matrix} \cos n\theta_1 \\ \sin n\theta_1 \end{matrix}\right\} = (-1)^n \sum_{m=0}^{\infty} H_m^{(1)}(\beta r)\frac{\varepsilon_m}{2}\left\{\begin{matrix} [J_{m+n}(\beta h) + (-1)^n J_{m-n}(\beta h)]\cos m\theta \\ -[J_{m+n}(\beta h) - (-1)^n J_{m-n}(\beta h)]\sin m\theta \end{matrix}\right\} \quad (r,\ \theta)\in R \tag{8}$$

Formula (8) are suitable for the exterior region R.Noting that the region R encloses the region D and substituting (8) into (1) leads to

$$u^{(d)}(r,\ \theta) = u_0 \sum_{m=0}^{\infty}\sum_{n=0}^{\infty} H_m^{(1)}(\beta r)[\delta_n^{(1)} A_n P_{m,\ n} \cos m\theta + \delta_n^{(2)} B_n Q_{m,\ n} \sin m\theta] \tag{9}$$

where

$$P_{m,\ l} = \frac{\varepsilon_m}{2}[J_{m+l}(\beta h) + (-1)^l J_{m-l}(\beta h)] \tag{10}$$

$$Q_{m,\ l} = \frac{\varepsilon_m}{2}[J_{m+l}(\beta h) - (-1)^l J_{m-l}(\beta h)] \tag{11}$$

For the circular–arc hill model, to avoid the singularity of the Hankel functions near the point o$_1$(Fig.3), the half–space can be divided into the two parts as shown in Fig.6.In the circle region, the following mixed boundary–value problem should be solved

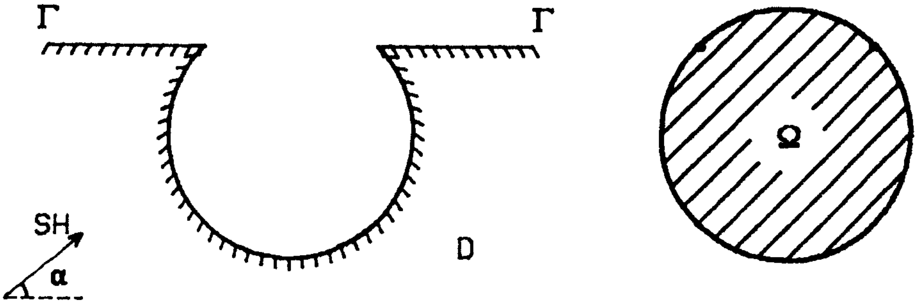

Fig.6 Division of the half–space for hill topography

$$\sigma_{rz}(a,\ \theta) = 0 \qquad -\varphi \leqslant \theta \leqslant \varphi \tag{12}$$

$$\sigma_{rz}(a,\ \theta) = \bar{\sigma}_{rz} \qquad \theta = others \tag{13}$$

$$u(a,\ \theta) = \bar{u} \qquad \theta = others \tag{14}$$

where equation (12) represents traction–free boundary condition on the hill topography and equations (13) and (14) represent the continiuty boundary conditions between the two regions. To solve the mixed boundary–value problem, we use the auxiliary functions, which are defined separately by

$$\Phi(\theta) = \begin{cases} \sigma_{rz}(a,\ \theta) & -\varphi + 2k\pi \leqslant \theta \leqslant \varphi + 2k\pi \\ \sigma_{rz}(a,\ \theta) - \bar{\sigma}_{rz} & \theta = others \end{cases} \qquad k = 0, \pm 1, \pm 2, \cdots \tag{15}$$

$$\Psi(\theta) = \begin{cases} 0 & -\varphi + 2k\pi \leqslant \theta \leqslant \varphi + 2k\pi \\ u(a,\ \theta) - \bar{u} & \theta = others \end{cases} \qquad k = 0, \pm 1, \pm 2, \cdots \tag{16}$$

then

$$\Phi(\theta)=0 \qquad -\pi \leqslant \theta \leqslant \pi \tag{17}$$

which is equivalent to satisfaction of the boundary condition (12) and the continuity condition (13), and

$$\Psi(\theta)=0 \qquad -\pi \leqslant \theta \leqslant \pi \tag{18}$$

which is equivalent to satisfaction of the continuity condition (14). Making $\Phi(\theta)$ and $\Psi(\theta)$ Fourier series expansions in $[-\pi, \pi]$ and letting the expansion coefficients equal zero, the boundary condition (12) as well as the continuity conditions (13) and (14) will all be satisfied.

For the circular–arc hill and canyon models, the constants A_n and B_n both can be determined by satisfying the corresponding boundary conditions and then the following infinite algebraic equations are yielded

$$\sum_{n=0}^{\infty} a_{mn} A_n = E_m \tag{19}$$

$$\sum_{n=0}^{\infty} b_{mn} B_n = F_m \tag{20}$$

$$m = 0,1,2,\cdots$$

where $E_m$and $F_m$are the known coefficients related with the incident waves.

Numerical Results

1.Accuracies of the solutions

Since the equation of wave motion and the boundary condition on the flat free surface are strictly satisfied, convergence of the numerical solutions to the exact ones will be checked using the boundary condition and the interface conditions with the increasing of the truncation order.The results shown in our research indicate that the maximum stress residual may be reduced to a sufficient small number if an appropriate truncation order n is adopted.The results also show that if the maximum stress and displacement residuals are limited within 5%the accuracies of the displacements can be guaranteed in the frequency range $0 \leqslant \eta \leqslant 3$, where

$$\eta = \frac{2L}{\lambda} = \frac{\beta L}{\pi} \tag{22}$$

2.Comparison with Cao and Lee′s results

The dimensionless displacements along the free surface are defined by

$$u_d = \{[Re(u)]^2 + [Im(u)]^2\}^{\frac{1}{2}} / u_0 \tag{23}$$

where Re(u) and Im(u) are the real and imaginary parts of the complex variable u, the total displacements.

The dimensionless displacements on the free surface are shown in Figs 7 and 8, where the solid and the dot lines represent the results obtained by the authors and Cao and Lee in reference 10, respectively.Fig.7 shows the numerical results for d / L = 0.5, $\eta = 2$ and incident angles $\alpha = 90°$ .Fig.8 shows the same results but for d / b = 0.25. In using the Cao and Lee′s method, the ratio of the radius of the big circle to the radius of the canyon is assumed to be 50, and in this case we found that the results obtained here are in agreement with the results in Fig.7 and Fig.10 in Cao and Lee′s paper.The comparison between the solid and dot lines shows that Cao and Lee′s results agree with ours quit well in the general trend, especially for the re–

sponse of the surface of the canyon. However, differences between the two methods appear in responses of the free surface away from the canyon, and become considerable as d / L is small. For example, as shown in Fig.8, the dimensionless displacement on y / L = 3.1 is 14% bigger than ours. Besides, less terms of the series are required for the convergence of the solution by ours method than by Cao and Lee's method. For example, for d / L = 0.5 and $\eta = 2$ the minimum number of the terms of the series is equal to 14 for our solution and equal to 20 for their solution. The above differences are come from the big circle assumption made by Cao and Lee to approximate the infinite half–space, which result in the multiple reflections of the waves inside the big circle, and therefore, stronger vibration phenomena appear in their results. Meanwhile, the reflections between the canyon and the big circle may result in more energy concentrated near the canyon and bigger displacements appear in some observation points of the ground surface.

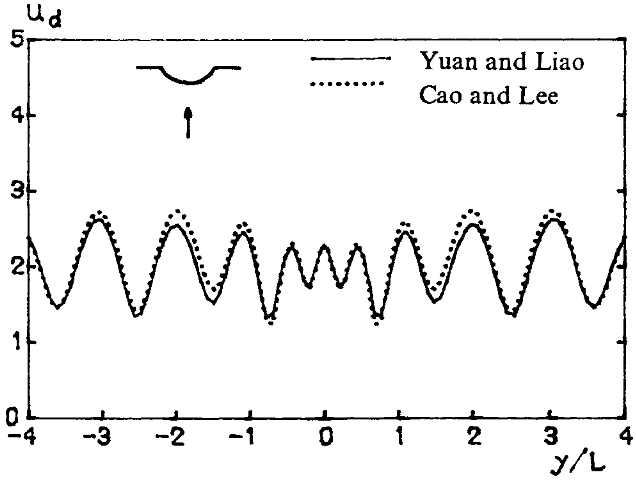

Fig.7 Comparison between authors' method and Cao and Lee's for canyon of d / L = 0.5

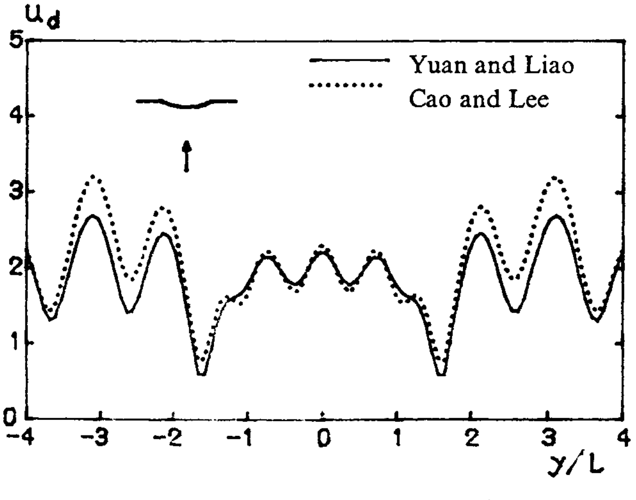

Fig.8 Comparison between authors' method and Cao and Lee's for canyon of d / L = 0.25

3.Surface ground motion near the topography

To exhibit the effects of the canyon and hill on surface ground motion, the displacements

u_d for some typical cases are shown in Fig.9 to Fig.12 for $d / L = 1$. From the Figures, it can be seen that the canyon mainly play a barrier role in the effects on surface motion, which develops a shadow zone behind the canyon and nearly sdanding wave motion in front of the canyon for acute and grazing incident waves. By camparion with canyon, the hill acts as receiver, which can get more energy from the incidence for vertical incident waves and then produce considerable amplification of surface motion.

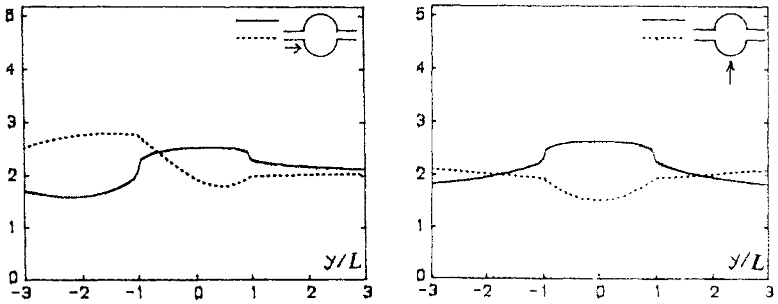

(a) Grazing incidence (b) Vertical incidence

Fig.9 Surface displacements of hill and canyon for $\eta = 0.15$

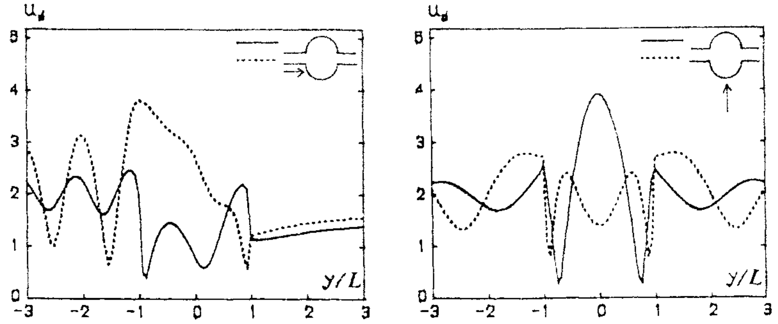

(a) Grazing incidence (b) Vertical incidence

Fig.10 Surface displacements of hill and canyon for $\eta = 1$

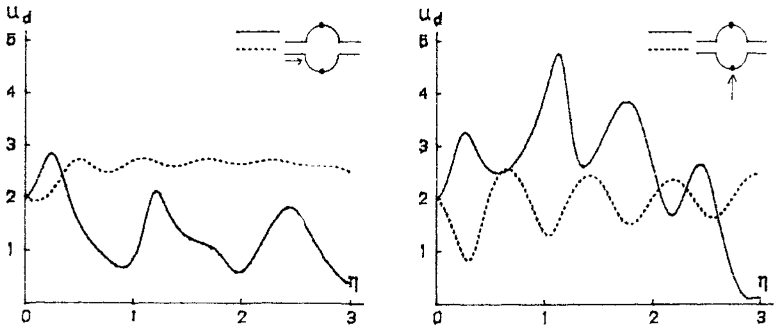

(a) Grazing incidence (b) Vertical incidence

Fig.11 Spectral amplification at hill top and canyon bottom

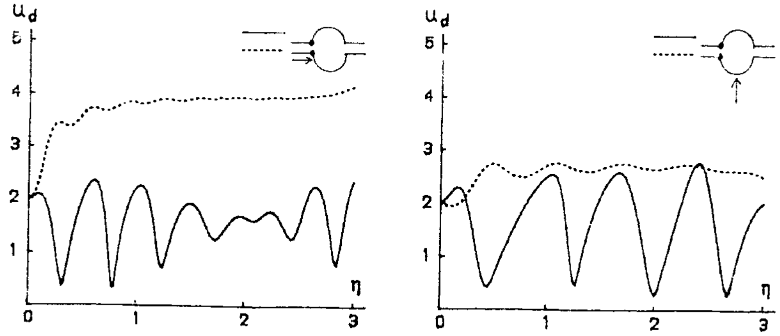

(a) Grazing incidence (b) Vertical incidence

Fig.12 Spectral amplification at hill and canyon rims

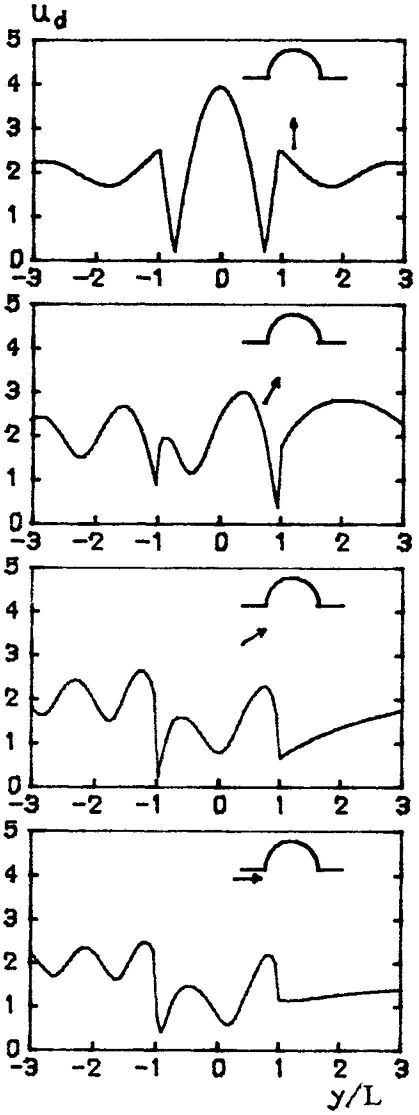

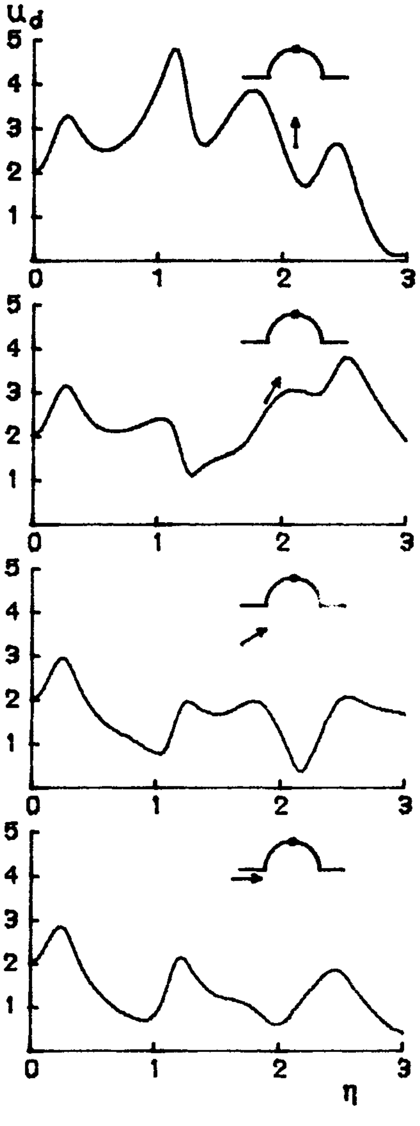

Fig.13 Displacements of hill versus y / L for $\eta = 1$ and d / L = 1 Fig.14 Spectral amplification of hill for d / L = 1

For checking accuracies of various numerical methods, Figs. 13 and 14 show the displacement u_d for $d/L=1$ and $\alpha=0°, 30°, 60°$ and $90°$. The displacement u_d versus y/L for $\eta=1$ is shown in Figure 13 and the displacement u_d versus η at top of the hill ($y/L=0$) is demonstrated in Figure 14. The corresponding numerical results of the Figs.13 and 14 are listed in Tables 1 and 2, separately. It can be seen that the effects of the hill on ground motion of the hill and its neighborhood are quite complicated. For example, the maximum u_d does not always occur at top of hill and does not always appear for vertical incidence of SH waves. The complicated effects depend strongly on the angle and the frequency of the incidence.

Table 1 Numerical results for Fig.13

y/L	$\alpha=0°$	$\alpha=30°$	$\alpha=60°$	$\alpha=90°$
−3.00	2.231	1.852	2.367	2.210
−2.50	1.775	2.162	1.927	2.138
−2.00	2.268	1.985	1.817	1.747
−1.90	2.088	1.710	2.082	1.702
−1.80	1.855	1.521	2.336	1.689
−1.70	1.657	1.535	2.536	1.711
−1.60	1.612	1.765	2.648	1.768
−1.50	1.762	2.095	2.650	1.855
−1.40	2.029	2.403	2.531	1.964
−1.30	2.292	2.604	2.280	2.086
−1.20	2.454	2.635	1.896	2.215
−1.10	2.443	2.451	1.379	2.349
−1.00	1.950	1.674	0.608	2.575
−0.90	0.386	0.666	1.946	1.826
−0.80	0.773	1.226	1.922	0.708
−0.70	1.136	1.511	1.699	0.376
−0.60	1.355	1.587	1.364	1.287
−0.50	1.452	1.551	1.165	2.089
−0.40	1.448	1.440	1.177	2.739
−0.30	1.361	1.262	1.359	3.243
−0.20	1.211	1.047	1.673	3.612
−0.10	1.019	0.859	2.046	3.843
+0.00	0.804	0.771	2.384	3.922
+0.10	0.614	0.829	2.644	3.843
+0.20	0.573	1.029	2.835	3.612
+0.30	0.752	1.322	2.969	3.243
+0.40	1.042	1.635	3.013	2.739
+0.50	1.358	1.911	2.914	2.089
+0.60	1.674	2.123	2.651	1.287
+0.70	1.963	2.267	2.251	0.376
+0.80	2.156	2.288	1.665	0.708
+0.90	2.168	2.038	0.750	1.826
+1.00	1.155	0.629	1.708	2.575
+1.10	1.127	0.721	1.957	2.349
+1.20	1.128	0.815	2.162	2.215
+1.30	1.141	0.902	2.328	2.086
+1.40	1.159	0.981	2.463	1.964
+1.50	1.178	1.052	2.573	1.855
+1.60	1.198	1.118	2.661	1.768
+1.70	1.217	1.179	2.728	1.711
+1.80	1.235	1.237	2.779	1.689
+1.90	1.253	1.290	2.811	1.702
+2.00	1.269	1.341	2.826	1.747
+2.50	1.339	1.562	2.691	2.138
+3.00	1.393	1.744	2.282	2.210

Table 2 Numerical results for Fig.14

η	$\alpha=0°$	$\alpha=30°$	$\alpha=60°$	$\alpha=90°$
0.01	2.005	2.005	2.005	2.005
0.06	2.110	2.114	2.121	2.124
0.11	2.310	2.323	2.350	2.364
0.16	2.566	2.598	2.663	2.696
0.21	2.792	2.854	2.981	3.045
0.26	2.846	2.945	3.150	3.255
0.31	2.658	2.794	3.076	3.224
0.36	2.333	2.497	2.846	3.030
0.41	2.000	2.188	2.594	2.813
0.46	1.719	1.928	2.389	2.643
0.51	1.494	1.723	2.244	2.536
0.56	1.315	1.565	2.151	2.490
0.61	1.171	1.441	2.102	2.496
0.66	1.050	1.341	2.087	2.547
0.71	0.946	1.255	2.099	2.637
0.76	0.855	1.175	2.130	2.765
0.81	0.775	1.097	2.175	2.927
0.86	0.712	1.014	2.229	3.124
0.91	0.680	0.925	2.286	3.360
0.96	0.711	0.841	2.350	3.646
1.01	0.826	0.764	2.388	3.968
1.06	1.070	0.782	2.392	4.340
1.11	1.454	1.011	2.299	4.689
1.16	1.894	1.446	1.993	4.760
1.21	2.134	1.834	1.479	4.232
1.26	2.050	1.952	1.138	3.392
1.31	1.827	1.893	1.145	2.818
1.36	1.617	1.795	1.264	2.617
1.41	1.456	1.716	1.370	2.648
1.46	1.340	1.669	1.445	2.788
1.50	1.260	1.657	1.500	2.977
1.60	1.166	1.730	1.602	3.405
1.70	1.094	1.881	1.808	3.776
1.80	0.950	1.954	2.210	3.826
1.90	0.711	1.747	2.659	3.374
2.00	0.595	1.270	2.957	2.620
2.10	0.813	0.652	3.054	1.914
2.20	1.188	0.407	2.980	1.697
2.30	1.544	1.043	2.959	2.149
2.40	1.803	1.668	3.323	2.619
2.50	1.805	2.036	3.770	2.456
2.60	1.481	2.030	3.640	1.640
2.70	1.093	1.889	3.147	0.830
2.80	0.783	1.785	2.662	0.311
2.90	0.546	1.727	2.260	0.103
3.00	0.413	1.667	1.895	0.140

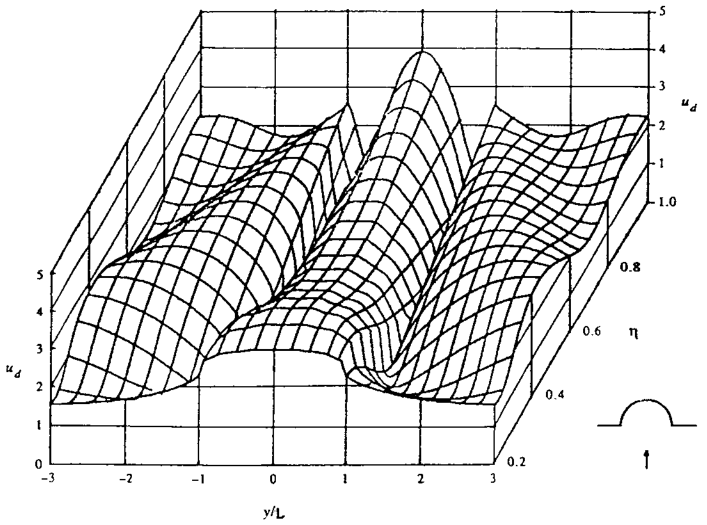

Fig.15 Displacements on the free surface of hill for d / L = 1

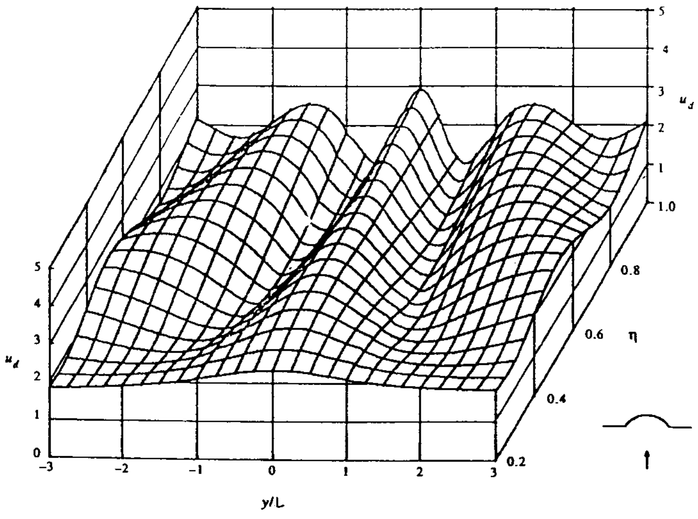

Fig.16 Displacements on the free surface of hill for d / L = 0.5

To exhibite the effects of the height–to–width ratio of the hill on the surface motion, 3–D plots of surface displacements u_d versus y / L and the dimensionless frequency η are presented in Figures 15, 16 and 17 for d / L = 1, 0.5 and 0.25, respectively. As expected, the effects of the hill decrease generally as d / L becomes smaller and the displacement for low d / L generally approaches to 2, the displacement of the free field in the obsence of hill. However, the effects are still quite considerable even for d / L = 0.25 if the excitation frequency is high. The amplification at the hill top is observed in the Figures. Yet this amplification does not appear systematicallly, and it depends significantly on the characteristics of both the incident waves and the hill structure. Although the dependence is complex, some general features can still be observed. First, the results presented here exhibit that the maximum response of the displacements at the hill top will occur as the incident wavelenghs are conparable with, or slightly shorter than the hill width. For $\eta = 1$ and the vertical incidence, for example, for the hill with d / L = 1, 0.5 and 0.25 the displacement u_d at the hill top are 95%, 40% and 20% higher than that in the free field in the obsence of the hill, respectively. The second feature we can observed is that the amplification at the hill top generally decreases with decreasing of the incident angle from $\alpha = 90°$ to $\alpha = 0°$, and deamplification at the hill top will occur for the grazing incidence of $\alpha = 0°$. In general trend, the above two feartures are agreeable to the results obtained by other methods. Besides, it can be seen from the results presented here that the degree of the complixity of the surface displacement pattern will increase with increasing of the frequency of the incident waves.

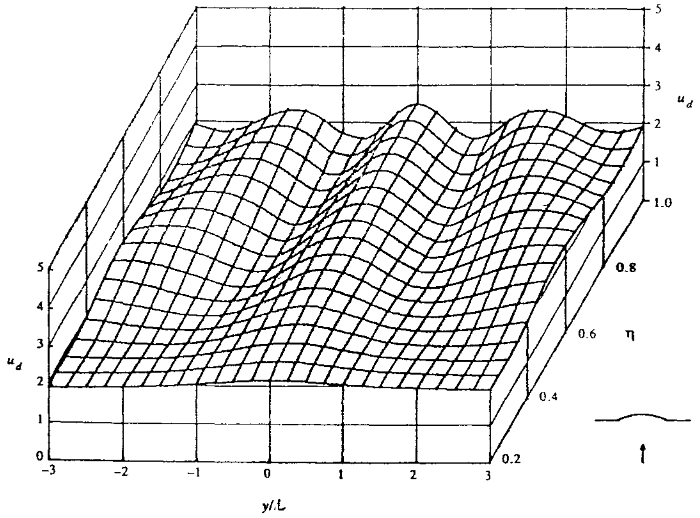

Fig.17 Displacements on the free surface of hill for d / L = 0.25

Conclusions

An analytical method is presented in this paper to obtain closed–form solutions of two–dimensional scattering of plane SH waves by cylindrical hill and canyon of circular–arc cross–section.Although truncation treatment of the infinite equations is inevitable for numerical solution, it has been tested that errors of the truncation converge to zero with increasing the truncation order. Complex effects of the height(depth)–to–width ratio of the topography on wave motion have been demonstrated by a series of numerical solutions using the method presented in the paper.

Acknowledgment

This research is sponsored jointly by National Natural Science Foundation of China and by Earthquake Science Foundation of China.

References

[1] Bouchon, M., Effect of topography on surface motion, Bull. Seism. and Soc.Amer.**63**(1973), 615–632.

[2] Sanchez–Sesma, F.J., I.Herrera and Aviles, I., A boundary method for elastic wave diffraction: application to scattering of SH waves by surface irregularities, Bull.Seism.and Soc.Amer.**72**(1982), 473–490.

[3] Bard, P.–Y., Diffracted waves and displacement field over two–dimensional elevated topographies, Geophy.J.R.astr.Soc.**71**(1982), 731–760.

[4] Sanchez–Sesma, F.J., Site effect on strong ground motion, Soil Dyn.and Earthq.Eng.**6**(1987), 124–132.

〔5〕 Trifunac, M.D., Surface motion of a semi–cylindrical alluvial valley for incident plane SH waves, Bull.Seism.and Soc.Amer.**61**(1971), 1755–1770.
〔6〕 Trifunac, M.D., Scattering of plane SH waves by a semi–cylindrical canyon, Earthq.Eng.and Struct.Dyn.**1**(1973), 267–281.
〔7〕 Wong, H.L.and Trifunac, M.D., Scattering of plane SH waves by a semi–elliptical canyon, Earthq.Eng.and Struct.Dyn.**3**(1974), 157–169.
〔8〕 Yuan, X. and Liao, Z.P., Scattering of plane SH waves by a cylindrical hill of circular–arc cross–section, Soil Dyn.and Earthq.Eng.**13**(1994), 407–412.
〔9〕 Yuan, X. and Men, F.L., Scattering of plane SH waves by a semi–cylindrical hill, Earthq.Eng.and Struct.Dyn.**21**(1992), 1091–1098.
〔10〕 Cao, H and Lee, V.W., Scattering of plane SH waves by circular cylindrical canyon with variable depth–to–width ratio, European J Earthq.Eng., Ⅲ(2)(1989), 29–37.
〔11〕 Eringen, A.C.and Suhubi, E.S., Elastodynamics, Vol.Ⅱ, Academic Press(1975).
〔12〕 Achenbach, J.D., Shear waves in an elastic wedge, Solids and Struct.**6**(1970), 379–388.

APPLICATIONS OF INFINITE ELEMENTS TO DYNAMIC SOIL-STRUCTURE INTERACTION PROBLEMS

Chongbin Zhao
(CSIRO Division of Exploration and Mining, Perth, WA 6009, Australia)

Abstract

This paper presents a brief summary on the research, which was mainly related to the applications of infinite elements to dynamic soil-structure interaction problems and carried out by the author and his coworkers during the last decade. Owing to the complex and complicated nature of practical engineering problems, infinite elements often need to be coupled with finite elements to deal with such problems. This has enabled the combination of infinite elements and finite elements to be used to successfully solve many practical problems in various engineering fields, such as earthquake engineering, structural engineering, geotechnical engineering, dam engineering and so forth. Several examples are given in this paper to show the applications of infinite elements to dynamic soil-structure interaction problems in engineering practice.

1 Introduction

It is well known that compared to the structural size in engineering practice, the Earth's crust is vast on the geometrical side, and therefore can be treated as an infinite medium on the mathematical analysis side. This poses a challenge problem for the conventional finite element method because the modelling domain must be finite in the conventional finite element analysis. The early treatment of this problem is to simply cut a finite region of the Earth's crust as the foundation medium of a structure, and then to model the structure and its foundation medium of finite size using the finite element method. This treatment may be acceptable for static problems, provided the foundation medium of a structure is taken large enough. However, this treatment does not work at all for dynamic problems because it cannot avoid the wave reflection and refraction behaviour on the artificially truncated boundary, no matter how large the foundation of a structure is taken.

To solve the above-mentioned problem more effectively and efficiently, great efforts have been made during the last a few decades. Among them the infinite element is one of the most powerful techniques to tackle the above problem [1-21]. The theory of infinite elements can be found in many open literatures [1-4, 6-7, 13] and will not be repeated in this paper. The infinite element was initially proposed for dealing with static problems in infinite elastic media [1, 4] and later extended to the solution of steady-state wave propagation problems in infinite elastic media [2-3, 6-7, 13]. Only very recently, the transient infinite element was developed for solving truly transient heat transfer, mass transport and pore-fluid flow problems in infinite media [11, 14, 18, 19].

Considering the relevance to the topic of this paper, we only present some numerical results obtained from using the combination of finite elements and infinite elements for solving dynamic soil-structure interaction problems. The basic idea behind using the combination of finite and infinite elements is as follows. The finite element is used to effectively model the geometric irregularities and material varieties in a structure and the near field of its foundation, while the infinite element is used to effectively and efficiently model the wave propagation behaviour in the far field of the foundation. To demonstrate the applicability of infinite elements to various practical engineering problems, several examples are given to show how to use the combination of finite and infinite elements for solving the dynamic soil-structure interaction problems in earthquake engineering, structural engineering, geotechnical engineering and dam engineering in the following sections.

2 Applications of Infinite Elements to Wave Propagation Problems in Earthquake Engineering

The free field distribution of a site due to an earthquake is a wave scattering problem in the infinite medium. This free field distribution is often affected by the site geometrical and geological conditions. Applications of the coupled method of finite elements and infinite elements to this kind of problem have been reported in several publications [7, 10]. An example are only given below to demonstrate the applicability of using infinite elements to solve some practical problems in earthquake engineering.

For the above-mentioned purpose, a V-shaped canyon with different ratios of top width to height is considered. H and L are used to stand for the height and top width of the canyon respectively. As shown in Fig. 1, the near field of the canyon is simulated by eight-node isoparametric finite elements, while the far field of the canyon is modelled by dynamic infinite elements. Since this study aims to investigate the displacement distribution pattern along the canyon surface, it is appropriate to use a unit plane harmonic wave in the analysis. To meet different needs for the study, the unit wave may be considered to have different wave types (i.e., P-wave or SV-wave), different circular frequencies and different incident angles. The horizontal line (Y=0) is chosen as the wave input boundary where the incident harmonic wave is transformed into dynamic loads using the elastic wave theory. The angle between the normal of the front of the plane harmonic wave and the vertical line is defined as the wave incident angle. According to this definition, $\theta = 0$ means that the harmonic wave is vertically propagating onto the wave input boundary, while $\theta \neq 0$ implies that the harmonic wave is obliquely propagating onto the wave input boundary. In order to reflect the effects of wave incident direction on free field motion, different incident angles have been considered in the analysis.

The following parameters are used in the computation: the height of the canyon is 100 m; the elastic modulus of the canyon rock mass is $24\times10^6 kPa$; the unit weight and Poisson's ratio of the canyon rock mass are $24kN/m^3$ and 1/3 respectively. For the purpose of investigating the effect of the circular frequency of the incident wave, the dimensionless frequency is defined as

$$a_0 = \frac{\omega H}{\pi C_s} \tag{1}$$

where a_0 is the dimensionless frequency; ω is the circular frequency of the incident harmonic wave; C_s is the S-wave velocity in the canyon rock mass.

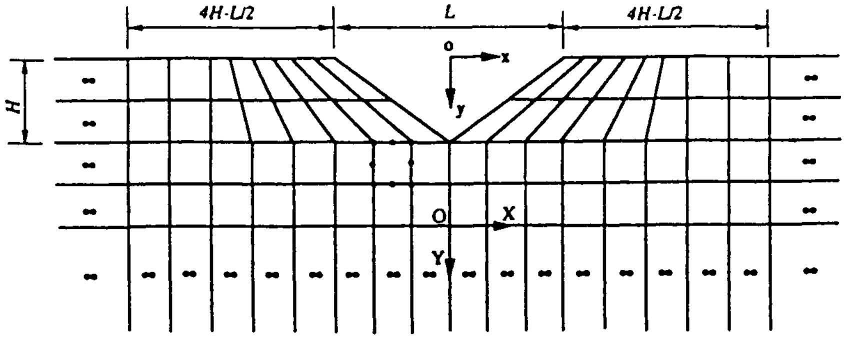

Fig. 1 Discretized mesh for a V-shaped canyon

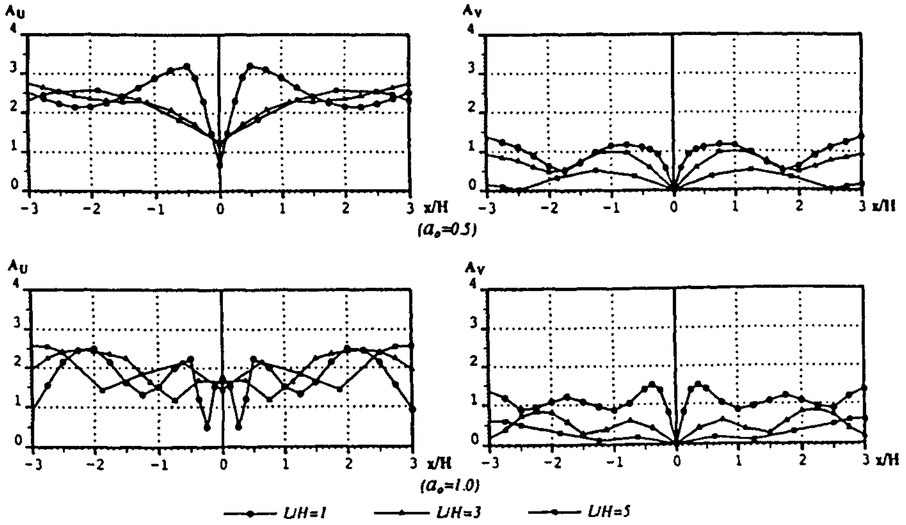

Fig. 2 Distributions of displacement amplitudes along V-shaped canyons due to SV wave vertical incidence

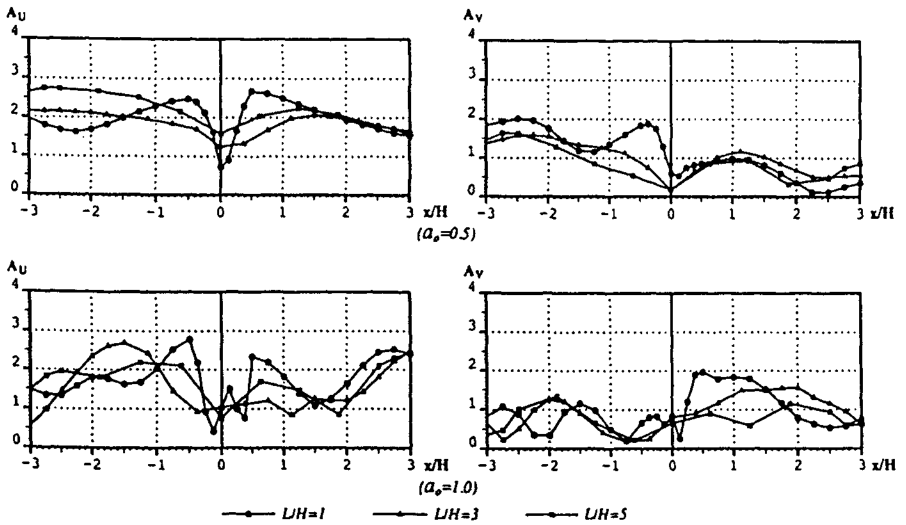

Fig. 3 Distributions of displacement amplitudes along V-shaped canyons due to SV wave oblique incidence

Fig. 2 and Fig. 3 show the displacement amplitude distribution along the V-shaped canyon due to harmonic SV wave incidences with different incident angles. In these figures, A_U and A_V are the displacement amplitudes in the horizontal and vertical directions respectively. It is clear that in the case of vertical incident waves (Fig. 2), the symmetric nature of the displacement pattern along the canyon surface is maintained for the SV wave incidence. Both the maximum value and the pattern of the displacement amplitudes are different for different ratios of canyon width to height (*L/H*), especially for higher frequency wave incidences ($a_0 = 1.0$). This indicates that the canyon topographic condition has significant effects on free field motions along the canyon surface. The maximum value of the displacement amplitude can reach over 3 for the SV wave vertical incidence. This maximum value appears at the top of the narrower canyon (*L/H*=1). Even though the input waves are vertical, both the horizontal and vertical displacement components are not zero for the SV wave incidences due to wave mode conversion. In the case of oblique incident waves (Fig. 3), the related results show that the pattern of the displacement amplitude appears to be asymmetric and its distribution along the canyon surface is also different due to different ratios of canyon width to height (*L/H*). This phenomenon can also be attributed to wave mode conversion along the canyon surface in the case of SV wave incidences.

3 Applications of Infinite Elements to Dynamic Soil-Structure Interaction Problems in Structural Engineering

To investigate the effect of foundation flexibility on the dynamic response of a structure with the soil-structure interaction included, a three dimensional multistorey frame structure with a plate foundation resting on a rock medium is considered. The frame structure is modelled using three dimensional frame elements, while the plate and the near field of the rock mass are modelled using the thick plate elements and solid elements respectively. To reflect the wave propagation between the near and far fields, the far field of the rock mass is modelled using three dimensional dynamic infinite elements [13]. Fig. 4 shows the discretized model of the frame structure-plate foundation-rock mass system. It needs to be pointed out that owing to the symmetric nature of the problem, only a quarter of the structure, the plate and the rock mass medium is considered and shown in Fig. 4. It is also assumed that only horizontal periodic loading is applied at the center of the plate (point O in Fig. 4). The plate foundation is considered both flexible and rigid so that the related results can be compared with each other.

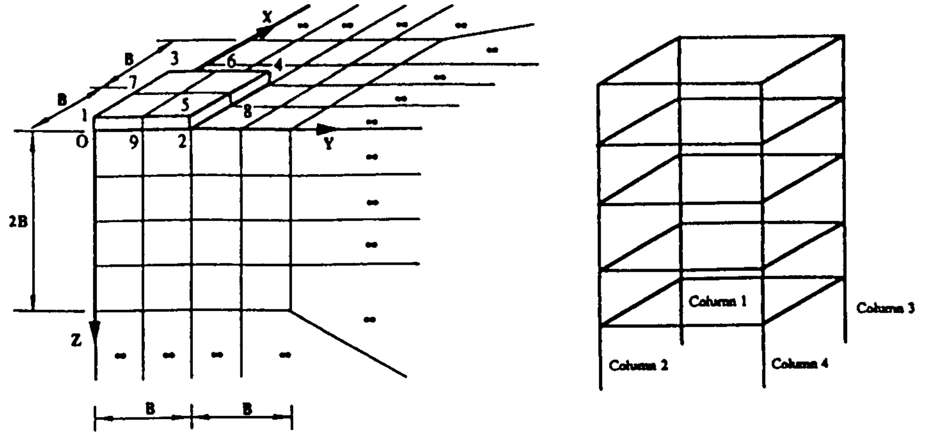

(a) (b)

Fig. 4 Discretized mesh for a frame-plate-soil system

The following parameters are used in the calculation. For the frame structure, the sections of columns and beams are $0.4\times0.4m^2$; the elastic modulus is $24\times10^6 kPa$; Poisson's ratio is 0.16; unit weight is $24kN/m^3$. For the plate foundation, the width and thickness are $10m$ and $1m$ respectively; the elastic modulus is $24\times10^{12} kPa$ for the rigid plate and $24\times10^6 kPa$ for the flexible plate, Poisson's ratio is 0.33. For the rock mass, the elastic modulus is $24\times10^6 kPa$; Poisson's ratio is 0.33; the unit weight is $24kN/m^3$.

Fig. 5 shows the dimensionless horizontal displacement distribution of the frame structure. In this figure, the solid triangle, the solid dot and the solid square represent the numerical results for column 1, column 2 and column 3 respectively. H is the height of the frame. It is observed that when the frame is subjected to a horizontal movement induced by the dynamic load on the plate, the maximum value of the displacement difference within each storey of the frame structure occurs in the ground storey of the frame for both rigid and flexible plate foundations. This implies that the safety of the columns in the ground storey is the controlling factor in the seismic design of frame structures. This is due to the fact that the repeated reflection within the columns between the ground floor and the first floor takes place and consequently, the wave energy is trapped in these regions. In addition, the flexibility of the plate foundation has a significant effect on the displacement response of the ground storey of the frame structure, as can be clearly seen in Fig. 5.

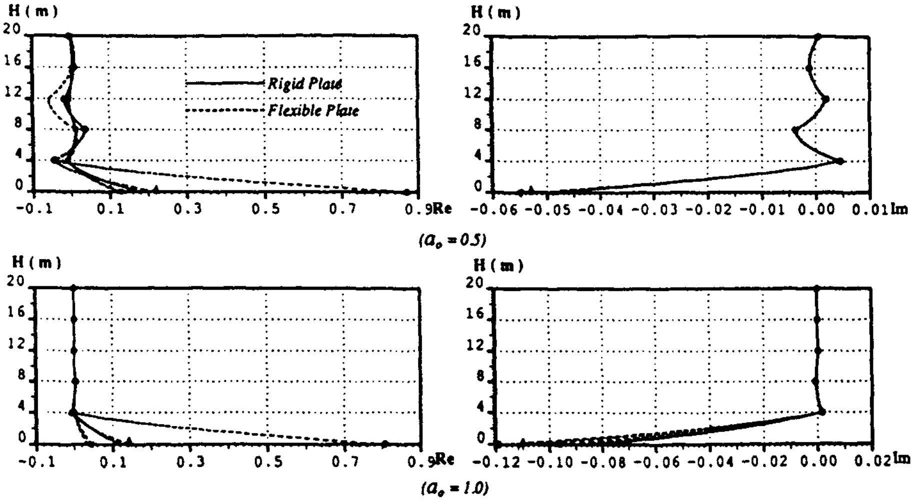

Fig. 5 Dimensionless horizontal displacement distribution of the frame columns

4 Applications of Infinite Elements to Dynamic Soil-Structure Interaction Problems in Geotechnical Engineering

Retaining walls are frequently used in geotechnical engineering. Once a retaining wall undergoes an earthquake event, the dynamic soil-structure interaction should be included in the seismic design of the retaining wall. Generally, a retaining wall is a finite structure, while its foundation soil is a infinite medium. Thus, the coupled method of finite and infinite elements is very suitable for solving this kind of problem.

Fig. 6 shows a typical soil-retaining wall system in geotechnical engineering. The near field of this problem consists of the retaining wall, the backfill soil and part of the natural soil, while the far field is comprised of the rest of the natural soil and the base rock mass. As was mentioned before, finite elements and dynamic infinite elements are used to model the near and far fields of the natural soil and rock mass respectively. The parameters used for the retaining wall, backfill soil, natural soil and rock mass can be found in a previous publication [12].

Fig. 7 shows the effect of different backfill soils on the acceleration amplitude distribution of the retaining wall due to plane SV wave vertical incidence. In this figure, $\ddot{u}_A$ and $\ddot{v}_A$ are the amplitudes of the horizontal and vertical acceleration components of the retaining wall; ω is the circular frequency of the incident harmonic wave; Stations 1, 2 and 3 represent the top, the middle and the bottom of the wall; Cases 1, 2 and 3 are corresponding to the softer, the medium and the stiffer backfill soil situations. It is clear that although the backfill soil has negligible influence on the dynamic response of the retaining wall in the case of low frequency wave incidences, it has a considerable effect on the response of the wall during high frequency wave incidences. This indicates that the change in mechanical properties of the backfill soil should be accounted for in the seismic design of a retaining wall. Since unit harmonic waves are used in the calculation, the acceleration amplitudes obtained here can serve as amplification factors of the wall to incident harmonic waves. It is concluded from the related results that the configuration of a retaining wall may affect significantly the amplification factor of the retaining wall to an input earthquake because an earthquake wave can be decomposed into several harmonic waves.

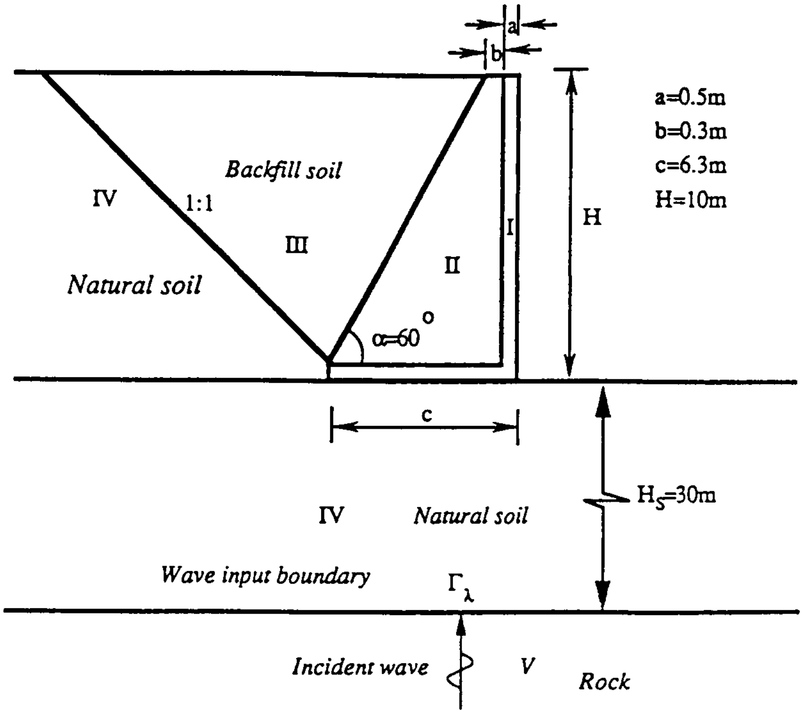

Fig. 6 Computing model of a soil-retaining wall system

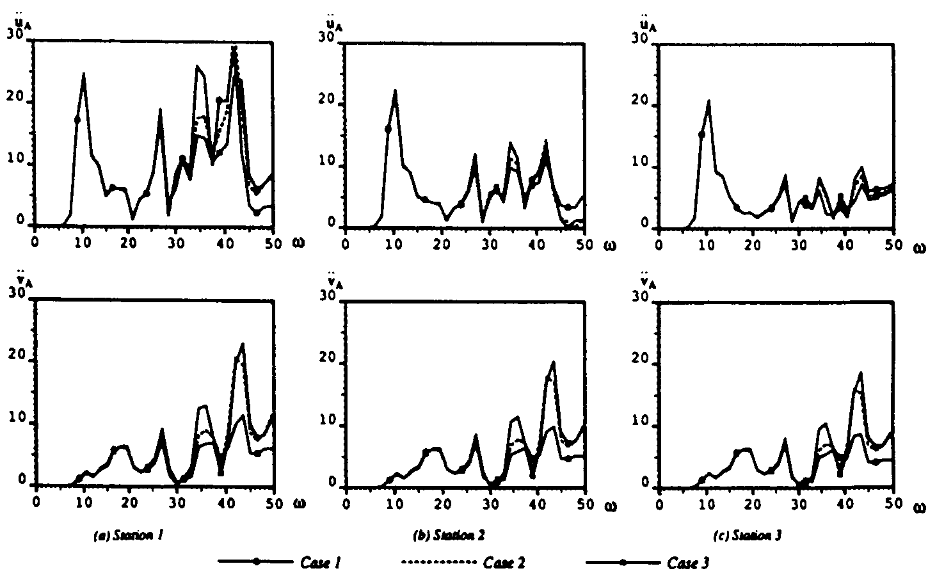

Fig. 7 Amplitudes of the acceleration distribution of the wall due to different backfill soils

5 Applications of Infinite Elements to Dynamic Soil-Structure Interaction Problems in Dam Engineering

In this section, an example is used to show how the infinite elements are applied to solve dynamic soil-structure interaction problems in dam engineering. A typical embankment dam with either a central clay core or an upstream inclined concrete apron is considered and shown in Fig. 8, where the dam and the near field of its foundation medium are modelled using finite elements, but the far field is modelled using dynamic infinite elements. The details about the configuration and the parameters of the dam-soil foundation system can be found in an open literature [17]. Only some results are briefly given and discussed below.

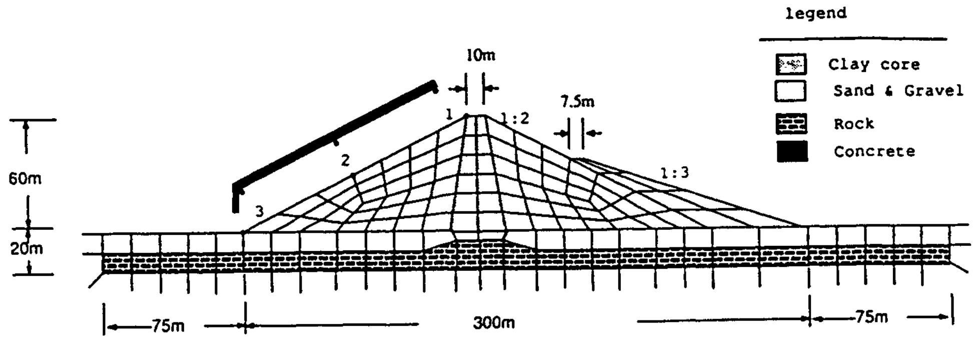

Fig. 8 Discretized mesh for an embankment dam-foundation system

Fig. 9 shows the dynamic response of an empty embankment dam on a layered foundation due to SV wave vertical incidence. In this figure, the solid lines represent amplification factors in the horizontal direction, while the dashed lines denote amplification factors in the vertical direction for several stations on the upstream surface of the dam. It is observed that the resonant frequencies of the system with an upstream inclined concrete apron are different from those of the system with a central clay core because the concrete apron is much stiffer than the central clay core. However, since the thickness of the inclined concrete apron is very small, the increase of the resonant frequencies of the dam with the concrete inclined apron is not profound although it deserves being considered in the analysis.

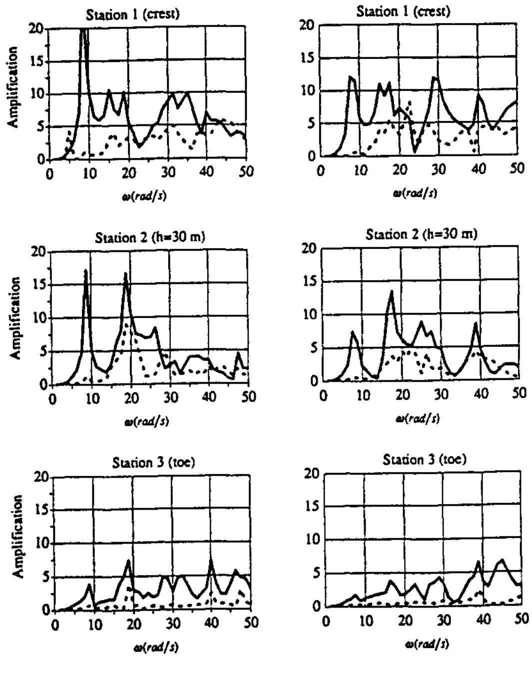

a) Upstream inclined concrete apron

b) Central clay core

Fig. 9 Dynamic response of the empty dam due to SV wave vertical incidence

In terms of the amplification factors of the system due to different impervious members, it has recognized that the types of impervious members have a significant influence on the dynamic response of the system in the low frequency range of excitation. The reason for this is that the material damping of the system plays a considerable role in the dynamic response of the system for low frequency excitation. In the case of the embankment dam with an upstream inclined concrete apron, the total material damping of the system decreases as the hysteretic coefficients of the related materials decrease, compared with the central clay core case. Thus, the amplification factors as well as the dynamic response of the dam with an upstream inclined concrete apron increase in the low frequency range. This leads to the conclusion that central clay cores are more suitable as impervious members for embankment dams, from the seismic resistant point of view. Since the dynamic response of a dam is dominated by the radiation damping of the system for high frequency excitation, the amplification factors for the dam with either an upstream inclined concrete apron or a central clay core are nearly the same due to the identical radiation damping of the foundation.

6 Conclusions

The dynamic infinite element has the following two main advantages. Firstly, the concept of the infinite element is very clear in physics. Secondly, the formulation of the infinite element is very easy to be include into the existing finite element codes. Thus, infinite elements have been widely used to solve dynamic soil-structure interaction problems in earthquake engineering, structural engineering, geotechnical engineering, dam engineering and so forth. However, further research is needed to develop the infinite element for solving dynamic soil-structure interaction problems in time domain, since the current dynamic infinite element can only be used to solve dynamic soil-structure interaction problems in frequency domain.

References

[1] Bettess P, *Int J Numer Methods Eng*, **11**(1977), 53-64.
[2] Chow Y K and Smith I M, *Int J Numer Methods Eng*, **17**(1981), 503-526.
[3] Medina F and Taylor R L, *Int J Numer Methods Eng*, **19**(1983), 699-709.
[4] Bettess P, Infinite Elements, Penshaw Press (1992).
[5] Zhao Chongbin and Valliappan S, *Int J Earthq Eng Struct Dyn*, **20**(1991), 1159-1177.
[6] Zhao Chongbin, Valliappan S, *Int J of Computers and Structures*, **41**(1991), 1041-1049.
[7] Zhao Chongbin, Valliappan S, *Int J Num Meth Eng*, **33**(1992), 1661-1682.
[8] Valliappan S and Zhao Chongbin, *Int J Num Anal. Meth Geomech*, **16**(1992), 79-99.
[9] Zhao Chongbin, Valliappan S, *Communications Numer Meth Eng*, **9**(1993), 407-415.
[10]Zhao Chongbin and Valliappan S, *Int J Num Analy Meth Geomech*, **17**(1993), 73-94.
[11]Zhao Chongbin, Valliappan S, *Int J Num Analy Meth Geomech*, **17**(1993), 324-341.
[12]Zhao Chongbin, Valliappan S, *Int J of Computers and Structures*, **47**(1993), 239-244.
[13]Zhao Chongbin and Valliappan S, *Int J Num Meth Eng*, **36**(1993), 2567-2580.
[14]Zhao Chongbin and Valliappan S, *Comput Meth Appl Mech Eng*, **108**(1993), 119-131.
[15]Zhao Chongbin and Valliappan S, *Computers and Structures*, **48**(1993), 227-239.
[16]Zhao Chongbin and Valliappan S, *Int J Soil Dyn Earthq Eng*, **12**(1993), 129-143.
[17]Zhao Chongbin et al., *Int J Soil Dyn Earthq Eng*, **12**(1993), 199-208.
[18]Zhao Chongbin, *Int J of Water Resources Engineering*, **1**(1993), 33-53.
[19]Zhao Chongbin and Valliappan S, *Int J Num Meth Eng*, **37**(1994), 1143-1158.
[20]Zhao Chongbin and Xu T P, *Computers and Structures*, **53**(1994), 105-117.
[21]Zhao Chongbin, Xu T P and Valliappan S, *Computers and Structures*, **54**(1995), 705-715.

NON-REFLECTING BOUNDARY CONDITIONS FOR WAVE PROPAGATION PROBLEMS AND THEIR STABILITY ANALYSIS

Shao Xiumin
(Institute of Mathematics, Academy of Sciences, Beijing, China, 100080)

Abstract

In this paper, a few kinds of non-reflecting boundary conditions are introduced, which have been used for a variety of wave propagation problems, such as acoustic waves, isotropic and anisotropic elastic waves, and waves in fluid saturated porous media. The stability of finite element methods for the acoustic wave equation with non-reflecting boundary conditions is discussed and the corresponding stability conditions are given. Some numerical results are presented to show the correctness of the theoretical analysis and the effectiveness of the boundary conditions suggested by the author of this paper and her cooperator.

§1. Introduction

In the numerical simulations of wave propagation in unbounded or semi-unbounded media artificial boundaries are usually introduced to obtain bounded computational regions. Then some artificial boundary conditions have to be imposed on these boundaries, which should eliminate the artificial (unphysical) reflection of waves on the boundaries so that the obtained solution rather accurately simulate the solutions on the unbounded regions, and therefore, are called non-reflecting boundary conditions.

In recent thirty years, a variety of non-reflecting boundary conditions have been developed (see [1]). They can mainly be divided into two classes. One class is called viscous (or damping) boundary conditions, which are analogous to have some viscous midia outside the computational domains to absorb, rather than reflect, the radiated energy. Among them are: The classical viscous boundary condition suggested by Lysmer and Kuhlemeyer[2], which use viscous damping forces to act along the boundary; Viscous strip along the boundaries, in which field variables are multiplied by a negative exponent factor to gradually reduce their amplitudes, i.e., a damping term is added into the differential equations, and so on. But generally speaking, the boundary conditions of this type is not very effective in absorbing the artificial reflecting waves. A possible exception is so-called PML (perfectly matched layer) technique which was suggested recently by Berenger[3] for the electromagnetic waves and then was applied to other fields.

Another class of non-reflecting boundary conditions is based on the one-way wave equations. Decomposite the wave operator into first-order operators, each one of which is a one-way wave equation, i.e., represents a wave propagating only in one direction. We can take the equations of outgoing waves as the artificial boundary conditions. They are generally of pseudodifferential operator forms, which are nonlocal and can not be calculated. Approximating them by using different formulas (Taylor, Chebyshev, Padé or least-squares), different boundary conditions of differential forms can be obtained. What is most widely used was given by clayton and Engquist[4], Engquist and Majda[5],[6], based on the Padé approximation of pseudodifferential operators. Let the artificial boundary be $x = 0$, and the domain be $t \geq 0, x \geq 0$. For the acoustic wave equation

$$\frac{\partial^2 u}{\partial x^2} + \frac{\partial^2 u}{\partial y^2} - \frac{1}{C^2(x,y)} \frac{\partial^2 u}{\partial t^2} = f(x,y,t), \tag{1.1}$$

the Clayton-Engquist-Majda conditions are the followings:

$$\begin{aligned} B_1 u|_{x=0} &= \left(\frac{1}{C}\frac{\partial u}{\partial t} + \frac{\partial u}{\partial x}\right)\Big|_{x=0} = 0, \\ B_2 u|_{x=0} &= \left(\frac{1}{C^2}\frac{\partial^2 u}{\partial t^2} + \frac{1}{C}\frac{\partial^2 u}{\partial t \partial x} - \frac{1}{2}\frac{\partial^2 u}{\partial y^2}\right)\Big|_{x=0} = 0, \\ B_{N+1}|_{x=0} &= \left(\frac{1}{C}\frac{\partial}{\partial t} B_N u - \frac{1}{4}\frac{\partial^2}{\partial y^2} B_{N-1} u\right)\Big|_{x=0} = 0. \end{aligned} \tag{1.2}$$

The corresponding condition for the elastic wave equations are complicated, and we are not going to write them here.

Higdon[7] proposed a more general boundary condition of the form

$$\prod_{j=1}^{m} \left((\cos \alpha_j)\frac{\partial}{\partial t} - C\frac{\partial}{\partial x}\right) u = 0 \tag{1.3}$$

which contains (1.2) as its special case. He also presented some discrete boundary conditions which are discrete counterparts of (1.3).

Modeling the physical processes of wave propagation, Liao Zhenpeng and others[8][9] developed a kind of discrete conditions of the form

$$U(x,y,t) = \sum_{j=1}^{N} (-1)^{j+1} C_j^N U(x - jC_A \triangle t, y, t - (j-1) \triangle t) \tag{1.4}$$

(which the authors call Multi-Transmitting Formula), where U is the unkonwn (scalar or vector); (x,y,z) point on the artificial boundaries; N positive integer not smaller than 1, which is just the order of boundary conditions; C_A artificial wave velocity, the range of which is given in the papers;

$$C_j^N = \frac{N}{(N-j)!j!}.$$

Liao's conditions have a wide range of applications. In fact, they are most general conditions.

Shao and Lan[10] suggested a improvement version of the Liao Zhenpeng conditions of the second order. They take the rectangular $\{-a \leq x \leq a, 0 \leq y \leq b\}$ as the computational domain, where $x = \pm a$ and $y = b$ are the artificial boundaries. First, they enlarge the domain to $\{-a - \Delta x - 2C_A \Delta t \leq x \leq a + \Delta x + 2C_A \triangle t, 0 \leq y \leq b + \Delta y + 2C_A \triangle t\}$, where Δx and Δy are mesh sizes in the original domain, C_A the artificial wave velocity. Then non-reflecting boundary conditions are imposed on the new boundaries $x = \pm a \pm \triangle x \pm 2C_A \triangle t$ and $y = b + \triangle y + 2C_A \triangle t$. For example, on the boundary $x = a + \triangle x + 2C_A \triangle t$, the condition is

$$\begin{aligned} U(a+\triangle x+2C_A \triangle t, y, t+\triangle t) &= \alpha_1 U(a+\triangle x+2C_A \triangle t, y, t) \\ +\alpha_2 U(a+\triangle x, y, t) &+ \alpha_3 U(a, y, t) - U(a+\triangle x, y, t-\triangle t), \end{aligned} \tag{1.5}$$

where

$$\alpha_1 = \frac{1+s}{1+2s}, \quad \alpha_2 = 1+s, \quad \alpha_3 = -\frac{2s^2}{1+2s},$$
$$s = \frac{C_A \triangle t}{\triangle x}.$$

The conditions on the other boundaries are similar. This kind of conditions has satisfactory accuracy and stability, and has been successfully applied to a variety of wave propagation problems, such as acoustic waves, isotropic and anisotropic elastic waves, and waves in fluid saturated porous media. The authors of [10] determine the wave velocity C_A by minimizing the reflecting coefficients. For the acoustic wave equation (1.1), $C_A = C$. For anisotropic elastic waves, C_A should be the minimal wave velocity among all velocities in different directions and of different kinds. In the special case of isotropic elastic waves, $C_A = C_s$. For the waves in the two-phase media mentioned above, $C_A = C_{p2}$, i.e., the velocity of dilatational wave of the second kind (the slow dilatational wave).

Numerical experiments have indicated that the stability is a serious problem when non-reflecting boundary conditions are used. The higher the order of boundary conditions the more unstable. It implies that the accuracy and the stability are contradictory requirements. In the next two sections, the stability of finite element methods for the wave equation (1.1) with the first and second order non-reflecting boundary conditions (1.2) is discussed. The stability conditions are presented. Comparing them with the stability conditions for the Dirichlet or Neumann boundary conditions, it can be discovered that the stability properties become much worse in the present case.

§2. Finite element-finite difference schemes

In this section, some knowledge and notations of the sobolev spaces will be used. It is necessary for the description of the numerical method and the proofs of the following theorems. The readers who are not familiar with them may ignor the details and only notice the conclusions.

Let the computational domain be $\overline{\Omega}, \Omega = \{(x,y) : -a < x < a, 0 < y < b\}; \Gamma_1 = \{(x,y) : -a \leq x \leq a, y = 0\}$ be a natural boundary, and $\partial\Omega' = \partial\Omega / \Gamma_1$ be the artificial boundary.

Introduce the inner product notations

$$(u,v) = \int\int_\Omega uv dx dy, \quad \langle u,v \rangle = \int_{\partial\Omega'} uv ds.$$

Define the space

$$H^{1,0}(\Omega) = \{v(x,y) \in H^1(\Omega) : v|_{\Gamma_1} = 0\}.$$

In the following discussion, let n denote outer normal direction, and s tangential direction of the boundary $\partial\Omega'$. Suppose that in (1.1), $C(x,y) \in L^\infty(\Omega)$ and $C(x,y) > 0; f(x,y,t) \in H_0^1(\Omega) \times C([0,T])$. Consequently, $f(x,y,t) \in L^2(\Omega) \times C([0,T])$. Hence $f(x,y,t) \in L^\infty(\Omega) \times C([0,T])$. For convenience of computation, we write $f(x,y,t)$ as $\overline{f}(x,y,t)/C^2(x,y)$, where $\overline{f}(x,y,t) = C^2(x,y) f(x,y,t)$.

Corresponding to the first-and seoncd-order non-reflecting boundary conditions in (1.2), consider the following generalized solutions of initial-boundary value problems of the equation (1.1).

Problem I: Find a function $u(x,y,t)$ which is second-order continuously differentiable with respect to t when $(x,y) \in \Omega$ and belongs to $H^{1,0}(\Omega)$ for any fixed $t \in [0,T]$, and satisfies the following equations

$$\begin{cases} \left(\frac{1}{C^2}\frac{\partial^2 u}{\partial t^2}, v\right) + (\nabla u, \nabla v) - \langle \frac{\partial u}{\partial n}, v\rangle + \left(\frac{1}{C^2}\overline{f}, v\right) = 0 \\ \langle \frac{\partial u}{\partial n} + \frac{1}{C}\frac{\partial u}{\partial t}, v\rangle = 0 \\ (u,v)|_{t\leq 0} = 0 \\ \left(\frac{\partial u}{\partial t}, v\right)|_{t\leq 0} = 0 \end{cases} \tag{2.1}$$

for every $v(x,y) \in H^{1,0}(\Omega)$.

Problem II: Find a function $u(x,y,t)$ which is second-order continuously differentiable with respect to t when $(x,y) \in \Omega$ and belongs to $H^{1,0}(\Omega)$ for any fixed $t \in [0,T]$, and satisfies the following equations

$$\begin{cases} \left(\frac{1}{C^2}\frac{\partial^2 u}{\partial t^2}, v\right) + (\nabla u, \nabla v) - \langle \frac{\partial u}{\partial n}, v\rangle + \left(\frac{1}{C^2}\overline{f}, v\right) = 0 \\ \langle \frac{\partial^2 u}{\partial n \partial t} + \frac{1}{C}\frac{\partial^2 u}{\partial t^2}, v\rangle + \frac{1}{2}\langle C\frac{\partial u}{\partial s}, \frac{\partial v}{\partial s}\rangle = 0 \\ (u,v)|_{t\leq 0} = 0 \\ \left(\frac{\partial u}{\partial t}, v\right)|_{t\leq 0} = 0 \end{cases} \tag{2.2}$$

for every $v(x,y) \in H^{1,0}(\Omega)$.

For the sake of simplicity and clearness of the conclusions, we will only consider the homogeneous media (i.e., $C(x,y) \equiv$ const.) and uniform right-angled triangle and square elements. The general cases will be discussed in the paper [11].

Discretise the spatial variables x and y by using the finite element method. Denote the nodes by $P_i (i = 1, \cdots, m)$. Suppose that S^h is a finite element space, $S^h \in H^1(\Omega)$, and its basis functions are $\varphi_i (i = 1, \cdots, m)$ which possess the feature $\varphi_i(P_j) = \delta_{ij}$. Take φ_i as the function v in (2.1) and (2.2) (except those φ_i which correspond to the nodes on Γ_1). Find the solutions of the problems I and II in the subspace S^h. Then the problems are reduced to the following initial value problems of ODEs

$$I': \begin{cases} M\ddot{U} + SU - W = MG(t) \\ W + M_B\dot{U} = 0 \\ U(0) = U_t(0) = W(0) = 0 \end{cases} \tag{2.3}$$

$$II': \begin{cases} M\ddot{U} + SU - W = MG(t) \\ \dot{W} + M_B\ddot{U} + S_B U = 0 \\ U(0) = U_t(0) = W(0) = 0 \end{cases} \tag{2.4}$$

where U is the nodal unknown vector, M the mass matrix, S the stiffness matrix, M_B the boundary mass matrix, S_B the boundary stiffness matrix, and W the vector related with the normal derivative on the artificial boundary. The elements of the matrices M, S, M_B, S_B and the vector W are, respectively,

$$\begin{aligned} &M_{ij} = \frac{1}{C^2}\iint_\Omega \varphi_i\varphi_j dxdy, \qquad S_{ij} = \iint_\Omega \nabla\varphi_i \cdot \nabla\varphi_j dxdy, \\ &(M_B)_{ij} = \frac{1}{C}\int_{\partial\Omega'} \varphi_i\varphi_j ds, \qquad (S_B)_{ij} = \frac{1}{2}C\int_{\partial\Omega'} \frac{\partial\varphi_i}{\partial s}\frac{\partial\varphi_j}{\partial s} ds \\ &(i,j = 1, 2 \cdots, m) \end{aligned} \tag{2.5}$$

$$W_i = \int_{\partial\Omega'} \frac{\partial u}{\partial n}\varphi_i dS, \qquad (i = 1, \cdots, m), \tag{2.6}$$

and $G(t)$ is a vector which consists of the values of the function $\overline{f}(x, y, t)$ at nodes.

Through a lumping process the matrices M and M_B are replaced by diagonal matrices. In the case of right-angled triangle elements mentioned above, the entrices of element mass matrix are

$$M^e_{ij} = \begin{cases} \frac{h^2}{6C^2} & i = j \\ 0 & i \neq j, \end{cases} \tag{2.7}$$

and the entrices of element boundary mass matrix are

$$(M_B)^e_{ij} = \begin{cases} \frac{h}{2C} & i = j \\ 0 & i \neq j. \end{cases} \tag{2.8}$$

In the case of square elements, the corresponding entrices are

$$M^e_{ij} = \begin{cases} \frac{h^2}{4C^2} & i = j \\ 0 & i \neq j \end{cases} \tag{2.9}$$

and (2.8), respectively. Here h is the mesh size.

Discretise the time variable in (2.3) and (2.4) by using the following finite difference schemes

$$\begin{cases} \frac{U^{n+1} - U^n}{\Delta t} = V^{n+1} \\ M\frac{V^{n+1} - V^n}{\Delta t} + SU^n - W^n = MG^n \\ W^{n+1} + M_B V^{n+1} = 0 \end{cases} \tag{2.10}$$

and

$$\begin{cases} \frac{U^{n+1} - U^n}{\Delta t} = V^{n+1} \\ M\frac{V^{n+1} - V^n}{\Delta t} + SU^n - W^n = MG^n \\ \frac{W^{n+1} - W^n}{\Delta t} + M_B\frac{V^{n+1} - V^n}{\Delta t} + S_B U^{n+1} = 0. \end{cases} \tag{2.11}$$

That is,

$$\begin{cases} MV^{n+1} = MV^n - \Delta tSU^n + \Delta tW^n + \Delta tMG^n \\ U^{n+1} = U^n + \Delta tV^{n+1} \\ W^{n+1} = -M_B V^{n+1} \end{cases} \tag{2.10$'$}$$

and

$$\begin{cases} MV^{n+1} = MV^n - \Delta tSU^n + \Delta tW^n + \Delta tMG^n \\ U^{n+1} = U^n + \Delta tV^{n+1} \\ W^{n+1} = W^n - M_B(V^{n+1} - V^n) - \Delta tS_B U^{n+1}. \end{cases} \tag{2.11$'$}$$

The initial values U^0, V^0 and W^0 are zero. Utilizing the formulas (2.13)' and (2.14)', U^{n+1}, V^{n+1} and W^{n+1} can be obtained successively from U^n, V^n and W^n.

§3. Stability of the schemes (2.10) and (2.11)

In the following discussions, $\lambda_{\max}$ and $\lambda_{\min}$ denote the maximum and minimum eigenvalues of a matrix, respectively.

Lemma 1. For the finite element space of right-angled triangle elements and linear basis functions, the following inequalities

$$\begin{aligned} &\lambda_{\max}(S) \le 9, \quad \lambda_{\min}(M) \ge \frac{h^2}{6C^2}, \\ &\lambda_{\max}(M_B) \le \frac{h}{C} \end{aligned} \tag{3.1}$$

are valid.

Proof. First, consider the maximum eigenvalue of the stiffness matrix S. As is well known,

$$\lambda_{\max}(S) = \max_{U \in R^m} \frac{U^T S U}{U^T U}. \tag{3.2}$$

For the nodal unknown vector U, we have

$$U^T S U = \sum_e (U^e)^T S^e U^e \le q \lambda_{\max}(S^e) U^T U,$$

where q is the maximum number of elements which meet at a node, and S^e the element stiffness matrix. In our case, $q = 6$ and

$$S^e = \frac{1}{2} \begin{pmatrix} 1 & -1 & 0 \\ -1 & 2 & -1 \\ 0 & -1 & 1 \end{pmatrix} \quad \text{or its transpose,}$$

so that $\lambda_{\max}(S^e) = 3/2$. From (3.2), the first inequality can be obtained.

The element mass matrix M^e and the element boundary mass matrix M_B^e are both diagonal matrices. It is easy to get their eigenvalues. From (2.7), $\lambda_{\min}(M^e) = \frac{h^2}{6C^2}$. And from (2.8), $\lambda_{\max}(M_B^e) = \frac{h}{2C}$. Utilizing again the fact that maximum and minimum eigenvalues of a matrix are equal to maximum and minimum of its Rayleigh quotient, respectively, and noticing that a node is at least a vertex of one element and a boundary node is at most vertex of two line elements, we have the second and third inequalities of (3.1), which completes the proof.

Lemma 2. For the finite element space of square elements and bilinear basis functions, the following inequalities

$$\begin{aligned} &\lambda_{\max}(S) \le 4, \quad \lambda_{\min}(M) \ge \frac{h^2}{4C^2}, \\ &\lambda_{\max}(M_B) \le \frac{h}{C} \end{aligned}$$

are valid.

Proof. The approach is similar to the Lemma 1. We have only to notice that in the present case, $q = 4$, and

$$S^e = \frac{1}{6} \begin{pmatrix} 4 & -1 & -2 & -1 \\ -1 & 4 & -1 & -2 \\ -2 & -1 & 4 & -1 \\ -1 & -2 & -1 & 4 \end{pmatrix}$$

So that $\lambda_{\max}(S^e) = 1$, and the entrices of the element mass matrix and the element boundary mass matrix are (2.9) and (2.8), respectively. The proof is completed.

Now we investigate the stability of the schemes (2.10) and (2.11).

Define the following inner products and norms of vectors:

$$\begin{aligned} &(U, V)_2 = U^T V, \quad \|U\|_2 = \sqrt{(U, U)_2}, \\ &(U, V)_M = U^T M V, \quad \|U\|_M = \sqrt{(U, U)_M}, \\ &(U, V)_S = U^T S V, \quad \|U\|_S = \sqrt{(U, U)_S}. \end{aligned}$$

The latter two definitions of norm are reasonable because of the positive-definiteness of the matrices M and S. For the norms $\|\cdot\|_2$ and $\|\cdot\|_M$, there is inequality

$$\frac{1}{\lambda_{\max}(M)}\|U\|_M^2 \le \|U\|_2 \le \frac{1}{\lambda_{\min}(M)}\|U\|_M^2.$$

About the scheme (2.10), i.e., the non-reflecting boundary condition of the first order, we have the following Theorem 1 and 2.

Theorem 1. For the finite element space of uniform right-angled triangle elements and linear basis functions, if the condition

$$\frac{C\,\Delta\, t}{h} \le 0.18 \tag{3.5}$$

is satisfied, then for any $T \in R$ and $N \in Z^+, 0 < (N+1)\,\Delta\, t < T$, there exists a constant C_1 such that the solution of (2.10) is subjuct to the inequality

$$\max_{0\le n\le N}\|U^{n+1}\|_M + \max_{0\le n\le N}\|V^{n+1}\|_M \le C_1\|f\|_\infty, \tag{3.6}$$

i.e., the scheme (2.10) is stable.

Proof. From (2.10),

$$M\frac{U^{n+1}-2U^n+U^{n-1}}{\Delta t^2} + SU^n + M_B\frac{U^n-U^{n-1}}{\Delta t} = MG^n. \tag{3.7}$$

Multiply the equation (3.7) by $\Delta t\left(\frac{U^{n+1}-U^{n-1}}{\Delta t}\right)^T$, and sum the obtained equation from 0 to N with respect to n. Since M is a diagonal matrix, the first term of the left-hand side can be reduced to

$$\begin{aligned}&\Delta t\left(\frac{U^{n+1}-U^{n-1}}{\Delta t}\right)^T M\frac{U^{n+1}-2U^n+U^{n-1}}{\Delta t^2}\\ &= \left(\frac{U^{n+1}-U^n}{\Delta t}\right)^T M\frac{U^{n+1}-U^n}{\Delta t} - \left(\frac{U^n-U^{n-1}}{\Delta t}\right)^T M\frac{U^n-U^{n-1}}{\Delta t}.\end{aligned}$$

After the summation, we obtain

$$\Delta t\sum_{n=0}^{N}\left(\frac{U^{n+1}-U^{n-1}}{\Delta t}\right)^T M\frac{U^{n+1}-2U^n+U^{n-1}}{\Delta t^2} = \left(\frac{U^{N+1}-U^N}{\Delta t}\right)^T M\frac{U^{N+1}-U^N}{\Delta t}.$$

Here the condition $U^0 = U^{-1} = 0$ has been used. For the second term of the left-hand side we have

$$\begin{aligned}\Delta t\left(\frac{U^{n+1}-U^{n-1}}{\Delta t}\right)^T SU^n &= \tfrac{1}{2}\{(U^{n+1})^T SU^{n+1} - (U^{n+1}-U^n)^T S(U^{n+1}-U^n)\\ &\quad -(U^{n-1})^T SU^{n-1} + (U^n-U^{n-1})^T S(U^n-U^{n-1})\}.\end{aligned}$$

After the summation it becomes

$$\begin{aligned}\Delta t\sum_{n=0}^{N}\left(\frac{U^{n+1}-U^{n-1}}{\Delta t}\right)^T SU^n &= \tfrac{1}{2}(U^{N+1})^T SU^{N+1} + \tfrac{1}{2}(U^N)^T SU^N\\ &\quad -\tfrac{1}{2}(U^{N+1}-U^N)^T S(U^{N+1}-U^N)\\ &= (U^{N+1})^T SU^{N+1} - (U^{N+1})^T S(U^{N+1}-U^N).\end{aligned}$$

For the third term, it can be proved that

$$\begin{aligned}&\Delta t\left(\frac{U^{n+1}-U^{n-1}}{\Delta t}\right)^T M_B\frac{U^n-U^{n-1}}{\Delta t} = \frac{1}{2\,\Delta\, t}(U^{n+1}-U^{n-1})^T M_B(U^{n+1}-U^{n-1})\\ &+\frac{1}{2\,\Delta\, t}(U^n-U^{n-1})^T M_B(U^n-U^{n-1}) - \frac{1}{2\,\Delta\, t}(U^{n+1}-U^n)^T M_B(U^{n+1}-U^n).\end{aligned}$$

It follows that

$$\begin{aligned}
&\Delta t\sum_{n=0}^{N}\left(\frac{U^{n+1}-U^{n-1}}{\Delta t}\right)^T M_B\frac{U^{n}-U^{n-1}}{\Delta t}\\
&=\frac{\Delta t}{2}\sum_{n=0}^{N}\left(\frac{U^{n+1}-U^{n-1}}{\Delta t}\right)^T M_B\left(\frac{U^{n+1}-U^{n-1}}{\Delta t}\right)\\
&\quad-\frac{\Delta t}{2}\left(\frac{U^{N+1}-U^{N}}{\Delta t}\right)^T M_B\left(\frac{U^{N+1}-U^{N}}{\Delta t}\right).
\end{aligned}$$

Thus the equation (3.7) is reduced to

$$\begin{aligned}
&\left(\frac{U^{N+1}-U^{N}}{\Delta t}\right)^T\left(M-\frac{\Delta t}{2}M_B\right)\frac{U^{N+1}-U^{N}}{\Delta t}+(U^{N+1})^T SU^{N+1}\\
&\quad-(U^{N+1})^T S(U^{N+1}-U^{N})+\frac{\Delta t}{2}\sum_{n=0}^{N}\left(\frac{U^{n+1}-U^{n-1}}{\Delta t}\right)^T M_B\left(\frac{U^{n+1}-U^{n-1}}{\Delta t}\right)\\
&=\Delta t\sum_{n=0}^{N}\left(\frac{U^{n+1}-U^{n-1}}{\Delta t}\right)^T MG^{n}.
\end{aligned}\tag{3.8}$$

From the Lemma 1,

$$\begin{aligned}
&\left(\frac{U^{N+1}-U^{N}}{\Delta t}\right)^T\left(M-\frac{\Delta t}{2}M_B\right)\frac{U^{N+1}-U^{N}}{\Delta t}\\
&\qquad\ge\left\{1-\frac{\Delta t}{2}\frac{\lambda_{\max}(M_B)}{\lambda_{\min}(M)}\right\}\left\|\frac{U^{N+1}-U^{N}}{\Delta t}\right\|_M^2\ge\left(1-\frac{3C\,\Delta\,t}{h}\right)\left\|\frac{U^{N+1}-U^{N}}{\Delta t}\right\|_M^2.\\
&(U^{N+1})^T S(U^{N+1}-U^{N})=(U^{N+1},U^{N+1}-U^{N})_S\le\|U^{N+1}\|_S\cdot\|U^{N+1}-U^{N}\|_S,
\end{aligned}$$

and

$$\Delta t\sum_{n=0}^{N}\left(\frac{U^{n+1}-U^{n-1}}{\Delta t}\right)^T M_B\left(\frac{U^{n+1}-U^{n-1}}{\Delta t}\right)\ge 0.$$

If we take Δt such that

$$\alpha=1-\frac{3C\,\Delta\,t}{h}>0,\tag{3.9}$$

then

$$\begin{aligned}
\text{left of (3.8)}\quad&\ge\alpha\left\|\frac{U^{N+1}-U^{N}}{\Delta t}\right\|_M^2+\|U^{N+1}\|_S^2-\|U^{N+1}\|_S\|U^{N+1}-U^{N}\|_S\\
&\ge\alpha\left\|\frac{U^{N+1}-U^{N}}{\Delta t}\right\|_M^2+\|U^{N+1}\|_S^2-\sqrt{\frac{\lambda_{\max}(S)}{\lambda_{\min}(M)}}\,\Delta\,t\|U^{N+1}\|_S\left\|\frac{U^{N+1}-U^{N}}{\Delta t}\right\|_M.
\end{aligned}$$

From the Lemma 1,

$$\begin{aligned}
\text{left of (3.8)}\quad&\ge\alpha\left\|\frac{U^{N+1}-U^{N}}{\Delta t}\right\|_M^2+\|U^{N+1}\|_S^2\\
&\quad-\frac{3\sqrt{6}C}{h}\,\Delta\,t\|U^{N+1}\|_S\left\|\frac{U^{N+1}-U^{N}}{\Delta t}\right\|_M\\
&=\left(1-\frac{3\sqrt{3}}{\sqrt{2\alpha}}\frac{C\,\Delta\,t}{h}\right)\left\{\alpha\left\|\frac{U^{N+1}-U^{N}}{\Delta t}\right\|_M^2+\|U^{N+1}\|_S^2\right\}\\
&\quad+\frac{3\sqrt{3}}{\sqrt{2\alpha}}\frac{C\,\Delta\,t}{h}\left\{\sqrt{\alpha}\left\|\frac{U^{N+1}-U^{N}}{\Delta t}\right\|_M-\|U^{N+1}\|_S\right\}^2\\
&\ge\left(1-\frac{3\sqrt{3}}{\sqrt{2\alpha}}\frac{C\,\Delta\,t}{h}\right)\alpha\left\|\frac{U^{N+1}-U^{N}}{\Delta t}\right\|_M^2
\end{aligned}\tag{3.10}$$

Take Δt once again such that

$$1 - \frac{3\sqrt{3}}{\sqrt{2\alpha}} \frac{C \, \Delta \, t}{h} \geq \varepsilon > 0, \tag{3.11}$$

where ε is a positive number small enough, which will be determined later. It implies

$$27 \left(\frac{C \, \Delta \, t}{h} \right)^2 + 6(1-\varepsilon)^2 \frac{C \, \Delta \, t}{h} - 2(1-\varepsilon)^2 \leq 0, \tag{3.12}$$

i.e.,

$$\frac{C \, \Delta \, t}{h} \leq \frac{-3(1-\varepsilon)^2 + (1-\varepsilon)\sqrt{9(1-\varepsilon)^2 + 54}}{27}. \tag{3.13}$$

It is easy to see that (3.12) (consequently, (3.13)) contains (3.9). (3.13) can be replaced by the following stronger condition

$$\frac{C \, \Delta \, t}{h} \leq (1-\varepsilon)^2 \frac{-3+\sqrt{63}}{27} = (1-\varepsilon)^2 \frac{-1+\sqrt{7}}{9}.$$

If we take $\varepsilon = 1 - \sqrt{\frac{1.62}{-1+\sqrt{7}}}$, the condition mentioned above becomes

$$\frac{C \, \Delta \, t}{h} \leq 0.18.$$

Then from (3.10),

$$\text{left of (3.8)} \quad \geq 0.0113 \left\| \frac{U^{N+1} - U^N}{\Delta t} \right\|_M^2. \tag{3.14}$$

For the right-hand side of (3.8) we have

$$\Delta t \sum_{n=0}^{N} \left(\frac{U^{n+1} - U^{n-1}}{\Delta t} \right)^T M G^n \leq 2 \, \Delta \, t \sum_{n=0}^{N} \left(\frac{U^{n+1} - U^n}{\Delta t} \right)_+^T M G_+^n,$$

where the notation $(\quad)_+$ denotes a vector the entries of which are absolute values of entries of the original vector. Obviously,

$$|G_i^n| \leq C^2 \|f\|_\infty \quad (i = 1, \cdots, m).$$

Introduce the m-dimensional vector

$$E = \{1, 1, \cdots, 1\}^T.$$

Then

$$\begin{aligned} \Delta t \sum_{n=0}^{N} \left(\frac{U^{n+1} - U^{n-1}}{\Delta t} \right)^T M G^n &\leq 2 \, \Delta \, t \sum_{n=0}^{N} \left(\frac{U^{n+1} - U^n}{\Delta t} \right)_+^T \cdot C^2 \|f\|_\infty M E \\ &= 2 \, \Delta \, t \sum_{n=0}^{N} \left(\left(\frac{U^{n+1} - U^n}{\Delta t} \right)_+, C^2 \|f\|_\infty E \right)_M \\ &\leq 2 \, \Delta \, t \sum_{n=0}^{N} \left\| \frac{U^{n+1} - U^n}{\Delta t} \right\|_M \cdot C^2 \|f\|_\infty \|E\|_M \\ &\leq 0.0113 \, \Delta \, t \sum_{n=0}^{N} \left\| \frac{U^{n+1} - U^n}{\Delta t} \right\|_M^2 + \frac{1}{0.0113} C^4 \|f\|_\infty^2 \, \Delta \, t \sum_{n=0}^{N} \|E\|_M^2. \end{aligned} \tag{3.15}$$

From (3.14) and (3.15), it is obtained that

$$\begin{gathered} \left\| \frac{U^{N+1} - U^N}{\Delta t} \right\|_M^2 \leq \Delta t \sum_{n=0}^{N} \left\| \frac{U^{n+1} - U^n}{\Delta t} \right\|_M^2 + K \|f\|_\infty^2, \\ K = \frac{C^4}{(0.0113)^2} \, \Delta \, t \sum_{n=0}^{N} \|E\|_M^2. \end{gathered}$$

From the discrete Gronwall's inequality[12] we get

$$\max_{0\leq n\leq N}\|V^{n+1}\|_M^2=\max_{0\leq n\leq N}\left\|\frac{U^{n+1}-U^n}{\Delta t}\right\|_M\leq K\|f\|_\infty^2\exp\{2T\}=C_1'\|f\|_\infty^2.$$

That is

$$\max_{0\leq n\leq N}\|V^{n+1}\|_M\leq\sqrt{C_1'}\|f\|_\infty. \tag{3.16}$$

Moreover,

$$\|U^{n+1}\|_M\leq\Delta t\{\|V^{n+1}\|_M+\|V^n\|_M+\cdots+\|V^1\|_M\}.$$

It follows

$$\max_{0\leq n\leq N}\|U^{n+1}\|_M\leq T\sqrt{C_1'})\|f\|_\infty. \tag{3.17}$$

Adding (3.16) and (3.17), we obtain (3.6), which completes the proof.

Theorem 2. For the finite element space of uniform square elements and bilinear basis functions, if the condition

$$\frac{C\triangle t}{h}\leq 0.3 \tag{3.18}$$

is satisfied, then the scheme (2.10) is stable in the sense of (3.6).

Proof. The approach is similar to the Theorem 1. But in the present case,

$$\alpha=1-\frac{2C\triangle t}{h}$$

and

$$\frac{\lambda_{\max}(S)}{\lambda_{\min}(M)}\leq\frac{16C^2}{h^2}$$

from the Lemma 2. Thus the condition corresponding to (3.11) should be

$$1-\frac{2C\triangle t}{\sqrt{\alpha}h}\geq\varepsilon>0.$$

The conditions (3.12) becomes

$$4\left(\frac{C\triangle t}{h}\right)^2+2(1-\varepsilon)^2\frac{C\triangle t}{h}-(1-\varepsilon)^2\leq 0.$$

If we take $\varepsilon=1-\sqrt{\frac{1.2}{-1+\sqrt{5}}}$, the stability condition

$$\frac{C\triangle t}{h}\leq 0.3$$

can be obtained, which completes the proof.

About the scheme (2.11), i.e., the non-reflecting boundary condition of the second order, we have the following Theorem 3 and 4. Their proofs are similar to those of the Theorem 1 and 2, but are more complicated. We will not write them, and only give the conclusions.

Theorem 3. Suppose that $\partial f/\partial t$ is bounded when $t\in[0,T],(x,y)\in\Omega$ and $a\leq CT,b\leq CT$. For the finite element space of uniform right-angled triangle elements and linear basis functions, if the condition

$$\frac{C\triangle t}{h}\leq\frac{h^2}{52.17C^2T^2} \tag{3.19}$$

is satisfied, then for any $N \in Z^+, 0 < (N+1)\triangle t < T$, there exists a constant C_2 such that the solution of (2.11) is subjuct to the inequality

$$\max_{0\leq n\leq N}\|U^n\|_M + \max_{0\leq n\leq N}\|V^n\|_M + \max_{0\leq n\leq N}\left\|\frac{V^{n+1}-V^n}{\Delta t}\right\|_M \leq C_2\left\|\frac{\partial f}{\partial t}\right\|_\infty, \tag{3.20}$$

i.e., the scheme (2.11) is stable.

Theorem 4. Suppose that $\partial f/\partial t$ is bounded when $t \in [0,T], (x,y) \in \Omega$ and $a \leq CT, b \leq CT$. For the finite element space of uniform square elements and bilinear basis functions, if the condition

$$\frac{C\triangle t}{h} \leq \frac{h^2}{40C^2T^2}$$

is satisfied, then the scheme (2.11) is stable in the sense of (3.20).

§4. Numerical experiments

In the numerical computation of the following examples of the acoustic wave equation the nonreflecting boundary conditions (1.2) and (1.5) were used. The results corresponding to the two kinds of boundary conditions cannot be distinguished.

Example 1. Acoustic wave equation. $\Omega = \{(x,y) : -1000m < x < 1000m, 0 < y < 1000m\}, C = 3200m/\sec$, and

$$f(x,y,t) = g(t)\delta(x)\delta(y-500),$$

where

$$g(t) = \begin{cases} 1000\sin 50t\cdot\exp\left\{-2500\left(t-\frac{\pi}{100}\right)^2\right\}, & 0 \leq t \leq \frac{\pi}{50} \\ 0 & t > \frac{\pi}{50}. \end{cases} \tag{4.1}$$

The square meshes are used. Take $h = 20m, T = 3\sec, \Delta t = 0.002\sec$. The numerical results are shown in Fig. 1.

Example 2. Acoustic wave equation. The computational domain is the same as in Example 1. It consists of two parts, in which the wave velocities are

$$C^I = 3300m/\sec, \qquad C^{II} = 2000m/\sec,$$

respectively. On the boundary $y = 0$ the following Dirichlet condition is imposed:

$$u(x,y,t)|_{y=0} = g(t)\delta(x),$$

where $g(t)$ is the function (4.1). The square meshes are used. We take $h = 10m, T = 3\sec$ and $\Delta t = 0.001\sec$. The numerical results are shown in Fig.2.

The results have shown the effectiveness of the non-reflecting boundary conditions and confirmed the theoretical conclusions, that is, the computations are stable when the stability conditions given in this paper are satisfied.

The non-reflecting boundary condition (1.5) has been also successfully applied to the isotropic and anisotropic elastic wave equations and the two-phase wave equation. Due to the limited space of paper, we will not exhibit the figures here.

The numerical experiments were conducted by using our program package SWS (a finite element program package for the numerical simulation of seismic wave propagation).

References

[1] D. Givoli, Numerical Methods for Problems in Infinite Domains, Elsevier Science Publishers B. V., 1992.

[2] J. Lysmer and R. L. Kuhlemeyer, Finite Dynamic Model for Infinite Media, J.Eng. Mech. Div. ASCE, Vol.95, pp.859–877, 1969.

[3] J. P. Berenger, A perfectly matched layer for the absorption of electromagnetic waves, J. Comput. Physics, Vol.114, pp.185–200, Oct. 1994.

[4] R. Clayton and B. Engquist, Absorbing Boundary Conditions for Acoustic and Elastic Wave Equations, Bull. Seismol. Soc. Amer., Vol.67, pp.1529–1540, 1977.

[5] B. Engquist and A. Majda, Absorbing Boundary Conditions for the Numerical Simulation of Waves, Math. Comput., V ol., 31, pp.629–652, 1977.

[6] B. Engquist and A. Majda, Radiation Boundary Conditions for Acoustic and Elastic Calculations, Comm. Pure Appl. Math., Vol.32, pp.313–357, 1979.

[7] R. L. Higdon,Absorbing Boundary Conditions for Difference Approximations to the Multi-Dimensional Wave Equations, Math. Comput., Vol.47, pp.437–459, 1986.

[8] Z. P. Liao, H. L. Wong, B. P. Yang and Y. F. Yuan, A Transmitting Boundary for Transient Wave Analysis, Scientia Sinica (Series A), Vol. XXVII, No.10, pp.1063–1076, 1984.

[9] Z. P. Liao and H. L. Wong, A Transmitting Boundary for the Numerical Simulation of Elastic Wave Propagation, Sil Dynamics and Earthquaka Engineering, Vol.3, No.4, pp.174–183, 1984.

[10] Xiumin Shao and Zhiling Lan, Absorbing Boundary Conditions for Anisotropic Elastic Wave Equations, J. Geophy., 1995, Vol.38, Suplement I, pp.56–73, 1995.

[11] Xiumin Shao and Zhiling Lan, Stability Analysis of Finite Element Methods for the Acoustic Wave Equation with Absorbing Boundary Conditions (to appear).

[12] Yulin Zhou, Applications of Discrete Functional Analysis to the Finite Difference Method, International Academic Publishers, 1990.

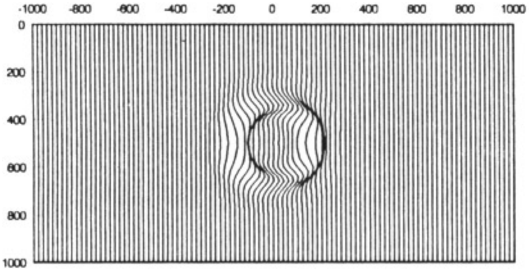

t=0. 10sec

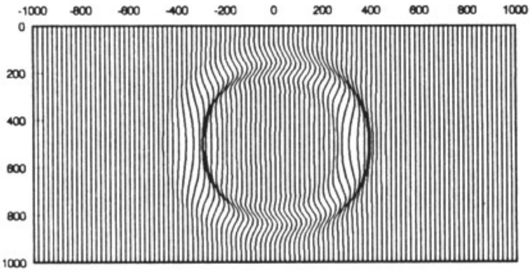

t=0. 16sec

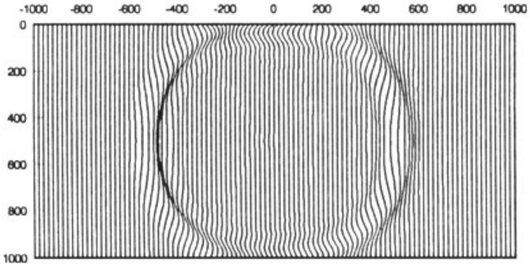

t=0. 22sec

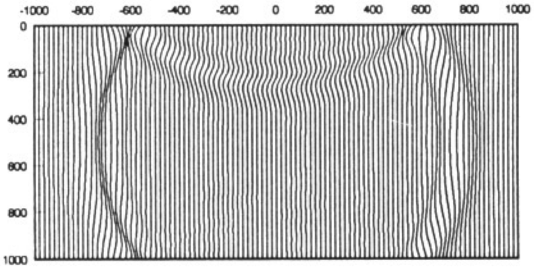

t=0. 30sec

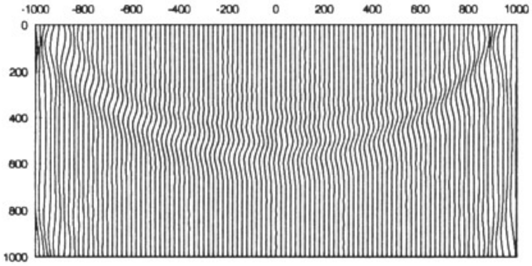

t= 0. 50sec

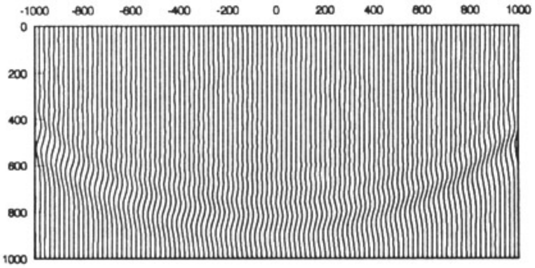

t=0. 60sec

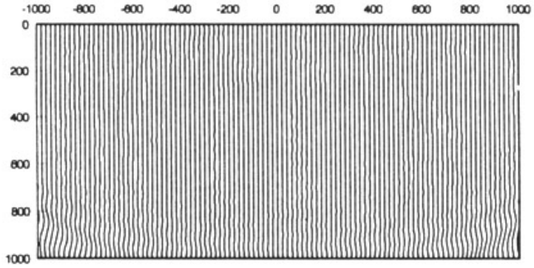

t=0. 80sec

Fig 1. Wave field of Example 1 with the second order absorbing boundary condition

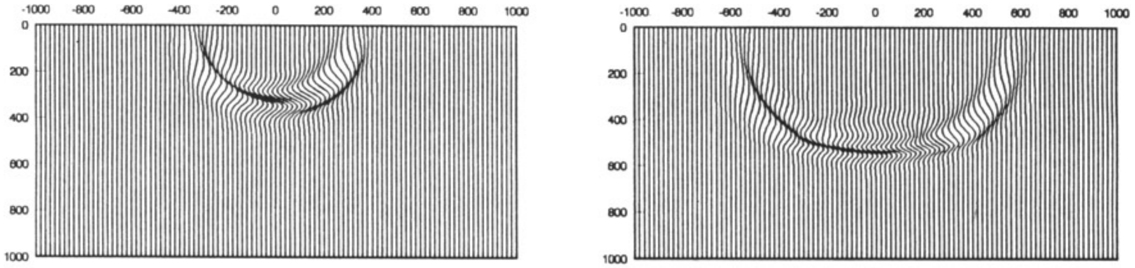

t=0. 150sec

t=0. 225sec

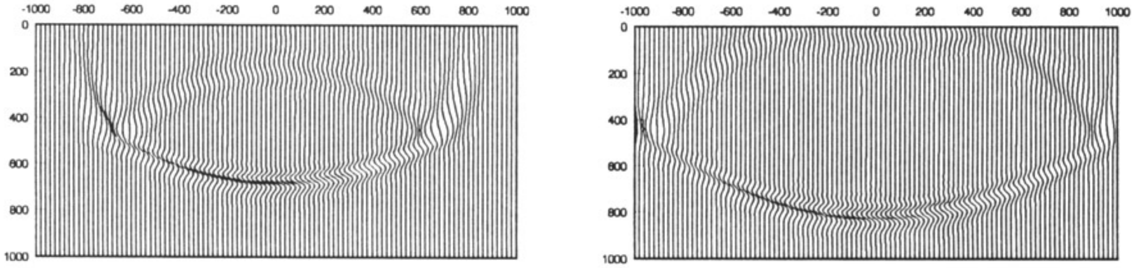

t=0. 300sec

t=0. 375sec

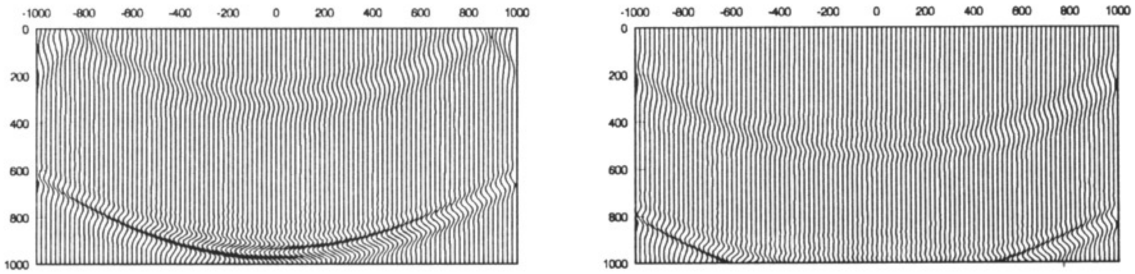

t=0. 450sec

t=0. 525sec

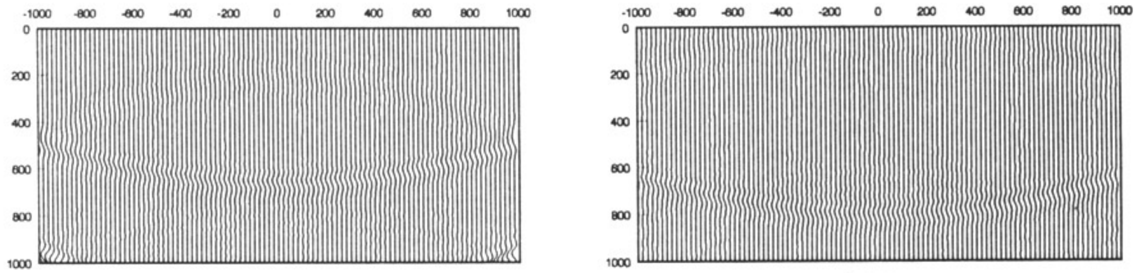

t=0. 600sec

t=0. 675sec

Fig 2. Wave field of Example 2 with the second order absorbing boundary condition

BOUNDARY ELEMENT METHOD FOR SH WAVES IN ELASTIC HALF PLANE WITH STOCHASTIC AND HETEROGENEOUS PROPERTIES

Yao, Z.H. and Xiang, J.L.
(Department of Engineering Mechanics, Tsinghua University, Beijing, China 100084)

Abstract

In this paper a scheme of stochastic boundary element method for wave propagation in elastic half plane with stochastic and heterogeneous properties has been presented. As an example the problem of SH wave propagation in random stratified media is studied. Some statistical measures of the response are presented in the corresponding numerical examples.

Introduction

Wave propagation is of great importance in earthquake engineering, ocean engineering and in noise control engineering. Heterogeneity is a common character of the medium in such problems, especially in earthquake and ocean engineering. On the other hand, randomness arises because of uncertainties associated with the geometry, boundary and initial conditions, and the applied loads. It is well known that the material properties of soil medium in seismic wave propagation problems are not well defined generally, and it can be addressed a random field. Although the randomness in wave propagation may be small, their combination may results in large and unexpected excursions of the response. Therefore it is of practical interest to develop methods to address the wave propagation problems in random heterogeneous medium.

At present a number of methods have been developed for the analysis of random or stochastic systems, such as Monte-Carlo method, perturbation methods, etc.[1-3]. In recent years, many researchers have begun developing stochastic finite element methods[3-6], as well as stochastic boundary element methods[7-11] for the engineering systems with randomness.

So far the stochastic boundary element method is based on the perturbation methods. The basic idea is to decompose the random operator (i.e., a partial differential equation with random coefficients) into a deterministic part and a zero-mean random part. Then the problem may be reduced into an integral equation with a random kernel. That is built using the Green's function of the deterministic part of the operator as a base, plus a random forcing function. The random kernel and the field variable can be written in terms of Neumann or Taylor series, a set of recursive integral equations is generated, and the equations can be solved by boundary element method. The main problem here is that although the solution process is recursive for the field variables, it is not so for the statistical measures of the field variable.

Boundary element methods are suitable for a wide range of engineering problems. It is well known that the boundary element methods are based on the knowledge of the fundamental solution or free space Green's function of the problem at hand. When the problem considered involves a heterogeneous medium, such fundamental solutions are not available. Some of the researchers use very complicated fundamental solution for problems in layered media[12], which is difficult and inefficient to implement in coding.

As to the wave propagation problem in heterogeneous media, there exists some methods to deal with the heterogeneity, such as the layered media model. In each layer the homogeneous free space Green's function can be used to generate the boundary element equation, then the connective conditions on the interfaces are used to get the global algebra equations. Other researchers use specific Green's function for the heterogeneous media, such as Shaw and Makris[13] used a transformation relation to reduce the heterogeneous Helmhlotz equation into a homogeneous one. The homogeneous Green's function is used to built a specific Green's function for wave propagation problem in heterogeneous media. Although their method requires that the material properties must satisfy a special relationship, it is justified that there still exist some degrees of freedom in this relationship to fit the real media. In this paper we have adopted the idea of transforming a heterogeneous Helmholtz equation into a homogeneous one in [13]. A deterministic boundary element formulation based on a boundary element method for harmonic SH wave propagation problem in homogeneous elastic half space is developed. It is applied to study the scattering of harmonic SH wave by sub-surface topography in a heterogeneous half space.

Thereafter, a heterogeneous random model for the material properties of the heterogeneous half space is proposed and a stochastic boundary element method is developed by introducing the perturbation technique.

The problem of harmonic SH wave propagation in a random stratified half space is studied. Some statistical measures of the response displacement on the surface of an irregular topography are presented in the corresponding numerical examples. It is demonstrated that the stochastic boundary element method is quite efficient.

Governing Equations

The time harmonic SH wave propagation problem in heterogeneous media is governed by the heterogeneous Helmholtz equation

$$\nabla\cdot\left[\mu(\boldsymbol{r})\nabla w(\boldsymbol{r})\right]+\rho(\boldsymbol{r})\omega^{2}w(\boldsymbol{r})=0 \tag{1}$$

where $\boldsymbol{r}$ stands for the position vector, $\mu(\boldsymbol{r})$, $\rho(\boldsymbol{r})$ stand for the shear modulus and the density of the material. They are position dependent material properties. The equation is written in the dimensionless form, where

$$\mu(\boldsymbol{r})=\mu_{(\text{dimensional})}/\mu_{\text{ref}},\quad \rho(\boldsymbol{r})=\rho_{(\text{dimensional})}/\rho_{\text{ref}},\quad \omega(\boldsymbol{r})=\omega_{(\text{dimensional})}/\omega_{\text{ref}}$$

$$w=w_{(\text{dimensional})}/L_{\text{ref}},\quad (x,y,z)=(x,y,z)_{(\text{dimensional})}/L_{\text{ref}},\quad \rho_{\text{ref}}\omega_{\text{ref}}^{2}L_{\text{ref}}^{2}/\mu_{\text{ref}}=1$$

As the referenced length it is taken the characteristic length of the sub-topography.

The boundary conditions at the free surface of a half space and at the surface of a sub topography on the half space (Fig. 1) are:

$$\left.\frac{\partial w}{\partial y}\right|_{y=0}=0,\qquad \left.\mu\frac{\partial w}{\partial n}\right|_{r\in S}=0 \tag{2}$$

By setting $N(\boldsymbol{r})=\rho(\boldsymbol{r})\omega^{2}$, a simple transform of the variable $\psi(\boldsymbol{r})=\mu^{1/2}(\boldsymbol{r})w(\boldsymbol{r})$ turns equation (1) into

$$\mu^{1/2}\nabla^{2}\psi+\left\{\frac{1}{4}\mu^{-3/2}(\nabla\mu\cdot\nabla\mu)-\frac{1}{2}\mu^{-1/2}\nabla^{2}\mu+\mu^{-1/2}N(\boldsymbol{r})\right\}\psi(\boldsymbol{r})=0 \tag{3}$$

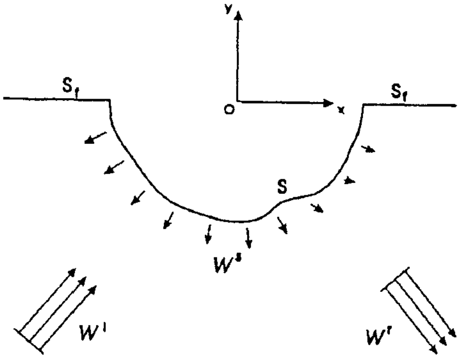

Fig. 1 Wave propagation in half space with sub-topography

By further requiring

$$(\nabla\mu\cdot\nabla\mu)/(4\mu^2)-\nabla^2\mu/(2\mu)+N/\mu=k^2 \tag{4}$$

where k is assumed to be a constant, equation (3) can be reduced to a standard Helmholtz equation

$$\nabla^2\psi+k^2\psi(\boldsymbol{r})=0 \tag{5}$$

The boundary condition equation (2) can be transformed into a new form as well, which is described by variable $\psi(\boldsymbol{r})$. Therefore $\psi(\boldsymbol{r})$ must satisfy the following differential equation and boundary conditions:

$$\begin{cases} \nabla^2\psi+k^2\psi=0 & \\ \left.\dfrac{\partial\left(\mu^{-1/2}\psi\right)}{\partial y}\right|_{y=0}=0 & \text{on } S_{\mathrm{f}} \\ \mu\dfrac{\partial\left(\mu^{-1/2}\psi\right)}{\partial n}=0 & \text{on } S \end{cases} \tag{6}$$

By further requiring the shear modulus of the material satisfies

$$\left.\frac{\partial\mu}{\partial y}\right|_{y=0}=0 \tag{7}$$

the boundary condition on the free surface of the half space can be simplified,

$$\left.\frac{\partial\psi}{\partial y}\right|_{y=0}=0 \qquad \text{on } S_{\mathrm{f}} \tag{8}$$

Hence we have transformed the problem of wave propagation in a heterogeneous media into solving a standard homogeneous Helmholtz equation with some restriction on material properties of the heterogeneous media. The Green's function of a homogeneous Helmholtz equation for elastic half space is well known, which can be written as

$$G^*=\frac{i}{4}\left[\mathrm{H}_0^{(2)}(k\sigma_1)+\mathrm{H}_0^{(2)}(k\sigma_2)\right] \tag{9}$$

where $\mathrm{H}_0^{(2)}(*)$ the second kind zero order Hankel function, and

$$\begin{cases} \sigma_1 = \sqrt{\left(x - x_{\rm p}\right)^2 + \left(y - y_{\rm p}\right)^2} \\ \sigma_2 = \sqrt{\left(x - x_{\rm p}\right)^2 + \left(y + y_{\rm p}\right)^2} \end{cases} \tag{10}$$

The total field $\psi(r)$ can be decomposed into an analytical part $\psi^{\rm a}$ and a scattering part $\psi^{\rm s}(r)$. The analytical part $\psi^{\rm a}$ satisfies Helmholtz equation and the free surface boundary condition (8), which is composed of the incident and reflective wave in a free surface half space without the irregular sub-topography. Therefore $\psi^{\rm s}$ satisfies not only Helmholtz equation and the free surface boundary condition on $S_{\rm f}$, but also the irregular sub-topography boundary condition

$$\begin{aligned} &\nabla^2 \psi^{\rm s} + k^2 \psi^{\rm s} = 0 \\ &\frac{\partial \psi^{\rm s}}{\partial y} = 0 \qquad \text{on } S_{\rm f} \\ &\frac{\partial \psi^{\rm s}}{\partial n} = \frac{1}{2\mu}\frac{\partial \mu}{\partial n}\psi^{\rm s} + \left(\frac{1}{2\mu}\frac{\partial \mu}{\partial n}\psi^{\rm a} - \frac{\partial \psi^{\rm a}}{\partial n}\right) \qquad \text{on } S \end{aligned} \tag{11a-c}$$

Boundary Element for Scattering Wave

By setting $Q^{\rm s} = \dfrac{\partial \psi^{\rm s}}{\partial n}$, $Q^* = \dfrac{\partial G^*}{\partial n}$, and $\dfrac{\partial}{\partial n}$ denoting the differentiation in the outward normal direction n on S, applying Green's theorem with Green's function on equation (9), the displacement function $\psi^{\rm s}$ and the derivative $Q^{\rm s}$ can be related through integral equation. This can be written as

$$C(p)\psi^{\rm s}(p) = \int_{\rm S} \left[G^*(p,q)Q^{\rm s}(q) - Q^*(p,q)\psi^{\rm s}(q)\right] {\rm d}S(q) \tag{12}$$

A numerical solution can be obtained by discretizing the surface S and approximating the integrals in equation (12) by a weighted sum of functions evaluated at the surface points. If m is the total number of points on the surface, then equation (12) can be approximated by a set of linear algebraic equations with order m,

$$\boldsymbol{H}\boldsymbol{\Psi}^{\rm s} = \boldsymbol{G}\boldsymbol{Q}^{\rm s} \tag{13}$$

where $\boldsymbol{H}$, $\boldsymbol{G}$ are square matrices whose elements are computed by numerical integration of the kernel functions. The elements of the vectors $\Psi^{\rm s}$ and $Q^{\rm s}$ are the displacements and derivatives at nodal points on surface S, respectively. In order to solve this algebraic equation (13), we should apply the corresponding boundary conditions. The boundary condition equation (11c) can be written in a matrix form

$$Q^{\rm s} = A\Psi^{\rm s} + Q^{{\rm a}*} \tag{14a}$$

$$Q^{{\rm a}*} = A\Psi^{\rm a} - Q^{\rm a} \tag{14b}$$

where A is a diagonal square matrix, the element can be evaluated by

$$A_{ii} = \left(\frac{1}{2\mu}\frac{\partial \mu}{\partial n}\right), \tag{15}$$

The elements of vector $Q^{{\rm a}*}$ are combination of the analytical displacements and their derivatives at the surface points. Substituting equation (14a) into (13) leads to the final algebraic equations

$$(H - GA)\Psi^{s} = GQ^{a*} \tag{16}$$

where the unknown displacements Ψ^{s} are on the left side and the known values Q^{a*} are on the right side. Solution of equation (16) yields approximate value for the unknown displacement on the surface points. Once the scattering displacement Ψ^{s} and its derivatives Q^{s} are known on the entire surface, the displacement of the total field Ψ can be calculated using the relationship between total field and the scattering and analytical fields. The original displacement in the heterogeneous media can also be calculated using the transformation relationship between $\psi(\boldsymbol{r})$ and $w(\boldsymbol{r})$.

Specific Material Variation

Equation (4) and (7) forces a relationship between $\mu(\boldsymbol{r})$ and $N(\boldsymbol{r})$, hence it is a limited approach to such problems. This restriction may be justified by the fact that the actual variations of material properties are generally only known at a few locations and fit by some convenient functional form anyway. The final judgement lies on how many degrees of freedom exist in this relationship. According to Shaw and Makris[11], equation (4) can be simplified by a transformation, $V = \mu^{1/2}$, leading to

$$\nabla^2 V - N/V + k^2 V = 0 \tag{17a}$$

$$\left.\frac{\partial V}{\partial y}\right|_{y=0} = 0 \tag{17b}$$

as the required relationship and boundary condition. If a relationship between N and V is allowed, one choice would be

$$N(\boldsymbol{r}) = A(\boldsymbol{r})V(\boldsymbol{r}) + B_0 V^2(\boldsymbol{r}) \tag{18}$$

where A is a function of position and B_0 is a constant. This leads to

$$\nabla^2 V + \left(k^2 - B_0\right)V = A(\boldsymbol{r}) \tag{19}$$

which is a linear Helmholtz equation with constant coefficients. There will be some degrees of freedom in the solution of homogeneous equation plus many degrees of freedom chosen for $A(\boldsymbol{r})$.

This approach may be illustrated by the special case of stratified media, where $\mu(\boldsymbol{r})$ and $\rho(\boldsymbol{r})$ depend only on one spatial coordinate, e.g., the depth y. Then equation (19) is reduced to an ordinary differential equation with constant coefficients whose solution can be written as

$$V(y) = a_1 \mathrm{e}^{-\lambda y} + a_2 \mathrm{e}^{\lambda y} + V^{c}(y) \tag{20}$$

where $\lambda = B_0 - k^2 > 0$, $V^{c}(y)$ is a particular solution of equation (19) corresponding to the forcing term $A(y)$. Consider a semi-infinite region with $y < 0$, then a_1 must vanish to have finite μ as y approaches infinity. If we chose a decaying exponential plus a constant term as $A(y)$, e.g.,

$$A(y) = \alpha_0 + \sum_{j=1}^{m} \alpha_j \mathrm{e}^{\gamma_j y} \tag{21}$$

Consider the case with a single exponential term in $A(y)$, i.e., m=1, the corresponding solution V is

$$V(y) = a_2 \mathrm{e}^{\lambda y} - \alpha_0/\lambda^2 + \alpha_1 \mathrm{e}^{\gamma_1 y}/\left(\gamma_1^2 - \lambda^2\right) \tag{22}$$

The boundary condition, e.g., equation (17b) requires

$$a_2 \lambda + \alpha_1 \gamma_1/\left(\gamma_1^2 - \lambda^2\right) = 0 \tag{23}$$

There will be five independent parameters, i.e., α_0, α_1, λ, γ_1, a_2, which can be determined by five independent parameters of material properties at different locations.

Two examples for the distribution of the material properties with coordinate y are illustrated in Fig. 2a, 2b. In Fig. 2a the values of the parameters are $\alpha_0 = -0.0387$, $\alpha_1 = 0.319$, $\lambda = 0.197$, $\gamma_1 = 3.05$, and $a_2 = -0.535$, and the corresponding material properties at different locations are $\mu(0) = 0.25$, $\mu(-\infty) = 1.0$, $\rho(0) = 0.4$, $\rho(-\infty) = 1.0$, $\mu(-5.0) = 0.64$, $\omega = 0.5\pi$. $C(y)$ is defined as $V/N^{1/2}$.

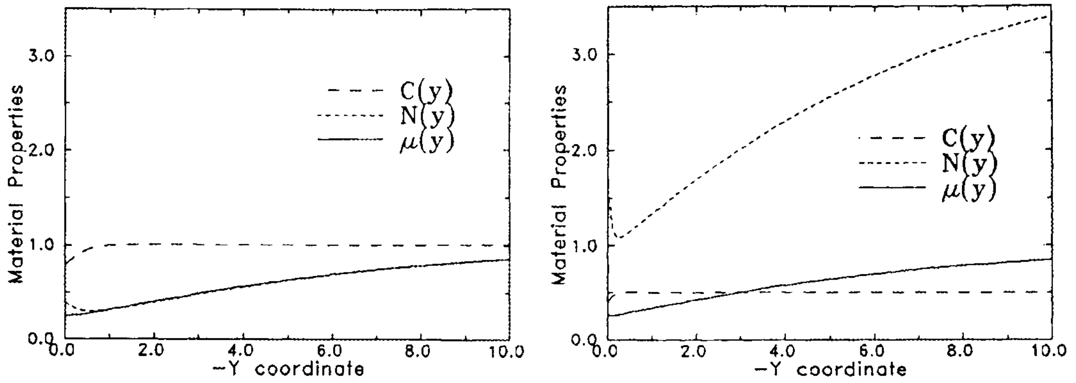

(a) Case 1 (b) Case 2

Fig. 2 Distributions of material properties along depth

In Fig.2b the material properties are the same as in Fig. 2a, at the given positions, the only difference is $\omega = 1.0\pi$, and the values of the corresponding parameters are $\alpha_0 = -0.0347$, $\alpha_1 = 1.22$, $\lambda = 0.184$, $\gamma_1 = 12.9$, $a_2 = -0.507$. These examples are hypothetical and are given to illustrate the potential uses of this approach.

Random Heterogeneous Model and Perturbation Expansions

1. Random heterogeneous model

Randomness arises because of uncertainties associated with material properties, geometry, boundary and initial conditions, and applied loads. The concept of uncertainties can be classified into three categories. (1) Uncertainty regarding constant system parameters results in a spread or density of possible parameter values, i.e., random variable model. (2) Uncertainty regarding of parameters as time-dependent processes, where the statistics of each process may be either time-dependent or -independent, i.e., random function model. (3) Uncertainty with respect to the behavior of parameters as functions of spatial coordinates, i.e., random stochastic field model.

In extending the boundary element formulation to include uncertainties, we have used the random field model for the heterogeneous media at first. Then we use the transformation technique again so as to transfer the random heterogeneous field model into a homogeneous random variable model.

Provided that the material properties of the stratified heterogeneous half space described above are random field, i.e., $\mu = \mu(r,\gamma)$, $\rho = \rho(r,\gamma)$, where γ represents one realization in a random experiment. By setting $N = \rho(r,\gamma)\,\omega^2 = N(r,\gamma)$, $V = \mu^{1/2} = V(r,\gamma)$, which are also random fields. Assuming μ and N are weak random field, we can decompose the random fields V and N into mean value parts, which are position dependent and deterministic, and random fluctuation parts, which are position-independent and have zero expectation values, i.e.,

$$V(r,\gamma) = \bar{V}(r) + \varepsilon V_1(\gamma) \tag{24a}$$

$$N(\boldsymbol{r},\gamma) = \overline{N}(\boldsymbol{r}) + \varepsilon N_1(\gamma) \tag{24b}$$

where $V_1(\gamma)$, $N_1(\gamma)$ are random variables which are position independent.

Now we restrict our work to the specific heterogeneous media described above. Hence the wave umber k in equation (17a) becomes a random variable, and can be expressed in terms of series of small parameter ε, which is deterministic, if the orders higher than one are omitted, we have

$$k(\gamma) = \bar{k} + \varepsilon k_1(\gamma) \tag{25}$$

Substituting equations (25) and (24a,b) into equation (17a), and equating terms of the same order in ε, produces

$$k(\gamma) = \frac{\overline{N}}{\overline{V}^2} - \frac{\nabla^2 \overline{V}}{\overline{V}} \tag{26a}$$

$$k_1 = f(\boldsymbol{r}) V_1(\gamma) + g(\boldsymbol{r}) N_1(\gamma) \tag{26b}$$

$$\begin{cases} f(\boldsymbol{r}) = -\dfrac{1}{2\bar{k}}\left(\dfrac{\overline{N}}{\overline{V}^3} - \dfrac{\bar{k}}{\overline{V}}\right) \\ g(\boldsymbol{r}) = \dfrac{1}{2\bar{k}\overline{V}^2} \end{cases} \tag{27}$$

where the over line denotes the mean values of the functions.

2. Perturbation expansion

Above we have transformed the wave propagation problem in heterogeneous media into a wave scattering problem in homogeneous media, which is determined by the wave number k, see equations (11a-c). Now the wave number k is random variable, the dependence on k in equation (16) is indicated explicitly by writing

$$\{\boldsymbol{H}(k) - \boldsymbol{G}(k)\boldsymbol{A}(k)\}\boldsymbol{\Psi}^{\mathrm{s}}(k) = \boldsymbol{G}(k)\boldsymbol{Q}^{\mathrm{a}*}(k) = \boldsymbol{G}\left(\boldsymbol{A}(k)\boldsymbol{\Psi}^{\mathrm{a}} - \boldsymbol{Q}^{\mathrm{a}}\right) \tag{28}$$

Expanding the matrices and vectors $\boldsymbol{H}$, $\boldsymbol{G}$, $\boldsymbol{\Psi}$ about the mean value $\bar{k}$ with $\delta = \varepsilon k_1$ yields

$$\boldsymbol{H}(k) = \overline{\boldsymbol{H}} + \delta \overline{\boldsymbol{H}}_k + \frac{1}{2}\delta^2 \overline{\boldsymbol{H}}_{kk} + \cdots \tag{29a}$$

$$\begin{aligned} \boldsymbol{G}(k) &= \overline{\boldsymbol{G}} + \delta \overline{\boldsymbol{G}}_k + \frac{1}{2}\delta^2 \overline{\boldsymbol{G}}_{kk} + \cdots \\ \boldsymbol{\Psi}(k) &= \overline{\boldsymbol{\Psi}} + \delta \overline{\boldsymbol{\Psi}}_k + \frac{1}{2}\delta^2 \overline{\boldsymbol{\Psi}}_{kk} + \cdots \end{aligned} \tag{29b,c}$$

where the subscript k denotes partial differentiation (no summation implied for repeated subscripts) and the over line denotes evaluation of the functions at the respective mean values.

In order to simplify the calculation, we assume that the analytical part of $\boldsymbol{\Psi}$, e.g. $\boldsymbol{\Psi}^{\mathrm{a}}$, $\boldsymbol{Q}^{\mathrm{a}}$ are given at the mean value of k, i.e.,

$$\boldsymbol{\Psi}^{\mathrm{a}} = \overline{\boldsymbol{\Psi}}^{\mathrm{a}}, \qquad \boldsymbol{Q}^{\mathrm{a}} = \overline{\boldsymbol{Q}}^{\mathrm{a}} \tag{30a,b}$$

Another assumption is about matrix $\boldsymbol{A}$, i.e., $\boldsymbol{A}(k)$ is approximated by its mean value,

$$\boldsymbol{A}(k) = \boldsymbol{A}(\bar{k}) \tag{31}$$

By substitution of equations (29)-(31) into equation (28), and equating terms of the same order δ, it produces a set of recursive relations:

$$\begin{aligned}
&\left(\overline{H}-\overline{G}\,\overline{A}\right)\overline{\Psi}^{s}=\overline{G}Q^{a*}\\
&\left(\overline{H}-\overline{G}\,\overline{A}\right)\overline{\Psi}_{k}^{s}=\left(\overline{G}_{k}\overline{A}-\overline{H}_{k}\right)\overline{\Psi}^{s}+\overline{G}_{k}Q^{a*}\\
&\left(\overline{H}-\overline{G}\,\overline{A}\right)\overline{\Psi}_{kk}^{s}=\left(\overline{G}_{kk}\overline{A}-\overline{H}_{kk}\right)\overline{\Psi}^{s}+2\left(\overline{G}_{k}\overline{A}-\overline{H}_{k}\right)\overline{\Psi}_{k}^{s}+\overline{G}_{kk}Q^{a*}
\end{aligned} \qquad (32a\text{-}c)$$

The recursive system can be solved efficiently since the coefficient matrix on the left hand side is the same for all orders. Equations (32a-c) are solved recursively for the unknown component of $\overline{\Psi}^{s}$, $\overline{\Psi}_{k}^{s}$ and $\overline{\Psi}_{kk}^{s}$. The solutions are substituted appropriately into equation (29c), which is used below to evaluate the first and second order moments (mean and standard deviation) of the response.

3. Expectation of the response

The total wave field displacement ψ and the displacement w in heterogeneous media can be considered as functions of wave number k, and can be expanded into series of small paramete δ about the mean value $\bar{k}$. By applying the expectation operation to the expansions, such as equation (29c), and consider the relationship between ψ and w, the mean and variance of the displacement w can be achieved.

Given the mean and variance, it is possible to establish confidence bounds on specific realization of the displacement w. One possible approach for a random variable x with mean value η is to use the Chebyshev inequality,

$$P\{\eta - a < x < \eta + a\} \geq 1 - \frac{\sigma^2}{a^2} \qquad (33)$$

or the one sided versions

$$P\{x < \eta + a\} \geq \frac{a^2}{\sigma^2 + a^2} \qquad (34)$$

$$P\{x > \eta - a\} \geq \frac{a^2}{\sigma^2 + a^2} \qquad (35)$$

where P stands for the probability, η is the mean value of the random variable x, σ is the variance.

If the probability P is given, the deviation of the random variable can be calculated as

$$a = \pm\sqrt{\frac{P}{1-P}}\,\sigma \qquad (36)$$

then the probability $P\{\eta - a < x < \eta + a\}$ will be not less than the given value P. Therefore the deviation calculated here can be used to determine the confidence bound of the random variable corresponding to the probability P.

The method in this section is used by Ettouney, Benaroya and Wright (1989) for probabilistic structural analysis[10] and also for probabilistic acoustics analysis[11]. We have adopted this method for the probabilistic analysis of wave propagation in random heterogeneous media. Some applications are introduced in the following section.

Numerical Examples

The boundary element methods for deterministic as well as for random wave propagation problems were introduced in the previous sections. In this section we will first apply the methodology to the solution of the wave propagation in a deterministic stratified media, and then to the solution of wave propagation in a random heterogeneous media.

1. Wave scattering by semi-circular canyon —deterministic case

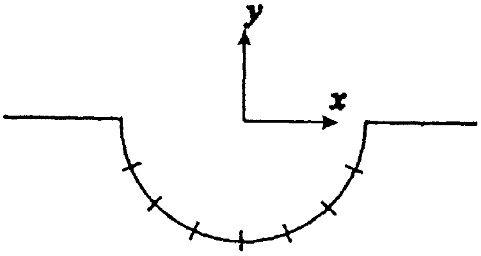

Fig. 3 Canyon Boundary Element Mesh

Consider a harmonic SH wave propagation in a heterogeneous half space, where exists a semi-circular canyon on the surface of the half-space, as depicted in Fig.3. The heterogeneous halfspace is assumed to be stratified media. The specific variations of the material properties are described above, e.g., the square root of shear modules $\mu(y)$ can be described by equation (22), and the function $N(y) = \rho\omega^2$ by equation (18). The material properties at different positions together with the corresponding parameters in equation (22) are listed at the end of that section.

Fig. 4a-b show the results of the displacement amplitude on the surface of the semi-circular canyon. The results of the displacement amplitude of a corresponding wave propagation problem in a homogeneous media are also depicted in Fig. 4a-b. The distributions of the material properties corresponding to Fig. 4a and Fig. 4b are shown in Fig.2a and Fig.2b respectively. The material properties of the corresponding homogeneous media are the same as the material properties of the heterogeneous media at infinity.

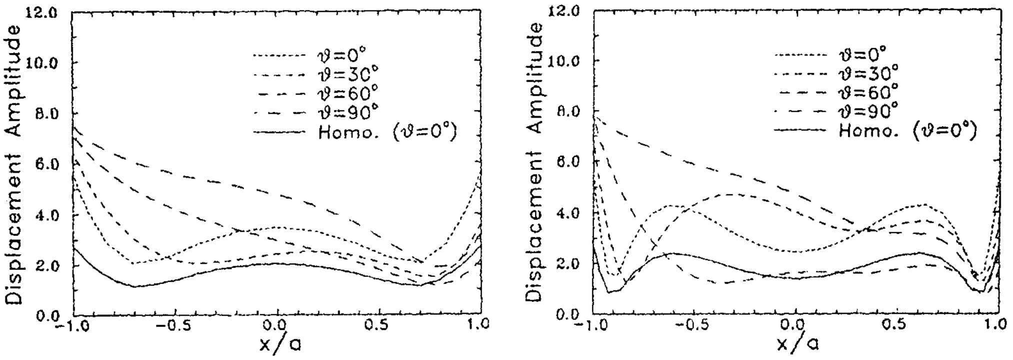

(a)

(b)

Fig. 4 Displacement amplitude along surface of the topography

Fig.4a and Fig.4b indicate that the structures of the displacement amplitude in the stratified media are analogous with those in the homogeneous media, and the magnitudes of the amplifications in the stratified media are greater than those in the homogeneous media. This may be justified that the velocity of shear wave near the surface of the stratified media is smaller than at infinity. In Fig. 2a and 2b the velocity on the surface is about 75% of the velocity at infinity, and a greater amplitude is needed to meet the requirement of the conservation of energy.

It should be pointed out that the purpose of the example problem is to illustrate the application of the boundary element method developed for wave propagation in heterogeneous media. More practical examples with actual stratified material behaviour as well as material with multi-dimensional variations should be studied in the future.

2. Wave scattering by sediment soil structure—deterministic case

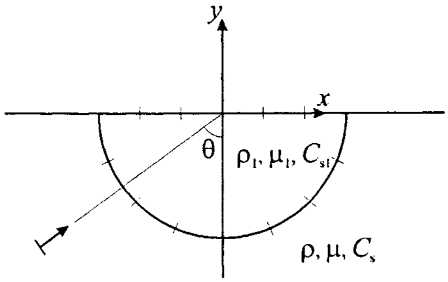

Fig. 5 Half plane with semi-circular sediment soil structure

On the elastic half plane, there is a semi-circular sediment soil structure as shown in Fig. 5. The material parameters for the elastic half plane and the sediment structure are different, and two pairs of examples have been analyzed.

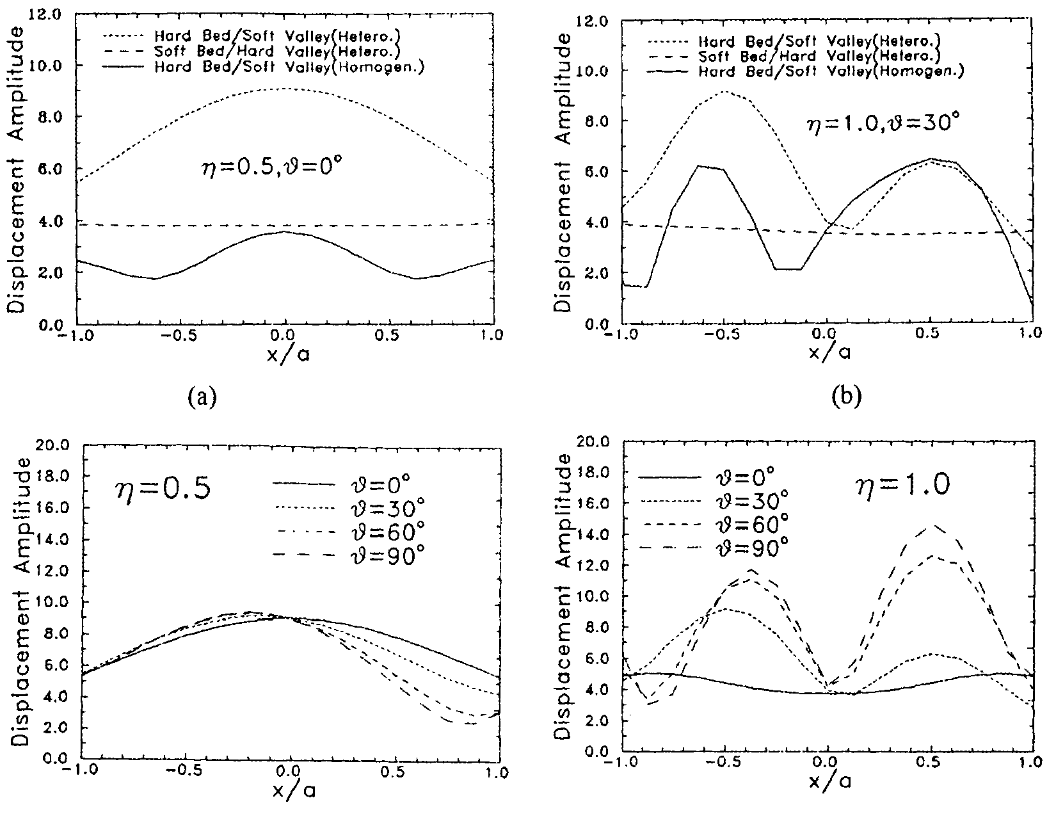

(c) (d)

Fig. 6 Displacement amplitude on the sediment surface

Case 1a, 1b: The material for the half plane is stratified, and the material parameters are the same as shown in Fig. 2a-b. In the heterogeneous case of Hard Bed / Soft Valley, the material parameters of the sediment structure are the same as those for the half plane media as $-y$ approaches infinity, i.e., $\rho_1 = 1.0$, $\mu_1 = 1.0$, $C_{s1} = 1.0$. In this case of Soft Bed / Hard Valley, the material parameters of the sediment are the same as those for the free surface of the half plane. The circular frequency of the incident wave is $\omega = \eta\pi$. The results of the displacement amplitude along the uper surface of the sediment structure are shown in Fig. 6a-b, corresponding to Fig. 2a-b.

Case 2a, 2b: The material for the half plane is the same as Hard Bed / Soft Valley heterogeneous case in Case 1a, 1b. The circular frequency of the incident wave is $\omega = \eta\pi$. The results of the displacement amplitude along the uper surface of the sediment structure are shown in Fig. 6c-d, corresponding to Fig. 2a-b and for a series of incident angle.

3. Wave propagation in random stratified media probabilistic case

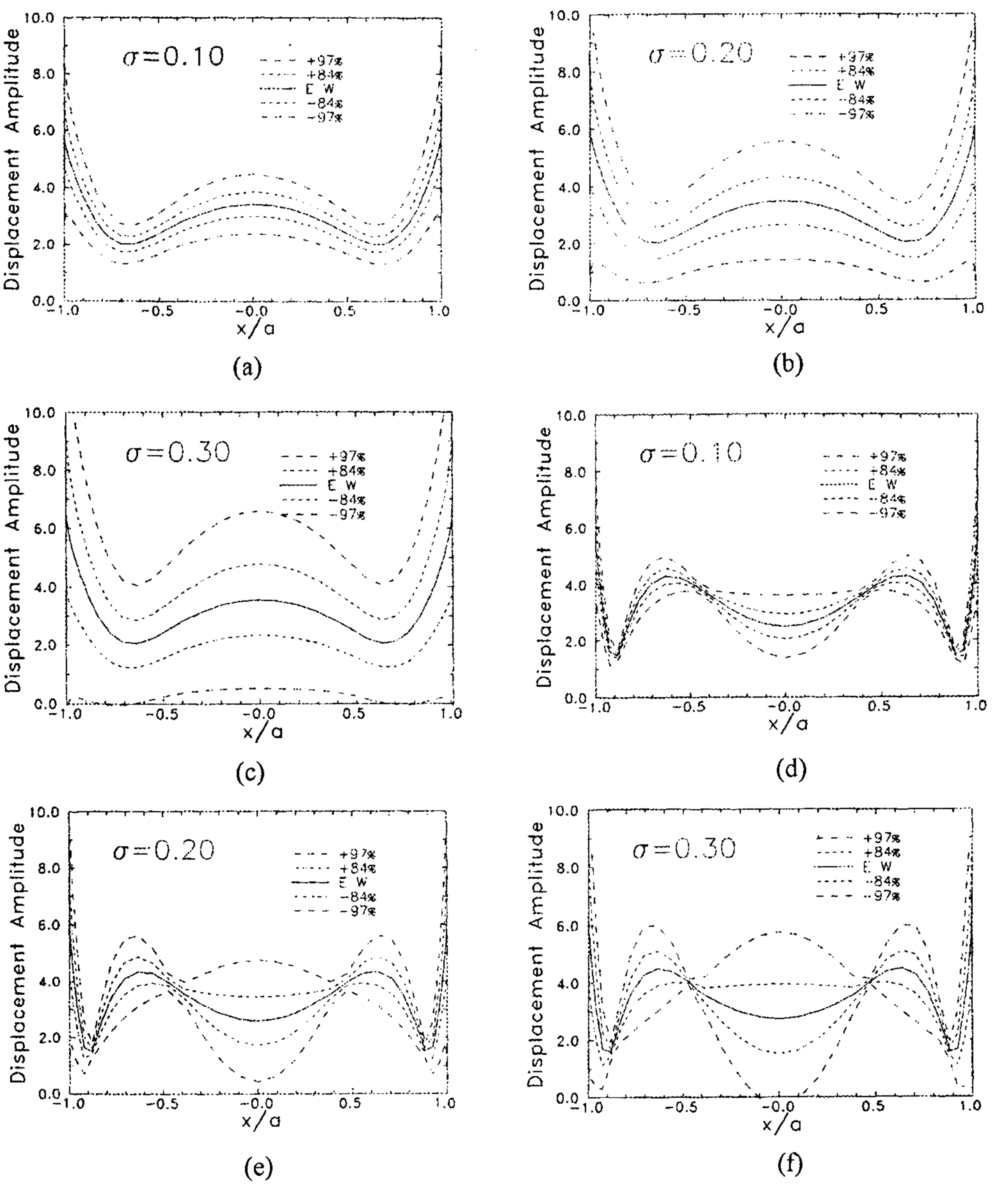

(a) (b) (c) (d) (e) (f)

Fig. 7 Confidence bound of displacements

We will now apply the stochastic BEM to solve the problem of wave scattering from a semi-circular canyon on random stratified media. The configure of the canyon is the same as in the previous section. The mean values of the random field $V(r,\gamma)$ and $N(r,\gamma)$ are also the same as in the previous section. The random variables $V_1(\gamma)$ and $N_1(\gamma)$ are assumed to have a normal probability density distribution, and the variances of $V_1(\gamma)$ and $N_1(\gamma)$ are set to be the same, i.e. $\varepsilon\sigma_{V_1} = \varepsilon\sigma_{N_1} = \sigma$, and we have set $\sigma = 0.1$, 0.2, 0.3 respectively, and $\varepsilon = 0.5$ for the following probabilistic analysis.

The displacement amplitudes of the canyon surface together with a probability of non-exceedence of 84% and 97% are calculated using the Chebyshev inequalities that were described above. These non-exceedence levels are chosen since they correspond to one and two standard deviations from the mean in a normal density function, hence they are widely used in engineering applications.

Fig. 7a through 7f show the results of the probabilistic analysis. The mean values of the material properties in Fig. 7a-c and Fig 7d-f are illustrated in Fig. 2a and Fig 2b respectively. The confidence bounds in Fig 7a-f can be interpreted as that the displacement amplitude will fall into the bounded zone with a given probability, e.g., 84% or 97%, when the material properties vary randomly. These confidence bounds can be used for design or analysis decision. This confidence estimate methodology has much advantage over the conventional "deterministic zone approach". The deterministic zone approaches use the "best guess" and upper and/or lower limits of the material properties as three levels to produce upper and lower bound values of the response quantities of interest. The deterministic zone, i.e., the space between the upper and lower bounds, is then used for design or analysis decision. The main drawback of the deterministic zone approach is that it cannot tell what are the probabilities that the response quantities will fall outside the deterministic zone, the confidence estimate methods can solve the dilemma.

It should be reiterated that the purpose of the examples is to illustrate the application of the stochastic boundary element method presented herein. Further studies will be concentrated on more realistic random heterogeneous media.

Summary

A boundary element formulation for wave propagation problem in heterogeneous media is introduced. The formulation assumes that the heterogeneous media is stratified and the material properties satisfy certain relationships. The wave propagation problems in the stratified half space are transformed into a wave scattering problem in a corresponding homogeneous media, which is solved by boundary element method.

The problem of wave scattering by a semi-circular canyon on a stratified heterogeneous half space was studied in order to demonstrate the use of the boundary element formulation for wave propagation in heterogeneous media. The surface displacement amplitudes of the canyon are given and compared to the results in the corresponding homogeneous media.

Then a stochastic boundary element presented for wave propagation in random stratified media is formulated. The formulation assumes that the shear modules and density of the heterogeneous media are random fields. A decomposition of the random fields is used to transform the wave propagation problem in random heterogeneous media into a wave scattering problem in a corresponding homogeneous media with a random wave number. A perturbation approach is used to solve the scattering problem in the homogeneous media. The statistical properties of the response measures, such as the means and mean square are evaluated. These statistical measures are used to evaluate the response measures at different confidence levels.

Again the problem of wave scattering by the canyon on the stratified random half space was studied. The displacement amplitudes on the canyon surface together with non-exceedence of 80% and 97% are given to illustrate the use and value of the formulation.

In conclusion, we should point out that the purpose of this work is to illustrate the potential of BEM in solving problems with heterogeneity and randomness. There are many works remains to be done in these areas.

References

[1] Nigam, N.C. 1983. Introduction to Random Vibrations. MIT press, Cambridge, MA.

[2] Benaroya, H. 1984. Stochastic structural dynamics. Tech Report No.1 , Weidinger Assoc, New York.

[3] Vanmarke, E., Shinozuka, M., Nagagiri, S, Schueller, G.I and Grigoriu, M. 1986. Random fields and stochastic finite elements, Structure Safety, 3, 141-166.

[4] Nakagiri, S., Hisada, T. and Tochimitsu, K. 1985. Stochastic time-history analysis of structural vibration with uncertain damping. In C Sundarerajan (eds), Probabilislic Structural Analysis. ASME PVP 93:109-120. New York.

[5] Lin, W.K., Buterfield, G. and Belytscke,T. 1988. Transient probabilistic systems Comp. Meth. Appl. Mech. Eng, 67:27-54.

[6] Cruse, T.A., Burnside, O.H., Hu, Y.T, Polch. E.Z. and Dias, J.B. 1988. Probabilistic structural analysis methods for select space problems system structural components (PSAM), Comp. and Structure. 29(5):891-901.

[7] Burczynski, T. 1985. The boundary element method for stochastic potential problems. Appl. Math. Modeling. 9:159-194.

[8] Benaroya, H. and Rehak, M. 1987. The Neumann series /Born approximations applied to parametrically excited systems, Prob. Eng. Mech. 2(2):474-481 .

[9] Manolis, G.D. and Shaw, R.P. 1992. Wave motion in a random hydroacoustic media using boundary integrals/element, Eng. Anal. Boundary Elements. 9:61-70.

[10] Ettouney, M., Benaroya, H. and Wright, J. 1989. Boundary element method in probabilistic structural analysis (PBEM) Appl. Math. Modeling. 3:432-441.

[11] Raymond, P.D. and Ettouney, M.M. 1991. Probabilistic acoustic analysis. Ch.5 in Boundary Element Methods in Acoustics. R.D. Ciskowski and C.A. Brebbia (eds) ,CMP and Elsevier, London.

[12] Luco, J.E., Apcel, R.J. 1983. On the Green's fonction for a layered half space, part I. Bull. Seism. Amer. 73.

[13] Shaw, R.P, Makris, N. 1992. Green's function for Helmholtz and Laplace equations in heterogeneous media. Eng. Anal. Boundary Elements, 10:179-183.

EFFECTS OF SOIL-STRUCTURE INTERACTION ON STRUCTURAL VIBRATION CONTROL

Lou Menglin and Wu Jingning
(Institute of Structural Theory, Tongji University, Shanghai, China, 200092)

Abstract

The control effectiveness of Tuned Mass Damper (TMD) device is studied in this paper for high-rising building rested on the soft soil, subjected to seismic excitation. Two approaches, random analysis in frequency domain and determinative analysis in time domain, are applied for evaluating the effects of soil-structure interaction (SSI) on the dynamic response of the structure with TMD device. The numerical results in the case studies show that the TMD effectiveness to reduce the seismic behavior of the structure decreases drastically due to the strong interaction between the structure and the soil. So that, the SSI effects should be taken into consideration in dynamic analysis and design of the TMD control of the structures subjected to earthquakes when the soil is soft.

Introduction

The theory of structure control has remarkably been developed in recent years since the new concept of the structure control in civil engineering was suggested by Professor Yao[1]. Many different types of active, passive and hybrid control techniques have been developed and studied through theoretical and experimental research. The structure control devices had been set upon many high-rising buildings in the word, to reduce the dynamic behavior of the structure. It has been shown that the structure control is coming critically important to suppress the dynamic response of the structures due to strong wind and earthquake excitations.

However, the soil-structure interaction is not considered in the most studies and designs of the structure control. In recent decades, the research results in the field of soil-structure interaction indicate that SSI has an important effect on the dynamic response of the structures when the soil is soft. In general, there are three major influences. (1) It will change the dynamic characteristics of the soil-structure system, such as modal frequencies and vibrating shapes. Especially, the fundamental frequency will have more decreases and rigid body motion of the structure will be produced or enhanced. (2) It will increase the modal damping as some vibrating energy in the structure will transfer to the soil. This type of damping is called radiation damping. (3) It will influence the free-field ground motion. Obviously, modal frequencies and damping of the system are also the important factors considered in the structure control.

Recently, the SSI effects on the structure control have been studied in several researches[2-7].

Most works focused on the SSI effects on the active control of the structures subjected to earthquakes. However, TMD control is one of the most popular and practicable control techniques used to suppress the seismic response of the high-rising buildings and the long-span bridges. Its effectiveness to reduce the dynamic behavior of the structure is more dependent upon the fundamental frequency of the system. In this paper, the SSI effects on the TMD control for seismic response of high-rising buildings are investigated.

Equation of Motion

1. Structure rested on rigid foundation

If the soil-structure interaction is not considered, the equation of motion for the structure with TMD device, under the seismic excitation including translational and rotational components $\ddot{x}_g(t)$ and $\ddot{\theta}_g(t)$, can be written as

$$[M]\{\ddot{u}_{\text{sup}}(t)\}+[C]\{\dot{u}_{\text{sup}}(t)\}+[K]\{u_{\text{sup}}(t)\}=-[M][\Gamma]\{\ddot{u}_g(t)\} \tag{1}$$

in which $[M]$、 $[C]$ and $[K]$ are (n × n) mass, damping and stiffness matrices respectively. n is the number of the degrees of freedom (DOF) of the structure-TMD system. $\{u_{\text{sup}}(t)\}$ is the relative displacement vector of the system with respect to the structure's base foundation. $[\Gamma]$ represents a (n × 2) quasistatic transformation matrix. $\{\ddot{u}_g(t)\}$ is the acceleration vector of the free-field ground motion,

$$\{\ddot{u}_g(t)\}=\begin{Bmatrix}\ddot{x}_g(t)\\ \ddot{\theta}_g(t)\end{Bmatrix} \tag{2}$$

In general, $\ddot{\theta}_g(t)$ is equal to zero in the structural seismic analysis.

2. Structure rested on soft soil

If the structure with TMD device is built on the soft soil, the equation of motion of the soil-structure system can be described by the equations of motion of two subsystems, structure-TMD subsystem and rigid base foundation subsystem including the effect of the soft soil.

For the structure-TMD subsystem, its equation of motion can be expressed as

$$[M]\{\ddot{u}_{\text{sup}}(t)\}+[C]\{\dot{u}_{\text{sup}}(t)\}+[K]\{u_{\text{sup}}(t)\}=-[M][\Gamma](\{\ddot{u}_f(t)\}+\{\ddot{u}_g(t)\}) \tag{3}$$

Eq. (3) is somewhat different to Eq. (1) as structure's base foundation has an additional motion $\{\ddot{u}_f(t)\}$ relative to the free-field ground motion $\{\ddot{u}_g(t)\}$ due to the SSI effect. Similar to $\{\ddot{u}_g(t)\}$,

$$\{\ddot{u}_f(t)\}=\begin{Bmatrix}\ddot{x}_f(t)\\ \ddot{\theta}_f(t)\end{Bmatrix} \tag{4}$$

The equation of motion for the rigid structure's base foundation can be written as

$$[M_f](\{\ddot{u}_f(t)\}+\{\ddot{u}_g(t)\})+[\Gamma]^T[M](\{\ddot{u}_{\sup}(t)\}+[\Gamma]\{\ddot{u}_f(t)\}+[\Gamma]\{\ddot{u}_g(t)\})=\{f_s(t)\} \tag{5}$$

where $[M_f]$ is a (2 × 2) mass matrix of the rigid structure's base foundation. $\{f_s(t)\}$ is a force vector including the horizontal force $p_s(t)$ and rotational moment $\mu_s(t)$. They represent the action of the soft soil on the structure's base foundation. They can be written in detail:

$$[M_f]=\begin{bmatrix} m_f & 0 \\ 0 & J_f \end{bmatrix} \tag{6}$$

$$\{f_s(t)\}=\begin{Bmatrix} p_s(t) \\ \mu_s(t) \end{Bmatrix} \tag{7}$$

in which m_f and J_f are mass and inertia moment of the structure's base foundation. The thickness of the base foundation is thought as small and negligible.

According to the results of the research in the field of soil-structure interaction, the force vector $\{f_s(t)\}$ can be expressed in frequency domain using the impedance matrix :

$$-\{F_s(\omega)\}=[\bar{S}_s(\omega)]\{U_f(\omega)\} \tag{8}$$

where $\{F_s(\omega)\}$ and $\{U_f(\omega)\}$ are the Fourier transformations of $\{f_s(t)\}$ and $\{u_f(t)\}$ respectively. $[\bar{S}_s(\omega)]$ is the impedance matrix of the soil, a (2 × 2) complex coefficient matrix. It can be written in detail:

$$\begin{aligned}[\bar{S}_s(\omega)]&=[K_s(\omega)]+i\omega[C_s(\omega)] \\ &=\begin{bmatrix} k_{xx}(\omega) & k_{x\theta}(\omega) \\ k_{\theta x}(\omega) & k_{\theta\theta}(\omega) \end{bmatrix}+i\omega\begin{bmatrix} C_{xx}(\omega) & C_{x\theta}(\omega) \\ C_{\theta x}(\omega) & C_{\theta\theta}(\omega) \end{bmatrix}\end{aligned} \tag{9}$$

Obviously, stiffness coefficient k_{ij} and damping coefficient c_{ij} are dependent on the exciting frequency ω. Some researchers[8,9] found that a frequency-independent impedance can be safely taken corresponding to the fundamental frequency of the soil-structure system. They also compared their results with the more rigorous analysis and showed that their results are within a reasonable agreement. Therefore, Eq. (8) can be written approximately in time domain as follows :

$$-\{f_s(t)\}=[K_s]\{u_f(t)\}+[C_s]\{\dot{u}_f(t)\} \tag{10}$$

in which $[K_s]=[K_s(\omega_0)],[C_s]=[C_s(\omega_0)]$. ω_0 is the fundamental frequency of the soil-structure system.

From Eq.(3), following relationship can be obtained:

$$[M](\{\ddot{u}_{\sup}(t)\}+[\Gamma]\{\ddot{u}_f(t)\}+[\Gamma]\{\ddot{u}_g(t)\})=-[C]\{\dot{u}_{\sup}(t)\}-[K]\{u_{\sup}(t)\} \tag{11}$$

Substituting Eqs. (10) and (11) into Eq. (5), a new equation can be arrived:

$$[M_f](\{\ddot{u}_f(t)\}+\{\ddot{u}_g(t)\})-[\Gamma]^T[C]\{\dot{u}_{\mathrm{sup}}(t)\}+[C_s]\{\dot{u}_f(t)\}$$
$$-[\Gamma]^T[K]\{u_{\mathrm{sup}}(t)\}+[K_s]\{u_f(t)\}=0 \tag{12}$$

Let

$$\{u(t)\}=\{u_{\mathrm{sup}}(t)\}+[\Gamma]\{u_f(t)\} \tag{13}$$

where $\{u(t)\}$ describes the displacement vector of the structure-TMD subsystem relative to the free-field ground motion $\{u_g(t)\}$.

Assembling Eqs. (3) and (12), the final equation of motion for the structure with (n+2) degrees of freedom can be obtained as follows,

$$\begin{bmatrix} M & 0 \\ 0 & M_f \end{bmatrix}\begin{Bmatrix} \ddot{u}(t) \\ \ddot{u}_f(t) \end{Bmatrix}+\begin{bmatrix} C & -C\Gamma \\ -\Gamma^T C & \Gamma^T C\Gamma+C_s \end{bmatrix}\begin{Bmatrix} \dot{u}(t) \\ \dot{u}_f(t) \end{Bmatrix}+\begin{bmatrix} K & -K\Gamma \\ -\Gamma^T K & \Gamma^T K\Gamma+K_s \end{bmatrix}\begin{Bmatrix} u(t) \\ u_f(t) \end{Bmatrix}$$

$$=-\begin{bmatrix} M & 0 \\ 0 & M_f \end{bmatrix}\begin{bmatrix} \Gamma \\ I_2 \end{bmatrix}\{\ddot{u}_g(t)\}=\{p_{eff}(t)\} \tag{14}$$

where $[I_2]$ is a (2 × 2) unit matrix. If the rotational component in $\{u_g(t)\}$ is neglected, that is $\ddot{\theta}_g(t)=0$, $\{p_{eff}(t)\}$ in Eq. (14) is becoming as

$$\{p_{eff}(t)\}=-\begin{bmatrix} M & 0 \\ 0 & M_f \end{bmatrix}\begin{bmatrix} \Gamma_1 \\ e \end{bmatrix}\ddot{x}_g(t) \tag{15}$$

in which $\{\Gamma_1\}$ is the first column in $[\Gamma]$ and $\{e\}^T=\{1,\ \ 0\}$. In this paper, seismic response analysis in time domain for the soil-structure system with TMD device is carried using Eq. (15). It means that only horizontal seismic excitation is taken into consideration.

3. Random Response Analysis

If the free-field ground motion $\ddot{x}_g(t)$ is mathematically assumed as a stationary random process, the mean square value of seismic response of the structure is given by following equation:

$$E[\delta^2]=\int_{-\infty}^{\infty}|H_\delta(\omega)|^2 S(\omega)d\omega \tag{16}$$

where $S(\omega)$ is the power spectral density function of the free-field ground motion $\ddot{x}_g(t)$. A filtered non-white noise model[10] is taken in this study:

$$S(\omega) = \frac{1+4\xi_g^2\frac{\omega^2}{\omega_g^2}}{\left(1-\frac{\omega^2}{\omega_g^2}\right)^2 + 4\xi_g^2\frac{\omega^2}{\omega_g^2}} \cdot \frac{S_0}{1+\frac{\omega^2}{\omega_h^2}} \tag{17}$$

in which the parameters ω_g, ω_h and ξ_g are dependent on the property of the soil.

In Eq. (16), the symbol δ represents the seismic response at any position of the structure, such as acceleration a_{top} and displacement u_{top} at the top of the structure or shear force Q_{base} at the structure's base. Usually, a_{top} , u_{top} and Q_{base} are the most important response required to check the safety or confortableness of the structure.

An influence factor is defined by following ratio:

$$R_\delta = \sqrt{\frac{E\left[\delta^2\right]}{E\left[\bar{\delta}^2\right]}} \tag{18}$$

where δ indicates the seismic response of the structure with TMD control as well as $\bar{\delta}$ indicates the seismic response at same position of the structure without TMD control. The value of R_δ is changeable with the shear wave velocity V_s of the soil and the dimensionless ratio ω_{TMD}/ω_0 . ω_{TMD} is the designed frequency of the TMD device. ω_0 is the fundamental frequency of the soil-structure system. Comparing R_δ values obtained from different shear wave velocity V_s of the soil can be reveal the SSI effects on the control effectiveness of the TMD device. The greater value of R_δ indicates the smaller effectiveness of the TMD control.

Case Study and Discussion

1. Parameters in case study

In this research, the shear buildings with (L × L) square cross-section, rested on half-space, are selected for illustration. As well as two types of structure's base foundation, surface foundation and group-piles foundation, are taken in consideration respectively. The TMD device is installed at the building top. Its damping ratio is designed as 8% and mass is equal to 2% of the first modal mass of the building. Details of the parameters are listed in Table 1 to Table 5.

Table 1. Parameters of building-TMD system

No.	width L (m)	height H (m)	TMD mass (kg)	floor mass (kg)	floor inertia moment	layer stiffness (N/m)
1	16	45 (12 F)	6.4×10^4	5.3×10^5	0	8.4×10^8
2		90 (24 F)	1.3×10^5			
3	24	45 (12 F)	1.3×10^5	1.06×10^6	0	1.68×10^9
4		90 (24 F)	2.6×10^5			

Table 2. Parameters of rigid structure's base mat

width L (m)	mass (kg)	inertia moment kg·m^2
16	9.8×10^5	4.9×10^7

Table 3. Parameters of group-piles

cat size (m^2)	cat mass (kg)	cat inertia moment (kg·m^2)	pile length (m)	pile diameter (m)	pile mass density (kg/m^3)	pile Young's modulus (Gpa)	pile span (m)
16×16	9.8×10^5	4.9×10^7	15	0.4	2.5×10^3	34	2m
24×24	2.0×10^6	2.1×10^8		0.6			3m

Table 4. Parameters of the soil

Poisson's	damping	shear elastic modulus (N/m^2)				
ratio	ratio	V_s=100m/s	V_s=150m/s	V_s=200m/s	V_s=350m/s	V_s=∞
0.35	0.125	1.7×10^7	4.3×10^7	8.4×10^7	2.8×10^8	∞

Table 5. Parameters of filtered non-white noise model

	kinds of soil	I	II	III	IV
ω_g	near field earthquake	41.89	31.42	25.13	16.75
(rad/s)	far field earthquake	35.90	25.13	19.33	13.23
	ξ_g	0.64	0.72	0.80	0.90
	ω_h (rad/s)	25.13			

In case study, El Centro and San Fernando earthquake records are selected as the horizontal seismic input $\ddot{x}_g(t)$. The acceleration peak value of El Centro wave is modified to $100\,cm/s^2$ as well as the peak value of San Fernando wave is $265.7\,cm/s^2$.

2. SSI effects on TMD control of soil-structure system without group-piles

In this case, the structure's base foundation is assumed as a rigid mat which keeps contact continuously with soft soil during earthquake. Building No.1 is selected as an example to analyze the SSI effects on effectiveness of the TMD control.

(1) Random analysis

Figure 1 and Figure 2 give the computing results from Eq. (18) according to different shear wave velocity V_s of the soil. In the figures, u_{top} and d_{top} represent the horizontal displacement at the building top with respect to the free-field ground motion and to the displacement of the base foundation respectively. Obviously, d_{top} is only the dynamic elastic deformation and u_{top} includes d_{top} and rigid body motion component. In the computing condition of $V_s \to \infty$, it represents the case that SSI is not taken into consideration.

From the numerical results, it is shown that if the building modal damping ratio is small, for example $\xi = 1\%$ in steel structure, the TMD still has an important function to reduce the dynamic behavior when the soil is stiff or rigid in the case of $V_s = 350m/s$ or $V_s \to \infty$. Otherwise, if the building is rested on soft soil, the TMD has a little function to reduce the dynamic behavior in spite of low modal damping of the structure.

(2) Determinative analysis in time domain

The designed frequency of TMD device ω_{TMD} is equal to $0.98\omega_0$. The time history of the seismic response of Building No.1 for two extreme cases ($V_s = \infty$, $100m/s$) are shown in Figure 3 and Figure 4. In the figures, the solid and dotted line represent the seismic response of the structure with and without TMD control respectively.

The results illustrate that when the soil is very soft, there is nearly no difference between seismic responses of the building with TMD and without TMD. This means that the strong SSI effect makes TMD lose its function.

3. SSI effects on TMD control of soil-pile-structure system

The main assumption in this study is that all of the discussed problems of the soil are limited in the range of the linear viscoelastics. The impedance matrix of the group-piles is obtained approximately through applying the interaction factor between two piles[11].

(1) Random analysis

The computing results of the SSI effects on the effectiveness factor R_δ of the TMD control are shown in Figure 5 to Figure 9. From the numerical results, it can be summarized that SSI brings down the TMD function to reduce the seismic response of the structures with the decrease of the shear wave velocity V_s of the soil.

(2) Determinative analysis in time domain

The seismic response of the soil-pile foundation-structure systems subjected to horizontal excitations of El Centro and San Fernando waves are shown in Figure 10 and Figure 11. In general, some conclusions similar to the ones in the case of random response analysis, can be obtained. But sometime the effectiveness of the TMD control does not decrease monotonously with the decrease of V_s, because resonance between the system fundamental frequency ω_0 and dominant frequency component ω_f in earthquake wave influences significantly the dynamic response of the building. The SSI effects on the resonance can not be described monotonously.

Conclusions

The SSI effects on the TMD control of the high-rising buildings have been investigated. The numerical case studies give us following several practical conclusions.

1. The function of TMD control to suppress the seismic response of the buildings is weakened by the soil-structure interaction with decrease of the shear wave velocity of the soil. The stronger interaction between the soil and the structure, the more reduction of the TMD control effectiveness.
2. If the high-rising building with higher modal damping, for example more than 5% in reinforced concrete structure, is rested on soft soil, TMD technique is not available to control the seismic response of the building efficiently.
3. If the soil is not very soft and damping of the building is small, for example about 1% or 2% in the steel structure, TMD control can still be applied to reduce the seismic response of the building. However, the frequency of the TMD device ω_{TMD} has to be designed to equal approximately to the fundamental frequency ω_0 of the soil-structure system rather than the fundamental frequency of the structure without considering the SSI effect.

Acknowledgments

The work done in this study has been supported by the Doctoral Discipline Foundation of State Education Committee of China. The authors are grateful for this support.

References

[1] J. T. P. Yao, Concept of Structural Control. J. Struc. Dic., ASCE, Vol.98, 1567-1574, 1972

[2] H. L. Wang and T. E. Luco, Structural Control Including Soil-Structure Interaction Effects. J. Engng. Mech. Div., ASCE, Vol.117, No.10, 2237-2250, 1991

[3] T.Sato and K.Toki, Predictive Control of Seismic Response of Structure Taking into Account the Soil-Structure Interaction. Proc. 1st Eur. Conf. on Smart Structures and Materials, Glagow, Switzerland, 245-250, 1982

[4] S. M. Alam and S. Baba, Robust Active Optimal Control Scheme Including Soil-Structure Interaction. J. Struc. Div., ASCE, Vol.119, No.9, 2533-2551, 1993

[5] H. A. Smith and W. Wu, Soil-Structure Interaction Transfer Function for Ground Motion and Control Force. Proc. 1st Word Conf. Struc. Control, FP2: 44-53, Los Angeles, USA, 1994

[6] H. A. Smith, W. Wu and R. Borja, Structural Control Considering Soil-Structure Interaction Effects. Earthquake Engineering and Structural Dynamics, Vol.23, No.6, 609-626,1994

[7] F. Y. Cheng, S. Suthiwong and P. Tian, Generalized Optimal Active Control with Embedded and Half-Space Soil-Structure Interaction. Analysis and Computation (F. Y. Cheng ed.), 337-346, 1994

[8] M. Ghaffar-Zadeh and F. Chapel, Frequency-independent Impedances of Soil-Structure System in Horizontal and Rocking Modes. Earthquake Engineering and Structural Dynamics, Vol.11, 523-540, 1983

[9] P. J. Wolf and D. R. Somaini, Approximate Dynamic Model of Embedded Foundation in Time Domain. Earthquake Engineering and Structural Dynamics, Vol.14, 653-703, 1986

[10] J. Ou and H. Liu, Random Seismic Response Spectrum and Application Based on the Random Seismic Ground Motion. Earthquake Engineering and Engineering Vibration(in Chinese), Vol.14, No.1, 14-23, 1994

[11] J. Wu, Soil-Structure Interaction and Structural Vibration Control. Doctoral Thesis, Tongji University, China, June, 1997

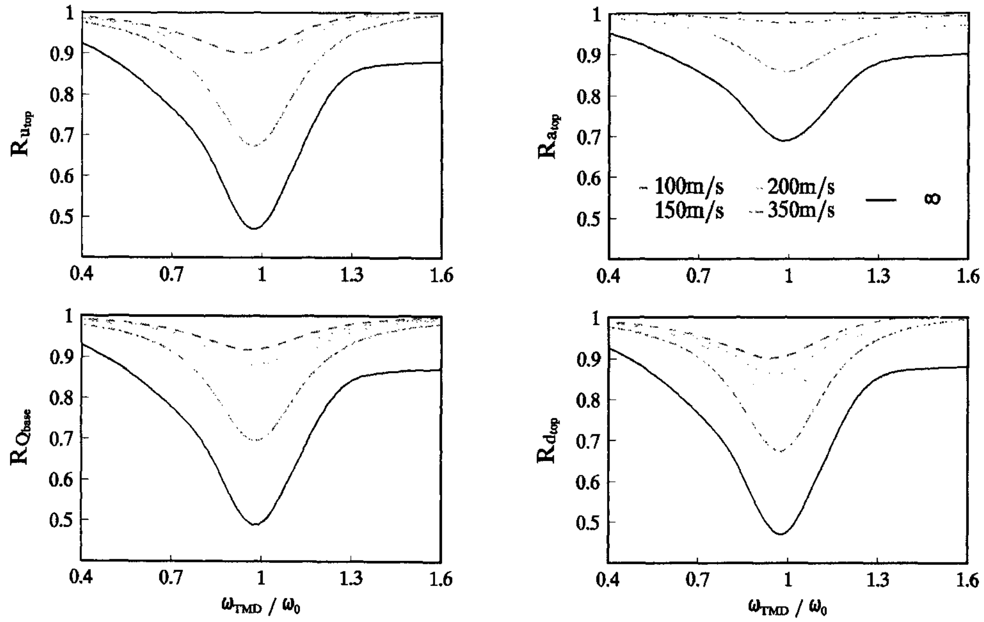

Fig. 1 Control influence factor R_δ of Building No.1 (rigid base mat; $\xi = 1\%$)

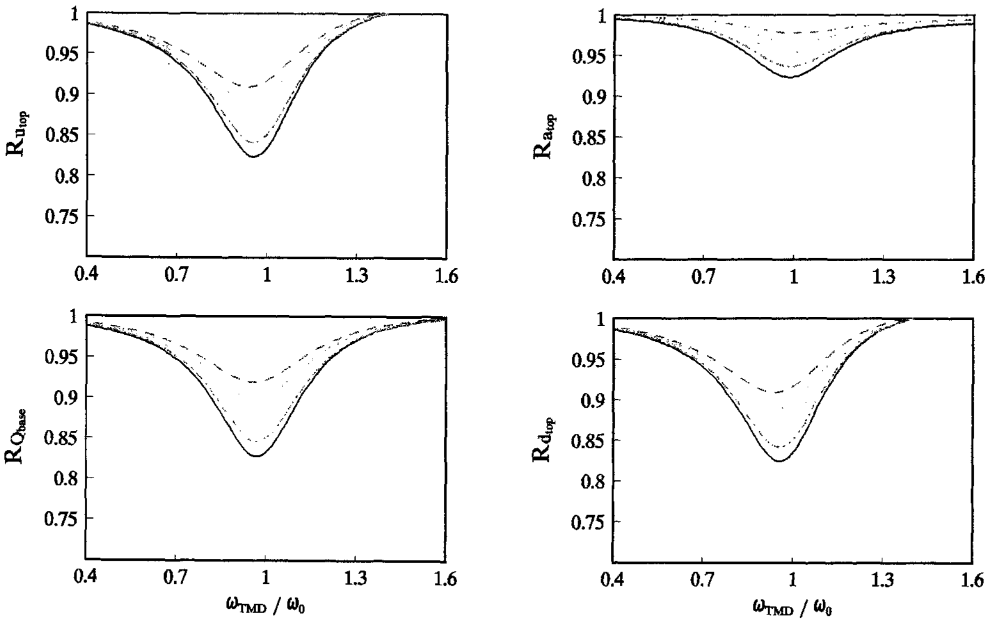

Fig. 2 Control influence factor R_δ of Building No.1 (rigid base mat; $\xi = 5\%$)

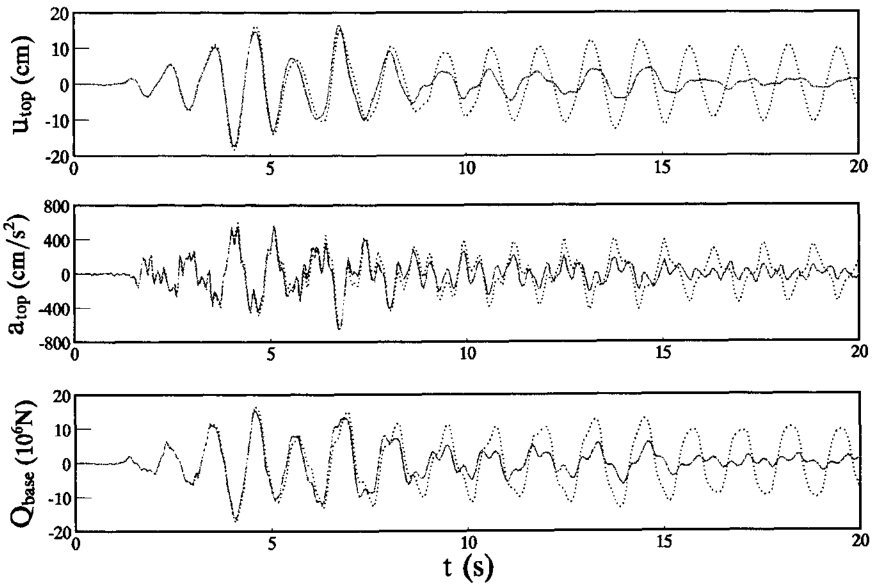

Fig. 3 Seismic response of Building No.1 subjected to El Centro wave (rigid base mat; $\xi = 1\%$; $V_s \to \infty$)

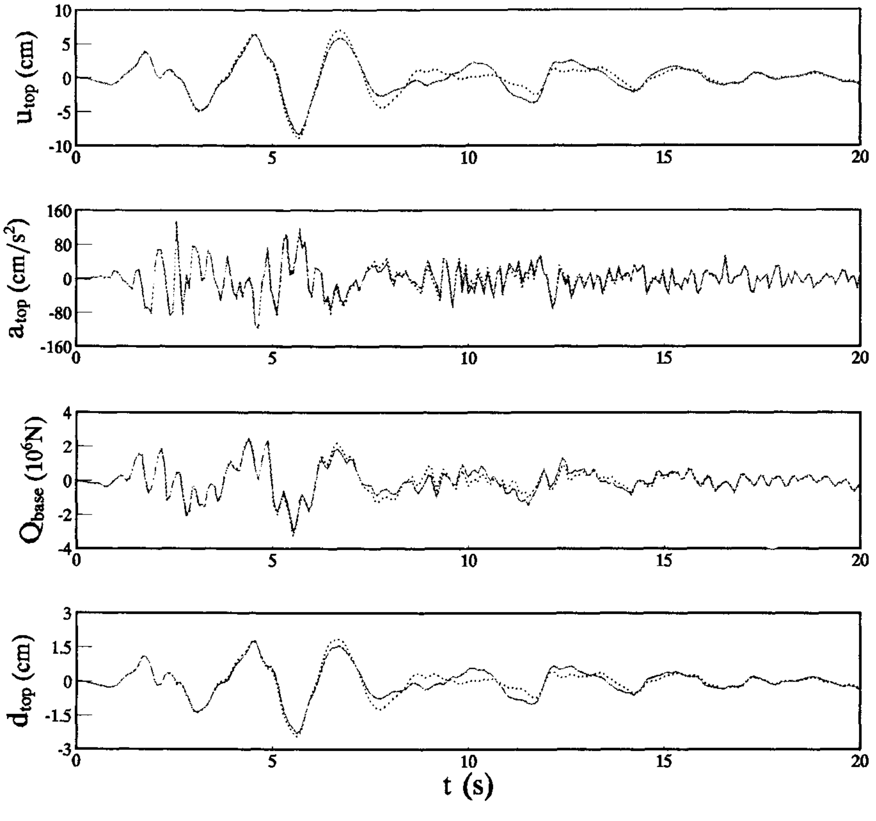

Fig. 4 Seismic response of Building No.1 subjected to El Centro wave (rigid base mat; $\xi = 1\%$; $V_s = 100 m/s$)

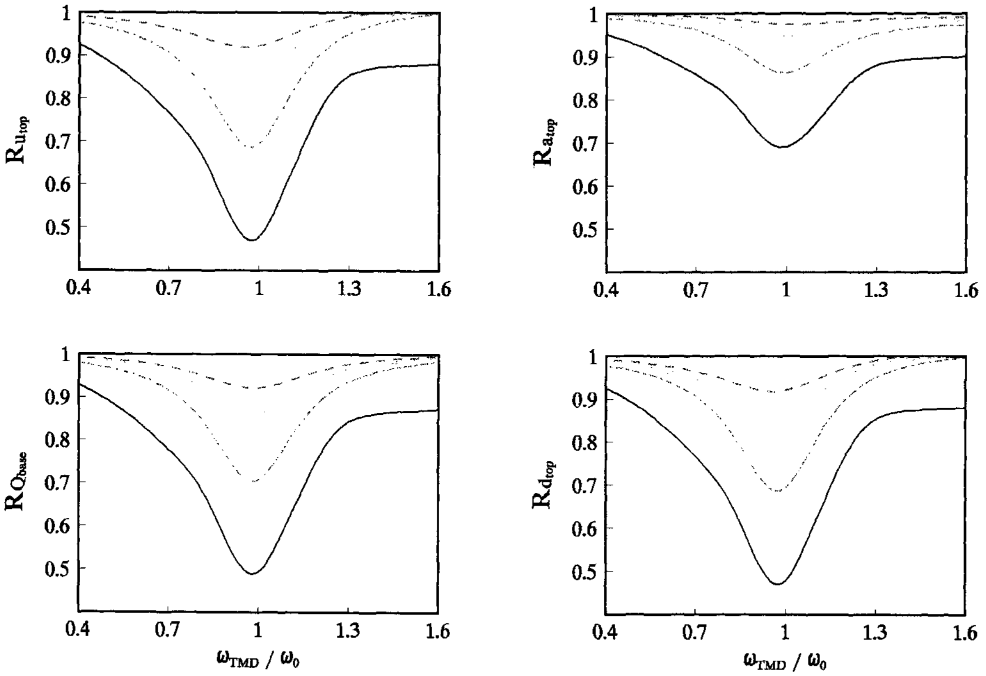

Fig. 5 Control influence factor R_δ of Building No. 1
(group-piles foundation; $\xi = 1\%$)

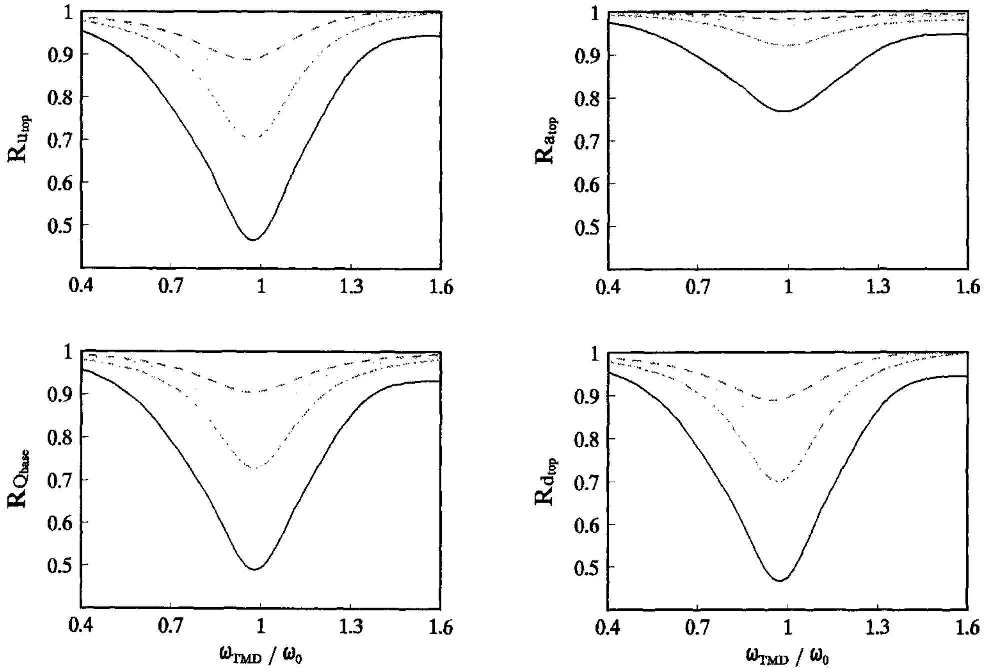

Fig. 6 Control influence factor R_δ of Building No. 2
(group-piles foundation; $\xi = 1\%$)

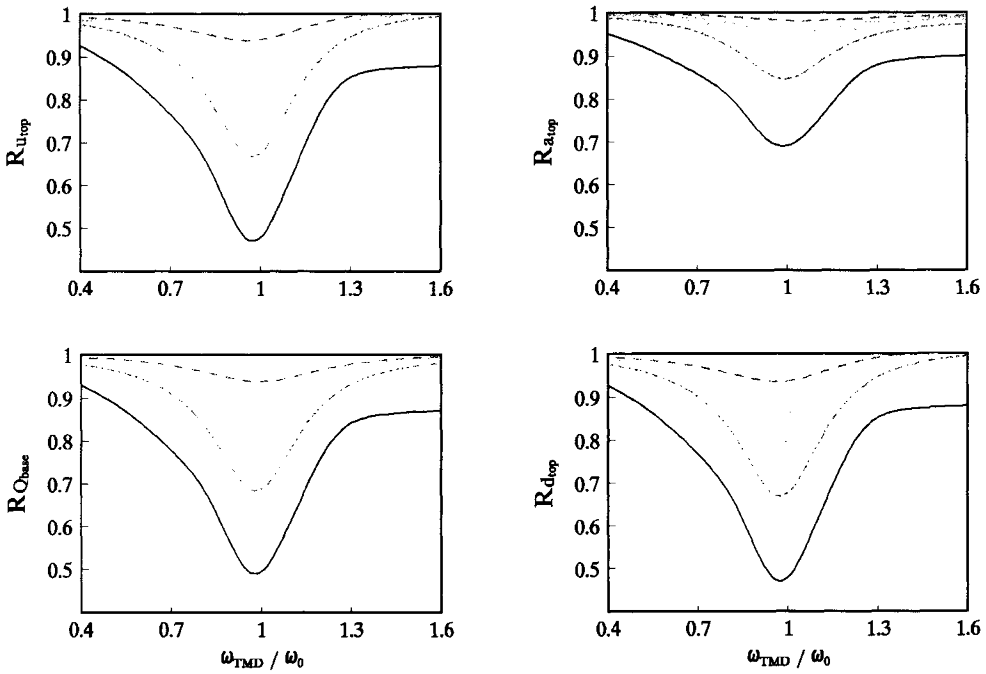

Fig. 7 Control influence factor R_δ of Building No. 3
(group-piles foundation; $\xi = 1\%$)

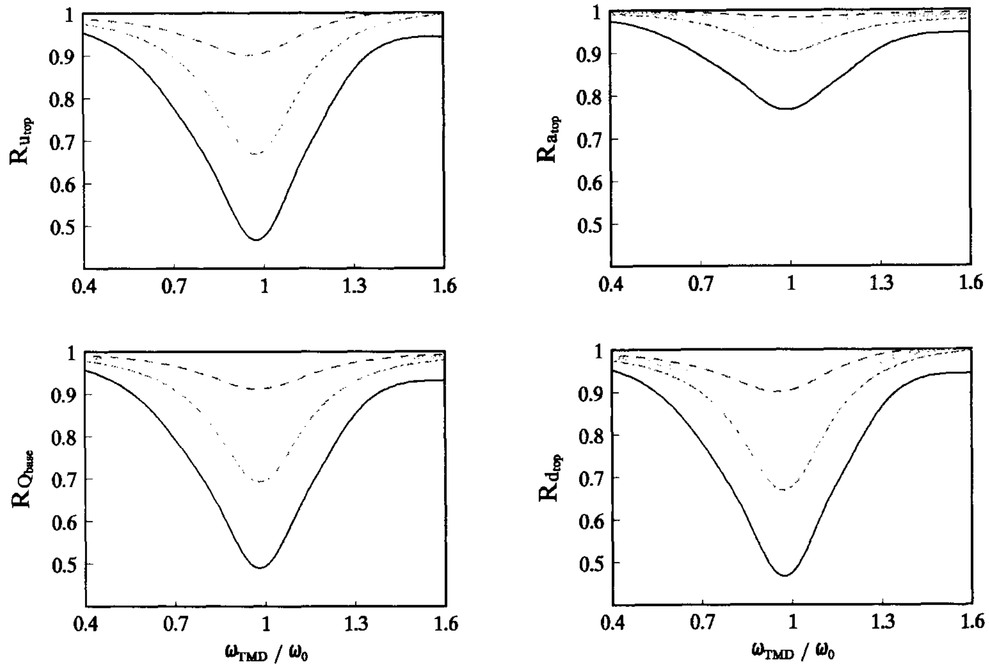

Fig. 8 Control influence factor R_δ of Building No. 4
(group-piles foundation; $\xi = 1\%$)

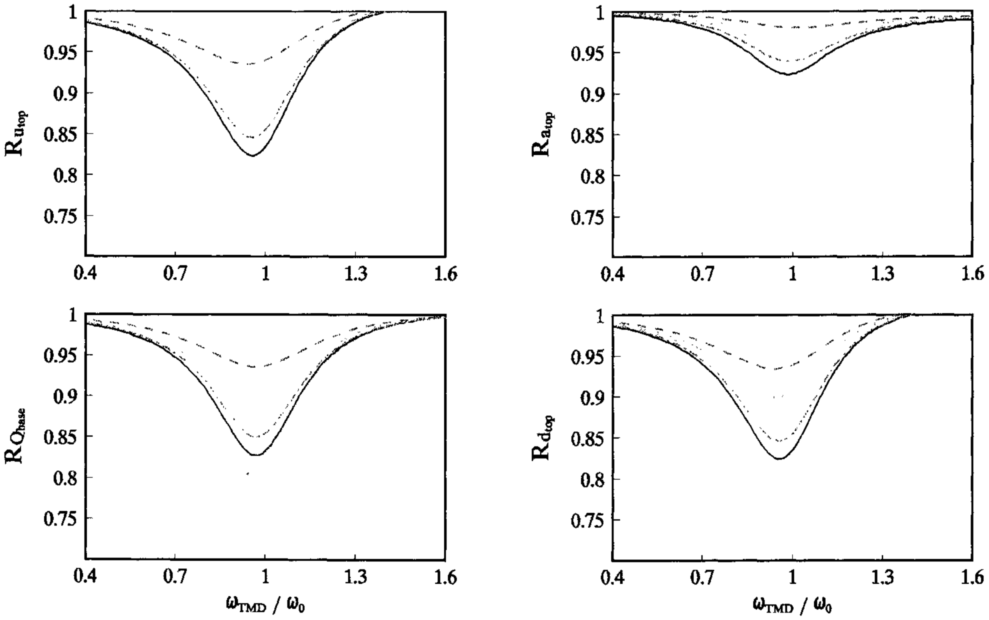

Fig. 9 Control influence factor R_δ of Building No. 1
(group-piles foundation; $\xi = 5\%$)

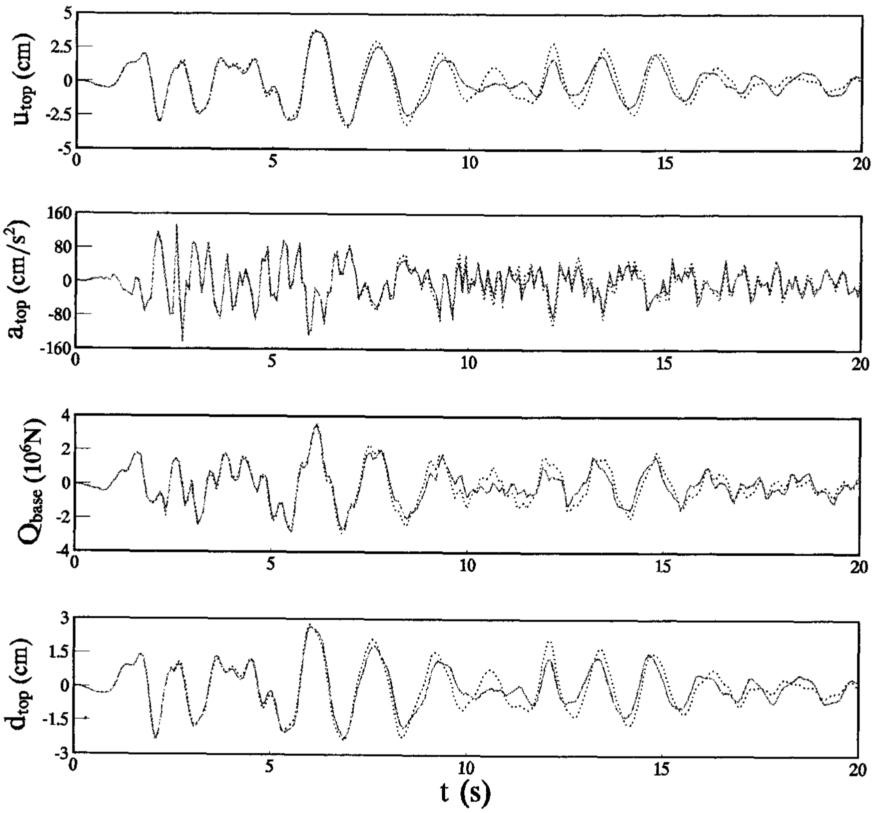

Fig. 10 Seismic response of Building No.1 subjected to El Centro wave
(group-pile foundation; $\xi = 1\%$; $V_s = 150 m/s$)

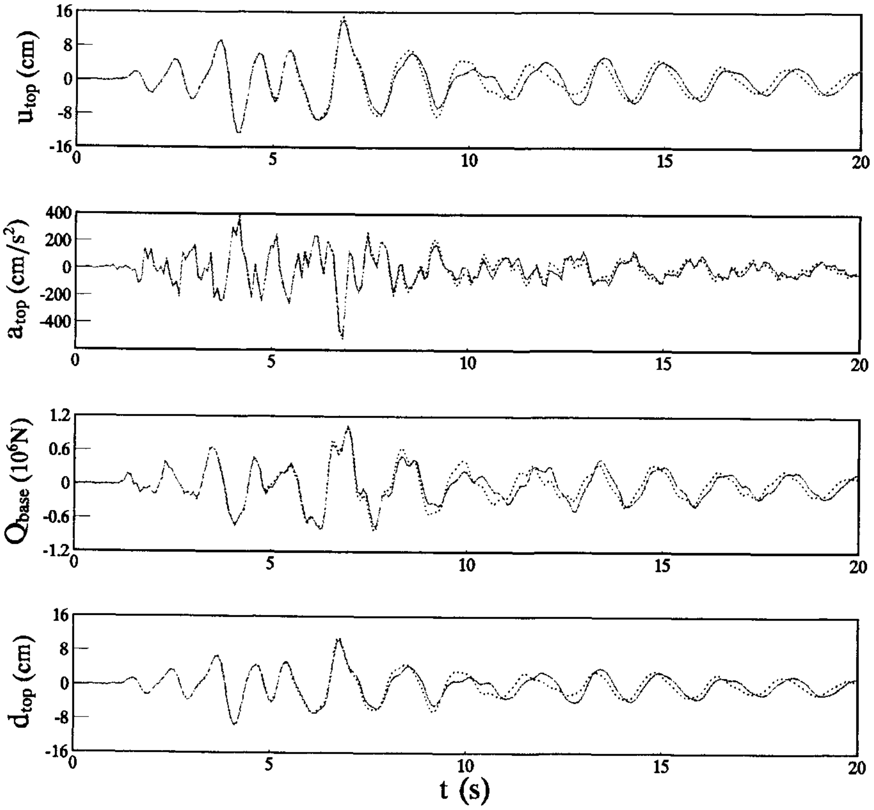

Fig. 11 Seismic response of Building No.1 subjected to San Fernando wave (group-pile foundation; $\xi = 1\%$; $V_s = 150m/s$)

DYNAMIC SOIL-STRUCTURE INTERACTION FOR HIGH-RISE BUILDINGS

Wu Shiming, Gan Gang
(Zhejiang University, Hangzhou, China 310027)

Abstract

The authors analyze vibration impedance function of raft and pill foundations on layered media with 3-D model consisting of spacial beam, columm and panel elements. The paper presents super-structure-foundation-soil 3-D dynamic interaction equations and corresponding program with substructure method. The recults are compared for commonly used frame and frame-shear wall structures on different subsoil, different types of foundation and different input of seismic waves. The results show variation of vibration period of structure, displacement, stresses under consideration of interaction. It can be seen that it is necessary to compile a soil-structure interaction program of dynamic analysis for high-rise buildings.

Introduction

The importance of dynamic soil-structure interaction for high-rise buildings has being recognized, because of two effects: (1) the feedback action from structure affects the composition of frequency spectrum of soil motion, resulting in increasing of component approaching that of natural frequency of the super-structure; (2) the soil flexibility affects the dynamic behavior of super-structure (including frequency and vibration mode) and damping of the whole structure resluting in part of vibration energy dissipating through hysteresis and wave radiation. It is necessary to take soil-structure interaction into account for seismic analysis, especially for a structure built on soft soil.

There are several approaches, such as finite element method, sub-structure method and hybrid method for analyzing soil-structure interaction, among which sub-structure method is widely used for its advantages which each system (including super-structure, foundation and soil) can be analyzed with its the most suitable approach within its zone [1]. In this method, the super-structure is often simplified as multi-nodel system of bending-shear or shear pattern, and vibration impedance function of massless rigid disc on homogeneous elastic half space, and is analyzed in plane domain [2]～[6]. However, since a real structure is in 3-D and dynamic soil-structure interaction is also a spacial problem, it is necessary to set up a model in 3-D.

Based on the characteristics of high-rise structures, the assumptions are made that box (raft) foundations with or without piles are resting on transversely layered isotropic visco-elastic half space (simplified as layered media). A model of 3-D with spacial beam, column and panel elements is used for analysis of vibration impedance function of box (raft) foundations embeded certain depth with horizontal and vertical vibration of piles in layered soils. Then, 3-D super-sturcture-foundation-soil dynamic interaction is analyzed with substructure method, and corresponding program is compiled. Examples of two types of structure on different soils and foundations, and different seismic input are given, and the results are compared. Some conclusions are drawn for reference of seismic design.

Motion Equations

With 3-D high-rise structure-foundation-soil dynamic interaction models as shown in Fig. 1(a), Fig. (b) and (c) represent motions in x and y direction resulting from seismic input on foundation approximately equal to the acceleration in free field $\ddot{u}_g(t)$ and $\ddot{v}_g(t)$.

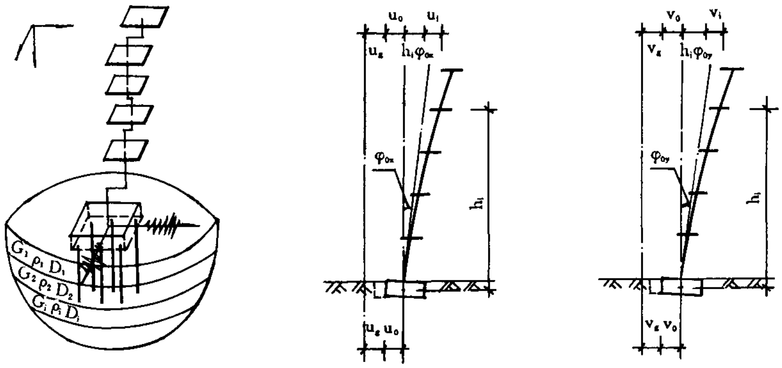

(a) (b) (c)

Fig. 1 3-D High-Rise Structure-Foundation-Soil Dynamic Interaction Models

1. Motion Equations of Super-Structure

Super-structure is discritized as spacial beam, column element and panel element which can simulate behavior of shear walls. The stiffness matix of each element can be found [10]. Gerenally, in a high-rise building with N floors, for its large size in horizontal plane of each floor and great stiffness of whole building, it is rational to assume that each floor has infinite stiffness in-plane. Therefore, each floor only has three degrees of freedom, i. e. two horizontal displacements and one rotational displacement around the vertical axis of mass centre of the structure, and the transversal stiffness matrices can be obtained by static congregation method [10].

From Fig. 1(b) and (c), the dynamic equilibrium equations of each floor can be expressed in terms of matrix as following:

$$\begin{bmatrix}[m] & & \\ & [m] & \\ & & [J]\end{bmatrix}\begin{Bmatrix}\{\ddot{u}\}+\{h\}\ddot{\varphi}_{0x}\}+\{\ddot{u}_g\}+\{\ddot{u}_0\} \\ \{\ddot{v}\}+\{h\}\ddot{\varphi}_{0y}\}+\{\ddot{v}_g\}+\{\ddot{v}_0\} \\ \{\ddot{\theta}\}\end{Bmatrix} + \begin{bmatrix}C_{xx} & C_{xy} & C_{x\theta} \\ C_{yx} & C_{yy} & C_{y\theta} \\ C_{\theta x} & C_{\theta y} & C_{\theta\theta}\end{bmatrix}\begin{Bmatrix}\{\dot{u}\} \\ \{\dot{v}\} \\ \{\dot{\theta}\}\end{Bmatrix} + \begin{bmatrix}K_{xx} & K_{xy} & K_{x\theta} \\ K_{yx} & K_{yy} & K_{y\theta} \\ K_{\theta x} & K_{\theta y} & K_{\theta\theta}\end{bmatrix}\begin{Bmatrix}\{u\} \\ \{v\} \\ \{\theta\}\end{Bmatrix} = 0 \tag{1}$$

Let

$$[M] = \begin{bmatrix}[m] & & \\ & [m] & \\ & & [J]\end{bmatrix}, [C] = \begin{bmatrix}C_{xx} & C_{xy} & C_{x\theta} \\ C_{yx} & C_{yy} & C_{y\theta} \\ C_{\theta x} & C_{\theta y} & C_{\theta\theta}\end{bmatrix}, [K] = \begin{bmatrix}K_{xx} & K_{xy} & K_{x\theta} \\ K_{yx} & K_{yy} & K_{y\theta} \\ K_{\theta x} & K_{\theta y} & K_{\theta\theta}\end{bmatrix}$$

where, $[M]$, $[C]$ and $[K]$ are mass matrix, damping matrix and stiffness matrix of superstructure, respectively, with $3N \times 3N$; Rayleigh damping for the structure, i. e. $[C] = a[M] + b[K]$; h_i , height of each floor to the mass centre of the foundation; u_0 and v_0 , displacements in x and y direction of the foundation, respectively; φ_{0x} and φ_{0y} , rotations of the foundation around y and x axices.

2. Motion Equations of Foundation

Assume P_x^* and P_y^* representing horizontal forces acting on the foundation from soil, and M_x^* and M_y^* representing moments acting on the foundation. Then, motion equations of the foundation can be expressed as shown in Eq. (2):

$$\left.\begin{aligned} & m_0(\ddot{u}_0+\ddot{u}_g)+\sum_{i=1}^{N} m_i(\ddot{u}_i+h_i\ddot{\varphi}_{0x}+\ddot{u}_0+\ddot{u}_g)+P_x^*=0 \\ & m_0(\ddot{v}_0+\ddot{v}_g)+\sum_{i=1}^{N} m_i(\ddot{v}_i+h_i\ddot{\varphi}_{0y}+\ddot{v}_0+\ddot{v}_g)+P_y^*=0 \\ & I_{x\varphi}\ddot{\varphi}_{0x}+\sum_{i=1}^{N} m_i h_i(\ddot{u}_i+h_i\ddot{\varphi}_{0x}+\ddot{u}_0+\ddot{u}_g)+M_x^*=0 \\ & I_{y\varphi}\ddot{\varphi}_{0y}+\sum_{i=1}^{N} m_i h_i(\ddot{v}_i+h_i\ddot{\varphi}_{0y}+\ddot{v}_0+\ddot{v}_g)+M_y^*=0 \end{aligned}\right\} \tag{2}$$

where, $I_{x\varphi}$ and $I_{y\varphi}$ representing summution of rotational moment of inertia of m_i , mass of each floor and m_0 , mass of foundation around their axices, x and y, respectively, in which the relationship between displacemants of foundation u_0, v_0, φ_{0x} and φ_{0y} , and forces, P_x^* , P_y^* , M_x^* and M_y^* can be expressed in terms of vibration impedance function of foundation.

(1) Impedance Foundation of Box (Raft) Foundation on Layered Media

Normally, the shape of foundation of high-rise building is most likely of rectangular or square. [8] presented vibration impedance function of rectangular foundation on layered madia with certain embeded depth, as following [7],

$$\left.\begin{aligned}
&K_{HH} = f_H(\alpha_H G_H r_H k_H + G_s l S_{u1}) \\
&K_{\varphi\varphi} = f_\varphi\{\alpha_\varphi G_\varphi r_\varphi^3 k_\varphi a_\varphi + \alpha_\varphi G_\varphi z_c^2 r_\varphi k \\
&+ G_s \delta_\varphi r_\varphi^3 [S_{\varphi 1} + (\frac{\delta_\varphi^3}{3} + \frac{z_c^2}{r_\varphi} - \delta_\varphi \frac{z_c}{r_\varphi}) S_{u1}]\} \\
&K_{H\varphi} = - f_H[\alpha_H G_H z_c r_H k_H + G_s l (z_c - \frac{1}{2} l) S_{u1}] \\
&C_{HH} = \frac{1}{\omega}[2(\eta_u + \eta_s) G_H r_H k_H + G_s l S_{u2}] \\
&C_{\varphi\varphi} = \frac{1}{\omega}[2(\eta_\varphi + \eta_s) G_\varphi r_\varphi^3 k_\varphi a_\varphi + 2(\eta_u + \eta_s) G_\varphi r_\varphi z_c^2 k_H \\
&+ G_s r_\varphi^3 \delta_\varphi [S_{\varphi 2} + \frac{\delta_\varphi^3}{3} + \frac{z_c^2}{r_\varphi^2} - \delta_\varphi \frac{z_c}{r_\varphi}) S_{u2}]\} \\
&C_{H\varphi} = - \frac{1}{\omega}[2(\eta_u + \eta_s) G_H z_c r_H k_H + G_s l (z_c - \frac{l}{2}) S_{u2}]
\end{aligned}\right\} \qquad (3)$$

in which, K_{HH}, $K_{\varphi\varphi}$, $K_{H\varphi}$and C_{HH},$C_{\varphi\varphi}$ and $C_{H\varphi}$ are stiffnesses in horizontal, rocking, and, coupled by horizontal and rocking, and their corresponding dampings.

(2) Vibration Impedance Function of Pile Foundation on Layered Media

Horizontal vibration impedance function of single pile [8],

for friction pile: $[K^s] = ([T_{21}] + [T_{22}][K_T])([T_{11}] + [T_{12}][K_T])^{-1}$ (4a)

for tip bearing pile: $[K^s] = [T_{22}][T_{12}]^{-1}$ (4b)

in which, $[K_T]$, dynamic stiffness of pile tip and $[T_{11}]$,$[T_{12}]$,$[T_{21}]$,$[T_{22}]$, block matrices of transfer matrix $[T]$.

Vertical vibration impedance function of single pile [9],

for friction pile: $k^s = (t_{21} + t_{22}k_w)/(t_{11} + t_{12}k_w)$ (5a)

for tip bearing pile: $k^s = t_{22}/t_{12}$ (5b)

in which, k_w , dynamic stiffness of pile tip and t_{11}, t_{12}, t_{21}, t_{22} , element of transfer matrix $[t]$.

The vibration impedance function of pile foundation with a group of n piles can be obtanied by superposing each single pile:

$$\left.\begin{aligned}
&K_{HH}^x = \sum_{i=1}^{n} k_{HH}^s \\
&K_{H\varphi}^x = \sum_{i=1}^{n} (k_{H\varphi}^s - k_{HH}^s z_c) \\
&K_{\varphi\varphi}^x = \sum_{i=1}^{n} (k_{\varphi\varphi}^s - 2k_{H\varphi}^s z_c + k_{HH}^s z_c^2 + k_{zz}^s x_i^2) \\
&C_{HH}^x = \sum_{i=1}^{n} c_{HH}^s \\
&C_{H\varphi}^x = \sum_{i=1}^{n} (c_{H\varphi}^s - c_{HH}^s z_c) \\
&C_{\varphi\varphi}^x = \sum_{i=1}^{n} (c_{\varphi\varphi}^s - 2c_{H\varphi}^s z_c + c_{HH}^s z_c^2 + c_{zz}^s x_i^2)
\end{aligned}\right\} \qquad (6)$$

where, K^y_{HH}, $K^y_{H\varphi}$, $K^y_{\varphi\varphi}$ and C^y_{HH}, $C^y_{H\varphi}$, $C^y_{\varphi\varphi}$ given by changing x and y with x_i and y_i, respectively; z_c, distance between mass centre of foundation to its bottom; and, x_i and y_i representing coordinates of its pile, respectively.

Then, following equations are given:

$$\left.\begin{aligned} P^*_x &= C^x_{HH}\dot{u}_0 + C^x_{H\varphi}\dot{\varphi}_{0x} + K^x_{HH}u_0 + K^x_{H\varphi}\varphi_{0x} \\ P^*_y &= C^y_{HH}\dot{v}_0 + C^y_{H\varphi}\dot{\varphi}_{0y} + K^y_{HH}v_0 + K^y_{H\varphi}\varphi_{0Y} \\ M^*_x &= C^x_{H\varphi}\dot{u}_0 + C^x_{\varphi\varphi}\dot{\varphi}_{0x} + K^x_{H\varphi}u_0 + K^x_{\varphi\varphi}\varphi_{0x} \\ M^*_y &= C^y_{H\varphi}\dot{v}_0 + C^y_{\varphi\varphi}\dot{\varphi}_{0y} + K^y_{H\varphi}v_0 + K^y_{\varphi\varphi}\varphi_{0y} \end{aligned}\right\} \tag{7}$$

For the case of foundation consisting of box (raft) and piles, its vibration impedance function can be obtained just simply superposing these two parts.

3. Motion Equations of 3-D System

Combining Eq. (1), (2) and (7), the motion equation of high-rise superstructure-foundation-soil 3-D dynamic interaction system in time domain can be obtained:

$$[\overline{M}]\{\ddot{\overline{D}}\} + [\overline{C}]\{\dot{\overline{D}} + [\overline{K}]\{\overline{D}\} = -[\overline{M}]\{\ddot{D}_g\} \tag{8}$$

in which,

$$[\overline{M}] = \left[\begin{array}{ccc:cccc} & & & \underline{m} & 0 & \underline{mh} & 0 \\ & [M] & & 0 & \underline{m} & 0 & \underline{mh} \\ & & & 0 & 0 & 0 & 0 \\ \hdashline \underline{m}^T & 0 & 0 & m_0 + \sum_{i=1}^{N} m_i & 0 & \sum_{i=1}^{N} m_i h_i & 0 \\ 0 & \underline{m}^T & 0 & 0 & m_0 + \sum_{i=1}^{N} m_i & 0 & \sum_{i=1}^{N} m_i h_i \\ \underline{mh}^T & 0 & 0 & \sum_{i=1}^{N} m_i h_i & 0 & I_{x\varphi} + \sum_{i=1}^{N} m_i h_i^2 & 0 \\ 0 & \underline{mh}^T & 0 & 0 & \sum_{i=1}^{N} m_i h_i & 0 & I_{y\varphi} + \sum_{i=1}^{N} m_i h_i \end{array}\right]$$

$$[\overline{C}] = \left[\begin{array}{c:cccc} [C] & & & [0] & \\ \hdashline & C^x_{HH} & 0 & C^x_{H\varphi} & 0 \\ [0] & 0 & C^y_{HH} & 0 & C^y_{H\varphi} \\ & C^x_{H\varphi} & 0 & C^x_{\varphi\varphi} & 0 \\ & 0 & C^y_{H\varphi} & 0 & C^y_{\varphi\varphi} \end{array}\right]$$

$$[\overline{K}] = \left[\begin{array}{c:cccc} [K] & & [0] & & \\ \hdashline & K^x_{HH} & 0 & K^x_{H\varphi} & 0 \\ [0] & 0 & K^y_{HH} & 0 & K^y_{H\varphi} \\ & K^x_{H\varphi} & 0 & K^x_{\varphi\varphi} & 0 \\ & 0 & K^y_{H\varphi} & 0 & K^y_{\varphi\varphi} \end{array}\right]$$

$$\underline{m} = \{m_1\ m_2 \cdots m_N\}^T$$

$$\underline{mh} = \{m_1 h_1\ m_2 h_2 \cdots m_N h_N\}^T$$

$$\{\overline{D} = \{u_1\ u_2 \cdots u_N\ v_1\ v_2 \cdots v_N\ \theta_1\ \theta_2 \cdots \theta_N\ u_0\ v_0\ \varphi_{0x}\ \varphi_{0y}\}^T$$

$$\{D_g\} = \{0\ 0 \cdots 0 \,|\, \ddot{u}_g\ \ddot{v}_g\ 0\ 0\}^T$$

It is to be mentioned that the stiffness matrix, $[\overline{K}]$, contains vibration impedance for taking soil-structure dynamic interaction into account, and the coefficents are frequency dependent. Taking natural frequency of the structure without dynamic interaction as an initial value, find the natural frequency of the system under considering dynamic interaction by iterative method, from which the vibration impedance of the foundation is determined, consequently, seismic response of super-structure can be continued.

Seismic Response Analysis For Different Types of Structure

1. Data for Analysis

Frame and frame-shear wall are common structure systems for high-rise buildings. Fig. 2 and 3 are examples of these two types of structure, both with 12 stories and height between each floor, 3. 6m. Size of cross-section of beam, column and shear-wall are shown in Table 1 and 2. Table 3 shows strengths of concrete for each floor. Raft foundations (32m×17m×0. 8m) with or without piles are adopted. Fig. 4 shows plane view of pile foundation arrangement, with coefficients shown in Table 4. Shear wave velocities for layers are given as 100m/s, 200m/s, 300m/s, 400m/s and 500m/s, respectively. El Centro and Taft are taken as seismic input with adjustment of peak acceleration to 35 gal.

Table 1. Cross-Section of Beam and Column for Frame Structure

Floor	Column (mm)	Beam 1 (mm)	Beam 2 (mm)
1~3	400×700	250×700	250×400
4~6	400×600	250×700	250×400
7~12	400×500	250×700	250×400

Table 2. Cross-Section of Beam, Column and Shear-Wall for Frame-Shear Wall Structure System

Floor	Column (mm)	Thickness of Shear-wall (mm)	Beam 1 (mm)	Beam 2 (mm)
1~4	400×700	200	250×700	250×400
5~7	400×600	200	250×700	250×400
8~12	400×500	180	250×700	250×400

Table 3 Strengths of Concrete

Floor	1~4	5~7	8~12
Grade of Concrete	C35	C30	C25

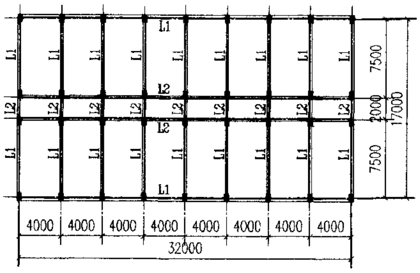

Fig. 2 Plane View of Frame Structure

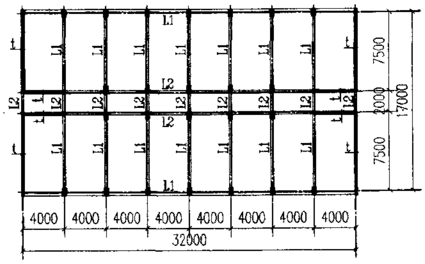

Fig. 3 Plane View of Frame-Shear Wall Structure System

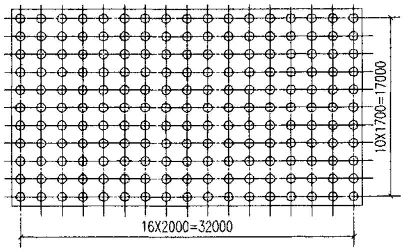

Fig. 4 Plane Arrangement of Pile Foundation

Table 4 Coefficients of Pile Foundation

Unit Weight (kN/m^3)	Yang's Modulus (MPa)	Diameter of the Pile (m)	Pile Length (m)
24.5	2.55×10^4	0.5	12.5

2. Results and Observations

(1) Natural Period

Table 5 shows ratio of natural period of first modes with or without taking interaction into account for two types of structure system, from which natural period of the structure increases as taking interaction into account and increases with increasing flexibility of soil. For a same site, the natural period of the structure with piles is smaller than that without piles, and corresponding natural periods of horizontal vibration have greater incremant than rotational vibration ($\bar{T}_3/T_3$, $\bar{T}_6/T_6$, $\bar{T}_9/T_9$), while the increments of natural period of first 3 modes are smaller than those of others. By comparing the ratio of there two types of structure system, it can be seem that the ratio of all modes of frame-shear wall structure is greater than that of frame structure, because of great stiffness of frame-shear wall structure, especially on flexible soil.

Table 5 Ratio of Period of Structures

type of structure	period ratio V_S(m/ s)	$\bar{T}_1/T_1$	$\bar{T}_2/T_2$	$\bar{T}_3/T_3$	$\bar{T}_4/T_4$	$\bar{T}_5/T_5$	$\bar{T}_6/T_6$	$\bar{T}_7/T_7$	$\bar{T}_8/T_8$	$\bar{T}_9/T_9$
Frame Structure	100	1.073 (1.005)	1.042 (1.005)	1.000 (1.000)	1.848 (1.033)	1.154 (1.032)	1.112 (1.000)	1.341 (1.090)	1.296 (1.058)	1.167 (1.000)
	200	1.014 (1.002)	1.013 (1.002)	1.000 (1.000)	1.151 (1.010)	1.078 (1.011)	1.000 (1.000)	1.252 (1.026)	1.105 (1.022)	1.027 (1.000)
	300	1.006 (1.001)	1.006 (1.001)	1.000 (1.000)	1.043 (1.005)	1.038 (1.007)	1.000 (1.000)	1.113 (1.015)	1.066 (1.013)	1.000 (1.000)
	400	1.003 (1.001)	1.003 (1.001)	1.000 (1.000)	1.020 (1.004)	1.021 (1.005)	1.000 (1.000)	1.054 (1.010)	1.040 (1.010)	1.000 (1.000)
	500	1.002 (1.001)	1.002 (1.001)	1.000 (1.000)	1.012 (1.003)	1.013 (1.003)	1.000 (1.000)	1.031 (1.007)	1.026 (1.007)	1.000 (1.000)
Frame-Shear Wall Structure	100	1.187 (1.021)	1.506 (1.045)	1.556 (1.001)	1.727 (1.639)	2.100 (1.589)	1.887 (1.326)	1.691 (1.164)	2.314 (1.515)	1.785 (1.588)
	200	1.031 (1.003)	1.063 (1.007)	1.059 (1.000)	1.724 (1.059)	1.625 (1.195)	1.487 (1.074)	1.205 (1.005)	1.567 (1.461)	1.598 (1.064)
	300	1.012 (1.002)	1.026 (1.004)	1.000 (1.000)	1.330 (1.031)	1.505 (1.100)	1.206 (1.043)	1.117 (1.001)	1.490 (1.340)	1.458 (1.056)
	400	1.007 (1.001)	1.014 (1.003)	1.000 (1.000)	1.144 (1.021)	1.365 (1.062)	1.127 (1.029)	1.059 (1.001)	1.486 (1.237)	1.213 (1.050)
	500	1.004 (1.001)	1.009 (1.002)	1.000 (1.000)	1.076 (1.015)	1.236 (1.043)	1.088 (1.021)	1.016 (1.000)	1.480 (1.161)	1.079 (1.046)

Note: Values in brackets refer to those with piles.

(2) Displacement of Floor

Because of flexibility of soil and spacial interaction, seismic input in x direction causes displacement at each floor in x direction, meanwhile, it also causes displacement in y direction and rotational displacement around mass centre; the similar for seismic input in y driection. The direction of seismic input is refered to primary one, the other is refered to secondary. From Table 6 and Fig. 5, one can find that displacement in primary direction will decrease for frame structure because of the rigid soil, while for frame-shear wall structure it may increase or decrease because of the rigid of soil; displacement in secondary direction and rotation increase dramatically especially for stiff structure and flexible soil. With increasing soil stiffness, displacement approaches to that of rigid soil. Pile foundation has an effect on restraining displacements of floor and foundation. An another important factor affecting floor displacement is spectrum characteristics of seismic input, as well as stresses, which causes different influences for two types of structure system, i. e. , frame and frame-shear wall structural systems.

Table 6 Floor Displacements in Superstructure

Type of Structure	Input in x Direction	Shear Wave Velocity	Displacement at Top Floor			Displacement at Foundation			
			U(m)	V(m)	θ(rad)	U_0(m)	V_0(m)	φ_{0x}(rad)	φ_{0y}(rad)
Frame Structure	El Centro Wave	∞	0.3695×10^{-1}	0.1966×10^{-8}	0.1213×10^{-7}	0	0	0	0
		100	0.3682×10^{-1} (0.3653×10^{-1})	0.1304×10^{-1} (0.2997×10^{-2})	0.9162×10^{-4} (0.2304×10^{-4})	0.2124×10^{-2} (0.4246×10^{-3})	0.1250×10^{-2} (0.1774×10^{-3})	0.1997×10^{-3} (0.2259×10^{-4})	0.2400×10^{-3} (0.3833×10^{-4})
		500	0.3693×10^{-1} (0.3695×10^{-1})	0.1490×10^{-2} (0.4282×10^{-3})	0.8853×10^{-5} (0.2153×10^{-5})	0.1264×10^{-3} (0.2975×10^{-4})	0.4763×10^{-4} (0.1343×10^{-4})	0.1286×10^{-4} (0.2473×10^{-5})	0.1455×10^{-4} (0.3720×10^{-5})
	Taft Wave	∞	0.2321×10^{-1}	0.1294×10^{-8}	0.9782×10^{-8}	0	0	0	0
		100	0.2085×10^{-1} (0.2276×10^{-1})	0.9829×10^{-2} (0.2366×10^{-2})	0.6658×10^{-4} (0.1957×10^{-4})	0.2147×10^{-2} (0.4454×10^{-3})	0.1194×10^{-2} (0.1548×10^{-3})	0.1598×10^{-3} (0.2399×10^{-4})	0.1725×10^{-3} (0.3071×10^{-4})
		500	0.2286×10^{-1} (0.2313×10^{-1})	0.9722×10^{-3} (0.2471×10^{-3})	0.5334×10^{-5} (0.1344×10^{-5})	0.8002×10^{-4} (0.1607×10^{-4})	0.4255×10^{-4} (0.1321×10^{-4})	0.7142×10^{-5} (0.1407×10^{-5})	0.1247×10^{-4} (0.3740×10^{-5})
Frame-Shear Well Structure	El Centro Wave	∞	0.1643×10^{-1}	0.9048×10^{-8}	0.1279×10^{-8}	0	0	0	0
		100	0.2011×10^{-1} (0.1683×10^{-1})	0.9720×10^{-2} (0.1413×10^{-2})	0.5851×10^{-4} (0.9365×10^{-5})	0.1761×10^{-2} (0.3183×10^{-3})	0.5798×10^{-3} (0.1722×10^{-3})	0.1158×10^{-3} (0.1550×10^{-4})	0.1804×10^{-3} (0.3123×10^{-4})
		500	0.1661×10^{-1} (0.1626×10^{-1})	0.8633×10^{-3} (0.2932×10^{-3})	0.5375×10^{-5} (0.1209×10^{-5})	0.1435×10^{-3} (0.2794×10^{-4})	0.7687×10^{-4} (0.1685×10^{-4})	0.1395×10^{-4} (0.2271×10^{-5})	0.2072×10^{-4} (0.5088×10^{-5})
	Taft Wave	∞	0.2148×10^{-1}	0.1015×10^{-7}	0.1205×10^{-8}	0	0	0	0
		100	0.2270×10^{-1} (0.2269×10^{-1})	0.9762×10^{-2} (0.1753×10^{-2})	0.3601×10^{-4} (0.9678×10^{-5})	0.1606×10^{-2} (0.3878×10^{-3})	0.8977×10^{-3} (0.2023×10^{-3})	0.1403×10^{-3} (0.2019×10^{-4})	0.2081×10^{-3} (0.3943×10^{-4})
		500	0.2100×10^{-1} (0.2162×10^{-1})	0.1037×10^{-2} (0.3064×10^{-3})	0.4090×10^{-5} (0.1092×10^{-5})	0.1138×10^{-3} (0.1954×10^{-4})	0.7402×10^{-4} (0.1686×10^{-4})	0.1146×10^{-4} (0.1725×10^{-5})	0.2379×10^{-4} (0.4867×10^{-5})

Note: Values in brackets refer to those with piles.

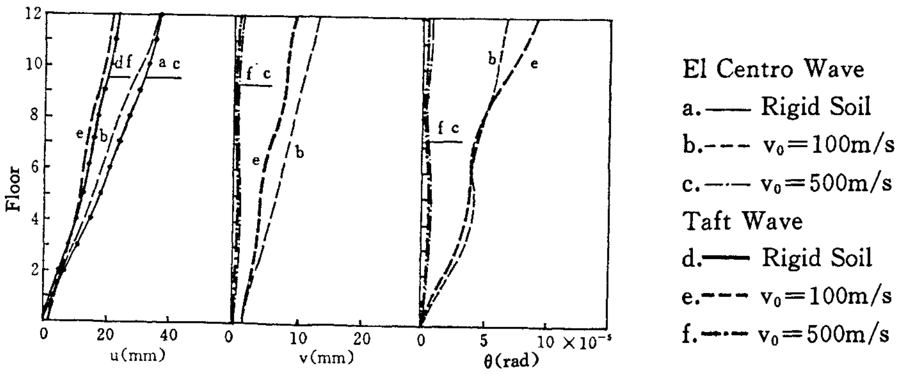

Fig. 5(a) Floor Displacements of Frame Structure

(3) Floor Shear Forces

$\overline{Q}_x^*$, $\overline{Q}_y^*$ and Q_x^*, Q_y^* listed in Table 7 represent shear forces at top of foundation in x and y input primary driections with and without dynamic interaction. Fig. 6 only gives out shear force envelope of super-structure in x input direction, from which shear force in primary direction at top of foundation increases considerablly under interaction condition, and its variation along height under interaction condition is quite different from stiff base condition, meanwhile it causes large floor shear forces in secondary direction, especially for frame-shear wall structure. It can be seen from Table 7 that floor forces in primary direction for both frame and frame-shear wall structural systems can possiblly increase or decrease. The possibility of increasing is greater than that of decreasing, and the increment and decrement values depend on stiffness of structure, stiffness of soil and type of foundation. The stiffer the structure and the more flexible the soil, the greater variation of shear force is. From the example, the range of shear force ratio at top of foundation for frame structure is about 0.807~1.087, and 0.470~1.578 for frame-shear wall structure. Not counting extremely soft case, shear forces at top of foundation for frame structure vary from −15% to 10%, while for frame-wall structure from −30% to 20%.

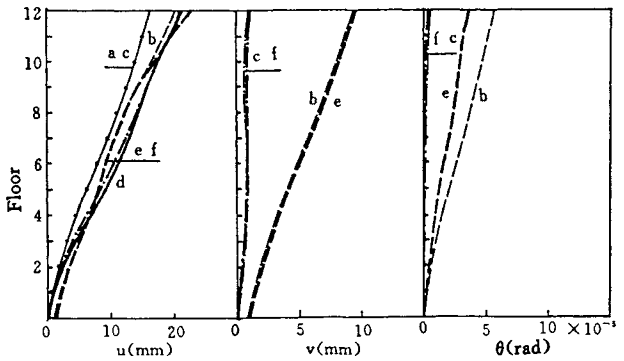

Fig. 5(b) Floor Displacements of Frame-Shear Wall Structure

Table 7 Shear Force Ratio at Top of Foundation of Sturctures

Type of Structures	Seismic Waves	Vs(m / s) Shear Force Ratio	100	200	300	400	500
Frame Structure	El Centro Wave	$\overline{Q}_x^*/Q_x^*$	0.863 (0.897)	0.959 (0.967)	0.902 (0.982)	0.921 (0.988)	0.960 (0.991)
		$\overline{Q}_y^*/Q_y^*$	0.897 (1.020)	0.876 (0.998)	1.042 (1.003)	0.973 (1.004)	0.993 (1.004)
	Taft Wave	$\overline{Q}_x^*/Q_x^*$	0.955 (0.971)	1.016 (0.945)	0.964 (0.961)	0.927 (0.973)	0.941 (0.980)
		$\overline{Q}_y^*/Q_y^*$	0.807 (1.048)	1.087 (1.009)	1.068 (1.017)	1.015 (1.013)	1.004 (1.009)

Type of Structures	Seismic Waves	V_S(m / s) Shear Force Ratio	100	200	300	400	500
Frame-Shear Wall Structure	El Centro Wave	$\overline{Q}_x^* / Q_x^*$	1.350 (0.772)	1.169 (0.908)	0.892 (0.850)	0.797 (0.694)	0.834 (0.709)
		$\overline{Q}_y^* / Q_y^*$	0.475 (0.981)	0.855 (0.802)	0.957 (0.832)	0.956 (0.768)	1.086 (0.899)
	Taft Wave	$\overline{Q}_x^* / Q_x^*$	1.578 (0.766)	0.867 (0.767)	0.939 (0.915)	0.976 (0.952)	0.986 (0.966)
		$\overline{Q}_y^* / Q_y^*$	0.470 (0.778)	1.003 (1.108)	1.050 (1.217)	1.019 (1.109)	1.016 (1.057)

Note: Values in brackets refer to those with piles.

(4) Overturning Moment

Table 8 Overturning Moment Ratio at Top of Foundation of Structures

Type of Structures	Seismic Waves	V_S(m / s) Overturning Moment Ratio	100	200	300	400	500
Frame Structure	El Centro Wave	$\overline{M}_x^* / M_x^*$	0.873 (1.005)	0.947 (1.002)	1.005 (1.001)	1.005 (1.001)	1.003 (1.001)
		$\overline{M}_y^* / M_y^*$	0.929 (0.997)	1.024 (0.993)	1.000 (0.996)	0.990 (0.997)	0.993 (0.998)
	Taft Wave	$\overline{M}_x^* / M_x^*$	0.896 (1.035)	1.032 (0.994)	1.068 (0.995)	0.998 (0.996)	0.996 (0.997)
		$\overline{M}_y^* / M_y^*$	0.782 (0.980)	0.912 (0.998)	0.981 (0.998)	0.994 (0.998)	0.997 (0.999)
Frame-Shear Wall Structure	El Centro Wave	$\overline{M}_x^* / M_x^*$	0.958 (0.928)	0.862 (0.965)	0.909 (0.988)	0.911 (0.996)	0.959 (0.997)
		$\overline{M}_y^* / M_y^*$	0.503 (0.995)	0.916 (1.004)	0.980 (1.014)	1.000 (1.006)	1.019 (1.002)
	Taft Wave	$\overline{M}_x^* / M_x^*$	0.607 (0.875)	0.955 (0.944)	0.898 (0.986)	0.921 (0.992)	0.915 (0.995)
		$\overline{M}_y^* / M_y^*$	0.719 (0.968)	1.051 (1.061)	0.969 (1.085)	0.945 (1.043)	0.996 (1.029)

Note: Values in brackets refer to those with piles.

$\overline{M}_x^*$ $\overline{M}_y^*$ and M_x^* M_y^* in Table 8 represent overturning moment at top of foundation in x and y seismic input primary directions with and without taking interaction into account. Fig. 7 only gives out envelope of overturning moment of super-structure in x direction with seismic input, from which one can see that there exist possibilities of increasing and decreasing of overturning moment both for two types of structure . Increasing of overturning moment most likely occurs at top part of the structure, while the decreasing occurs at the low part of the structure, meanwhile accompanyed with greater overturning and torsional moments in secondany direction, especially for frame-shear wall structure, which may be harmful during earthquake. From Table 8, there are several factors affecting the value of overturning moment, such as stiffness of structure, stiffness of soil and their relative ratio, type of foundation and spectrum characteristics of seisumic input. From the example, the variation range of overturning moment ratio at top of foundation of frame structure is around 0.782～1.068; while the range for frame-shear wall structure is about 0.503～1.085. Not counting extremely soft soil (V_s=100m/s), overturning momnet at top of foundation of frame structure varies from −10% to 10%, for frame-shear wall structure from -15% to 10%.

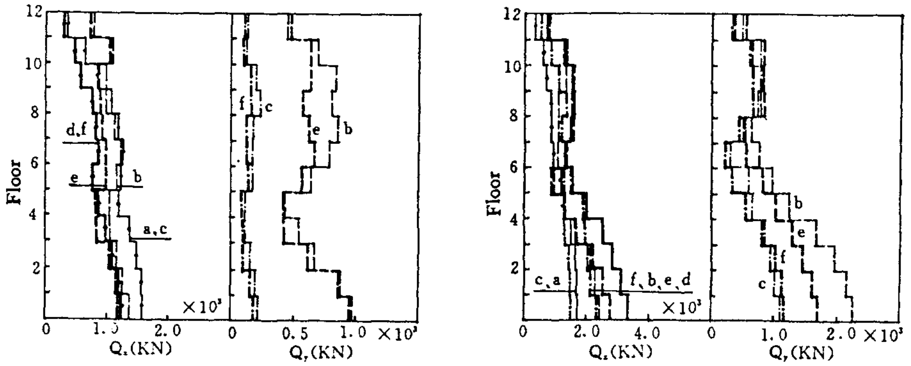

(a) Frame Structure (b) Frame-Shear Wall Structure

Fig. 6 Shear Force Envelopes of Floors in Superstucture

Conclusions

The anthors established a 3-D dynamic high-rise structure-foundation-soil interaction model based on substructure method, and a compiled computer program, which makes it possible to take interaction into account for high-rise buildings quantitatively under earthquake condition. Compare the results of dynamic interaction for different types of structure, foundations, soils and seismic input waves, some conclusions can be drawn:

1. Natural period of each mode of the structure under consideration of interaction is greater in varying degree than that without interaction, varying with stiffness of structure, soil and types of foundation. The stiffer the structure and the softer of the soil, the greater increase of natural period is. For a same soil, increase of natural period for foundation with piles is smaller than that without piles. Increase of natural period of torsional vibration is smaller than that of horizontal vibration.

2. The interaction obviously causes 3-dimensional displacements, one of which, displacment in primary disection may increase or decrease, the variation depends on stiffness of structure and soil, i.e., the greater the stiffness of structure and the softer the soil, the greater the variation is; For a same soil, pile foundation can restrain

the variation of displacement; the other two displacements, secondary transverse and torsion displacements, increase drameticaly compared to those for stiff base (without interaetion). The secondary transverse and torsional displacements caused on foundation have little effects on floor displacemants in the superstructure.

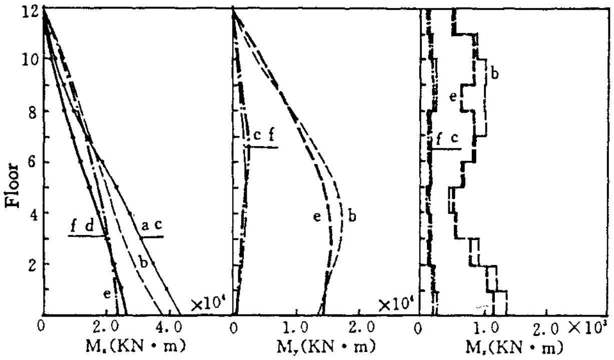

(a) Frame Structure

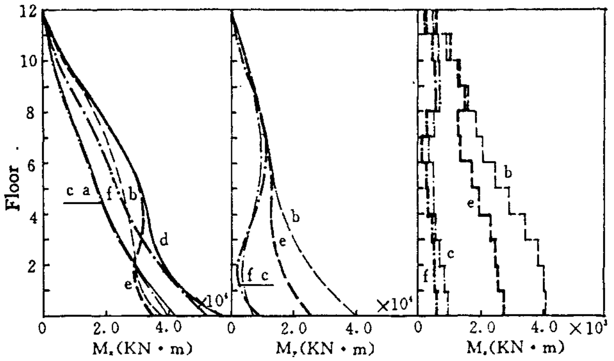

(b) Frame-Shear Wall Structure

Fig. 7 Overturning Moment Envelope of Superstructure

3. The interaction also obviously causes 3-dimensional stresses in structure. The stress in primary direction may increase or decrease compared to stiff base (without interaction), meanwhile, it causes stresses and torsional moment in secondary directions. Stress distribution along the height of the structure is different from that in stiff base (without interaction), which may be greater than that for stiff base, especially top part of the structure. Therefore, it is not rational to consider dynamic interaction just reducing peak value of acceleration and analyzing stress distribution for stiff base condition.

4. Dynamic characteristics and seismic response of the structure taking interaction into account depend not only upon stiffness of structure itself, also upon stiffness of soil, type of foundation and spectrum chanacteritics of seismic input. Therefore, it is necessary to compile a set of computer program of 3-D superstructure-foundation-soil dynamic interaction.

REFERENCES

[1] J. P. Wolf, *Dynamic Soil-Structure Interaction*, Prentice-Hall, (1985).

[2] M. Novak, Effect of soil on structure response to wind and earthquake, *EESD* , **3** (1974).

[3] N. C. Tsai, et al. , The use of frequency independent soil-structure interaction parameters, *Nuclear Eng. and Design* , 31(1974).

[4] K. Ahn, P. L. Gould, Soil-pile-structure interaction effects on the seismic response of a cooling tower, *EESD* , 18(1989).

[5] K. S. Wang, et al. , Soil-structure interaction earthquake response and practical analysis, *J. of Architecture structure* , **7**(2),(1986)(in Chinese).

[6] Y. W. Wang and K. S. Wang, Structure-pile-soil interaction earthquake response analysis, *J. of Architecture Structure* , **6**(5), (1985) (in Chinese).

[7] G. Gan and S. M. Wu, Horizontal dynamic characteritics of pile foundation, *J. of Zhejiang University*, **30**(5), (1996)(in Chinese).

[8] G. Gan and S. M. Wu, Calculation of dynamic impedance function of foundation on layered soils, *Proc. 7th Conf. of SMFE Zhejiang Province* , Nuclear Press, (1996) (in Chinese).

[9] G. Gan and S. M. Wu, Vertical dynamic characteristics of pile foundation, *Proc. 2nd Intl. Syp. of Struct. and Found. Eng* . Hongkong (1997) (in Chiense).

[10] G. Gan, 3-D dynamic high-rise strucutre-foundation-soil interaction, *Ph. D, thesis* , Zhejiang University, (1996) (in Chinese).

NONLINEAR DYNAMIC ANALYSIS OF SATURATED SOIL-STRUCTURE INTERACTION BY FEM[*]

Song Erxiang, Yao Zhiquan and Qiu Zonglian
(Tsinghua University, Beijing, China, 100084)

Abstract

Nonlinear dynamic interaction of saturated soil and structure is analyzed by using the direct finite element method. Undrained conditions are assumed and an overlay model is proposed to describe both plastic deformation and pore pressure build up in the porous soil. In order to model the infinite soil region by a finite element mesh appropriately, the viscous boundary with minor modifications is applied to the nearly incompressible soil. Some numerical examples are presented to show the performance of the analysis procedure and to investigate some influence factors.

1. Introduction

Since the last two decades, much efforts have been devoted to the study of dynamic soil-structure interaction, and considerable progress has been made in understanding this problem as well as in the analysis methods. For a comprehensive review of the state of the art one may refer to the paper by Zhang[1], Xiong[2] and the monographs by Wolf [3][4] and many other papers.

In most of the papers published, the soil is often assumed to be a linear elastic or visco-elastic material. This is appropriate for vibrations in relatively small amplitude, and is also valuable for giving insight into more complex response of SSI system. However, for the vibration under relatively strong earthquake, the soil may show strong non-linearity, and a linear analysis may not sufficient. Although the equivalent linear analysis method has been proposed to treat the nonlinearity of the soil, its disadvantages are obvious compared with a truly nonlinear analysis. For instance, it does not calculate any residual deformation, and for some cases it may predict a false resonance. Therefore, truly nonlinear analysis is necessary for important structures.

Soil can be considered as the most complicated engineering material, especially when considering dynamic repeated loading. Under relatively low load level, it already shows nonlinearity. And another well known fact is that soil under repeated shearing may densify in drained condition and in undrained conditions pore pressure may build up, or even cause liquefaction of the soil. Past earthquake hazards, such as those happened during the Niigata earthquake in Japan and Tangshan earthquake in China, showed that soil liquefaction may cause collapses of many buildings.

---

[*] This project is financially supported by the National Natural Science Foundation of China

In this paper attempts are made to study the nonlinear analysis of soil-structure interaction. The soil is seen as a two phase material, and special attention is paid to consider the plastic deformation and pore pressure build up in the porous soil. An overlay model is proposed to describe the soil plasticity and pore pressure build up. The direct finite element method together with the viscous boundary is employed to model the soil-structure system. Some numerical examples are presented to show the performance of the analysis procedure and to investigate some influence factors.

2. Equation of Motion of Saturated Soils

The dynamic equation of motion for saturated soil was first derived by Biot[5] and later was developed by many researchers. Here we use the formulation given by Zienkiewicz[6].

The overall equilibrium equation of the saturated soil is written as

$$\sigma_{ij,j} + b_i = \rho \ddot{u}_i + \rho_f \ddot{w}_i \tag{1}$$

where σ_{ij} are the total stresses, i.e. the effective stress plus the pore water pressure p, b_i is the body force, ρ the density of the soil-water mixture, and ρ_f is the density of the water, w_i is the averaged displacement of pore water relative to the soil skeleton. The two superimposed dots represent second derivative with respect to time. In the last term, the actual fluid mass in a unit total volume should be $n\rho_f$, the drop of n is due to that w_i is defined as the ratio of the displaced fluid quantity over the total cross sectional area.

The continuity equation is written according to the principle that the out flow of pore fluid must be equal to the decrease of the pore volume and the volume expansion of the pore fluid, thus we have

$$\dot{w}_{i,i} = -\dot{\varepsilon}_{ii} - (1-n)\dot{p} / K_s + \dot{\sigma}'_{ii} / (3K_s) - n\dot{p} / K_f \tag{2}$$

The first 3 terms on the right hand side are all pore volume decrease due respectively to the rearrangement of soil particles, compression of soil particles by the pore pressure p, compression of soil particles by the effective mean stress, and the last term represents the pore fluid expansion. In the above equations, the stress is defined as positive for tension, whereas the pore pressure is positive for compression.

Considering the equilibrium of the flowing fluid, on which the seepage force, the pressure difference, the water weight and the inertia forces are acting, we may obtain the dynamic form of the Darcy's law relating the seepage velocity with the water pressure as follows

$$-p_{,i} + \rho_f g_i = k_{ij}^{-1} \dot{w}_j + \rho_f (\ddot{u}_i + \ddot{w}_i / n) \tag{3}$$

Eqs. (1)-(3) together with the strain-displacement relation and the strain-effective stress relation, which are all similar to those in continuum mechanics, define the whole problem. By eliminating the stresses, strains and pore pressure variables, two sets of equations governing the six displacement variables u_i and w_i may be obtained.

For engineering application it is often more convenient to use some simplified form of the above equations. For some limit conditions simplification is also necessary to get better numerical performance of the solution procedure. For medium speed phenomena, a so called U-p formulation is preferred. In this case $\ddot{w}_i$ is relatively small and can be neglected. Then the variable w_i can be simply eliminated by using equation (2) and (3) to give

$$(k_{ij}p_{,j})_{,i} - \dot{\varepsilon}_{ii} = -(k_{ij}\rho_f \ddot{u}_j)_{,i} + \left(\frac{n}{K_f} + \frac{1-n}{K_s}\right)\dot{p} - \dot{\sigma}'_{ii} / (3K_s) \tag{4}$$

Consequently the number of variables is reduced.

Under earthquake excitation, the loading rate is too rapid to allow significant dissipation of the pore fluid, even for a sandy soil. Hence, undrained conditions may be assumed. In undrained conditions, the seepage velocity and displacement can never reach significant values, then we obtain the limiting case of untrained behavior. The equations are obtained by making $k_{ij}=0$, thus Eq. (4) reduces further to

$$-\dot{\varepsilon}_{ii} = n\dot{p} / K_f + (1-n)\dot{p} / K_s - \dot{\sigma}'_{ij} / (3K_s) \tag{5}$$

As K_s is much greater compared with K_f for soil, the terms containing K_s can be neglected. Then p, with its positive definition being changed now to be the same as the normal stress, is related with the volume strain as

$$\dot{p} = K_w \dot{\varepsilon}_{ii} \qquad \text{with} \qquad K_w = \frac{K_f}{n} \tag{6}$$

Then an explicit relation between the total stress and the strain can be obtained, allowing the displacement field to be solved with a procedure similar to that used for one phase material. After the solution of the displacements, the strains and then the effective stress and the pore pressure can be determined. Hence the influence of the pore pressure can be considered with minor extra efforts. This is the so called effective stress method, which will be applied later in this paper.

3. Stress-Strain Relationship of Saturated Soil

Much efforts have been made to study the behavior of soil under repeated loading. Basically, there are two lines which can be followed for the analysis of soil under repeated loading. One is within the framework of elasto-plasticity theory. A complicated stress-strain model should first be developed to model the cyclic behavior of soil, such as the nested yield surface model[7] and the bounding surface model[8]. While this method is good for its solid theoretical background, it also has some serious disadvantages. As pointed out by Finn et al[9], none of these models can predict the volume change satisfactorily, and formidable costs prevent them from being used for practical analysis. Another line we may follow is that we construct a model based directly on cyclic loading tests to describe the soil behavior for a certain type of loading. Analysis with this kind of models is considered to be more reliable and more economical, at least in the present stage of development.

In this study we will follow the second line. A densification model is proposed to model the pore pressure build up in the soil during repeated loading. The soil failure is described by the well established Mohr-Coulomb model. Then the two models are combined to form an overlay model to give a reasonable description of the soil behavior.

(1) Failure condition of soil

Soil under dynamic loads shows a relatively high strength and high stiffness. This is more pronounced for clay under undrained dynamic loading. However, the difference under earthquake conditions, the loading rate of which is relatively low, is not large, and can be neglected for an engineering analysis [10]. Under many cycles of repeated loading, the soil always shows a densification or pore pressure build up. At the same time the strength and stiffness degrade. This will be modeled here with the densification model. Experiments also show that the effective soil strength parameters are about the same as those under static loading. Therefore the well established Mohr-Coulomb model is employed in this study to model the failure of a sandy soil. The failure surface of the model is expressed as

$$0.5(\sigma_1-\sigma_3)+0.5(\sigma_1+\sigma_3)\sin\phi-c\cos\phi=0 \tag{7}$$

Nonassociated plastic flow is assumed to give a more realistic prediction of the plastic volume change of the soil. The plastic potential function takes the same form as the yield function with only the friction angle being replaced by the dilatancy angle. An efficient procedure is proposed in reference [11] to integrate this model.

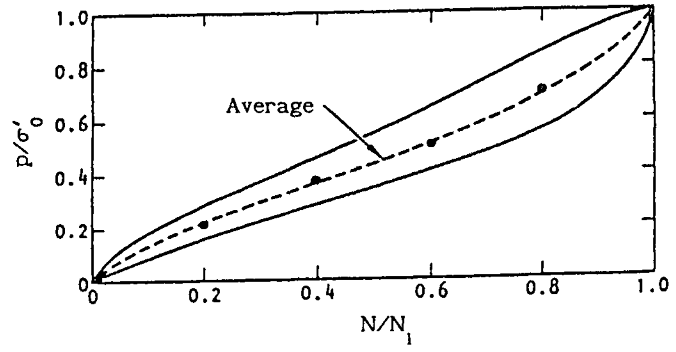

Fig. 1 Pore pressure build-up in undrained cyclic tests (Seed et al, 1976)

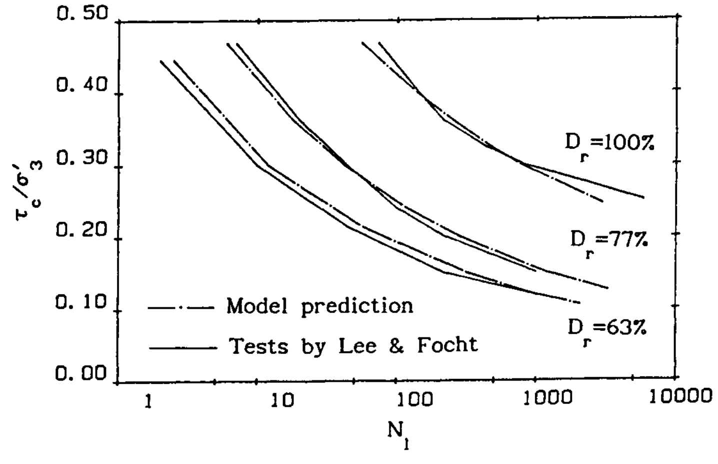

Fig. 2 Cyclic loading strength from undrained tests

(2) The densification model

Many tests have been reported on the cyclic behavior of soil. The main results about the pore pressure build up can be summarized as two curves, one is the p/σ'_0 versus N/N_l curve (Fig. 1), and the other the N_l versus τ_c/σ'_0 curve (Fig. 2), where N_l is the number of cycles to liquefaction. The first curve was proposed by Seed [12]. It expresses that there exists a nearly unique relation between the normalized pore pressure and the normalized cyclic loading cycles. The function of this curve can be written as

$$\frac{p}{\sigma'_{mo}} = \frac{1}{2} + \frac{1}{\pi}\arcsin[2(\frac{N}{N_l})^{1/\eta} - 1] \tag{8}$$

where η is a constant. The average curve in Fig. 1 is corresponding to $\eta = 0.7$. The second figure indicates that the number of cycles to liquefaction depends strongly on the shear stress ratio and the relative density.

The densification model proposed here is based on these two curves. It is intended to predict directly the volume densification instead of pore pressure increase. This is to make it applicable both for undrained and partially drained conditions. In order to use undrained test results to predict the densification, we need to relate the densification to the excess pore pressure. In an undrained test the total stress remains the same after one cycle, hence the change of pore pressure dp and the effective mean stress $d\sigma'$ should be equal in magnitude and opposite in sign, i.e.

$$dp = -d\sigma' \tag{9}$$

The effective isotropic stress $d\sigma'$ can be estimated as

$$d\sigma' = K(d\varepsilon_v - d\varepsilon_{vc}) \tag{10}$$

where K is the compression modulus of the soil skeleton, and $d\varepsilon_v$ and $d\varepsilon_{vc}$ are the total and plastic volume strain (densification) increment respectively. Under undrained conditions $d\varepsilon_v$ can be neglected compared to $d\varepsilon_{vc}$. Thus from the above two equations we get

$$dp = Kd\varepsilon_{vc} \tag{11}$$

This equation enables us to estimate the densification from the pore pressure induced by cyclic loading. Indeed, K will also change with the stress state. However an average value of interest will be used herein to simplify the numerical procedure. In this way the densification estimated may be not so accurate, but the pore pressure build-up under undrained and partially drained conditions is believed to be modeled properly.

By using the above relation between densification and pore pressure build up and the two test curves we are able to give a formula to predict the densification under cyclic loading. However the model proposed here is not just by curve fitting. Attention is paid to make the model give reasonable prediction not only for undrained but also partially drained conditions. To this end consideration is given to the fact that as densification is accumulating, it will be more and more difficult to achieve further densification. Therefore a hardening term is included in the model. Here we just write out the formulas below, for detailed derivation the reader is refereed to reference [13].

$$d\varepsilon_{vc} = F(\frac{\tau_c}{\sigma'_m}, \varepsilon_{vc})dN \tag{12}$$

$$F(\frac{\tau_c}{\sigma'_m}, \varepsilon_{vc}) = D_1(\frac{\tau_c}{\sigma'_m} - S_{\min})^{\frac{1}{2}}(\frac{\tau_c}{\sigma'_m})^{\theta}\exp(-D_2\varepsilon_{vc}) \tag{13}$$

$$D_1 = D_1^*\sigma'_{m0}/K \qquad D_2 = D_2^*K/\sigma'_{m0} \tag{14}$$

where ε_{vc} is the densification, N is the number of loading cycles, D_1^*, D_1^*, θ and $S_{\min}$ are material parameters describing soil behavior under cyclic loading and can be determined by cyclic undrained tests, $S_{\min}$ is the threshold cyclic shear stress ratio below which no densification occurs; σ'_{m0} is the initial consolidation stress, σ'_m is the present effective stress, τ_c is the shear stress induced by cyclic loading.

For anisotropicly consolidated soil, it is generally realized that the pore pressure build up will be limited [14].The limit of the pore pressure in undrained tests can be estimated by the following formula (see Fig. 3)

$$p_{\max} = \sigma'_{m0} - \sigma_{d0} / M \tag{15}$$

where $\sigma_d = \sigma_1 - \sigma_3$ is the deviator stress, and M is the slope of the failure line and can be related with the angle of internal friction. Here we just use the slope of the Mohr-Coulomb failure line.

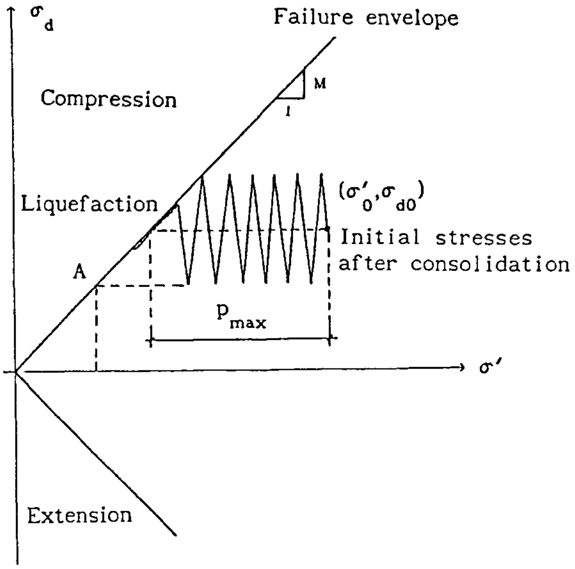

Fig. 3 Limiting value of pore pressure in soil under anisotropic conditions

The explanation for this pore pressure limitation is that when the soil approaches failure, more dilatancy will be developed so that the pore pressure will remain stable around some value. This means that no densification can be achieved any more. However, this is only true for undrained conditions. For partially drained conditions further densification may be expected, at a more or less lower rate. According to the discussion above, the effect of static shear stress is considered in an approximate way. That is, the densification ratio will be reduced to a very small amount when the failure line is approached.

The model given so far is only applicable to uniform cyclic loading. In order to apply it for earthquake loading an approximate procedure is used to transform the load cycles to the length of the dynamic shear stress path, i.e. to write the densification model as

$$d\varepsilon_{vc} = f(\frac{\tau}{\sigma'_m}, \varepsilon_{vc})d\tau \tag{16}$$

One cycle of loading can be seen as that the shear stress goes form 0 to τ_c four times. By further assuming a uniform densification during the whole stress path, we have

$$4\int_0^{\tau_c} f d\tau = F \tag{17}$$

By analyzing each factor in F, we see the change of $\exp(-D_2\varepsilon_{vc})$ within one cycle is very small, hence it can be seen as a constant. Besides, θ is usually much larger than 1, the change of $(\tau_c / \sigma'_m - S_{\min})^{0.5}$ is much slower than that of $(\tau_c / \sigma'_m)^{\theta}$. Hence as an approximation, only the factor $(\tau_c / \sigma'_m)^{\theta}$ is considered as a varying term in considering the integration, and even one step further only τ is seen as a variable. Then we have

$$f(\frac{\tau}{\sigma'_m}, \varepsilon_{vc}) = \overline{D}_1 (\frac{\tau}{\sigma'_m} - S_{\min})^{\frac{1}{2}} \frac{\tau^{\theta-1}}{(\sigma'_m)^{\theta}} \exp(-D_2\varepsilon_{vc}) \tag{18}$$

where $\overline{D}_1 = \theta D_1 / 4$, and the original dynamic cyclic shear stress amplitude τ_c in F is replaced by the current cyclic shear stress τ and all the other variables remain the same as above.

The densification is actually a plastic volume strain and it can be treated in the system response analysis in a similar way as for ordinary plasticity. Densification will reduce the effective stress and at the same time increase the pore pressure.

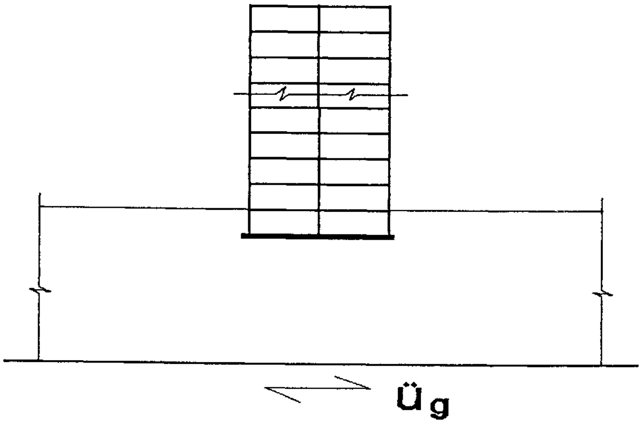

Fig. 4 A soil-structure system

4. Analysis of the Soil-Structure System

For definiteness, the soil considered here in the soil-structure system is assumed to lie above a relatively hard layer, such as a rock or a very dense sand layer (Fig. 4). Then only the soil above this hard layer is discretized into finite elements. Earthquake input can be prescribed on the lower boundary. The superstructure can be ether a frame or a shear-wall structure. The soil and the shear wall are discretized into 6 node triangle elements. The lowest order element is rejected for its serious shear locking for incompressible material. The frame structure is discretized into 3 node Mindlin beam elements, which enables the consideration of shear deformation in beams and columns. More important is that this type of beam elements can easily insure deformation compatibility with the surrounding soil elements. Since the soil layer extends to infinity in both directions, a transmitting boundary is applied on the vertical artificial boundary to maintain the mesh in a manageable size.

(1) The transmitting boundary

Many types of transmitting boundaries are proposed to model the infinite soil region. Some of these boundaries are frequency dependent and cannot be applied for time domain analysis. The most suitable transmitting boundary for time domain analysis by finite elements should be the viscous boundary, first developed by Lysmer and Kulehmeyer [15] and then improved by White et al [16], and the interpolation transmitting boundary by Liao and Wong [17]. The higher order Liao boundary has a high accuracy, but it may have stability problem. The first order Liao boundary and the viscous boundary are mathematically the same. For simpleness and efficiency, the viscous boundary is employed in this study. That is both normal and tangential surface tractions are applied on the vertical boundary and they are calculated as

$$\sigma = a\rho V_p \qquad \tau = b\rho V_s \tag{19}$$

As suggested by White et al, the constants a and b should be dependent on the Poisson's ratio. Here we just take an average value for a and b, namely we take a=1.0 and b=0.74. To determine the surface tractions we also need the P and S wave velocities. As here we are considering undrained soil, the P wave velocity should be calculated as

$$V_p = \sqrt{(K + K_w} + 4G/3)/\rho \tag{20}$$

whereas the S wave velocity is calculated as usual. Obviously, V_p is much greater than V_s. As stated in Eq. (19), the P wave velocity should be applied in the normal direction of the artificial boundary and the S wave velocity in the tangential direction. However numerical calculations show that it gives poor results when doing in this way for undrained soil. Somewhat better results can be obtained by applying the S wave velocity in both directions.

To investigate the accuracy of such a boundary treatment , the vertical vibration of a footing on a horizontal soil layer is analyzed by using several meshes, the distance from the footing edge to the artificial boundary ranges from 3 to 8 times the footing width. The fundamental period of the soil layer is estimated to be 1s, and the period of the load is 0.25s. Hence it ensures the existence of energy transmission to the far region in the reality. Both the free boundary and the two versions of viscous boundary are employed for the analysis. It is found by examining the displacement time history of the footing that the present version of viscous boundary performs better than all the other boundaries. However, a little damping is always needed to get satisfactory results.

When there is plasticity close to the artificial boundary, the S wave velocity V_s must be reduced. As an elasto-perfectly plastic model is employed here, a zero value for V_s is used in the incremental equilibrium equations when this occurs. The validity of this treatment requires still some study.

(2) Governing Equation of the Soil-Structure System

The dynamic equation of motion of the SSI system can be written as

$$[M]\{\ddot{u}\}+[C]\{\dot{u}\}+[K]\{u\}=-[M]\{m\}\ddot{u}_g+\{F_v\} \tag{21}$$

where $\{u\}$、$\{\dot{u}\}$、$\{\ddot{u}\}$ are respectively the nodal displacements, velocities and accelerations with respect to the underlying rock layer.[M], [C] and [K] are respectively the mass matrix, damping matrix and stiffness matrix. When plasticity presents, it is more appropriate to use the incremental form of Eq. (21) and then the matrix [K] should be the tangential matrix. $\ddot{u}_g$ is the earthquake induced acceleration of the underlying hard layer. If only the horizontal acceleration is considered, for instance, then $\{m\}=[1,0,1,0......1,0]^T$. $\{F_v\}$ is the force vector corresponding to the viscous dampers on the artificial boundary. It is nonzero only when there is difference between the motion on the near side of the artificial boundary and the motion in the free field. Hence it is written as

$$\{F_v\}=-[C_b](\{\dot{u}_b\}-\{\dot{u}_{bf}\}) \tag{22}$$

where

$$[C_b]=\int[N]^T\begin{bmatrix} a\rho V_p & 0 \\ 0 & b\rho V_s \end{bmatrix}[N]dA \tag{23}$$

$$[N]=\begin{bmatrix} N_1 & 0 & \dots & \dots & N_n & 0 \\ 0 & N_1 & \dots & \dots & 0 & N_n \end{bmatrix} \tag{24}$$

ρ is the mass density of the soil, V_p and V_s are the P and S wave velocities respectively. $\{\dot{u}_b\}$ and $\{\dot{u}_{bf}\}$ are respectively the nodal velocities on the boundary and in the corresponding free field.

Substituting Eq.(22) into Eq. (21) and moving the term containing the unknown nodal velocities to the left, we have

$$[M]\{\ddot{u}\}+[\tilde{C}]\{\dot{u}\}+R(u)=-[M]\{m\}\ddot{u}_g+\{\tilde{F}_v\} \tag{25}$$

where

$$\{\tilde{F}_v\}=[C_b]\{\dot{u}_{bf}\} \qquad [\tilde{C}]=[C]+[C_b] \tag{26}$$

The mixed mass matrix, i.e. a combination of the consistent and the lumped mass matrix, is employed, in order to enhance the accuracy and allow somewhat coarser mesh [18]. For the 6 node triangle element the lumped mass matrix is calculated by using the Newton-Kotes integration, which lumps the mass just to the 3 nodes on the middle of the element sides. By using the mixed mass matrix, the element size can be $\lambda_{min}/4$, where λ_{min} is the minimum wave length to be considered. This is checked by doing calculations with different element sizes.

The determination of damping matrix is still a difficult problem. As nonlinearity has been considered, a part of the damping may be thought as included in the plasticity. However, damping and plasticity are not exactly the same. Besides, what we apply here is an elasto-perfectly plastic model, which predicts no plasticity for low level deformations. Hence, an explicit damping matrix [C] is still included. Here [C] is assumed to be a linear combination of the mass and stiffness matrix, but now this is done at element level, i.e.

$$[C]^e = a_0[M]^e + a_1[K]^e \tag{27}$$

where$[M]^e$ and $[K]^e$ are respectively the element mass and stiffness matrix. The 2 constants a_0 and a_1 are estimated as below

$$a_0 = \xi\omega \qquad a_1 = \xi / \omega \tag{28}$$

where ω and ξ are respectively the fundamental frequency and the corresponding damping ratio for each part of the structure, i.e. the soil or the superstructure.

In the above equation for establishing the damping matrix, the element stiffness matrix $[K]^e$ can be taken in several different ways, such as the elastic stiffness matrix, the tangential stiffness matrix or a combination of them [19]. It may be more proper to use the tangential stiffness, but many tests are interpreted by using the elastic stiffness and satisfactory results are claimed. Hence here we just use the elastic stiffness, which also makes the analysis simpler.

The free field motion is calculated by assuming an upwards propagating shear wave. This assumption is reasonable for soil underlay by rock layers.

To solve Eq. (25) Newmark's method is applied to treat the time variable and the initial stiffness method is used to treat the material plasticity. In order to avoid error accumulation, it is suggested to use the global equilibrium equations instead of the incremental equilibrium equations to estimate the out of balance error. Comparisons show that this procedure is much more accurate with only minor extra computational effort.

5. Numerical Examples and Discussions

As numerical examples the earthquake response of a soil-structure system is analyzed by the above numerical procedures. The structure considered is a framed structure of 15 storeys high on raft foundation. One building unit is taken for the analysis and two dimensional deformation is assumed. The stiffness is calculated from the frame structure and the masses are due to the whole unit of the building. Detailed information is given in reference [20].The soil layer is assumed to be 20m thick. The Tianjin record of the Tangshan earthquake, with the maximum acceleration being adjusted to 0.1g, is used as the earthquake input on the bottom boundary. Strictly speaking it is not proper without doing a back calculation to find the motion of the underlying rock layer, but considering the random nature of any earthquake, it can be seen as acceptable to do in such a way. Before performing the earthquake response analysis, a static analysis is first carried out to obtain the initial stresses in the soil. The time history of the displacement at the top of the structure and the base shear forces are shown in Fig.5 and 6. The contour of residual pore pressure is shown in Fig.7.

From Fig. 7 we note that the maximum pore pressure occurs relatively far from the structure and close to the ground surface. This is in agreement with the pore pressure build up mechanism recognized through experiments. Just beneath the structure, the normal stress is in a greater magnitude, and consequently the shear stress ratio is smaller. Next to the structure, the pore pressure is also smaller due to the existence of a much greater static shear stress. As here completely undrained conditions are assumed, the maximum pore pressure occurs very close to the surface. In reality pore pressure dissipation may easily occur close to the free surface, then we may expect the maximum pore pressure will occur at somewhat deeper position. This is in agreement with field observations.

For the same structure, analysis is also carried out by the conventional procedure, that is without the consideration of soil-structure interaction. In this analysis the soil is assumed to be completely rigid and only the superstructure is taken for the analysis. The earthquake input is prescribed at the raft foundation. In order to see the interaction effect by comparing this analysis with the former one, this earthquake input is calculated from the free field response analysis by using the same earthquake excitation on the bottom boundary. The results are shown in Fig. 8 and 9. By comparing them with Fig. 5 and 6 we see that the interaction analysis gives a somewhat greater displacement and lower base shear.

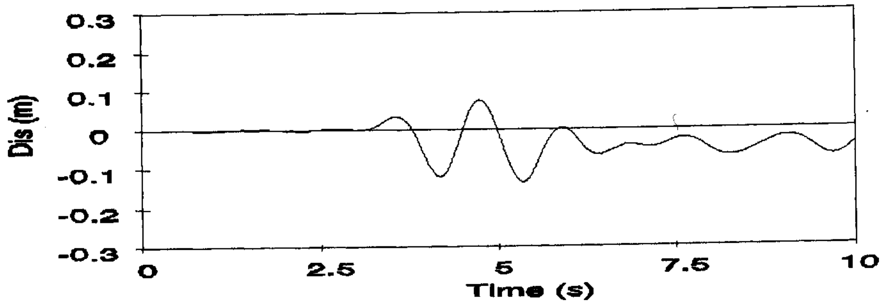

Fig. 5 Displacement at top of the structure with SSI

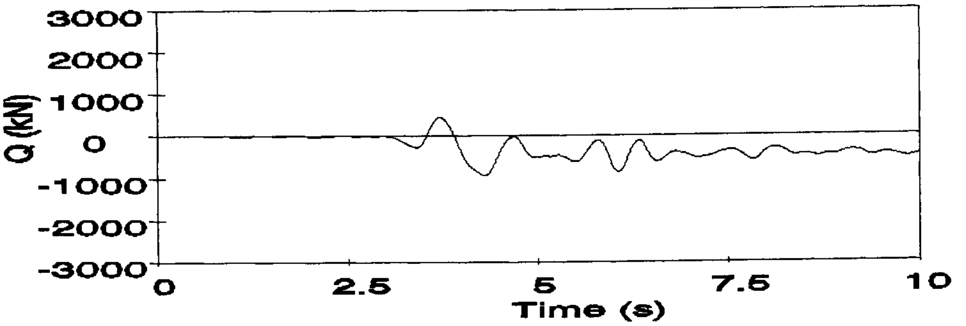

Fig. 6 Base shear force of the structure with SSI

Completely undrained assumption is an extreme condition. Another extreme is to assume totally drained condition, namely to completely neglect the influence of the pore water during the dynamic analysis. To get some insight into the influence of the pore water, drained analysis is also carried out. The results are shown in Fig. 10 and 11. Here we note a reduction of displacement response and an increase in base shear. However, we cannot conclude that it is on the safe side if pore water is not considered. As pore pressure build up reduced the strength and stiffness of the soil. It may cause failure of the structure after the earthquake.

All the calculations above were carried out on a 586 micro computer, the computer time consumed for each interaction analysis was about 2 hours. For each time step only 3-4 iterations were needed, and no numerical instability was noted for this type of nonlinear problem with non-proportional damping.

6. Conclusion

Numerical procedures are discussed for the nonlinear analysis of dynamic soil-structure interaction. The soil is seen as a two phase material and undrained conditions are assumed. Attention is paid to consider the elasto-plastic deformation and the pore pressure build up in the porous soil. For this purpose an overlay model is proposed which combines the well established Mohr-Coulomb model for the soil plasticity and a densification model for the pore pressure build up. Calculations show the efficiency of this model.

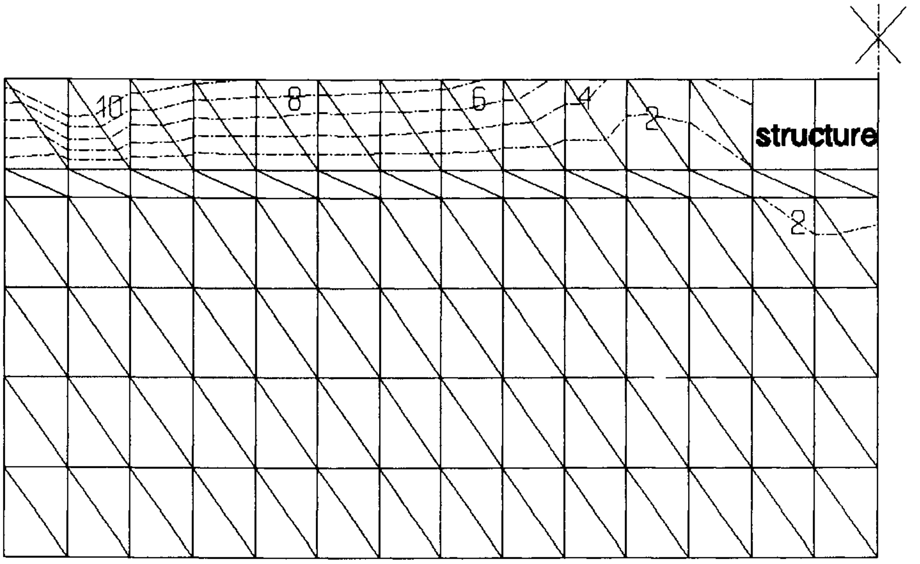

Fig. 7 Contour of the steady pore pressure at t=10s

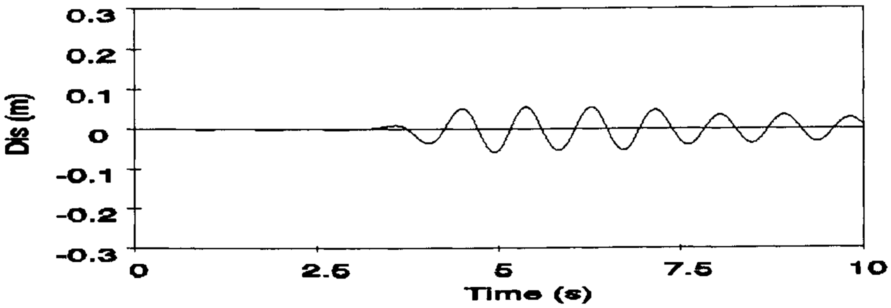

Fig. 8 Displacement at top of the structure without SSI

In order to model the infinite soil region by finite elements, the viscous boundary with minor modifications is tried for the undrained incompressible soil. The accuracy seems acceptable. However, it still requires some research into its application when nonlinearity exists close to the artificial boundary.

Some numerical examples showed a satisfactory performance of the numerical model and the computational procedure, although both nonlinearity and nonproportional damping are involved here. The computer time for an interaction analysis is quite modest. This is encouraging for doing truly nonlinear analysis

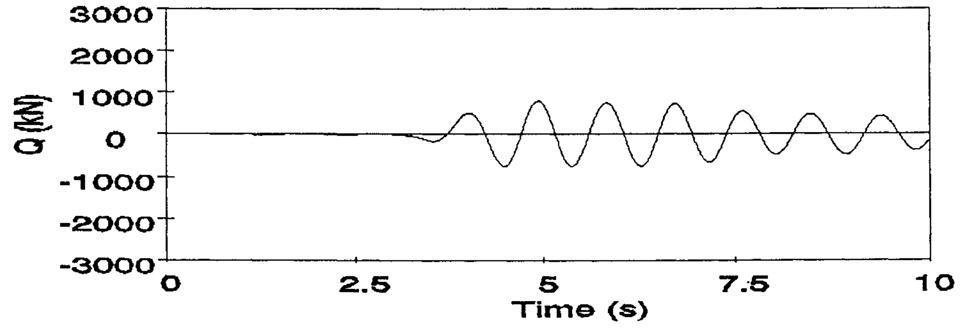

Fig. 9 Base shear force of the structure without SSI

What worth mentioning is that calculations show plasticity and pore pressure build up are more prominent in the far field. Therefore, it is imperative to study transmitting boundaries for such kind of problems.

Nonlinear dynamic soil structure interaction is a very complex problem. This study is still to be continued further. Much has to be done in investigating the performance of the model and the numerical procedures as well as the various influence factors on the response of a soil-structure system.

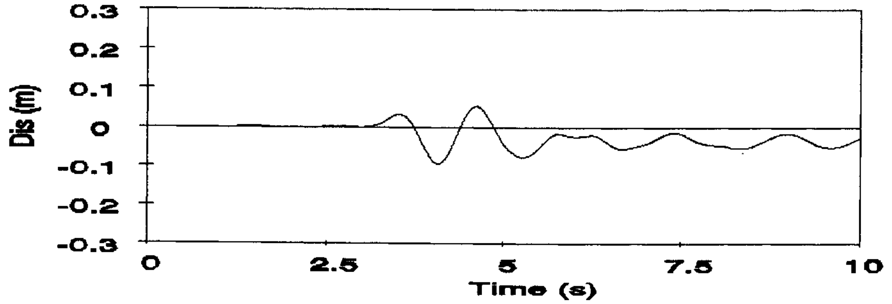

Fig. 10 Displacement at top of the structure on drained soil

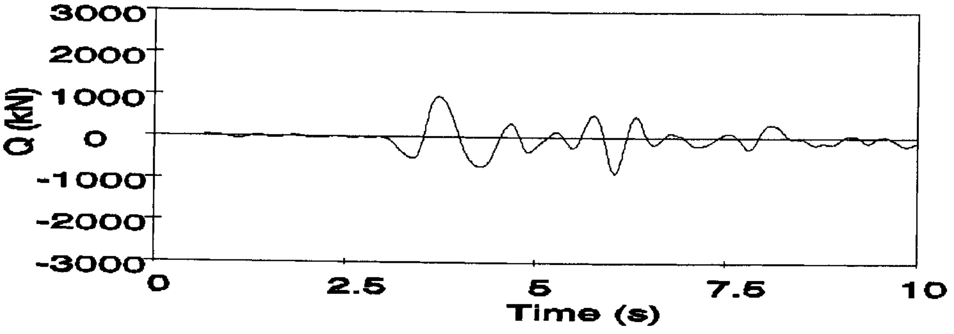

Fig. 11 Base shear force of the structure on drained soil

7. References

[1] Zhang Chuhan, On the dynamic soil-structure interaction, *Proc. of 1st National Conference on Structure-Medium Interaction,* 1993. (in Chinese)

[2] Xiong Jianguo, Recent advances in research on dynamic soil-structure interaction, *Protective Engineering,* (3), 1993, 27-41. (in Chinese)

[3] Wolf, John P., *Dynamic Soil Structure Interaction,*Prentice-Hall, Englewood Cliffs, NJ. 1985.

[4] Wolf, John P., *Dynamic Soil-Structure Interaction in Time domain,* Prentice-Hall, Englewood Cliffs, NJ. 1988

[5] Biot M.A., Theory of propagation of elastic waves in fluid saturated porous solid, *J. Acoust. Soc. of America,* **28**(2), 1956, 168-191.

[6] Zienkiwicz O.C. and Shiomi T., Dynamic behavior of saturated porous media; the generalized Biot formulation and its numerical formulation, *Inter. J. Num. Analy. Methods Geomech.* **8**(1), 1984, 71-96.

[7] Mroz Z. et al, An anisotropic hardening model for soils and its application to cyclic loading, *Int. J. Num. Analy. Methods Geomech.,***2**, 1978, 203-221.

[8] Dafalias Y.F. and Herrmann L.R., Bounding surface formulation of soil plasticity, in *Soil Mechanics-Transient and Cyclic Loads,* Wiley, London, 1982, 253-282.

[9] Finn W.D.L. et al. Comparative assessment of methods for dynamic effective stress analysis, *Proc. of NUMOG III,* Niagara Falls,Canada, May, 1989.

[10]Xie Dingyi, *Soil Dynamics,* Earthquake Engineering Press, 1977 (in Chinese)

[11]Song Erxiang and Vermeer P.A., Implementation and application of Mohr-Coulomb model with tension cut off for limit load analysis, *Proc. of Inter. Conf. on Comp. Meth.in Struct. and Geotech. Eng.*, Hong Kong, Dec. 1994.

[12]Seed H.B. et al. Pore pressure changes during soil liquefaction, *J. of Geotechnical Engineering, ASCE,* **102**(4), 1976. 323-346.

[13]Song Erxiang, Analysis of pore pressure build up by overlay models, *Proc.of 4th Inter. Conf. on Polar and Offshore Eng.*,Osaka, Japan, April, 1994.

[14]Vaid Y.P. and Chern J.C., Effect of static shear on resistance to liquefaction, *Soils and Foundations,* **23**(1), 1983, 47-60.

[15]Lysmer J. and Kulehmeyer R.L., Finite dynamic model for infinite media, *J. of Engineering Mechanics, ASCE.* **95**(4), 1969. 859-877.

[16]White W. et al. Unified boundary for finite dynamic models, *J. of Engineering Mechanics, ASCE.* **103**(5), 1977. 949-964.

[17]Liao Z.P. and Wong H.L., A transmitting boundary for the numerical simulation of elastic wave propagation, Soil *Dynamics and Earthquake Engineering,* **3**(4), 1984, 174-183.

[18]Liu Jingbo, *Finite element simulation of wave propagation and analysis of earthquake response of complex ground,* PhD. thesis, Engineering Mechanics Institute of National Seismic Bureau, 1989. (in Chinese)

[19]Huang Zongming et al, On the damping estimation in time domain analysis of earthquake response of structures, *Earthquake Engineering and Engineering Vibration,* **16**(2), 1996, 95-105. (in Chinese)

[20]Yao Zhiquan, *Nonlinear finite element analysis of dynamic undrained soil-structure interaction,* Thesis, Tsinghua University, Beijing, China, 1997. (in Chinese)

DYNAMIC SOIL-STRUCTURE INTERACTION ON LAYERED STRATA UNDER SEISMIC WAVE INCIDENCE

Xu Zhixin and Liao Heshan
(Institute of Structural Theory, Tongji University, Shanghai, China, 200092)

Abstract

Soil-structure interaction solved by means of boundary element method in frequency domain is presented. Some examples illustrate the practical use of this method. A new type of two dimensional boundary element method in time domain, velocity type boundary element method, is also presented.

Introduction

Amplification of earthquake ground motion on soft soil deposit is well known and verified by recent earthquakes and downhole recordings [1], [2], [3]. This phenomena is most significant in basin type soft alluvium. Soil-structure interaction has been studied by many authors using various methods [4], [5], [6]. Presented here is the soil structure interaction problem solved by means of boundary element method in frequency domain which can treat the irregularity at surface as well as on substrata easily. Also presented is a new type of boundary element method, the velocity type boundary element method in which the traction and velocity are used as unknowns. The merits of this method are that the singular integrals are of same order of singularity and that in calculating acceleration time history only derivative once to time is needed .

Boundary Element Method in Frequency Domain

On the boundary of a certain elastic medium under harmonic excitation, the following integral equation holds. The time factor $\exp(i\omega t)$ is omitted here and hereafter.

$$c_{ij}u_j^p = \int_s (U_{ij}t_j - T_{ij}u_j)dS \tag{1}$$

where

$$c_{ij} = \delta_{ij} + \lim_{\varepsilon \to 0} \int_{S\varepsilon} T_{ij} dS \tag{2}$$

is the free term. The direct calculation of c_{ij} can be found in [7]. U_{ij} is the Green's function for infinite region. T_{ij} is the traction component corresponding to U_{ij} [6].

$$u_{ij} = \frac{1}{4\pi\mu}(\psi\delta_{ij} - \chi r_{,i} r_{,j}) \tag{3}$$

$$\psi = (1 - \frac{c_s}{\omega^2 r^2} + \frac{c_s}{i\omega r})\exp(-i\omega r / c_s)/r - \frac{c_s^2}{c_p^2}(-\frac{c_p}{\omega^2 r^2} + \frac{c_p}{i\omega r})\exp(-i\omega r\, c_p)/r$$

$$\chi = (-\frac{3c_s^2}{\omega^2 r^2} + \frac{3c_s}{i\omega r} + 1)\exp(-i\omega r\ c_s)/r - \frac{c_s^2}{c_p^2}(-\frac{3c_p^2}{\omega^2 r^2} + \frac{3c_p}{i\omega r} + 1)\exp(-i\omega r\ c_p)/r$$

c_p and c_s are the longitudinal and transverse wave velocity respectively.
For the region where incident wave exists, the following equation is used:

$$c_{ij}(u_j^p - u_{(f)j}^p) = \int_S [U_{ij}(t_j - t_{(f)j}) - T_{ij}(u_j - u_{(f)j})]dS \tag{4}$$

where $u_{(f)i}$ and $t_{(f)i}$ are the displacement and traction components of the incident wave. u_i and t_i are the displacement and traction components of the total wave field. On free boundary, $t_i = 0$. On interior boundary conditions of continuity and equilibrium have to be fulfilled. To solve Eq. (4), boundary element is used. For calculating c_{ij} on nonsmooth boundary and the singular integral for quadrilateral isoparametric element, a closed form expression of c_{ij} and direct calculation of the singular integral by Liao and Xu [7] reduces the computing effort and increases the accuracy.

Soil-structure interaction can be easily treated. The structure can be represented by an impedance. The structure is modelled as a multi-degree-of-freedom system. The equation of motion can be expressed as:

$$[M]\{\ddot{u}\} + [C]\{\dot{u}\} + [K]\{u\} = -[M][N]\{\ddot{u}_0\} \tag{5}$$

where $\{\ddot{u}_0\}$ is the excitation at the base of the structure with frequency ω. Putting $\{u\} = [\phi]\{y(t)\}$, setting $[\Phi]^T[M][\Phi] = [I]$, then $[\Phi]^T[K][\Phi] = [\Omega]^2$, assuming $[\Phi]^T[C][\Phi] = 2[\xi][\Omega]$, then relation between the force acting upon the base of structure $\{F_0\}$ and the displacement $\{u_0\}$ is:

$$[K_0(\omega)]\{u_0\} = \{F_0\} \tag{6}$$

where

$$K_0(\omega) = -\omega^2([N]^T[M][N] + [H]^T[D(\omega)][H])$$

$$[H] = [\phi]^T[M][N]$$

$$D(\omega) = \omega^2(-\omega^2[I] + 2i[\xi][\Omega]\omega + [\Omega]^2)^{-1}$$

Assuming that the foundation base and the soil is in full contact, the relation between $\{F_0\}$ and $\{u_0\}$ with t_i and u_i on the soil can be formulated according to condition of continuity and equilibrium.

Examples

1. Effect of soft layer on the amplification of ground motion for inclined incident SH wave is shown in Fig.1 and Fig.2 . It can be seen that near the edge of the soft deposit the amplification factor is much higher than that on the part away from the edge. Also noticed is that the amplification varies rapidly on the region near the edge.

2. A containment structure was built on the cut of a slope of a mountain. The raft foundation of the containment is modelled as medium I , while the mountain is modelled as medium II . The containment structure and the primary loop are modelled as lumped mass system (Fig.3) . The input ground motion is assumed to be comprised in P , SV and SH waves with incident angle θ . One set of bed rock motion and the motion of the base of the structure is shown in Fig.4 . Twenty sets of bed rock ground motion and seismic input for the structure are calculated. In this case the average amplification of peak ground acceleration is around 1 for vertical incidence ($\theta = 0^\circ$) and 1.1 for inclined incidence ($\theta = 30^\circ$) with maximum of 1.33 .

Velocity Type Boundary Element Method

1. Velocity Type Boundary Integral Equation

The computing effort of boundary element method in time domain is much higher than in frequency domain. Therefore it is not used as frequently as in frequency domain. Here a new type, the velocity type, boundary element method devised by the authors is presented. The merits of this type of boundary element method are that the singular integral are of the same order of singularity and that in computing acceleration only differentiation to time once is necessary. The method is illustrated here for two dimensional problem. The boundary integral equation in time domain is

$$c_{ij}(Y)u_i(Y,t) = \int_S [G_{ij}(X-Y,t)*t_i(X,t) - F_{ij}(X-Y,t)*u_i(X,t)]dS(X) \tag{7}$$

where $*$ means convolution, G_{ij} is the two dimensional Stoke's solution, F_{ij} is the stress kernel derived from G_{ij}. $i,j=1,2$.

The body force is neglected here. Zero initial condition is implied. c_{ij} is the free term.

$c_{ij} = \delta_{ij}$ when Y is in the interior of the domain,

$c_{ij} = 0$ when Y situates outside of the domain,

$c_{ij} = \frac{1}{2}\delta_{ij}$ when Y is on the smooth boundary,

$$c_{ij} = \frac{1}{4\pi(1-\nu)} \times \begin{bmatrix} 2(1-\nu)(\varphi_1-\varphi_2)+(\sin 2\varphi_1 - \sin 2\varphi_2)/2 & \sin^2\varphi_1 - \sin^2\varphi_2 \\ \sin^2\varphi_1 - \sin^2\varphi_2 & 2(1-\nu)(\varphi_1-\varphi_2)-(\sin 2\varphi_1 - \sin 2\varphi_2)/2 \end{bmatrix}$$

when Y situates at nonsmooth boundary point. φ_1 and φ_2 are the angles between the tangents of the boundary segments with the x axis, $\varphi_1 > \varphi_2$.

The stress in the interior of the domain can be computed from:

$$\sigma_{ij}(Y,t) = \int_S [K_{kij}(X-Y,t)*t_k - L_{kij}(X-Y,t)*u_k]dS(X) \tag{8}$$

$$K_{kij} = \lambda\frac{\partial G_{km}}{\partial y_m}\delta_{ij} + \mu\left(\frac{\partial G_{ki}}{\partial y_j} + \frac{\partial G_{kj}}{\partial y_i}\right) \tag{9}$$

$$L_{kij} = \lambda\frac{\partial F_{km}}{\partial y_m}\delta_{ij} + \mu\left(\frac{\partial F_{ki}}{\partial y_j} + \frac{\partial F_{kj}}{\partial y_i}\right) \tag{10}$$

The expressions of K_{kij} and L_{kij} are omitted for simplicity. G_{ij} and F_{ij} are shown in the Appendix. It can be seen that the singularity of F_{ij} is one order higher than that of G_{ij} on the wave front. This handicaps the use of the same integration scheme for these two integrations. To overcome this difficulty, improve the smoothness of the solution and make the acceleration time history which is the wanted one in seismic response analysis more accurate, a new type of integral equation is devised. Differentiating Eq.(7) with respect to time results in

$$c_{ij}v_i(Y,t) = \int_S (\dot{G}_{ij}*t_i - F_{ij}*v_i)dS(X) \tag{11}$$

Here the zero initial condition for displacement and velocity has been used.

The stress field in the interior can be expressed as

$$\sigma_{ij}(Y,t) = \int_S (K_{kij}*t_k - L'_{kij}*v_k)dS(X) \tag{12}$$

Eq.(11) is called velocity type integral equation. A dot over a function means its time derivative, t over a function means its integration over time.

2. Discretization and Way of Solution

Eq.(11) is solved by discretization in both time domain and space domain. In time domain t_i and v_i are discretized at constant interval using the same interpolation function.

$$t_i(X,t)=\sum_{n=1}^{N}\varphi_n(t)t_{in}(X) \tag{13}$$

$$v_i(X,t)=\sum_{n=1}^{N}\varphi_n(t)v_{in}(X) \tag{14}$$

$$\varphi_n(t)=\begin{cases} 1-\dfrac{|t-T_n|}{\Delta T} \quad , & T_{n-1}\le t\le T_{n+1} \\ 0 \quad , & t<T_{n-1} \quad or \quad t>T_{n+1} \end{cases} \tag{15}$$

where $T_i = i\Delta T$, $i=1, 2, \cdots, N$.

φ_n (t) can also be expressed as

$$\begin{aligned}\varphi_n(t)&=\frac{(t-T_{n+1})H(t-T_{n+1})+(t-T_{n-1})H(t-T_{n-1})-2(t-T_n)H(t-T_n)}{\Delta T}\\ &=\frac{1}{\Delta T}\Delta_n^2[(t-T_n)H(t-T_n)]\end{aligned} \tag{16}$$

H(t) is the Heaviside function, Δ_n^2 represents the second order difference operator.

Inserting Eqs. (13), (14) and (16) into Eqs. (11) and (12), the following equations can be obtained:

$$c_{ij}v_i(Y,T_N)=\frac{1}{\Delta T}\sum_{n=1}^{N}\int_s\left\{\left[\Delta_n^2G_{ij}^{t}(X-Y,T_N-T_n)\right]t_{in}-\left[\Delta_n^2F_{ij}^{tt}(X-Y,T_N-T_n)\right]v_{in}\right\}dS(X) \tag{17}$$

$$\sigma_{ij}(Y,T_N)=\frac{1}{\Delta T}\sum_{n=1}^{N}\int_s\left\{\left[\Delta_n^2K_{kij}^{tt}(X-Y,T_N-T_n)\right]t_{kn}-\left[\Delta_n^2L_{kij}^{ttt}(X-Y,T_N-T_n)\right]v_{kn}\right\}dS(X) \tag{18}$$

The expressions of G_{ij}^{t}, F_{ij}^{tt} are shown in the Appendix, K_{kij}^{tt} and L_{kij}^{ttt} are omitted here. These expressions have no singularity on the wave front. t_{in} and v_{in} are function of space. The solution for quadratic isoparametric element is worked out. It is easy to extend to other types of element. The following expressions are assumed:

$$t_{in}=\sum_{l=1}^{3}N_l(\zeta)t_{inl} \tag{19}$$

$$v_{in}=\sum_{l=1}^{3}N_l(\zeta)v_{inl} \tag{20}$$

$$x_i=\sum_{l=1}^{3}N_l(\zeta)x_{il} \tag{21}$$

$$N_1(\zeta)=\zeta(\zeta-1)/2,\quad N_2(\zeta)=1-\zeta^2,\quad N_3(\zeta)=\zeta(\zeta+1)/2$$

Where $N_l(\zeta)$ is the shape function, t_{inl} and v_{inl} are the value of t_{in} and v_{in} at node l respectively. Eq.(21)

expresses the transform of boundary element e to coordinate ζ, x_{il} is the component of the position vector of node l of element e. Eq. (17) and Eq. (18) can be expressed as:

$$c_{ij}v_i(Y,T_N)=\sum_{n=1}^{N}\sum_{e=1}^{M}\frac{1}{\Delta T}\int_{S_e}\left\{\left[\Delta_n^2 G'_{ij}(X-Y,T_N-T_n)\right]N_l(\zeta)t_{inl}-\left[\Delta_n^2 F''_{ij}(X-Y,T_N-T_n)\right]N_l(\zeta)v_{inl}\right\}dS(X) \quad (22)$$

$$\sigma_{ij}(Y,T_N)=\sum_{n=1}^{N}\sum_{e=1}^{M}\frac{1}{\Delta T}\int_{S_e}\left\{\left[\Delta_n^2 K''_{kij}(X-Y,T_N-T_n)\right]N_l(\zeta)t_{knl}-\left[\Delta_n^2 L'''_{kij}(X-Y,T_N-T_n)\right]N_l(\zeta)v_{knl}\right\}dS(X) \quad (23)$$

Repeated indices of i, k, l imply summation. S_e means boundary element e. M is the number of elements. At each node Y, $v_i(Y,T_N)$ can be expressed as v_{iNp}, p is the numerical order of the node Y. Thus Eq. (22) takes the form

$$\sum_{n=1}^{N}([G]_{N-n}\{T\}_n-[F]_{N-n}\{V\}_n)=0 \quad (24)$$

Where subscript n means the traction and velocity associated with $\phi_n(t)$ or at time T_n. The element of $\{T\}_n$ and $\{V\}_n$ are t_{inp} and v_{inp} respectively. n means at time T_n. p is the numerical order of the node. Subscript N-n means the matrices resulting from G'_{ij} and F''_{ij} at time T_N-T_n. Eq. (24) can be expressed as

$$[G]_0\{T\}_N-[F]_0\{V\}_N=-\{Q\}_N \quad (25)$$

$$\{Q\}_N=\sum_{n=1}^{N-1}([G]_{N-n}\{T\}_n-[F]_{N-n}\{V\}_n) \quad (26)$$

For the region where incident wave acts, replacing $v_i(Y,t)$ and $t_i(Y,t)$ by $v_i(Y,t)-v_{(f)i}(Y,t)$ and $t_i(Y,t)-t_{(f)i}(Y,t)$ respectively, and $v_{(f)i}(Y,t)$ and $t_{(f)i}(Y,t)$ being discretized in the same way as $v_i(Y,t)$ and $t_i(Y,t)$, Eq.(22) becomes :

$$c_{ij}[v_i(Y,T_N)-v_{(f)i}(Y,T_N)]=\sum_{n=1}^{N}\sum_{e=1}^{M}\frac{1}{\Delta T}\int_{Se}\left\{\left[\Delta_n^2 G'_{ij}(X-Y,T_N-T_n)\right]N_l(\xi)(t_{inl}-t_{(f)inl})\right.$$

$$\left.-\left[\Delta_n^2 F''_{ij}(X-Y,T_N-T_n)\right]N_l(\xi)(v_{inl}-v_{(f)inl})\right\}dS(X) \quad (27)$$

Eq.(25) becomes:

$$[G]_0\{T\}_N-[F]_0\{V\}_N=-[Q]_N+[R]_N \quad (28)$$

$$[R]_N=\sum_{n=1}^{N}([G]_{N-n}\{T_{(f)}\}_N-[F]_{N-n}\{V_{(f)}\}_n) \quad (29)$$

The elements of $\{T_{(f)}\}_n$ and $\{V_{(f)}\}_n$ are $t_{(f)inp}$ and $v_{(f)inp}$ respectively.

When the traction and velocity before and at $T_{N-1}=(N-1)\Delta T$ are known, $\{Q\}_N$ is known. $\{R\}_N$ is known since the incident wave field is known. On the surface boundary either $\{V\}_N$ or $\{T\}_N$ or some combination of them is given for the first, second or third boundary value problem respectively. On interior boundary the number of equations from neighbouring domains are the same as the total number of unknown elements of $\{T\}_N$ and $\{V\}_N$ on that boundary. Thus starting from $N=1$, the unknowns can be solved. The computation effort is low since the inverse of matrix is necessary only at the first time step.

3. Integration of the Cauchy Integral

Similar to static elastic boundary element, in transient dynamic problem the two kernel functions have logarithmic and Cauchy singularities respectively when the coordinate of integration approaches the source. Here the method presented by the authors [7] is used. This method makes the singular integral a sum of regular integral and an algebraic expression.

It can be shown that (see Appendix, Equation A1- A5) when $r \to 0$

$$F''_{ij}(x,t) \to F^s_{ij}\, tH(t) \tag{30}$$

where

$$F^s_{ij} = \frac{-1}{4\pi(1-\nu)r}\{\frac{\partial r}{\partial n}[(1-2\nu)\delta_{ij} + 2r_{,i}r_{,j}] - (1-2\nu)(r_{,j}n_i - r_{,i}n_j)\} \tag{31}$$

is the static kernel, and

$$\frac{1}{\Delta T}\Delta^2_n F''_{ij}(X, T_N - T_n) \to \begin{cases} F^s_{ij}\,, & n = N \\ 0\,, & n < N \end{cases} \tag{32}$$

when $r \to 0$, $\frac{\partial r}{\partial n} \to 0$, thus the Cauchy's singularity comes from the last term in Eq. (31). It can be seen from Eq. (32) that in calaculating $[F]_k$ singular integral appears only when k=0, or at the first time step.

If e_1 and e_2 are the boundary elements connecting at singular point A(Fig. 5), then for calculating $[F]_0$, the following integral needs to be calculated.

$$I_{ij} = \int_{e_1} F''_{ij}(X - X_A, \Delta T)N_3 dS + \int_{e_2} F''_{ij}(X - X_A, \Delta T)N_1 dS \tag{33}$$

I_{ij} can be written as

$$I_{ij} = \int_{e_1} F''_{ij} N_3 dS - \beta\int_{\tilde{e}_1}\frac{1}{R^2}(M_iR_j - M_jR_i)dS + \int_{e_2} F''_{ij} N_1 dS - \beta\int_{\tilde{e}_2}\frac{1}{R^2}(M_iR_j - M_jR_i)dS + \tilde{I}_{ij} \tag{34}$$

where

$$\tilde{I}_{ij} = \beta\int_{\tilde{e}_1+\tilde{e}_2}\frac{1}{R^2}(M_iR_j - M_jR_i)dS$$

$$\boldsymbol{R} = \boldsymbol{r}_A + \boldsymbol{p}(\zeta - \zeta_A) \tag{35}$$

$$R = |\boldsymbol{R} - \boldsymbol{r}_A|\,, \quad R_i = p_i(\zeta - \zeta_A)$$

$$i = 1, 2\,, \quad \beta = \frac{1-2\nu}{4\pi(1-\nu)}$$

$$\boldsymbol{p} = \frac{\partial \boldsymbol{r}}{\partial \zeta}\Big|_{\zeta_A}$$

is the tangent vector of the element at A.

$$\boldsymbol{r} = \boldsymbol{r}_A + \boldsymbol{p}(\zeta - \zeta_A) + \boldsymbol{q}(\zeta - \zeta_A)^2$$

M is the outward normal of the element at A. $\tilde{e}_1$, $\tilde{e}_2$ are the tangent element at A defined by Eq.(35) corresponding to e_1 and e_2 respectively. Changing variable in Eq. (34)

$$I_{ij} = \int_{-1}^{1}[F''_{ij} N_3 J_1(\zeta) - \beta\frac{1}{R^2}(M_iR_j - M_jR_i)\tilde{J}_1(\zeta)]d\zeta + \int_{-1}^{1}[F''_{ij} N_1 J_2(\zeta) - \beta\frac{1}{R^2}(M_iR_j - M_jR_i)\tilde{J}_2(\zeta)]d\zeta + \tilde{I}_{ij} \tag{36}$$

J_1, J_2, $\tilde{J}_1$ and $\tilde{J}_2$ are the Jacobian of e_1, e_2, $\tilde{e}_1$ and $\tilde{e}_2$ respectively. It can be seen from the asymptotic behaviour of $F_{ij}^{tt}(X, \Delta t)$ that there is no singularity in the integral in Eq. (36). The integral can be calculated by means of ordinary Gauss integration scheme. $\tilde{I}_{ij}$ can be integrated analytically.

$$\tilde{I}_{12} = \int_{\tilde{e}_1+\tilde{e}_2} \beta \frac{1}{R^2}(M_1R_2 - M_2R_1)dS = \beta \ln(l_2 / l_1) \tag{37}$$

$\tilde{I}_{21} = -\tilde{I}_{12}$, $\tilde{I}_{11} = \tilde{I}_{22} = 0$

where l_1 and l_2 are length of element e_1 and e_2 respectively.

When the singular point locates on the interior of the element (Fig . 6),

$$I_{ij} = \int_e F_{ij}'' N_2(\zeta)dS = \int_{-1}^{l} [F_{ij}'' N_2(\zeta)J(\zeta) - \beta \frac{1}{R^2}(M_iR_j - M_jR_i)\tilde{J}(\zeta)]d\zeta + \bar{I}_{ij} \tag{38}$$

$$\bar{I}_{ij} = 0, \qquad i, j = 1,2$$

The integral in Eq. (38) can be calculated by means of ordinary Gauss integration.

The integral involving kernel G_{ij}^t can be treated in the same way. The results are given here. For singular point at edge node,

$$J_{ij} = \int_{-1}^{1} [G_{ij}^t(\Delta T)N_3(\zeta)J_1 + \alpha\delta_{ij}\tilde{J}_1 \ln R]d\zeta + \int_{-1}^{1} [G_{ij}^t(\Delta T)N_1(\zeta)J_2(\zeta) + \alpha\delta_{ij}\tilde{J}_2 \ln R]d\zeta$$
$$-\alpha\delta_{ij}(l_1 \ln l_1 + l_2 \ln l_2 - l_1 - l_2) \tag{39}$$

where
$$\alpha = \frac{3-4\nu}{8\pi(1-\nu)\mu}$$

For singular point at interior node,

$$J_{ij} = \int_{-1}^{1} [G_{ij}^t(\Delta T)N_2(\zeta)J + \alpha\delta_{ij}\tilde{J} \ln R]d\zeta - \alpha\delta_{ij}[\ln(\frac{l}{2}) - 1]l \tag{40}$$

l is the lengths of element e.

4. Examples

(1) Suddenly applied uniform pressure on circular cavity in an infinite plate (Fig.7)

This axisymmetrical problem has been solved by Chou and Koenig [8] by means of method of characteristics. For verification of the present method, the same parameters used in Chou and Koenig's paper are used: a=0.25 in., E=3 × 10^7 psi, ρ=0.000793 lb-sec^2/in^4, ν=0.3, ΔT=0.25 μ sec. The results are shown in Fig.8. As can be seen that they agree very well.

(2) The cross section of an earth dam is shown in Fig.9. ρ=2.0 T/m^3, c_s=200m/s, c_p=400 m/s. The seismic input of vertical incident horizontal acceleration time history at the bed rock is shown in Fig.10. The response at crest of dam is shown in Fig.11.

5. Soil-Structure Interaction

Soil-structure interaction can also be solved in time domain. A structure can be represented as a multi-degree-of-freedom lumped mass system. The equation of equilibrium under seismic excitation can be expressed as

$$[M]\{\ddot{u}\} + [C]\{\dot{u}\} + [K]\{u\} = -[M][N]\{\ddot{u}_0\} \tag{41}$$

As usual, here $\{u\}$ is the relative displacement of the lumped mass, $\{u_0\}$ is the displacement of the base of the structure. For two dimensional problem $\{u_0\} = (u_{x0}, u_{z0}, \varphi_{y0})^T$. Eq.(41)is solved through modal superposition. Putting

$$\{u\} = [\phi]\{y(t)\} \tag{42}$$

$$[\phi] = [\phi_1, \phi_2, \cdots, \phi_n], \quad \phi_i \text{ is the ith eigenvector}.$$

$$[\phi]^T[M][\phi] = [I], \quad \text{assuming} \quad [\phi]^T[C][\phi] = diag[2\xi_i\omega_i],$$

Eq.(41) is decoupled as

$$\ddot{y}_i + 2\xi_i\omega_i\dot{y}_i + \omega_i^2 y_i = -\{\phi_i\}^T[M][N]\{\ddot{u}_0\} \qquad i = 1, 2, \ldots, n. \tag{43}$$

$$y_i(t) = \frac{1}{\omega_{di}}\{\phi_i\}^T[M][N]\{\ddot{u}_0(t)\} * \left[e^{-\xi\omega_i t}\sin\omega_{di}t\right] \tag{44}$$

$$\omega_{di} = \omega_i(1-\xi_i^2)^{1/2}$$

The absolute displacement of the structure is

$$\{u_t\} = [N]\{u_0\} + [\phi]\{y(t)\}$$

The force acting upon the base of structure is

$$\{F_0\} = [N]^T\{[M][N]\{\ddot{u}_0(t)\} + [M][\Phi]\{\ddot{y}(t)\}\} \tag{45}$$

or

$$\{F_0\} = F\{\ddot{u}_0(t)\} \tag{46}$$

is a function of $\{\ddot{u}_0(t)\}$

Under the base of the structure, full contact between the base of the structure and the soil beneath it is assumed. The traction $\{T\}$ and velocity $\{V\}$ on the soil beneath the base of structure are in equilibrium with F_0 and continuous with $\{\ddot{u}_0\}$ respectively. The boundary condition together with $\{T\} = 0$ on the free surface enables one to solve the soil-structure interaction problem.

Conclusive Remark

Boundary element method is most suitable for soil-structure interaction with irregular surface topography and arbitrary substrata. The new method for calculating the free term and singular integral facilitates the use of this method. Practical applications illustrate the capability of this method.

A new type of boundary element method in time domain, the velocity type boundary element method devised by the authors is also presented. Example shows that the result of this method agrees well with analytic solution. Further study of the three dimensional problem will be reported later.

References

[1] Benuska, L., "Loma Prieta earthquake reconnaissance report", *Earthq, Spectra, Supl.* to **6** (1990), 106 —114.

[2] Naeim, E., "On seismic design implications of the 1994 Northridge earthquake records", *Earthq. Spectra,* **11** (1) (1995), 91—110.

[3] Huang, H. C. and Chiu, H. C., "Estimation of site amplification from Dahan downhole recordings" *Earthq. Eng. and Struct. Dynam.,* **25** (4) (1996), 319—322.

[4] Wolfe, J. P., *Dynamic Soil-structure Interaction,* Prentice Hall (1985), London.

[5] Liao, Z. P., Wong, H. L., Yang, B. P., and Yuan, Y. F., "Transmitting boundary for transient wave", *Scientia Sinica* (A), **6** (1984), 556—564.

[6] Kitahara , M. and Nakagawa , K. , “Boundary integral equation methods in three dimensional elastodynamics”, *Boundary Element Methods, VII*, Springer-Varlag (1985), 627-636.

[7] Liao, H. and Xu, Z., “A method for direct evaluation of singular integral in direct boundary element method”, *Int. J. Numer. Methods Eng.*, **35**(7) (1992), 1473-1485.

[8] Chou, P. C. and Koenig, H.A., "A unified approach to cylindrical and spherical elastic waves by method of characteristics", *J. Appl. Mech.* **33**, *Trans ASME* 88(1966), 159-167.

Appendix

(1) Expression of G_{ij} and its time integral:

$$G_{ij} = \frac{-1}{2\pi\rho r}[\sum_{m=1}^{2}\frac{(-1)^m}{c_m} r,_i r,_j \frac{2z_m^2 - 1}{\beta_m} + \delta_{ij}(\frac{\beta_1}{c_1} - \frac{z_2^2}{c_2\beta_2})] \qquad \text{(A1)}$$

where

$$\beta_i = \sqrt{z_i^2 - 1}$$

$$z_i = \frac{tc_i}{r}\ , \quad i,j = 1,2\ , \quad c_1 = c_p\ , \quad c_2 = c_s\ .$$

Integrate over time:

$$G_{ij}^t = \frac{1}{4\pi\rho}\sum_{m=1}^{2}\frac{1}{c_m^2}[\delta_{ij} ch^{-1}(z_m) + (-1)^m \beta_m z_m(\delta_{ij} - 2r,_i r,_j)] \qquad \text{(A2)}$$

(2) Expression of F_{ij} and its time integral:

$$F_{ij} = \frac{\mu}{2\pi\rho r^2}\sum_{m=1}^{2}\frac{(-1)^{m+1}}{c_m}(F_m \frac{1}{\beta_m^3} + 2F\frac{2z_m^2 - 1}{\beta_m}) \qquad \text{(A3)}$$

where

$$F = n_i r,_j + n_j r,_i + \frac{\partial r}{\partial n}(\delta_{ij} - 4r,_i r,_j)$$

$$F_1 = \frac{\lambda}{\mu} n_i r,_j + 2r,_i r,_j \frac{\partial r}{\partial n}$$

$$F_2 = -n_j r,_i + (2r,_i r,_j - \delta_{ij})\frac{\partial r}{\partial n}$$

Integrate over time:

$$F_{ij}^t = \frac{\mu}{2\pi\rho r}\sum_{m=1}^{2}\frac{(-1)^m}{c_m^2}(F_m \frac{z_m}{\beta_m} - 2F\beta_m z_m) \qquad \text{(A4)}$$

Integrate over time again:

$$F_{ij}^{tt} = \frac{\mu}{2\pi\rho}\sum_{m=1}^{2}\frac{(-1)^m}{c_m^3}(\beta_m F_m - \frac{2}{3}F\beta_m^3) \qquad \text{(A5)}$$

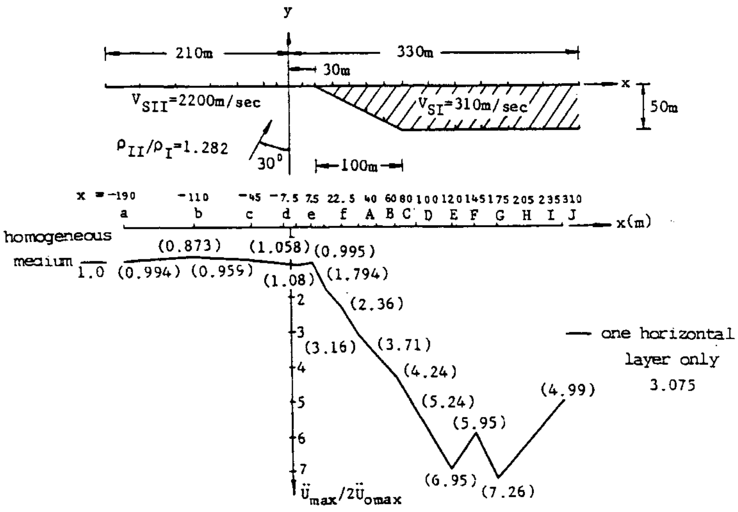

Fig.1 Distribution of peak ground acceleration (A)
(Input: EI Centro 1940 NS record assumed to be SH wave)

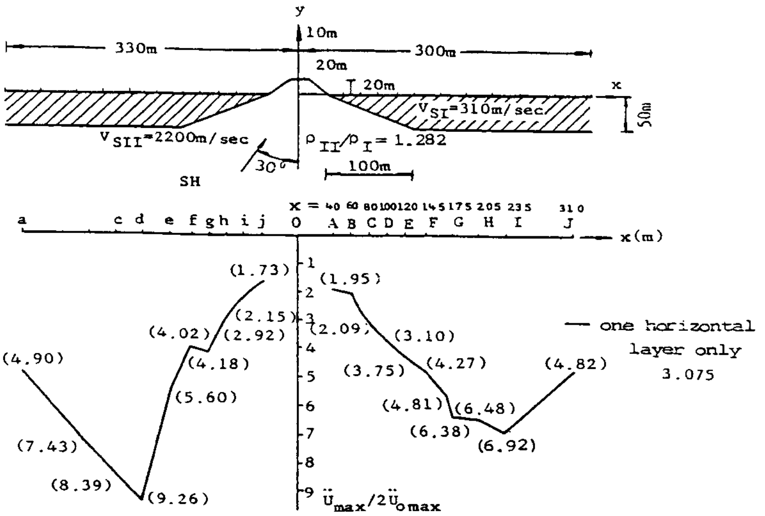

Fig.2 Distribution of peak ground acceleration (B)

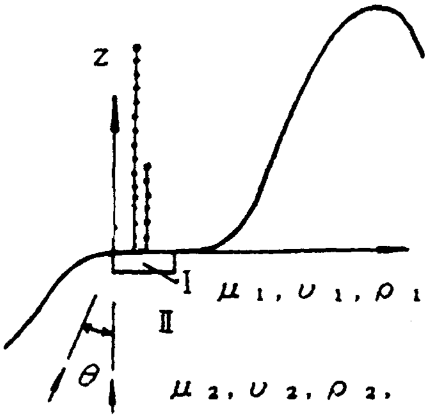

P SV or SH wave (θ = 0°,30°)

Fig.3 Modelling of a containment structure and sketch of the site

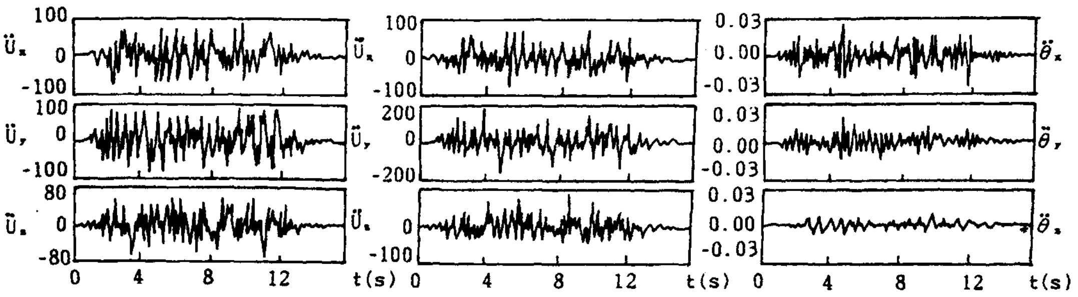

Earthquake ground motion at bed rock (cm/s^2)

Displacement input at the base of structure (cm/s^2) θ = 30°

Rotation input at the base of structure (rad./s^2) θ = 30°

Fig.4 Seismic input for a containment structure

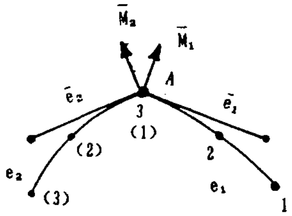

Fig.5 Quadratic elements and their tangent elements (the singular point is at edge of nodes)

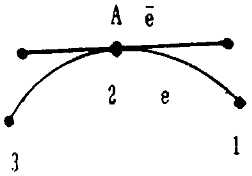

Fig.6 Quadratic elements and their tangent elements (the singular point is at interior of nodes)

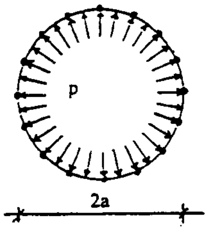

Fig.7 Radiation of cylindrical wave in an infinite sheet

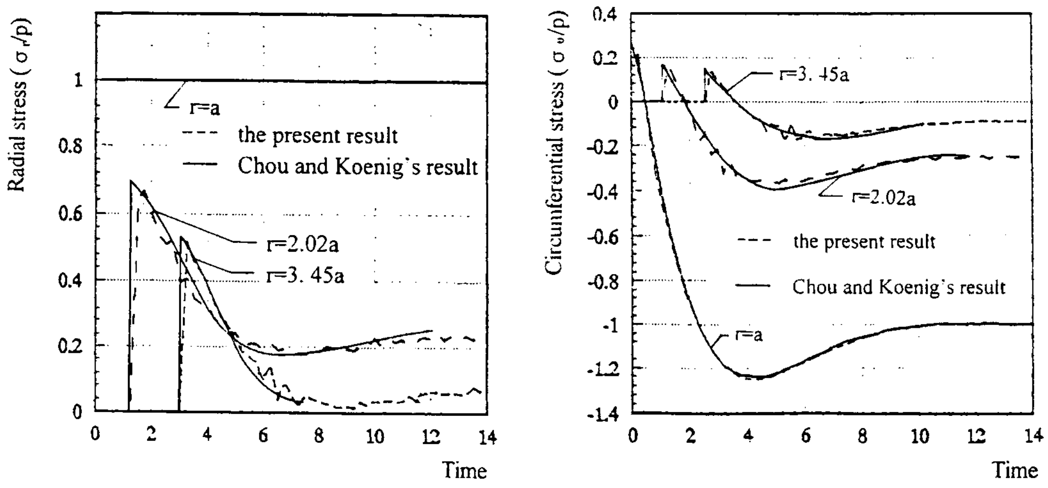

(a). Radial stress (b). Circumferential stress

Fig.8 Comparison of the present result with Chou and Koenig's result

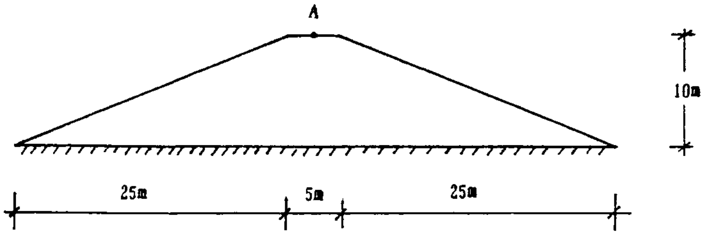

Fig.9 Profile of earth dam on bedrock

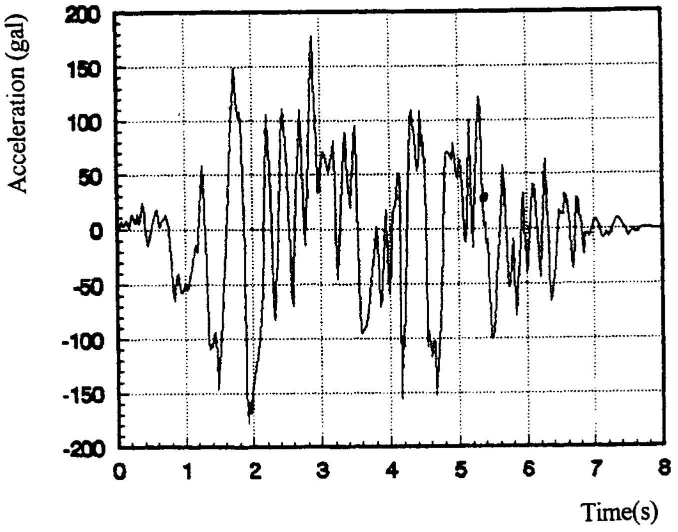

Fig.10 Acceleration time history input at bedrock

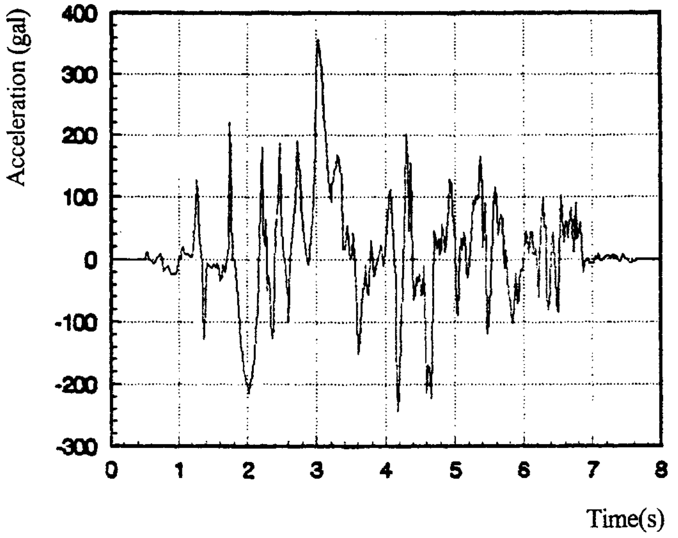

Fig.11 Acceleration time history at crest of dam (point A)

NONLINEAR SSI --SIMPLIFIED APPROACH, MODEL TEST VERIFICATION AND PARAMETER STUDIES FOR SEISMIC AND AIR-BLAST ENVIRONMENT

Xiong Jianguo, Wang Danming*, Fu Tieming and Liu Jun
(Institute of Engineering Mechanics,State Seismological Bureau,Harbin, 150080, China)
(*North-East University, Shenyang, 110006, China)

Abstract

In the paper a modified lumped parameter model for nonlinear soil-structure interaction (SSI) analysis is described, in which the nonlinearities associated with the inelastic soil behavior and the uplift of the rectangular foundation from surrounding soil are properly accounted for. In order to verify the simplified analysis model two types of model tests had been performed. Finally, the simplified analysis model is applied to the nonlinear response analysis of the SSI under seismic and air-blast loading conditions.

Introduction

With SSI analysis there are two kinds of nonlinearities. The first one, that has received most attention from researchers and practicing engineers, is associated with the nonlinear behavior of the soil. The second kind is associated with the partial separation (uplift) of the foundation from the soil mass, resulting from the inability of the soil to resist tension. The numerical simulation of the inelastic soil behavior in a soil-structure system may be divided into two categories: the equivalent linearization analysis [1,2] and the true nonlinear analysis. In the later case the soil-structure system is simulated by some sophisticated models, i.e. the complete finite element model [3], substructure or hybrid model [4].These sophisticated models are also available for the analysis of the nonlinearities of SSI induced by uplift by incorporating some special elements at the interface between the foundation and the surrounding soil [5-10].The lumped parametric model or the sway-rocking spring model, sometimes referred to as the S-R model, widely used in the linear SSI analysis is also widely adopted in studying the effect of uplift of the structure foundation from the soil [11,12]. Nevertheless, for most investigators the nonlinear S-R model differs from the linear one only in the nonlinearities of the rocking stiffness and damping of the foundation soil (or the foundation impedance). In the nonlinear S-R model the stiffness and damping of the soil springs (dashpots) are in general evaluated from the frequency-independent stiffness and damping adopted in the linear S-R model multiplied by some coefficients depending on the ratio of the effective contact area of the foundation base [11, 13-15], or determined by some nonlinear moment-rotation relationships established by assuming the distribution of contact stresses developed after uplift occurs [16-18]. Moreover, in the nonlinear S-R model the vertical component of the response and the effect of the embedment of the foundation are ignored.

Besides remarkable progress having been made in the numerical simulation of the SSI effects, in recent years a great deal of experimental studies [19-22] had been carried out aimed at assessing the capability of the analysis model to predict structure response. However, few studies have been done on examine the effectiveness for evaluating the nonlinear response of the soil-structure system by comparing the numerical results with the observed ones.

Based on the previous studies [23,24] performed by the author a modified lumped parametric model had been proposed [25,26]. In the model the above two kinds of nonlinearities, the vertical component of the response and the embedment of the foundation etc. have been properly taken into account. In order to verify the availability of the proposed analysis model two types of model tests had been performed. Furthermore, parametric studies have been carried out by applying the proposed analysis model to two cases: the analyses of response of structures to earthquake and to air-blasting.

Analysis Model, Expressions and Equations of Motion

(1) Basic assumptions

In establishing the analysis model following basic assumptions have been made:

(a) The foundation is of rigid rectangular;

(b) The stiffness of the soil springs for a buried rectangular foundation is composed of three portions contributed from the base, the sidewalls of the foundation with normal parallel to the direction of the excitation (hereafter it's called the 'parallel' sidewalls) and the sidewalls perpendicular to the direction of the excitation (the 'perpendicular' sidewalls), where the stiffness of the base soil springs is the same as for a surface foundation. The radiation damping is the same as in the linear SSI analysis for a buried foundation;

(c) Before uplift of the foundation from the supporting soil, i.e. at the linear response stage, the stiffness of the soil springs is estimated from the existed information [27]. After uplift the stiffness of the base soil spring is given by functions of the effective width of the foundation base, these functions are the same as those before uplift. The stiffness of the soil spring associated with parallel sidewalls decreases with a factor identical to that of the base spring. The stiffness of the soil spring associated with the perpendicular sidewalls is constant without change during uplift. No sliding between the foundation base and the soil occurs;

(d) The impedance-frequency dependency of the soil springs is approximately considered by substituting the fundamental frequency of the linear soil-structure system in the initial impedance-frequency relationships;

(e) The inelastic soil behavior is approximately evaluated by supposing the shear modulus (G) to be equal to the initial modulus (G_o) multiplied by a function of the uplift ratio γ as [23]

$$G = [\,1 - 0.9\,\gamma + 0.1\,\sin(2.5\,\pi\,\gamma)\,]\,G_o \tag{1}$$

where $\gamma = (B - \bar{B})/B$, here B and $\bar{B}$ denote respectively the initial width and the current effective width of the foundation base at each time step during numerical calculation process.

A schematic representation of the equivalent soil-spring model proposed is shown in Fig.1.

(2) Impedance of a rectangular buried foundation

The foundation impedance is generally written in the complex form

$$K_i^d = K_i + i K_i' \tag{2}$$

in which K_i^d denotes the foundation impedance, K_i the soil stiffness, K_i' the radiation damping, the subscript i denotes the i-th mode of the vibration, i = z, x, r., with z, x, and r denoting respectively modes of the vertical and horizontal translation and rocking around the horizontal axis perpendicular to the transversal axis, while $\imath = \sqrt{(-1)}$.

The soil stiffness for a buried rectangular foundation can be represented by

$$K_i = K_i^{os}\ (1 + \eta_i)\, k_i \tag{3}$$

where K_i^{os} is the static stiffness for the surface foundation, η_i the coefficients of the embedment effectiveness depending on the aspect and buried depth-width ratios of the foundation, k_i dynamic stiffness coefficients being function of the aspect ratio of the foundation and dimensionless frequency a_0, $a_0 = \omega B_o / (2V_S)$, here ω is the circular frequency, B_o the original width of the foundation and V_S the velocity of shear wave in soil. The coefficients η_i and k_i can be evaluated by using formulas given by Pais and Kausel [27] by introducing the effective width ratioβ, $\beta = \overline{B}\ /\ B = 1 - \gamma$. With consideration of the uplift we present the K_i^{os} as

$$K_z^{os} = G\,(B_o/2)\,/\,(1-\nu)\,Z \tag{4a}$$

$$K_x^{os} = G\,(B_o/2)\,/\,(2-\nu)\,X \tag{4b}$$

$$K_i^{os} = G\,(B_o/2)^3/\,(1-\nu)\,R \tag{4c}$$

in which G and ν denote respectively the shear modulus and Poison's ratio of the soil , and

$$Z = \beta\,[\,2.46\,(L/B_o/\beta) + 18.5\,(L/B_o/\beta)^{--0.2} - 3.3\,(L/B_o/\beta)^{-1.4} - 13.0\,] \tag{5a}$$

$$X = \beta\,[\,4.2\,(L/B_o/\beta) + 33.0\,(L/B_o/\beta)^{--0.2} - 6.4\,(L/B_o/\beta)^{-1.4} - 21.6\,] \tag{5b}$$

$$R = \beta^3\,[\,3.2\,(L/B_o) + 0.8\,] \tag{5c}$$

where L is the length of the rectangular foundation.

According to assumptions (b) and (c) we may write

$$K_i = K_i^o + \overline{K_i} + \overline{\overline{K_i}} \tag{6}$$

in which K_i^o, $\overline{Ki}$ and $\overline{\overline{Ki}}$ denote the contributions associated with the base, the parallel sidewalls and the perpendicular sidewalls respectively. For K_i^o, $\overline{Ki}$ and $\overline{\overline{Ki}}$ the following expressions can be derived [26]:

$$K_z^o = [\,GB_0/2\,/\,(1-\nu)\,]\,Z\,k_z \tag{7a}$$

$$K_x^o = [\,GB_0/2\,/\,(2-\nu)\,]\,X \tag{7b}$$

$$K_r^o = [\,G\,(B_0/2)^3\,/\,(1-\nu)\,]\,R\,k_r \tag{7c}$$

$$\overline{Kz} = 0.369\,[\,GB_0/2\,/\,(1-\nu)\,]\,(L/B_0)\,[\,H/(B_0/2)\,]^{0.8}\,Z/Z|_{\beta=1} \tag{8a}$$

$$\overline{Kx} = 1.386\,[\,GB_0/2\,/\,(2-\nu)\,]\,(L/B_0)\,[\,H/(B_0/2)\,]^{0.8}\,X/X|_{\beta=1} \tag{8b}$$

$$\overline{Kr} = 3.2\,[\,G\,(B_0/2)^3\,/\,(1-\nu)\,]\,(L/B_0)\,[\,H/(B_0/2)\,]\,[\,1 - 0.576\,a_0^2\,/\,(2.4 + a_0^2)\,]\,R/R|_{\beta=1} \tag{8c}$$

$$\overline{\overline{Kz}} = [\,GB_0/2\,/\,(1-\nu)\,]\,\{\,Z\,(\eta_z\,k_z)|_{\beta=1} - 0.369\,(L/B_0)\,[\,H/(B_0/2)\,]^{0.8}\,\} \tag{9a}$$

$$\overline{\overline{Kx}} = [\,GB_0/2\,/\,(2-\nu)\,]\,\{\,X\,(\eta_x\,k_x)|_{\beta=1} - 1.386\,(L/B_0)\,[\,H/(B_0/2)\,]^{0.8}\,\} \tag{9b}$$

$$\overline{\overline{Kr}} = [\,G(B_0/2)^3\,/\,(1-\nu)\,]\{\,R\,(\eta_r\,k_r)|_{\beta=1} - 3.2\,(L/B_0)[\,H/(B_0/2)\,]\}[\,1 - 0.576a_0^2\,/\,(2.4 + a_0^2) \tag{9c}$$

In the above expressions H is the buried depth of the foundation, $(Z, X, R)|_{\beta=1}$ represents the Z, X and

R with $\beta = 1$. For the radiation damping we may obtain from Ref.[27]

$$K_z^{'} = \omega\rho\,[\,V_L A_b + V_S(A_x + A_y)\,] \tag{10a}$$

for the vertical mode, and

$$K_x^{'} = \omega\rho\,[\,V_L A_x + V_S(A_b + A_y)\,] \tag{10b}$$

for the horizontal mode, and

$$K_r^{'} = \omega\rho\,\{[\,V_L(I_b + I_x) + V_S I_y\,]\,a_o^2\,/\,(f + a_o^2) + [\,V_L(B/2) + V_S(L/2)\,]H^3 f\,/\,(f + a_o^2)\,\} \tag{10c}$$

for the rocking mode. In the above expressions ρ stands for the mass density of the soil, $V_L = 3.4\,V_S\,/\,[\,\pi\,(1-\nu)\,]$, $A_b = L\,B$, $A_x = 2\,H\,B$, $A_y = 2\,H\,L$, $I_b = L\,B^3/\,12$, $I_x = L\,H(\,2H^2/3 + B^2/\,2\,)$, $I_y = 2\,B\,H/\,3\,[\,B^2/\,4 + H^2\,]$.

(3) Distribution of the contact stresses and estimation of the effective width of the foundation

From numerical comparison [26] it has been found that the quasi-static distribution is more appropriate than the linear and the bilinear distributions and the effective width ratio of the foundation can be estimated by

$$\beta = 2\,[\,1 - 2\,F_r\,/\,(\,F_z\,B\,)\,] \tag{11}$$

where F_r and F_z are respectively the overturning moment and the vertical force acting on the foundation base, which will be given later.

(4) Fundamental equations of motion

By using the substructure technique the motion equation of the superstructure can be written in the well-known form as follows

$$[\,M\,]\,\{\ddot{u}\} + [\,C\,]\,\{\dot{x}\} + [\,K\,]\,\{x\} = \{\,0\,\} \tag{12}$$

in which [M], [C]and [K] denote the mass, damping and the stiffness matrices of the structure respectively, the elements in the displacement vector {u} are $u_i = u_g + u_b + \varphi_b\,(\,h_i + H\,) + x_i$ here u_g is the horizontal displacement of the input motion, u_b and φ_b denote the horizontal displacement of the foundation base and the rotation of the foundation respectively, h_i are the distances from the i-th mass point to the foundation top and x_i the elements of the relative displacement vector { x }.

For the foundation-soil system , assuming the base and the parallel sidewall springs being located at the centre of the effective width of the foundation base and the perpendicular sidewall springs at the original centre of the foundation base the following motion equations can be written

$$M_b(\,\ddot{w}_b + z_o\ \ddot{\varphi}_b\,\varphi_b\,) + K_z^d\,w_b + (\,K_z^{do} + \overline{K_z^d}\,)\,e\,|\,\varphi_b\,| = F_z(\,t\,) \tag{13a}$$

$$M_b\,(\,\ddot{u}_b + z_o\ddot{\varphi}_b\,) + K_x^d\,u_b = -M_b\ \ddot{u}_g + F_y\,(\,t\,) \tag{13b}$$

$$M_b\,z_o\,(\,\ddot{w}_b\,\varphi_b + \ddot{u}_b + z_o\ddot{\varphi}_b\,) + I_b\ddot{\varphi}_b + K_r^d\,\varphi_b + (\,K_z^{do} + \overline{K_z^d}\,)\,e\,[w_b\,(\varphi_b) + e\,\varphi_b] = M_b\,z_o\,(g\,\varphi_b - \ddot{u}_g) + F_r\,(\,t\,) \tag{13c}$$

where M_b stands for the mass of the foundation, z_o the height of the c.g. of the foundation measured from its base, e the eccentricity of the middle point of the effective contact area of the foundation base during uplift relative to that before uplift, $K_z^{do} + \overline{K_z^d}$ denote the sum of the complex stiffness of the soil springs associated with the foundation base and the parallel sidewall, w_b the vertical displacement of the original centre of the foundation base, g the gravity acceleration, F_x and F_z the horizont and vertical forces and F_r the overturning moment acting on the original centre of the foundation base are as follows

$$F_x = -\sum_{i=1}^{N} m_i \ddot{u}_i \tag{14a}$$

$$F_z = -\sum_{i=1}^{N} m_i \ddot{w}_b \tag{14b}$$

$$F_r = -\sum_{i=1}^{N} m_i \ddot{u}_i \,(h_i + H) - \ddot{w}_b \sum_{i=1}^{N} m_i \,[\,\varphi_b\,(h_i + H) + x_i\,] \tag{14c}$$

with m_i being the mass of the i-th mass point of the superstructure, N the total number of the mass points.

Model Test Verification

(1) Shaking table test

A series of shaking table tests was carried out for investigating the nonlinear earthquake response of a one story building with rigid footing rested on/ or buried in a soil deposit.The model ground was made of prepared clay laid in a container and compacted layer by layer. The container made from thick wood plate had an inner size of 120 cm in length, 40 cm in width and 50 cm in depth, its base was fixed on the shaking table. In order to minimize the wave reflection a piece of foam-rubber cushion was placed at each inner sides of the container. The basic characteristics of the model ground are: shear modulus--$3.2\text{x}10^6$ Pa, mass density-- 1.35g/cm^3 and water content --9.8%. The SDOF model structure consisted of a top mass of 11.12 kg supported by a steel cantilever and a concrete block used for simulating the rigid footing. The cantilever had a height of 32 cm measured from the upper surface of the concrete block to the center of the top mass and a transversal stiffness of $1.35\text{x}10^4$ N/m, the concrete block had a mass of 9.30 kg and dimension of 8.6 cm (height) x 20.0 cm (width) x 23.6 cm (length).

Tests of following four groups were performed:

(1) Free field test (No. I). The free field test was aimed at: (a) estimating the characteristics of the model ground by the measured data of the response, (b) examining the availability of the model ground for simulating approximately the infinite extension of the ground in the direction of shaking and (c) observing the nonlinearities associated with the inelastic behavior of the soil.

(2) Test of scattering field or the effective input motion (No. II). It was performed by using a rigid light-weight box made of plywood buried in the model ground to simulate the massless rigid foundation, the outer size of the box was the same as that of the concrete block of the footing of the model structure.

(3) Test of SDOF structure model with buried footing (No. III) and

(4) Test of SDOF structure model with ground surface supported footing (No. IV)

A typical scheme of the model of the soil-structure system and the arrangement of the transducers are shown in Fig.2. Besides the accelerometers at the base of the footing and in the neighboring soil there were 5 pairs of switches to observe the occurrence of the uplift of the footing from the supporting soil. During all tests the tested models were subjected to increasing excitation by small increament of peak acceleration. The accelerogrom (N-S component) for the El Centro earthquake of 1940 with reduced time scale of 1 : 6 was used as the input motion.

The variation of the amplification factor (ξ) with peak acceleration of the input motion at the shaking table (a_g) is shown in Figs.3 and 4 for tests of No. I and No. II respectively. The amplification factor is defined as the ratio of the peak acceleration of the response to a_g. From Figs.3 and 4 we see: (i) In the free field test for a given a_g the responses at all measured points on the model ground surface differ very small. It indicates the availability of the model ground for simulating the infinite extension in the shaking direction. With increasing a_g the response acceleration decreases, this implies the nonlinearilities associated with the inelastic soil behavior. (ii) In the scattering field test, contrary to the free field test case, the amplification factor ξ of the scattering field increases slightly with increasing a_g. Comparing Fig.4 with Fig.3 one finds that for a given input motion a_g the acceleration in the scattering field is higher than that in the free field for our tested case. It is contrary to the theoretical results. This may result from the buried box used in the scattering field test deviating from the massless footing. Moreover, from the test results the rocking and the vertical components are obviously due to wave scattering.

Fig.5 shows the horizontal acceleration time histories (A_1) of the model superstructure of test No. IV and No. III under different input motion levels of a_g. In the figure the time history of the input motion a_g (t) signed with A_6 is also given. From Fig.5 we see that the horizontal response of the model structure with buried footing exhibits behavior of typical periodical damped vibration, specially under low level of input motion. Does it imply that the damping in the model structure with buried footing is smaller than that with surface footing? The relationship of the apparent fundamental frequencies of natural vibration of tests of No.III and No. IV obtained from the Fourier spectra of the $A_1(t)$ with a_g are shown in Fig.6. It shows that the frequencies of natural vibration of the system decrease with increasing a_g due to soil flexibility and the nonlinearilities associated with inelastic soil behavior and resulting from loss of contact between structure and surrounding soil, particularly in case of surface foundation. From Fig.6 and the detection of the uplift by using switchs at the footing base it was found that the uplift of the foundation base occurs under a relatively low level of input motion.

With purpose of direct measuring the natural vibration behavior of the model structure under different foundation conditions free vibration test induced by striking had also been performed . The results obtained are listed in Table I. It illustrates that the phenomenon of the damping generated in the model structure with buried foundation being lower than that in structure with surface foundation discovered in the earthquake-simulation tests is proved by the free vibration test. A reasonable explanation may be that for our test the effective depth of the soil layer corresponding to a ratio of the effective depth of soil layer to the width of the model footing base of near 5 seems to be less sufficient for simulating a half-space.

Table 1. Behavior of natural vibration of model structure under different foundation conditions

Foundation condition	Fundamental frequency (Hz)	Damping ratio (%)
Absolutely fixed	6.75	0.48
Buried in model ground	6.73 (6.60*)	1.73
Supported on model ground	6.12	4.70

* Obtained from the earthquake-simulating tests.

The amplification factors (ξ) versus a_g for tests No. III and No. IV are shown in Figs.7 and 8 respectively. The comparison indicates that the response of the model structure with buried foundation is higher than that with surface foundation under identical input motion. This may be due to the fact that the structure with buried foundation has natural frequency more closing to the predominant frequency of the input motion (6.85 Hz), and a lower damping as mentioned above. Comparing Fig.3 with Figs.7 and 8 indicates that the nonlinearities developed in the soil-structure system is much remarkable than that in the free field. With respect to the response of the footing, Fig.7 along with Fig.8 show that the response of the foundation is independent of whether the foundation is buried or ground supported and differs little from that in the scattering field, with exception of the rocking and vertical components of the response under a higher level of input motion

The acceleration time histories for test model III obtained from the shaking table tests and numerical calculation by using the proposed analysis model are represented in Fig.9. In the numerical calculation for the model ground the initial shear modulus G_0 =5.05 MPa and the Poisson's ratio ν =0.4 and for the input motion the acceleration time histories of the massless footing model measured during the scattering field test (No. II) were utilized. The comparison illustrates that not only the peak values but also the whole process obtained from the tests and calculations agree well.

(2) Air-blast loading test

An inverted " T " type rigid specimen made from concrete was used in the air-blast loading model test. The model footing simulating the basement of buildings had 40 cm in length, 16 cm in height and a width of 20 cm .The impulsive horizontal loading generated by shock tube was applied to the lateral surface of the model tested. The tested model and the arrangement of the accelerometers and displacement transducers are shown in Fig.10. Before the impulsive loading test a series of statically lateral loading tests were performed with purpose of investigating the effects of the dimensionless of the footing and the constitution of the model ground : dense sand and dense clay. Besides, the results of the static loading tests were also used to evaluate the value of the initial modulus of the model ground through conducting an inverse analysis.

Several runs of test under loading with different magnitude of the overpressures had been carried out. Before each test the model ground was reconstructed. Approximately identical conditions of the model ground were maintained through keeping constant water content and density of the clay used for simulating the ground soil.

A comparison of the horizontal accelerations and the rotations of the model footing obtained from the model tests and numerical calculations using the present analysis model for test with incidental overpressure of 3.61 kN is presented in Fig.11. It is seen that from both the peak values and the wave forms the numerical calculations yield satisfactory results.

Parametric Studies

The proposed analysis model is applied to study the dynamic responses of structures to earthquake and air-blast loading.

(1) Seismic response analysis of structures.

A typical reactor containment building modeled with a 16 lumped mass system and connected to a rigid base slab is studied. The foundation slab is rectangular in plan 50.0m by 50.0m and 3.0m in thick with a buried depth of 15m. All numerical analyses for the seismic response analysis have been performed for four different site soil with shear wave velocity of 350, 450, 600 and 1000 m/s. These sites are assumed to be homogeneous half-space. The accelerogram (N-S component) for the El Centro earthquake of 1940 is employed as the horizontal ground motion applied to the analysis model and scaled to have different peak accelerations: 0.2, 0.3, 0.4 and 0.5g. To investigate the effects of the soil-structure interaction with each soil site and input motion level the following cases are studied [28]:

(a) Neglecting the effect of SSI, i.e. assuming the structure being fixed at its base;

(b) Linear SSI, i.e. both the inelastic behavior of the site soil and the uplifting of the foundation from the soil being ignored;

(c) Nonlinear SSI neglecting the inelastic soil behavior; and

(d) Complete nonlinear SSI. Hereafter , it is refer to this case, if no specification is given.

The results of some typical time histories of responses obtained for condition of peak acceleration a_g = 0.4g and site soil with initial shear wave velocity V_S=350 m/ s are shown in Fig.12. From the figures it is seen that for the studied structure and the input motion the time histories of the horizontal acceleration and displacement of the structure at its top and the rotation of the foundation have identical phase angles or a angle of 180° with exception of some additional components of high frequencies happening in the acceleration response. Besides, there are vertical acceleration response due to uplift of the foundation even under no vertical component of the input motion in the single impulse form. The calculation results indicate that the harder is the site soil, the earlier the uplift occurs.

In Figs.13 comparisons of the in-structure spectra generated at the top of the structure under a_g = 0.4g and V_S= 350, 600 and 1000 m/s are presented for four cases considered. All spectra have been generated at damping taken to be 5% of critical viscous damping. It is evident that for soft soil site the effect of the SSI is significant, causing a significant frequency shift in the frequency of peak spectral response, while the nonlinear SSI has minor effect in this case. As the site soil becomes harder, the overall effect of the SSI decreases, however , the influence of the inelastic soil behavior remains remarkable. For stiff soil site with shear wave velocity of 1000 m/s the peak spectral responses from the linear and the nonlinear SSI analyses become higher than those from the analysis neglecting the effect of SSI.

Fig.14 showing the distributions of the shear forces and the bending moments developed along the height of the structure under input motion with a_g=0.4g for different site soil conditions further illustrates the significant effect of the nonlinear SSI taking place mainly in condition of moderately stiff soil site. Furthermore, the computed results indicate that the analysis neglecting the effect of the SSI always leads to an overestimation of the shear forces and the bending moments in the structure. Comparing with the analysis of the linear SSI the nonlinear analysis, in general, yields minor responses of the structure with exception of the shear forces developed near the base of the structure.

In the seismic design of the structures of nuclear power plant the ratio of the effective contact area of the base slab is one of the important parameters. The relationship between the ratio of the effect contact area of the base slab, the relative base shear and the overturning moment versus the peak accelerations of the input motion for site soil with shear wave velocity V_S=350 m/s are shown in Fig.15. In which the results corresponding to the two nonlinear SSI cases (c) and (d) considered in this section are given. We see that for the studied structure and the environment conditions the uplifting off of the base slab of the structure occurs under excitation of the input motion with a_g of a little higher than 0.2g. Under a_g=0.5g half of the base slab will lift off from the beneath soil. Besides, an approximate linear relationship exists between the ratio of the effective contact area and the input motion level. In Fig.15 the relative base shear and the overturning moment are defined as

$$F_x^* = F_x / [(\sum_{i=1}^{N} m_i) a_g] \quad \text{and} \quad F_r^* = F_r / [(\sum_{i=1}^{N} m_i) a_g \times 0.77 H_0] \qquad (15)$$

where H_0 is the total height of the superstructure.

(2) Dynamic response of basement shelter under high-rise building subjected to air-blast loading

Besides the earthquake response related problems , the response of buildings to air-blast loading constitutes another task encountered in dynamic engineering practice. In this section the proposed analysis model is applied to the analysis of the dynamic response of basement shelters under high-rise buildings to air-blast loading. The buildings considered have various configurations in plan as shown in Fig.16.

In applying expressions of impedance for rectangular foundations to nonrectangular ones the first thing is to find the equivalent width and length of the footing base under assumption of the buried depth being constant during uplift process. The equivalent characteristics of the footing base for a nonrectangular foundation is easy to determined to be

$$B_e = \sqrt{(12 I_0 / A_0)} \qquad \text{and} \qquad L_e = A_0 / B_e \tag{16}$$

where B_e and L_e are respectively the width and the length of the base of the equivalent rectangular foundation, A_0 and I_0 denote respectively the original area and the moment of inertia around the axis through the c.g. and parallel to the longer side of the base of the foundation. It should be notice that the B_e and L_e obtained were based on the initial parameters of the footing base and they are available only before the uplift occurring. After uplift the effective contact area is varying and at each time step it is necessary to evaluate a new set of B_e and L_e by using Eq.15 with the subscript " o " refereed to the associated characteristics during the last time step. Moreover, due to no symmetric axis for a nonrectangular foundation under lateral loading the uplift of the base may take one of two possible states, taking the " L " footing for instance, namely the state (a) and the state (b) shown in Fig.17, where the shadow area denotes the contact area of the base. It is easy to prove that among states (a) and (b) with equal contact area the last one which has a minor moment of inertia has predominate effect, therefore the state (b) is hereafter adopted as the basis in the uplift analysis.

Based on similar principle for the "parallel" sidewalls, another set of equivalent width B_{es} and length L_{es} of the foundation can be obtained. Therefore, in applying the stiffness expressions for rectangular foundations to nonrecatngular ones different equivalent characteristics of the base for the base and the sidewalls of the nonrectangular foundation should be used. In order to avoid confusion possibly happening in the numerical calculation the initial equivalent characteristics of the base i.e. B_{eo} and L_{eo} is adopted by introducing correction stiffness coefficients in Eqs.7 and 8. The correction coefficients are determined based on the following consideration, taking the contribution of the parallel sidewalls to the foundation $\overline{Kz}$ for instance, from Eqs.7 and 8 it is seen that the $\overline{Kz}$ is proportional to a factor of $(L/ B^{0.8})$. Therefore for $\overline{Kz}$ we have correction factor $(L_{es}/L_{eo})\times(B_{eo}/B_{es})^{0.8}$. Substituting the values of the corresponding equivalent characteristics we obtain , for example for the L-shaped in plan footing, the correction factor equals to 0.369 and the stiffness coefficient of $\overline{Kz}$ becomes $0.369\times3.51 = 1.30$ instead of 3.51 for the rectangular foundation.

For the radiation damping of the nonrectangular foundations, owing to the assumption (b) introduced Eq.9 used for the rectangular foundations remains available if the A_x and A_y in it are defined as the area of the sidewalls of the foundation projected on the plans perpendicular to the x- and y-axis respectively.

In the dynamic response analysis of the high-rise buildings with basement shelters subjected to air-blast loading the net lateral loading from computation with consideration of the incident overpressure and the structural configuration of interest is utilized[28]. For all buildings studied the incident overpresures and the tall height of the structure are identical, the buried depth of the basement and the initial shear modulus of the site soil are 8.5m and 25 MPa respectively except for the building with piles, for which the corresponding values are 3.2m and 12 MPa respectively.

The computed responses of the basement shelters are presented in Figs.18 and 19 for a rectangular and Y-shaped in plan buildings and a rectangular building with pile foundation respectively. The areas of the footing bases, the minimum effective ratios of the contact area and the peak values of the horizontal translation and rotation are listed in Table 2.

Table 2. Some basic characteristics of the studied buildings

Footing with plan	Footing base area (m^2)	Maximum translation (mm)	Maximum rotation (10^{-2} rad)	Ratio of effective contact area
Rectangular	937.04	25.0	0.43	0.35
L	1218.20	12.0	0.25	0.86
П	1068.00	17.0	0.24	0.87
Y	1349.40	15.0	0.22	1.00
Rectangular with piles	937.04	21.0	0.05	1.00

From the above results it can be concluded that the configuration of the foundation in plan has significant influence on the translations and rotations of the basement under identical other conditions, a small variation in the footing base area would result in significant different in the response of the basement shelter due to great difference in the foundation stiffness caused by the difference in the configurations. Besides, for building with pile foundation the rotation of the basement is much less than other buildings owing to its higher rocking stiffness of the foundation contributed by the pile system.

Conclusions

(1) A modified lumped parametric model of analyzing the soil-structure interaction with partial lifting-off is proposed, in which the inelastic soil behavior and the embedment of the foundation are properly accounted for.

(2) Verification of the proposed analysis model is performed through two kinds of model tests: one under earthquake simulation environment and one under air-blast loading. It is shown that the proposed model predicts well the nonlinear responses of the soil-structure system.

(3) Even at nonlinear state the soil-structure system exhibits an apparent behavior of natural vibration. Comparing with the surface foundation case , the embedment of the foundation leads to an increase in the natural frequencies of the system. With increasing input motion level the apparent natural frequencies of the system with buried foundation decreases more slowly than that with surface foundation . In circumstances, for instance, when the fundamental natural frequency of the system with buried foundation is close to the predominant frequency of the input motion, the response of the system would higher than that with the surface supported foundation. However, with increasing input motion level the nonlinear effect increase and the embedment effect decreases.

(4) For the performed test cases it seems the nonlinearities resulted from the loss of contact of the foundation with its surrounding soil have a more remarkable effect on the structure response than the nonlinearities associated with the inelastic soil behavior.

(5) From the parametric studies on the seismic response of a typical nuclear containment building it is recommended that for soft soil site with shear wave velocity $V_S < 350$ m/s, to carrying out a linear SSI analysis is necessary and adequate, however, under input motion with higher level the inelastic soil behavior should be taken into account. For moderately stiff soil site ($V_S = 350 \sim 450$ m/s) it is appropriate to consider the inelastic soil behavior neglecting the uplift effect of the foundation. With stiff soil site ($V_S >$ 450 m/s) it seems necessary to account for both the effect of the inelastic behavior and the uplift effect of

the foundation.

(6) The results of the dynamic response analysis of structures subjected to intensive air-blast loading illustrate that the configuration of the foundation in plan has great influence on the response of the basement shelters due to the significant difference in the foundation impedance resulted from the variation in the configuration of the foundation. The numerical examples performed indicate the pile foundation is beneficial to the reduction of the rotation of the basement shelters under air-blast loading condition.

Finally, further study is needed in respect of the modeling inelastic soil behavior, the simulation of buried cylindrical foundations etc.

References

[1] Schnabel, P.B., Lysmer, J. & Seed, H.B.,*Report EERC* 72-12, (1972).
[2] Lysmer, J., Udako, T., Seed, H.B. & Hwang, R.N., *Report EERC* 74-4, (1974).
[3] Ferritto, J.M.,Shock and *Vibration Bulletin,* 52(5),(1982), 29-38.
[4] Wolf, J. P.,*Nuclear Engineering and Design,* 111(1989) , 381-393.
[5] Toki, K and Miu ra, F., *Earthquake engineering and Structure Dynamics,* 11(183), 77-89.
[6] Miura, F., *Proc.8th WCEE,* III(1984), Prentice Hall, 485-492.
[7] Desai, c. G. and Zamm, M.M., *Proc. 8th WCEE,* III(1984), Prentice Hall, 1049-1056.
[8] Zhao Zhendong et el., *Explosion and Shock Waves,* 11(4), (1991), 301-330. (in Chinese)
[9] Hayashi, Y. et al., *Proc. 9th WCEE* VIII(1988), 265-270.
[10] Aihara, S. et al., *Trans. 7th SMiRT,* K9/1(1973).
[11] Kennedy, R. P., *Nuclear and Design*, 38(1976), 323-355.
[12] Wolf, J. P., *Nuclear and Design*, 38(1976), 357-383.
[13] Sotomura, K. et al., *Trans. 7th SMiRT,* K5/^(1983).
[14] Kobori, T. et al., *Proc. 8th WCEE,* III(1984), Prentice Hall, 897-904.
[15] Ohtomo, K. et al., *Proc. 9th WCEE,* III(1984), 277-282.
[16] Unemori, a. l., *PB-256794,* 1976.
[17] Izumi, M et al., *Proc. 4th Japanese Earthquake Engineering Symposium*, (1975), 727-734.
[18] Zinn, R. and Stangenberg, F., *Trans. 7th SMiRT,* K9/3(1983).
[19] Weissman, K and Prevost, J. H., *NCEER Technical Report* NCEER-890040, (1989).
[20] Tang, H. T. et al., *Nuclear Engineering and Design*, 111(1989), 371-379.
[21] Tajimi, H., *Proc. 9th WCEE,* III(1989), 297-308.
[22] Ishimura, K., *Proc. 10th WCEE,* III(1992), 1897-1903.
[23] Xiong Jianguo et al., *Computers and Geotechniques*, 8(1989), 157-174.
[24] Xiong Jianguo et al., *Proc. 9th ECEE* 7B(1990), 66-75.
[25] Xiong Jianguo et al., *Inst. of Eng. Mechanics, Research Report.* (1992), (In Chinese).
[26] Xiong Jianguo, *Soil Dynamics and Earthquake Engineering,* 12(1993), 273-282.
[27] Pais, A. and Kausel, E., *Soil Dynamics and Earthquake Engineering,* 2(1), (1983), 213-227.
[28] Xiong Jianguo et al., *Building Science*, 4(1996),6-11. (In Choinese)

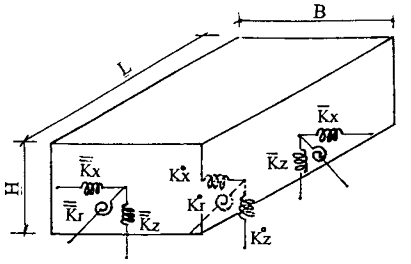

Fig. 1 Equivalent soil-spring model of soil stiffness. (Dashpods not shown)

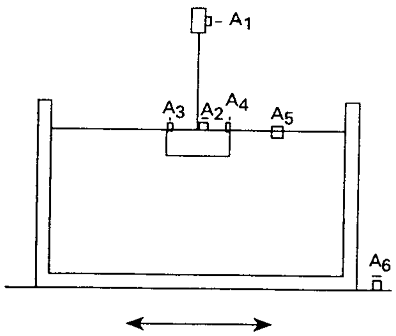

Fig. 2 Experimental model for earthquake excitation test (No. III).

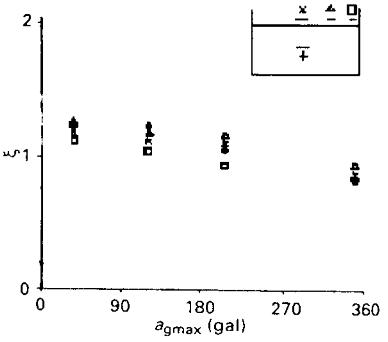

Fig. 3 Amplification factor (ξ) vs. peak acceleration of input motion (a_g) (No. I).

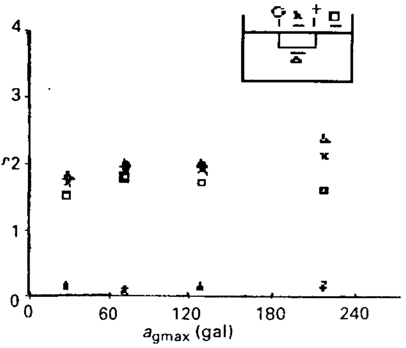

Fig. 4 Amplification factor (ξ) vs. peak acceleration of input motion (a_g) (No. II).

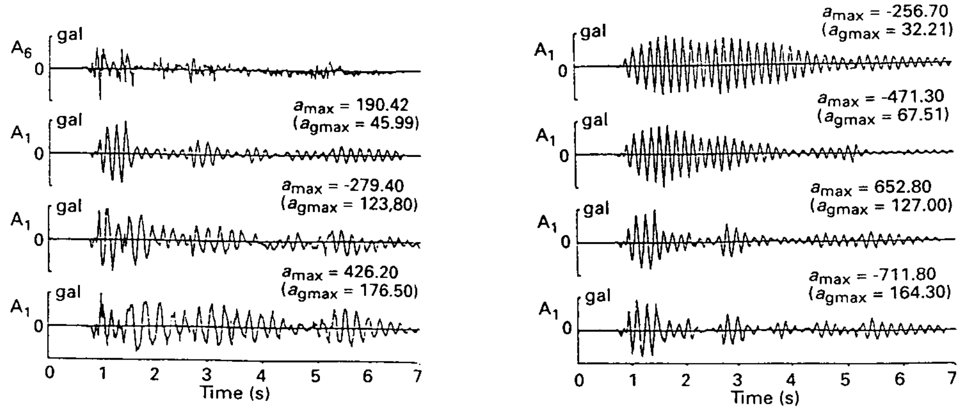

No. IV

No. III

Fig. 5 Acceleration time histories of A_1

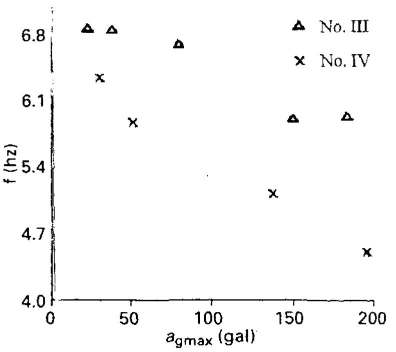

Fig. 6 Apparent natural frequencies (f) vs. a_g.

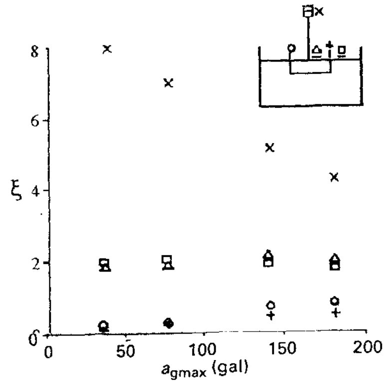

Fig. 7 Amplification factor (ξ) vs. peak acceleration of input motion (a_g) (No.III).

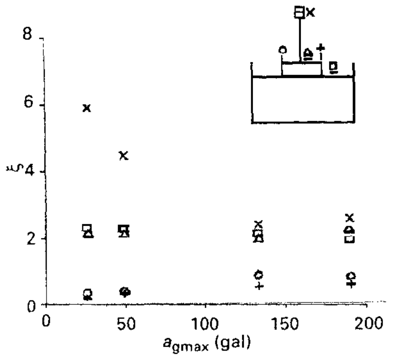

Fig. 8 Amplification factor (ξ) vs. peak acceleration of input motion (a_g) (No. IV).

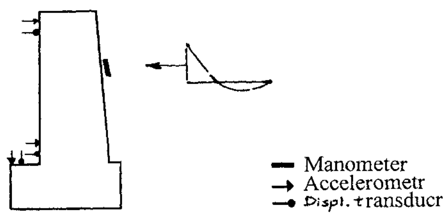

Fig. 10 Experimental model for air-blast loading test

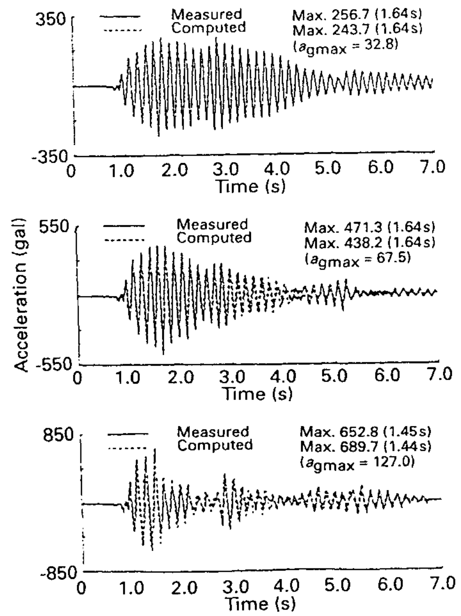

Fig. 9 Comparisons between acceleration responses at structure top obtained from tests and calculation (No.III).

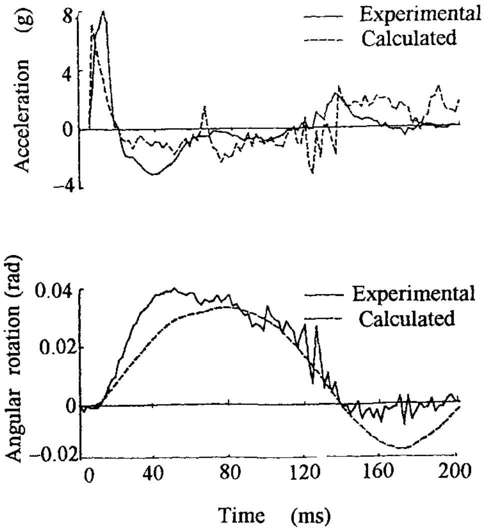

Fig. 11 Time histories of acceleration at the structure top (a) and rotation of the footing (b) under incidental peak overpressure Δp=3.61 Mpa

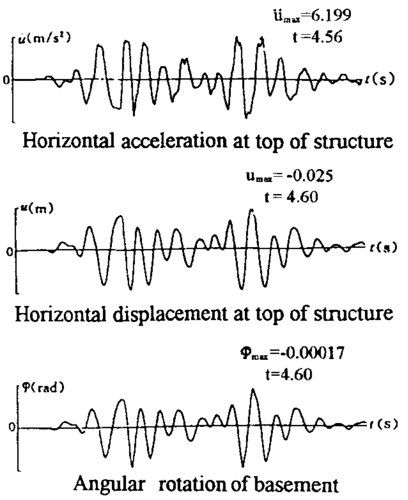

Horizontal acceleration at top of structure

Horizontal displacement at top of structure

Angular rotation of basement

Fig. 12 Time histories of reponses of the structure at its top and the footing, $a_g = 0.4$ g, $V_{so}=350$ m/s

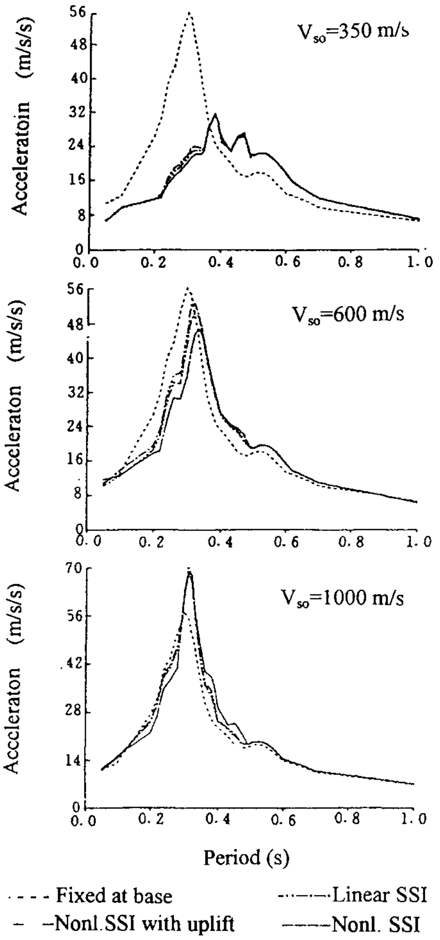

Fig. 13 Computed in-structure response spectra top of structure, $a_g = 0.4$ g, 5% damping

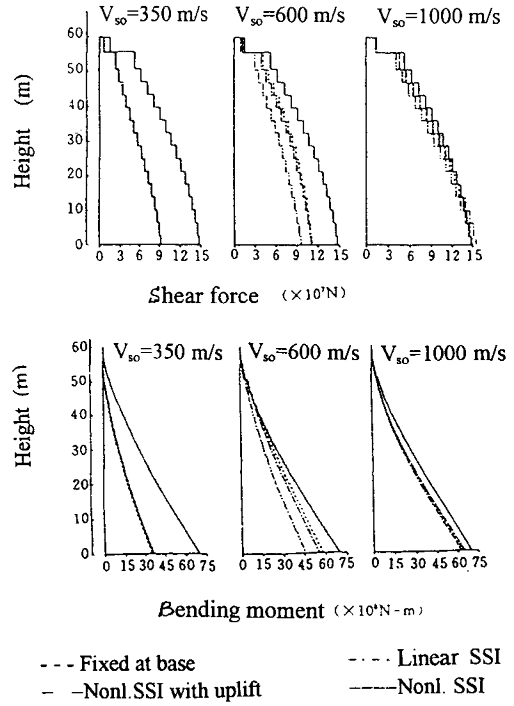

Fig. 14 Variation of shear force and bending moment along structure height , $a_g = 0.4$ g

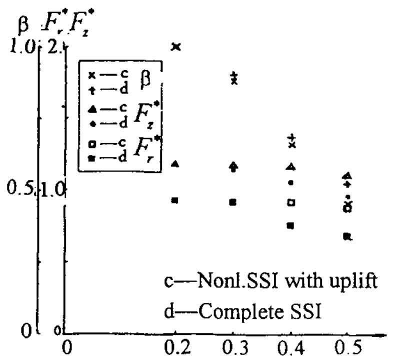

Fig 15 Ratio of effective contact area and relative base shear and overturning moment vs. acceleration a_g

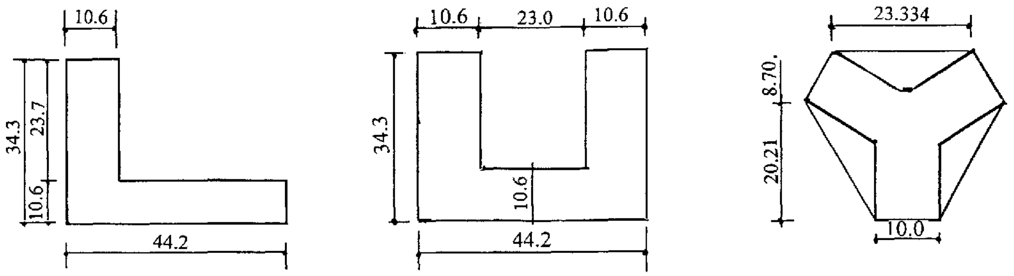

Fig. 16 Configuration in plan of studied structures

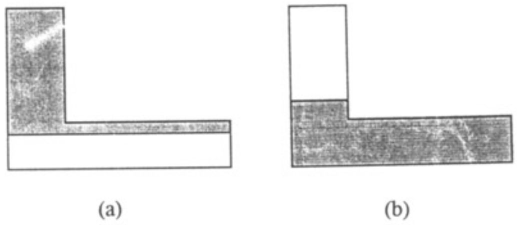

Fig. 17 Possible uplift states, L-shaped in plan of foundation

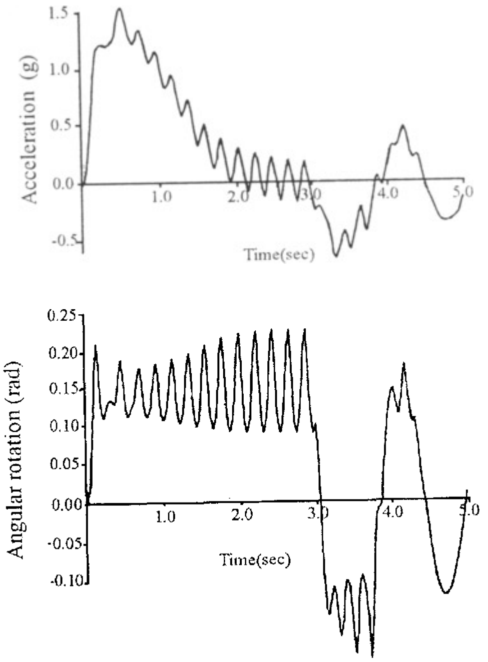

Fig. 18 Acceleration and rocking of basement shelter Y-shaped in plan

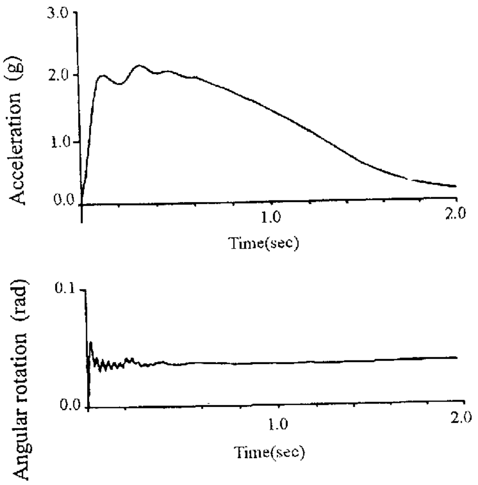

Fig. 19 Acceleration and rocking of basement shelter Rectangular in plan with pile foundation

A DIRECT METHOD FOR ANALYSIS OF DYNAMIC SOIL-STRUCTURE INTERACTION BASED ON INTERFACE IDEA

Liu Jingbo Lu Yandong
(Department of Civil Engineering, Tsinghua University, Beijing China)

Abstract

This paper presents a direct finite element method for analysis of dynamic soil-structure interaction based on the large general structure analysis software. The method can simulate not only the absorption of infinite soil to the scattering wave but also the elasticity recovery capacity of the far field media on the boundary. A new input method of wave motion dealing with dynamic soil-structure interaction is also proposed which can be used to exactly simulate seismic wave input with any angle. The accuracy of the methods presented in this paper is demonstrated by the numerical examples.

Ⅰ. Introduction

In the practices of earthquake engineering, it is recognized that the dynamic interaction of soil-structure may have a significant effect on the response of the structure to earthquake. At the recent twenty years, a great achievement on the research of soil-structure interaction have been achieved, computational models and methods have been improved progressively, actual data of earthquake observation and large scale model experiments on site have been accumulated constantly[1,2]. But researchers should continue working to find more reasonable and practicable methods to consider the influence of an infinite soil and input problems of wave motion.

With constructions of tall buildings, large nuclear power station as well as large dams, dynamic interaction of soil-structure in earthquake has become an important research subject in the field of earthquake engineering. This subject includes two main problems. One is the dynamic response of structure and the other is the input method of seismic wave motion. Now great improvements have been achieved in the field of dynamic response of structure, in which theories and analytical software have been mature. Expending a great deal of manpower, material and financial resources, a great number of large general structural analysis software have been developed based on these achievements in the world, such as Super SAP, ANSYS and NASTRAN, etc., which can compute dynamic response of a complex structure system to a dynamic load. These software can meet the needs of common project. Further more, there are not only a complete element but also elements addition or expansion functions in these software, with which they can also satisfy the needs of research work to some degrees. In addition, great progress have been made on the problem of wave propagation in complex media, the input methods of seismic wave motion and the modeling of the radiation condition of wave motion. Now seismic wave response in a heterogeneous media including a local complex field can be analyzed.

Although a great achievement have been achieved, many analytical methods have been developed and many papers have been published, as we face a real project, we find that except for the nuclear power station, in the other fields of structure engineering the dynamic interaction of soil-structure is always ignored in the analysis of seismic resistance. Even a tall building or a super tall building is constructed on some deep and soft soil, something like that has been done. For example, in Shanghai city, although the depth of the soft soil reaches 80 meters, seldom do the designers consider the dynamic interaction as designing a tall building or a super tall building. Many reasons lead to the serious problem. Complexity of the problem is one of the reasons. But another main reason is that the achievements of the two research fields mentioned above are not combined well. On the one hand the input of seismic wave motion is not considered or roughly considered in large general software, which can not reasonably reflect the phase feature of input seismic wave motion and simulate the absorption to the scattering wave. So they can not well treat the dynamic interaction of soil-structure. On the other hand the earth media can be well described in some analytical methods for seismic wave and the corresponding software, but they are too coarse to be employed in the significant structural analysis.

The main reason for hindering the organic combination of the achievement of the two aspects is that generally only the executable file of an advanced dynamic structural analytic software is given, especially the latest version. It is difficult to combine the wave motion input method and the artificial boundary into the current general software. Although some source programs of a general software, which can be obtained, can be reformed, with the appearance of the new version, it is difficult to renew them. At present, in some better methods well considering the dynamic soil-structure interaction, generally the stiffness of part of the interacting structures is amended-adding stiffness coefficient reflecting the influence of soil resistance, which needs to amend the stiffness and mass matrixes generated by a general software on the large scale and is in great difficulty. In addition, further work of wave motion input method(such as a slant incident wave) in a general situation while analyzing seismic wave motion in a local heterogeneous field is needed to develop a method that can accurately and reliably simulate the seismic wave input from an infinite media to a local heterogeneous field.

This paper gives a set of methods combining dynamic structural analysis and wave motion analysis in complex media, which can analyze the dynamic interaction of soil-structure by using the latest general structural analysis software. They consider not only the effect of varying of amplitude and phase to structural response, but the absorption of a scattering wave. we take advantage of the functions of a general software themselves and combine the artificial boundaries into them. At the same time we give a input method of seismic wave to exactly simulate the procedure of wave motion input which do not decrease the accuracy of the scattering wave handled by the artificial boundaries. All these work is done by making exterior appending programs and not changing the general software.

II. Viscous-Spring Boundary

When we analyze the dynamic interaction of soil-structure by using the finite element method, we must cut out a finite computational region of interest from the infinite media of the earth. It is necessary to set up an artificial boundary to simulate the absorption of the continua to the scattering wave on the boundary of the region, which ensure that the scattering wave does not reflect while passing through the boundary[3]. Generally two kinds of methods are used to set up the artificial boundaries-precise boundary and local boundary. In the former the artificial boundary satisfies the field equation, the boundary condition and the radiation condition of the infinite media. This kind of boundary is precise in the finite element sense and can be set up on the surface of the construction with an irregular configuration or surrounding media. Although this kind of boundary is effective in many cases, besides others limitations, the main shortcoming is cohesion of all the nodes motion on the artificial boundary, which lead to more cost of computer memory and computational time. Although the second method is not strictly precise, it can give enough accuracy in needed frequent band if the local artificial boundary is arranged suitably. The prominent character of the local boundary is that the nodal displacements on the boundary are incoherent with others (except for the near nodes). It is practical for less memory and time consuming. Now there are many kinds of artificial boundaries, such as the viscous boundary[4], the consistent boundary[5], the superposition boundary [6], the paraxial boundary [7], the transmitting boundary[8], the dynamic infinite element boundary [9]etc. Many kinds of artificial boundaries are compared each other in reference[10] and [11]. In these kinds of boundaries, the viscous boundary, the paraxial boundary, transmitting boundary belong to the artificial boundary in time-domain, in which the paraxial boundary and the transmitting boundary have a higher accuracy. But for a real project within two order accuracy is often taken for the two methods because of the complexity of the higher order one. Although the viscous boundary has only one order accuracy, its idea is clear and easy to make program and widely used. Its shortcoming is only considering the absorption of the energy of the scattering wave and can not simulate the elasticity recovery capacity of the infinite soil. In physical meaning, the mechanical model exerted the viscous boundary can be regarded as a separate body floating in the air, which may drift entirely been subject to a load with low frequency. This is so-called low frequency stability. A novel artificial boundary is introduce in this paper, which can simulate absorption to scattering waves and the elasticity recovery capacity of infinite soil at the same time[12].

2.1 Formulation of Artificial Boundary

The artificial boundary introduced in the analysis of the dynamic interaction of soil-structure is derived under the assumption of non-reflecting energy such as the viscous boundary. In the following, the artificial boundary condition is derived base on exterior propagation wave[12].

In a real problem, because scattering waves caused by a local irregular region or foundation of structure generally exist geometric diffusion, it is reasonable to adopt cylindrical waves(2D) or spherical waves(3D) to simulate the scattering waves. Only 2D problem is considered in the paper, in which cylindrical waves were adopted to simulate the scattering waves radiating in infinite media. In polar coordinate system the motion equation of planar cylindrical waves is

$$\frac{\partial^2 w}{\partial t^2} = c_s^{\,2}\left(\frac{\partial^2 w}{\partial r^2} + \frac{1}{r}\frac{\partial w}{\partial r}\right) \tag{2.1}$$

where, w is anti-plane displacement of media, c_s is propagation velocity of shear wave, $c_s = \sqrt{G/\rho}$, G is the shear modulus and ρ mass density.

The solution form of a cylindrical wave ejaculated from the source point can be written as[13]

$$w(r,t) = \frac{1}{\sqrt{r}} f\left(t - \frac{r}{c_s}\right) \tag{2.2}$$

One can obtain the shear stress at any point in the media employing Eq.(2.2) and the computational formulation of shear stress $\tau(r,t) = G\partial w / \partial r$

$$\tau(r,t) = -G\left[\frac{1}{2r\sqrt{r}} f\left(t - \frac{r}{c_s}\right) + \frac{1}{c_s\sqrt{r}} f'\left(t - \frac{r}{c_s}\right)\right] \tag{2.3}$$

where, f' denotes the differentiation of f with respect to the variable in the parenthesis. The velocity of any point can be written as

$$\frac{\partial w(r,t)}{\partial t} = \frac{1}{\sqrt{r}} f'\left(t - \frac{r}{c_s}\right) \tag{2.4}$$

Substituting Eq.(2.2), (2.4) into Eq.(2.3), one can obtain the following relationship between the stress on the element at any radius r_b, whose normal is radius vector $\vec{r}_b$, and velocity as well as displacement at the same point

$$\tau(r_b,t) = -\frac{G}{2r_b}w(r_b,t) - \rho c_s \frac{\partial w(r_b,t)}{\partial t} \tag{2.5}$$

It can be seen that if the media is truncated at radius r_b where the distributive physical components are exerted, a viscous damper C_b and a linear spring K_b

$$C_b = \rho c_s, \quad K_b = \frac{G}{2r_b} \tag{2.6}$$

It can be seen that the artificial boundary condition where $r=r_b$ is the same as Eq.(2.5). If one can precisely determine the distance r_b from the wave source to the artificial boundary, one can obtain the coefficient of the physical component exerted on the artificial boundary using Eq.(2.6). Thus the reflection of a scattering wave on the artificial boundary can be completely eliminated. That is to say one can precisely simulate the propagation of waves from a finite region to an infinite one. In this paper we call the artificial boundary combining a viscous damper and a linear spring as viscous-spring boundary. If the spring is ignored, the boundary degenerates into Lysmer's viscous boundary. It is easy to implement the viscous-spring boundary into some large general software. Now we have done it in the program Super SAP.

2.2 Reflective Coefficient of Viscous-Spring Boundary

Because the assumption of cylindrical waves is adopted in the derivation of the artificial boundary, it can prefigure that a high accuracy can be obtained if the arc artificial boundary is employed practically. However it is more convenient to adopt a linear artificial boundary in the finite element analysis of dynamic interaction of soil-structure(although lose accuracy to some degree). Thus only coefficient of the linear artificial boundary is studied in the following.

The incident waves equation can be given according to Eq.(2.2)

$$w_I(r,t) = \frac{A}{\sqrt{r}}e^{i\omega(t-r/c_S)} \tag{2.7$_1$}$$

When an incident wave $w_I(r,t)$ with an angle θ reaches a linear artificial boundary, it will produce an reflective wave $w_R(r,t)$ written as the following according to the mirror image law.

$$w_R(r',t) = \frac{B}{\sqrt{r'}}e^{i\omega(t-r'/c_S)} \tag{2.7$_2$}$$

In Eq. (2.7) ω is frequency, A and B represent the amplitude coefficient of the incident wave and the reflective wave caused by the artificial boundary respectively. It is convenient to use two different coordinates *r* and *r'* for the incident wave and the reflective wave respectively, whose source points are symmetric to the artificial boundary(see Fig. 2.1). Thus the reflective wave has the same form as the incident wave. The total wave field is the sum of the incident wave and the reflective wave,

$$w(r,t) = w_I(r,t) + w_R(r',t) \tag{2.8}$$

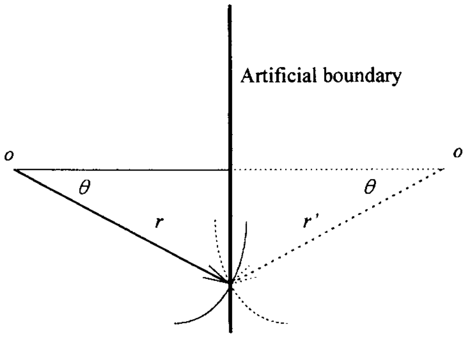

Fig.2-1 Coordinates system of the incident and reflective wave

On the artificial boundary, $r=r'=r_b$, substituting Eq.(2.8) into Eq.(2.5), one can obtain the artificial boundary condition

$$\tau_B = -\left(\frac{G}{2r_b} + i\omega\rho c_s\right)(A + B)\frac{1}{\sqrt{r_b}}e^{i\omega(t - r_b/c_s)} \tag{2.9}$$

The stresses caused by the incident and reflective wave on the artificial boundary are

$$\tau_{bI} = G\frac{\partial w_I}{\partial r}\bigg|_{r=r_b}\cos\theta = -A\frac{G}{\sqrt{r_b}}\left(\frac{1}{2r_b} + \frac{i\omega}{c_s}\right)\cos\theta e^{i\omega(t-r_b/c_s)} \tag{2.10$_1$}$$

$$\tau_{bR} = -G\frac{\partial w_R}{\partial r'}\bigg|_{r'=r_b}\cos\theta = B\frac{G}{\sqrt{r_b}}\left(\frac{1}{2r_b} + \frac{i\omega}{c_s}\right)\cos\theta e^{i\omega(t-r_b/c_s)} \tag{2.10$_2$}$$

On the artificial boundary, the stresses caused by the incident and reflective wave satisfy the boundary condition.

$$\tau_{bI} + \tau_{bR} = \tau_B \tag{2.11}$$

Substituting Eq.(2.9), (2.10) into Eq.(2.11), the reflective coefficient of the artificial boundary R=|B/A| can be obtained,

$$R = (1 - \cos\theta)/(1 + \cos\theta) \tag{2.12}$$

It can be seen that the formulation (2.12) is the same as Lysmer's viscous boundary, which indicates the reflective coefficient of viscous-spring boundary will increase with the incident angle θ. Although the two artificial boundaries have the same accuracy, it can be proved by numerical examples that the accuracy of the viscous-spring boundary is generally higher than the viscous boundary, because the assumption to a scattering wave field as deriving the viscous-spring boundary is more suitable for the practice.

2.3 The Accuracy of Viscous-Spring Boundary

When an artificial boundary is set up, the coefficients of viscous damper are constant which do not change with the distance r_b from the scattering wave source to the boundary, but the stiffness of the spring should change with the distance r_b. Because in a real problem, the source is not a point, but a distributive linear or surface one in space, r_b is only elected averagely. In the numerical examples in the paper, r_b has the same value on every linear artificial boundary, which is the shortest distance from the source point to the boundary.

Wave problems in a continua include two aspects. One is source problem, the other is scattering problem. Generally there are more high frequency components in the former, which often make the boundary produce errors. Here we consider source problem as an example to test the accuracy and efficiency of the elastic artificial boundary used in it.

The first example is a source problem with SH wave in a homogeneous elastic half space, whose mechanical model is shown in Fig. 2.2 . The shear modulus G=1, density ρ=1, the shear wave velocity c_s=1. Wave source is a transient distributive load along z direction on the surface of the half space F(t, x)=T(t)S(x), where T(t) is a triangular pulse whose duration is 1, spatial distributive function of focus S(x) is well-distributed in a finite region, which can be expressed as follow,

$$\mathrm{T(t)} = \begin{cases} 2\mathrm{t} & 0 \le \mathrm{t} \le 0.5 \\ 2(1-\mathrm{t}) & 0.5 < \mathrm{t} \le 1 \\ 0 & \text{others} \end{cases} \tag{2.13}$$

$$\mathrm{S(x)} = \begin{cases} 1 & |\mathrm{x}| \le 1 \\ 0 & \text{others} \end{cases} \tag{2.14}$$

The computational region is $|x| \le X_b$ and $0 \le y \le Y_b$, $X_b = Y_b = 2$, which is discretized by square elements.

The element length and width $\Delta x = \Delta y = 0.05$. The central difference method is employed to compute the step-by-step integration in time domain and the time step is chosen as $\Delta t = 0.025$.

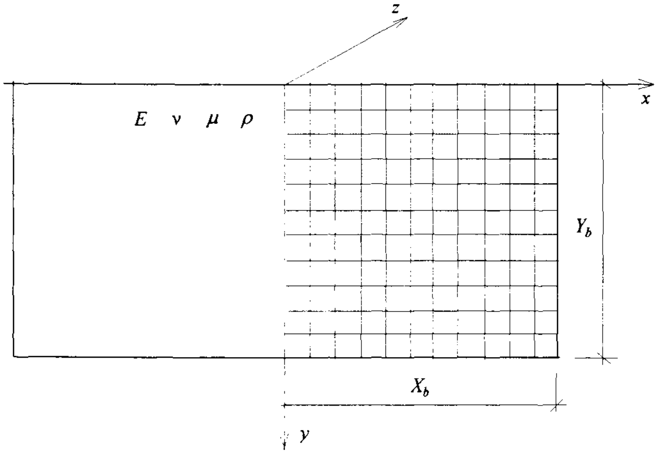

Fig.2.2 Mechanical model for a homogeneous elastic half space

Three observation points, A, B, C, are chosen, whose coordinates are (x, y)=(0, 0), (2, 0) and (0, 2) respectively. The theoretical seismogram are shown in Fig. 2.3, In the figure V.S.B. is the result by the finite element method (super SAP) combined with viscous-spring boundary. The responding exact solution (finite element solution with expansion boundary) and the numerical solution obtained by adopting fix boundary and viscous one are also shown in Fig.2.3, marked with E.S., R.B. and V.B. respectively. The results demonstrate the solution obtained by using viscous-spring boundary is much closer to the exact solution than that using viscous one, and the computational displacement obtained by using the viscous-spring boundary converges to zero as time going on, but the one obtained by using viscous boundary converges to an non-zero. Thus the viscous-spring boundary is better than the viscous one and the fix boundary is the worst. Because what we adopt as r_b is only the shortest distance from the source point to the artificial boundary, not ones to the different points on the boundary, while determining the stiffness of the spring on the artificial boundary, the stiffness determined is wholly bugger, for which the velocity of recovering to zero of computational displacement becomes faster. Otherwise the results may be improved further.

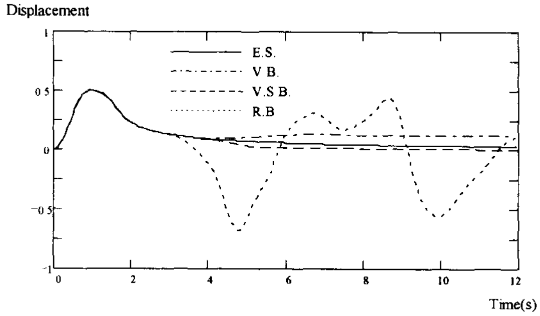

Time history of the displacement at observation point A

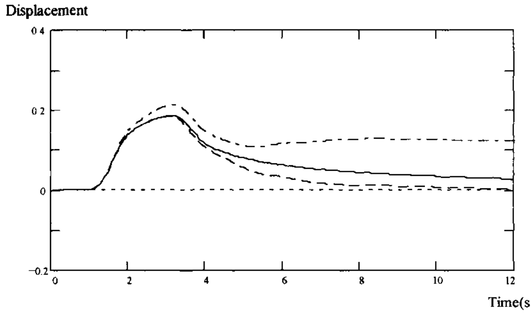

Time history of the displacement at observation point C

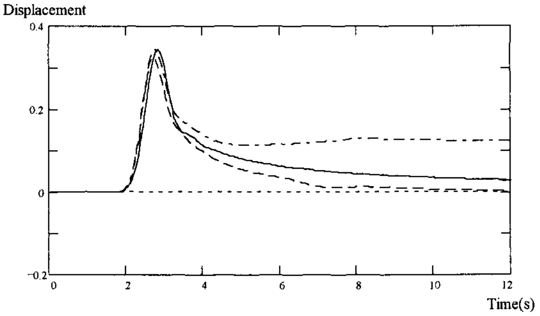

Time history of the displacement at observation point D

Fig.2.3 The anti-plane wave motion example with artificial boundaries

The second example is an in-plane wave motion problem, whose model is the same as the first example. The elastic modulus E=2.5, Poisson's ratio ν =2.5, mass density ρ =1, SV wave velocity c_s=1 and P wave velocity $c_p=\sqrt{3}$, the surface wave load is the same as the first example except that the direction is along y axis and the duration is 2. In an in-plane wave motion problem, the damper and spring must be exerted on the boundary along tangent and normal direction. The components along the tangent direction is the same as the first example, but the ones along the normal must derive theoretically again. But in the example we simply substitute E and c_p for G and c_s in Eq. (2.6). Four observation points are chosen, whose coordinates are (x, y)=(0, 0), (1, 0), (2, 0), (0, 2) respectively. Their theoretical seismogram are shown in Fig.2.4. It can be seen from Fig.2.4, which demonstrate the viscous-spring boundary to be better than the viscous one.

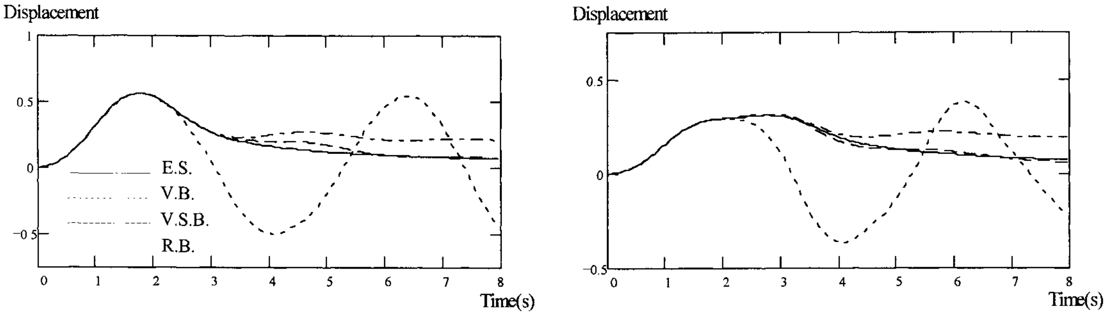

Time history of the displacement at observation point A

Time history of the displacement at observation point B

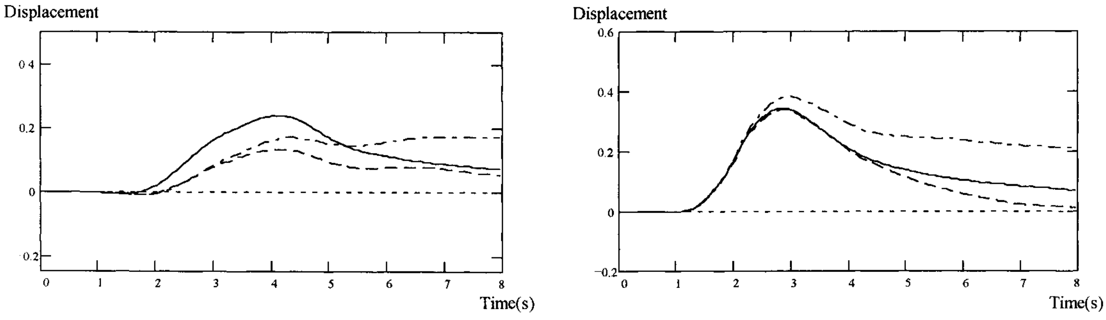

Time history of the displacement at observation point C

Time history of the displacement at observation point D

Fig.2.4 The in-plane wave motion example with artificial boundaries(the vertical displacement)

It can be seen from the above results that the viscous-spring boundary has a good stability and does not produce unstability caused by artificial boundary. Thus it can be used to compute long duration wave motion, for example , it can be adopted for a real seismic wave input. By comparing the results with the exact solution and the numerical solution obtained by using adopting the standard viscous boundary, it can be stated the accuracy of the viscous-spring boundary can satisfy the needs of engineering.

III Input Method of Seismic Wave

In the problem of dynamic interaction of soil-structure subjected to a seismic wave, whether or not the wave motion input to be treated well decides weather or not the situation of wave motion to be successful, which directly influences the accuracy of results and its creditability. In boundary element method, wave motion input is not difficult, which can be solved by converting seismic wave input into an equivalent load acted on the boundary. But in finite element method, in order to model wave radiation to a far field, an artificial boundary is needed to introduce in when wave motion is input to the artificial boundary, different artificial boundary conditions may sometime influence the input method. For viscous boundary, Joyner successfully solved the wave motion input for one dimensional model by means of converting incident motion into an equivalent load acted on the artificial boundary. Yasui amended Joyner's methods, who can treat approximately slant body wave input in finite element method. In reference[16] a method was proposed in which the scattering wave problem was converting into a wave source problem. A fixing-releasing boundary method was introduced to treat wave motion input problem in reference[17], in which the author adopted the infinite element artificial boundary. In this paper a new input method of wave motion which is suitable for the viscous-spring boundary is presented. Its fundamental theory and method are also appropriate for some others artificial boundary, such as viscous boundary and infinite boundary. Finally we give some numerical example to test the effect of the input method.

3.1 Input Method of Wave Motion

In this paper the problem of seismic wave input is converted into a wave source problem. That is to say that the input motion is converted into an equivalent load been directly subject to the artificial boundary to simulate the wave motion input.

The motion of an artificial boundary is made up with a known incident wave and a scattering wave caused by the soil of the structure. The scattering wave is absorbed by the artificial boundary, the incident wave should be inputted into the computational region with some methods. Because in this paper we adopt the method in which the input problem is converted into a wave source problem to treat wave motion input, suppression low of force is satisfied, the incident wave field and the scattering wave field do not effect each other. Thus the incident wave and the scattering wave can be considered separately. In the following discussion only the incident wave field is considered.

Assuming that $w_0(x, y, t)$ is known incident wave fields, so-called free wave field, with any incident angle, which produces the displacement $w_0(x_B,y_B,t)$ on the artificial boundary. If a finite computational region is cut out from in an infinite half space with artificial boundaries, the exact wave motion input condition is that the equivalent load exerted on the artificial boundary makes the displacements and stresses on the artificial boundary are the same as that of the former free wave field. The condition can be written as follow

$$w(x_B,y_B,t)=w_0(x_B,y_B,t) \tag{3.1}$$

$$\tau(x_B,y_B,t)=\tau_0(x_B,y_B,t) \tag{3.2}$$

where, τ_0 is the stress caused by w_0 in the former continua.

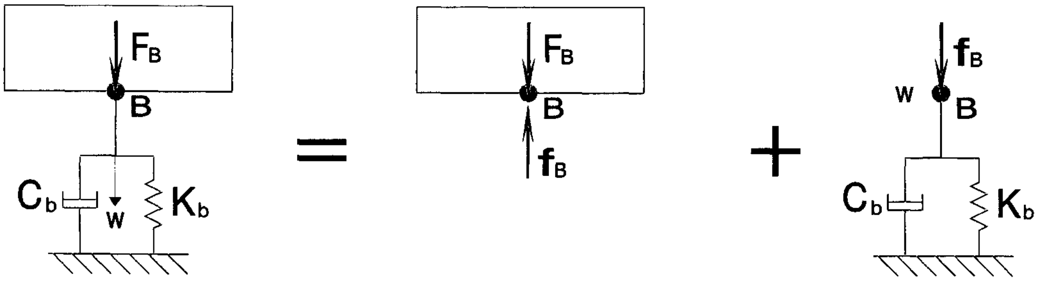

Fig.3.1 The artificial boundary and its separated body

In order to present wave motion input, assuming that the stress exerted on the artificial boundary point B is $F_B(t)$. Using concept of separate body in general mechanical analysis, the artificial boundary and physical components (damper and spring) appended to it(see Fig.3.1) are separated. $f_B(t)$ is the interior force between computational region and component of the artificial boundary. The stress at point B is

$$\tau(x_B, y_B, t) = F_B(t) - f_B(t) \tag{3.3}$$

Substituting Eq.(3.2) into Eq.(3.3) leads to

$$F_B(t) = \tau_0(x_B, y_B, t) + f_B(t) \tag{3.4}$$

The motion equation made up with the spring and the damper is

$$C_b \dot{w}(x_B, y_B, t) + K_b w(x_B, y_B, t) = f_B(t) \tag{3.5}$$

Substituting Eq.(3.1) into Eq.(3.5) results in

$$f_B(t) = C_b \dot{w}_0(x_B, y_B, t) + K_b w_0(x_B, y_B, t) \tag{3.6}$$

Substituting Eq.(3.6) into Eq.(3.4) yields

$$F_B(t) = \tau_0(x_B, y_B, t) + C_b \dot{w}_0(x_B, y_B, t) + K_b w_0(x_B, y_B, t) \tag{3.7}$$

In Eq.(3.7), w_0 is known and velocity $\dot{w}_0$ and stress τ_0 are determined by w_0. Thus according to Eq.(3.7), one can obtain the total load $F_B(t)$ exerted on the artificial boundary and wave motion input can be presented on the viscous-spring boundary.

For more general condition, if the motion equation of the component exerted on the artificial boundary satisfies

$$f_B(t) = f_B(w, \dot{w}, \ddot{w}, t) \tag{3.8}$$

the stress exerted on the artificial boundary as wave field input is

$$F_B(t) = \tau_0(x_B, y_B, t) + f_B(t) \tag{3.9}$$

Eq.(3.9) is also suitable for the viscous boundary and infinite element boundary. For example, for a viscous boundary, a slant wave propagates into a half space(see Fig.3.2),

$$w_0 = w_0(x \sin\theta - y \cos\theta - c_s t) \tag{3.10}$$

on the bottom of the artificial boundary,

$$\tau_0 = \rho c_s \cos\theta\, \dot{w}_B \tag{3.11}$$

where $w_B = w_0(x_B, y_B, t)$, $\dot{w}$ represents differentiation of w with respect to time t. $f_B(t)$ is

$$f_B(t) = \rho c_s \dot{w}_B \tag{3.12}$$

Thus the stress needed to be exerted on the artificial boundary can be obtained according to Eq.(3.9)

$$F_B(t) = \rho c_s (1 + \cos\theta) \dot{w}_B \tag{3.13}$$

when $\theta = 0$,

$$F_B(t) = 2 \rho c_s \dot{w}_B \tag{3.14}$$

The above results is complete the same as that given by other authors which belongs to the precise method for one dimensional wave motion input[14,18]

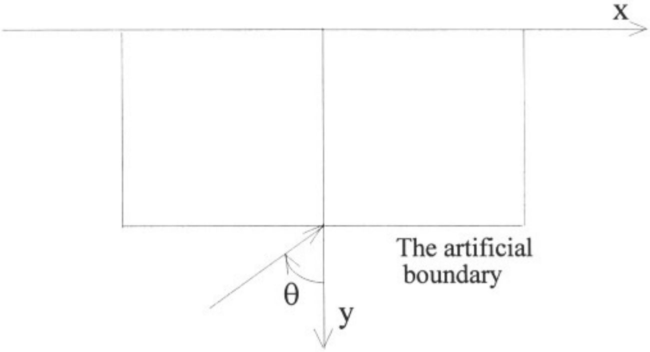

Fig.3.2 A slant incident wave

It is worthy to point out that other authors only gave the incident wave propagating vertically, which belongs to the precise input method of one dimensional wave motion input. But the input method proposed in this paper can deal with a slant wave motion input. That is to say it can simulate the input procedure of multiple point.

For a 2-D or 3-D problem, one can exert physical component on the boundary point in two direction(2D) or three direction(3D) to form an artificial boundary. Firstly, stress caused by the incident wave field on the artificial boundary is determined. Then by using Eq.(3.7), stress exerted on every direction is obtained, which complicate the input of wave motion.

3.2 Numerical Examples of Wave Motion Input

In the following, a homogeneous elastic half space subjectd to an plane incident wave is considered as an example to verify the accuracy of the input method of wave motion proposed in this paper. The mechanical model employed in the example is an elastic half space as shown in Fig.3.3, the mechanical parameters are: shear modulus $G=5.292\times10^6$Pa, elastic modulus $E=1.323\times10^7$Pa, Poisson's ratio $\nu=0.25$, mass density $\rho=2.7$ kg/m^3, wave velocity $c_s=1400$m/s, $c_p=2425$m/s. The range of computational region is $X_b=Y_b=381$m. The size of the finite element are $\Delta x=\Delta y=19.05$m. Time step is chosen as $\Delta t=0.005$s. The elastic half space is subject to a incident SV wave with angle $\theta=0°$ and 30° respectively, whose time history is shown in Fig.3.4.

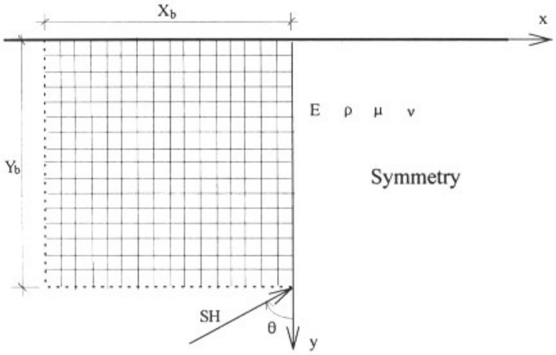

Fig.3.3 Modeling of elastic half space

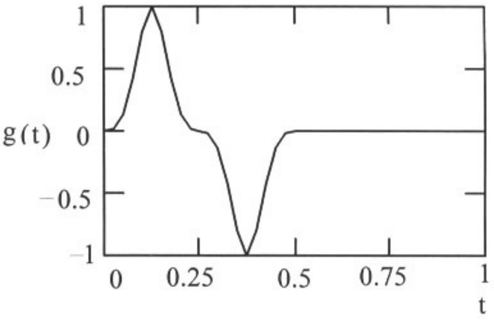

Fig.3.4 The time history of the incident wave

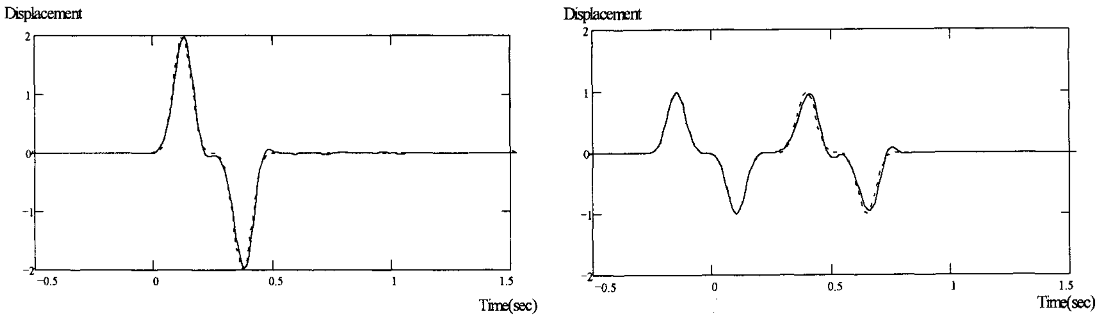

Observation point A

Observation point B

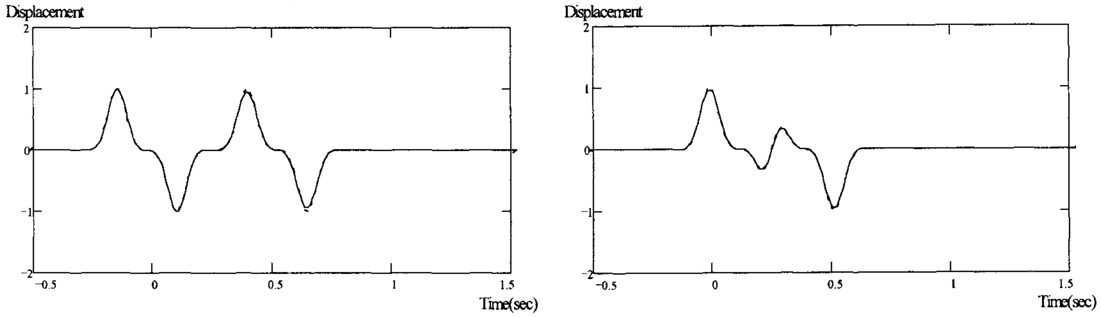

Observation point C

Observation point D

Fig.3.5 The horizontal displacement time history of the elastic half space subjected to an incident SV wave(θ =0 °)

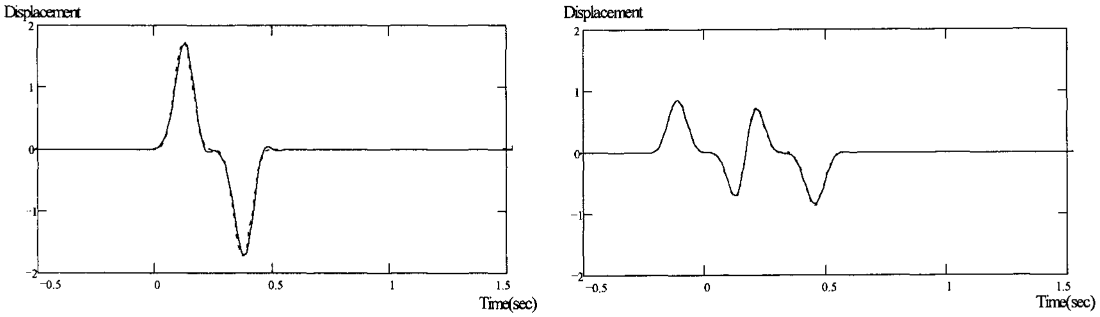

Observation point A

Observation point B

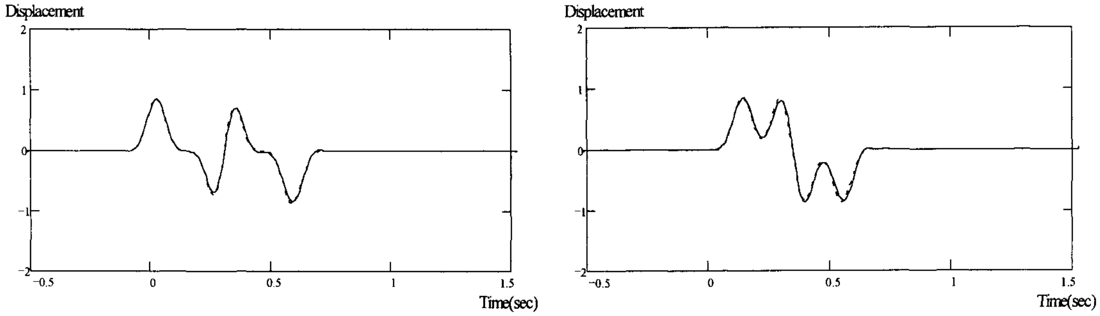

Observation point C

Observation point D

Fig.3.6 The horizontal displacement time history of the elastic half space subjected to an incident SV wave (θ =30 °)

The displacement in time domain of the four observation points A, B, C, D, whose coordinates are (0, 0), (0, 381), (381, 381), (381, 0) respectively, is presented in Fig.3.5 and 3.6. In these figures, the dashed lines represents the analytical solution and the solid lines represent the numerical solution employing the input method and the viscous-spring boundary proposed in this paper. It can be clearly seen from the Fig.3.5 and 3.6 that the results adopting the proposed input method are well agreeable with the analytical solutions, which demonstrate that the proposed input method is accurate as treating SV wave input.

At the same time, we also consider the situation for incident plane SH and P wave especially the one with an large angle. Also the results are well agreeable with the analytical solutions, which state that the proposed input methods is also precise while treating the incident SH and P wave inputs.

IV. Numerical Example of Seismic Wave Scattering

The response of a two dimensional semicircular valley subjected to a SV wave is computed in this section based on the proposed viscous-spring boundary and wave motion input method by using finite element software (Super SAP). By comparing the results obtained by proposed method with the analytical solutions given in[19], the accuracy and efficiency of the proposed method are verified.

The computational model and coordinate system employed in the following example is shown in Fig.4.1. The parameters of the model are chosen as follows: shear modulus G=5.292 × 10^6Pa, mass density ρ =2.7kg/m^3, shear wave velocity c_s=1400m/s.

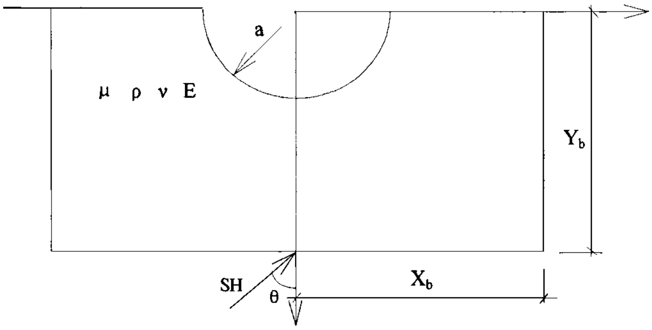

Fig.4.1 Modeling of the semicircular valley subjected to an incident SH wave

A finite computational region is cut out from an infinite media, which is discretized by the finite element method. The size of the element close to the boundaries is $\Delta x = \Delta y = 19.05m$ along x and y direction respectively and the elements close to the semicircular valley are fined down, and the time step is chosen as $\Delta t = 0.01s$, the computational area, X_b=Y_b=476.25m, the radius of the valley a=190.5m.

The incident SH wave in time domain is a pulse. The displacement at the surface of semicircular valley caused by the incident SH wave are obtained by employing the finite element method. In order to compare with the analytical solutions, the numerical solutions are transformed from time domain into frequent domain by using Fourier transformation.

Define a non-dimensional frequency

$$\eta = 2a / \lambda = \omega a / \pi c_s \tag{4.1}$$

where λ is the wavelength, ω is frequency, c_s is SH wave velocity. It can be stated that η is the characteristic coefficient of the ratio of the diameter of the semicircular valley and the wavelength of the incident SH wave.

The amplify coefficients of the ground motion caused by the incident SH waves with angle θ =0 °, 30 °, 60 °, 90 ° and non-dimensional frequency η =0.25, 0.50, 0.75, 1.0, are presented in Fig. 4.2 to 4.5, where

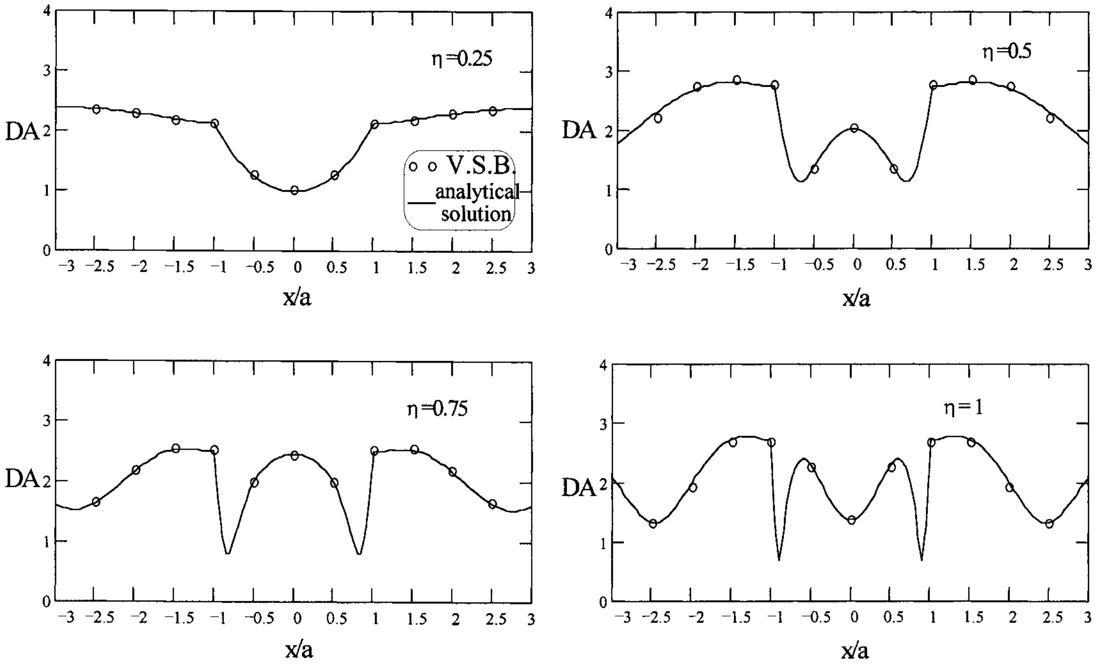

Fig.4.2 The magnification coefficient of the ground motion of the semicircular valley subjected to an incident SH wave motion with the angle θ =0 °

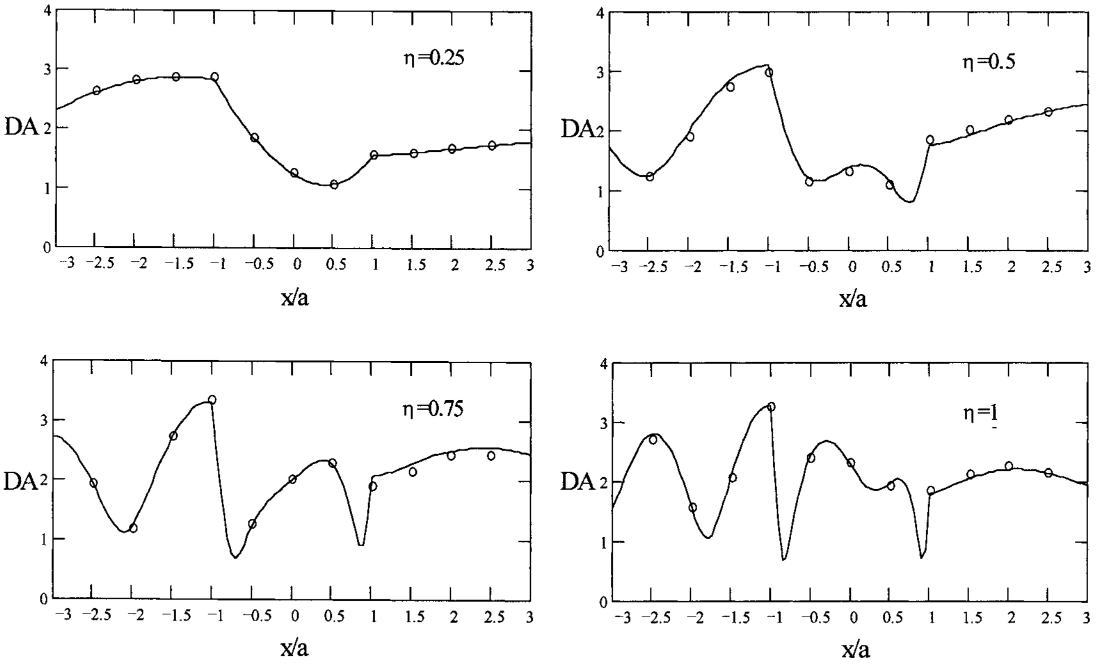

Fig.4.3 The magnification coefficient of the ground motion of the semicircular valley subjected to an incident SH wave motion with the angle θ =30 °

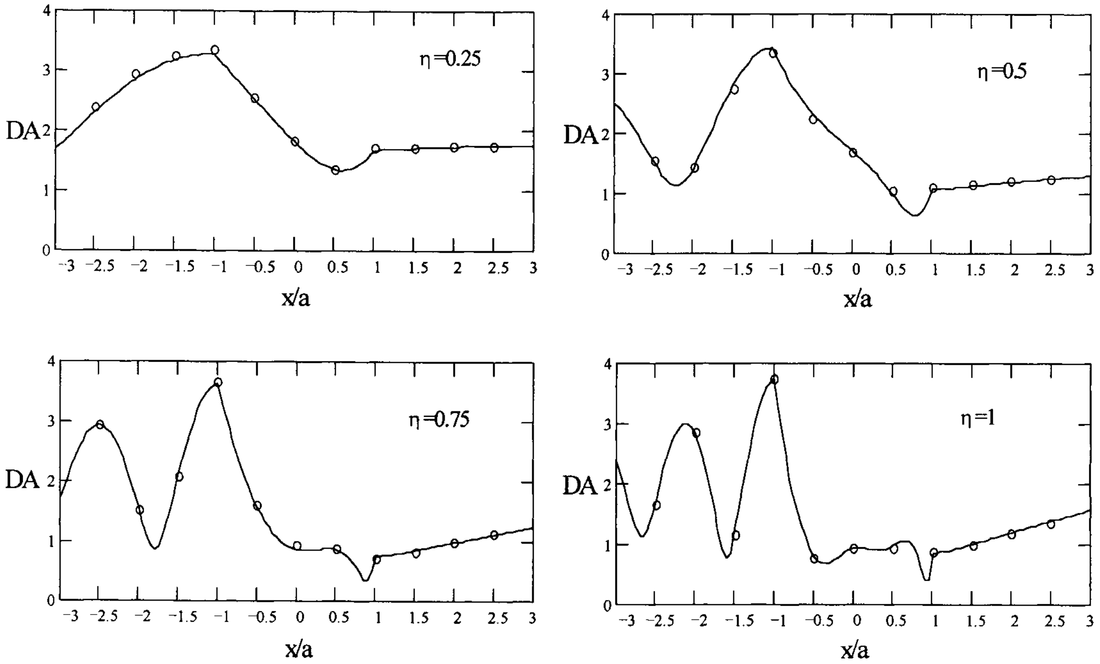

Fig.4.4 The magnification coefficient of the ground motion of the semicircular valley subjected to an incident SH wave motion with the angle θ =60 °

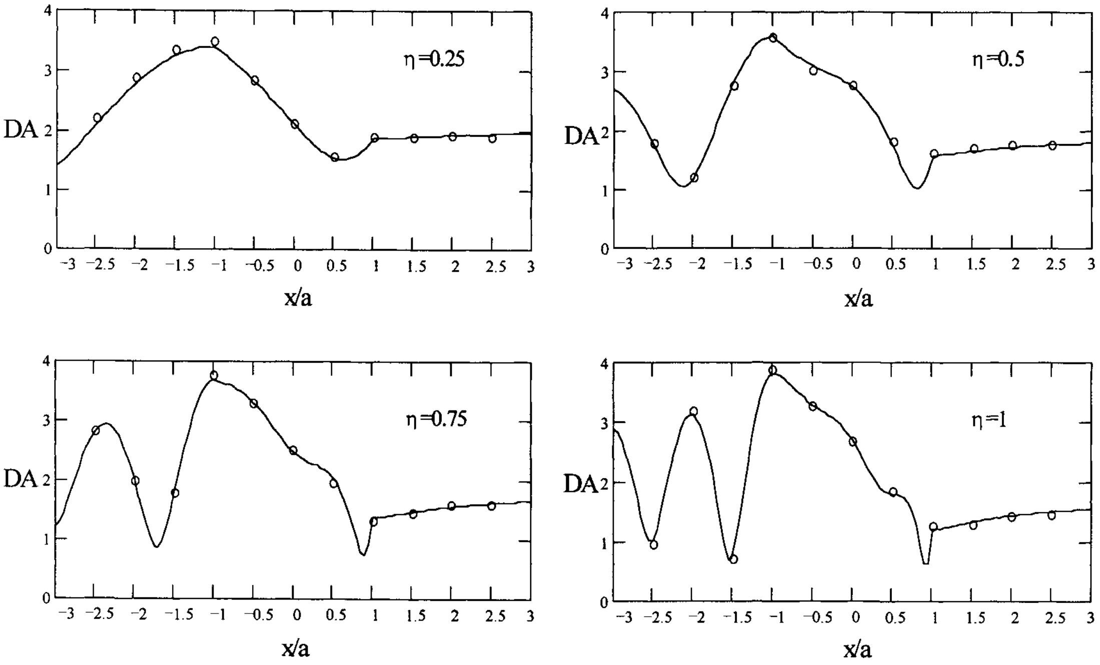

Fig.4.5 The magnification coefficient of the ground motion of the semicircular valley subjected to an incident SH wave motion with the angle θ =90 °

the horizontal coordinate is position, the vertical coordinate is the magnification coefficients of the ground motion, the solid lines represent the analytical solution, the discretized dots represent the numerical solutions obtained by using the proposed method. By comparing the results obtained by using the proposed method with close form solutions, it can be clearly seen that the agreement is satisfactory. It can be stated once more that the input method given in this paper is exact and the viscous-spring boundary has a satisfactory accuracy. Thus the set of proposed methods are practicable for analyzing the dynamic interaction of soil-structure.

V. Conclusions

A direct method for analysis of dynamic soil-structure interaction is presented in this paper. Some of conclusions are obtained as following

1. In the problem of dynamic soil-structure interaction, viscous-spring boundary can be employed to simulate the absorption of infinite soil to the scattering wave. Compared with others artificial boundaries, this kind of boundary can simulate not only the absorption of infinite soil to energy of scattering wave, but also elasticity recovery capacity of the exterior media. Numerical examples demonstrate that the accuracy of the viscous-spring boundary is higher than the viscous one and the stability of the former is better.
2. The physical concept of the new seismic wave input method proposed in this paper is clear and simple. Compared with the others input method of wave motion, it expands the exact wave motion input method from one dimensional problem to two dimension and in principle is suitable for three dimension.
3. By making the exterior appending programs, the method is combined into a large general structural analysis software (i.e. Super SAP). Numerical examples state that the method has a higher accuracy.

Finally the proposed method not only makes it possible to analyze the dynamic soil-structure interaction employing a large general structural analysis software, but also provides a platform to trace the renewing and developments of the large general software and be sure to use the latest software to analyze the dynamic soil-structure interaction in time.

References

[1] Zhang Chuhan, Problems of dynamic soil-structure interaction, *Theory and Application for Interaction of Structure and Media*, Hehai University Press(1993).

[2] Lin Gao, Seismic response and resistance design of dynamic soil-structure interaction system, *progress in earthquake engineering in China*, Seismological Press(1992).

[3] Liao Zhenpeng, Normal transmitting boundary conditions, *Scientia Sinica (Series E)*, **39**(3), 244-254, 1996.

[4] Lysmer J. and R. L. Kulemeyer, Finite dynamic model for infinite media, *J. Engng. Mech. Div. ASCE*, **95**, 759–877, 1969.

[5] Lysmer J. and G. Wass, Shear waves in plane infinite structures , *J. Engng. Mech. Div., ASCE*, **98**, 85–105, 1972.

[6] Smith W. D., A nonreflecting plane boundary for wave propagation problems, *J. Comp. Phys.*, **15**(4), 492–503, 1974.

[7] Clayton R. and B. Engquist, Absorbing boundary conditions for acoustic and elastic wave equations, *Bull. Seism. Soc. Amer.*, **67**(6), 1529–1540, 1977.

[8] Liao Zhenpeng, A finite model for problems of transient scale waves in an infinite elastic medium, *Earthquake Engineering and Engineering Vibration*, **2**(4), 38-53, 1984.

[9] Zhao Chongbin, Zhang Chuhan and Zhang Guangdou, Analysis of 3-D foundation wave problems by mapped dynamic infinite elements, *Science in China*, **32**(4), 1989.

[10] Kausel E., Local transmitting boundaries, *J. Engng. Mech.*, **114**(6), 1011–1027, 1988.

[11] Wolf J. P., A comparison of time-domain transmitting boundaries, *Earthq. Engng. Struct. Dyn.*, **14**, 655–673, 1986.

[12] Deeks A. J. and Randolph M. F., Axisymmetric time-domain transmitting boundaries, *Journal of Engineering Mechanics*, **120**(1), 25-42, 1994.

[13] Whitham G. B., *Linear and nonlinear waves*, Wiley, New York, 1974.

[14] Joney W. B. and A. T. F. Chen, Calculation of nonlinear ground response in earthquake, *Bull. Seism. Soc. Amer.*, **65**(5), 1315-1336, 1975.

[15] Yasui Y., S. Takano T. Takeda, A. Miyamoto O. Kurimoto and R. Ishikawa, Finite element method for obliquely incident seismic wave problems, *Proc. Ninth World Conference on Earthquake Engineering,* Vol.III, Tokyo-Kyoto, Japan, 447-452, 1988.

[16] Liao Zhenpeng, A Finite element method for near-field problems of wave motions in heterogeneous materials, *Earthquake Engineering and Engineering Vibration*, **4**(2), 1-14, 1984.

[17] Zhao Chongbin, Simulation of infinite soil of arch dam and study of input method of seismic wave, *Doctoral Dissertation of Tsinghua University*, 1987.

[18] Wang Mingyang, Zhao Yuetang and Qian Qihu, Two problems in setting up artificial boundary while analyzing soil-structure interaction by finite element method for wave motion, *Chinese Journal of Geotechnical Engineering*, **17**(1), 92-95, 1995.

[19] Trifunac M. D., Scattering of plane SH-waves by a semi-cylindrical canyon, *Earthq. Engng. Struct. Dyn.*, **1**, 267–281, 1973.

AN ANALYTICAL APPROACH FOR EVALUATION OF GLOBAL DYNAMIC IMPEDANCE OF SEMI-CIRCULAR DAM CANYON CUT IN AN ELASTIC HALF-SPACE

Lin Gao , Chen Jianyun and Sun Keming
(Dept. of Civil Engineering ,Dalian University of Technology,Dalian 116023, China)

Abstract

An analytical approach for evaluation of global dynamic impedance of semi-circular dam canyon cut in an elastic half-space is presented. From the study of the behaviour of complex frequency response functions for radial displacements and the dynamic impedance of the canyon surface, a suitable way for simplifying the computation of the dynamic impedance of dam canyon is suggested.

Introduction

Dynamic soil-structure interaction has significant effect on the seismic response of dam structures. Nevertheless, determination of the foundation impedance of the dam canyon, especially for a three-dimensional space structure such as arch dam associates with large computational effort and it is too complicated for design engineers. For practical engineering implementation, simplifying the computation of dynamic foundation impedance is a task which demands paying attention to. For this purpose , a rather simple example of the global dynamic impendance of a semi-circular dam canyon cut in an elastic half-space is first evaluated analytically, then based on the study of the characteristics of frequency-dependent dynamic impedance of the dam canyon, a suitable way for simplifying the computation of foundation impedance is suggested.

Modeling and Assumptions

The dam canyon is assumed as semi-circular with radius of R, and the foundation medium is assumed to be linear visco-elastic, homogeneous and isotropic. The dam-foundation interface is simulated by a ring shaped area of width b and the external load P is assumed uniformly distributted along the surface of canyon. The coordinate system and the displacement components are illustrated in Fig.1

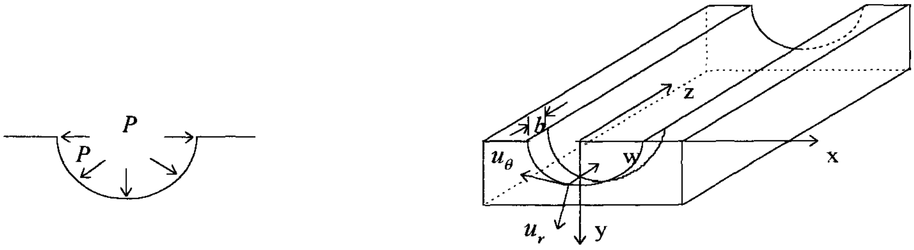

Fig.1 Modeling of the Problem

The equations of motion of the system expressed in the cylindrical coordinate system are given as follows

$$\left.\begin{aligned}
&\frac{\partial\sigma_r}{\partial r}+\frac{1}{r}\frac{\partial\tau_{\theta r}}{\partial\theta}+\frac{\partial\tau_{zr}}{\partial z}+\frac{\sigma_r-\sigma_\theta}{r}+F_r=\rho\frac{\partial^2u_r}{\partial t^2}\\
&\frac{\partial\tau_{r\theta}}{\partial r}+\frac{1}{r}\frac{\partial\sigma_\theta}{\partial\theta}+\frac{\partial\tau_{z\theta}}{\partial z}+\frac{2\tau_{r\theta}}{r}+F_\theta=\rho\frac{\partial^2u_\theta}{\partial t^2}\\
&\frac{\partial\tau_{rz}}{\partial r}+\frac{1}{r}\frac{\partial\tau_{\theta z}}{\partial\theta}+\frac{\partial\sigma_z}{\partial z}+\frac{\tau_{rz}}{r}+F_z=\rho\frac{\partial^2u_z}{\partial t^2}
\end{aligned}\right\}\tag{1}$$

where u_r, u_θ and u_z are the radial, tangential and longitudinal displacements respectively; σ_r, σ_θ , σ_z and $\tau_{r\theta}$, $\tau_{\theta z}$, τ_{zr} are corresponding normal and tangential stresses respectively; F_r , F_θ and F_z are unit volumetric force. The complex modulus of elasticity of the foundation medium is expressed as

$$E^*=E\cdot(1+i\cdot2\mu)$$

μ is the hysteretic material damping.

In order to simplify the derivation, some assumptions have to be introduced. The displacements is regarded uniformly distributed along any arbitrary radius r, and the displacement components u_θ and u_r associated with provided external load are considered as negligibly small and the radial displacements components is approximated by separable function of the cylindrical coordinates z and r . Accordingly, the displacement field is expressed by

$$\begin{cases}u_r=F(z)\cdot\phi(r)\\u_\theta=u_z=0\end{cases}\tag{2}$$

where $F(z)$ and $\phi(r)$ are the variation and decay of u_r along the longitudinal and radial direction respectively.

The appropriateness of these assumptions was examined by a numerical example of the same canyon with radius *r=10,* but subjected to static load excitation only. The calculated radial and tangential displacement components for *r=10, 12.5, 16.0, 20.5, 26.0, 32.5* at *z=0* are illustrated in Fig.2 and Fig.3 respectively. And distribution of longitudinal displament component along *z* axis for various *r* is illustrated in Fig.4.

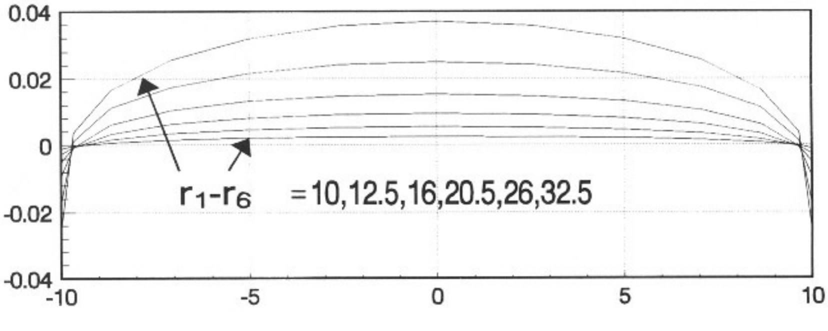

Fig.2 Distribution of radial displacement components along x axis for various r

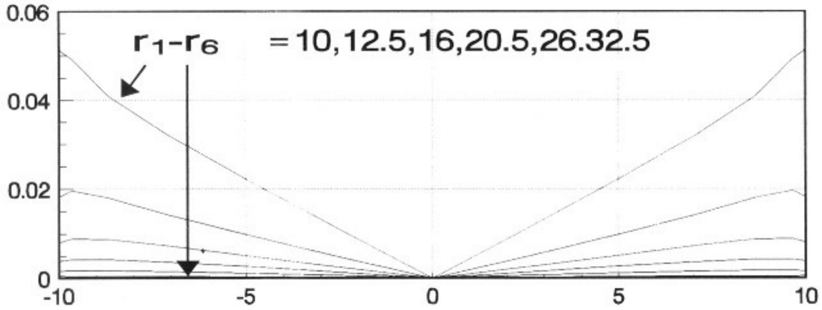

Fig.3 Distribution of tangential displacement components along x axis for various r

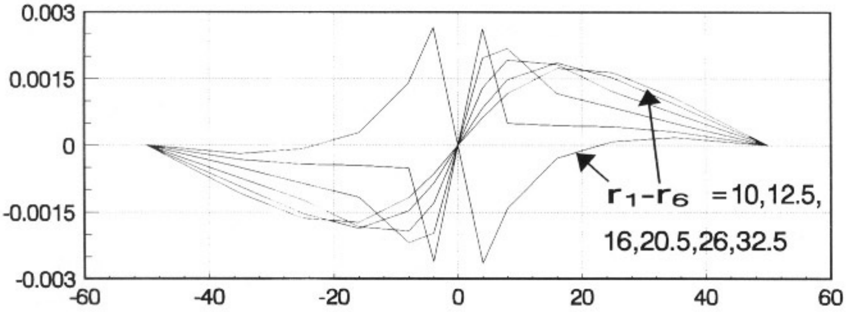

Fig.4 Distribution of longitudinal displacement components along z axis for various r

It can be seen from these figures that u_z is small compared with u_r, the largest value of u_z is about *10% of* u_r in the vicinity of $z=0$ and it reduces remarkably with increasing z, the assumption of $u_z = 0$ is reasonable. Some discrepancies from the assumptions given in Eq.(2) are found for u_θ, particularly near the horizontal free surface notabale deviations exists, The averaged u_θ accounts for about *70 %* of u_r at the canyon surface and it reduces to about *20%* of u_r at $r=20$. However, the computed average radial impedance along canyon surface is $1213\,N/m$, which is close to the value $1453\,N/m$ of global impedance given by Eq.(59) at $\omega = 0$. The error is about *12%*. Hence, from the point of view of global impedance, though the assumotions made by Eq.(2) seem rather arbitrary, they are acceptable.

Eventually, based on Eq.(2), the strain components and stress components are formulated as follows:

$$\varepsilon_r = \frac{\partial u_r}{\partial r} = F(z)\cdot\frac{\partial \phi}{\partial r} \quad , \quad \varepsilon_\theta = \frac{1}{r}\frac{\partial u_\theta}{\partial \theta} + \frac{u_r}{r} = \frac{1}{r}F(z)\cdot\phi(r) \quad , \quad \varepsilon_z = \frac{\partial u_z}{\partial z} = 0$$

$$\gamma_{\theta z} = \frac{1}{r}\frac{\partial u_z}{\partial \theta} + \frac{\partial u_\theta}{\partial z} = 0 \quad , \quad \gamma_{rz} = \frac{\partial u_r}{\partial z} + \frac{\partial u_z}{\partial r} = \frac{\partial F}{\partial z}\cdot\phi(r) \quad , \quad \gamma_{r\theta} = \frac{\partial u_\theta}{\partial r} + \frac{1}{r}\frac{\partial u_r}{\partial \theta} - \frac{u_\theta}{r} \qquad (3)$$

and

$$\sigma_r = 2G\varepsilon_r + \lambda e = (2G+\lambda)\cdot F\cdot\frac{\partial \phi}{\partial r} + \frac{\lambda}{r}F\cdot\phi \quad , \quad \tau_{\theta z} = G\gamma_{\theta z} = 0$$

$$\sigma_\theta = 2G\varepsilon_\theta + \lambda e = (2G+\lambda)\cdot\frac{1}{r}\cdot F\cdot\phi + \lambda\cdot F\cdot\frac{\partial\phi}{\partial r} \quad , \quad \tau_{\theta z} = G\gamma_{rz} = G\cdot\frac{\partial F}{\partial z}\cdot\phi \qquad (4)$$

$$\sigma_z = 2G\varepsilon_z + \lambda e = \lambda\cdot F\cdot(\frac{\partial\phi}{\partial r} + \frac{\lambda}{r}\cdot\phi) \quad , \quad \tau_{\theta z} = G\gamma_{r\theta} = 0$$

in which $e = \varepsilon_r + \varepsilon_\theta + \varepsilon_z \quad , \quad \lambda = \dfrac{E^* v}{(1+v)\cdot(1-2v)} \quad , \quad G = \dfrac{E^*}{2(1+v)}$

Governing Equations of the Foundation Impedance

A convenient approach of deriving the governing equations of motion for a complex medium problem such as the one discussed here is to make use of scalar energy quantities and the variational calculus. The most generally applicable variational concept is Hamilton principle, which may be expressed as:

$$\int_{t_1}^{t_2} \delta(T - I)\cdot dt + \int_{t_1}^{t_2} \delta(W_{nc})\cdot dt = 0 \qquad (5)$$

where T and I denote total kinetic energy and potential energy of the system respectively ;W_{nc} denotes work done by the nonconservative forces acting on the system and δ represents variation taken during the indicated time interval (t_1, t_2).

For a harmonic motion, the kinetic and potential energy functions for the soil domain can be expressed in terms of the frequency ω and the displacement amplitude. Taking variations of T, I and W_{nc}, we find

$$T = \frac{1}{2}\int_0^\infty \int_R^\infty \int_0^\pi \rho\cdot w^2 u_r^2 r\cdot dr\cdot d\theta\cdot dz = \frac{\pi}{2}\int_0^\infty \int_R^\infty \rho\cdot w^2 u_r^2 r\cdot dr\cdot dz \qquad (6)$$

Let $m = \int_0^\infty F^2 dz \quad , \quad \xi = \int_R^\infty r\cdot\phi^2 dr$

Then $\delta T = \pi\int_R^\infty \rho\cdot\omega^2 m\cdot\phi\cdot r\cdot\delta\phi\cdot dz + \pi\int_0^\infty \rho\cdot\omega^2\xi\cdot F\cdot\delta F\cdot dz \qquad (7)$

For the work done by the external force

$$W_{nc} = -\int_0^\pi 2b\cdot R\cdot P\cdot F(z)\cdot\phi(r)\cdot d\theta\Big|_{z=0,r=R} = -\pi\cdot 2bPR\cdot F(z)\cdot\phi(r)\Big|_{z=0,r=R} \qquad (8)$$

$$\delta W_{nc} = -\pi\cdot 2bPR\cdot F\cdot\delta\phi\Big|_{z=0,r=R} - \pi\cdot 2bPR\cdot\phi\cdot\delta F\Big|_{z=0,r=R} \qquad (9)$$

and, for the potential energy

$$I = \frac{1}{2}\int_0^\infty \int_R^\infty \int_0^\pi (\sigma_r\varepsilon_r + \sigma_\theta\varepsilon_\theta + \sigma_z\varepsilon_z + \tau_{r\theta}\gamma_{r\theta} + \tau_{\theta z}\gamma_{\theta z} + \tau_{rz}\gamma_{rz})\cdot r dr d\theta dz$$
$$= \pi\cdot(I_1 + I_2 + I_3 + I_4) \qquad (10)$$

where

$$I_1 = \frac{1}{2}\int_0^\infty \int_R^\infty (2G+\lambda)\cdot F^2 (\frac{\partial\phi}{\partial r})^2 r\cdot drdz$$

$$I_2=\frac{1}{2}\int_0^{\infty}\int_R^{\infty}(2G+\lambda)\cdot\frac{1}{r}F^2\phi^2drdz$$

$$I_3=\int_0^{\infty}\int_R^{\infty}\lambda\cdot F^2\phi\cdot\frac{\partial\phi}{\partial r}\cdot drdz$$

$$I_4=\frac{1}{2}\int_0^{\infty}\int_R^{\infty}G\cdot(\frac{\partial F}{\partial z})^2\phi^2r\cdot drdz \qquad (11)$$

Substituting (3) and (4) into (10) and taking variation of it leads to

$$\begin{aligned}\delta(\frac{I}{\pi})=&\int_0^{\infty}(2G+\lambda)\cdot\zeta\cdot F\cdot\delta F\cdot dz+\int_0^{\infty}(2G+\lambda)\cdot\eta\cdot F\cdot\delta F\cdot dz\\&+(\phi^2\big|_R^{\infty})\cdot\int_0^{\infty}\lambda\cdot F\cdot\delta F\cdot dz-\int_0^{\infty}G\cdot\xi\cdot\frac{\partial^2F}{\partial z^2}\cdot\delta F\cdot dz\\&-\int_R^{\infty}(2G+{}_{\lambda})\cdot m\cdot(r\frac{\partial^2\phi}{\partial r^2}+\frac{\partial\phi}{\partial r})\cdot\delta\phi\cdot dr+\int_R^{\infty}(2G+\lambda)\cdot m\cdot\frac{1}{r}\cdot\phi\cdot\delta\phi\cdot dr+\int_R^{\infty}G\cdot n\cdot{}_{\phi}\cdot r\cdot\delta\phi\cdot dr\\&+(2G+\lambda)\cdot m\cdot\frac{\partial\phi}{\partial r}\cdot r\cdot\delta\phi\big|_R^{\infty}+\lambda\cdot m\cdot\phi\cdot\delta\phi\big|_R^{\infty}+G\cdot\xi\cdot(\frac{\partial F}{\partial z})\cdot r\cdot\delta F\big|_0^{\infty}\end{aligned} \qquad (12)$$

In which

$$m=\int_0^{\infty}F^2dz\quad,\quad n=\int_0^{\infty}(\frac{\partial F}{\partial z})^2dz$$

$$\xi=\int_R^{\infty}r\cdot\phi^2dr\quad,\quad\zeta=\int_0^{\infty}r\cdot(\frac{\partial\phi}{\partial r})^2dr\quad,\quad\eta=\int_R^{\infty}\frac{1}{r}\cdot\phi^2dr \qquad (13)$$

Substituting (7), (9) and (12) into (5) and making rearrangement of the terms, finally we get

$$\begin{aligned}&\int_0^{\infty}\left\{\left[(2G+\lambda)\cdot(\zeta+\eta)+\left(\phi^2\big|_R^{\infty}\right)\cdot\lambda-\rho\cdot\omega^2\xi\right]\cdot F-G\cdot\xi\cdot\frac{\partial^2F}{\partial z^2}\right\}\cdot\delta F\cdot dz\\&-\int_0^{\infty}\left\{\left[(2G+\lambda)\cdot m\cdot\left(r\cdot\frac{\partial^2\phi}{\partial r^2}+\frac{\partial\phi}{\partial r}-\frac{1}{r}\cdot\phi\right)-\left(G\cdot n+\rho\cdot\omega^2m\right)\cdot r\cdot\phi\right]\cdot\delta\phi\cdot dr\right\}\\&+\left[(2G+\lambda)\cdot m\cdot\frac{\partial\phi}{\partial r}\cdot r+\lambda\cdot m\cdot\phi\right]\cdot\delta\phi\big|_R^{\infty}+2bPR\cdot F\cdot\delta\phi\big|_{r=R,z=0}\\&+G\cdot\xi\cdot\frac{\partial F}{\partial z}\cdot\delta F\big|_0^{\infty}+2bPR\cdot\phi\cdot\delta F\big|_{r=R,z=0}=0\end{aligned} \qquad (14)$$

As $\delta\phi$ and δF can be chosen arbitrarily, the terms included in the brackets must turn to zero. Thereby, the following governing equations for determining the function F and ϕ are obtained.

$$A\cdot F-G\cdot\xi\cdot\frac{\partial^2F}{\partial z^2}=0\quad,\quad(0\le z\le\infty) \qquad (15)$$

$$r^2\frac{\partial^2\phi}{\partial r^2}+r\frac{\partial\phi}{\partial r}-\left(\frac{\gamma^2}{R^2}r^2+1\right)\cdot\phi=0\quad,\quad(R\le r\le\infty) \qquad (16)$$

where

$$A=(2G+\lambda)\cdot(\zeta+\eta)+\left(\phi^2\big|_R^{\infty}\right)\cdot\lambda-\rho\cdot\omega^2\xi \qquad (17)$$

$$\left(\frac{\gamma}{R}\right)^2=\frac{G\cdot n}{(2G+\lambda)\cdot m}-\frac{\rho\cdot\omega^2}{2G+\lambda} \qquad (18)$$

And the corresponding boundary conditions are given by

$$\left[(2G+\lambda)\cdot m\cdot\frac{\partial\phi}{\partial r}\cdot r+\lambda\cdot m\cdot\phi\right]\cdot\delta\phi\Big|_R^\infty+2bPR\cdot F\cdot\delta\phi\Big|_{r=R,z=0}$$
$$+G\cdot\xi\cdot\frac{\partial F}{\partial z}\cdot\delta F\Big|_0^\infty+2bPR\cdot\phi\cdot\delta F\Big|_{r=R,z=0}=0 \qquad (19)$$

According to the assumptions concerning radial components of the displacement $u_r=F(z)\cdot\phi(r)$, they are symmetrical with respect to z axis

$$\frac{\partial F}{\partial z}\Big|_{z=0}=0 \qquad (20)$$

It is reasonable to assume $F\big|_{z=0}=1\ ,\quad \delta F\big|_{z=0}=0$ (21)

And accordingly, the boundary conditions for determining ϕ and F are given by

$$F=1\ ,\quad \frac{\partial F}{\partial z}=0 \qquad (z=0) \qquad (22)$$

$$\begin{aligned}&(2G+\lambda)\cdot m\cdot r\cdot\frac{\partial\phi}{\partial r}+\lambda\cdot m\cdot\phi-2bPR=0 && (r=R)\\ &(2G+\lambda)\cdot m\cdot r\cdot\frac{\partial\phi}{\partial r}+\lambda\cdot m\cdot\phi=0 && (r\to\infty)\end{aligned} \qquad (23)$$

Solution of the Equations

1. Solution of the function $\phi(r)$

In the formula (16), let x be denoted by $x=\frac{\gamma}{R}\cdot r$, then (16) becomes

$$x^2\frac{\partial^2\phi}{\partial x^2}+x\frac{\partial\phi}{\partial x}-(x^2+1)\cdot\phi=0 \qquad (24)$$

It is the modified Bessel Equation of first order, and the general solution takes the form

$$\phi(r)=C_1I_1(x)+C_2k_1(x)$$

As $I_1(x)\to\infty$ with $|x|\to\infty$, the constant C_1 should be taken equal to zero, and $\phi(r)$ becomes

$$\phi(r)=C_2k_1(x) \qquad (25)$$

where k_1(x) is the first order modified Bessel function of second kind.

At the canyon surface $x = \frac{\gamma}{R} \cdot R = \gamma$

Substituting it into boundary condition (23) , we obtain

$$C_2 = \frac{2bPR}{(2G+\lambda) \cdot m \cdot \gamma \cdot k_1'(\gamma) + \lambda \cdot m \cdot k_1(\gamma)} \tag{26}$$

and $\phi(r)$ is expressed as

$$\phi(r) = C_2 k_1(x) = \frac{4bPR}{2\lambda \cdot m \cdot k_1(\gamma) - (2G+\lambda) \cdot m \cdot \gamma \cdot (k_0(\gamma) + k_2(\gamma))} \cdot k_1\left(\frac{\gamma}{R} \cdot r\right) \tag{27}$$

2. Determining the Parameters ξ , ζ and γ

(1) Parameter ξ

$$\xi = \int_R^\infty r \cdot \phi^2 dr = \frac{R^2 C_2^2}{2\gamma^2}\left[\left(x^2 k_2(x)\right)\Big|_R^\infty - \left(x \cdot k_1'(x) \right)^2 \Big|_R^\infty + k_2(x)\Big|_R^\infty \right] \tag{28}$$

Taking into consideration, that $\underset{x|\to\infty}{k_1(x) = 0}$, $\underset{|x|\to\infty}{k_1'(x) = 0}$

finally we get

$$\xi = \frac{c_2^2 R^2}{2}\left[k_1'^2(\gamma) - \left(1 + \frac{1}{\gamma^2}\right) \cdot k_1^2(\gamma) \right] \tag{29}$$

(2) Parameter ζ

$$\zeta = \int_R^\infty r \left(\frac{\partial \phi}{\partial r}\right)^2 dr = c_2^2 \int_R^\infty x \cdot k_1'^2(x) \cdot dx$$

Using the recurrence relation $k_0 + k_2 = -2k_1'$ (30)

leads to $\zeta = C_2^2 \int_R^\infty \left(x \cdot k_0^2 + x \cdot k_2^2 + 2x \cdot k_0 k_2\right) \cdot dx \Big/ 4$

Noting that $k_0' = -k_1$, $x \cdot k_2 - x \cdot k_0 = 2k_1'$ (31)

we get $\zeta = C_2^2 \left[3\int_R^\infty x \cdot k_0^2 dx + \int_R^\infty x \cdot k_2^2 dx - 4\int_R^\infty k_0 dk_0 \right] \Big/ 4$

In the same manner as the derivation of $\xi = \int_R^\infty x \cdot k_1^2 dx$, it can be found that

$$\int_R^\infty x \,.\, k_0^2 dx = \left[\gamma^2 \left(k_0'^2(\gamma) - k_0^2(\gamma) \right) \right] \Big/ 2$$
$$\int_R^\infty x \,.\, k_2^2 dx = \left[\gamma^2 k_2'^2(\gamma) - (\gamma^2 + 4) \cdot k_2^2(\gamma) \right] \Big/ 2$$
$$\int_R^\infty k_0 dk_0 = \frac{1}{2} k_0^2 \Big|_R^\infty = -k_0^2(\gamma)/2$$

Then ζ is expressed as

$$\zeta = \frac{1}{8}c_2^2\gamma^2\left[\,3k_0'^2(\gamma) - 3k_0^2(\gamma) + k_2'^2(\gamma) - k_2^2(\gamma)\right] - \frac{1}{2}c_2^2\left[\,k_2^2(\gamma) - k_0^2(\gamma)\,\right] \qquad (32)$$

(3) Parameter η

$$\eta = \int_R^\infty \frac{1}{r}\phi^2 dr = -c_2^2\left[\gamma\cdot k_1(\gamma)\cdot k_1'(\gamma)\right] - \zeta - \xi\cdot\frac{\gamma^2}{R^2} \qquad (33)$$

where
$$k_1'(\gamma) = -\left[\,k_0(\gamma) + k_2(\gamma)\right]/2 \qquad (34)$$

Solution of the function $F(z)$

According to Eq.(15), let
$$\alpha = \sqrt{\frac{A}{G\cdot\xi}} \qquad (35)$$

Eq.(15) becomes
$$\frac{\partial^2 F}{\partial z^2} = \alpha^2 F \qquad (36)$$

The general solution of it is expressed as

$$F(z) = D_1 e^{-\alpha z} + D_2 e^{\alpha z}$$

Let the real part of α be greater than or equal to zero, the radiation condition requires that $D_2 = 0$, and $F(z)$ becomes
$$F(z) = D_1 e^{-\alpha z}$$

According to the boundary condition (23)

$$D_1 = 1 \text{ and } F(z) = e^{-\alpha z} \qquad (37)$$

Foundation compliance

Substituting (27) and (37) into (2), the radial components of the displacement field are expressed in the form

$$u_r = C_2 e^{-\alpha z} k_1\left(\frac{\gamma}{R}\cdot r\right) \qquad (38)$$

where according to (26), the coefficient C_2 is given by

$$C_2 = \frac{2bPR}{m\cdot\left[\,(2G+\lambda)\cdot\gamma\cdot k_1'(\gamma) + \lambda\cdot k_1(\gamma)\,\right]\cdot F(z)}\cdot F(z)\Big|_{z=0} \qquad (39)$$

Hence
$$u_r = \frac{2bP}{m\cdot\sigma_r(r=R)}\cdot e^{-\alpha z} k_1\left(\frac{\gamma}{R}\cdot r\right) \qquad (40)$$

Or, in the abbreviated form
$$u_r = F_r\cdot P \qquad (41)$$

where

$$F_r = \frac{2bR}{m\cdot[\ (2G+\lambda)\cdot\gamma\cdot k_1'(\gamma)+\lambda\cdot k_1(\gamma)\ ]}\cdot e^{-\alpha z}k_1\left(\frac{\gamma}{R}\cdot r\right) \tag{42}$$

$F_r(z=0)$ is exactly the global foundation compliance of the semi-circular dam canyon

$$F_r(z=0) = \frac{2bR}{m\cdot[\ (2G+\lambda)\cdot\gamma\cdot k_1'(\gamma)+\lambda\cdot k_1(\gamma)\ ]}\cdot k_1(\gamma) \tag{43}$$

Determination of Iteration Parameter γ

To obtain solutions of the functions $F(z)$ and $\phi(r)$, the value of the parameter γ defined by (18) is needed. Note that γ depends on the quantities m and n, which in turn depend on $F(z)$ (See Eq.13). As shown in (37), $F(z)$ is a function of α, and the variable A contained in α (See Eq.35) depends on the quantities ξ ,ζ and η, which are also function of γ. As γ is not known a priori, iterative techniques are required to evaluate it .

Here, an iterative approach is used to obtain γ for the static loading case, and a special semi-analytical approach is proposed to obtain γ for the dynamic loading case.

From (18), it is obvious that γ is a function of quadratic frequency ω^2, and the ratio n/m can be written as (See Eq.13)

$$\frac{n}{m} = \frac{\int_0^\infty F_{,z}^2(z)dz}{\int_0^\infty F^2(z)dz} = \frac{\rho}{G}\cdot\frac{\int_0^\infty G\cdot F_{,z}^2(z)dz}{\int_0^\infty \rho\cdot F^2(z)dz} \tag{44}$$

Making use of (37), we get

$$\begin{aligned} m &= \int_0^\infty F^2(z)dz = \int_0^\infty e^{-2\alpha z}dz = (2\alpha)^{-1} \\ n &= \int_0^\infty F_{,z}^2(z)dz = \alpha^2\int_0^\infty F^2(z)dz = \alpha^2\cdot m \end{aligned} \tag{45}$$

Hence

$$\frac{n}{m} = \alpha^2 \tag{46}$$

As shown in (44) ,n/m is equivalent to the ratio of the maximum potential energy to the maximum kinetic energy of a shear beam or a soil column. Although, (44) is not an explicit expression of ω^2, it is obviously, that n/m bears some analogy to the Rayleigh's quotient for evaluating approximate vibration frequencies of the struture. The fact that the Rayleigh's quotient provides an upper bound to the vibration frequency of the structure, sheds some light to the evaluation of the parameter γ . As any assumed shape of $F(z)$,which is the best choice of γ ,will minimize the frequency. Thus , the true value of γ is the one that minimizes the ratio n/m. Therefore,

$$\frac{\partial(n/m)}{\partial(\omega^2)} = 0 \tag{47}$$

serves the basic equation for evaluating γ .

According to (18): $$2\frac{\gamma}{R^2}\frac{\partial\gamma}{\partial(\omega^2)}=\frac{G}{(\lambda+2G)}\cdot\frac{\partial\left(n/m\right)}{\partial\gamma}\frac{\partial\gamma}{\partial(\omega^2)}-\frac{\rho}{(\lambda+2G)} \qquad (48)$$

defining the square of the volumetric wave speed as

$$c_p^2=\frac{(\lambda+2G)}{\rho} \qquad (49)$$

Eq.(48) gives $$\frac{\partial(\gamma^2)}{\partial(\omega^2)}=-\frac{R^2}{c_p^2}$$

Integrating both side of it, leads to $$\gamma^2=\gamma_0^2-\frac{R^2\omega^2}{c_p^2}$$

Introducing dimensionless frequency $$\overline{\omega}=\frac{\omega\cdot R}{c_p} \qquad (50)$$

and solving for γ yields $$\gamma=\sqrt{\gamma_0^2-\overline{\omega}^2} \qquad (51)$$

where γ_0 is the value of γ corresponding to the static loading case $\omega=0$, which can be found as follows.
Let $\omega^2=0$,and take a first approximation of γ_0 as $\gamma_0^{(1)}=1.0$
Introducing dimensionless quantities

$$\overline{\xi}=\frac{\xi}{C_2^2R^2},\quad \overline{\zeta}=\frac{\zeta}{C_2^2},\quad \overline{\eta}=\frac{\eta}{C_2^2},\quad \overline{A}=\frac{A}{C_2^2},\quad \overline{\alpha}=\alpha\cdot R \qquad (52)$$

From (29), (32) and (33) , $\xi_0^{(k)}$, $\zeta_0^{(k)}$ and $\eta_0^{(k)}$ are calculated (k=2,3,.....)

$$\xi_0^{(k)}=\frac{C_2^2R^2}{2}\left[k_1'^2\left(\gamma_0^{(k)}\right)-\left(1+\frac{1}{\gamma_0^{(k)2}}\right)\cdot k_1^2\left(\gamma_0^{(k)}\right)\right]=\overline{\xi}_0^{(k)}C_2^2R^2$$
$$\zeta_0^{(k)}=\frac{1}{8}C_2^2\gamma_0^{(k)2}\left[3k_0'^2\left(\gamma_0^{(k)}\right)-3k_0^2\left(\gamma_0^{(k)}\right)+k_2'^2\left(\gamma_0^{(k)}\right)\right.$$
$$\left.-k_2^2\left(\gamma_0^{(k)}\right)\right]-\frac{1}{2}C_2^2\left[k_2^2\left(\gamma_0^{(k)}\right)-k_0^2\left(\gamma_0^{(k)}\right)\right]=\overline{\zeta}_0^{(k)}C_2^2 \qquad (53)$$
$$\eta_0^{(k)}=C_2^2\left(-\left[\gamma_0^{(k)}\cdot k_1\left(\gamma_0^{(k)}\right)\cdot k_1'\left(\gamma_0^{(k)}\right)\right]-\overline{\zeta}_0^{(k)}-\overline{\xi}_0^{(k)}\cdot\gamma_0^{(k)2}\right)=\overline{\eta}_0^{(k)}C_2^2$$

Then , from (17), $A_0^{(k)}$ is evaluated

$$A_0^{(k)}=C_2^2\left((2G+\lambda)\cdot\left(\overline{\zeta}_0^{(k)}+\overline{\eta}_0^{(k)}\right)-\lambda k_1^2\left(\gamma_0^{(k)}\right)\right)=\overline{A}_0^{(k)}\cdot C_2^2 \qquad (54)$$

and from (35), $\alpha_0^{(k)}$ is determined

$$\alpha_0^{(k)} = \sqrt{\frac{A_0^{(k)}}{\xi_0^{(k)}G}} = \frac{1}{R}\sqrt{\frac{\bar{A}_0^{(k)}}{G\bar{\xi}_0^{(k)}}} = \bar{\alpha}\cdot\frac{1}{R} \qquad (55)$$

New value of γ_0 is obtained by using (18)

$$\gamma_0^{(k+1)} = \sqrt{\frac{GR^2}{(2G+\lambda)}\cdot\left(\alpha_0^{(k)}\right)^2} = \sqrt{\frac{G}{(2G+\lambda)}\cdot\left(\bar{\alpha}_0^{(k)}\right)^2} \qquad (56)$$

The iterative process is continued until the difference between the *i*th and (*i*+*1*)th value of γ_0 becomes less than the specified tolerance ε.

$$\left|\frac{\gamma_0^{(k+1)} - \gamma_0^{(k)}}{\gamma_0^{(k)}}\right| \le \varepsilon \qquad (57)$$

Convergence is very fast and the correct value of γ_0 is obtained in five or six iterations even if the first estimation of γ_0 is far from the exact value. Once γ_0 is evaluated, Eq.(51) is used to calculate the value of γ for different value of ω^2. The iterative procedure is not employed again.

Behaviour and Properties of Dynamic Foundation Impedance

The solution given above is derived based on the presupposition that $\phi(r)$ satisfies the modified Bessel differential equation. In fact, behaviour of the solution depends on whether γ is real, imaginary or complex to a greater degree.

In the following, solutions associated with the foundation medium being of pure elastic and visco-elastic case are discussed, in the later case frequency scattering and amplitude attenuation take place, wave speed varies with the change of wave number.

1. Foundation material is pure elastic

In this case, Lame constants λ and G are all real, the foundation compliance takes the form

$$F_r = \frac{2bR}{m\cdot[\ (2G+\lambda)\cdot\gamma\cdot k_1'(\gamma)+\lambda\cdot k_1(\gamma)\ ]}\cdot e^{-\alpha z}k_1\left(\frac{\gamma}{R}r\right)$$

Integrating over the z-axis yields

$$F_b = \int_0^\infty F_r(z)dz = \frac{bR}{(2G+\lambda)\cdot\gamma\cdot k_1'(\gamma)+\lambda\cdot k_1(\gamma)}\cdot k_1\left(\frac{\gamma}{R}r\right) \qquad (58)$$

Define foundation impedance as $\qquad K_b = (F_b)^{-1} \qquad (59)$

The following behaviour of K_b can be found.

There exist a cut-off frequency $\bar{\omega}_0 = \sqrt{\gamma_0}$. In case of $\bar{\omega} \le \bar{\omega}_0$, $\gamma = \sqrt{\gamma_0^2 - \bar{\omega}^2}$ is real. $k_1\left(\frac{\gamma}{R}\cdot r\right)$ is also a real function without oscillation and it decays with increasing of r.

In case of $\overline{\omega} > \overline{\omega}_0$, γ is a pure imaginary number. Let

$$\gamma_a = i\gamma \tag{60}$$

Then γ_a is real, Eq.(16) becomes

$$r^2\frac{\partial^2\phi}{\partial r^2} + r\frac{\partial\phi}{\partial r} + \left(\frac{\gamma_a^2}{R^2}r^2 - 1\right)\cdot\phi = 0 \tag{61}$$

It is a Bessel function of the first order and the solution gives

$$F_b = \frac{bR}{i\cdot(2G+\lambda)\cdot\gamma_a\cdot H_1^{(1)'}(\gamma_a) + \lambda\cdot H_1^{(1)}(\gamma_a)}\cdot H_1^{(1)}\left(\frac{\gamma_a}{R}r\right) \tag{62}$$

where $H_1^{(1)}\left(\frac{\gamma_a}{R}r\right)$ is a Hankel function of first kind. It is a real function , which oscillates and attenuates with γ ,the attenuation factor is $\sqrt{2}(\pi r)^{-1/2}$. And K_b is complex valued, which indicates, that wave motion occurs in the elastic half-space and also radiation damping takes place, in despite of the fact , that no material damping exists. Such a phenomena is analogous to the wave propagation in the half-space modeled as one-dimensional rod with exponentially varying area[2],[3].

2. Foundation material is visco-elastic

In this case, λ and G are all complex, thus, the impedance of K_b is also complex even at $\omega = 0$.

Now , let
$$\frac{\gamma}{R} = a + ib\,,\quad S = a^2 - b^2\,,\quad T = 2ab\,,\quad (\,a \neq 0, b \neq 0\,) \tag{63}$$

and put
$$\phi = \phi_1 + i\phi_2 \tag{64}$$

we obtain
$$\begin{gathered} r^2\frac{\partial^2\phi_1}{\partial r^2} + r\frac{\partial\phi_1}{\partial r} + \left(Sr^2 - 1\right)\cdot\phi_1 + Tr^2\phi_2 = 0 \\ r^2\frac{\partial^2\phi_2}{\partial r^2} + r\frac{\partial\phi_2}{\partial r} + \left(Tr^2 - 1\right)\cdot\phi_2 + Sr^2\phi_1 = 0 \end{gathered} \tag{65}$$

In fact, Bessel's differential equation (24) holds whether x or γ is real, imaginary or complex, and its solution has the same form expressed in terms of $k_1\left(\frac{\gamma}{R}\cdot r\right)$ or $H_1^{(1)}\left(\frac{\gamma_a}{R}\cdot r\right)$. Note that, for modified Bessel's differential equation, if the solution keeps single valued and satisfies the Sommerfeld radiation condition at infinity, the real part of it should not equal to zero and its argument should satisfy the following conditions :

$$|\arg x| < \pi \quad \text{or} \quad |\arg\gamma| < \pi \ \text{and} \quad a \neq 0$$

In comparison with the pure elastic case, in the visco-elastic case, no cut-off frequency $\bar{\omega}_0$ will take place. Because γ is always complex, except at $\omega = 0$ (See after). That is, at the real beginning wave propagation occurs, and the attenuation behaves faster than that in the pure elastic space, in addition, the attenuation behaves different for material with different wave speed. The problem is,. we have to clarify , whether there is discontinuity or singularity at $\omega = 0$ or not. In case of two dimensional wave propagation, such a phenomenon really exists. In views of this, we proceed as follows:

From (4) , for visco-elastic medium

$$\lambda = \frac{\nu E^*}{(1+\nu)\cdot(1-2\nu)}, \quad G = \frac{E^*}{2(1+\nu)}, \quad E^* = E(1+i\mu) \tag{66}$$

λ may be expressed also in the form of

$$\lambda = \frac{2\nu}{1-2\nu}G \tag{67}$$

According to the iterative process of γ (52) ~ (56), we have

$$\overline{A}_0^{(k)} = 2G\cdot\left(\frac{1-\nu}{1-2\nu}\right)\cdot\left(\overline{\zeta}_0^{(k)} + \overline{\eta}_0^{(k)} - k_1^2(\gamma)\right) \tag{68}$$

$$\overline{\alpha}_0^{(k)} = \sqrt{\frac{\overline{A}_0^{(k)}}{G\cdot\overline{\xi}_0^{(k)}}} = \sqrt{\frac{\left(\overline{\zeta}_0^{(k)} + \overline{\eta}_0^{(k)} - k_1^2(\gamma)\right)}{\overline{\xi}_0^{k}}}\cdot\left(\frac{2\nu}{1-2\nu}\right)^{1/2} \tag{69}$$

$$\left(\gamma_0^{(k+1)}\right)^2 = \frac{G}{2G+\lambda}\cdot\left(\overline{\alpha}_0^{(k)}\right)^2 = \frac{1-2\nu}{2(1-\nu)}\cdot\left(\overline{\alpha}_0^{(k)}\right)^2 \tag{70}$$

From (69) and (70), It is easy to find that $\overline{\alpha}_0$ and γ_0 are real, in spite of λ and G are complex. This means γ tends to become real as ω approaches zero, and in the meanwhile , wave propagation vanishes (See Eq.59). The imaginary part of the impedance at $\omega = 0$ results from the imaginary part of λ and G, which reflects the effect of material damping. The problem may also be studied from another point of view, we define the dimensionless impedance of the canyon foundation in the form of

$$\overline{K}_b = \frac{K_b}{G/Rb} = \frac{Rb}{F_b G} \tag{71}$$

Then

$$\overline{K}_b = \left(\frac{(1-2\nu)\cdot k_1\left(\frac{\gamma}{R}r\right)}{2(1-\nu)\cdot\gamma\cdot k_1'(\gamma) + 2\nu\cdot k_1(\gamma)}\right)^{-1} \tag{72}$$

Based on the above analyses, in case of visco-elastic material , the behaviour of $\overline{K}_b$ depends fully on the property of γ . And at $\omega = 0$, γ_0 is real, $\overline{K}_b$ is also real, we arrive at the same conclusion as before.

After rearrangement, the dimensionless impedance at the canyon surface $r=R$ is expressed in a more general form

$$\overline{K}_r(r) = \frac{2(1-\nu)}{(1-2\nu)} \cdot \frac{k_1'\left(\frac{\gamma}{R}\cdot r\right)}{k_1(\gamma)} \cdot \gamma + \frac{2\nu}{(1-2\nu)} \qquad (73)$$

It may be served for the study of the variation of complex impedance with respect to the variation of frequency for both pure elastic and visco-elastic material.

Numerical Examples and Conclusions

Based on (73), the complex frequency response functions for radial displacements of the canyon surface subjected to harmonic excitations are calculated with $E = 2.7 \times 10^4 MPa$, $\rho = 2400kg$ and $R = 400^m$, the results are depicted in Fig.5 for two different values of Poisson's ratio ν and two different values of hysteretic damping factor μ. As shown in these figures, the Poisson's ratio of the foundation material has great effect on its fundamental frequency and on dynamic amplification at this frequency. The dynamic amplification of the displacement amplitude at the fundamental frequency is very sensitive to the change of hysteretic damping. In case of hysteretic damping $\mu = 0$, the dynamic amplification does not approach infinity due to the existence of radiation damping.

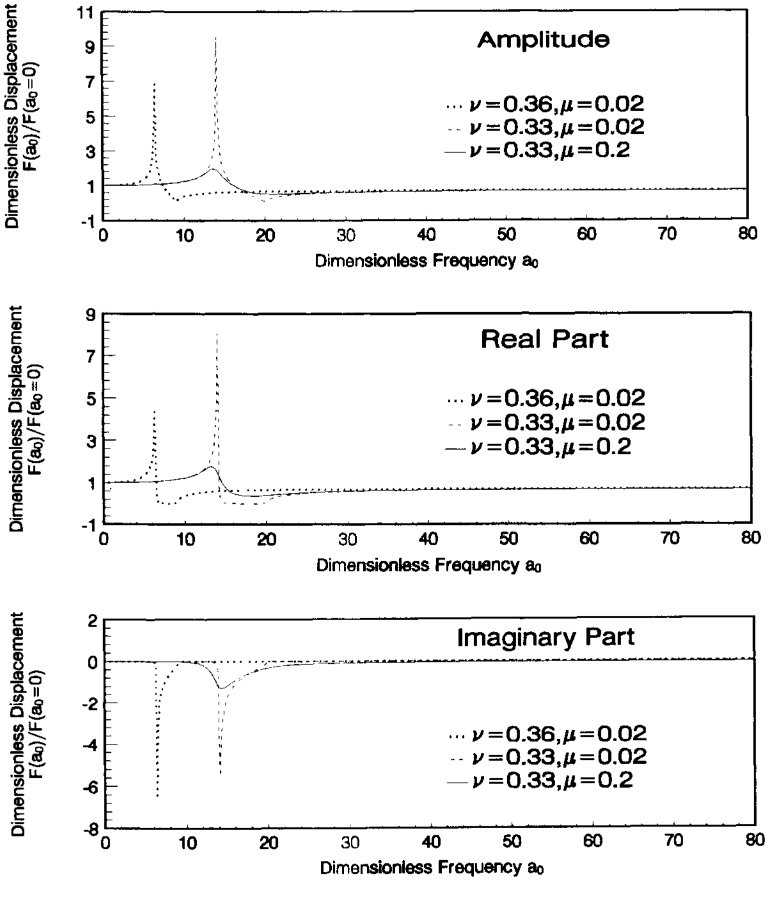

Fig.5 Complex Frequency Response Function for Radial Displacements of Canyon Foundation

The dynamic impedance of the canyon foundation for $\nu = 0.33$ and $\mu = 0.3$ is illustrated in Fig.6. It can be seen that in the low frequency range of seismic interest, the variation of the real part with frequency can be fitted by a parabola, and the imaginary part can be approximated by a straight line, that is

$$K_r(\omega) = K_0 + i\omega C_0 - \omega^2 M_0 \tag{74}$$

where K_0 is the stiffness for $\omega = 0$; C_0 is the slope of the approximated straight line, and M_0 depends on the degress of flatness of the real part of the curve. Thus, a conventional spring-dashpot-mass model is reached.

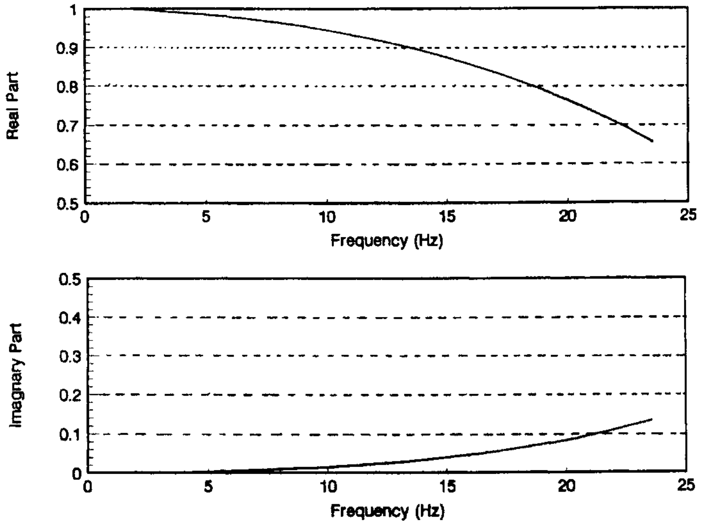

Fig.6 Dynamic Impedance of the Dam Canyon

In the earthquake analyses of a 300^m high arch dam in China, based on the Green's function of the elastic half-space similar curves of the dynamic impedance of dam canyon were obtained[4]. Because the foundation rock of high arch dams is usually very stiff, the dynamic impedance of it is less sensitive to the variation of exciting frequency. We may approximate them by the similar expression as (74)

$$[K_r(\omega)] = [K_0] + i\omega[C_0] - \omega^2[M_0] \tag{75}$$

$[K_0]$ is the matrix of static impedance, $[C_0]$ and $[M_0]$ are found by curve-fitting technique. Since $[K_0]$、$[C_0]$ and $[M_0]$ are all frequency independent, the analyses were easy to be carried out in the time domain and the non-linearity of the structure could be taken into consideration.

From the above study, some enlightenment for simplifying the computation of the dynamic impedance of dam canyon can be obtained. Since $[K_0]$ is the stiffness matrix for $\omega = 0$, it can be determined by a static approach. $[C_0]$ represents the slope of the imaginary part and $[M_0]$ reflects the degree of flatness of the real part, they can be found empirically. Eq.(75) significantly reduces the computational effort of the dynamic structure-foundation interaction analysis of arch dams.

References

[1]Sun K . and Pires J .A ., Simplified Approach for Pile and Foundation Interation Analysis , *J. Geotech. Engrg. Div.* , ASCE , 119(9) (1993) ,1462-1479.

[2]Chen J . , Dynamic Interaction and Stochastic Multi-Point Excitation Analyses of Structure-Foundation System , *Doctoral Thesis* , Dalian University of Technology, Dalian , China(1997).

[3]Wolf J .P .,*Dynamic Soil-structure Interaction* .Prentice-Hall (1985).

[4]Lin G . , Aseismic Design of Arch Dams , *Paper No .2070* , Eleventh World Conference on Earthquake Engineering , Elsevier Science (1996).

A COUPLING MODEL OF FE-BE-IE-IBE FOR NONLINEAR LAYERED SOIL-STRUCTURE INTERACTIONS

Zhang Chuhan, Wang Guanglun and Chen Xinfeng
(Dept. of Hydraulic Eng.,Tsinghua University, Beijing, China, 100084)

Abstract

A coupling model of finite elements(FE$_S$), boundary elements(BE$_S$), infinite elements(IE$_S$) and infinite boundary elements(IBE$_S$) is presented for analysis of soil-structure interaction(SSI). The radiation effects of the infinite layered soil are taken into account by FE-IE coupling, while the underlying bed rock halfspace is discretized into BE-IBE coupling whereby the non-horizontal bed rock surface can be accounted for. Displacement compatibilities are satisfied for all types of aforementioned elements. The equivalent linear approach is employed for approximation of nonlinearity of the near field soil. This model has some advantages over the current SSI program in considering the bed rock halfspace and non-vertical wave incidence from the far field. Examples of verification demonstrate the applicability and accuracy of the method when compared with the FLUSH[2] program. Finally, the effects of the relative modulus ratio E_r/E_s of rock and soil and the incident angles of non-vertical waves on the responses of the structure and the soil are examined.

Introduction

In analysis of dynamic soil-structure interactions(SSI) for important projects such as nuclear structures(power plants and other structures) built on sites of alluvial deposit, it is of importance that the layered and nonlinear properties of the soil can be considered. However, since the dynamic stress-strain behavior of soils and the factors affecting the behavior are not easily quantifiable in the current state-of-the-art, the soil is commonly modelled as an equivalent linear viscoelastic medium[1] in SSI analyses for earthquake motion, in which the nonlinearities of the soil are accounted for in an approximate manner. This simplified procedure is used in the most popular computer codes of SSI analyses for nuclear structures such as FLUSH[2] and SASSI[3] in the current design practice. Another important consideration in performing SSI analyses is that the soil model possesses the capability of properly simulating the radiation damping mechanism. The discretization of the layered halfspace using the finite element method requires the use of wave-transmitting side-boundaries to simulate the lateral radiation effects. Another alternative for simulating the radiation effect of infinite soil is simply to use a truncated halfspace model in which a sensitivity study must be performed to demonstrate the effects on the impedances of the foundation due to the wave diffractions and reflections by the truncated boundaries are negligible.

In many practical cases for simulating soil foundation system, a 2-D horizontally layered stratum overlying a rigid base may be assumed such as in FLUSH. In this case, the rigid base boundary may be placed at a layer at which the shear wave velocity equals or exceeds 1100m/s[4]. However, if a deep soft soil or semi-rock is encountered, the rigid base assumption will not be appropriate to describe the radiation effects of the lower boundary or will lead to an expensive cost for discretization of the soil to a great extent of depth. Another limitation of placing the rigid base at the lower boundary is that the inclined wave input can not be performed in the analysis. However, it is important to consider the inclined wave input mechanism which causes rocking and torsional motions of the foundation and may significantly affect the foundation motion and the structural response.

With the above-mentioned considerations, this paper presents a coupling model of finite elements(FE$_s$)-boundary elements(BE$_s$)-infinite elements(IE$_s$) and infinite boundary elements (IBE$_s$) for simulation of soil-structure system for nuclear structures built on a deep soft soil. As shown in Fig.1, FE is employed for discretization of the structure and the near field soil, in which the linear equivalent viscoelastic assumptions can be applied and the layered characteristics can also be considered. The soil underlying the FE region is a uniform elastic halfspace which can be discretized into BE$_s$. The propagating waves from the far field incident to the halfspace surface at varying angles can be applied. To achieve the coupling of the FE region with the lateral layered soil, an improved type of infinite element(IE) which is able to transport SV and P waves simultaneously is presented to be installed at the side-boundaries. For discretization of the boundary interface between the IE region and the uniform halfspace, a type of infinite boundary element(IBE) which is compatible with the IE$_s$ is employed. This IBE possesses the same attenuation behavior of the tractions as the displacements at the far-field. Thus, a complete coupling model of FE$_s$-BE$_s$-IE$_s$-IBE$_s$ is formed to simulate the linear equivalent and layered soil overlying the elastic halfspace. The use of BE-IBE coupling to discretize the underlying bed rock provides advantages over the halfspace solution in dealing with special cases as the bed rock surface is not horizontal or the bed rock medium is not entirely homogeneous. In this case, the discretization method has to be used. On the other hand, if the bed rock surface is honizontal and the medium is homogeneous, to analyze the entire system more efficiently, the substructure technique using analytical solution may be employed. The entire soil medium is divided into the near and the far fields so that the linear equivalent region of the soil and the computational efforts can be reduced as much as possible. Finally, as a test example, the earthquake response of a structure founded on a soft soil foundation is analyzed using the presented model. Verification of accuracy is first achieved by comparing the results with that analyzed by FLUSH. To demonstrate the applicability of the presented coupling system, the responses of the structure under the incidence of the waves at different inclined angles are analyzed.

Numerical Modelling

1. Infinite Boundary Elements(IBE$_S$) with Decaying Tractions

The idea of infinite boundary elements(IBE) is borrowed from that of infinite elements[5]. It was presented by Zhang and Song[6,7] and later was extended to model the far field of arch dam canyons by Zhang and Jin[8]. This paper extends the function of IBE to discretize the interface between the bottom layers on the two sides and the underlying halfspace, in which a decaying variation of displacements and tractions from the near to the far field needs to be simulated.

As shown in Fig.2, a two node element is developed and is mapped from the global into the local coordinate system using the following mapping relationship:

$$r = r_1 + \frac{1+\xi}{2}\lambda_s + (m-1)\lambda_s \qquad m = 1,2,3\cdots \tag{1}$$

where r and ξ are the global and local coordinate respectively; λ_s is the wave length for s component; m denotes the number of wave length to be integrated; r_1 is the distance between node 1 and 2 which is also defined as the distance from the origin to node 1.

By using the mapping function given in equation(1), for m=1, the node 1 with $r = r_1$ is mapped into $\xi = -1$ while the point $r = r_1 + \lambda_s$ is mapped into $\xi=1$. Thus, for m=1,2,3 $\cdots$ the global coordinate r is completely transformed into the local coordinate ξ from one wave length to another until $r \to \infty$.

Since the asymptotic behaviors of the fundamental solutions U_{ij}^* and P_{ij}^* are of following forms

$$\begin{aligned} U_{ij}^* &\propto 0\left(\frac{1}{\sqrt{r}}e^{-ikr}\right) \\ P_{ij}^* &\propto 0\left(\frac{1}{\sqrt{r}}e^{-ikr}\right) \end{aligned} \tag{2}$$

the shape functions of the displacements of the IBE with two nodes can be assumed as

$$U = \frac{1}{\sqrt{r}}\left(a_u e^{-ik_p r} + b_u e^{-ik_s r}\right) = \sum_{i=1}^{2} \overline{N}_i(\xi) U_i \tag{3}$$

where k_P, k_S are wave numbers of P and S waves respectively; a_u, b_u are coefficients; $\overline{N}_i$ are displacement shape functions.

From equation(3) and the nodal displacement of the element, the displacement shape function $\overline{N}_i$ can be derived as

$$\bar{N}_1(r) = \frac{\sqrt{r_1}}{\sqrt{r}\Delta}\left(e^{-ik_s r_2} e^{-ik_p r} - e^{-ik_p r_2} e^{-ik_s r}\right)$$
$$\bar{N}_2(r) = \frac{\sqrt{r_2}}{\sqrt{r}\Delta}\left(-e^{-ik_s r_1} e^{-ik_p r} + e^{-ik_p r_1} e^{-ik_s r}\right) \tag{4}$$

where Δ is the determinant

$$\Delta = \begin{vmatrix} e^{-ik_p r_1} & e^{-ik_s r_1} \\ e^{-ik_p r_2} & e^{-ik_s r_2} \end{vmatrix} \tag{5}$$

The same shape functions as equation(4) are used for traction approximation since both the displacements and the tractions have the same form of asymptotic behavior as shown in equation(2).

The shape functions are plotted in Fig.3 from which the decaying trigonometric characteristics of the functions are evident.

To obtain the contributions of the infinite boundary elements, the integrations $\int_{\Gamma e} P^* \bar{N} d\Gamma$ and $\int_{\Gamma e} U^* \bar{N} d\Gamma$ need to be calculated. A scheme of integration is performed from one wave length to another in the global coordinate system until the contribution of further wave lengths is negligible. The above integrations are assembled into the coefficient matrices H and G of the normal boundary element system. Thus, the halfspace surface with decaying tractions can be simulated by BE-IBE coupling system.

2. Infinite Elements(IE$_S$) with Multi-wave Numbers

The concept of infinite elements was first presented by Ungless[9] and Bettess[10], and subsequently studied by a number of researchers[11] - [13]. Zhang and Zhao[14][15] studied the infinite elements comprehensively for simulation of infinite foundations. A review of this element was given by Zhang and Wang[16]. Herein, an improved type of the IE in compatible with the IBE described above is presented for modelling of the layered soil beyond the near field. The innovative point is that it allows P and SV waves to propagate within the element.

In order to have a displacement compatibility with the IBE$_S$, the mapping relationship of the IE is depicted in Fig. 4, where r, t and ξ, η represent the global and local coordinate system respectively, whereas x, y represent the original coordinate system. Assuming that the same mapping functions for IBE in equation(1) are again used for IE in infinite r direction and that the linear interpolation is employed for finite t direction, the mapping relationship between the original coordinate x, y system and the local ξ, η system can be derived as

$$x = \left(\frac{1+\eta}{2}x_1 + \frac{1-\eta}{2}x_2\right) + \left[\frac{1+\xi}{2}\lambda_s + (m-1)\lambda_s\right]\cos\theta$$
$$y = \left(\frac{1+\eta}{2}y_1 + \frac{1-\eta}{2}y_2\right) + \left[\frac{1+\xi}{2}\lambda_s + (m-1)\lambda_s\right]\sin\theta \tag{6}$$

where x_1,y_1, and x_2,y_2 are original coordinates of points 1 and 2 respectively; θ denotes the angle between

r and x coordinates.

With this mapping functions of equation(6), the original x, y coordinates can be mapped into the local ξ, η coordinate system from one wave length to another when m=1,2,3 ⋯.

The same decaying patterns of the displacement shape functions as equation(4) are used for attenuation in r direction of infinite elements and have the form

$$\begin{aligned} N_1 &= \frac{1+\eta}{2}\overline{N}_1(r);\ N_2 = \frac{1-\eta}{2}\overline{N}_1(r) \\ N_3 &= \frac{1-\eta}{2}\overline{N}_2(r);\ N_4 = \frac{1+\eta}{2}\overline{N}_2(r) \end{aligned} \qquad (7)$$

Thus, the conditions of displacement compatibility between the $\mathrm{IBE_s}$ and $\mathrm{IE_s}$ are assured. Since the asymptotic behaviors of N_i and $\frac{\partial N_i}{\partial r}$ when $r \to \infty$ have the following forms

$$\left.\begin{aligned} N_i &\propto 0\left(\frac{1}{\sqrt{r}}e^{-ikr}\right) \\ \frac{\partial N_i}{\partial r} &\propto 0\left(\frac{1}{\sqrt{r}}e^{-ikr}\right) \end{aligned}\right. \qquad (i=1,2,3,4) \qquad (8)$$

the stiffness and mass matrices $[K]^e$ and $[M]^e$ of the infinite elements are convergent when $r \to \infty$.

The integration for obtaining $[K]^e$, $[M]^e$ for the infinite elements is performed in the global coordinate system and executed from one wave length to another as done for infinite boundary elements. Assembling the contributions of $\mathrm{IE_s}$ to the corresponding stiffness and mass matrices of the FE, the coupling system of FE and IE can be constructed.

3. FE-BE-IE-IBE Coupling for Modelling Soil-Structure Interaction

The schematic system shown in Fig.5a is a typical soil-structure interaction problem. The seismic input waves are propagating upward from the bed rock halfspace underneath the soil layers. The time histories of these waves may be obtained by deconvolution technique after the design ground motion is specified as free-surface motion on the top of competent foundation material or the outcrop at the site. The structure and the near field soil shown in Fig.5b are discretized into finite elements of which the linear equivalent model can be applied to the latter. A transition ring of finite elements between the two vertical dash lines of Fig.5f may also be set up for better connection of the near field FE region with the far field layers and with the halfspace. Beyond the transition zone the soil is discretized into $\mathrm{IE_s}$ on two sides and into $\mathrm{BE_s}$-$\mathrm{IBE_s}$ on the halfspace interface. Thus, the whole system under wave propagation shown in Fig.5a can be divided into two subdomains, i.e. the structure and the near field soil with interaction traction -Pc (Fig.5b) and remainder of the layers and the halfspace under the wave incidence and the traction Pc on the near field boundaries (Fig.5c). Again, the system of Fig.5c can be redivided into the incident wave field of horizontal layers (Fig.5d) and the corresponding scattering field depicted in Fig.5e, the latter may be redivided into two subdomains as shown in Figures 5f and 5g.

The dynamic equation for harmonic problems can be written as

$$SU=F \tag{9}$$

where U represents the nodal displacement amplitudes; F is the amplitudes of harmonic loads; and S denotes the dynamic stiffness matrix.

First, as shown in Figures 5a, 5b the degrees of freedom of the structure and near field soil are divided into interior domain d and the common boundary c, thus the equation(9) can be partitioned as follows

$$\begin{bmatrix} S_{dd} & S_{dc} \\ S_{cd} & S_{cc} \end{bmatrix} \begin{Bmatrix} U_d \\ U_c \end{Bmatrix} = \begin{Bmatrix} 0 \\ F_c \end{Bmatrix} \tag{10}$$

in which the nodal forces F_c are transformed from boundary traction P_c, i.e. $F_c = -M_P P_c$ in which M_p is the transformation matrix constructed from the interpolation shape functions.

Secondly, the transition ring and the remainder of the infinite soil layers can be divided based on degrees of freedom associated with c, i and b shown in Figures 5a and 5f and the dynamic equation of this subregion can be partitioned as

$$\begin{bmatrix} S_{cc} & S_{ci} & 0 \\ S_{ic} & S_{ii} & S_{ib} \\ 0 & S_{bi} & S_{bb} \end{bmatrix} \begin{Bmatrix} U_c^s \\ U_i^s \\ U_b^s \end{Bmatrix} = \begin{Bmatrix} -F_c + F_c^f \\ 0 \\ F_b \end{Bmatrix} \tag{11}$$

where superscripts s and f represent the scattering and the free fields; again, $F_c^f = -M_P P_c^f$ and $F_b = -M'_p P_b$, in which M'_p is the transformation matrix of the shape functions of the halfspace boundary.

Third, for the domain of halfspace with traction P_b shown in Fig.5g, the formulations of coupling $\mathrm{BE_s}$ and $\mathrm{IBE_s}$ are derived as

$$H_b U_b^s = G_b P_b \tag{12}$$

where H_b and G_b are the coefficient matrices derived from the halfspace boundaries by coupling $\mathrm{BE_s}$ and $\mathrm{IBE_s}$. Premultiplying equation(12) by $M'_p G_b^{-1}$ yields

$$S' U_b^s = -F_b \tag{13}$$

where $$S' = M'_p G_b^{-1} H_b \tag{14}$$

Substituting equation (13) into (11) and combining U_b^s and U_i^s as U_e^s yields

$$\begin{bmatrix} S_{cc} & S_{ce} \\ S_{ec} & S_{ee} \end{bmatrix} \begin{Bmatrix} U_c^s \\ U_e^s \end{Bmatrix} = \begin{Bmatrix} -F_c + F_c^f \\ 0 \end{Bmatrix} \tag{15}$$

or $$S'_{cc} U_c^s = -F_c + F_c^f \tag{16}$$

in which $$S'_{cc} = S_{cc} - S_{ce} S_{ee}^{-1} S_{ec} \tag{17}$$

and noting that

$$U_c = U_c^s + U_c^f \tag{18}$$

Combining equations(10), (16) and (18) provides the equations for a complete system in the form

$$\begin{bmatrix} S_{dd} & S_{dc} \\ S_{cd} & S_{cc} + S'_{cc} \end{bmatrix} \begin{Bmatrix} U_d \\ U_c^s \end{Bmatrix} = \begin{Bmatrix} -S_{dc} U_c^f \\ -M_p P_c^f - S_{cc} U_c^f \end{Bmatrix} \tag{19}$$

where U_c^f and P_c^f are the free field displacements and tractions of the layered halfspace shown in Fig.5d of which the solutions are available in referance [17].

By solving equation(19), the displacement fields $[U_d \;\; U_c^s]^T$ can be obtained. Then, using the relationship of equation(18) the total responses of displacement fields of the structure and the near field soil $[U_d \;\; U_c]^T$ are solved.

4. Equivalent Linear Model for Near Field Soil[1]

An approximation of a truly nonlinear soil, the equivalent linear model replaces the nonlinear constitutive relation with a secant modulus and material damping values selected to be compatible with the average shear strains induced during the earthquake motion. The parameters required for the analysis are low strain shear modulus and Poisson's ratio, material damping values, and their variations with strain level.

The equivalent average shear strain γ_{eff} is expressed as

$$\gamma_{eff} = 0.65 \max_t |\gamma_{\max}| \tag{20}$$

in which $\max_t$ denotes the maximum value for time history; $|\gamma_{\max}|$ represents the strain history in the plane of maximum shear strain; 0.65 is an empirical coefficient.

The Root Mean Square method is employed to obtain the maximum shear strain $\max_t |\gamma_{\max}|$, and the procedure is summarized as follows:

Considering the relationship

$$\gamma_{\max}^2 = (\varepsilon_x - \varepsilon_y)^2 + \gamma_{xy}^2 \tag{21}$$

yields
$$\mathrm{RMS}^2(\gamma_{\max}) = \mathrm{RMS}^2(\varepsilon_x - \varepsilon_y) + \mathrm{RMS}^2(\gamma_{xy}) \tag{22}$$

where $\varepsilon_x, \varepsilon_y, \gamma_{xy}$ are strain components in *x*, *y* coordinate system. The right hand side of (22) can be obtained using Parseval equation, i.e.

$$\mathrm{RMS}^2(f) = \frac{1}{2}\sum_{s=0}^{N/2}|F_s|^2 \tag{23}$$

in which F_s (s=0,1,$\cdots$ N/2) are the amplitude coefficients of the following Fourier's Series:

$$f(t) = \mathrm{Re}\sum_{s=0}^{N/2} F_s \exp(i\omega_s t) \tag{24}$$

From equation (23) and (24) yields

$$\mathrm{RMS}^2(\gamma_{\max}) = \frac{1}{2}\sum_{s=0}^{N/2}(|E_s|^2 + |\Gamma_s|^2) \tag{25}$$

in which E_s and Γ_s are the amplitudes of the Forier's Series of $(\varepsilon_x - \varepsilon_y)$ and γ_{xy} respectively and they can be calculated from displacement amplitude [U_s] in the frequency domain.

The maximum shear strain can be approximately expressed as

$$\max_t|\gamma_{\max}| \approx C\cdot\mathrm{RMS}(\gamma_{\max}) \tag{26}$$

where C denotes a coefficient of the shear strain ratio which may be derived using the same definition as the ratio for the ground motion, i.e.

$$C = \max_t|\ddot{y}(t)|/\mathrm{RMS}(\ddot{y}) \tag{27}$$

where $\ddot{y}(t)$ is the control motion of the design earthquake. Combining the equations (20), (26) and (27) provides the equation for the equivalent average shear strains in the form

$$\gamma_{eff} \approx 0.65\frac{\mathrm{RMS}(\gamma_{\max})}{\mathrm{RMS}(\ddot{y})}\max_t|\ddot{y}(t)| \tag{28}$$

The procedure of the linear equivalent method includes the following steps: First, using the low strain shear modulus G_0 and damping ratio ξ_0 (i.e. initial values) the linear strains $\varepsilon_x, \varepsilon_y, \gamma_{xy}$ for each frequency component ω_s are calculated, and the squares of the amplitudes $|E_s|^2$ and $|\Gamma_s|^2$ can be obtained;

Secondly, using equation (25) for RMS ($\gamma_{\max}$) the first approximation of $\gamma_{\max}$ for each element can be solved by equation(28); Third, using the current values of $\gamma_{\max}$, new values of shear modulus $G_1(\gamma_{eff})$ and the damping ratios $\xi_1(\gamma_{eff})$ for each element can be found from the variation curves of $G(\gamma)$ and $\xi(\gamma)$. These new values of $G_1(\gamma_{eff})$ and $\xi_1(\gamma_{eff})$ are subsequently used as new parameters for further iteration. Repeat the same process until the errors between $G_{i+1}(\gamma_{eff})$ and $G_i(\gamma_{eff})$, and $\xi_{i+1}(\gamma_{eff})$ and $\xi_i(\gamma_{eff})$ are within a predetermined tolerance. Thus, the values $G_{i+1}(\gamma_{eff})$ and $\xi_{i+1}(\gamma_{eff})$ are selected to be the equivalent linear modulus and damping ratios for nonlinear soil. The corresponding response of the structure or the free field motions can be obtained. Two important points are noteworthy in practical computation.

(1) After a preliminary convergence of the iteration for the near field soil, the material parameters G and ξ of the finite elements for transition zone and the infinite elements for the far field are changed accordingly to be the same as that of the neighboring finite elements of the near field. Additional iterations are needed for final convergence.

(2) The free field solution of the layers overlying the halfspace U_c^f and P_c^f in Fig.5d is also repeated accordingly using the updated values of the parameters.

Numerical Verification and Application

1. Free Field Response of a Soil Layer Overlying on Elastic Halfspace

The example shown in Figure 6 is a linear soil layer with linear variation of increasing stiffness with depth. The velocity of S wave at the bottom of the layer is as five times as that of the surface. Underlying is a bed rock halfspace with elastic property. The same problem was solved analytically by Wolf[17]. The following nondimensional parameters are defined

$$\overline{C}_s = {C_S^R}\big/{C_S^L}; \quad \overline{\rho} = {\rho^R}\big/{\rho^L}; \quad a_0 = \frac{\omega d}{C_S^L}$$

in which C_S^R and C_S^L are S wave velocities for bed rock and soil layer(average) respectively; ρ^R and ρ^L are mass density respectively; $\overline{C}_S, \overline{\rho}$ are ratios of velocity, and mass density respectively; a_0 is the nondimensional frequency; d is the depth of the soil layer. Also, the average velocity of the soil layer is defined as

$$C_S^L = \frac{d}{\int_0^d {dz}\big/{C_S(z)}}$$

In this analysis, $\overline{C}_S$=2.012; $\overline{\rho}$=1.0; $\eta^R=\eta^L$=0.1; $\nu^R = \nu^L$ =0.33 are assumed, in which η and ν are viscous damping and Poisson's ratio respectively.

As shown in Fig.6a, the propagating waves with amplitudes A_P^R and A_{SV}^R represent the incident P and SV waves from rock with incident angles of ψ_P^R and ψ_{SV}^R respectively; u_t and v_t are horizontal and vertical displacement responses on the top of the soil layer. The definition of other symbols is described in Fig.6a.

The soil medium is divided into six layers as shown in Fig.6b. 24 four-node finite elements and 12 infinite elements are used for discretization of the layers, while the bed rock halfspace is discretized into 4 BE_s and 2 IBE_s. The region of FE_s with shadow in Fig.6b is selected for the solution domain of the near field soil, while the surrounding ring of FE_s is the transition zone for better connection with the far field layers of IE_s and the BE-IBE halfspace. The comparison of magnification factors of the responses between the present results and that given by Wolf[17] is shown in Figures 7 and 8. The agreement between the two methods is excellent. Thus, the high accuracy of the presented model is verified.

2. The Response of a Soil-Structure Interaction System

Shown in Fig.9 is a typical test example of soil-structure interaction system given in reference [2]. Lysmer et. al. studied this example for verification of the computer program FLUSH. Herein, the structure is modelled as beam elements and the embeded foundation of concrete is simulated as solid finite elements. The soil profile is assumed to have 8 layers of which the first two are clay and the rest are sand. The soil layers within the dash line region denoted by elements A_i and D_i (i=1,2,⋯ 7) are selected as the near field of equivalent linear soil region. As mentioned previously, two stages of interation need to be set up. After a preliminary convergence of the iteration is obtained, the modulus and damping ratios of the transition and infinite elements B_i ,C_i and E_i ,F_i are changed to be the same as that of elements A_i and D_i respectively. Then, additional iterations are needed for final convergence. This technique ensures the compatibility of parameters at the far field with that of the equivalent linear region while keeping the computation price at a reasonable level.

The typical normalized modulus and damping ratios versus shear strains provided by Seed[18] are used in the analysis.

In order to compare the present results with that obtained by FLUSH, a high value of modulus as 10^4 times as that of the neighboring soil layer is assumed for the bed rock halfspace. This high value of stiffness is equivalent to the rigid boundary assumption restricted in FLUSH. The horizontal ground motion with a maximum acceleration of 0.2g shown in Fig.10 is assumed to be acting at the rigid boundary for FLUSH. For present analysis, one half of the above ground motion history is assumed as SV waves travelling from the bed rock. Thus, the earthguake input are approximately equivalent for the two methods. To demonstrate the effects of far field on the response, a study of boundary truncation by eliminating the IE_s or the transmitting boundaries(TB_s) of the two methods respectively is also performed.

The comparisons of responses of the structure and the soil layer between the two methods are shown in Figures 11 and 12. The agreement between the two is seen to be satisfactory for both cases of with and without IE_s or transmitting boundaries(TB_s). It is evident that the truncation of boundaries gives a significantly larger response than the results of considering the far field effects. It can be concluded that the radiation damping is an important factor affecting the responses.

3. Effects of Bed Rock Stiffness and Non-vertical Wave Input

In order to examine the effects of the bed rock stiffness on the response of the structure and the soil, a series of different ratios of bed rock modulus are assumed, i.e. (E_r/E_s)=1,2,4,6,9, where E_r and E_s are modulus of the bed rock and the neighboring soil layer respectively. Figures 13 and 14 show the acceleration distribution along the depth of the soil and the response spectra at the soil surface and the top of the structure.

The results with $(E_r/E_s)=10^4$ for rigid boundary are also included in the Figures for comparison. It appears that the response increases with the increase of rigidity of the bed rock. The most significant difference is seen at the bottom of the layers between the case of $(E_r/E_s)=1.0$ and the other ratios. This fact indicates the effects of wave amplification are significant at the interface between the bed rock and the soil layers. For the current example the ratio of $(E_r/E_s)=9.0$ can be viewed as a rigid base condition.

Further study is to examine the influences of non-vertical wave input on the response. SV waves with different incident angles: i.e. $\theta=0°$, $30°$, $60°$ are assumed as the input. $(E_r/E_s)=1.0$ is assumed in this example. The results are shown in Figures 15 and 16. Observations arising from the results are summarized as follows: (1) When SV wave incidence is vertical (i.e. $\theta=0°$) the dominant responses in the soil and the structure are in horizontal, and the vertical responses are insignificant. (2) When SV wave incidence is non-vertical, both horizontal and vertical responses are important. For example, when $\theta=30°$, the horizontal responses are smaller than the case of $\theta=0°$, but the vertical responses become more significant. In addition, the rocking motion produced from the phase difference due to inclined wave incidence may also become significant. Therefore, the resultant effects of non-vertical wave input may or may not increase in foundation motion and structural response depending on specific soil conditions and characteristics of the input waves. It is suggested that the input waves with different incident angles need to be considered for obtaining the critical response for analysis.

Conclusions

In aseismic design and analysis of nuclear structures founded on sites of layered soil deposit, it is necessary to consider the following aspects in SSI analysis: (1) infinite and layer characteristics; (2)nonlinear behaviors of the soft soil; (3)different input mechanism of earthquake waves from the bed rock. The objective of this study is to develop a coupling method of FE-BE-IE-IBE to satisfy the above requirements in an approximate manner. Based on the previous research on $\mathrm{IE_s}$ and $\mathrm{IBE_s}$, some improvements on these special elements are made for purpose of intercoupling. This includes development of a four-node IE capable of transporting multi-waves and a type of IBE with traction attenuation. The FE-IE coupling is then used for simulation of infinite layered soil, and BE-IBE coupling is used to discretize the bed rock halfspace. Thus, a complete model of structure-soil-bed rock system can be constructed.

With regard to the nonlinearity of soil, the equivalent linear approach is employed allowing the system to be solved in the frequency domain. A substructuring technique is also adopted to restrict the solution domain to the near field soil and the computational efforts can be reduced. The applicability and the accuracy of the method has been verified by comparing the present results of a test example with that by FLUSH program. Studies on the effects of relative stiffness of the bed rock halfspace and of different incident earthquake waves are also conducted. This method is being employed for analysis of a nuclear plant built on deep soft soil and the results may be reported in the near future.

References

[1] Seed, H. B., Idriss, I. M., " Influence of soil conditions on ground motions during earthquake " , J. Soil Mech. Found Div., ASCE, 1969, 94(SMI) 99-137.

[2]Lysmer, J., Udaka, T., Tsai, C.F. and Seed, H. B., " FLUSH-A computer program for Approximate 3-D analysis of soil-structure interaction problems " , Report No. EERC-75-30, University of California, Berkeley, 1975.

[3]Lysmer, J., Tabatabaic-Raissi, Tajirian, F., Vandani, S. and Ostadan, F., " SASSI-A system for analysis of soil-structures interaction " , Report No. UCB/GT/81-02, University of California, Berkeley, 1981.

[4]ASCE Standard: " Seismic analysis of safety-related nuclear structures and commentary on standard for seismic analysis of safety related nuclear structurs " , Published by ASCE, Sept., 1986.

[5] Bettess, P., " More on infinite elements " , Int. J. Numer Methods, Eng. 15, 1613-1626(1980).

[6]Zhang, C.H., Song, C.M., " Boundary element technique in infinite and semi-infinite plane domain " , Proc.Int, Conf.BEM, Pergaman Press, 1986.

[7]Zhang, C.H., Song, C.M., and Pekau, O.A. " Infinite boundary elements for dynamic problems of 3-D halfspace " , Int. J. Numer Methods Eng., 31, 447-462(1987).

[8]Zhang, C.H., Jin, F., Pekau, O.A., " Time domain procedure of FE-BE-IBE coupling for seismic interaction of arch dams and canyons " , Earth, Eng. Struc. Dyn., 1995.

[9]Ungless, R.F., " An infinite finite element: [M A S_c Thesis]" University of British, Columbia, 1973.

[10] Bettess, P., " Infinite element " , Int. J. Numer Methods Eng., 11,53 ~ 64(1977).

[11]Saini, S.S., Bettess, P., Zienkiewicz, O.C., " Coupled hydro-dynamic response of concrete gravity dams using finite and infinite elements " , Earth. Eng. Struc. Dyn., 6, 363 ~ 374(1978).

[12]Chow, Y.K., Smith, I.M., " Static and periodic infinite solid elements " , Int. J. Meth. Eng., 17, 503 ~ 526(1981).

[13]Medina, F., Penzien, J., " Infinite elements for elastodynamics " , Earth. Eng. Struc. Dyn., 10, 699-709(1982).

[14]Zhang, C.H. and Zhao, C.B., " Coupling method of finite and infinite elements for strip foundation wave problems " , Earth. Eng. Struc. Dyn., 15, 839 ~ 851(1987).

[15]Zhao, C.B., Zhang, C.H. and Zhang, G.D., " Analysis of 3-D foundation wave problems by mapped dynamic infinite elements " , Science in China, 32, No.4(1989).

[16]Zhang, C.H. And Wang, G.L., " Numerical model of the infinite domain and infinite elements " , Proceedings of the 1st national conference on combination method of analytic and numerical solutions,

Hunan University Press, 1989.

[17]Wolf, J.P., " Dynamic soil-structure interaction " , New Jersey, Prentice-Hall Englewood Cliffs, 1985.

[18]Seed, H.B., Idriss, I.M., " Soil moduli and damping factors for dynamic response analysis " , Report No. EERC-70-10, University of California, Berkeley, 1970.

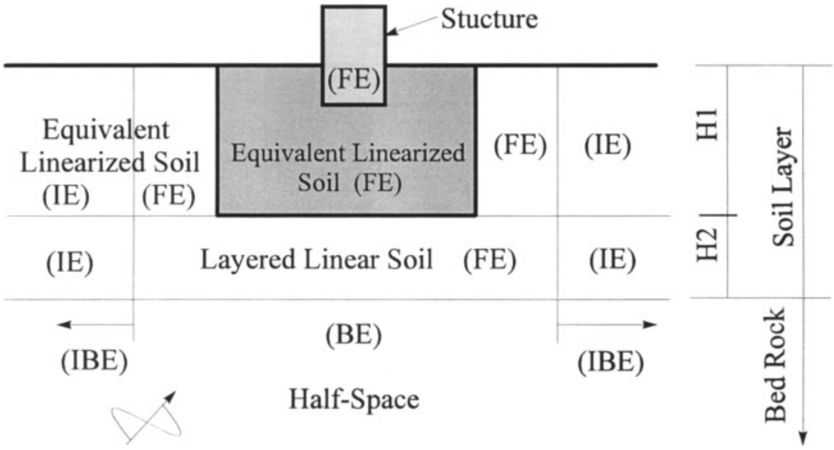

Fig. 1 Discretization of soil-structure system

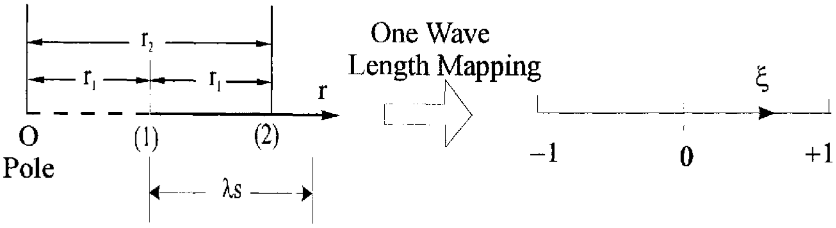

Fig. 2 Mapping relationship of the IBE

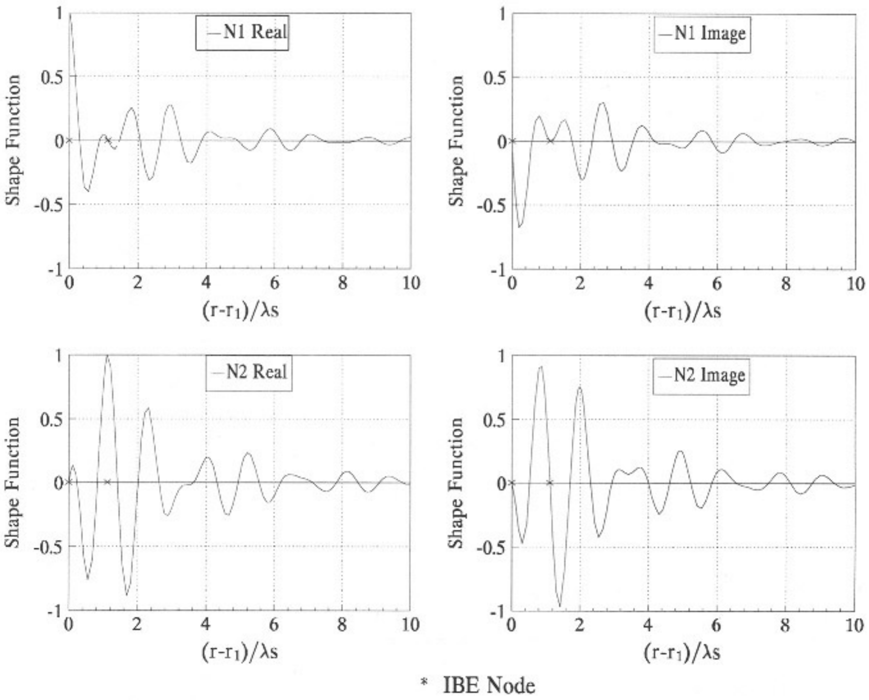

Fig. 3 Shape functions of the IBE

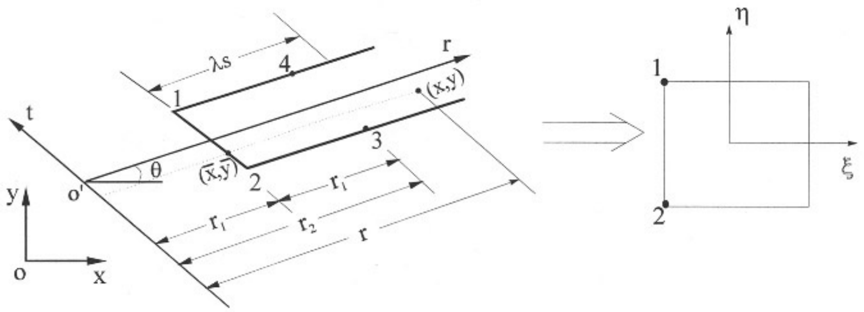

Fig. 4 Mapping relationship of the IE

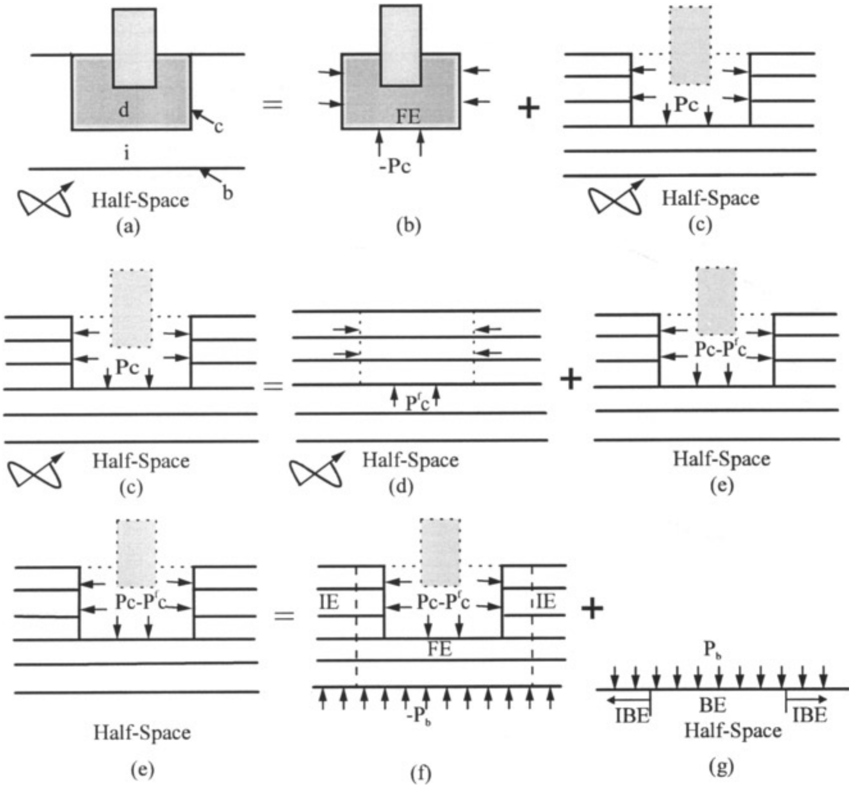

Fig. 5 Schematic representation of SSI

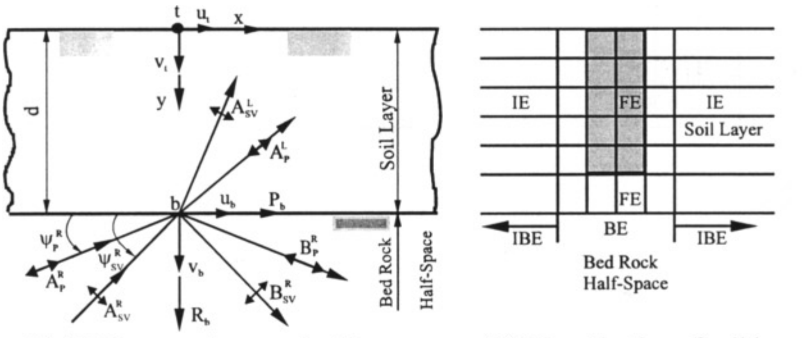

(a) Soil layer under wave incidence (b) Discretization of soil layer

Fig. 6 Soil layer and underlying halfspace

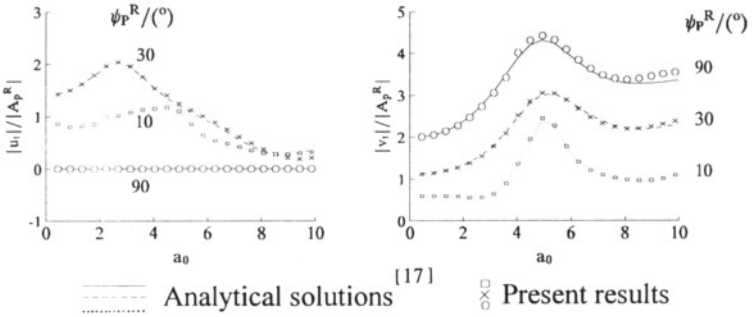

Fig. 7 Comparison of free field response of soil layer under P wave incidence

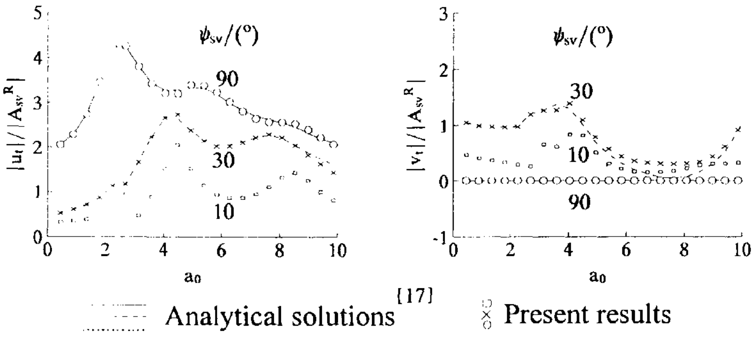

Fig. 8 Comparison of free field response of soil layer under SV wave incidence

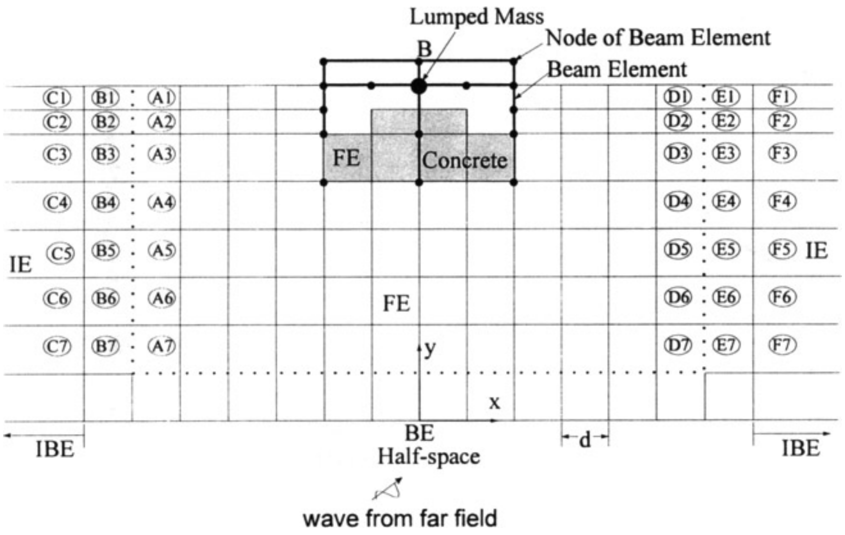

Fig. 9 Soil-structure interaction system

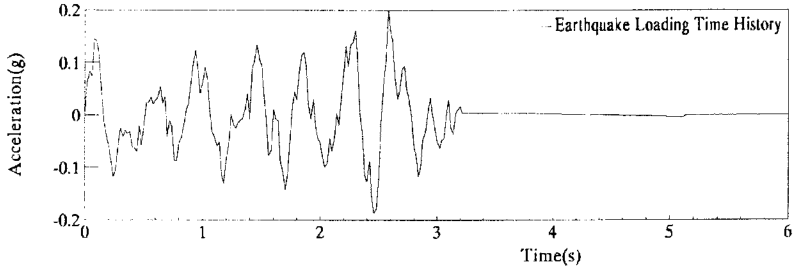

Fig. 10 Earthquake time history

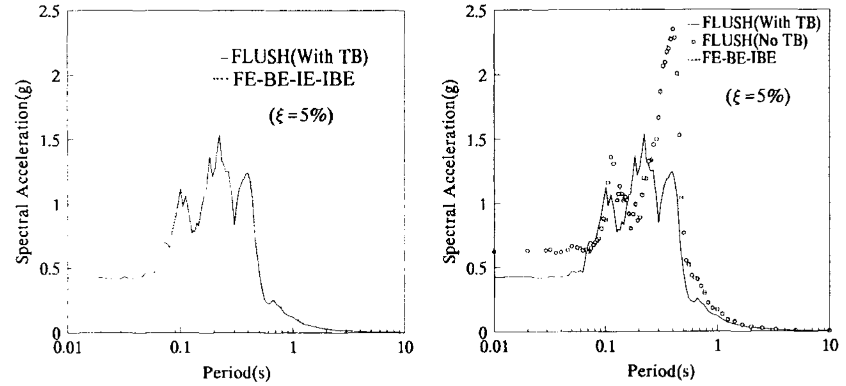

Fig. 11 Comparison of response spectra at the top of structure with results by FLUSH Program

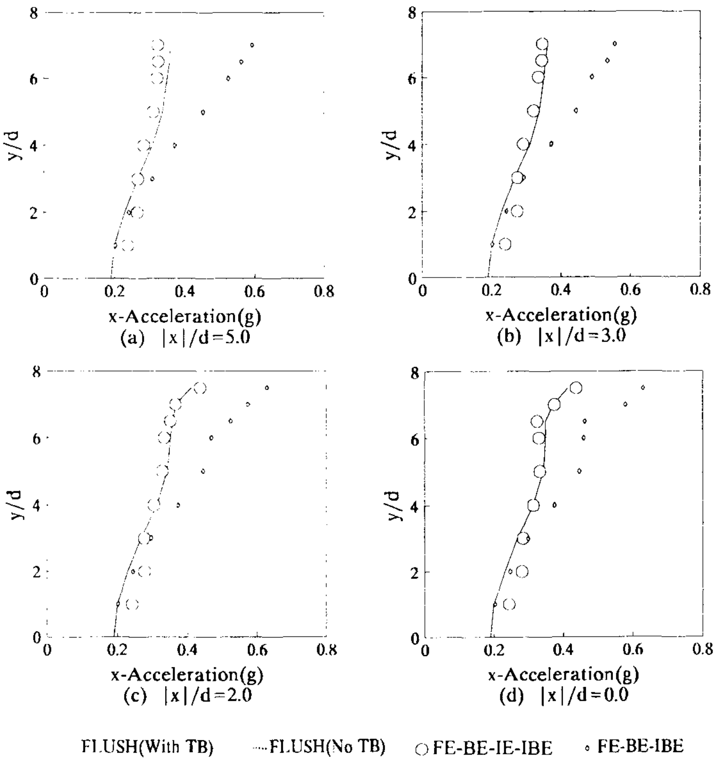

(a) |x|/d=5.0

(b) |x|/d=3.0

(c) |x|/d=2.0

(d) |x|/d=0.0

Fig. 12 Comparison of responses at different sections with results by FLUSH Program

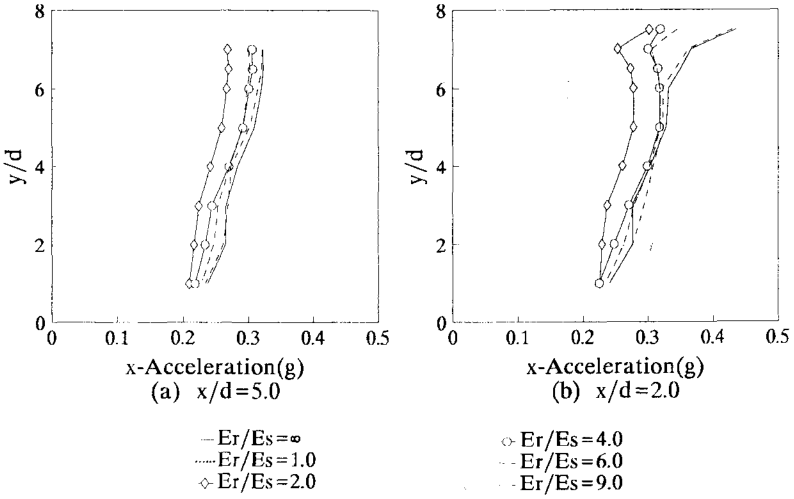

Fig. 13 Effects of modulus ratio Er/Es on the soil structure response

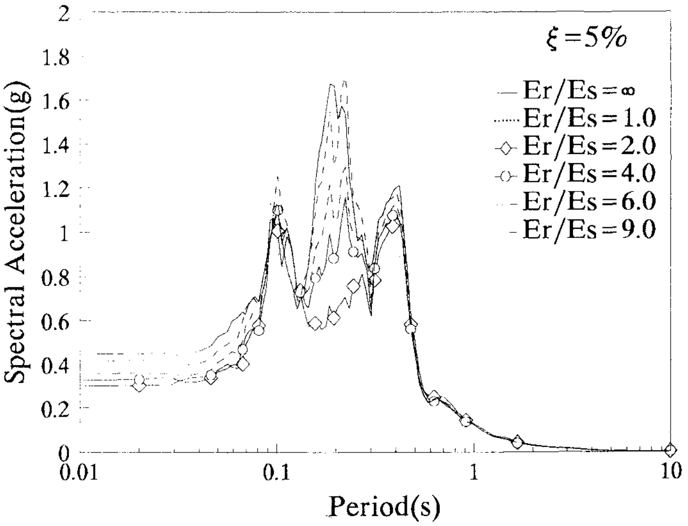

Fig. 14 Effects of modulus ratio Er/Es on response spectra at top of the structure

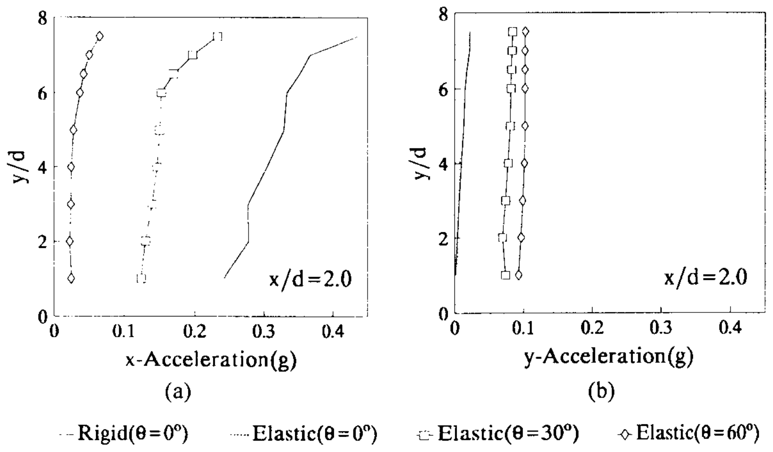

Fig. 15 Effects of incident angles of waves on soil structure response

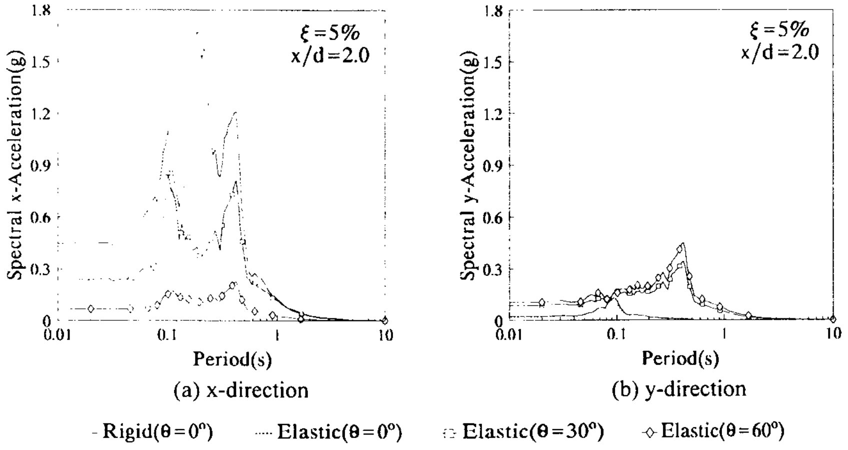

Fig. 16 Effects of incident angles of waves on response spectra at top of the structure

A HYBRID PROCEDURE OF DISTINCT - BOUNDARY ELEMENT FOR DISCRETE ROCK DYNAMIC ANALYSIS

Jin Feng, Wang Guanglun and Zhang Chuhan
(Tsinghua University, Beijing, China, 100084)

Abstract

A hybrid procedure of distinct element - time domain boundary element for discrete rock dynamics analysis is presented, in which the boundary element domain is embedded into DEM procedure as a distinct block. Combining the advantages of DEM and BEM, this coupling model not only can model the dynamic behaviour of discrete rock medium, but also can simulate the radiation damping of far field and non-uniform input of dynamic loading such as earthquake or blasting wave. A simple problem is studied to verify the presented procedure.

Introduction

Distinct element method(DEM) is a useful tool to study static and dynamic response and stability of discrete rocky tunnels or slopes. Since the emergence of the first discrete element model, i.e. distinct element method (DEM) proposed by Cundall[1] in the 1970's, significant developments have taken place both in numerical simulation and engineering applications. Fully deformable distinct element methods[2,3,4] for two- and three-dimensional problems have been reported, which are gaining increasingly more users in rock mechanics and engineering. Meanwhile, some other numerical techniques for simulating discontinuous medium have been presented. For example, a discontinuous deformation analysis method (DDA) has been proposed by Shi and Goodman[5,6], who used strain mode superposition rather than the finite difference scheme of DEM to account for element deformation. Another discrete element model proposed by Williams and Mustoe[7] uses orthogonal modes to approximate the deformation patterns of block elements, in which only a few lower modes are needed to describe complex deformation. On the other hand to simulate granular material, Ghaboussi et al.[8] presented a special rigid discrete element. Additionally, as applications of DEM in dynamic analysis of rocky slopes and structures, Iwashita and Hakuno[13] studied the dynamic failure process of a cliff using the extended DEM, while Meguro et al.[14] also studied the seismic collapse of concrete structures by modelling the structure as a system comprising numerous discrete particles.

One outstanding feature of DEM is its ability to consider the slip and separation behaviours of contact joints as well as the deformation of solid rock, in which any constitutive law for the material can be implemented. The second important feature of DEM is its inherent suitability for non-linear dynamic problems including earthquake shaking and rock blasting. This is due to its explicit time marching scheme for solving the dynamic equilibrium equations and its incremental formulation of the constitutive behaviour in response to stress increments, where linear and static problems are viewed as special cases of the solution.

In coupling the DEM with another numerical scheme, Lorig et al.[9] developed a hybrid distinct-boundary element system for jointed - intact rock interaction. Huang and Ma[10] presented a couple procedure of distinct element and boundary element which simulate a granular soil deposit as a two-dimensional, circular disk assembly. They used this hybrid model to study the behaviour of granular materials under cone penetration tests. But the above two hybrid distinct-boundary element procedures are only for static analysis.

In the context of dynamic problems, to simulate the effects of radiation damping of far field, hybrid schemes have significant advantages. Lemos[11] developed a dynamic DEM program for studying seismic response of a dam-foundation system. Non-reflecting lateral free-field boundaries are imposed to simulate radiation effects. Similarly, Dowding et al.[12,13] studied the dynamic response of an underground cavern using a model for coupling near-cavern rigid blocks with surrounding finite elements. The far-field effects were considered by introducing a viscous boundary, and the results were compared with a physical model test.

The dynamic boundary element method(BEM) has the advantages of simplicity to model far field, as the radiation conditions can be satisfied in the analytical fundamental solutions. In the early of 1980s, two approaches of two-dimensional dynamic BEM employing time domain fundamental solutions for transient elastodynamics were developed. Niwa et al.[16] solved two-dimensional dynamic problems utilising a simplified three-dimensional time domain fundamental solution. Mansur and Brebbia[17,18] presented a BEM procedure based on two-dimensional fundamental solutions. They systematically studied the integral techniques and singularity of each term of fundamental solutions and concluded that the accuracy and efficiency of the time domain BEM can be enhanced by analytical integration of the time domain integral and the singularity can be treated only at the first time step. The numerical results by these authors are very encouraging. Rice and Sadd[19] developed a time domain BEM for problems with a regular free surface without discretization of the surface by utilising time domain fundamental solutions of the half-plane. Jin et al.[20] developed a simplified procedure to simulate the effects of the material damping in time domain BEM, which employs time domain fundamental solutions of linear elastic medium. As applications of the time domain BEM, some simple two- and three-dimensional soil-structure interaction problems have been studied by Spyrakos and Beskos[21], and Karabalis and Beskos[22].

This paper presents a hybrid scheme of DEM and time domain BEM, which can study the effects of radiation damping of far field and non-uniform input mechanism on discontinuous medium with continuous far field. To the authors' knowledge, there is little work to study these influences. At first, the basic outline of distinct element method for deformable blocks and time domain boundary element method with material damping are reviewed. Then, the coupling procedure is presented and a simple benchmark problem is studied to verify its validation.

Distinct element method

As shown in Figure 1(a), the system is divided into blocks by contact joints and the interior region of the blocks are discretized into triangular elements which are assumed to be fully deformable. The geometry of the joints can be specified individually or stochastically generated according to statistical data from field measurements.

It is assumed that normal and shear springs with stiffness k_n and k_s, respectively, represent the force-displacement relationship of the joints. The latter are assumed to exhibit zero tension in the normal direction and follow Coulomb's friction law for shear, i.e.

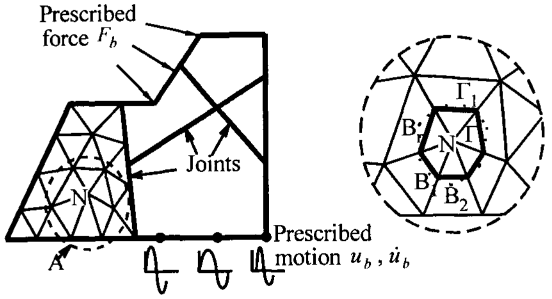

(a) System (b) Detail A

Fig. 1 Deformable DEM system

$$\begin{aligned} F_{cn} &= k_n u_n && \text{if} \quad u_n \le 0 \\ F_{cn} &= 0 && \text{if} \quad u_n > 0 \\ F_{cs} &= k_s u_s && \text{if} \quad |F_{cs}| \le f\,|F_{cn}| + cL \\ F_{cs} &= \operatorname{sign}(\dot{u}_s)\left(f\,|F_{cn}| + cL\right) && \text{if} \quad |F_{cs}| > f\,|F_{cn}| + cL \end{aligned} \tag{1}$$

where F_{cn} and F_{cs} are, respectively, the normal and tangential components of the contact force vector F_c; k_n and k_s represent the normal and shear stiffness of the joints; u_n and u_s are the corresponding components of the relative joint displacement; f, c are friction and cohesion coefficients of the joint material; and L denotes the length of the contact boundary.

The technique by Cundall to determine the deformation of the interior region of blocks employs triangular finite difference elements of the constant-strain type. As shown in Figure 1(b), the grid point N is a common node surrounded by elements B_1 B_2 ... B_n. The inertial mass of each element is assumed to be equally distributed to the three vertices of the element yielding a mass of the polygon area confined by Γ_1 be lumped at node N. In order to maintain consistency in computing inertial and elastic forces, the boundary Γ_1 should also be used as the integration route for elastic stresses. Since constant strain elements are assumed, the following equation defines the force vector F_e at node N due to elastic deformation of the blocks:

$$F_e = \int_{\Gamma_1} \sigma_{ij} n_j \, ds = \int_{\Gamma} \sigma_{ij} \, n_j \, ds = \sum_{k=1}^{n} \sigma_{ij}^k n_j^k \Delta s^k \qquad i,j = 1,2 \tag{2}$$

where σ_{ij} is the stress tensor in the element; n_j denotes the unit normal vector of the integration boundary; Γ_1 and Γ are, respectively, the polygon boundaries denoted by dashed and solid lines; and n represents the number of boundary segments surrounding node N.

In DEM solutions, damping is regarded as the dissipater of vibration energy for both static and dynamic loading. In both cases, mass proportional damping and stiffness proportional damping may be used separately or in combination. In the dynamic case, Rayleigh damping for continuous media yields the following equations:

$$\begin{aligned} F_{dm} &= -\alpha m \dot{u} \\ F_{dk} &\approx -\beta \frac{\Delta F}{\Delta t} \end{aligned} \tag{3}$$

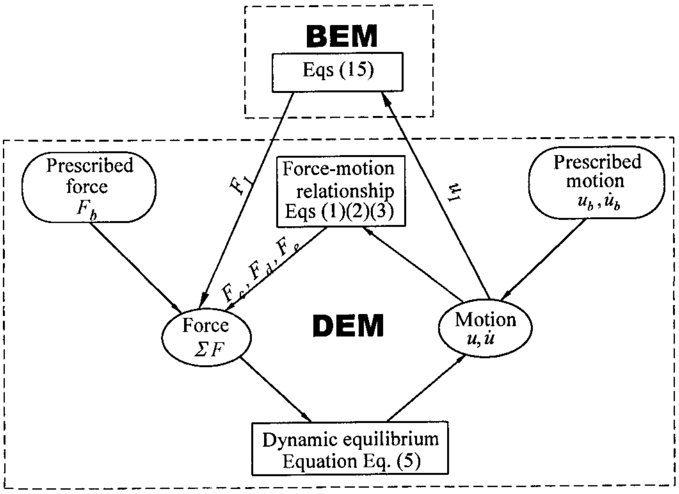

Fig. 2 Schemetic flow chart of DE-BE hybrid procrdure

where F_{dm}, F_{dk} are damping forces due to mass and stiffness, respectively; m represents the lumped mass of the node; α, β represent corresponding damping constants; and ΔF denotes the incremental total force vector including joint contact and internal deformation. Empirical values of damping ratios can be assumed to determine α and β.

The solution scheme of DEM is illustrated briefly in Figure 2. For each time step $\Delta\tau$, the incremental forces acting at each node due to deformation of the surrounding contact joints and the internal deformation of the material are determined from incremental joint displacements and internal strains by constitutive relationships shown in the upper box of Figure 2. The summation of the forces F goes to the lower box, where the dynamic equilibrium equations are applied, namely:

$$m\ddot{u} + \alpha m\dot{u} = F + mg \tag{4}$$

where, mg is gravity force.

By employing the central difference method for the acceleration on the left hand side of equation (4), one obtains

$$\dot{u}\left(t + \Delta\tau/2\right) = \left(\dot{u}\left(t + \Delta\tau/2\right)(1 - a\Delta\tau/2) + (F/m + g)\Delta\tau\right)/\left(1 + a\Delta\tau/2\right) \tag{5}$$

The new velocities and displacements, hence the new coordinates, are updated at each time step by equation (5). Note that the damping force in equation (5) is centred at time τ.

Time domain boundary element method with damping

Under zero initial conditions, the time domain boundary integral equation for a two-dimensional linear elastic body without body force is given by

$$c_{\alpha\beta}\, u_\beta(S,t) = \int_0^t \left[\int_\Gamma u^*_{\alpha\beta}(Q,t;S,\tau)\, p_\beta(Q,t) - p^*_{\alpha\beta}(Q,t;S,\tau)\, u_\beta(Q,t)\, d\Gamma \right] d\tau \tag{6}$$

where $\alpha,\beta = 1, 2$; u_β, p_β are, respectively, the displacement and traction vectors; $u^*_{\alpha\beta}$, $p^*_{\alpha\beta}$ represent the corresponding displacement and traction impulse fundamental solutions and $c_{\alpha\beta}$ is a constant related to the boundary geometry at source point S. Q represents the field point and Γ denotes the boundary of the two-dimensional body.

Integrating by parts and considering zero initial conditions lead to the following alternative form of boundary integral equation Eq. (6):

$$\begin{aligned} c_{\alpha\beta} u_\beta(S,t) &= \int_0^t \left[\int_\Gamma U^*_{\alpha\beta}(Q,t;S,\tau)\, p_\beta(Q,t) d\Gamma \right] d\tau + \int_0^t \left[\int_\Gamma V^*_{\alpha\beta}(Q,t;S,\tau)\, v_\beta(Q,t)\, d\Gamma \right] d\tau \\ &\quad - \int_0^t \left[\int_\Gamma P^*_{\alpha\beta}(Q,t;S,\tau)\, u_\beta(Q,t)\, d\Gamma \right] d\tau \end{aligned} \tag{7}$$

where v_β is the velocity vector and $U^*_{\alpha\beta}, V^*_{\alpha\beta}, P^*_{\alpha\beta}$ denote fundamental solutions whose expressions can be found in Reference [18] .

Discretizing the boundary into boundary elements and assuming that velocities and tractions remain constant over time increment Δt transform the integrals of Eq. (7) into the summations given below:

$$\begin{aligned} \int_0^t \left[\int_\Gamma P^*_{\alpha\beta}(Q,t;S,\tau)\, u_\beta(Q,t)\, d\Gamma \right] d\tau &= \sum_{m=0}^{M} [D]^{M-m} \{u\}^m \\ \int_0^t \left[\int_\Gamma V^*_{\alpha\beta}(Q,t;S,\tau)\, u_\beta(Q,t) d\Gamma \right] d\tau &= \sum_{m=0}^{M} [E]^{M-m} \{u\}^m \\ \int_0^t \left[\int_\Gamma U^*_{\alpha\beta}(Q,t;S,\tau)\, p_\beta(Q,t) d\Gamma \right] d\tau &= \sum_{m=0}^{M} [G]^{M-m} \{u\}^m \end{aligned} \tag{8}$$

where $t = M\Delta t$; D, E, G are coefficient matrices and superscripts m and $M\text{-}m$ indicate that the variable relates to the corresponding time step.

A time domain boundary element matrix equation for time step M can established as follows:

$$[H]^0 \{u\}^M = [G]^0 \{p\}^M + \{B\}^M \tag{9}$$

where

$$\begin{aligned} &[H]^0 = [C] + [H']^0 \\ &\{B\}^M = \sum_{m=1}^{M-1} \left([G]^{M-m} \{p\}^m - [H']^{M-m} \{u\}^m \right) \\ &[H']^n = [D]^n + [E]^n \qquad\qquad n = 0, 1, \ldots M \end{aligned} \tag{10}$$

in which C is a matrix related to the shape of the boundary and vector B is known from previous calculation.

When proportional decay damping model applied, boundary integral equation Eq. (2) takes the following modified form: [20]

$$\begin{aligned} c_{\alpha\beta}u_{\beta}(S,t) = & \int_0^t \left[\int_\Gamma U^*_{\alpha\beta}(Q,t;S,\tau)\, p_{\beta}(Q,t) d\Gamma \right] (1-\eta)^{(t-\tau)/2T} d\tau \\ & + \int_0^t \left[\int_\Gamma V^*_{\alpha\beta}(Q,t;S,\tau)\, v_{\beta}(Q,t)\, d\Gamma \right] (1-\eta)^{(t-\tau)/2T} d\tau \\ & - \int_0^t \left[\int_\Gamma P^*_{\alpha\beta}(Q,t;S,\tau)\, u_{\beta}(Q,t)\, d\Gamma \right] (1-\eta)^{(t-\tau)/2T} d\tau \end{aligned} \tag{11}$$

Where T is a characteristic time and the damping coefficient of proportional decay damping[20]

$$\eta = 1 - \exp(-4\pi\xi) \tag{12}$$

Where ξ is the damping ratio of BEM domain.

When material damping is sufficiently small, the assumption that $(1-\eta)^{(t-\tau)/2T}$ remains constant over a time increment Δt is justified. Accordingly, $u^m_{\beta j}, p^m_{\beta j}$ should be modified to $u^m_{\beta j}(1-\eta)^{(M-m)\Delta t/2T}$ and $p^m_{\beta j}(1-\eta)^{(M-m)\Delta t/2T}$, respectively. This results in the boundary element equation with proportional decay damping possessing the same form as Eq.(9), but with one term changed in order to incorporate proportional decay damping, namely the term B^M is modified to

$$\{B\}^M = \sum_{m=1}^{M-1} \left([G]^{M-m}\{p\}^m - [H']^{M-m}\{u\}^m \right) (1-\eta)^{(M-m)\Delta t/2T} \tag{13}$$

Hybrid procedure of DEM - BEM

The domain shown in Fig. 3 can be separated into two sub-domain: (1) a discrete elastic blocky domain modelled by DEM and (2) an infinite or semi-infinite homogeneous continuous elastic domain modelled by BEM, where the vibration energy in the DEM domain will transmit to infinite or the earthquake energy will propagate and input into the system.

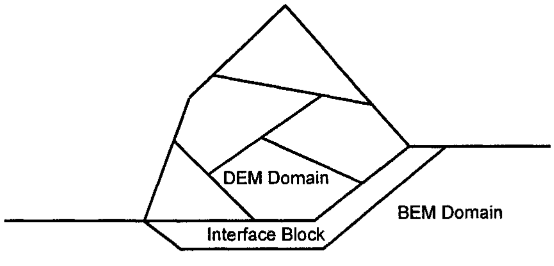

Fig. 3 DE-BE hybrid system

For assurance of compatibility, a block, named interface block, is set along the interface between the two domains. The boundary grid points along the interface of the interface block is called interface grid points. After the length of boundary element chosen, some interface grid points, whose distance between each other is approximate the chosen length of boundary element, are set to be the nodes of boundary element. So, the displacement of these interface grid points is same as that of boundary element nodes. Other interface grid points will be approximate consistent with BEM domain. But the interface force is distributed to all interface grid points linearly.

Employing the boundary conditions of free surface, condense BEM Eq. (9) to the interface, one can obtain

$$[H_I]\{u_I\}^M = [G_I]\{p_I\}^M + \{B_I\}^M \tag{14}$$

where, u_I, p_I denote the displacement and traction vector on the interface, respectively; B_I is a vector whose components are all known; H_I and G_I are coefficient matrixes. Eq. (13) can be transformed into

$$\{F_I\} = [A_I]\{u_I\}^M + \{C_I\}^M \tag{15}$$

where, F_I is the interface force vector of interface grid points and

$$[A_I]=[R][G_I]^{-1}[H_I] \qquad \{C_I\}^M=-[R][G_I]^{-1}\{B_I\}^M \tag{16}$$

where, R is the transform matrix from traction of BEM to interface force.

Let the time increment Δt of BEM to be K times of the time increment $\Delta\tau$ of DEM, namely, $\Delta t = K\Delta\tau$. In a time increment Δt, The relation between interface force F_I and the displacement u_I as shown in Eq. 14 can be assumed as identity. Then, the whole BEM domain can be treated as a DEM block in a time increment Δt. Under the assumption of constant velocity in a Δt, the displacements of interface nodes

$$\{u_I\}^M=\{u_I\}^{M-1}+\left(\{u^k\}-\{u_I\}^{M-1}\right)\frac{K}{k} \qquad k=1,2,\ldots K \tag{17}$$

where, u^k is the displacement vector of grid point connected with corresponding BEM nodes. When $k = K$, the traction vector of BEM p^M will be updated as follow

$$\{p_I\}^M=\frac{\sum_{k=1}^{K}[R]^{-1}\{F_I^{\,k}\}}{K} \tag{18}$$

Then, B^M of BEM is updated.

As shown in Fig. 2, for the interface grid points, the interface force F_I can determined by Eq. (15). So, the BEM domain can be embedded into the DEM procedure as a distinct block.

Verification of coupling technique

To verify the validation of proposed hybrid procedure, a column comprised of 4 rock blocks, as shown in Fig. 4, is studied and the dynamic displacement histories of point A, B, C and D are compared with that obtained by time domain BEM. The top block is discretized by 16 boundary elements. The bottom one is modelled by a rigid block and is fixed. The other two blocks are simulated by discrete deformable blocks. A uniform distributed step load with amplitude of p = 1MN/m^2 is applied at the top boundary. The Young's module $E = 3\times10^{10}$Pa, density ρ = 2000 kg/m^3,Poisson's ratio $\nu = 0$, damping ratio $\xi = 0.1$, $k_n = k_s = 10^{11}$N/m, f= 1.18 and c = 0.1MPa. The displacement histories of point A, B, C and D are calculated by time domain BEM and the hybrid scheme of distinct element and time domain boundary element, as shown in Fig. 5.

Because in the case of analysis the interfaces between blocks keeps contact and the stiffness of contact springs is big enough, the dynamic behaviour of block system which is simulated by the hybrid scheme is just as same as that of a continuous column modelled by TDBEM. The displacements of all nodes reach their corresponding static one after a few cycles of oscillation. The displacement histories of points calculated by the two method concord with each other very well. It means that the deformable distinct element method can simulate the wave propagation behaviour of blocks and the hybrid scheme works well.

Conclusion

A hybrid procedure of dynamic boundary element in time domain and deformable distinct element is presented. Comparison of the results of time domain boundary element and that of the presented hybrid procedure shows that the coupling procedure works well.

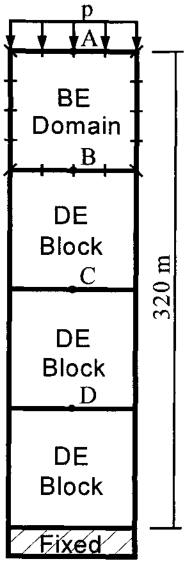

Fig. 4 Column studied

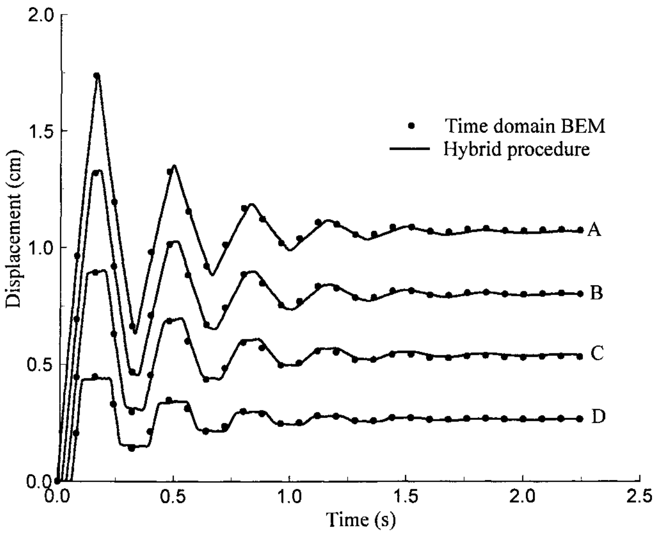

Fig. 5 Comparison of TDBEM and hybrid procedure

Reference

[1] P.A. Cundall, A computer model for simulating progressive large scale movement in blocky systems, *Proc. of symp. of int. soci. rock mech.*, Vol. 1, Nancy, France, 1971, paper no. II-8.

[2] P.A. Cundall, UDEC-A generalized distinct element program for modelling jointed rock, *Final technical report to European research office, U.S. Army*, 1980.

[3] P.A. Cundall, Formulation of three-dimensional distinct element model, Part I, A scheme to detect and represent contact in system composed of many polyhedral blocks, *Int. J. rock mech. min. sci. & geomech. abstr.*, **25**(3) , 1988, 107-116.

[4] R. Hart, P. A. Cundall, and J. Lemos, Formulation of three-dimensional distinct element model, Part II, mechanical calculation of a system composed of many polyhedral blocks, *Int. J. rock. mech. min. sci. & geomech. abstr*, **25**(3), 1988, 117-125.

[5] G.H. Shi and R.E. Goodman, Two dimensional discontinuous analysis, *Int. J. numer. anal. methods geomech.*, **9**, 1985, 541-556.

[6] G.H. Shi and R.E. Goodman, Generalization of two-dimensional discontinuous deformation analysis for forward modelling, *Int. J. numer. anal. methods geomech.*, **13**, 1989, 359-380.

[7] J. R. Williams and G. G. W. Mustoe, Modal methods for the analysis of discrete systems, *Computers and Geotechnics*, **4**, 1987, 1-19.

[8] J. Ghaboussi and R. Barbosa, Three-dimensional and discrete element method for granular materials, *Int. J. numer. anal. methods geomech.*, **14**, 1990, 451-472。

[9] L. J. Lorig, B. H. Brady and P. A. Cundall, Hybrid distinct element-boundary element analysis of jointed rock, *Int. J. rock. mech. min. sci & geomech. abstr.*, **23**(4), 1986, 303-312.

[10] A. B. Huang and M. Y. Ma, An analytical study of cone penetration tests in granular material, *Can. Geotech. J.*, **31**, 1994, 91-103.

[11] J. Lemos, A distinct element model for dynamic analysis of jointed rock with application to dam foundations and fault motion, *Ph.D. thesis, University of Minnesota*, 1987

[12] C. H. Dowding, T. B. Belytschko and H. J. Yen, A coupled finite element-rigid block method for transient analysis of rock caverns, *Int. J. numer. anal. methods geomech.*, **7**, 1983, 117-127.

[13] C. H. Dowding, T. B. Belyschko and H. J. Yen, Dynamic computational analysis of opening in jointed rock, *J. geotech. eng., ASCE*, **109**, 1983, 1551-1566.

[14] K. Iwashita and M. Hakuno, Granular assembly simulation for dynamic cliff collapse due to earthquake, *Proc. 9th world conf. earthquake eng.*, 3, Tokyo-Kyoto, 1988, 175-180.

[15] K. Meguro and M. Hakuno, Simulation of collapse of structures due to earthquake using extended distinct element method, *Proc. 10th world conf. earthquake eng.* 7, Madrid, 1992, 3793-3796.

[16] Y. Niwa, T. Fukui, S. Kato and K. Fujiki, An Application of the Integral Equation Method to two-dimensional Elastodynamics, *Theor. Appl. Mech.*, 28,Univ. Tokyo Press, 1980, 282 - 290.

[17] W. J. Mansur and C. A. Brebbia, Transient Elastodynamics Using a Time-stepping Technique, *Boundary Elements*, Springer-Verlag, 1983

[18] W. J. Mansur and C. A. Brebbia, Transient Elastodynamics, *Topics in Boundary Element Research*, 2, Springer-Verlag, 1984, 124-155.

[19] J. M. Rice and M. H. Sadd, Propagation and Scattering of SH Waves in Semi-Infinite Domain - Using a Time-Dependent Boundary Element Method, *J. Appl. Mech.* **51**, 1984, 641-645.

[20] F. Jin, O. A. Pekau and Ch. H. Zhang, A 2-D time domain boundary element method with damping, submitted *Int. J. Num. Methods Eng.*

[21] C. C. Spyrakos and D. E. Beskos, Dynamic response of rigid strip-foundations by time domain boundary Element Method, *Int. J. Num. Methods Eng.*, **23**, 1986, 1547-1565.

[22] D. L. Karabalis and D. E. Beskos, Dynamic response of 3-D flexible foundations by time domain BEM and FEM, *Soil Dyn. Earthquake Eng.*, **4**, 1985, 91-101.

Author Index